1993

The aerodynamics of a baseline supersonic throughflow fan rotor

Daniel Lawrence Tweedt
Iowa State University

INFORMATION TO USERS

This manuscript has been reproduced from the microfilm master. UMI films the text directly from the original or copy submitted. Thus, some thesis and dissertation copies are in typewriter face, while others may be from any type of computer printer.

The quality of this reproduction is dependent upon the quality of the copy submitted. Broken or indistinct print, colored or poor quality illustrations and photographs, print bleedthrough, substandard margins, and improper alignment can adversely affect reproduction.

In the unlikely event that the author did not send UMI a complete manuscript and there are missing pages, these will be noted. Also, if unauthorized copyright material had to be removed, a note will indicate the deletion.

Oversize materials (e.g., maps, drawings, charts) are reproduced by sectioning the original, beginning at the upper left-hand corner and continuing from left to right in equal sections with small overlaps. Each original is also photographed in one exposure and is included in reduced form at the back of the book.

Photographs included in the original manuscript have been reproduced xerographically in this copy. Higher quality 6" x 9" black and white photographic prints are available for any photographs or illustrations appearing in this copy for an additional charge. Contact UMI directly to order.

UMI®

Bell & Howell Information and Learning
300 North Zeeb Road, Ann Arbor, MI 48106-1346 USA
800-521-0600

The aerodynamics of a baseline supersonic throughflow fan rotor

by

Daniel Lawrence Tweedt

A Dissertation Submitted to the

Graduate Faculty in Partial Fulfillment of the

Requirements for the Degree of

DOCTOR OF PHILOSOPHY

Department: Mechanical Engineering
Major: Mechanical Engineering

Approved:

Signature was redacted for privacy.

In Charge of Major Work

Signature was redacted for privacy.

For the Major Department

Signature was redacted for privacy.

For the Graduate College

Iowa State University
Ames, Iowa

1993

TABLE OF CONTENTS

SYMBOLS AND NOTATION iv

ABSTRACT vii

CHAPTER 1. INTRODUCTION 1
The Supersonic Throughflow Fan Engine 2
Historical Considerations of Supersonic Compressor Development 6
NASA Lewis Supersonic Throughflow Fan Program 9
Purpose and Scope of Dissertation 11

CHAPTER 2. BASELINE FAN DESIGN 13
Design Philosophy and Approach 13
Description of Fan Design 15

CHAPTER 3. EXPERIMENTAL FACILITY 21
Description of Facility 21
Facility Instrumentation and Data Acquisition 26
Data Reduction 31

CHAPTER 4. COMPUTATIONAL FLUID DYNAMICS 35
Description of Codes 36
Application of Codes 39

CHAPTER 5. ROTOR OPERATING CHARACTERISTICS AND PERFORMANCE 56
One-Dimensional Steady-Flow Analysis 58
Subsonic Throughflow Operation 77
Axial-Subsonic Rotor-Inflow Characteristics 82
Rotor Inflow Starting and Unstarting 112

Impulse-Type Operation 149
Supersonic Throughflow Operation 169
Shock-in-Rotor Operation 215

CHAPTER 6. CONCLUDING REMARKS 219

REFERENCES 225

ACKNOWLEDGEMENTS 233

APPENDIX A. SUPERSONIC NOZZLE PERFORMANCE AND EXIT FLOW QUALITY 235

APPENDIX B. PROBLEMS IN COMPARING COMPUTATIONAL AND EXPERIMENTAL RESULTS 250

APPENDIX C. AVERAGING METHODS FOR COMPUTED FLOW FIELDS 263

APPENDIX D. APPROXIMATE TWO-DIMENSIONAL CALCULATION METHODS 275

APPENDIX E. A TOTAL-PRESSURE LOSS MODEL FOR SUPERSONIC THROUGHFLOW FAN BLADE ROWS 290

SYMBOLS AND NOTATION

A	cross-sectional area of stream-tube or duct
a	sonic speed; half-thickness of blade leading edge
c	aerodynamic chord
h	specific enthalpy; streamtube height
M	Mach number
m	meridional location
$\dot{m}$	mass flow rate
N	rotational speed in revolutions per unit-time
Pr	Prandtl number
p	static pressure
R	gas constant; annulus height fraction $= \dfrac{r - r_{hub}}{r_{tip} - r_{hub}}$
Re	Reynolds number
r	radial location; radius
s	circumferential blade spacing; specific entropy
T	absolute static temperature
U	circumferential blade speed
V	velocity magnitude
x	axial location
α	absolute circumferential flow angle with respect to meridional flow direction; flow "yaw" angle measured by a cone probe or rake element
β	relative circumferential flow angle with respect to meridional flow direction
γ	ratio of specific heats
δ	deviation angle; flow deflection angle through an oblique shock wave
ε	ellipse eccentricity parameter

η_F fan adiabatic efficiency

η_R rotor adiabatic efficiency

θ circumferential location; oblique shock wave angle; fan inlet total-temperature correction parameter = $T_{t0}/518.7$ (temperature in °R)

ι incidence angle

κ blade metal angle

λ area blockage factor = $1 - (A_{eff}/A)$

μ Mach angle = $\sin^{-1}(1/M)$

ν Prandtl-Meyer angle = $\sqrt{\frac{\gamma+1}{\gamma-1}}\tan^{-1}\sqrt{\frac{\gamma-1}{\gamma+1}(M^2-1)} - \tan^{-1}\sqrt{M^2-1}$

ρ static density

σ blade element solidity = c/s

ϕ dimensionless mass-flux parameter = $M\left(1+\frac{\gamma-1}{2}M^2\right)^{-(\gamma+1)/(2\gamma-2)}$

Ω rotational speed in radians per unit-time

ψ meridional flow angle with respect to axial direction; flow "pitch" angle measured by a cone probe or rake element

$\bar{\omega}$ total-pressure loss coefficient = $\frac{\bar{P}'_{t2\,i} - \bar{P}'_{t2}}{\bar{P}'_{t1} - \bar{P}_1}$

Subscripts

ax component in axial or meridional direction

cb nozzle centerbody

d design condition

e free-stream or boundary-layer-edge condition

eff condition which effectively exists

eq equivalent condition

hub annulus hub condition or quantity

i	condition reached through an isentropic process
le	leading edge condition or quantity
m	component in meridional direction
N	nozzle condition or quantity
p	Pitot condition, which for supersonic flow is the total condition downstream of a steady normal shock introduced actually or hypothetically into the flow field
ps	blade pressure-surface quantity
R	rotor quantity
r	component in radial direction
ss	blade suction-surface quantity
t	total condition
tip	annulus tip condition or quantity
x	component in axial direction
θ	component in circumferential direction
$*$	critical (sonic flow) condition
0	plenum condition; station within nozzle; aircraft flight condition
1	upstream condition; station at rotor inlet (nozzle exit)
2	downstream condition; station at rotor exit

Superscripts and Diacritics

q'	condition or quantity relative to blade
$\bar{q}$	average quantity
${}^{e}\bar{q}$	*energy-average* quantity from a circumferential integration (see Appendix C)
${}^{m}\bar{q}$	*momentum-average* quantity from a circumferential integration (see Appendix C)
${}^{s}\bar{q}$	*entropy-average* quantity from a circumferential integration (see Appendix C)
${}^{\bar{s}}\bar{q}$	*entropy-average* quantity from a spanwise integration in an axisymmetric flow field (see Appendix C for general notation)
${}^{\bar{s}s}\bar{q}$	overall *entropy-average* quantity from a circumferential and spanwise integration in a three-dimensional flow field (see Appendix C for general notation)

ABSTRACT

A baseline supersonic throughflow fan has been designed and tested at the NASA Lewis Research Center in order to demonstrate proof-of-concept and provide an experimental data base for this unique type of turbomachine. The aerodynamics of the rotor, which was tested in both an isolated and a stage configuration, is discussed in somewhat generic terms for conditions covering most of the practical operating range. Much detailed and quantitative information is also included. In addition to the experimental results, viscous computational fluid dynamics (CFD) results and simple analytical solutions are discussed, having been used extensively to understand and assess the aerodynamic performance of the rotor and to understand and interpret the experimental results. In general, most of the operational and performance characteristics for steady-state rotor operation can be explained and quantified using the various analytical methods.

The experimental rotor performed much as designed, and off-design operation involved stable operational characteristics with no unusual instabilities, even during transitional phases of operation where transient discontinuities traversed the rotor flow field. Rotor inflow starting, involving the propagation of a normal shock wave into the rotor from upstream, was accompanied by only minor discontinuities in rotor performance and blade loading.

Two- and three-dimensional viscous CFD simulations for several rotor operating points exhibited good agreement with the experimental data. The lack of harsh dynamic effects on rotor blade loading and performance during rotor inflow starting was also predicted using the analytical methods.

The application of a simple total-pressure loss model in conjunction with the experimental and CFD results allowed a fairly accurate determination of the first-order loss sources and their magnitudes for a wide range of operating conditions. For design-point operation it is shown that viscous losses account for about 51 percent of the total mixed-out loss, bow shock wave losses account for about 44 percent, and oblique shock losses

contribute the remaining 5 percent. Mixing losses, which are included as part of the viscous and the bow shock losses in the simple model, account for about 28 percent of the total mixed-out loss.

CHAPTER 1.
INTRODUCTION

Revived interest in developing an advanced supersonic transport (SST) for commercial air travel in the early twenty-first century [1-3] has led to intensified efforts to identify acceptable propulsion systems for such aircraft. These efforts reflect a general consensus that engine requirements offer some of the most difficult challenges to the successful development of a new SST. In fact, over the years the problems associated with supersonic propulsion and flight have actually increased despite many advances in the state-of-the-art for aircraft propulsion systems. For example, environmental restrictions related to aircraft engine noise and emissions have become progressively more stringent. Further, the airline business has become highly competitive and thus the demands placed on engine designers have increased. Indeed, these and other factors present formidable obstacles to the near-term design of an environmentally acceptable and economically viable commercial SST. The technical and economic risks involved require that improved propulsion system technologies continue to be developed [4].

Engine performance, weight, and mission studies involving different propulsion system concepts for long-range supersonic cruise aircraft have been carried out during the past few decades [5-10], many conducted under NASA sponsorship. Conventional and variable cycle engine concepts have been evaluated. Included are the variable stream control engine (VSCE), the double bypass engine (DBE), the turbine bypass engine (TBE), the mixed-flow turbofan (MFTF) engine, the supersonic throughflow fan (SSTF) engine, and the tandem fan engine, to name just a few. Increasingly stringent takeoff noise requirements have rendered some of these engines unacceptable, and the projected performance levels of more recent prospects such as the TBE and MFTF depend on successful development of effective noise-suppressors (mixer-ejector nozzles), a key technical problem [11] which cannot be underestimated. If the required degree of jet-noise suppression

is not realized [1], then the current estimates for engine size are too small and larger engines would be necessary with a corresponding penalty in performance.

The Supersonic Throughflow Fan Engine

An advanced concept, the variable cycle engine equipped with a supersonic throughflow fan (SSTF) has undergone scrutiny since the early 1970's. The initial study, by Advanced Technology Laboratories [12] under NASA contract through the Lewis Research Center, was completed in the early 1970's under the technical direction of Dr. Antonio Ferri who first proposed the concept of a variable cycle SSTF engine. Since then, related studies of the SSTF engine cycle have also been performed by Franciscus [13-16] at the Lewis Research Center, as well as by others under NASA grants and contracts [17,18].

In general, the results from these studies have shown that the SSTF engine has the potential to substantially improve the mission capabilities of long-range supersonic cruise aircraft for both civilian and military applications. A comparison study done in the mid 1970's by Franciscus [13] using the VSCE as a reference engine, for an all-supersonic cruise mission at cruise Mach 2.32, indicated 20 percent more range, 12 percent lower specific fuel consumption, and 30 percent less installed weight for the SSTF engine. Although the technology available for use in aircraft engines continues to improve, the more recent studies by Franciscus [14-16], including a comparison of the SSTF engine to the TBE and VSCE, still indicate a significant improvement potential. As already mentioned, takeoff noise is an important factor in the selection and sizing of an engine, and in this regard the SSTF engine is an attractive alternative. Some results from the TBE and

---

[1] European companies do not share the optimistic view prevalent in the United States regarding the probability of achieving, in the near future, required levels of noise suppression while maintaining an efficient engine installation [9,10]. As a result, they virtually exclude the single-compressor family of variable cycle engines (for example, the TBE, VSCE, MFTF, etc.) from serious consideration for applications below cruise Mach 2.5, and instead appear to be opting for the tandem fan as a probable solution to the noise problem.

SSTF engine studies of Franciscus (unpublished, but see References 14 to 16 for similar studies) are compared in Figure 1.1, which shows supersonic transport range as a function of engine airflow — a measure of engine size. Note in the figure that the noise levels (EPNdB) along the curve for the TBE indicate noise suppression needed at the corresponding engine airflows to meet Federal Aviation Regulation (FAR) part 36 stage-III noise requirements. For example, about 18 EPNdB of takeoff jet-noise suppression would allow the near-optimum engine size for the TBE. So far, however, experience indicates [19] that this will be very difficult to achieve without excessive thrust loss and/or weight and complexity, and indeed may be beyond the grasp of near-term technology. If the full noise suppression cannot be realized in a practical way, the engine will need to be oversized accordingly (see the 15 and 10 EPNdB noise suppression levels indicated in Figure 1.1) in order to keep takeoff noise at the required level. Observe, on the other hand, that the SSTF engine is projected to need only about 5 to 10 EPNdB of noise suppression, which is well within current technology. Note also in Figure 1.1 the effect of fan adiabatic efficiency, a relatively uncertain parameter at the present, on the SSTF engine cycle. A fan efficiency of about 76 percent is expected to result in nearly the same range as the "silenced" TBE. These somewhat favorable predictions for the SSTF engine depend, of course, on the assumed component weight and performances for the primary inlet, the bypass nozzle, and the so-called "core inlet", as well as for the fan itself, but recent unpublished research suggests that the estimates used are reasonable. To be sure, other yet uncertain factors can be expected to alter the final outcome; nevertheless, the indicated potential benefits are large enough to warrant serious investigation of the concept in order to resolve some of the more critical issues, and thereby allow more accurate comparisons with other engine concepts.

The payoffs predicted for the SSTF engine derive largely from engine inlet considerations. Typically, after ingesting supersonic flow, the inlet to an engine in supersonic flight is required to diffuse the airflow to the subsonic conditions needed upstream of the fan or compressor. The use of a supersonic throughflow fan eliminates this supersonic-to-subsonic diffusion in the primary inlet, and thereby circumvents many of the problems associated with this diffusion, directly (design-point inlet operation) and indirectly (off-design inlet operation). By incorporating a single-stage fan capable of ingesting axial-supersonic flow directly into its blade rows, a shorter, lighter, and more efficient

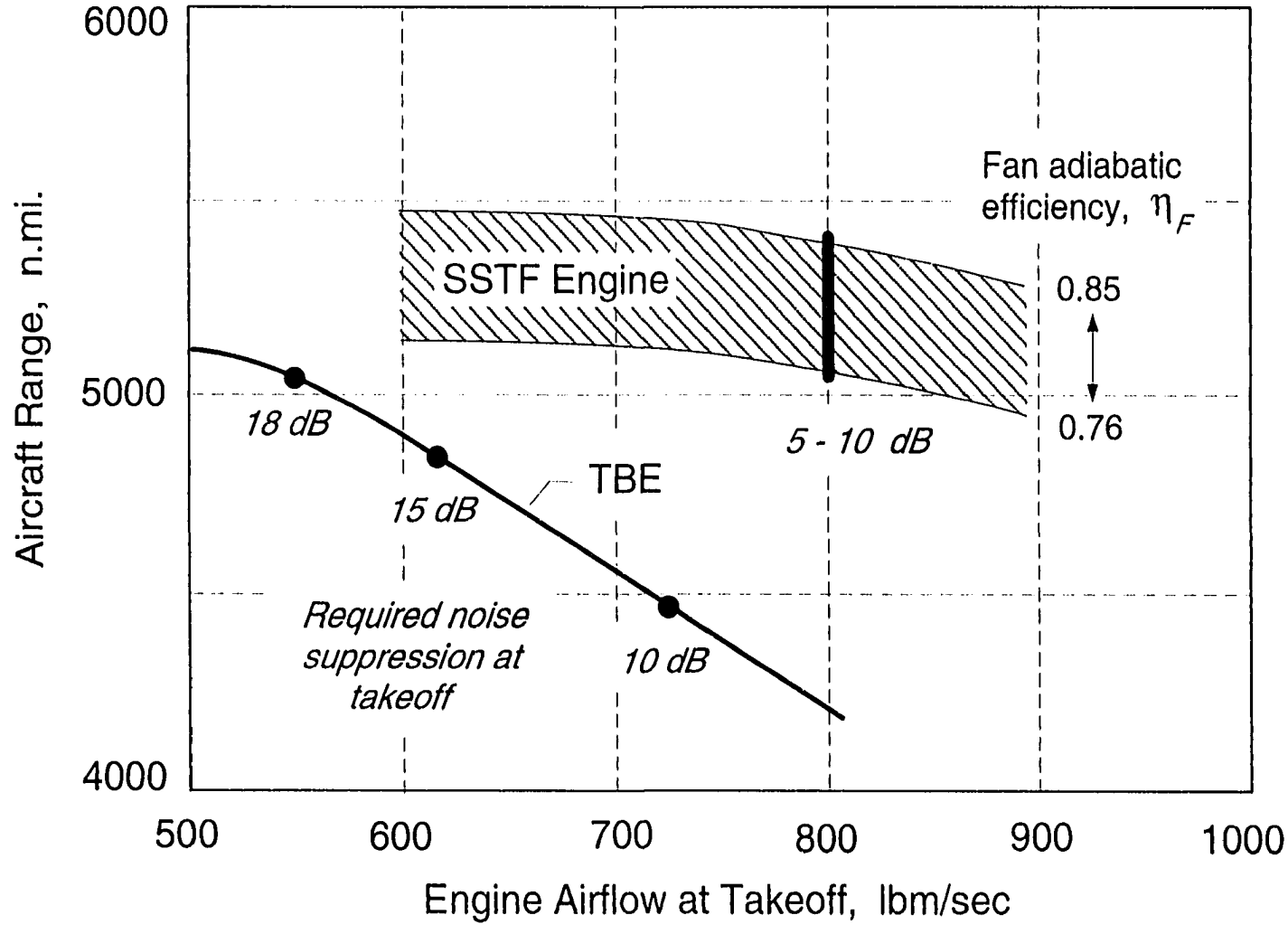

Figure 1.1 Estimated mission benefit of the SSTF engine over the TBE, for aircraft with 2.4 cruise Mach number, 700,000 lb takeoff gross weight, and 11,000 ft takeoff distance

engine installation can be achieved, at least in principle. The potential impact of this is large since for conventional installations the inlet, fan nozzle, and nacelle make up to 50 percent of the propulsion system weight. In addition, due to an inherently high rotor-work-input capability, the SSTF requires only a single stage to achieve the desired fan total-pressure ratio, in contrast to multiple stages for conventional turbofans. Finally, it is worth noting that the fan performance characteristics of the SSTF are naturally suited to the desired engine cycle variation [2]. At a given corrected rotational speed, a wide range in corrected mass flow accompanied by only minor changes in fan total-pressure ratio (and adiabatic efficiency) results in a more natural bypass flow variation and fan/core-compressor match over the entire flight envelope [12-18].

Before proceeding to some historical considerations of supersonic compressor development, a definition and some comments regarding the supersonic throughflow fan and its relationship to supersonic fans and compressors in general are in order. First, by definition the term *supersonic throughflow fan* will be used to denote any fan designed to operate with axial-supersonic [3] velocities throughout all of its blade rows. It is a special type of supersonic fan, even a subclass of the supersonic compressor, and is usually conceived of as having only a single, axial-flow stage, with or without inlet guide vanes [4]. It will be distinguished from other types of supersonic fans and compressors by its designation, and care must be taken to do this when considering it from a historical perspective or when surveying the literature. The terms *supersonic fan* and *supersonic compressor* are occasionally encountered in the literature, and they generally apply to any type of fan or compressor which operates with supersonic blade-relative velocities along the entire blade span, in one or more of the blade rows, regardless of the flow regime based on axial Mach

---

[2] The basic idea behind the variable cycle engine is to match the engine cycle to the different flight regimes; that is, to operate the engine as a turbofan at subsonic flight and as a turbojet at supersonic flight.

[3] The terms *axial-subsonic* and *axial-supersonic* are used frequently to denote conditions where the meridional flow component is subsonic or supersonic, respectively, even though the flow may not necessarily be strictly axial as, for example, in the case of a mixed-flow fan or compressor.

[4] Only the rotor/stator type of stage is considered here, although other possibilities certainly exist such as, for example, the stator/rotor stage, and the counter-rotating fan stage.

number component. Note that the SSTF does not function as a compressor in the literal sense, at least near its design point, since it normally produces little or no static pressure rise (compression), and may actually involve a decrease in static pressure through the stage. Thus, this so-called *impulse-type* of supersonic fan generates thrust by accelerating the airflow through the stage, increasing its axial-momentum and kinetic energy, with little or no increase in static enthalpy. Finally, in that the distinction between fans and compressors is somewhat arbitrary, and that the term "compressor" might generally refer to a device for increasing the total pressure of the working fluid, the SSTF will be considered a type of supersonic compressor.

Historical Considerations of Supersonic Compressor Development

Experimental research on supersonic compressors began in the late-middle 1930's and was actively pursued by the NACA during the 1940's and 1950's at the Lewis Flight Propulsion Laboratory and the Langley Aeronautical Laboratory, as they were then named. Historical information summarizing much of the NACA research at the two facilities can be found in References 20 and 21, and a review of supersonic compressor development in general, up to the year 1961, has been presented by Klapproth [22]. One of the primary motivations behind the development of the supersonic compressor was the potential for high work-input per stage [5], thus allowing the possibility of reducing the number of axial-flow stages in multi-stage compressors. Furthermore, high mass flows per fan frontal area, approaching the maximum possible, would be achievable with this type of fan. It was held, and not without justification, that if the total-pressure losses were maintained at reasonable levels then fairly high adiabatic efficiencies were still possible, even with a normal shock and separated blade-boundary-layers [22], due to the large total-pressure increases. The modern transonic fan, the development of which is recognized as a major success in the field of aircraft gas turbine engines, demonstrates the practicality of this concept.

---

[5] Total-pressure ratios of up to 9.6 have been obtained across a single, axial-flow rotor blade row [22].

Most supersonic compressors operated with axial-subsonic flow into the rotating blade row, except for two documented cases which will be discussed below. All of them were operated as a single blade row (isolated rotor) or as a single stage. The rotor exit flow was either axial-subsonic or axial-supersonic depending on the design configuration, the operating point, and whether or not stators were installed downstream of the rotor. It should be pointed out that these two types of rotor exit flows involve two fundamentally different operating modes for the rotor, and at least two for the stage as well. Supersonic rotor operation with (relative) subsonic flow at the rotor exit involves the effects of a normal-shock compression to achieve most of the work interaction. This mode of operation, conventionally referred to as shock-in-rotor [20-22], is typically associated with a relatively high stage-reaction due to the resulting large static pressure (or enthalpy) rise through the rotor shock. Conversely, operation of a supersonic rotor at low back-pressure, often with axial-supersonic exit flow, involves little or no static-pressure rise through the rotor, and may even involve a substantial decrease in static pressure. A rotor designed to operate in this so-called impulse-type [21-22] manner accomplishes the work input mostly through flow turning rather than compression, with an accompanying increase in the kinetic energy of the fluid.

Historically, impulse-type compressors relied on the stator to diffuse the supersonic rotor exit flow down to subsonic conditions, and thereby recover some of the static pressure. By and large, these shock-in-stator supersonic compressors were not very successful due to the relatively high loading of the stator blade row, and to radial distributions of the flow parameters at the rotor exit which were not anticipated in the design [21]. The difficulties associated with high stator loading have also been confirmed in fairly recent experimental research involving a supersonic compressor stage with a variable-geometry stator, and with the rotor operating in an impulse-type mode [23].

Interestingly, a possible solution to the stator loading problem was considered in the mid 1950's, and even pursued to the extent of hardware construction; however, termination of the supersonic compressor program occurred before any useful results were obtained. The proposed concept employed a supersonic stator to turn the flow back to the axial direction, thus eliminating much diffusion in the stator. The diffusion was to be done downstream in an annular duct with provision for boundary-layer control and variable

geometry [21]. The current significance of such a concept is that it is similar in many respects to some features of the SSTF.

Axial-supersonic rotor inflow

The basic idea of a compressor designed to accept axial-supersonic inflow is not new, but it appears to have not been vigorously pursued for any protracted length of time, and so only limited analytical and experimental research has been done to assess the feasibility and operational characteristics of such a device. In as early as 1946, Kantrowitz [24] mentioned in a now classic paper the possible advantage of such a compressor as a means of avoiding some inlet loss by the elimination of the subsonic portion of the inlet. In the early 1950's, Ferri [25,26] addressed this concept in some detail from the perspective of inlet and compressor performance and matching, including an analysis of the trade-off between inlet and compressor efficiencies on the overall compression system efficiency.

Based on a personal survey of the literature, it appears that there are only two documented cases prior to 1989 involving successful experiments where axial-supersonic flow into a rotating blade row was established, and in both of these cases only shock-in-rotor operation was examined, as was probably intended. Indeed, prior to recent efforts at the NASA Lewis Research Center [27-31] there appears to have been no reported experimental work aimed at directly investigating a supersonic throughflow rotor [6] or stage, although detailed design studies [32,33] were done in the mid 1960's which included experimental research on a supersonic throughflow rotor cascade [34]. Linear cascade tests with axial-supersonic flows into or through blade passages are not particularly scarce. Some early examples include three-dimensional (single passage) stator cascade tests [35] in 1954, two-dimensional rotor cascade tests [36] in 1955, and three-dimensional rotor cascade tests [37] in 1958. Axial-supersonic flow has also been established into a stator blade row downstream of a rotor (impulse-type rotor operation), as demonstrated somewhat recently in a single-stage supersonic compressor [23].

---

[6] The SSTF rotor can be generally classified as an impulse-type rotor with axial-supersonic inflow.

Information reported in Reference 21, and the apparent lack of any similar information elsewhere, suggests that the first successful tests of a rotor (isolated; no stator) with axial-supersonic inflow velocities were performed at the NACA Langley Aeronautical Laboratory in the late 1950's. As described in the reference, an axial inlet Mach number of about 1.5 was established into the rotor through the use of a fixed-geometry, annular nozzle upstream. The static pressure ratio across the rotor is reported to have been about 4, indicating shock-in-rotor conditions. The second, and apparently only other rotor tested with axial-supersonic inflow is the one studied by Breugelmans [38]. These rotor experiments, conducted at the von Karman Institute, involved a range of supersonic axial inlet Mach numbers up to about Mach 1.5 which were generated using an annular, variable-geometry nozzle upstream of the rotor. The reported results are more extensive than those for the NACA Langley rotor and, again, all of the data indicate shock-in-rotor conditions. Unfortunately, a mechanical failure prevented completion of the test program so that only a fairly limited amount of data were acquired, with none at the design speed.

NASA Lewis Supersonic Throughflow Fan Program

In 1986, the NASA Lewis Research Center began a program aimed at demonstrating the feasibility and performance potential of the SSTF. In its general scope the program addresses all of the supersonic throughflow system components required for a variable cycle engine application [39]; namely, the primary inlet, the fan stage, the bypass nozzle, and the core inlet which diffuses part of the fan exit airflow to subsonic conditions for ingestion by the core-engine compressor. Although other possible applications exist for the SSTF, its application to the variable cycle engine is currently very relevant and leads to guidelines for establishing many of the design parameters.

The objective of the SSTF technology program is to resolve several key issues concerning the supersonic throughflow fan system, with special emphasis placed on the fan stage since it is the least understood, as well as the most aerodynamically complex of the components. The following are some of the more commonly recognized key technological issues:

- Fan overall performance and operability, at design and off-design conditions.

- Fan aerodynamic and aeromechanical characteristics during transition from subsonic to supersonic throughflow conditions, and vice-versa.
- Successful integration of the fan into the overall system.
- Fan performance and durability under service operating conditions, e.g., performance degradation in moist ambient air or due to foreign object damage (FOD), and the influence of inlet flow distortion on fan performance and stability.

Although other important issues could be cited, these are some of the more fundamental and reflect several of the technological risks associated with practical application of the SSTF concept. From this perspective it is interesting to note that these and other difficulties, whether real or imagined, have caused many to criticize or reject the concept at the outset, without any serious investigation or study. Therefore, it is within the intent of the Lewis program to eliminate much of the conjecture and provide a sound basis for comparing SSTF systems with other airbreathing propulsion systems. The primary goals of the Lewis program can be summarized as follows:

- Demonstrate the feasibility and performance potential of the SSTF, and related system components.
- Provide a fundamental understanding of the SSTF aerodynamics over the practical range of its operation.
- Develop an experimental data base for the assessment or validation of design and analysis (computational) codes.
- Develop the technology necessary for the practical application of the SSTF.

The basic approach for achieving the program goals involves conducting, in parallel, experimental and analytical research so as to take advantage of the strengths inherent in each. A somewhat "conservative" baseline proof-of-concept fan design has served as the starting point for the program, where heavy reliance on advanced computational fluid dynamics (CFD) codes was necessary since no relevant experimental data base existed for such designs [27,28]. Details of the baseline fan design and the basic design philosophy used are reviewed in the next chapter. The information and knowledge gained from the baseline fan investigation are being used to assess the analysis (mostly computational) and design tools, as well as the design assumptions and methodology. Concurrently, the analytical results are being used for assessing and better understanding the experimental

results. As this approach is applied to successive designs aimed at improving stage performance and other characteristics, the technology for supersonic throughflow fans can be expected to advance if given the opportunity.

Purpose and Scope of Dissertation

The purpose of this dissertation is to describe and quantify the essential steady-state aerodynamic features of the baseline SSTF rotor. Although the fan stage (rotor and stator) is also of much interest, the scope is limited here to the rotor. Where practical, the aerodynamic descriptions are formulated so as to be fairly general and potentially applicable to future SSTF rotor designs. Nearly the entire range of practical rotor operation is addressed, that is, off-design as well as design-point operation, with varying degrees of emphasis on different operating modes, or throughflow regimes.

Unique to this type of rotor is the necessity for operation in several very different operating modes. These modes involve axial-subsonic and axial-supersonic flow conditions, sometimes with both types of conditions existing simultaneously at different axial locations. Several of these modes are necessary during initial start-up and final shut-down of the system, but based on more recent cycle and system studies it is expected that sustained operation in some off-design modes may also be required, depending on the overall compression system design and operation and how it relates to the aircraft mission profile. Hence, addressing the general off-design characteristics and performance is important.

The transitional phases of operation where the rotor is transited between different throughflow regimes (operating modes), with local changes from axial-subsonic to axial-supersonic conditions and vice versa, involve qualitative changes in the blade-row aerodynamics and overall operating characteristics. The severity of these changes and the impact that they have on factors such as aerodynamic blade loading, blade row performance, aeroelasticity, stress and vibration, and so on, are critical issues that largely determine the feasibility and acceptability of the concept. Therefore considerable attention is devoted to the aerodynamics associated with transitional operation.

The analytical and experimental findings are presented and discussed within the framework of gas dynamic theory to promote a basic understanding of the general operating characteristics and performance of the rotor, including how the characteristics relate to the system in which the rotor was tested. Although the performance and aerodynamics of only a specific rotor design are examined and demonstrated, it is maintained that many of the results obtained from this investigation are generic enough to qualitatively apply to most, if not all, fixed-geometry rotors designed at a supersonic throughflow operating point. An important facet of this study is the explanation of how certain key geometric features and operating conditions relate to the observed operating characteristics and performance. Consideration of the rotor as part of a larger system is important since under most operating conditions the rotor and other system components are strongly coupled. This coupling determines, for instance, whether or not certain operating modes are attainable for the system, the dynamic and quasi-steady behavior of the system during transitional operation between the different modes, and possible alternative sequences for transiting from subsonic to supersonic throughflow conditions.

Many important issues are not addressed since they are beyond the scope of this dissertation. These include, but are not limited to the following: fan stage operating characteristics and performance, circumferential flow-field distortion effects, high air-humidity effects, the influence of endwall bleed, and large-scale unsteady aerodynamic and gas dynamic effects. Some of these items are discussed in References 40 and 41, which deal with results from experimental investigations of the fan stage.

Finally, to reiterate, the main purpose of this dissertation is to describe in fairly general terms the essential steady-state aerodynamics of the baseline SSTF rotor. An implicit secondary theme throughout this work, however, relates to the extensive use of computational methods to acquire a better understanding of the aerodynamics than the experiments alone would allow, while at the same time using the experimental data to ensure that the computational results are reasonable. In this context, it should not be overlooked that the experimental research covers a much broader range of phenomena and operating conditions, but computational results at few selected operating points provide useful and needed insight into the detailed aerodynamics. Furthermore, the comparisons between experimental and computational results allow a better quantification of the rotor performance and its associated uncertainties.

CHAPTER 2.
BASELINE FAN DESIGN

The baseline SSTF was designed in-house at the NASA Lewis Research Center in 1986. The design is reviewed in this chapter, which contains information previously reported in two NASA Technical Memorandums [27,28]. Only a summary is presented here since complete details can be found in the references. The basic design philosophy and approach are discussed first, followed by a brief description of the final baseline fan design.

Design Philosophy and Approach

The approach taken in designing the baseline fan was, to a large extent, determined by the lack of any prior experience or relevant experimental data for supersonic throughflow blade rows. At the time the design process was initiated, the fairly recent availability of advanced CFD codes, especially viscous flow codes [42], provided an essential means for approaching a new design in a manner which greatly reduced many of the uncertainties involved. Considerable doubt and skepticism based on past experiences — which were not really directly related to the SSTF concept — cast a shadow, as it were, on the workability and potential success of such a design, which represented a substantial departure from conventional fan and compressor technology. Many of the concerns were related not just to design-point operation of the fan, but also to whether or not such a fan could be started [1] in the first place. Thus, in the design of the baseline fan it was desirable to consider fan off-design performance and starting [28], at least indirectly, by checking the final design for possible problems in these areas.

---

[1] As used here, the term starting refers to the transition from axial-subsonic to axial-supersonic throughflow velocities.

From its inception, the baseline fan was intended to demonstrate proof-of-concept, where success in terms of overall operability and start/unstart transition were of paramount importance. This major consideration coupled with the lack of experience and virtually no experimental data base led to the selection of several guidelines and parameters for the aerodynamic design:

- Constant hub and casing radii were used throughout the fan stage in order to avoid potentially severe three-dimensional flow effects [2] arising from endwall slopes and curvatures, and annulus-area reductions.
- Moderate values for overall total-pressure ratio (2.45) and rotor tip speed (1500 ft/sec corrected) [3] were selected. A design deemed aggressive in terms of high blade loading was avoided.
- Blade passage shock waves were to be weak and contained within the bladed passages. This implied oblique waves and the cancellation, or near cancelation, of reflected shocks.
- Static-pressure gradients on blade surfaces were to be weak. This guideline avoided the generation or reflection of strong shocks from the blade surfaces. "Strong" in this sense referred to oblique shocks with significant entropy rise.
- Static pressures on the suction and pressure surfaces were to match as the trailing edge was approached, i.e., the blade loading distribution was to "close" at the trailing edge, thus avoiding an abrupt flow adjustment at the trailing edge and the accompanying strong "fish-tail" shocks.

Note that, by definition, velocities were to be axial-supersonic throughout the stage. Also note that near-optimal aerodynamic performance and a high fan efficiency were *not* objectives in the baseline design.

---

[2] This constraint was also related to the CFD codes available in-house at the time of design. Initially, a two dimensional viscous blade-to-blade solver was used, followed later in the design process by a quasi-three-dimensional viscous solver as it became available. Three-dimensional viscous CFD codes for turbomachinery were not readily available at the time.

[3] The corrected tip speed of 1500 ft/sec is relatively high for the design point of an actual flight system. At a cruise Mach number of 2.4, this corrected speed corresponds to a mechanical tip speed of 1908 ft/sec (standard day; altitudes 40,000 to 80,000 ft).

The method for generating an aerodynamic design was iterative and consisted of three basic steps which were repeated until convergence was achieved. The first step involved generation of a fan geometry. This was done using a modified version of the axisymmetric compressor design code developed at NASA by Crouse and Gorrell [43]. This design code, which is based on the streamline curvature method, was modified to handle axial-supersonic flows [4]. As the second step, the resulting blade geometries were analyzed aerodynamically at several streamlines (blade elements) using the two-dimensional or quasi-three-dimensional CFD codes of Chima [42]. The third step consisted of using an interactive, blade element geometry code (undocumented) to modify, based on the CFD results, parameters controlling the blade profile geometry.

Convergence on an acceptable aerodynamic design involved the guidelines listed earlier, as well as close agreement between the blade exit flow deviation angles input to the compressor design code and those obtained from the CFD analysis. After achieving an aerodynamic design, a finite-element structural analysis was performed using the NASTRAN code to determine blade stresses, as well as vibration modes and frequencies. This was followed by an analysis to check for flutter potential [44,45]. If unacceptable structural or aeroelastic properties were indicated, then the blades were redesigned so as to satisfy both the aerodynamic and mechanical criteria [5]. The iterative design procedure just described is illustrated schematically in Figure 2.1.

Description of Fan Design

The overall parameters selected for the SSTF design are presented in Table 2.1, while in Table 2.2 parameters specific to each blade row are listed. Many of the quantities contained in Table 2.2 resulted from the design procedure just summarized, and descriptions

---

[4] Due to calculation instabilities associated with its application to axial-supersonic conditions, however, it was necessary to highly dampen the streamline curvature terms to the point where they contributed little to radial equilibrium [27].

[5] A potential flutter problem was indicated for the rotor of the first design, leading to a redesign involving 30 percent longer blade chords.

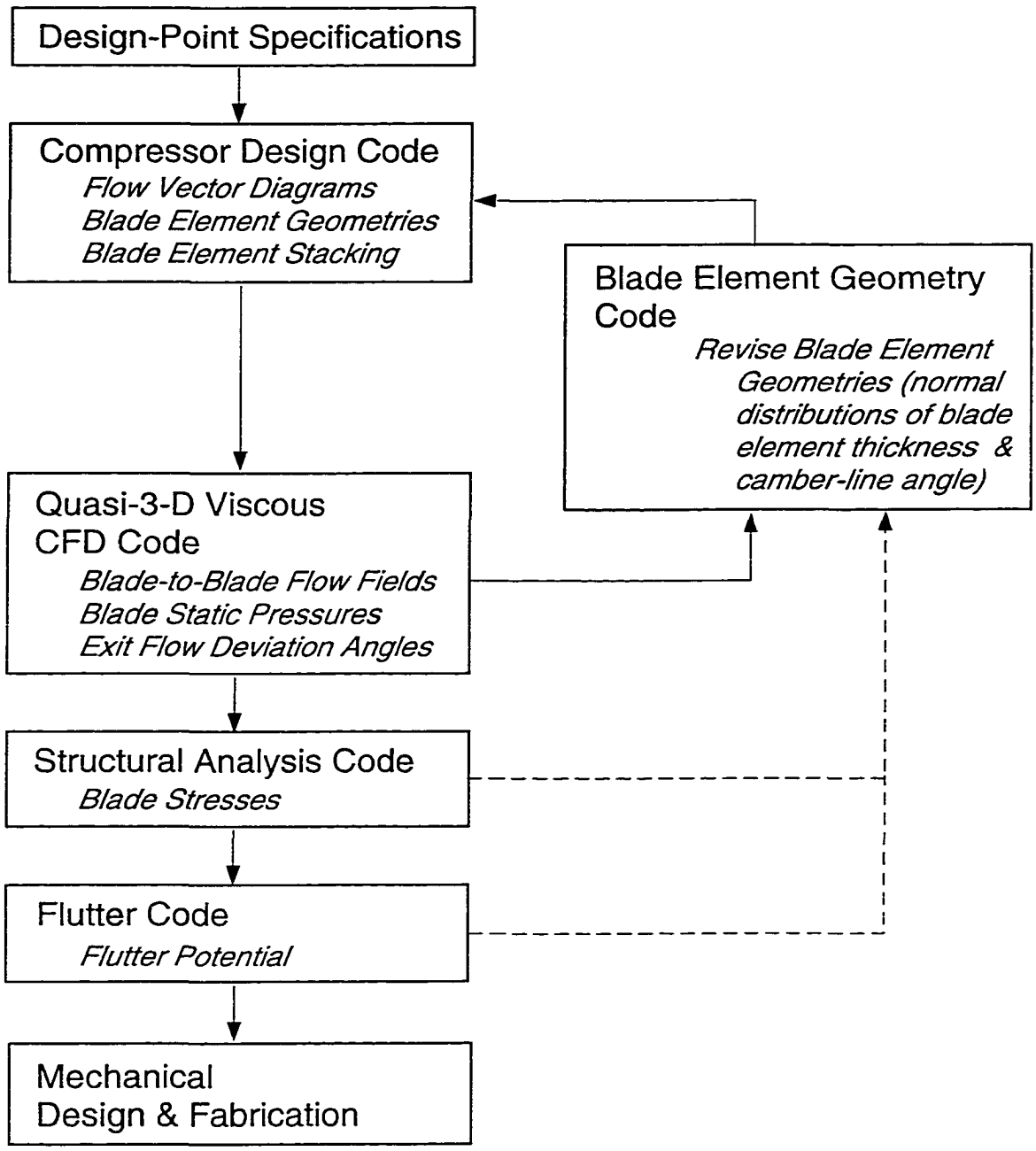

Figure 2.1 Schematic of fan design procedure

Table 2.1 Baseline SSTF overall design parameters

Total pressure ratio	2.45
Mass flow, lbm/sec	31.5
Axial inlet Mach number	2.00
Tip speed, ft/sec	1500
Tip radius, inches	10.0
Hub-tip radius ratio (constant)	0.700

Table 2.2 Rotor and stator design parameters

	Rotor	Stator
Rotational speed, rpm	17188.7	—
Total-pressure ratio	2.70	—
Blade number	44	52
Tip radius, inches (constant)	10.0	10.0
Hub radius, inches (constant)	7.0	7.0
Aerodynamic chord, inches (tip/hub) [a]	4.45/3.56	3.65/3.28
Aspect ratio, span to mean chord	0.97	0.86
Blade element solidity, σ (tip/hub)	3.11/3.56	3.02/3.88
Max. thickness/chord, percent (tip/hub)	4.0/7.0	5.0/5.0
L.E. thickness/chord, percent (tip/hub) [b]	0.45/0.56	0.41/0.46
T.E. thickness/chord, percent (tip/hub)	0.81/1.12	0.82/0.82

[a] The aerodynamic chord and the maximum-thickness to chord ratio both vary linearly from tip to hub.

[b] The leading edge (L.E.) and trailing edge (T.E.) thicknesses as listed here represent the full thickness of the particular edge, which is about the length of the minor axis for the edge-ellipse. The ellipse major/minor axis length ratio is 1.5 for all edges. The rotor and stator L.E. thicknesses are 0.020 and 0.015 inches, respectively, constant from tip to hub.

of how many of the values were obtained are in Reference 28. The quantities in Table 2.1, on the other hand, were selected at the beginning of the design process and, therefore, were independent of it. Although the overall design parameters are somewhat arbitrary, an attempt was made to choose values believed, at the time, to be fairly representative for this type of fan as employed in a flight propulsion system [6].

Mach number vector diagrams for the baseline SSTF at the tip, pitchline (or mean-line), and hub are shown in Figure 2.2. Notice in this figure that the flow enters the fan at an axial inlet Mach number of 2.0 (no swirl), and exits the stage at an axial Mach number of about 2.9 (no swirl). The corresponding static pressure ratio between fan inlet and exit is about 0.67, clearly revealing the impulse-type nature of the design. Interestingly, for axial-supersonic flows in a straight, constant-area annulus, the stator and rotor blade rows both function as nozzles to accelerate and expand the flow, rather than diffusing it as in the case of subsonic blade rows [7]. Only by incorporating annulus area convergence can supersonic diffusion occur through the blade rows.

A meridional plane view of the fan stage is shown in Figure 2.3, which also includes hub and tip blade profiles for the rotor and a pitchline blade profile for the stator. Blade-relative Mach number contours for computed rotor and stator pitchline flow fields are shown in Figure 2.4. These computations were done using the quasi-three-dimensional CFD code of Chima [42], and are included here mostly to show the relatively high blade-element solidities which resulted from the design process, and to provide an impression of the design-point, blade-to-blade flow field in the SSTF. It might be emphasized that throughout the design process, involving the viscous blade-to-blade CFD analysis, blade-element solidity emerged as a parameter of first-order importance. High solidities were clearly needed in order to turn the supersonic flow through a system of weak internal waves, while also minimizing shock/boundary-layer interaction effects, including large-scale flow separation under some conditions (see Reference 28 for details). More will be said in later chapters about the computational methods, codes, and results.

---

[6] The size, mass flow, and rotational speed are sub-scale. A full-scale fan would have a tip diameter of around six feet.

[7] An increasing flow area is associated with either a supersonic expansion or a subsonic diffusion, depending on the upstream and downstream boundary conditions.

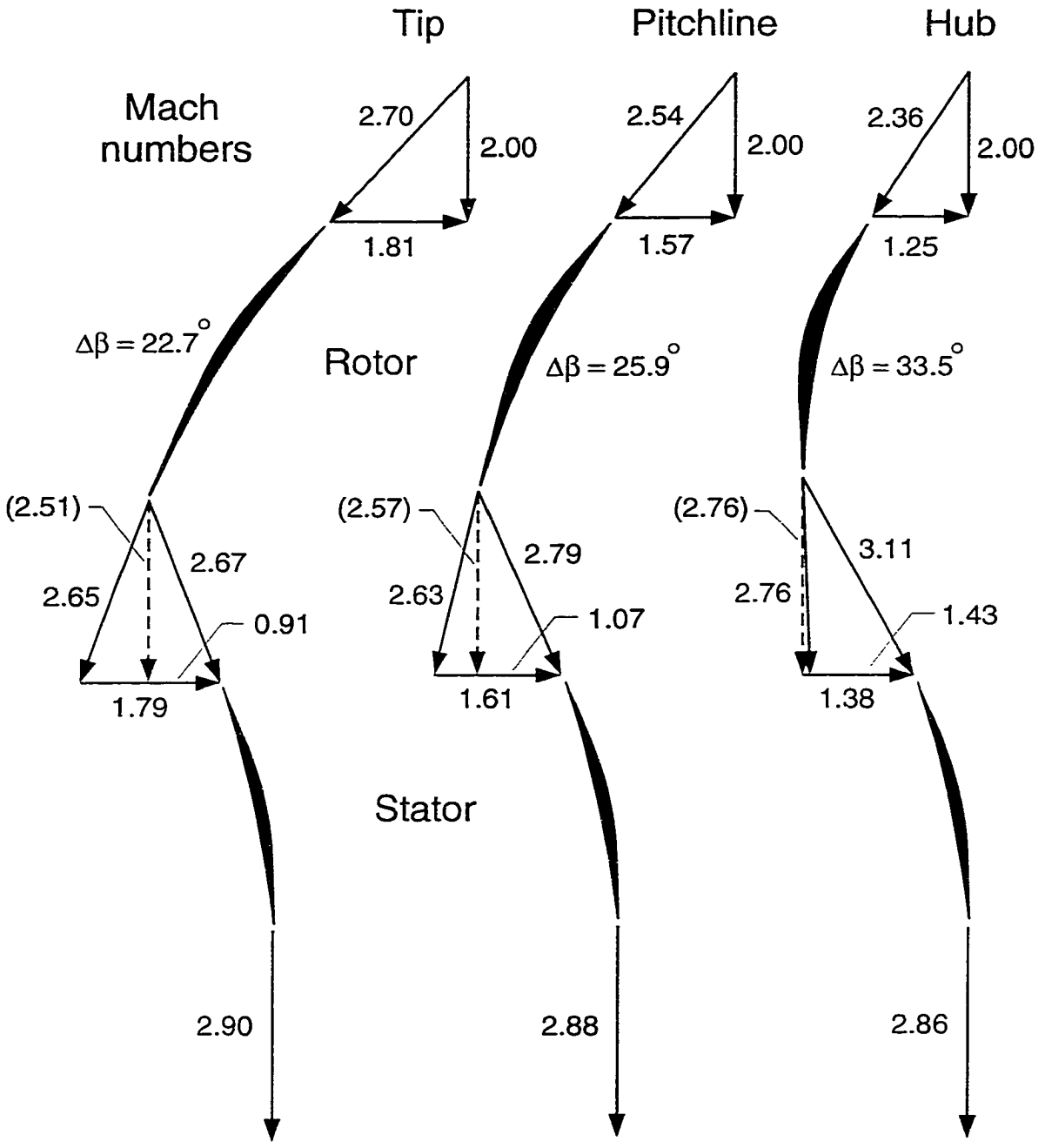

Figure 2.2 Mach number vector diagrams for the baseline SSTF

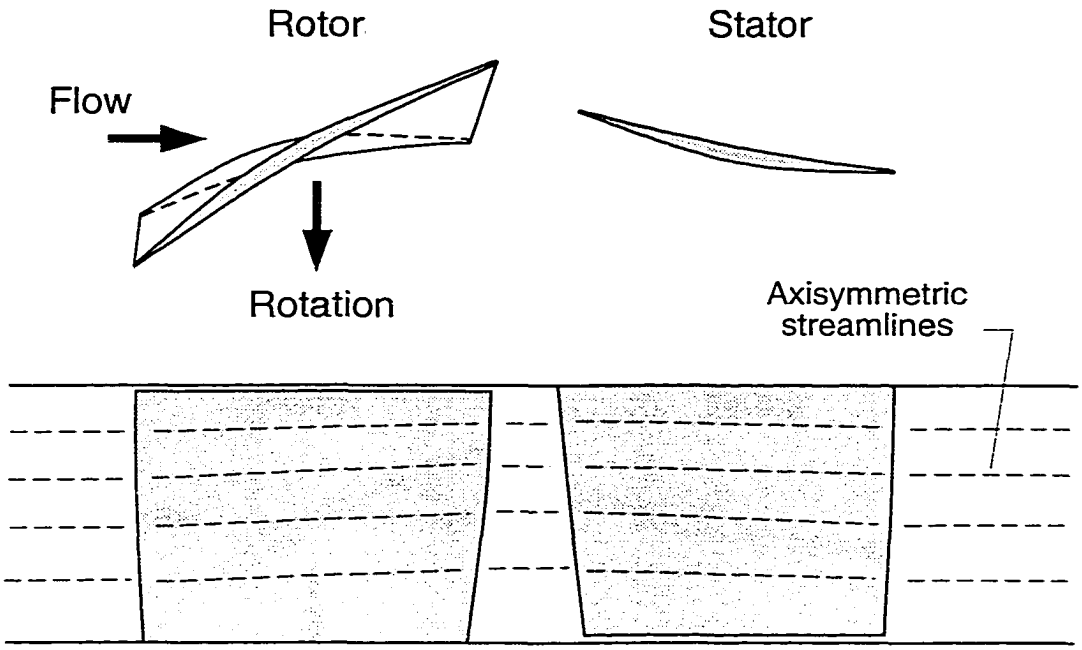

Figure 2.3 *Meridional view of baseline SSTF stage*

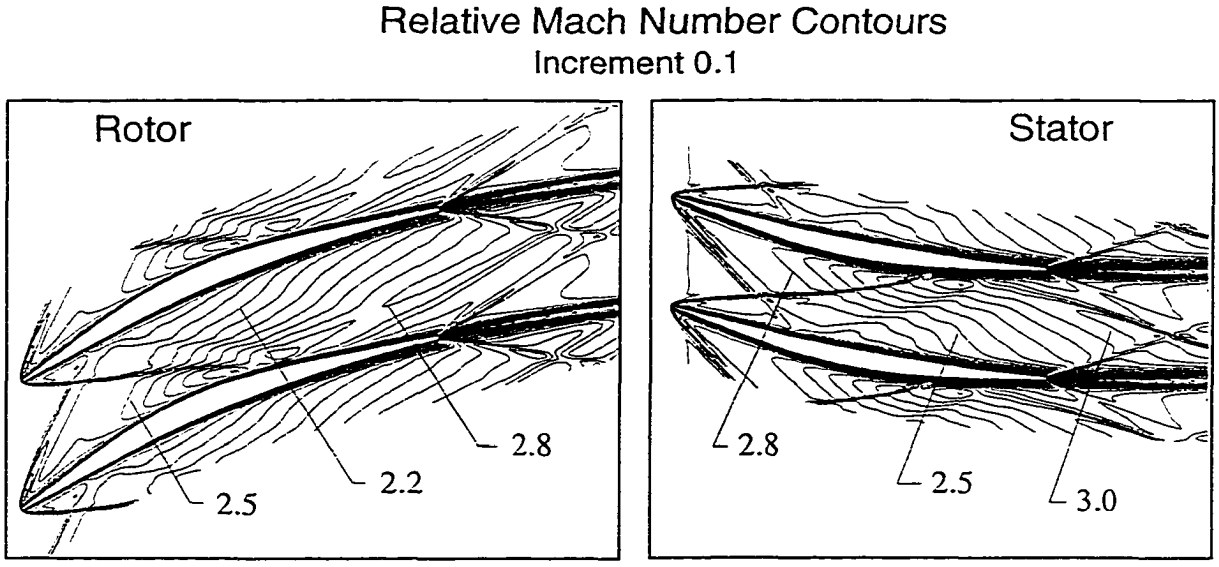

Figure 2.4 Pitchline Mach number contours for the baseline SSTF at the design operating point, computed using quasi-three-dimensional viscous CFD

CHAPTER 3.
EXPERIMENTAL FACILITY

The many unique aerodynamic features of the supersonic throughflow fan made necessary a special facility for its operation and testing. To this end, the Multistage Compressor Test Facility at the Lewis Research Center was extensively modified to accommodate the SSTF, as described in detail by Urasek et al. [46]. An overview describing the facility, including important instrumentation and data acquisition and reduction features, is provided in this chapter.

Description of Facility

The facility for testing the SSTF included a special test package which contained the fan and closely-related components. The test package, illustrated in Figure 3.1, consisted of an inlet strut housing with three hollow struts (one for instrumentation-leads and two for bleed flow removal), a variable-geometry inlet nozzle, the fan, and a variable-geometry supersonic exit-diffuser. A photograph of the test package is shown in Figure 3.2 with several major components identified. Photographs of the rotor and stator blades are shown in Figure 3.3.

Two different versions of the fan test package were used in the facility: one version for testing the isolated rotor, and the other for testing the fan stage. Note that the fan casing, as well as the instrumentation hardware, differed between the two versions. Since most of the experimental data presented in this dissertation were obtained in connection with the isolated-rotor casing, the description here is limited primarily to it and its related hardware. Descriptions of the other casing and its associated hardware can be found in References 40 and 41.

The aerodynamic design of the nozzle and diffuser components is discussed in Reference 27. For both the nozzle and diffuser, the geometry was varied by translating the cen-

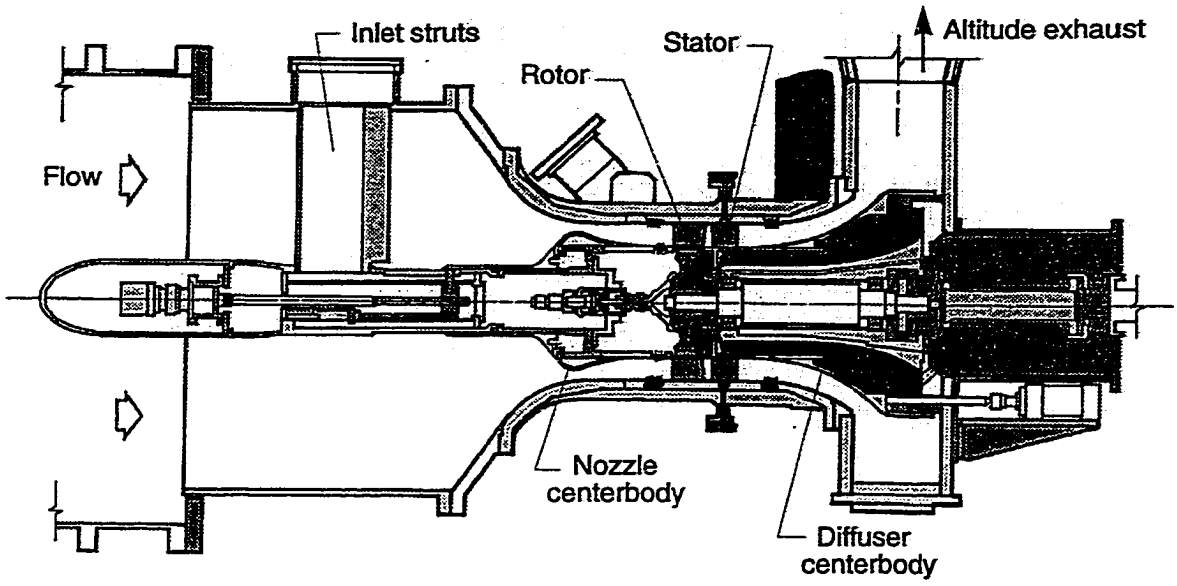

Figure 3.1 Illustration of supersonic throughflow fan test package

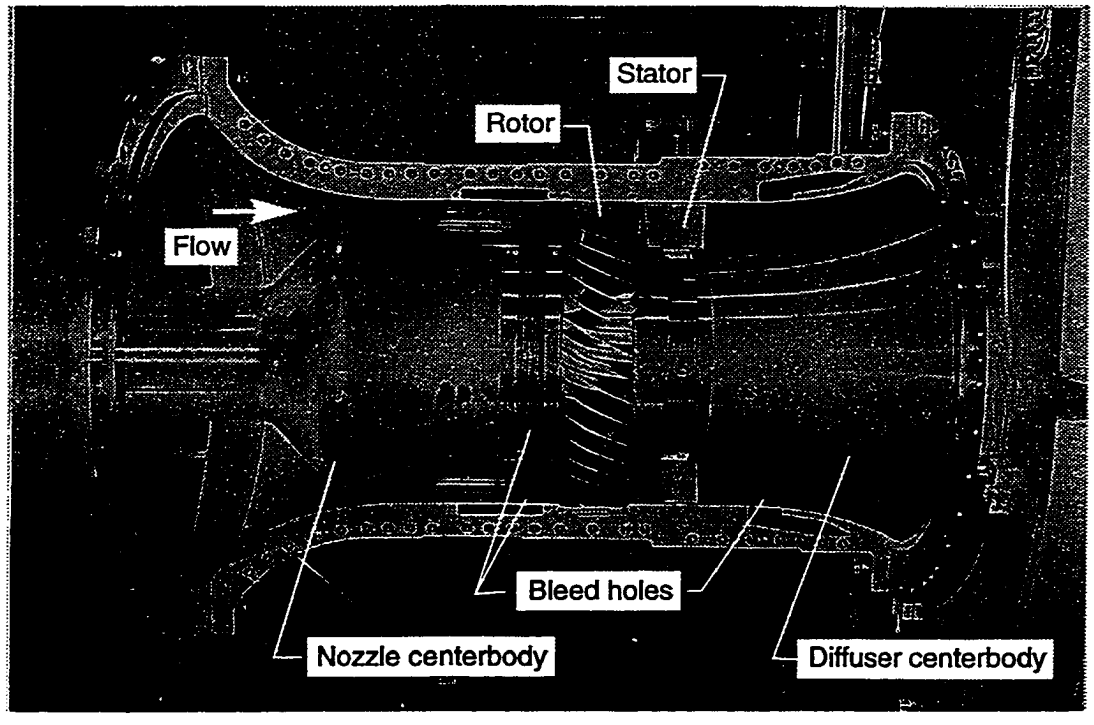

Figure 3.2 Photograph of supersonic throughflow fan test package

C-88-08525

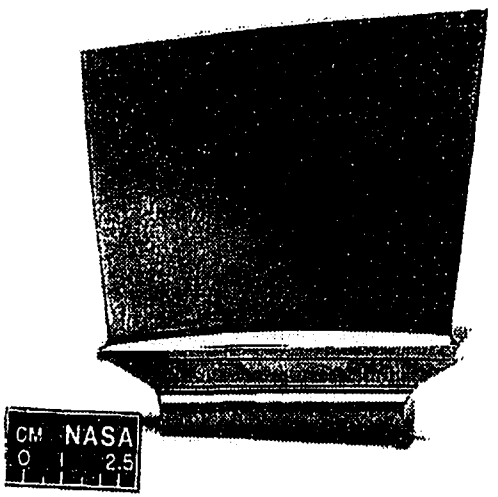

C-88-04489

(a) rotor blade

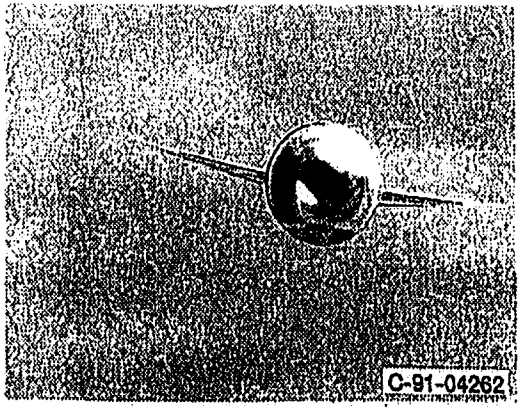

C-91-04262

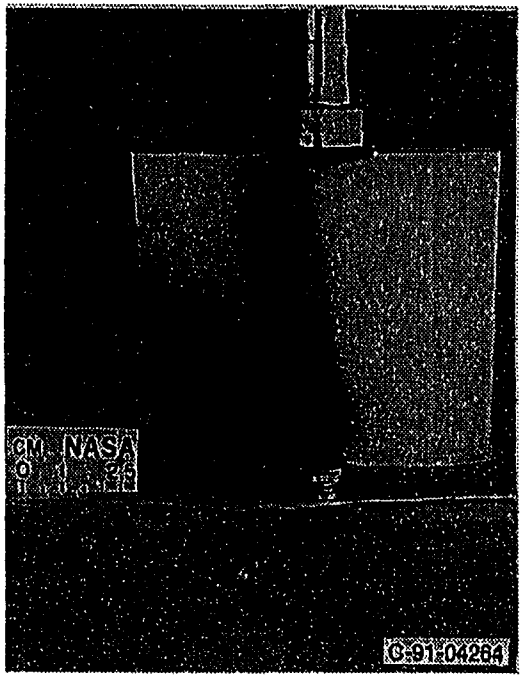

C-91-04264

(b) stator blade

Figure 3.3 Photographs of baseline supersonic throughflow fan rotor and stator blades

terbody (for that component). The inlet nozzle functioned as a subsonic duct when in the fully-open position (centerbody forward), or as a converging-diverging (c-d) supersonic nozzle when in the partially to fully-closed range of positions. The exit diffuser functioned as an all-supersonic diffuser, or as a throttle for the fan when diffuser conditions were subsonic and the diffuser was choked at its exit.

Perforated "bleed" rings for endwall boundary-layer air removal were located on the hub and casing endwalls just upstream of the rotor, and on the casing endwall just downstream of the stator exit location (see Figure 3.2). A thin circumferential bleed slot was located on the hub endwall at the diffuser entrance. Details of the bleed ring and bleed slot geometries are reported in Reference 47. Three vacuum pumps exhausting to a low-pressure exhaust system (altitude exhaust; see discussion below) provided manifold bleed static pressures low enough to allow bleeding from the supersonic flows [46,47]. Bleed flow rates were designed to be 0.5 lbm/sec at both casing locations, 0.35 lbm/sec at the nozzle hub location, and 1.0 lbm/sec at the diffuser hub slot.

The test package was connected to the rest of the test facility as shown schematically in Figure 3.4, and in the photograph provided in Figure 3.5. Dry air, necessary for avoiding condensation (shocks) in the supersonic flow, was supplied to the facility from the laboratory central *40-psig pressurized air system* (dew point -40°F), or from the *refrigerated air system* delivering air at temperatures down to about 0°F [1]. If desired, an *atmospheric air system* could be used to supply outside (humid) air to the facility.

After entering the facility, the supply air first encountered a flow measuring orifice, followed by two inlet throttle valves and then a plenum (see Figure 3.4). The pressure in the plenum was automatically maintained at a prescribed level by the inlet throttle valves. From the plenum, the airflow entered the test package and was then exhausted through a collector. The exhaust air normally exited the facility to an *altitude exhaust system*, maintained at about 2 psia. but could also be exited to an *atmospheric exhaust system*. As men-

---

[1] The refrigerated air system has enough capacity to deliver air at temperatures down to -75°F, but materials limitations for the SSTF facility allowed temperatures down to only about 0°F.

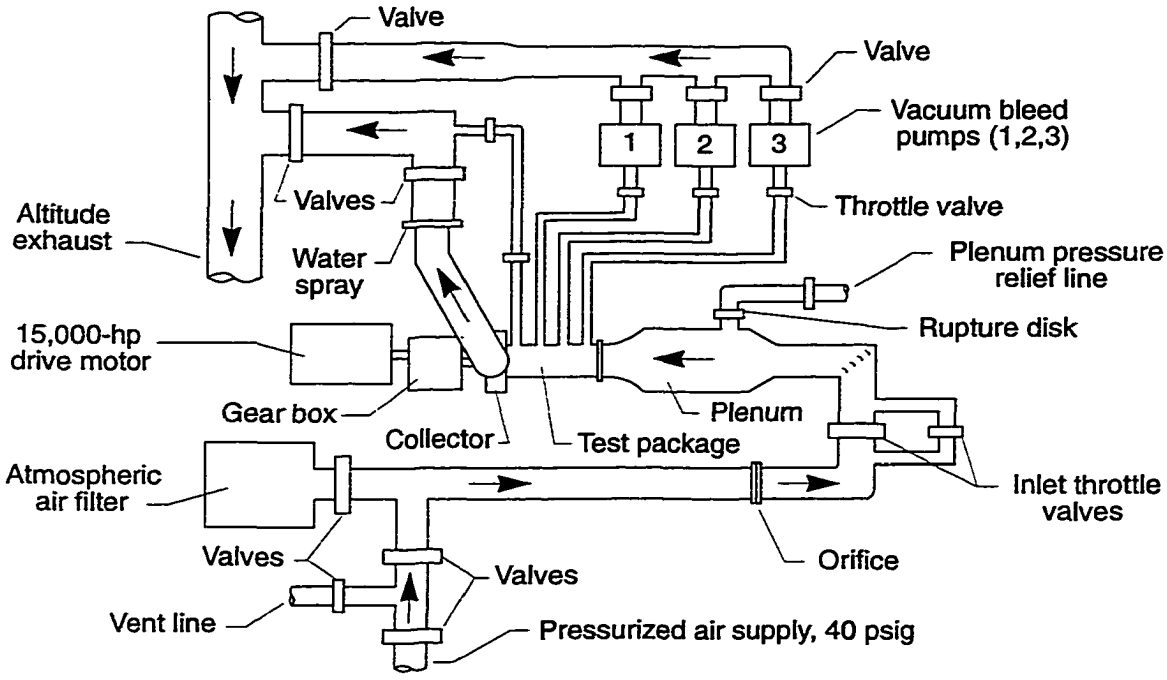

Figure 3.4 Schematic of supersonic throughflow fan facility

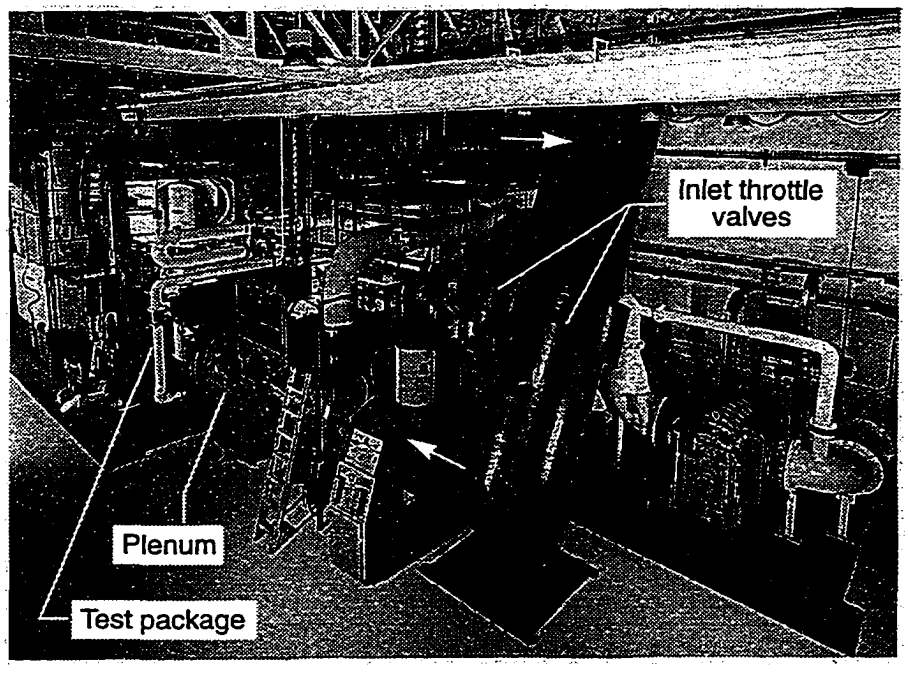

Figure 3.5 Photograph of supersonic throughflow fan facility

tioned above, the bleed air was also exhausted from the bleed pumps [2] to the altitude exhaust system.

Maximum limitations for the facility included a 25 psig plenum pressure, a mass flow rate of 100 lbm/sec, and a fan rotational speed of 18,600 rpm. Due to blade stress limitations, however, the maximum rotational speed for the SSTF was 17,600 rpm. A 15,000-hp synchronous electric motor supplied power to the fan through a 5.21:1 step-up gearbox.

Facility Instrumentation and Data Acquisition

The facility was instrumented for acquiring a variety of measurements related to the fan aerodynamics and to the health of various facility components. A state-of-the-art, real-time data acquisition system, designated Escort D [48], was used to acquire and record test data, including pressures, temperatures, flow rates, vibrations, and stress levels. Continuously monitored (analog) signals indicating stress and vibration levels were also recorded on magnetic tape for later analysis if problems were encountered.

The ASME standard orifice upstream of the plenum (see Figure 3.4) was used to measure fan inlet airflow. Bleed flow rates were measured using Annubars (averaging Pitot tubes). Temperatures were measured using thermocouples connected to a floating-point reference block, and pressures were measured using a periodically calibrated electronic pressure system or, for selected pressures, individual pre-calibrated pressure transducers. The facility was not equipped with any fast-response pressure instrumentation, and so only steady-state aerodynamic measurements were acquired.

Static pressure taps were located on the hub and casing endwalls, upstream and downstream of the rotor. The axial and circumferential locations of the casing taps for the isolated-rotor tests are shown in Figure 3.6. These locations (and the same casing) were also used for facility flow tests [47] performed before the rotor tests. The zero-reference axial location is at the rotor hub leading edge.

---

[2] The diffuser hub bleed slot was designed to exhaust bleed air directly to the altitude exhaust system. It was not needed, however, and therefore was not used.

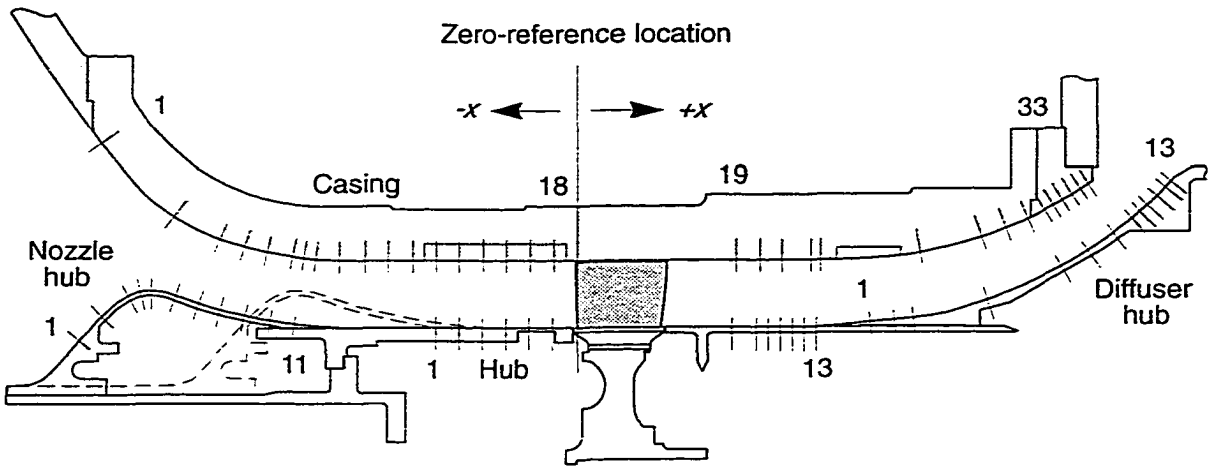

Nozzle casing

Tap	Axial location, x, inches
1	-20.000
2	-17.000
3	-15.000
4	-14.000
5	-13.000
6	-12.000
7	-11.477
8	-11.000
9	-10.000
10	-9.000
11	-8.000
12	-7.000
13	-6.000
14	-5.000
15	-4.000
16	-3.000
17	-2.000
18	-1.000

Diffuser casing

Tap	Axial location, x, inches
19	6.514
20	7.519
21	8.419
22	9.689
23	10.144
24	14.269
25	16.849
26	17.829
27	18.779
28	19.519
29	19.879
30	20.239
31	20.599
32	20.949
33	21.299

Nozzle hub

Tap	Axial location[a], x, inches
1	-20.94
2	-19.94
3	-18.94
4	-18.42
5	-17.94
6	-16.94
7	-15.94
8	-14.94
9	-13.94
10	-12.94
11	-11.94

Hub

Tap	Axial location, x, inches
1	-5.990
2	-4.990
3	-3.990
4	-2.990
5	-1.990
6	-0.990
7	6.414
8	7.419
9	7.919
10	8.419
11	8.919
12	9.419
13	9.919

Diffuser hub

Tap	Axial location[b], x, inches
1	12.21
2	13.20
3	14.00
4	17.16
5	20.20
6	21.30
7	22.29
8	23.08
9	23.44
10	23.76
11	24.17
12	24.49
13	24.75

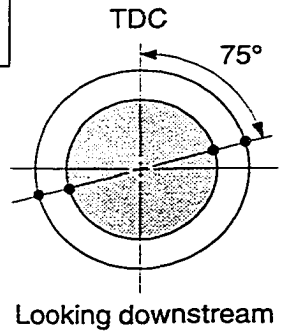

[a]Nozzle centerbody is at most forward position.

[b]Diffuser centerbody is at most rearward position.

Figure 3.6 Locations of endwall static pressure taps for isolated-rotor tests

Rakes were installed downstream of the isolated rotor. Traversing-probes were used for measurements downstream of the stage, and also for measurements at the nozzle exit during facility flow tests. Since the probes were used to measure the supersonic nozzle exit flow [3], a brief description of them is also given below after first discussing the rakes.

Detailed information about the location of the radial rakes is provided in Figure 3.7, where the axial and circumferential locations of the three-element rakes are shown, including the radial location of each rake element. A photograph of one of the pressure

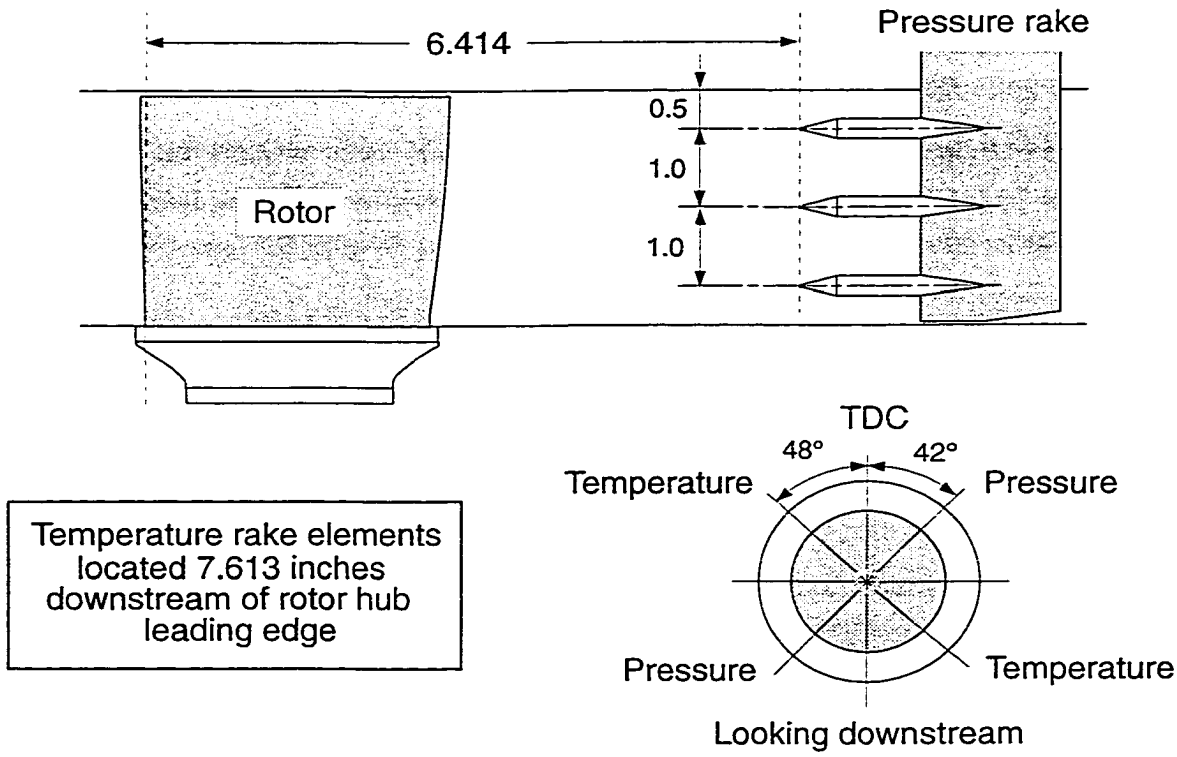

Figure 3.7 Axial and circumferential locations of downstream measurement rakes (dimensions in inches)

[3] Radial traverses were made at the rotor hub leading edge axial location (rotor not installed) for the entire range of practical flow conditions. See Appendix A for details about the nozzle flow.

rakes and one of the temperature rakes is shown in Figure 3.8. The pressure rake design was based on information reported in Reference 50. Each element of the pressure rake had a five-hole probe which was aerodynamically calibrated over a wide range of applicable conditions, in a steady flow, to measure local total and static pressure, and local yaw (circumferential) and pitch (radial) flow angle. Each element of the temperature rake contained a chromel-constantan thermocouple, and was also aerodynamically calibrated over a range of Mach numbers to measure local total temperature. The rakes were set at a fixed yaw-angle of 25 degrees to be somewhat aligned with the average rotor exit flow at design operating conditions.

A photograph of one of the pressure and one of the temperature traversing-probes is shown in Figure 3.9. The design of these probes was based on information reported in

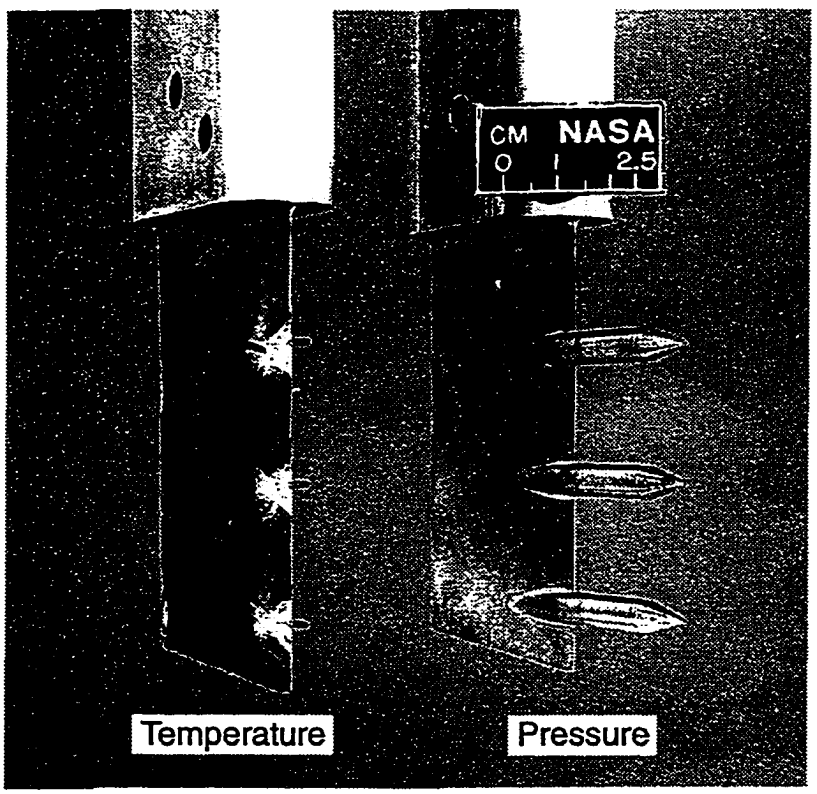

Figure 3.8 Photograph of downstream measurement rakes

References 51 and 52. As with the rake elements, each five-hole pressure probe was aerodynamically calibrated over a wide range of relevant steady-flow conditions to measure local total and static pressure, and local flow pitch-angle. Local flow yaw-angle was determined by a null-balance of probe static pressures [4]. Each chromel-constantan thermocouple was calibrated for total temperature, and the temperature probes were slaved to the pressure probes in order to yaw-align them with the flow.

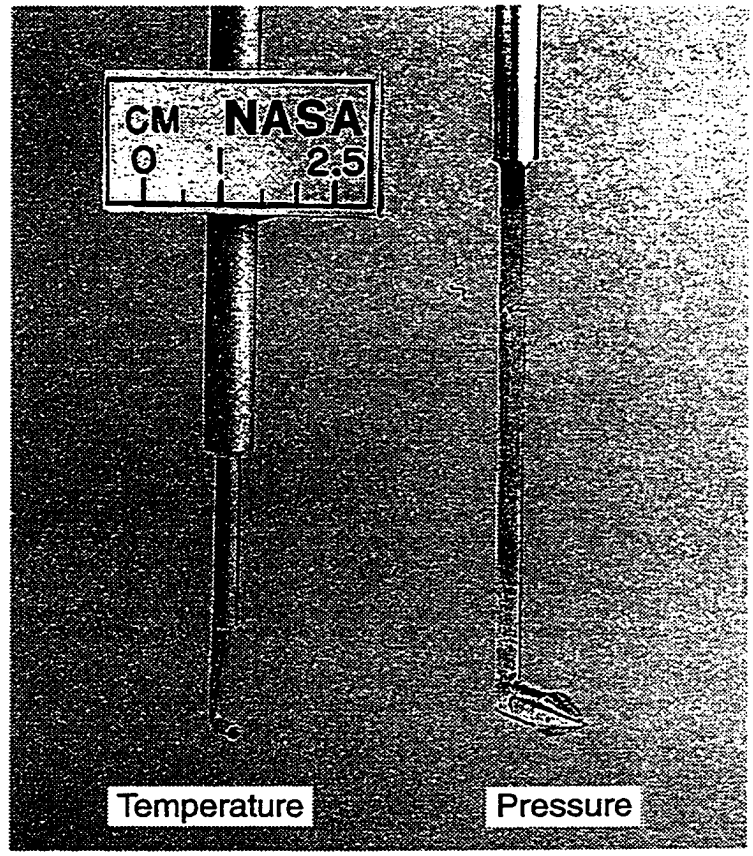

Figure 3.9 Photograph of measurement probes

[4] Only the two "side", or "yaw", ports on the cone-probe were balanced.

Experimental results obtained from the various tests performed in the SSTF facility have been reported in a series of NASA Technical Papers. These include the facility flow tests [47], the isolated-rotor tests [49], and the stage tests [40,41]. Estimated uncertainties for primary measurement quantities were reported in these papers, and for convenience they are also repeated here in Table 3.1. Note that these uncertainties correspond to a one percent of full-scale measurement uncertainty.

Table 3.1 Estimated uncertainties for primary measurement quantities

Orifice mass flow, lbm/sec	± 0.5
Bleed mass flow, lbm/sec	± 0.1
Flow angle, degrees	± 1.0
Temperature, °R	± 1.0
Static pressure, psia	± 0.15
Total pressure, psia	± 0.50

Data Reduction

The calculation methods for reducing the experimental data to the results commonly used and reported are reviewed in the following discussion, since familiarity with those methods can be useful in assessing and interpreting the experimental results. The data reduction was performed on a computer using a program which received, as input, primary measurement data including local temperatures and pressures, the orifice flow and bleed flow rates, and the fan rotational speed. Also received were aerodynamic calibration data for the rakes or probes [5]. The computer program processed the data by applying the calibrations, the equations from one-dimensional gas dynamics [6], and a variety of averag-

[5] Electronic calibrations for the pressure transducers were applied by the Escort D system during data acquisition.

[6] Air was assumed to be a perfect gas with a specific heat ratio γ of 1.40.

ing procedures which are described below. As is standard practice, corrections were applied such that all reduced output quantities reflect a standard-day condition in the facility plenum (see Figure 3.4).

Integration and averaging

Several of the measurements involved redundant instrumentation at two different circumferential locations. Specifically, dual measurements of endwall static pressures and downstream flow quantities were made [7]. The endwall static pressures at corresponding taps (same endwall and axial location) were arithmetically averaged to obtain the reduced values. Similarly, for the rakes, corresponding dual measurements of Mach number, total pressure, total temperature, and pitch and yaw flow angles were arithmetically averaged.

Overall mass-average quantities were obtained by integration of the radial rake distributions. Four quantities were directly mass-averaged through integrations in the radial direction; namely, total pressure, total temperature, Mach number, and flow pitch angle were averaged. For each of these quantities, represented generically by q, the following general form of integration was applied:

$$\bar{q} = \frac{\int q \delta \dot{m}}{\int \delta \dot{m}} \tag{3.1}$$

where locally [8]

$$\delta \dot{m} = \rho V_x \, dA \tag{3.2}$$

Note that all local thermodynamic and kinematic properties were calculated from the known quantities — known directly from the measurement data — using isentropic flow

---

[7] See Figures 3.6 and 3.7, and note the circumferential locations for the hub and casing endwall static pressure taps and the pressure and temperature rakes.

[8] The term *local* refers to *radially local* for the purpose of radial integration and averaging. Note that the "local" quantity is a circumferential (or time) average, where the slow-response instrumentation did the "averaging".

relations, the equations for a perfect gas, and flow vector relationships. For example, the local mass flux ρV_x in Equation (3.2) could be expressed as follows:

$$\rho V_x = \rho V \cos\alpha \cos\psi = \sqrt{\frac{\gamma}{RT_t}} p_t \phi \cos\alpha \cos\psi \tag{3.3}$$

where all quantities on the right-hand-side were known, the mass-flux parameter ϕ being a function of Mach number:

$$\phi = M\left[1 + \frac{\gamma - 1}{2} M^2\right]^{-(\gamma+1)/(2\gamma-2)} \tag{3.4}$$

The two angles α and ψ are the local yaw and pitch flow angles, respectively. The overall-average axial velocity component $\overline{V_x}$ for the annulus cross-section was determined using the overall-average static density [9] and the orifice-measured overall mass flow rate:

$$\overline{V_x} = \frac{\dot{m}}{\overline{\rho} A} \tag{3.5}$$

That is, the overall mass flow rate was used instead of an overall mass-average yaw angle (or tangential velocity). The overall-average yaw angle $\overline{\alpha}$ was determined using the overall-average values for the axial velocity component, the velocity magnitude, and the flow pitch angle:

$$\overline{\alpha} = \cos^{-1} \frac{\overline{V_x}}{\overline{V} \cos\overline{\psi}} \tag{3.6}$$

Radial and overall values of adiabatic efficiency were determined from the respective total pressures and total temperatures using the standard well-known definition of adiabatic efficiency, and assuming a perfect gas. The efficiencies were calculated between the upstream plenum condition and the condition at the rake measurement station.

---

[9] The overall-average density was calculated in the same way as the local density, that is, by applying isentropic flow and perfect gas relations to overall-average values of total temperature, total pressure, and Mach number, rather than by direct averaging of density itself.

Calculation of endwall Mach numbers

Local hub and casing endwall Mach numbers were calculated using the measured endwall static pressures and the plenum total pressure in the following well-known one-dimensional gas dynamic relation for the isentropic flow of a perfect gas [53]:

$$M_i = \sqrt{\frac{2}{\gamma - 1}\left[\left(\frac{P_t}{p}\right)^{(\gamma-1)/\gamma} - 1\right]} \tag{3.7}$$

Mach numbers calculated this way are sometimes referred to as *isentropic endwall Mach numbers*. Also calculated this way were the so-called *nominal* rotor-inlet (nozzle-exit) Mach numbers, where the static-pressure data from the taps located 1.0 inch upstream of the rotor leading edge (see Figure 3.6) [10] were used, but with the hub and casing static-pressure values first being arithmetically averaged together.

---

[10] For axial-subsonic rotor inflow conditions the static-pressure data from the taps located 2.0 inches upstream were used. This applies only to the results reported herein, and was done because the static-pressure values based on the taps at the 1.0 inch location usually appeared to be too low. It is suspected that the bleed rings influenced the static-pressure measurements there.

CHAPTER 4.
COMPUTATIONAL FLUID DYNAMICS

Continued advances in computer technology coupled with improved computational fluid dynamics (CFD) methods have made it practical to apply increasingly sophisticated CFD codes to solving turbomachinery fluid dynamics problems. Fairly recent advances in the field of turbomachinery CFD include the progression from inviscid to viscous, and from two-dimensional to three-dimensional analysis. With these advances it now appears possible in some cases, particularly for isolated blade rows, to apply computational methods and obtain reasonable predictions of blade row performance and efficiency [54].

As is generally known, three-dimensional CFD methods require more extensive computer resources than similar two-dimensional methods. Viscous three-dimensional CFD simulations are particularly demanding, even for steady flow calculations in an isolated blade row. The additional fluid dynamic information gained from such simulations, however, can often justify the increased expenditure, depending on the problem being investigated and the availability of computer resources. Fortunately, rapid progress in the computer industry has made the application of viscous three-dimensional CFD codes fairly practical.

Several CFD codes have been applied in the analysis of the baseline SSTF [27]. Included are codes by Chima [42,54-56], Jorgenson and Chima [57], Denton [58], and Whitfield, et al. [59]. The CFD codes of Chima have been applied extensively by the author as an integral part of this work, and so general descriptions of these codes are provided in this chapter. Basic information concerning the type, formulation, and application of the codes is included, as are descriptions of typical computational grids used with the codes.

Three different codes are discussed:

- RVCQ3D, a quasi-three-dimensional viscous code for turbomachinery [42].
- RVC3D, a three-dimensional viscous code for turbomachinery [54,55].
- DVC2D, a two-dimensional viscous code for planar and axisymmetric duct flows.

The latter code was developed by Chima and Tweedt (unpublished), and was used for computations of the inlet nozzle flow as reported in Appendix A.

All three CFD codes are similar in terms of their computational schemes, scheme implementation, and structure. In fact, the axisymmetric duct code was developed directly from the quasi-three-dimensional turbomachinery code, also borrowing parts and techniques from the three-dimensional turbomachinery code. Due to code similarities a general description pertaining to all three codes will be covered first, followed by specific details relevant to each code.

Description of Codes

The RVCQ3D, RVC3D, and DVC2D codes are all finite difference formulations of the Reynolds-averaged, thin-layer Navier-Stokes equations, where the thin-layer approximation is made in the streamwise direction, i.e., the streamwise viscous terms are neglected. Second-order central finite differences are used in an explicit multistage (usually four-stage) Runge-Kutta time-marching scheme. For stability, fourth-difference artificial dissipation terms are added, and for shock capturing, second-difference artificial dissipation terms are added. Implicit residual smoothing and a spatially-varying time step are normally used to accelerate convergence to a steady-state condition, although unsteady flow simulations can also be performed using a spatially-uniform time step (time-accurate integration). All of the codes can also be used to integrate the Euler equations simply by neglecting the viscous terms. An algebraic, eddy-viscosity turbulence model is used for closure of the Reynolds-averaged equations, with two turbulence models optionally available: the Baldwin-Lomax model [60] or a modified form of the Cebeci-Smith model [1] [61]. The equation of state for a perfect gas is employed in dimensionless form, and the power law is used for laminar viscosity.

---

[1] The Cebeci-Smith model was only introduced into the codes as this work neared completion, and so it was not applied in most cases.

RVCQ3D code

The quasi-three-dimensional blade-to-blade turbomachinery code, RVCQ3D, is applicable to single blade passages and solves a two-dimensional form of the Navier-Stokes equations as formulated along an axisymmetric stream surface. Local stream surface radii and corresponding stream-tube heights are input as a function of streamwise distance, so that the effects of rotation, radius change, and stream-tube thickness are modeled in the analysis. In a standard application of the code this stream surface information might be obtained, for example, from an axisymmetric throughflow calculation as part of a design or an analysis procedure.

The code uses body-fitted C-type computational grids which are normally generated using a version of the GRAPE code developed by Sorensen [62]. The physical (m,θ)-coordinates [2] of the blade-to-blade periodic grid are mapped to body-fitted computational (ξ,η)-coordinates by using standard methods.

The inlet and exit boundary conditions can each be either axial-subsonic or axial-supersonic. The method of implementing axial-subsonic boundary conditions is described in Reference 42. Briefly, at the inlet it involves specifying the total pressure, total temperature, and tangential velocity at the boundary, and extrapolating the upstream-running Riemann invariant from the interior. At the exit, the static pressure is specified and the density and momentum conservation variables are extrapolated from the interior. The method of implementing axial-supersonic boundary conditions is simpler: at the inlet *all* quantities are held constant at their initial values, and at the exit all of the conservation variables are extrapolated from the interior.

RVC3D code

The three-dimensional turbomachinery code, RVC3D, is applicable to single blade passages involving either Cartesian or cylindrical geometries. The Navier-Stokes equations are formulated in a Cartesian coordinate system with the (x,y,z)-coordinates mapped

---

[2] The meridional coordinate m is defined such that $dm^2 = dx^2 + dr^2$. The circumferential coordinate θ is an angle such that $\theta = \theta_0 - \Omega t$, where θ_0 is fixed in space, Ω is the rotational speed, and t is time.

to general body-fitted (ξ,η,ζ)-coordinates. The coordinate system rotates with angular velocity Ω about the x-axis. C-type computational grids, which are basically the same as the type used for the RVCQ3D code, are stacked in the spanwise direction. A three-dimensional grid generation program, TCGRID (unpublished, but see Reference 54 for a brief description), which internally incorporates a version of the GRAPE code, is used to generate the grids.

Inlet and exit boundary conditions are applied in a manner similar to that in the RVCQ3D code, except that for axial-subsonic boundary conditions the formulations are slightly more complex due to the third (spanwise) dimension. For axial-subsonic conditions at the exit, the *hub* static pressure is specified, and simple radial-equilibrium is solved as part of the exit boundary condition in order to determine the remaining exit static pressures. A more complete description of how both the inlet and exit boundary conditions are implemented can be found in references 54 and 55.

DVC2D code

The two-dimensional duct code, DVC2D, can be used to simulate compressible fluid flows in two-dimensional planar duct geometries or in three-dimensional axisymmetric duct geometries. In either case the grids are two-dimensional and the physical coordinates (x,y or x,r) are mapped to body-fitted computational (ξ,ζ)-coordinates. For axisymmetric cases the circumferential angle θ is mapped to the computational direction η, such that $\eta = \theta$. Although the code and its development are presently undocumented, the general formulations of the axisymmetric thin-layer Navier-Stokes equations used in the code were obtained from the work of Nietubicz, et al. [63].

Computational grids for the code can be obtained using a variety of grid generation programs. For the present work the grids were generated using an interactive grid generation program, TIGGERC, developed at the Lewis Research Center [64]. Inlet and exit boundary conditions are handled in a manner similar to that in the turbomachinery codes; for example, simple radial-equilibrium is solved at the exit boundary for axial-subsonic axisymmetric flows.

Application of Codes

A variety of computational grids have been employed in conjunction with the many CFD solutions presented in this work, and so an exhaustive description of all of them would be impractical. Most of the grids of a particular type have several basic similarities, including grid density, and so a few examples suffice to describe the different grids used. With this in mind, a few representative grids for each code are presented, and some related computational details are discussed. Note that the grids are presented here, rather than with the CFD solutions, to minimize distractions from discussions of the results.

RVCQ3D computations

Computational results obtained using the RVCQ3D code involved, by far, the largest variety of grids and flow conditions. Furthermore, a relatively large time span was associated with the various applications of this code so that different solutions sometimes reflect different versions of the code as improvements and modifications were implemented into it. The impact of the code variations was generally small, however, appearing mostly as minor perturbations in the viscous regions of the flow field, and therefore in the computed total pressure losses and efficiencies. For virtually all of the presented results these perturbations were well within the general approximation of the quasi-three-dimensional approach. In all cases the Baldwin-Lomax turbulence model was used with original values for the constants in the model [42,60].

Most of the CFD work using RVCQ3D involved axial-supersonic rotor exit conditions, although a few cases with axial-subsonic exit conditions were also examined. All of the rotor aerodynamic simulations were performed assuming sea-level-standard total conditions far upstream and in the absolute frame of reference; that is, all simulations were at corrected flow and rotational speed conditions. Only steady-flow simulations were performed, although it would have been possible to simulate unsteady rotor/stator interactions using a code by Jorgensen and Chima [57,] which is an extension of the RVCQ3D code. Note that when the flow at the rotor exit is axial-supersonic, the rotor flow field is not coupled to the stator flow field (through potential flow effects); that is, flow "information" propagates downstream only, and the rotor flow field is steady and independent of whether the rotor is isolated or in a stage configuration.

In general, grid sizes were on the order of 200 to 400 nodes in the ξ-direction (streamwise direction) and 45 to 49 nodes in the η-direction (surface normal direction). Note that for the C-type grids used here the 45 to 49 nodes implies 89 to 97 nodes, respectively, blade-to-blade. An example of a rotor pitchline [3] grid with dimensions 385×49 is shown in Figure 4.1. The grid density apparent in this figure is relatively high, allowing good resolution of oblique shock waves. A commonly-used rotor pitchline grid with smaller dimensions 257×45 is shown in Figure 4.2. The density of this grid is similar to that of the other grid, despite the smaller dimensions, because it also involved much less downstream extension. Grid spacing at and normal to the blade surface was generally between 0.0002 and 0.0005 inches, which for most flow conditions and turbulent boundary layers put at least one internal grid line within the viscous sublayer of the turbulent boundary layer. For cases where several spanwise locations were investigated — usually a near-hub, pitchline, and near-tip streamline — all of the grids were similar except for the basic differences in the blade geometry.

Formal studies to determine whether or not particular CFD solutions were grid-independent have not been performed, although several informal studies were done and a considerable amount of experience was gained in using the RVCQ3D code for a variety of related flow cases and different grid densities. These factors lead the author to infer that increased grid-densities would not substantially alter the computed results, at least in terms of integrated flow properties and performance parameters. Higher grid densities would improve the resolution of certain local flow features, for example shock waves, but in general would not be expected to have a large impact on global (integrated) flow properties. It is believed that for the cases studied, the limitations of the code due to turbulence modeling and boundary-layer-transition effects probably exceed those related to grid density.

The informal grid studies revealed certain key aspects of the computational grids which should be controlled in order to insure some degree of grid independence. In general it was determined that the grid spacing in the ξ-direction was relatively unimportant

---

[3] Pitchline refers in this case to the axisymmetric streamline representing 50 percent of the total mass flow, as determined either from the design code or from three-dimensional viscous CFD solutions.

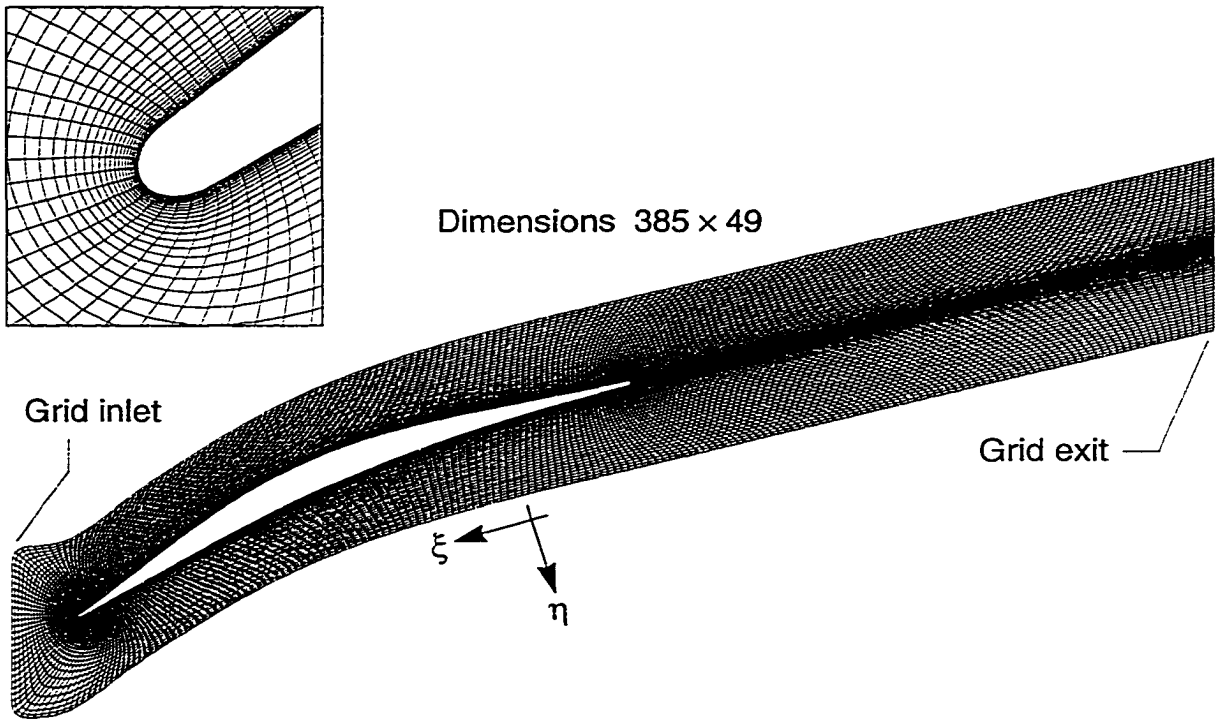

Figure 4.1 Rotor pitchline grid for RVCQ3D viscous computations (extended grid)

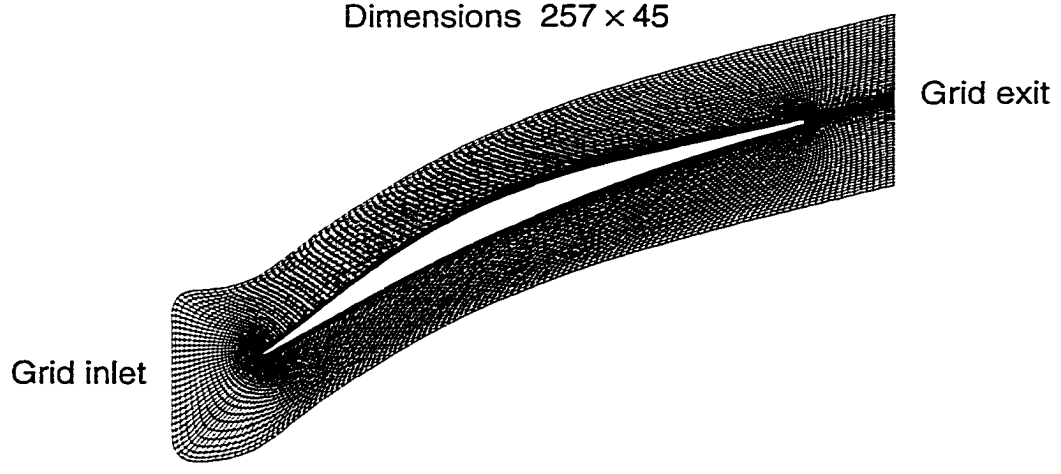

Figure 4.2 Rotor pitchline grid for RVCQ3D viscous computations (short grid)

in terms of integrated flow quantities, whereas the spacing in the η-direction *within the boundary-layer regions* was important. Near the wall boundaries at least one or two grid ξ-lines should be within the viscous sublayer (for turbulent boundary layers), and beyond that the grid should be only moderately stretched in the η-directions with around 20 (or more) grid ξ-lines within the turbulent layer. When these conditions were met, the solutions examined were nearly grid independent in terms of integrated performance and flow properties.

Execution of the code on a Cray X-MP computer normally involved less than one Mword of core memory, and a solution with 2000 iterations on a 385×49 grid required just under 6 CPU minutes. Convergence histories, especially in terms of density residuals, varied dramatically from case to case depending on the flow field, but they usually were well-behaved. The more recent versions of the code exhibited better convergence characteristics, and flow simulations involving supersonic throughflow velocities tended to converge better and faster than those involving subsonic throughflow conditions. An example of the convergence history for a supersonic throughflow rotor computation at the pitchline and for the design operating condition is shown in Figure 4.3. In this case the reduction in the density residuals was not very good, as is often the case for viscous computations [4], but the solution still "converged" in terms of global parameters, e.g., the total-pressure loss coefficient. The solution of Figure 4.3 was run on an SGI 4D/440 workstation (four RISC 4000 CPU's in parallel), and required about 35 CPU minutes for 2000 iterations on a 385×49 grid.

RVC3D computations

The steady-flow CFD solutions obtained for the rotor by using the RVC3D code involved three different grids. Although different three-dimensional grids were involved, they all had similar grid densities in all three directions, and most of the comments made

---

[4] Local instabilities (unsteadiness effects) in the viscous regions cause the associated local residuals to remain fairly large. Sometimes only a very minor change in flow conditions (on the same grid) can cause the instabilities to disappear, with a subsequent drop in the residuals by several orders of magnitude.

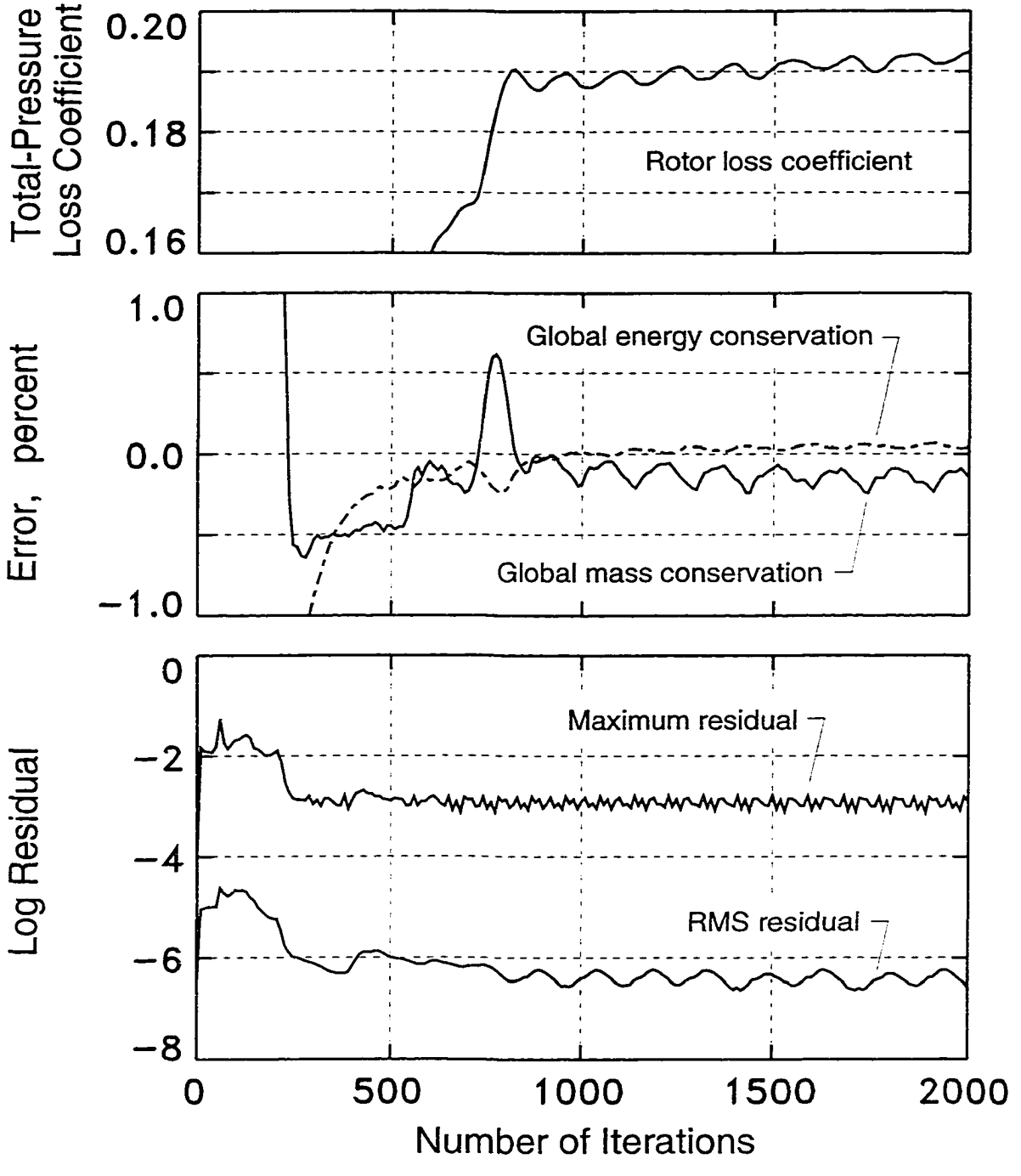

Figure 4.3 Convergence history of an RVCQ3D viscous computation for the rotor at the design operating condition

above regarding grid densities for the quasi-three-dimensional code also apply to the RVC3D code. The influence of grid density will therefore not be discussed in connection with the three-dimensional CFD analysis.

Seven different rotor operating points have been simulated using the RVC3D code, five of which involved axial-supersonic velocities throughout. The other two operating points had axial-subsonic flow into the rotor, but axial-supersonic velocities within and downstream of the rotor [5]; that is, all simulations involved an axial-supersonic exit boundary condition. Of the three rotor grids, one, designated RG-A, was used for four of the five supersonic throughflow cases, including the design operating point [6]. The other two rotor grids were very similar to it, except that they did not extend as far downstream. As with the quasi-three-dimensional code, all aerodynamic simulations were performed for corrected flow and rotational speed conditions.

The rotor grid RG-A had dimensions $281 \times 45 \times 60$ and is shown in Figure 4.4. The last dimension of 60 is in the spanwise ζ-direction. This grid extends fairly far downstream of the blade row to an axial location of 8.513 inches (relative to the rotor hub leading edge), as illustrated in Figure 4.5, allowing direct comparisons with the experimental rake data at the axial location of 7.840 inches. The grid spacing at the hub and casing endwalls was 0.0005 and 0.0010 inches, respectively, and the spacing at the blade surface was 0.0003 inches. These spacings allowed proper resolution of the near-wall viscous flows by including at least one internal grid line well within the viscous sublayer for all rotor operating points which were simulated. Note, however, that no fillets were modeled at the blade-hub intersections, although fillets existed for the experimental rotor geometry.

The other two rotor grids, designated RG-E and RG-S, had dimensions $201 \times 45 \times 60$, where the ξ-dimension of 201 does not imply a grid density lower than that of the larger grid with 281 nodes, but rather it corresponds to a shorter axial grid length, where both grids extended downstream to the axial location 5.213 inches as indicated in Figure 4.5.

---

[5] This operating mode is designated in Chapter 5 as *impulse-type* operation.

[6] For possible later reference, the four supersonic throughflow operating points were the following: axial inflow Mach number 2.0 at rotational speeds 75 and 100 percent of design speed, and axial inflow Mach number 1.4 at rotational speeds 75 and 100 percent of design speed.

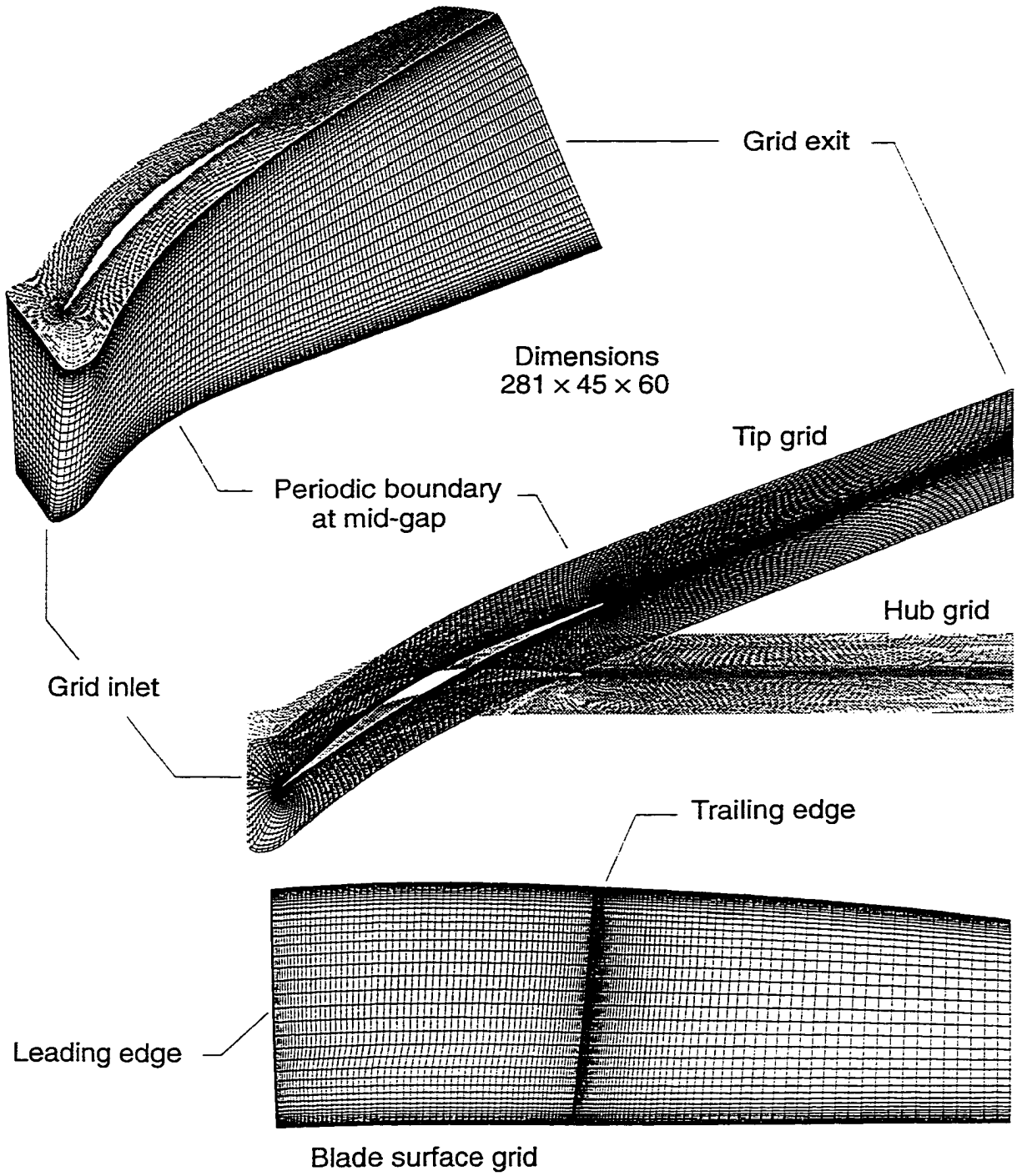

Figure 4.4 Three-dimensional rotor grid RG-A for RVC3D viscous computations

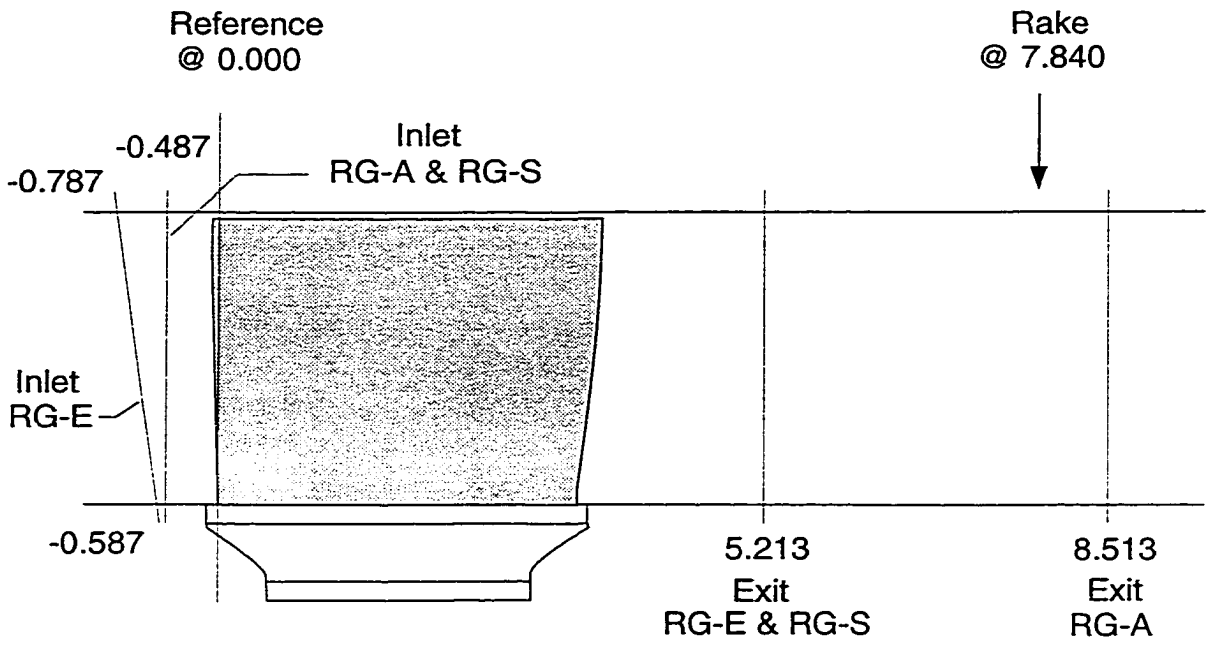

Figure 4.5 Axial locations of the grid inlet and exit stations for the three-dimensional rotor grids (dimensions in inches)

In other respects all three rotor grids were nearly the same. The difference between the two shorter grids is that one (RG-E) extended slightly farther upstream than the other (RG-S), the former grid being used in the two (impulse-type) cases with axial-subsonic rotor inflow velocities [7], and the latter being used for a single supersonic throughflow computation [8].

All of the rotor simulations except the design point were computed with a zero tip clearance; that is, the blade scraped along the casing with no clearance. The simulations

---

[7] One impulse-type simulation for 75 percent of design rotational speed, and the other for 100 percent of design rotational speed.

[8] Simulation for 50 percent of design rotational speed at axial inflow Mach number 2.0.

were done using earlier versions of the RVC3D code which did not have a model for tip clearance. The design point simulation was also originally computed with no tip clearance model, and was then recomputed later, after the model was added, using the design tip clearance value of 0.010 inches (0.33 percent span). No significant effect on integrated performance due to the clearance was observed for the CFD solution, which is not surprising considering the tight clearance and the high throughflow velocities.

The rotor aerodynamic simulations with axial-supersonic inflow velocities involved specifying the spanwise distribution of all inlet flow quantities. The basic form of the spanwise velocity profile consisted of a uniform inlet flow with compressible turbulent (flat plate) boundary layers at the hub and casing endwalls. In specifying the profiles it was necessary to estimate the endwall boundary layer thicknesses for the supersonic (nozzle exit) flow entering the rotor. Only two axial-supersonic inflow conditions were simulated, namely, Mach 1.4 and 2.0, for which cases the endwall boundary layers were estimated to be about 0.25 and 0.20 inches thick (8.3 and 6.7 percent span), respectively. Note that both the hub and the casing boundary layers were assumed to have the same thickness.

Computational results for the nozzle flow field could have directly provided the supersonic upstream boundary conditions for the rotor simulations; however, subsequent analysis of the nozzle flow field using the DVC2D code [9] (see Appendix A) revealed that the above estimates were reasonable, so no refinements were attempted. The spanwise Mach number profiles used in the rotor computations are graphed in Figure 4.6, where they can also be compared with the profiles obtained from DVC2D computations of the nozzle flow.

Axial-subsonic inlet boundary conditions for the rotor were provided by loosely coupling the RVC3D analysis with a CFD analysis of the inlet duct using the DVC2D code. This is discussed later, in the next subsection.

The RVC3D code was in all cases executed on the Cray Y-MP computer where adequate storage was available and execution speeds were relatively fast. Solutions on the

---

[9] Most of the three-dimensional CFD work preceded the development of the DVC2D code.

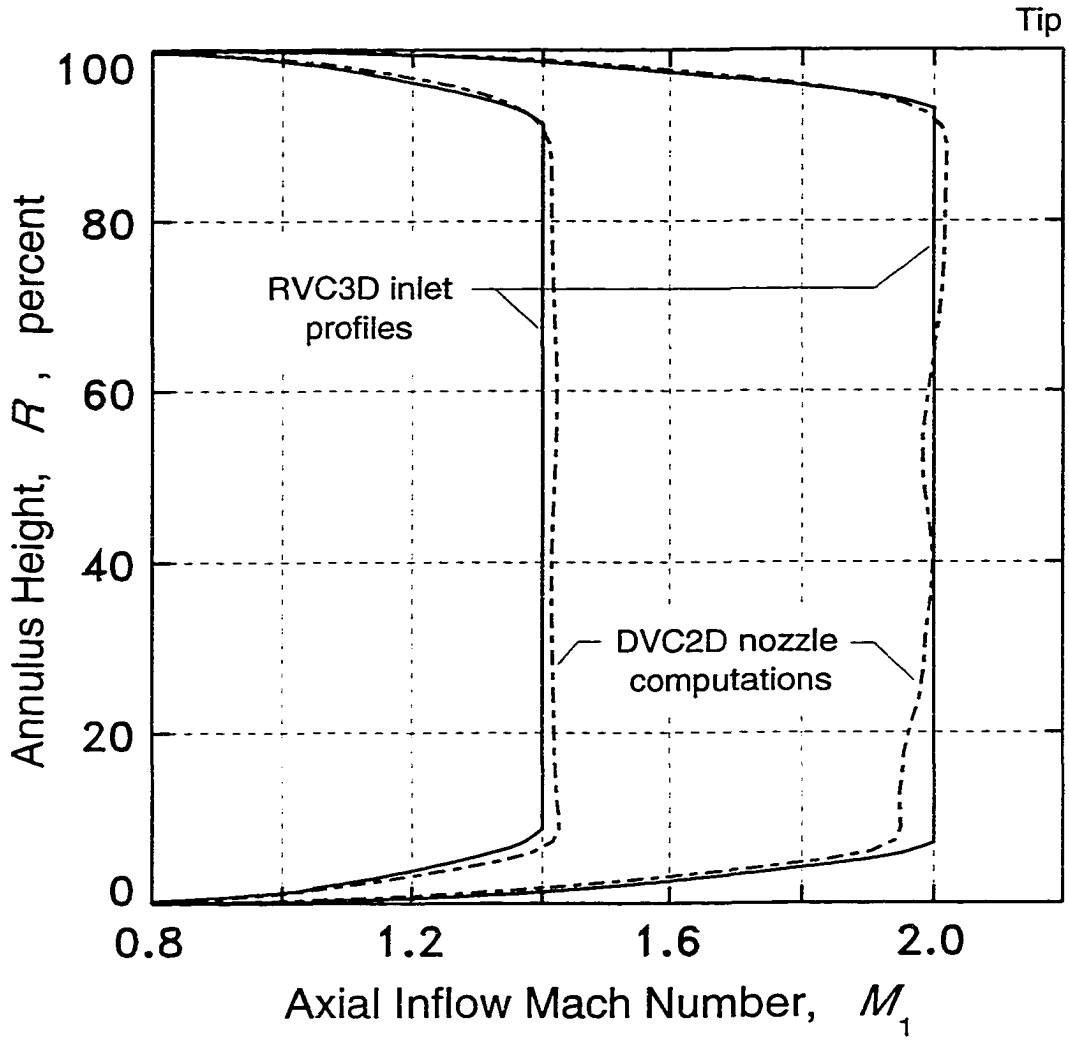

Figure 4.6 Spanwise Mach number distributions at the rotor grid inlet for RVC3D viscous computations with supersonic throughflow velocities

$281 \times 45 \times 60$ rotor grid RG-A required about 21 Mwords of core memory [10], and 295 CPU minutes for the typical 1800 iterations needed to insure convergence. The convergence history [11] for the design-point rotor simulation is shown in Figure 4.7.

To conclude this subsection on the RVC3D code, a few comments regarding the turbulence model should be made. First, in all rotor computations except for the design operating point the Baldwin-Lomax model [60] with original values for all constants was used [12]. Further research [61] and some (undocumented) computational studies performed subsequent to most of the baseline rotor CFD analysis revealed that an adjustment to the parameters C_{Kleb} and C_{cp} yielded more accurate solutions for flat-plate boundary layers. The new parameter values are

$$C_{Kleb} = 0.646 \tag{4.1}$$

$$C_{cp} = \max\,(1.216,\ 0.8M_e) \tag{4.2}$$

where M_e is the local Mach number at the edge of the boundary layer. Notice in Equation (4.2) that C_{cp} has a constant value of 1.216 for local Mach numbers less than 1.52. The adjustment for higher Mach numbers is only a first-order approximation and was determined from computations of turbulent boundary layers on a flat plate with freestream Mach number 2.4. Comparisons between experimental [65] and computed Mach number profiles in the wake region of the boundary layer indicated that a value of 3.0 was significantly better, at free-stream Mach 2.4, than the value of 1.216 recommended for subsonic

---

[10] The code could also be executed using a solid-state storage device (SSD) to reduce the necessary amount of core memory. Using the SSD the same solution required under 14 Mwords of core memory, but CPU requirements were greater due to the additional I/O operations.

[11] The convergence history shown for the rotor is the result of a "restarted" simulation from an already converged solution, but for different constants in the Baldwin-Lomax turbulence model.

[12] The Cebeci-Smith model of Reference 61 behaved poorly in the near-wall shear-flows produced on the blade surfaces downstream of the curved bow-shock wave. In the SSTF blade rows a bow shock wave normally exists due to relative inflow Mach numbers which are supersonic, at levels usually exceeding Mach 2.

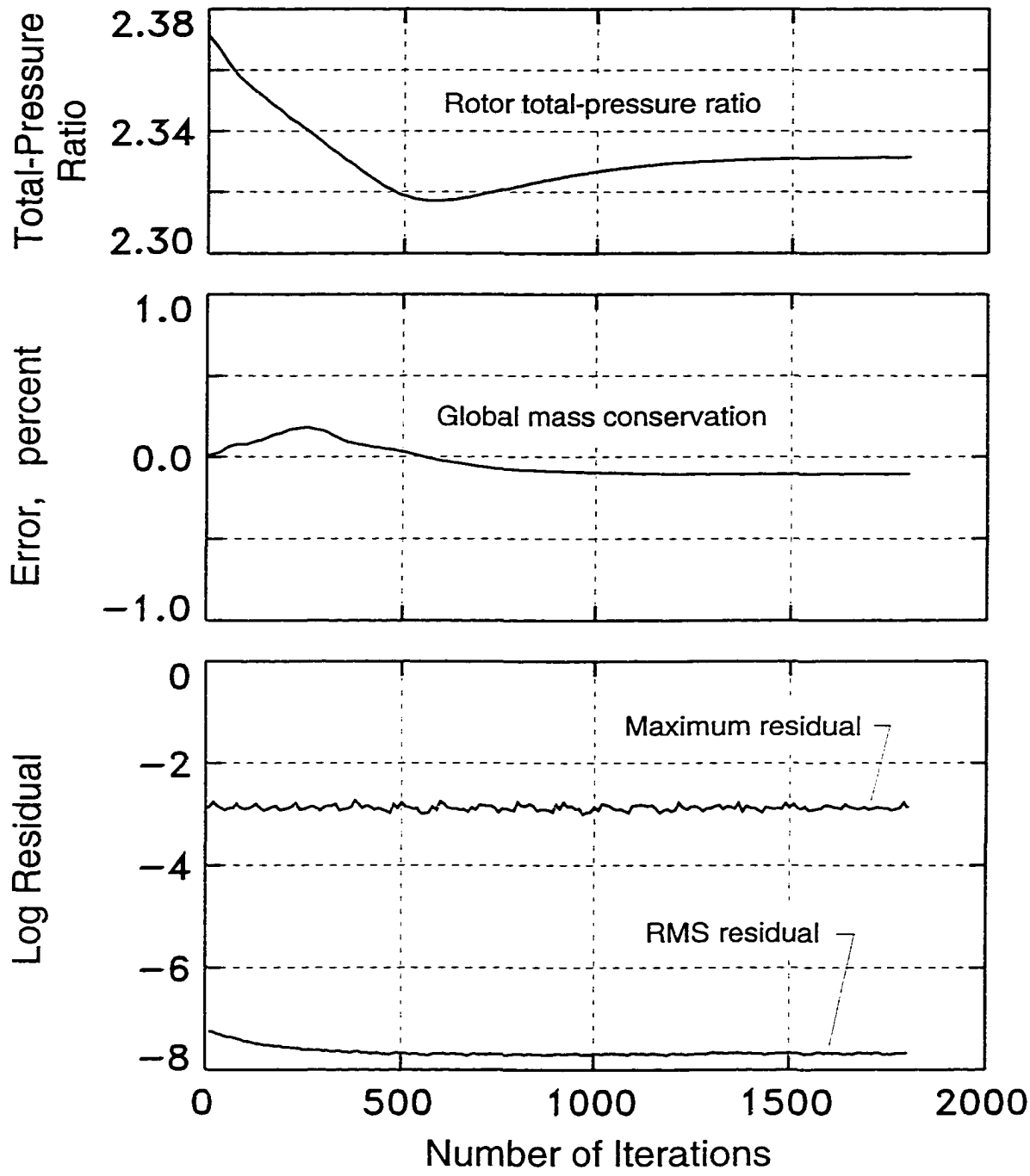

Figure 4.7 Convergence history of the RVC3D viscous computation for the rotor at the design operating condition (simulation restart at zero iterations)

(incompressible) boundary layers [61]. The general effect of increasing C_{cp} at the higher Mach numbers was to increase the turbulent eddy viscosity in the outer region, generating a thicker boundary layer with more total-pressure loss. The new parameters were used to recompute the design-point solution for the rotor, the convergence history for which is shown in Figure 4.7.

DVC2D computations

The DVC2D code was applied to the axisymmetric inlet nozzle in order to compute the flow fields for subsonic and supersonic nozzle operation. During supersonic operation the nozzle flow field is virtually independent of the downstream conditions, i.e., the rotor inlet flow field, thus allowing the nozzle and rotor components to be analyzed independently. During subsonic operation the "nozzle" functions as an inlet duct, and the flow field in the duct is dependent on the downstream pressure. The results of this subsonic analysis are, therefore, closely related to the rotor inlet flow field.

For supersonic nozzle operation five different computational grids were used to analyze five different operating points, as discussed in Appendix A. In all five cases the grids were similar except for differences in the nozzle hub geometry, corresponding to different nozzle centerbody positions (see Appendix A). Therefore only one of the grids is shown, in Figure 4.8, which contains the design-flow-condition grid for the centerbody located 6.22 inches downstream of the fully-open (reference) position. The grid dimensions were 165×75, with a wall-normal grid spacing of 0.0005 inches at each endwall.

The nozzle inlet and exit boundary conditions for supersonic operation were of the (axial-) subsonic and supersonic types, respectively. At the grid inlet, profiles for total pressure and total temperature were specified, where the profiles consisted of a free-stream flow with uniform total pressure and total temperature, and turbulent boundary layers at each endwall. The endwall boundary layers were specified to be 0.25 inches thick, which was somewhat arbitrary but relatively unimportant. The free-stream total conditions were equivalent to sea-level-static conditions, and the same inlet flow profiles were specified for all five cases. Tangential velocities were zero, and the flow direction in the meridional plane was aligned with the ξ-lines at the grid inlet boundary.

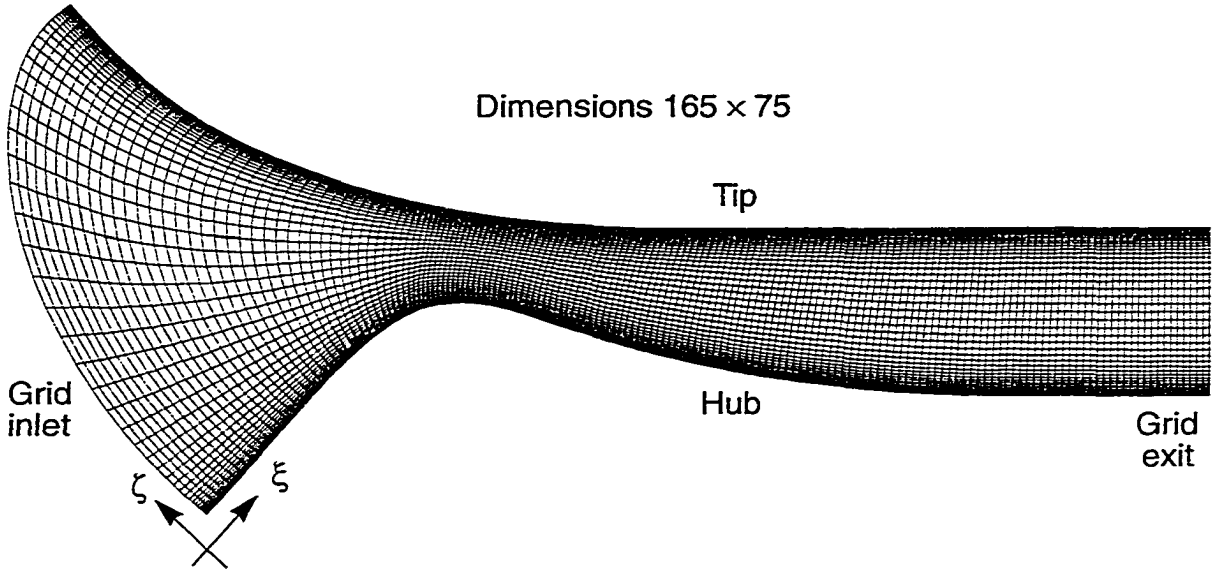

Figure 4.8 Nozzle grid for DVC2D viscous computation at the design flow condition (Mach 2.0 at nozzle exit; centerbody translated 6.22 inches downstream)

For subsonic nozzle operation the grid inlet boundary condition was identical to that just described, with the same values being used for all quantities specified. At the grid exit, however, an axial-subsonic type of boundary condition was also required, thus involving a specification of static pressures at that boundary. It was recognized that the static pressure field at the nozzle exit was the same as the field at the rotor inlet, and so an approach was taken to couple, albeit only loosely, the nozzle exit and rotor inlet flow fields of the respective CFD simulations; that is, the nozzle grid exit static-pressure distribution was obtained from the rotor inlet flow field, and the appropriate rotor grid inlet boundary quantities [13] were obtained from the nozzle exit flow field. The coupling of the nozzle and rotor CFD solutions was accomplished by alternately applying both codes (RVC3D and DVC2D) at a fairly low coupling-frequency, typically 150 RVC3D iterations to 1000

[13] These quantities were total pressures, total temperatures, tangential velocities (which were zero in this case), and the meridional flow directions.

DVC2D iterations (internal to each), repeated about 10 times until the rotor solution converged. A slight overlapping of the rotor and nozzle grids was conveniently employed, as illustrated in Figure 4.9, and it was necessary to circumferentially average [14] the rotor inlet flow field to match it with the axisymmetric nozzle flow field. Notice in Figure 4.9 the use of the term *pseudo grid inlet*, which is not the actual rotor grid inlet, but instead corresponds to the plane in the inlet region where the outer boundary of the rotor grid first becomes "periodic" in the circumferential direction, i.e., the computational domain first becomes continuous and periodic in the circumferential direction.

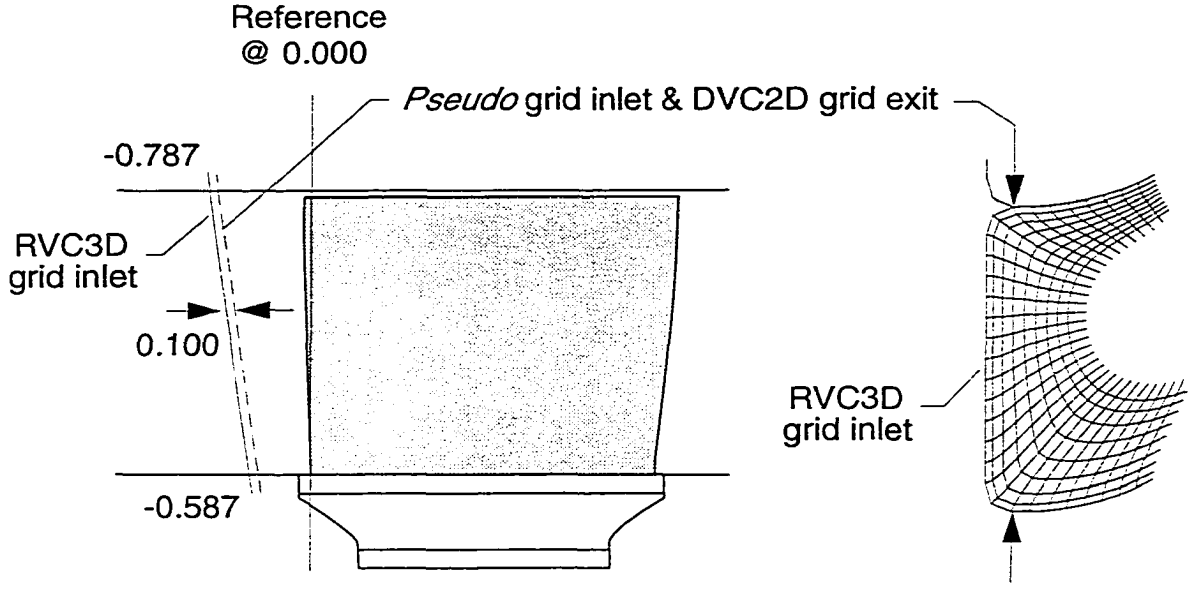

Figure 4.9 Overlapping of nozzle and rotor grids for coupled DVC2D and RVC3D viscous computations (dimensions in inches)

[14] The *entropy-averaging* procedure (see Appendix C) was used. The circumferential gradients at the rotor inlet averaging plane are small, however, so that the exact method of averaging is not critical.

Two different grids were used for computations of "subsonic" nozzle flows: one corresponding to the nozzle in the fully-open configuration and therefore involving wholly subsonic flow fields, and the other corresponding to the nozzle centerbody located 2.44 inches downstream of the fully-open position. The latter grid was used to compute a supercritical "shock-in-nozzle" condition, encountered during the nozzle starting process. The supercritical condition involved subsonic and supersonic flows within the (choked) nozzle, with subsonic flow at the nozzle exit. Dimensions of the first grid, for the fully-open configuration, were 150×65, and at each endwall the wall-normal spacing was 0.0010 inches. The second grid had dimensions 200×75, with a wall-normal grid spacing of 0.0005 inches at each endwall.

Execution of the DVC2D code was normally done using the Cebeci-Smith type of turbulence model, although the Baldwin-Lomax model produced nearly the same results when the constants in the model were adjusted to the values suggested in Reference 61. Convergence characteristics were similar to that of the other two CFD codes, being often better for the DVC2D solutions due to less complex viscous regions in the nozzle flow fields. The convergence history for the design-point (exit Mach number 2.0) nozzle computation is shown in Figure 4.10. Computer requirements were relatively small, with the code normally using less than one Mword of core memory. Solution times on an SGI 4D/440 workstation were about 25 CPU minutes for 2000 iterations on a 165×75 grid. When coupling the code with the RVC3D code on the Cray Y-MP, solution times for the DVC2D code were small compared to those for the three-dimensional code. For example, 1000 iterations on the 200×75 nozzle grid required under 2 CPU minutes, compared to about 20 CPU minutes for 150 iterations on a $201 \times 45 \times 60$ rotor grid.

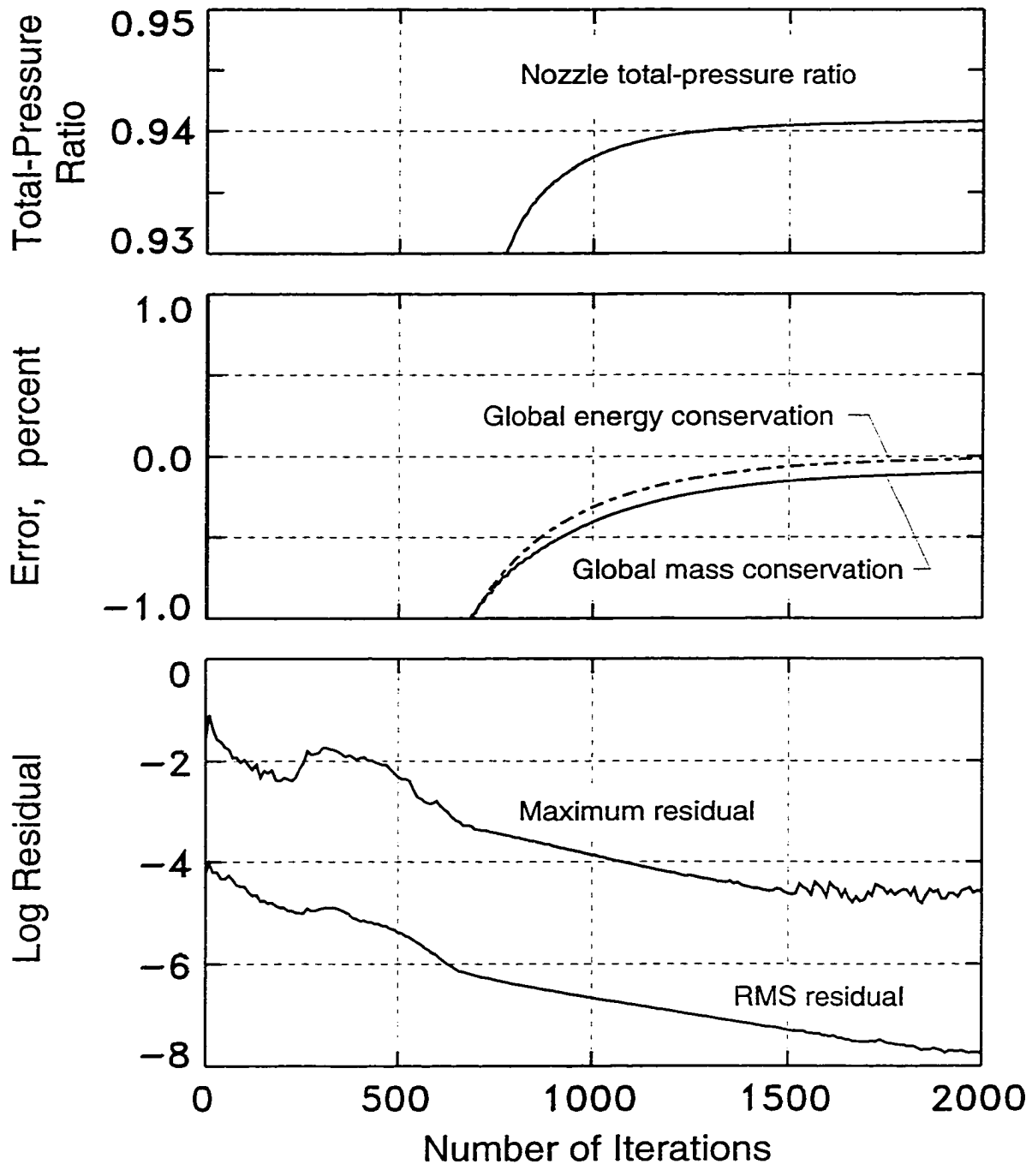

Figure 4.10 Convergence history of the DVC2D viscous computation for the nozzle flow field at the design operating condition

CHAPTER 5.
ROTOR OPERATING CHARACTERISTICS AND PERFORMANCE

Results from analytical and experimental research performed on the baseline SSTF rotor are discussed in this chapter. One-dimensional gas dynamic analyses, CFD simulations, and experimental results are all presented in an effort to describe and quantify the basic gas dynamic and aerodynamic features, the operating characteristics, and the performance of the baseline rotor.

The steady-state operating modes of a supersonic throughflow rotor can be conveniently classified into four basic types depending on whether the throughflow conditions at the inlet and exit of the blade row are axial-subsonic or axial-supersonic. The rotor operating modes and the terminology used to *define* them are listed in Table 5.1.

Table 5.1 Rotor operating modes

Operating Mode	Rotor Inflow	Rotor Outflow
subsonic throughflow	axial-subsonic	axial-subsonic
impulse-type	axial-subsonic	axial-supersonic
shock-in-rotor	axial-supersonic	axial-subsonic
supersonic throughflow	axial-supersonic	axial-supersonic

It should be carefully noted that by definition the term *subsonic throughflow* refers only to conditions where the blade-row inlet and exit velocities are axial-subsonic, although in many such cases axial-supersonic velocities exist within the blade row. Also, for the sake of brevity the terms *impulse-type* and *shock-in-rotor* are used here in a more restricted sense than usual. That is, their usage is as specifically defined in Table 5.1, even though the terms can generally apply to other operating modes. Two cases are particularly

relevant in this regard: supersonic thoughflow operation which can also generally be classified as an impulse-type mode; and subsonic throughflow operation which at higher rotational speeds almost always involves a shock-in-rotor condition.

All four rotor operating modes are addressed in this chapter. In addition to discussing the performance and steady-state operating characteristics of the rotor in the different modes, the aerodynamic aspects of rotor inflow transition from axial-subsonic to axial-supersonic conditions, and vice versa, are addressed at length. By way of definition, the process of inducing axial-supersonic rotor inflow conditions is termed *rotor inflow starting*, and the reverse process is termed *rotor inflow unstarting*. In the experimental facility, rotor inflow starting involves the final phase in the supersonic starting of the upstream nozzle, whereas in an aircraft propulsion system rotor inflow starting can coincide with the starting of the engine inlet [1].

This chapter is divided into several major sections. These sections are listed below in the order of their presentation:

- One-Dimensional Steady-Flow Analysis
- Subsonic Throughflow Operation
- Axial-Subsonic Rotor-Inflow Characteristics
- Rotor Inflow Starting and Unstarting
- Impulse-Type Operation
- Supersonic Throughflow Operation
- Shock-in-Rotor Operation

Before proceeding, several comments are in order regarding the general nature of the experimental and computational results. Many subtle, yet important assumptions are implicit in the majority of data which are presented and compared. In particular, all of the experimental data and any averaged forms of computational data involve important assumptions which are often ignored. One of the primary issues concerns the type of cir-

---

[1] The process involved in rotor inflow starting depends on the type of primary inlet. One possibility, the so-called *ground-start system*, would involve rotor inflow starting while the aircraft is on the ground. A more likely possibility, the so-called *air-start system*, would involve starting the rotor inflow and the inlet simultaneously, or nearly so, during supersonic flight.

cumferential, or blade-to-blade, averaging being affected, either directly or indirectly. The experimental data typically involve some form of circumferential-averaging resulting from the process of acquiring the data, from the method of reducing the data, or from both, such that the *type of average* represented by the data is uncertain. This is especially true for slow-response aerodynamic measurements downstream of a rotating blade row. The computational results, on the other hand, are averaged using a known, well-defined method so that the uncertainty does not lie in the type of average, but rather in the computed flow solution itself. Due to the relevance of these and other related issues, some discussion is provided in Appendix B which examines some of the problems encountered in attempting to make a valid comparison between the CFD and experimental results. A brief description of averaging methods for CFD solutions is provided in Appendix C.

One-Dimensional Steady-Flow Analysis

The general operation of the basic system consisting of nozzle, rotor, and diffuser can be described in a relatively simple way by using a one-dimensional steady-flow gas dynamic model. This model is especially useful for showing the system changes associated with the transition between different operating modes, as well as for providing a first-order theoretical basis for understanding and quantifying the rotor and system behavior. A general understanding of one-dimensional gas dynamics by the reader is assumed in the following discussion, particularly as it relates to supersonic wind tunnel starting behavior and theory. For more information on gas dynamic and compressible flow theory, see for example References 66 to 68.

A one-dimensional model of the SSTF (rotor only) is illustrated in Figure 5.1, where five components are depicted; namely, the plenum, nozzle, rotor, diffuser, and collector. Three locations where an area reduction potentially exists are also indicated: the nozzle minimum area N, which exists only when the nozzle is in a converging-diverging (c-d) configuration; the rotor minimum area R, which effectively varies with rotational speed; and the diffuser minimum area D near the diffuser exit, which exists for all but "wide open" diffuser settings.

During normal testing in the experimental facility the plenum total pressure was near standard sea-level pressure, while the static pressures in the downstream collector were relatively low at about 20 percent of standard pressure. A total-to-static pressure ratio, therefore, of about five-to-one from plenum to collector required that at least one of the smaller areas be choked at any given time. Initially, during facility start-up, choking occurred at the diffuser throat *D*, which made the diffuser throat the test facility throttle regulating the mass flow.

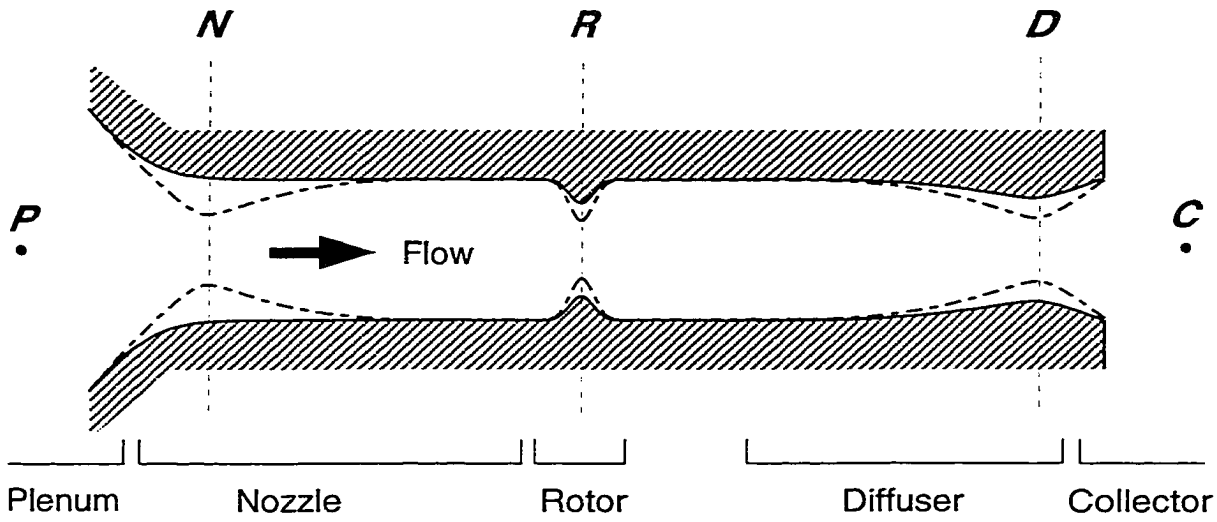

Figure 5.1 One-dimensional model of SSTF test section for the isolated rotor

Subsonic throughflow operation

The general flow conditions corresponding to low-speed, throttled-rotor operation are depicted in Figure 5.2, which represents subsonic throughflow rotor operation. The collector shock normally exists to match the diffuser exit flow to the subsonic, low-pressure collector flow. In the experimental facility this matching occurs through a complex structure of oblique and normal shock waves, shock/boundary-layer interactions, and separated flows at the diffuser exit where the flow dumps into the collector. Only at considerably higher collector static pressures (or lower plenum total pressures) would this exit shock-system not exist, in which case the diffuser exit flow would be entirely subsonic.

Strictly speaking, the flow situation indicated in Figure 5.2 only exists for the baseline rotor at the lower rotational speeds (below around 60 percent of design speed). And even at the lower speeds the situation ceases to exist when the rotor is sufficiently un-throttled by opening the diffuser throat *D*. That is, opening the diffuser causes the mass flow to increase until the rotor chokes, at which condition there becomes two choked areas in the system — one in the rotor and one at the diffuser exit — and the regulation of mass flow shifts upstream to the rotor throat *R*. Opening the diffuser further causes the formation of a "normal" shock in the rotor, downstream of the rotor throat, as depicted in Figure 5.3.

At higher rotational speeds (75 percent and above) the flow enters the baseline rotor with supersonic blade-relative velocities, and rotor choking and normal-shock formation occur as a natural consequence of the rotor inflow conditions. Therefore the situation

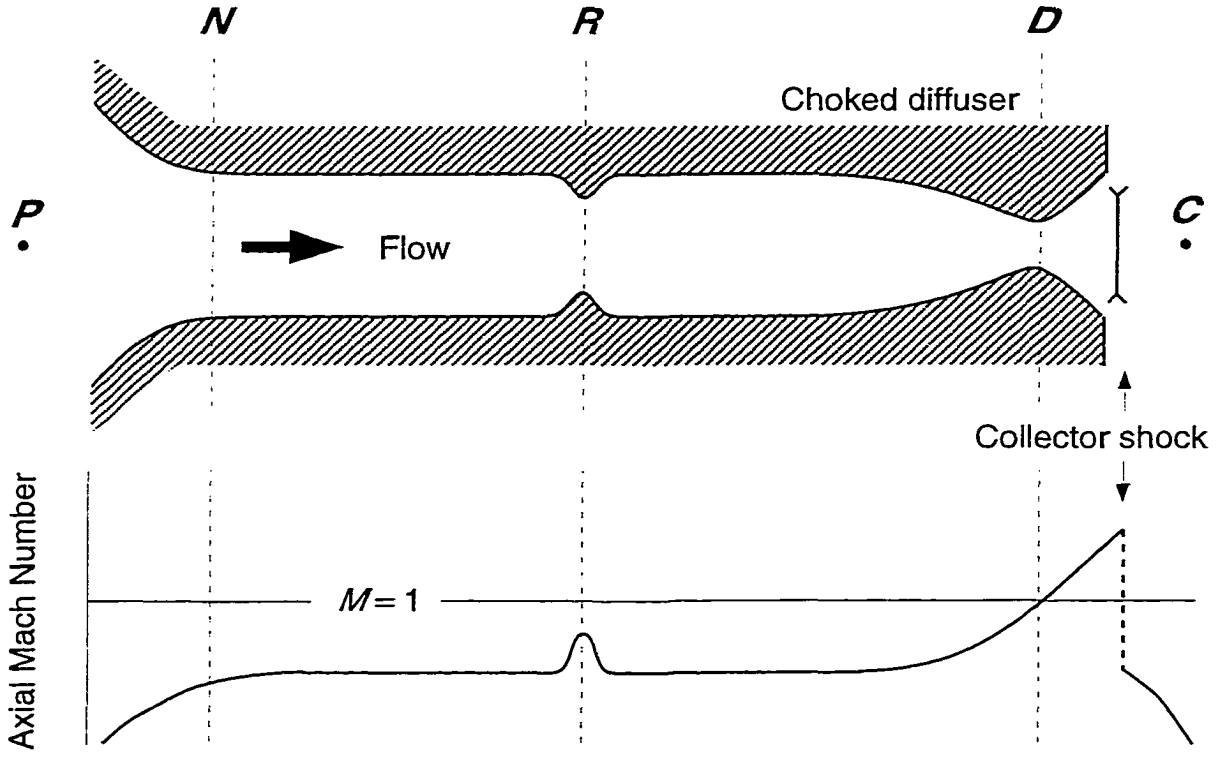

Figure 5.2 Subsonic throughflow operation without rotor choking

shown in Figure 5.3 practically always exists at the higher rotational speeds [2], except when the rotor is stalled. Note that this case still corresponds, by definition, to subsonic throughflow operation even though the flow reaches axial-supersonic velocities within the blade row itself.

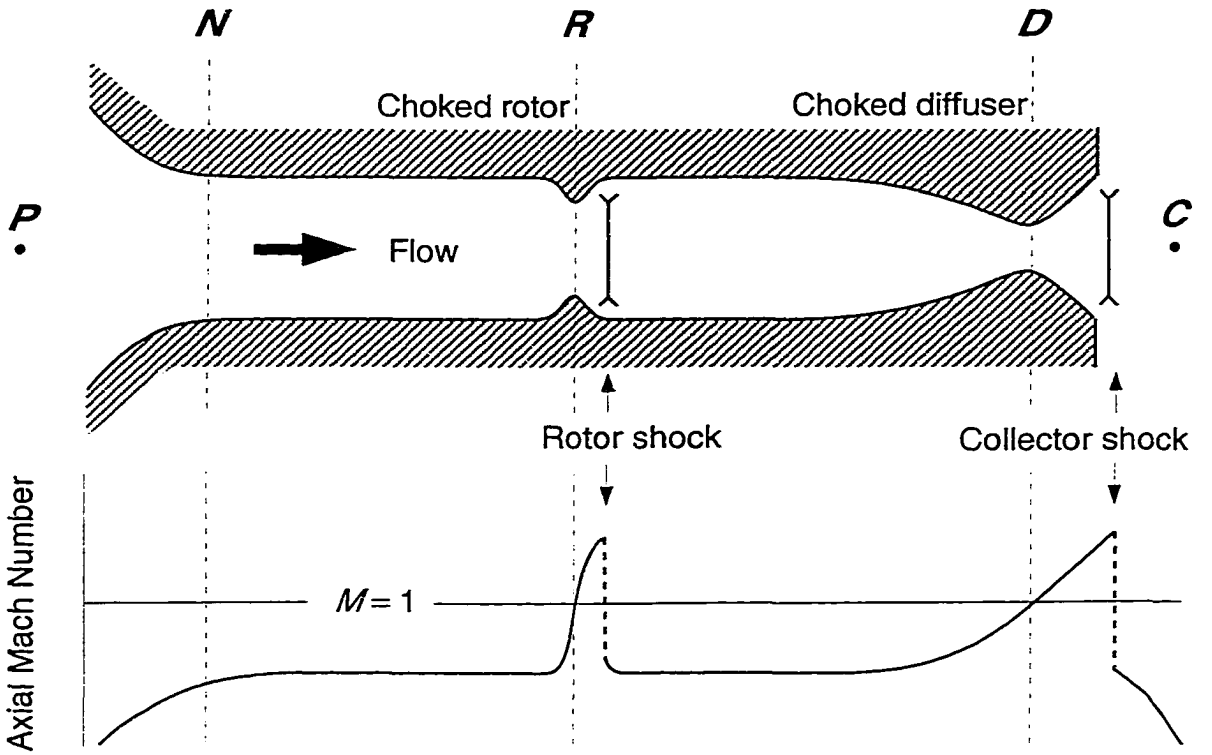

Figure 5.3 Subsonic throughflow operation with rotor choking

[2] This behavior can be contrasted with that of most conventional types of rotors, e.g., transonic and even supersonic rotors, where axial-subsonic flow exists through the entire blade row at all practical rotational speeds. The exception occurs in high-speed rotors designed for impulse-type operation, where the blade exit angles are oriented more or less toward the axial direction.

Theoretically speaking, the rotor shock is the gas dynamic mechanism which provides the necessary conditions for the steady-state coexistence of the two choked areas at *R* and *D*. A situation similar to that in the rotor-diffuser system also occurs upstream in the nozzle-rotor system as the nozzle geometry is varied into a c-d configuration. Gradually closing down the nozzle throat area for a particular rotor operating point causes the nozzle to eventually choke, at which time the regulation of mass flow transfers to the upstream nozzle throat *N*. Further reductions in nozzle throat area are accompanied by the formation and subsequent strengthening of a normal shock in the diverging section of the c-d nozzle. If the rotor is not choked then a situation as depicted in Figure 5.4 exists, whereas if the rotor is choked then Figure 5.5 illustrates the appropriate quasi-steady flow condition involving three choked throat areas. In both of these cases the nozzle shock provides the gas dynamic mechanism for the coexistence of the choked nozzle throat *N* and the choked throat *R* or *D*, downstream of the nozzle shock.

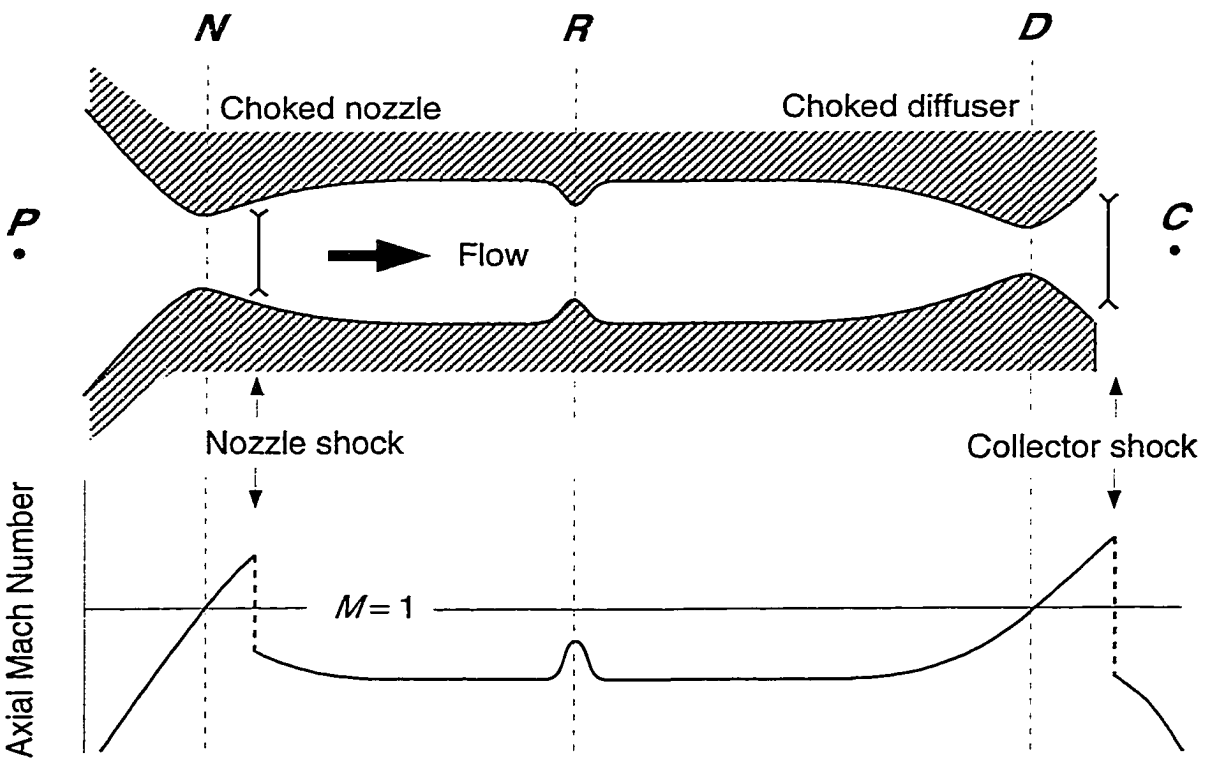

Figure 5.4 Subsonic throughflow operation with choked nozzle, and without choked rotor

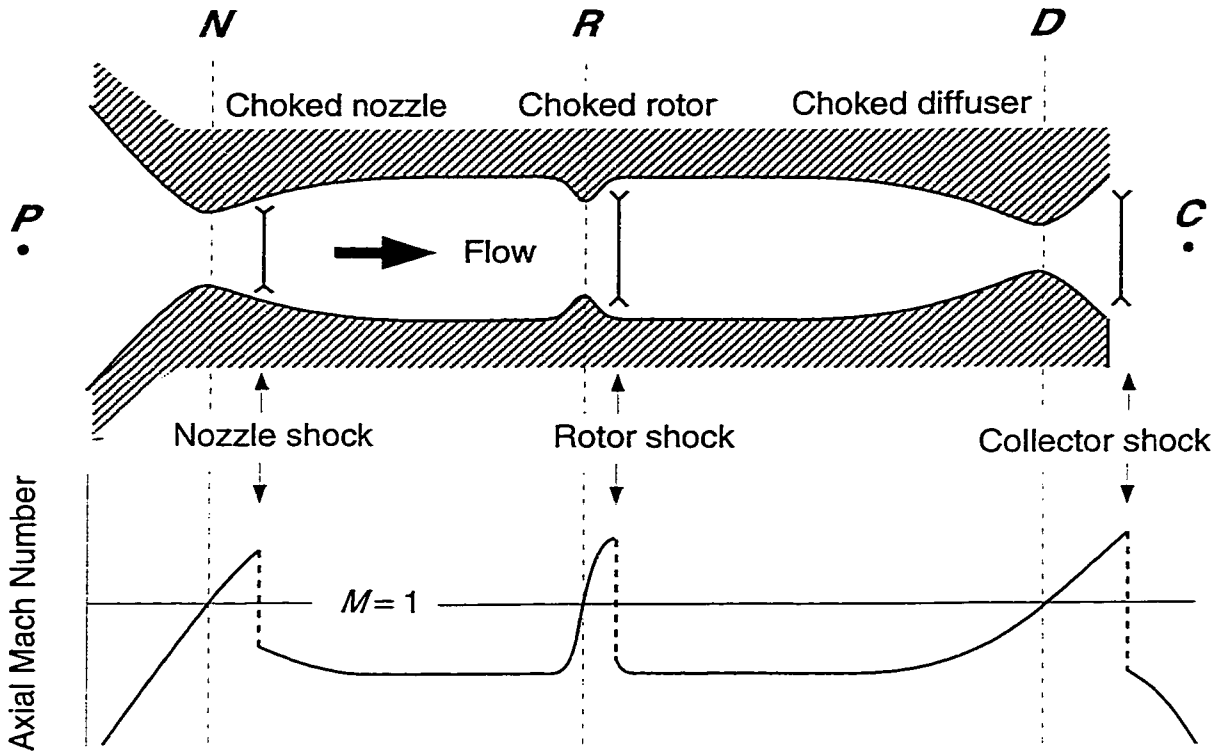

Figure 5.5 Subsonic throughflow operation with choked nozzle and rotor

Isoenergetic duct starting

The steady-state condition of a normal shock located between two choked throats is a well-known gas dynamic problem encountered, for example, in supersonic wind tunnels during the starting phase of their operation. For an adiabatic, isoenergetic (no work), and steady flow, the one-dimensional analysis is fairly simple. In the SSTF facility, such an analysis can be applied to the nozzle flow upstream of the rotor. Within and downstream of the rotor the flow is not isoenergetic, however, and tangential flow (swirl) effects complicate the gas dynamics even further. Fortunately the general qualitative behavior related to supersonic starting of the flow between two choked throats is not significantly altered by these effects. Thus, this general behavior can be usefully discussed next in the context of isoenergetic flow.

An important parameter controlling the behavior of the flow between two choked throats, illustrated in Figure 5.6, is the throat area ratio A_{*2}/A_{*1}. The maximum effective flow area A_{max}, located between the throats, is also important, but this aspect will be ignored for the moment. If the throat area ratio is gradually increased, either by decreasing the upstream throat area or increasing the downstream area, then the strength of the "normal" shock between the throats will increase by an amount producing a total-pressure loss commensurate with the change in throat area ratio. For the simple case of an adiabatic, isoenergetic, steady, one-dimensional flow, the following well-known relationship applies [68]:

$$\frac{A_{*2}}{A_{*1}} = \frac{p_{t1}}{p_{t2}} \geq 1 \tag{5.1}$$

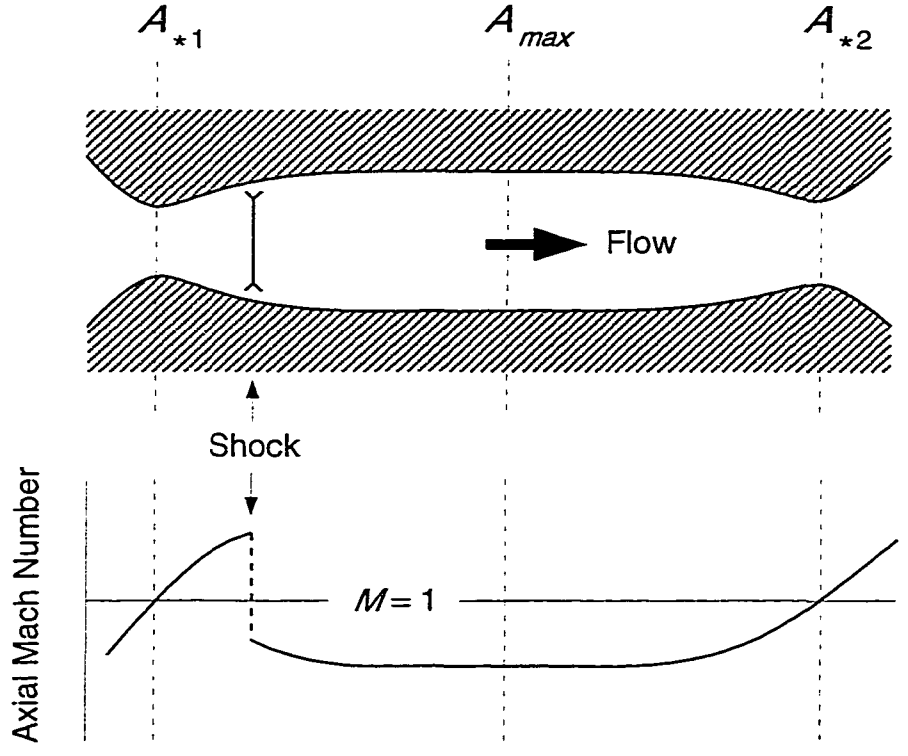

Figure 5.6 One-dimensional isoenergetic flow in a duct with two choked throat areas

In this case the downstream throat area must be larger than the upstream throat area in order to accommodate the total-pressure losses generated between the throats. To produce an increase in total-pressure loss, i.e., decrease in downstream total pressure p_{t2}, the shock location must shift downstream to a larger effective flow area and correspondingly higher shock-incident, supersonic Mach number. The local area at the shock location must diverge for a stable, or at least quasi-stable, shock to exist, which is a well-established fact of gas dynamics [66-68]

Further increases in throat area ratio eventually cause a limiting *unstarted* condition to be reached, where the effective flow area downstream of the shock no longer diverges; that is, the shock is situated at the location of maximum effective flow area between the throats. At this condition a further increase in throat area ratio is accompanied by an unstable shock position with the shock propagating rapidly downstream to a new stable location. During this start-transient the flow is unsteady and the second throat has a higher mass flow than the first. The transient ends when the shock has been swallowed by the second throat, and the duct is in the *started* condition, as shown in Figure 5.7, where the flow is supersonic between the first throat and some location downstream of the second throat. Note that after starting, the second throat is no longer choked. The throat area ratio at which the duct starts depends on the maximum effective flow area between the throats, or rather the area ratio A_{max}/A_{*1}, which also determines the maximum supersonic Mach number level in the started duct section.

The gas dynamic behavior involved in the unstarting of the supersonic duct flow is basically the reverse of that of starting. Note, however, that there is a hysteresis between the started and unstarted states due to the difference in the duct total-pressure losses for the two states. Just prior to starting, the unstarted duct has a total pressure loss from the normal shock, whereas just after starting this loss has been eliminated (from between the throats) by the swallowing of the shock.

Turning back now to the model of the SSTF facility (see Figure 5.1), the starting behavior just described will be related to the nozzle and diffuser duct sections, and to the rotor operating modes listed in Table 5.1.

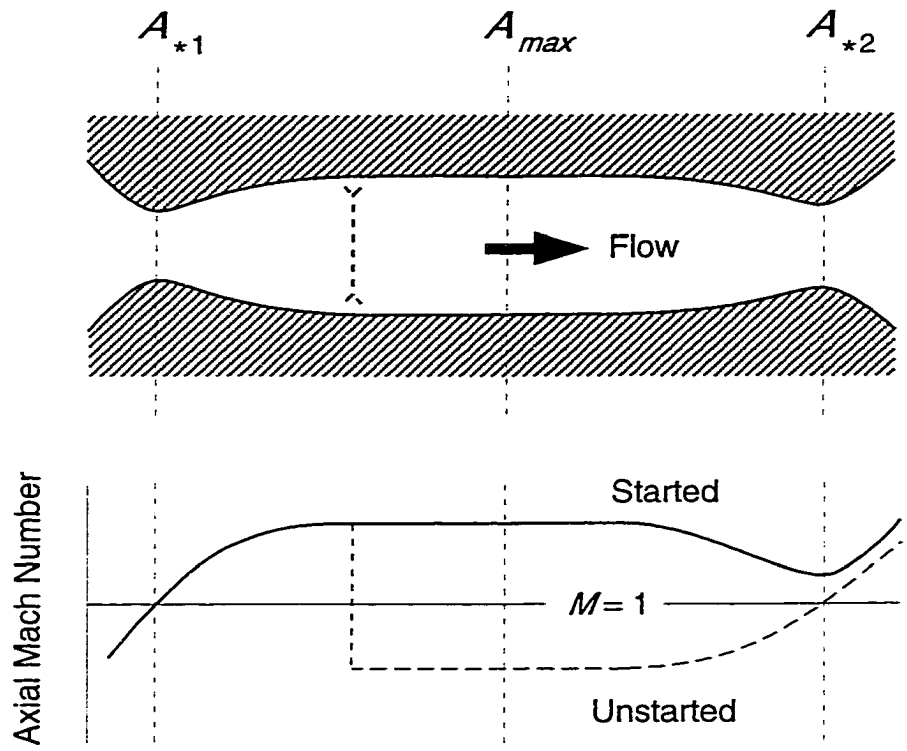

Figure 5.7 Started and unstarted conditions for a one-dimensional isoenergetic flow in a duct with two throat areas

Shock-in-rotor operation

Beginning with the subsonic throughflow operating condition, indicated in either Figure 5.3 or Figure 5.4, consider first the case of decreasing the nozzle throat area to levels beyond nozzle choking. As this is done the mass flow through the system decreases, being controlled by the nozzle throat area, and the nozzle shock progressively strengthens and moves further downstream until, eventually, the nozzle starts. The started-nozzle condition coincides with the establishment of axial-supersonic rotor inflow, and the generally expected post-start condition for the rotor and diffuser is depicted in Figure 5.8, where shock-in-rotor operation is indicated. In this case the nozzle shock has propagated downstream into the rotor and stabilized at a new location.

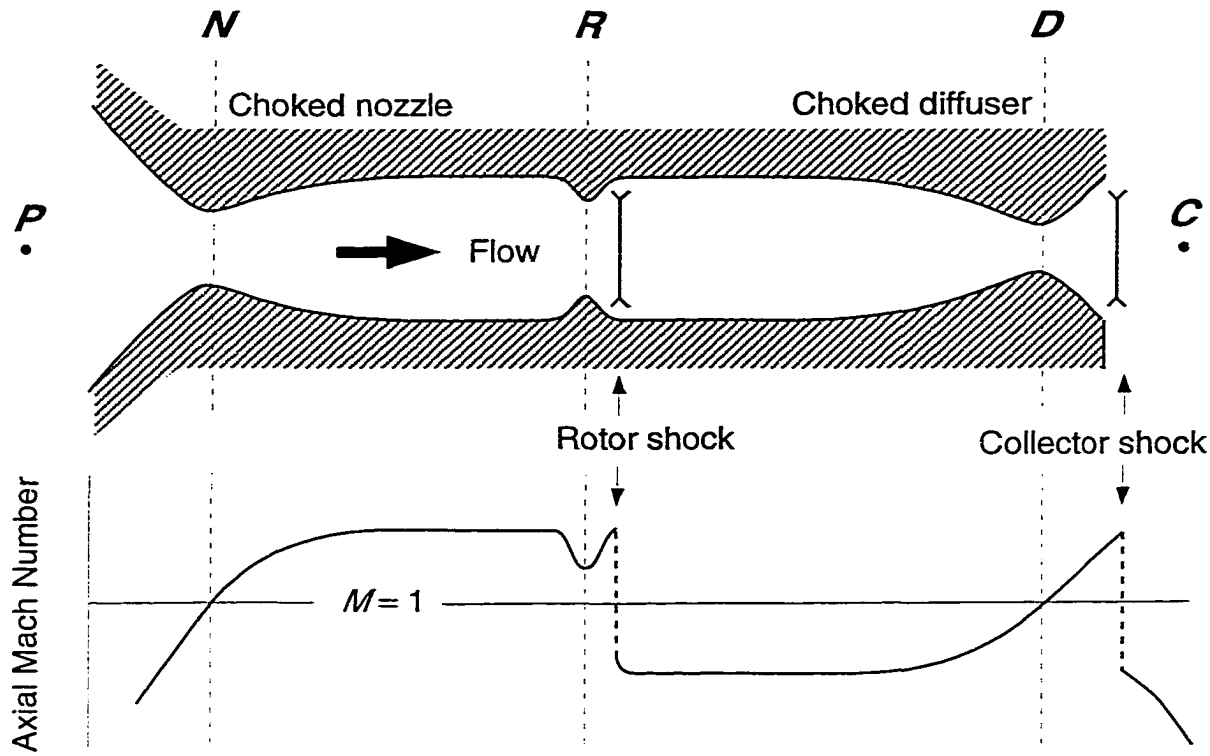

Figure 5.8 Shock-in-rotor operation

At this point a question naturally arises regarding the general existence of stable shock locations within the rotor. Without such locations the nozzle shock would continue to propagate through the rotor, and then through the diffuser duct as well, resulting in the entire nozzle-rotor-diffuser system starting simultaneously. Before addressing that issue, however, descriptions of the more commonly occurring start-transitions to the various operating modes will be completed.

Supersonic throughflow operation

When the system is operating in a shock-in-rotor configuration (see Figure 5.8), then the rotor throat is not choked, but the nozzle and diffuser throat areas N and D are. Note that in this case the flow between the choked throats is not isoenergetic, and that flow swirl

exists in the diffuser duct. The diffuser can be started by increasing the throat area ratio A_D/A_N by opening the diffuser throat, by closing the nozzle throat, or by adjusting both [3]. Closing the nozzle throat, however, is also accompanied by an increasing supersonic Mach number into the rotor, and drives the system toward a stronger starting shock. It is therefore a generally less-desirable method of starting the diffuser. Once the diffuser is started, then only one choked area remains in the system, at the nozzle throat *N*, and the flow is axial-supersonic from there on downstream into the collector, as depicted in Figure 5.9. At this condition the rotor is operating with supersonic throughflow, and the diffuser no longer throttles the rotor from downstream.

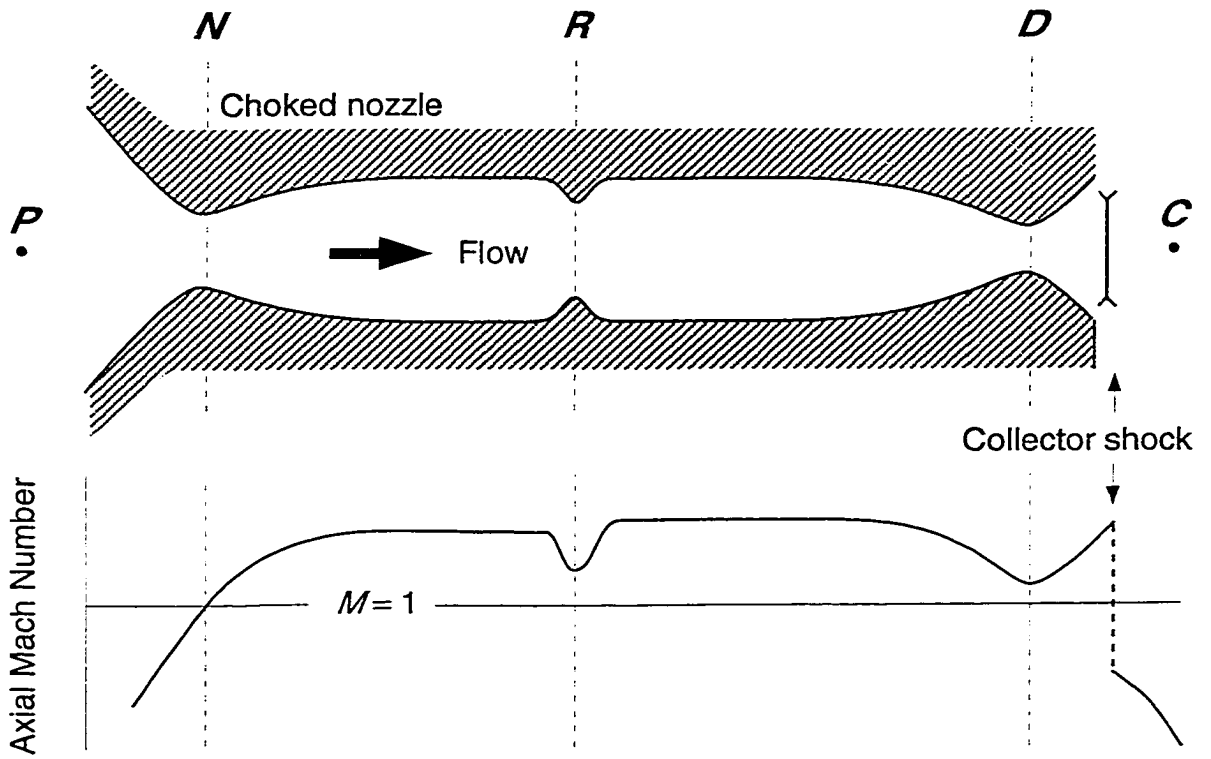

Figure 5.9 Supersonic throughflow rotor operation

[3] Another possibility, that of increasing the rotor speed and, hence, the energy addition, may also cause the diffuser to start for a sufficiently-open diffuser throat.

Impulse-type operation

The diffuser need not be started after the nozzle, as described above, but can instead be started first. In fact, in the experimental test facility the diffuser was virtually always started prior to the inlet nozzle being started [49]. Furthermore, the procedures used to unstart the system typically involved unstarting the nozzle first. Thus, experimentally the condition of a started diffuser in conjunction with an unstarted nozzle was commonly induced. In this condition the rotor operates in the impulse-type mode where, as in the supersonic throughflow mode, the rotor is not throttled from downstream. The transitions to this mode from subsonic throughflow and supersonic throughflow conditions are indicated in Figures 5.10 and 5.11, respectively, where the former case normally involves opening the diffuser throat to start the diffuser, and the latter case involves opening the nozzle throat to unstart the rotor inflow and nozzle.

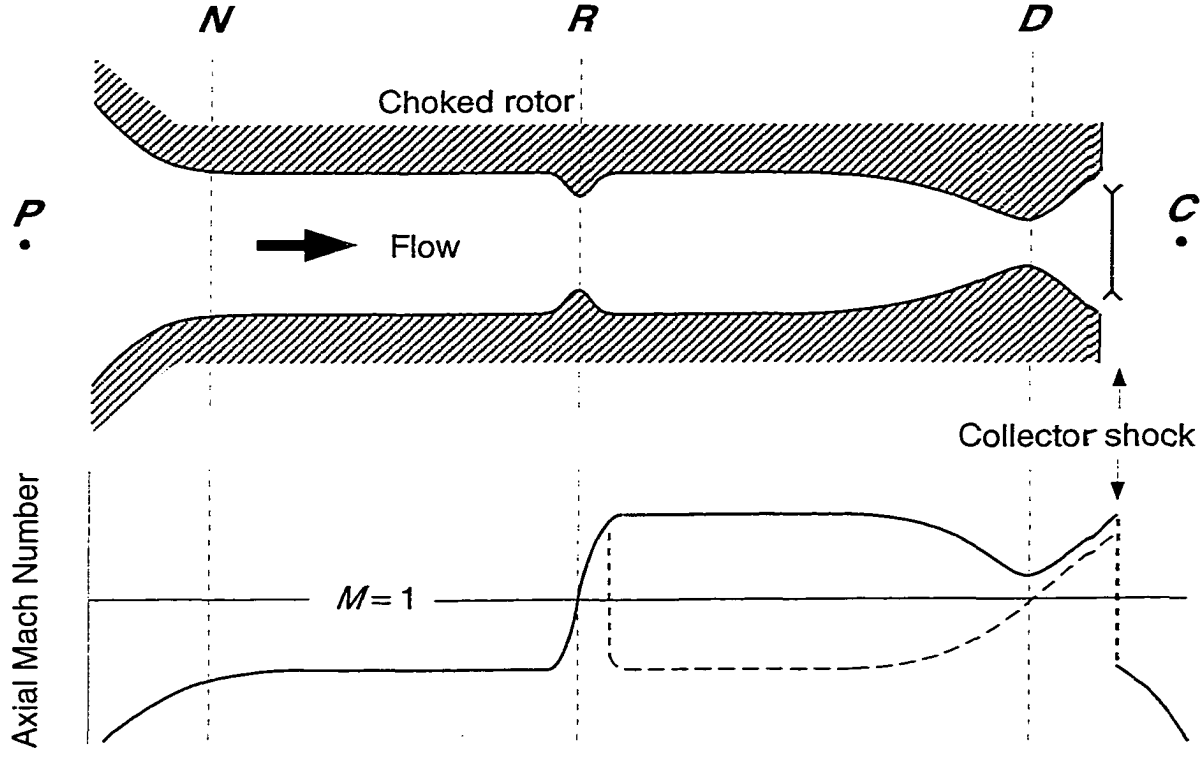

Figure 5.10 Transition to rotor impulse-type operation from subsonic throughflow operation

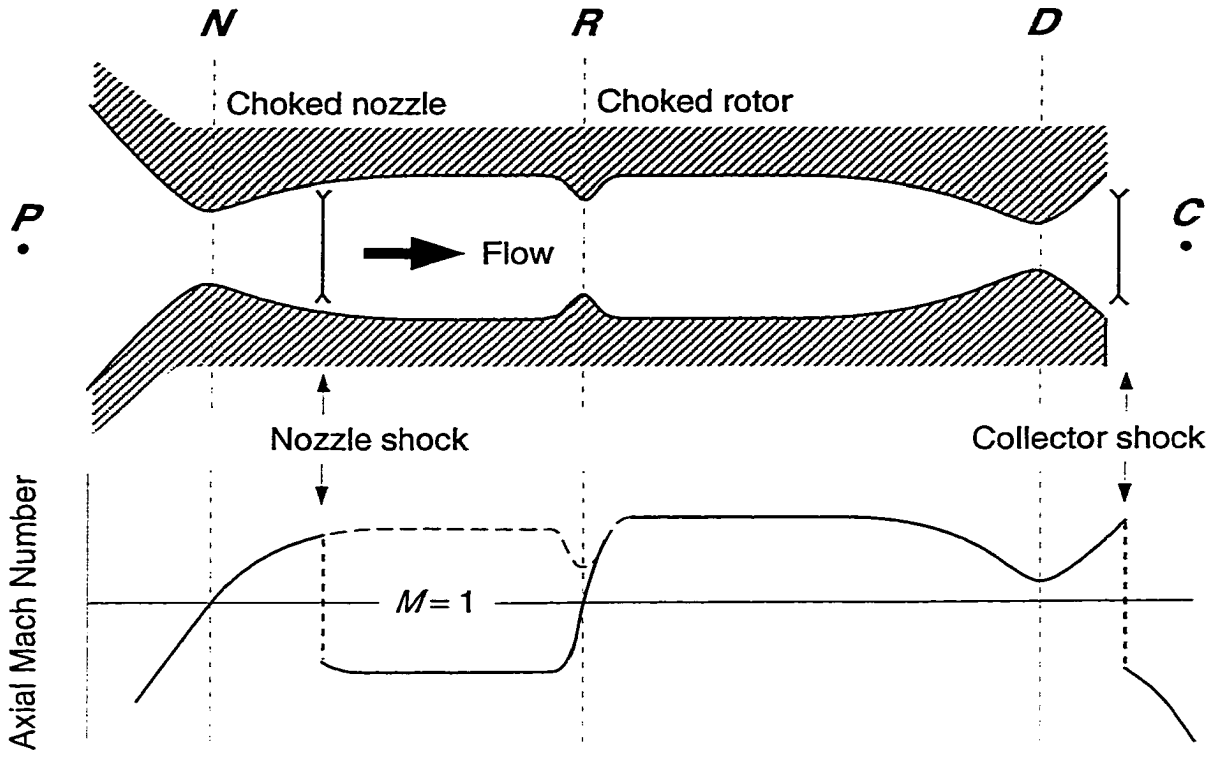

Figure 5.11 Transition to rotor impulse-type operation from supersonic throughflow operation

Non-isoenergetic duct starting

Having covered all four rotor operating modes and how they relate to the overall nozzle-rotor-diffuser system, the previously raised question regarding the existence of stable shock locations within the rotor will now be examined. To do this a simple quasi-two-dimensional axisymmetric model will be analyzed which includes the effects of rotor work and the resulting circumferential flow swirl. The flow model is illustrated in Figure 5.12, where the upstream and downstream flows are uniform and at the same radius, and

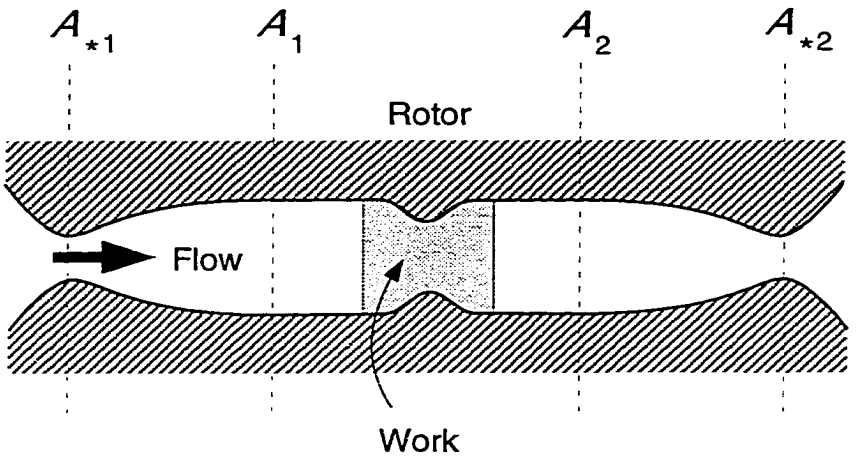

Figure 5.12 Quasi-two-dimensional flow model of the nozzle-rotor-diffuser system

the flow areas are equal. The continuity equation for an adiabatic and steady flow can be expressed in terms of the critical area ratio [4]:

$$\frac{A_{*2}}{A_{*1}} = \frac{\sqrt{T_{t2}/T_{t1}}}{p_{t2}/p_{t1}} \frac{\phi_1 \cos\alpha_{*1}}{\phi_2 \cos\alpha_{*2}} \tag{5.2}$$

In this equation the critical angles α_*, between the flow vector and the axial direction, represent the condition where the absolute flow velocity is supersonic and the axial component is sonic. At the upstream condition the critical flow is axial, and downstream the axial velocity component is sonic so that the following relationships apply:

$$\phi_1 \cos\alpha_{*1} = \phi_1 = \phi_* \tag{5.3}$$

$$M_2 \cos\alpha_{*2} = 1 \tag{5.4}$$

---

[4] The critical condition is considered here to exist where the axial velocity component is sonic.

The total pressure and total temperature ratios can be related through the adiabatic efficiency of the process, which for the compression of a perfect gas can be expressed in the following form:

$$\eta_R = \frac{(p_{t2}/p_{t1})^{(\gamma-1)/\gamma} - 1}{(T_{t2}/T_{t1}) - 1} \tag{5.5}$$

where η_R is the rotor adiabatic efficiency. Since the rotor is isolated, the tangential flow velocity at its exit is directly related to the amount of energy addition (or extraction) and the rotational speed at which it occurs. Applying the Euler momentum equation (tangential momentum) to an isolated fan rotor with no inlet swirl gives the following relationship between the exit tangential velocity and the total temperature ratio:

$$\frac{V_{\theta 2}}{a_{t2}} = \frac{(T_{t2}/T_{t1}) - 1}{(\gamma-1)\,(U_2/a_{t1})\sqrt{T_{t2}/T_{t1}}} \tag{5.6}$$

The dimensionless wheel speed parameter U_2/a_{t1} is a constant for a particular rotational speed and exit radius, e.g., the mean radius. Flow vector triangles at the rotor exit can be used to determine the exit Mach number from the tangential velocity:

$$M_2^2 = \frac{(V_{\theta 2}/a_{t2})^2 + 1}{1 - \frac{\gamma-1}{2}(V_{\theta 2}/a_{t2})^2} \tag{5.7}$$

There are a variety of ways to generate parameter curves from the above system of equations, i.e., Equations (5.2) through (5.7), and it is by no means obvious how the problem should be approached. One method provides considerable insight into the influence of rotor work and it will be discussed below. The main advantage of this approach is that it provides a minimal amount of quantitative information, while at the same time yielding a great deal of qualitative information. In this method, the system of equations is always solved for a critical area ratio of unity, and with adiabatic efficiency as the independent parameter:

$$\eta_R = f\left(\frac{p_{t2}}{p_{t1}}, \frac{U_2}{a_{t1}}\right) \tag{5.8}$$

Thus, a curve of adiabatic efficiency versus total pressure ratio can be obtained for a specific rotational speed. The significance of such a curve is viewed in a larger context, however, where the curve is seen only as a delimiter between qualitatively different conditions; namely, the conditions where the rotor exit critical area is less or greater than the inlet critical area. An example of such a curve is shown in Figure 5.13, which was generated for the baseline rotor at 60 percent of design rotational speed, and using the midspan radius as representative for the entire rotor.

The coordinate space in Figure 5.13 can be divided into four quadrants, where the curve for 60 percent rotational speed lies in the upper-right quadrant. In general, this quadrant represents isolated fan and compressor rotors operating with positive adiabatic efficiencies. As indicated, the area (in this quadrant) below the curve corresponds to conditions where the rotor exit critical area exceeds that at the rotor inlet, whereas above the curve the opposite applies. The lower-left quadrant also represents isolated fan and compressor rotors, but only for operating conditions with negative adiabatic efficiencies, in which case the exit critical area always exceeds that at the inlet. Finally, the upper-left quadrant represents isolated turbine rotors where again, as indicated, the exit critical area must always exceed the inlet critical area. Note that nothing is indicated for the case of turbines operating with negative efficiencies (lower-right quadrant) since such operation is impossible, i.e., a turbine with negative adiabatic efficiency — generating work output and a total-pressure rise in the working fluid — would violate the second law of thermodynamics.

In attempting to interpret the significance of the critical area ratio, an analogous flow-equivalent is conceptually very useful, and allows one to consider the problem in more familiar terms. Recall that the purpose of this analysis is to examine the general conditions necessary for stable shock locations in an isolated rotor, with a view toward better understanding the fundamental gas dynamic behavior associated with starting the axial-supersonic flows upstream and downstream of the rotor. The analogy is fairly simple and involves equating the non-isoenergetic flow which actually exists, to a hypothetical isoenergetic and isentropic flow which is similar. Similarity in this case is maintained in terms

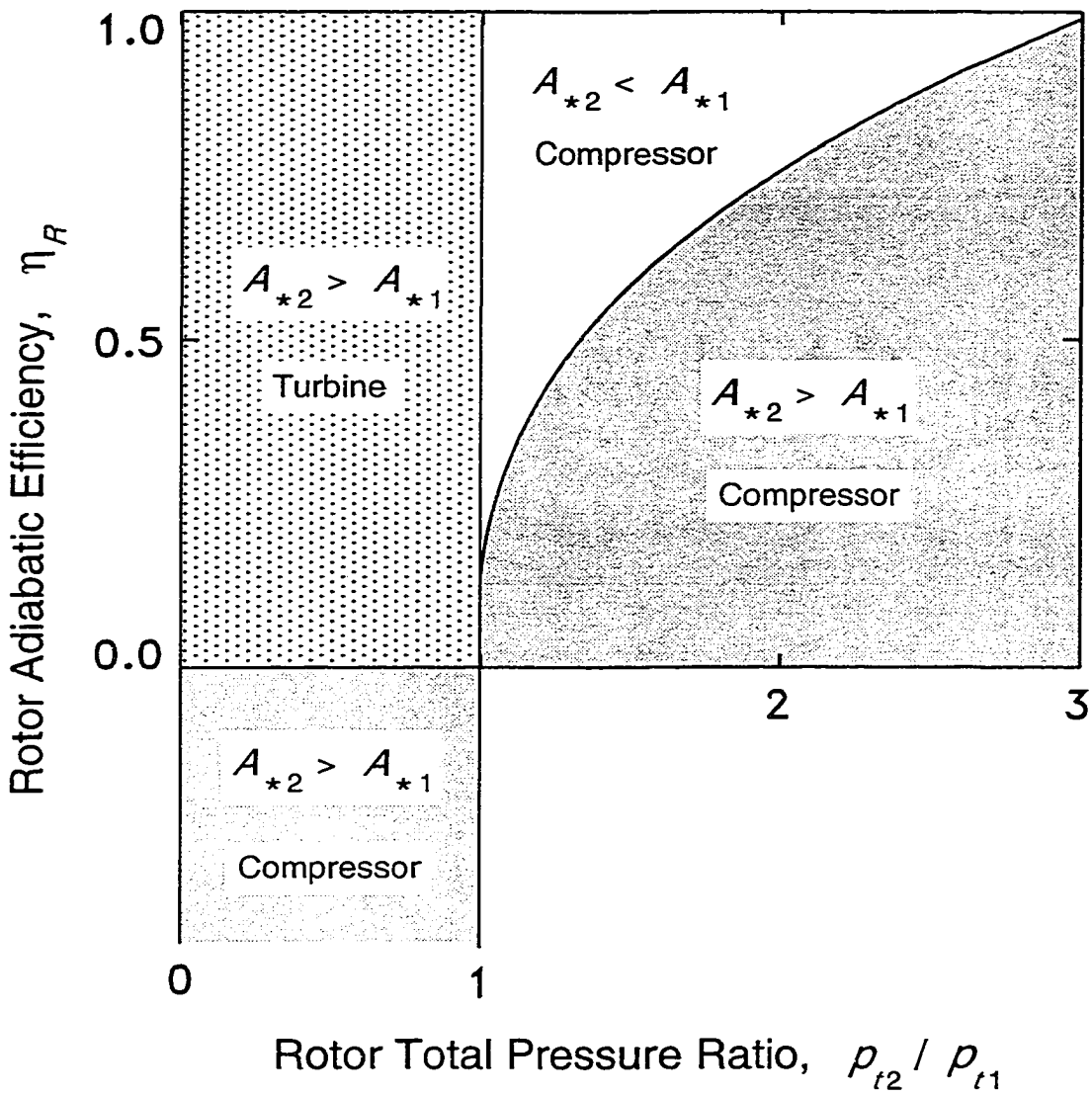

Figure 5.13 General influence of rotor work on the exit flow critical area, for a specific case corresponding approximately to the baseline rotor at 60 percent of design rotational speed

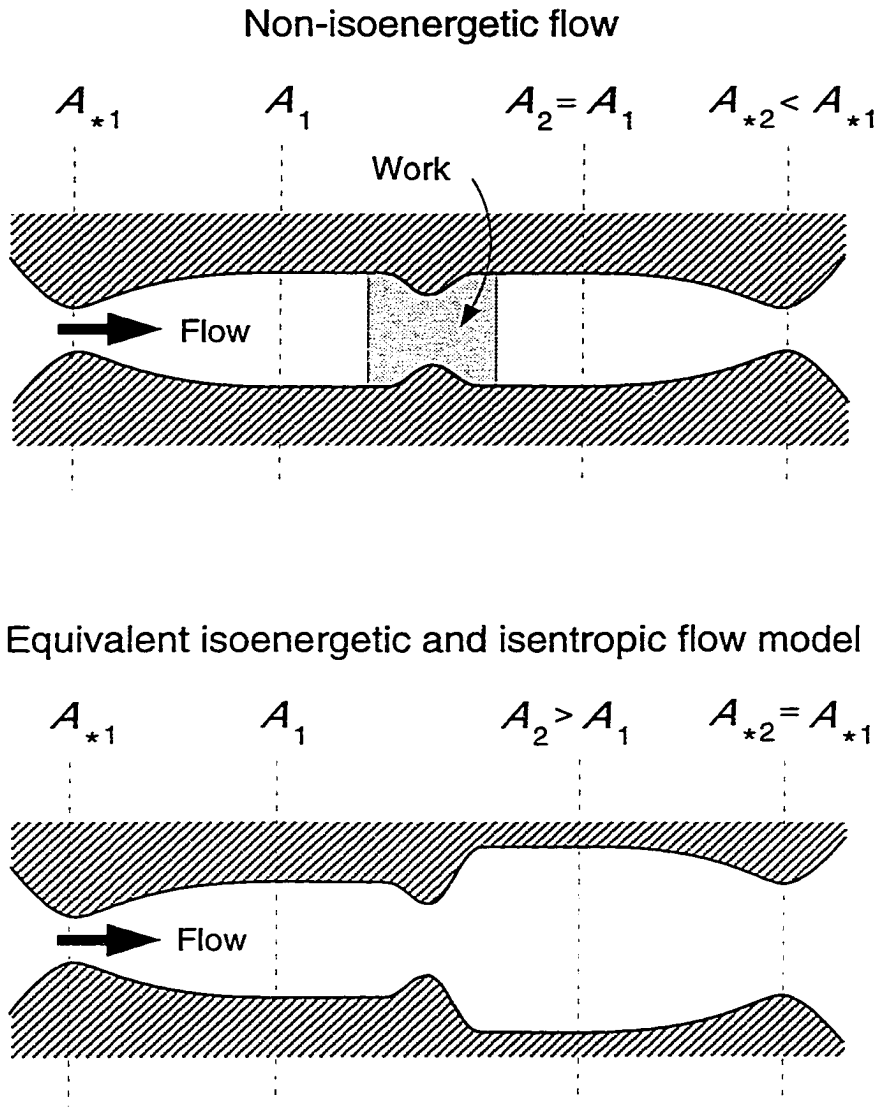

Figure 5.14 Analogous non-isoenergetic and isoenergetic one-dimensional duct flows

of Mach number levels. The analogous cases are shown in Figure 5.14, where it can be seen that a reduction in the critical area ratio through the rotor can be modeled by an isoenergetic flow with area divergence. Conversely, an increase in the critical area ratio, such as with a turbine or an inefficient compressor (see Figure 5.13), is comparable to an area convergence.

The proof for the analogy follows from the well-known isentropic area-ratio function of Mach number [53]:

$$\frac{A_*}{A} = \frac{\phi}{\phi_*} = f(M) \tag{5.9}$$

where $\phi_* = 125/216$ for air ($\gamma = 1.4$). For the non-isoenergetic flow model discussed above, the upstream and downstream areas can be related to the upstream and downstream Mach numbers using Equation (5.9):

$$\frac{A_2}{A_{*2}}\frac{A_{*1}}{A_1} = \frac{\phi_1}{\phi_2} \tag{5.10}$$

For an isoenergetic and isentropic flow the critical area A_* is constant, so that the analogous flow with the same Mach numbers has the following "equivalent" area ratio:

$$\left(\frac{A_2}{A_1}\right)_{eq} = \frac{\phi_1}{\phi_2} \tag{5.11}$$

Since the actual area ratio A_2/A_1 is unity for the baseline rotor, then the reciprocal of the critical area ratio is the same as the "equivalent" isoenergetic flow area ratio:

$$\frac{A_{*1}}{A_{*2}} = \left(\frac{A_2}{A_1}\right)_{eq} \tag{5.12}$$

The usefulness of the analogy lies in recognizing that an effectively divergent flow area is necessary for a normal shock (entering the rotor from upstream or downstream) to potentially stabilize somewhere in the rotor. Thus, only for rotor operating points where

the critical area ratio is less than unity can a transition to shock-in-rotor operation be expected [5]. Three examples for the baseline rotor operating with subsonic throughflow are shown in Figure 5.15. In this figure, theoretical [6] and experimental results for 50, 60, and 75 percent of design rotational speed are included, revealing that the critical area ratio is typically less than unity. As such, at any of these operating points it is expected that rotor inflow starting induced by contraction of the nozzle throat will terminate in the shock-in-rotor mode. One exception to this can be found in Figure 5.15 (top) at 50 percent rotational speed, where a rotor choking point [7] lies below the curve. Rotor inflow starting at this operating point would probably terminate in the supersonic throughflow mode; that is, immediately upon rotor inflow starting the diffuser would also start. Two more examples are shown in Figure 5.16, this time for the baseline rotor in supersonic throughflow operation. In this case experimental results for 75 and 100 percent rotational speed are presented, indicating again that the critical area ratio is less than unity. This implies that for any of these operating points diffuser unstarting, caused by contraction of the diffuser throat, should terminate in a shock-in-rotor mode. In other words, the rotor inflow should remain started as the diffuser is unstarted. Further reductions in the diffuser throat area, or increases in the nozzle throat area, would be subsequently needed in order to unstart the rotor inflow.

Subsonic Throughflow Operation

The practical operation of any supersonic throughflow device, including the SSTF rotor, inevitably involves subsonic throughflow operation. As a minimum the rotor must be operated in this mode during initial start-up and final shutdown. Probably the most important aspect of this operating mode, however, is the impact that it has on the aerody-

---

[5] An implicit assumption here is that the performance does not change too dramatically when the shock enters the rotor.

[6] Based on the rotor midspan wheel speed.

[7] On the performance map, this point lies far down on the vertical "choking" portion of the speed line.

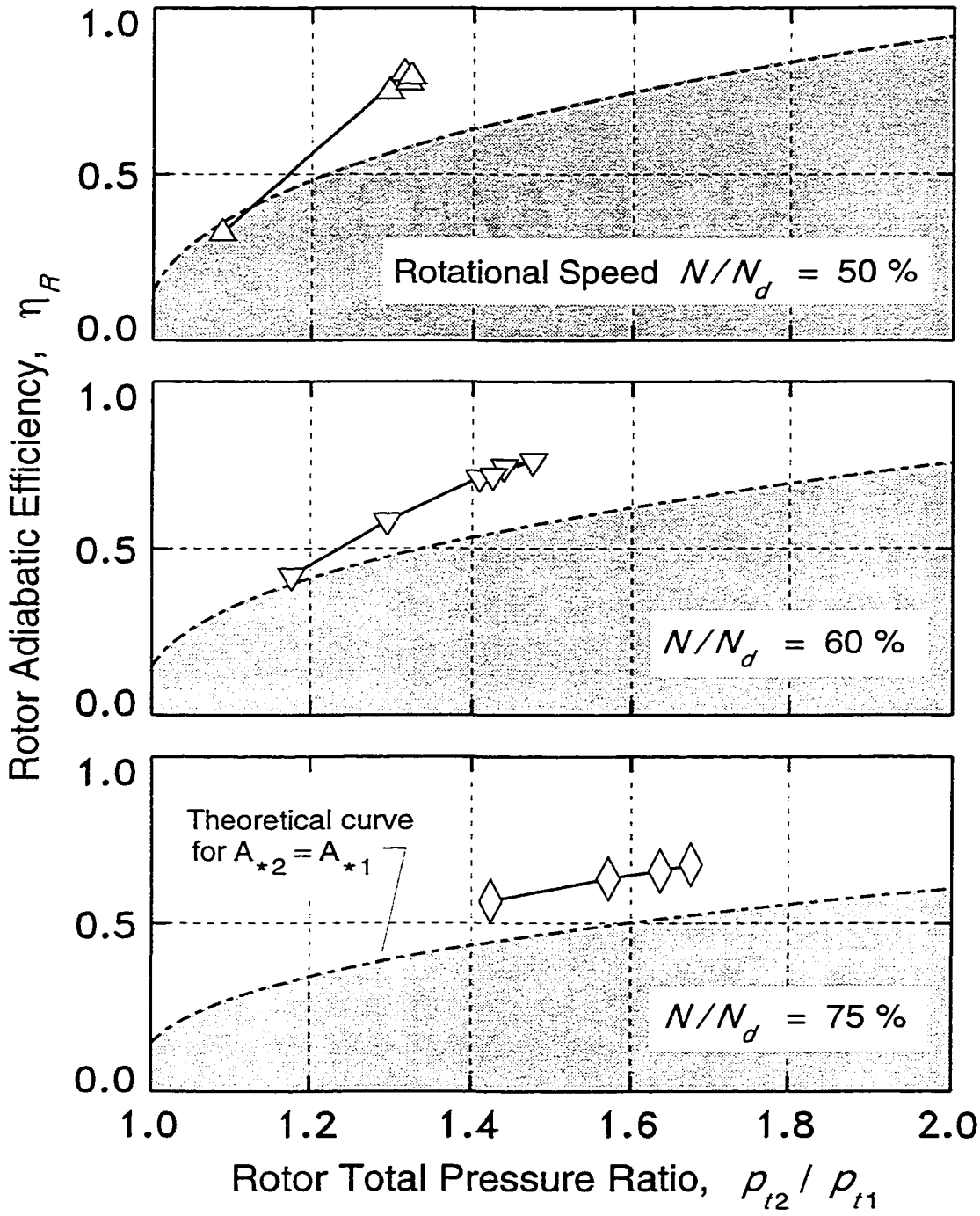

Figure 5.15 Experimental subsonic throughflow performance of baseline rotor at 50, 60, and 75 percent of design rotational speed; points above theoretical curve indicate potentially stable shock-in-rotor operation

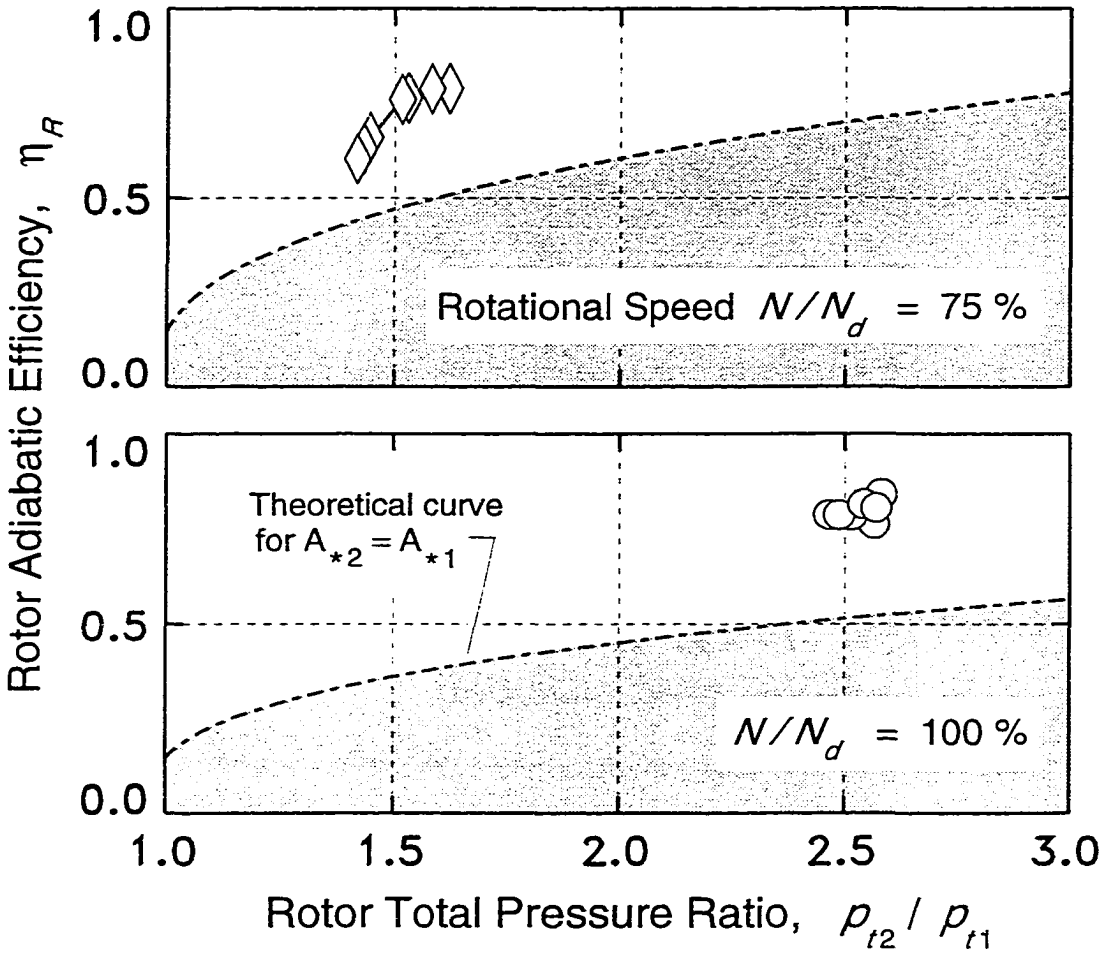

Figure 5.16 Experimental supersonic throughflow performance of baseline rotor at 75 and 100 percent of design rotational speed; points above theoretical curve indicate potentially stable shock-in-rotor operation

namics of the transition to and from axial-supersonic conditions. For this reason considerable attention is devoted to certain aerodynamic features associated with subsonic throughflow operation. This section is fairly brief and introduces the subsonic performance of the baseline rotor. The next section will expand on some of the features introduced here.

The overall subsonic performance measured for the isolated baseline rotor [49] is presented in Figure 5.17. Rotor total pressure ratio [8] versus axial inflow Mach number is shown in the bottom half of the figure, and corresponding adiabatic efficiencies are shown in the top half. Also included is a scale indicating approximate corrected mass flow rates at different axial inlet Mach numbers [9]. The performance, shown only for rotational speeds at and below 75 percent of design speed, is generally similar to that of typical, conventional-type fan rotors designed to operate with subsonic throughflow. A major point worth emphasizing is that these experimental results demonstrate the capability of this rotor to operate far off-design, in the subsonic throughflow regime, with reasonably good performance.

Transonic rotor operation begins at rotational speeds around 60 percent of design speed, where the rotor inflow becomes *relative* supersonic near the tip. Transonic and supersonic conditions can exist in the blade row at lower speeds, but only in conjunction with rotor choking. Near the rotor hub, relative supersonic inflow velocities are achieved, and thus exist over the entire blade span, in the 70 to 75 percent speed range. The establishment of supersonic relative inflow to all blade elements accounts for the virtually zero mass-flow range at 75 percent speed (see Figure 5.17). At this rotational speed a condition, referred to sometimes as *unique-incidence*, has been reached over the entire span of the blade so the mass flow into the rotor is determined solely by rotor blade geometry and rotational speed, being nearly independent of downstream static pressure until stall occurs. In addition to this, the baseline rotor has the unusual characteristic of achieving its maximum theoretical mass-flow limit at the same time that unique-incidence is established near the hub. An interesting and unusual implication of this is that increasing the

---

[8] Referenced to the plenum total pressure p_{t0}, which for the instrumentation used should be practically the same as referencing to the rotor inlet total pressure p_{t1}.

[9] Axial inflow Mach number is preferable to corrected mass flow for this type of fan since axial-subsonic and axial-supersonic inflows are both common. A particular mass flow rate generally corresponds to two inflow Mach numbers: an axial-subsonic and an axial-supersonic one. Furthermore, for axial-supersonic conditions the reverse trend of decreasing mass flow with increasing inflow Mach number can lead to some confusion. The mass flow rates indicated in the figure where determined assuming an inlet annulus blockage of 1.0 percent, which is based on the inlet results presented in the next section.

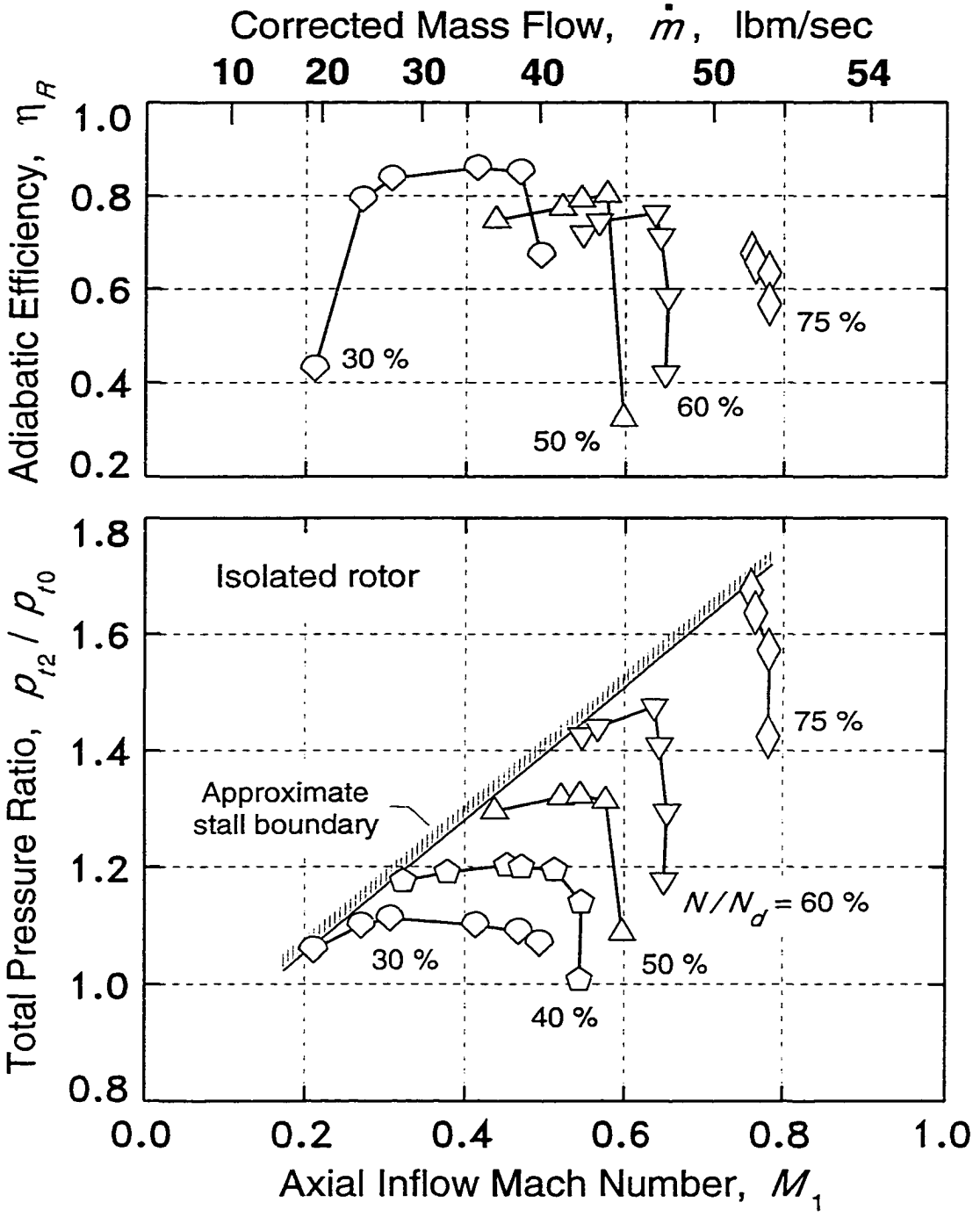

Figure 5.17 Subsonic throughflow performance of baseline rotor

rotor speed above 75 percent does not induce an increase in mass flow rate as might typically be expected. Paradoxically, in fact, it causes the mass flow rate to decrease slightly. This peculiar behavior is predictable, and will be addressed in the next section along with unique-incidence and other significant characteristics associated with axial-subsonic flow into the rotor.

Axial-Subsonic Rotor-Inflow Characteristics

The axial-subsonic inflow characteristics of the baseline rotor have special significance for this type of fan since these characteristics have a quantitative impact on the severity encountered in rotor inflow starting and unstarting. The most important parameter influencing rotor inflow transition is the axial component of the inflow Mach number which, since there are no inlet guide vanes, is equivalent to the absolute inflow Mach number. The mass flow rate can be directly related to an "average" axial inflow Mach number by accounting for inlet annulus blockage and spanwise non-uniformities in the rotor inflow [10]. For a constant rotational speed the mass flow typically varies greatly as the rotor is throttled or unthrottled, but as the data in Figure 5.17 so clearly show, the range in flow can decrease considerably, and eventually disappear under conditions of transonic operation (compare 60 and 75 percent speed). In any case, a maximum mass flow is achieved at any given rotational speed when the rotor blade row chokes, and it is this limiting condition which is of primary interest in this section. Reasons why the choking limit is considered especially important will be elaborated later, but it is sufficient here to say that rotor choking is generally associated with the condition of least severity, at a particular rotational speed, for rotor inflow starting. Besides this, the rotor is always choked at rotational speeds exceeding 75 percent anyway, as will be described in more detail below.

Most of the discussion in this section centers around analytical results, but experimental results are presented where possible in order to verify the analysis. The general

---

[10] Corrected mass flow rate and rotational speed are similarity parameters which preserve Mach number conditions in a turbomachine, at least as long as Reynolds number effects are not overly significant.

approach is to present two-dimensional results first, using these results to describe the blade-to-blade flow field features relevant to the rotor inflow characteristics. This is followed by three-dimensional CFD results and a discussion of the three-dimensional effects in the rotor entrance region. Finally, computed and measured overall flow rates induced by the choked rotor over most of the rotational speed range are presented and compared. Note that it is these final results which will be most useful in the following section on rotor inflow starting and unstarting.

In analyzing the rotor inflow, that is, in quantifying the axial inflow Mach numbers associated with rotor choking at various rotational speeds, some simple and fast two-dimensional calculation methods have been applied in addition to the more sophisticated quasi-three-dimensional and fully three-dimensional CFD codes, RVCQ3D and RVC3D. One of the simple techniques is an approximate procedure for calculating blade element inflow conditions corresponding to a choked blade-passage minimum area. The other simple technique provides a direct approximate calculation of the two-dimensional unique-incidence (U-I) relationship for a particular blade element. Although the CFD solutions provide much more information and are considered more accurate, the results obtained with the approximate methods are included since they provide additional insight into the rotor inflow behavior and help to interpret the CFD solutions. It is beyond the scope of this work to discuss the approximate unique-incidence technique in full detail, but many of the essential features of it are described in Appendix D, which also provides a brief description of the two-dimensional blade-element choking model.

Calculated axial-subsonic rotor-inflow conditions for *two-dimensional* blade elements near the tip, pitchline, and hub are presented in Figure 5.18, where axial inflow Mach number versus percent of design rotational speed is shown for each blade element. The solid lines indicate the solutions obtained using the simpler methods, whereas the symbols represent solutions obtained using the quasi-three-dimensional RVCQ3D code. Note that for the CFD results the streamtubes in the entire inlet region of the blade row were two-dimensional, i.e., the radii and streamtube-heights were constant. Also, the conditions shown were reduced from the CFD flow fields by blade-to-blade integration and averaging at a location near the grid inlet, which is about 14 percent of axial chord upstream of the rotor leading edges. These analytical results will now be discussed in more detail since they provide considerable insight into the axial-subsonic inflow aerodynamics of the rotor.

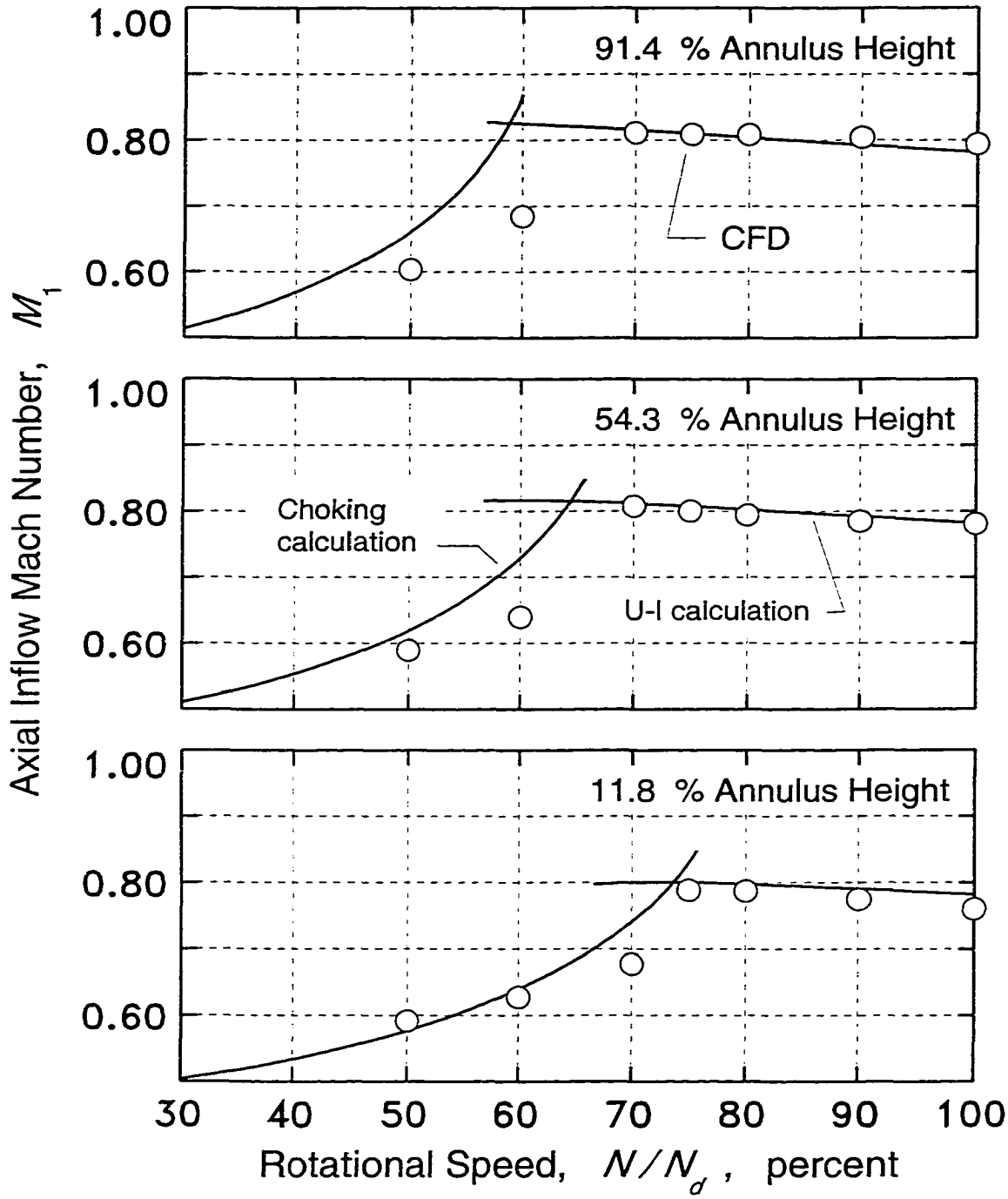

Figure 5.18 Maximum subsonic axial inflow Mach numbers for the rotor as a function of rotational speed; results based on two-dimensional CFD analysis and simple choking and unique-incidence calculations

Referring to Figure 5.18, the solid-line segment on the left half of each graph indicates the approximate limit for choking at the blade passage minimum-area location, assuming no inlet swirl and no total pressure loss between the inlet flow and the choked throat (see Appendix D). The solid-line-segment on the right half of each graph indicates the unique-incidence solution calculated using the fast, approximate method. The rotational speed at which the choking curve intersects the unique-incidence curve represents the approximate lower limit for unique-incidence; that is, unique-incidence conditions are unattainable for rotational speeds below that limit, for that particular blade element.

The term unique-incidence refers to a unique [11] functional relationship between the relative inflow angle β_1 and the supersonic relative inflow Mach number M_1'. In general, for a specific blade element the unique-incidence condition exists only in conjunction with supersonic relative inflow Mach numbers. Furthermore, the relative Mach numbers must be high enough for the supersonic flow into the covered blade passages to be started, under which condition the passage minimum-area is not choked. The absolute inflow Mach number, being in the axial direction, is a simple function of the relative Mach number and flow angle:

$$M_1 = M_{ax\,1} = M_1' \cos\beta_1 \tag{5.13}$$

The corresponding wheel speed U_1 can be expressed in dimensionless form using the absolute Mach number and the relative flow angle:

$$\frac{U_1}{a_{t1}} = \frac{M_1 \tan\beta_1}{\sqrt{1 + \frac{\gamma - 1}{2} M_1^2}} \tag{5.14}$$

---

[11] The uniqueness strictly applies only to a particular inflow streamtube geometry, which in this case is two-dimensional. Varying the streamtube geometry in order to account for three-dimensional effects will alter the unique-incidence relationship.

Therefore, from Equation (5.13) and (5.14) it becomes apparent that the establishment of unique-incidence on a particular rotor blade-element implies that the inflow conditions to that element become virtually a function of the rotational speed [12].

Virtually all conventional-type transonic fan designs exhibit a general trend of increasing flow rate, or similarly, axial inflow Mach number, as the rotational speed increases. This trend in flow induction occurs even at the near-tip blade elements when they are operating with unique-incidence. Interestingly, however, this is not the case for any of the baseline SSTF rotor blade elements, as can be seen in Figure 5.18. More will be said about this peculiar behavior as the discussion progresses.

Comparing the CFD results with the "approximate" curves in Figure 5.18 reveals very good agreement, under conditions of unique-incidence, for all three blade elements. The comparisons at blade-passage choking conditions are not in such good agreement, but this is not really surprising when it is considered that the approximate curves were calculated assuming no total-pressure loss. The effect of a total-pressure loss upstream of the choked throat would be to shift the choking curve down and to the right, which is where the CFD results lie. Also, any curvature in the sonic line, assumed to be straight in the simple approximation, would produce a shift in the same direction. It is significant that all of the CFD results conform to the expected direction of this shift.

As already pointed out, the unique-incidence axial inflow Mach number remains nearly constant for each blade element as the rotational speed varies. Additionally, all blade elements represented in Figure 5.18 have nearly the same level of maximum axial inflow Mach number, which is approximately 0.8. A comparison of the three elements reveals that unique-incidence conditions are established first near the tip, at rotational speeds just above 60 percent when the tip velocities become relative supersonic and the covered passage "starts". Increasing the rotor speed beyond that point causes the relative supersonic inflow condition to progressively advance toward the hub until finally, at about 75 percent speed, the unique-incidence condition is established at the hub as well. Thus, at around 75 percent rotational speed a unique-incidence axial inlet Mach number of about 0.8 is attained over the entire blade span, excluding the endwall boundary layer regions.

---

[12] In the absence of significant three-dimensional effects in the inlet region.

Further increases in rotational speed are associated with gradually decreasing axial inflow Mach numbers. Based on these computed results, therefore, it can be concluded that a *maximum* axial inflow Mach number condition, and corresponding maximum mass flow rate, occurs for the baseline rotor at about 75 percent speed.

The reason for the above behavior is discussed in somewhat generic terms in Appendix D, under the section entitled **Unique-Incidence for a Flat Plate Cascade.** Briefly summarized and applied to the baseline rotor, it can be stated that the baseline rotor design results in a condition where, with the onset of unique-incidence, the axial flow entering the blade row virtually always chokes in the plane of the blade leading edges. The geometric feature of the rotor design which produces this effect is the relatively low stagger angle of the blades, or more precisely, the relatively low blade-suction-surface angle in the entrance region of the rotor blade passages. In the blade-relative frame-of-reference the *first captured Mach wave* [13] associated with unique-incidence (see Appendix D) nearly always originates from the leading edge of a blade, from there extending across the passage to the bow shock wave at the leading edge of the adjacent blade. Although this Mach wave is oblique to the relative supersonic inflow, it is practically normal (perpendicular) to the axial, absolute inflow. Since the Mach number component normal to a Mach wave is always unity, the absolute flow is therefore choked at the first captured wave location. The axial inflow Mach number and corresponding mass flow are fairly high under this condition because the blade row blockage at the leading edge plane is low.

The maximum mass flow induced by the rotor apparently occurs at the minimum rotational speed at which the above condition is first realized over the entire blade span, excluding the endwall regions. Rotational speeds exceeding this minimum do not alter the entrance flow field in a *qualitative* way, but they do tend to increase the effective leading-edge blockage by increasing the relative inflow Mach number, and thus the bow shock losses [69,70].

Turning now to examine the two-dimensional CFD solutions in more detail, and thereby show many of the above aerodynamic features, Mach number contour plots for the

---

[13] This wave determines the mass flow entering the blade passage.

computed inlet flow fields at the rotor pitchline (54.3 percent annulus height) are provided in Figures 5.19, 5.20, 5.21, and 5.22, for choked rotor conditions at rotational speeds of 50, 60, 75, and 100 percent, respectively. The top part of each figure shows *relative* Mach number contours, while the bottom part shows *absolute* Mach number contours. The absolute Mach contours can be thought of as providing a stationary frame-of-reference "snapshot" of the flow field. In each of these figures the sonic condition is indicated by a thick dashed line.

The computed pitchline flow field for 50 percent speed (see Figure 5.19) indicates that the blade row is choked in both frames of reference, just upstream of the minimum area of the blade passage. The relative inflow Mach number in this case is calculated to be 0.841, at an inflow angle and suction-surface incidence of 45.5 and 7.6 degrees, respectively. As a point of added interest, notice in the top part of the figure the supersonic bubble behind the leading edge on the blade suction surface. The computed flow fields near the rotor hub and tip at this speed (not shown) are qualitatively similar to the pitchline flow field, except that the supersonic bubble is smaller near the hub and larger near the tip.

Increasing the rotational speed to 60 percent does not produce a large qualitative change in the computed flow fields. Near midspan (see Figure 5.20) the supersonic bubble has grown considerably as the computed relative inlet Mach number, equal to 0.966, approaches the sonic condition. Near the tip the computed inflow Mach number is relative supersonic at a value of 1.070, so that the bubble (not shown) has disappeared, having grown to include the entire upstream region. However, because the "covered passage" has not started yet, the passage minimum area is still choked and a weak normal shock stands directly in front of the covered-passage entrance. Increasing the rotational speed somewhat beyond 60 percent causes the near-tip covered passage to start, thereby establishing unique incidence with axial flow choking between the blade leading edges. Note that only the near-tip entrance flow is started at this point since the pitchline and hub covered-passages are not predicted to start until rotational speeds of around 65 and 75 percent, respectively, are reached (see Figure 5.18).

The Mach contours for the computed pitchline flow field at 75 percent rotational speed (see Figure 5.21) reveal all of the inflow features discussed so far in connection with unique-incidence. From the contours in Figure 5.21, it is apparent that the rotor inflow is relative supersonic and started, and the absolute flow entering the rotor is choked between

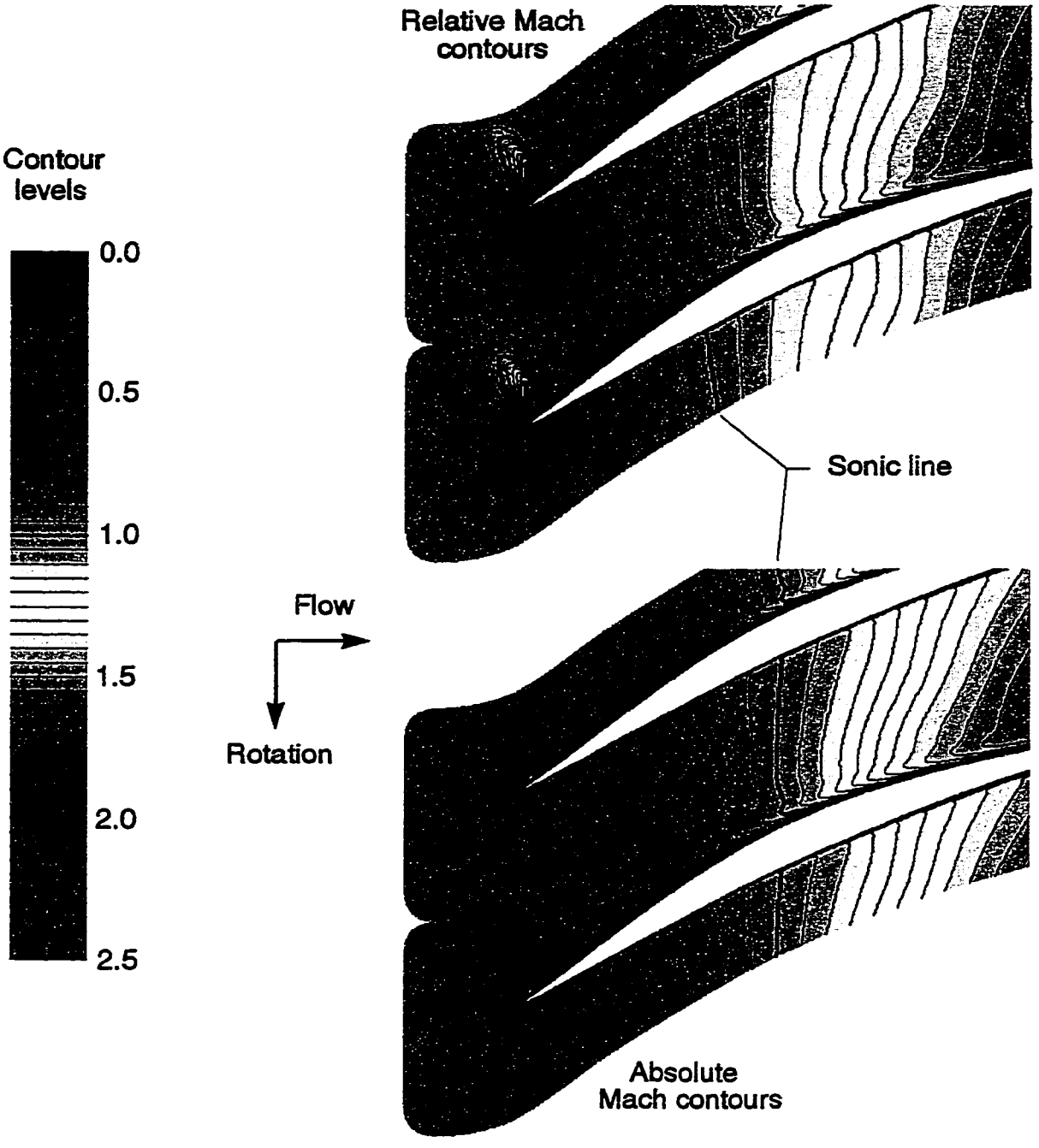

Figure 5.19 Viscous two-dimensional CFD Mach number contours for the rotor pitch-line at 50 percent of design rotational speed with choked axial-subsonic inflow conditions

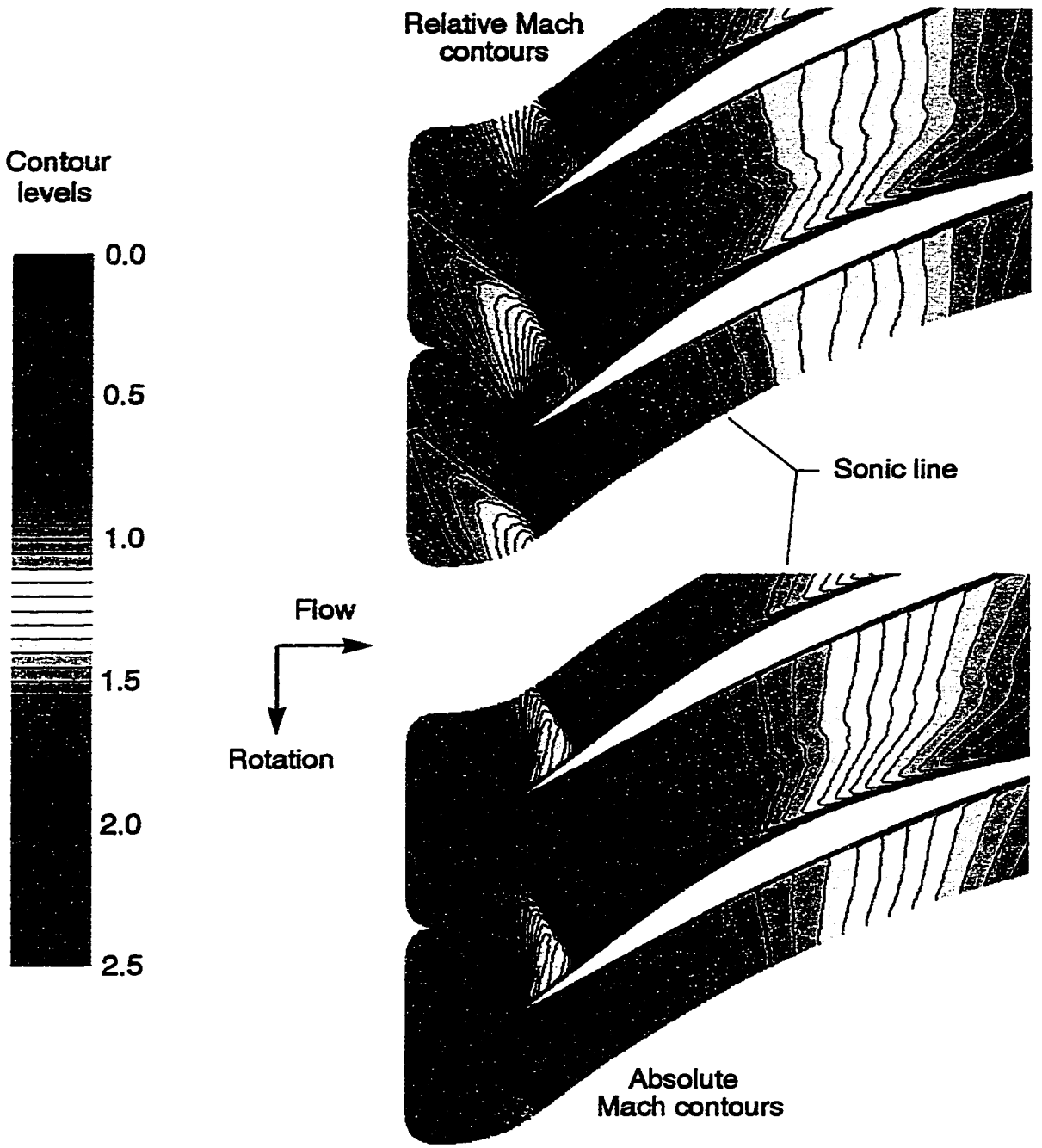

Figure 5.20 Viscous two-dimensional CFD Mach number contours for the rotor pitch-line at 60 percent of design rotational speed with choked axial-subsonic inflow conditions

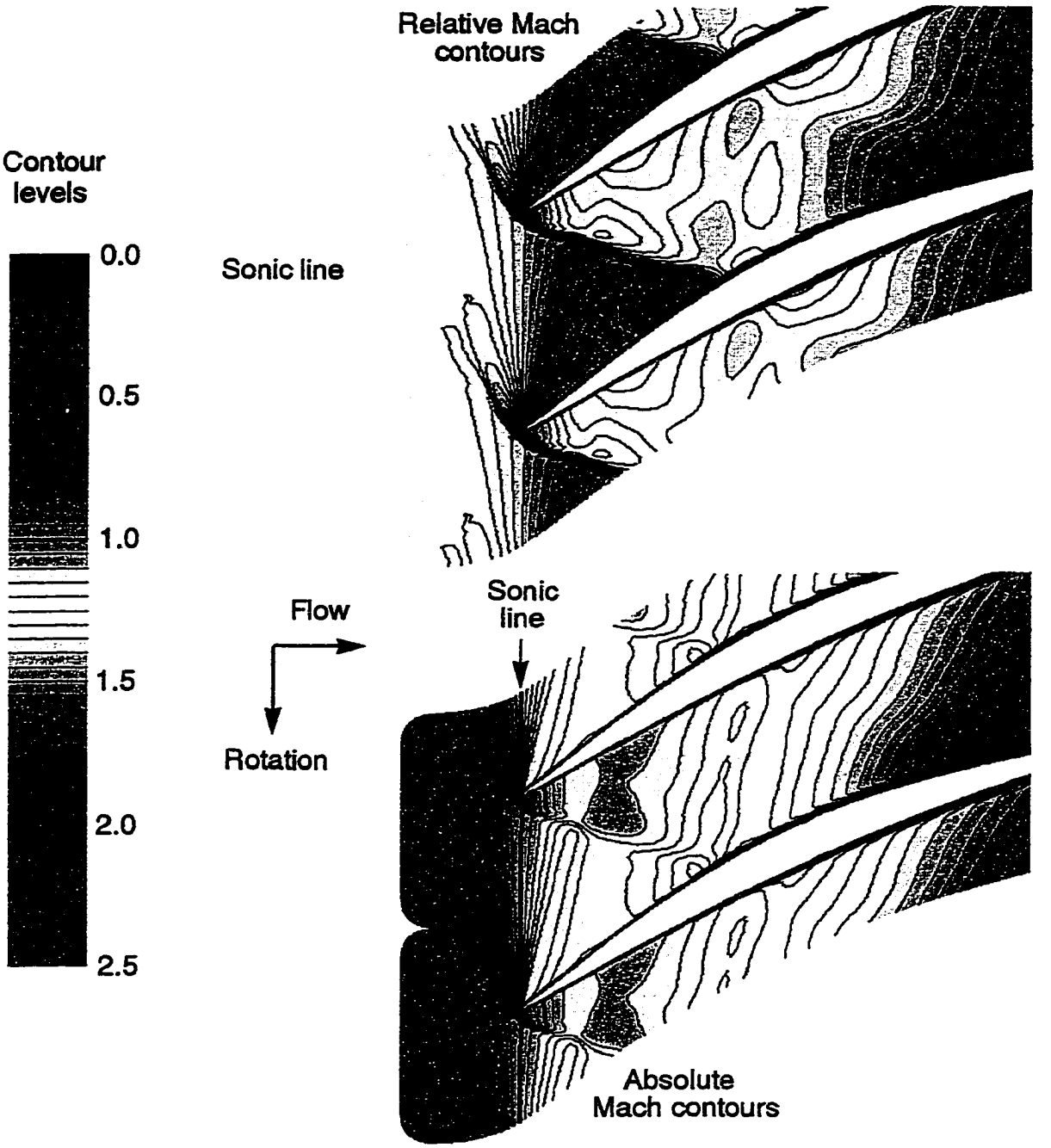

Figure 5.21 Viscous two-dimensional CFD Mach number contours for the rotor pitch-line at 75 percent of design rotational speed with choked axial-subsonic inflow conditions

the blade leading edges, as indicated by the sonic line (see Figure 5.21, bottom). Notice that the sonic line does not actually extend completely from leading edge to leading edge, but is significantly shorter, thus indirectly showing the added blockage from the leading edge bow shock waves. The Mach number contours also allow the sonic line to be identified as part of an essentially two-dimensional expansion fan which emanates from the blade leading edge, and which is close in appearance to the classical Prandtl-Meyer expansion fan. It is significant that the iso-Mach lines which make up the expansion fan are nearly straight, since this verifies the assumption used in the approximate unique-incidence calculation method; namely, the assumption that the entrance region can be modeled as a simple-wave flow field (see Appendix D).

In terms of absolute Mach numbers, the blade-to-blade expansion fan system can be seen to rapidly accelerate the rotor inflow from an upstream axial Mach number of about 0.8 to about Mach 1.2 just downstream of the leading edge plane (see Figure 5.21, bottom). The flow then remains at low supersonic Mach numbers until reaching the blade passage minimum area, located at around 40 to 50 percent chord, where it begins to accelerate again. Depending on the downstream boundary conditions, this flow may remain axial-supersonic as it exits the rotor blade row (impulse-type operation), or it may shock back down to axial-subsonic conditions (subsonic throughflow operation) through a terminal shock located downstream of the blade passage minimum area.

At 100 percent rotational speed (see Figure 5.22) the computed pitchline flow field is quite similar to that for 75 percent rotational speed, as a comparison of Figures 5.21 and 5.22 reveals. Notice, again, the choking between the blade leading edges. For both speeds the flow fields upstream of the blade row are quantitatively similar in the absolute frame-of-reference, even though the relative Mach number levels are substantially different. It is not until the flow is within the blade row that a large difference in the absolute Mach number levels for the two speeds is induced.

So far the discussion of the axial-subsonic rotor-inflow characteristics has mostly considered analytical and computational results obtained assuming two-dimensional inlet streamtubes, i.e., rotor inlet streamtubes with constant radius and height. The influence that three-dimensional effects have on the inflow characteristics will now be examined by considering results from two fully three-dimensional viscous CFD simulations: one computation at 75 percent of design rotational speed and another at 100 percent speed. The

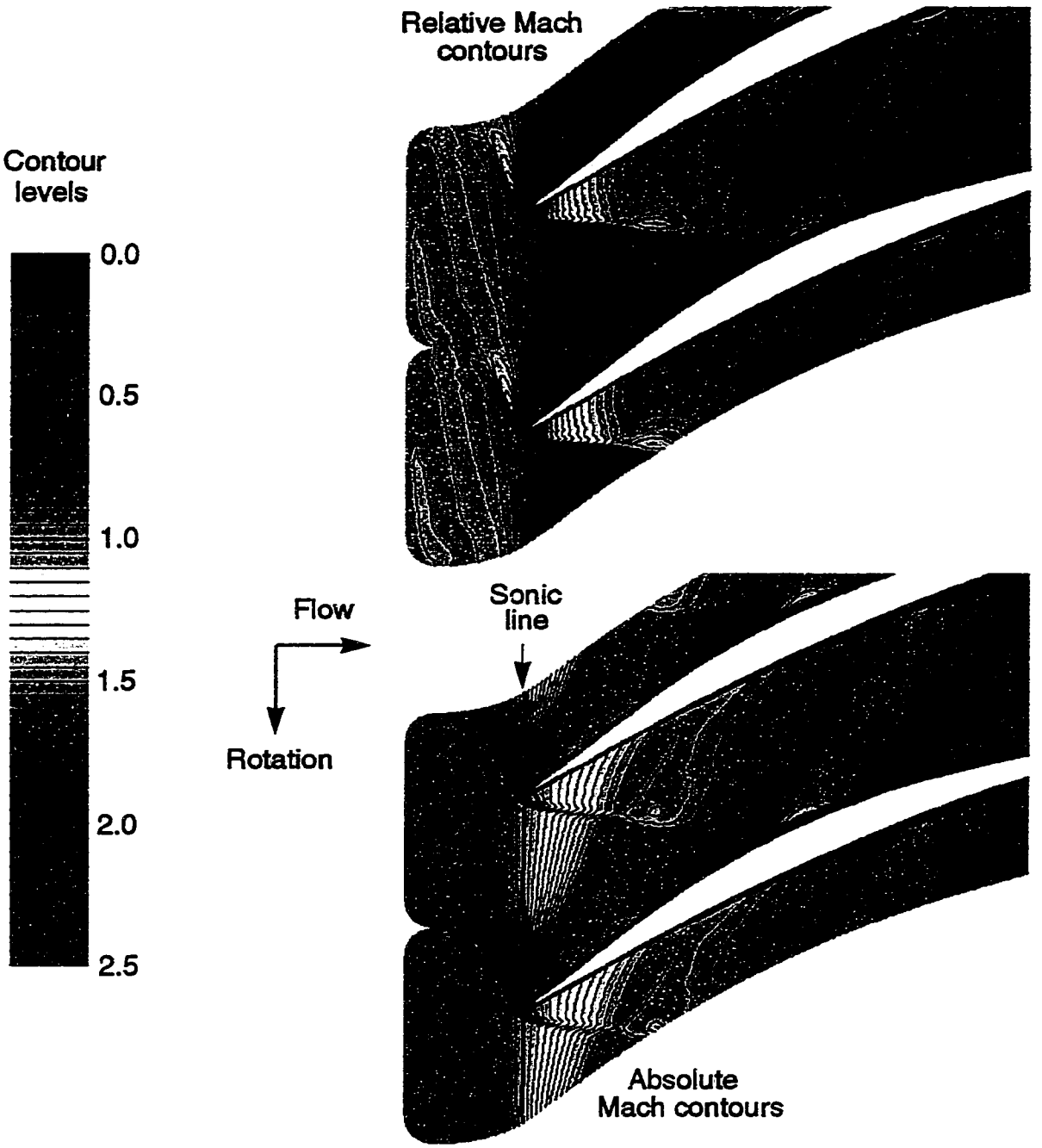

Figure 5.22 Viscous two-dimensional CFD Mach number contours for the rotor pitchline at 100 percent of design rotational speed with choked axial-subsonic inflow conditions

bulk of the discussion focuses on the results for 75 percent speed; however, the three-dimensional effects are similar at both speeds so the conclusions reached generally apply to the range of speeds between 75 and 100 percent.

In order to verify the accuracy of the analytical tools being applied, experimental results are also introduced now where appropriate. The subsequent discussion will conclude this section by providing a summary of the *overall* axial-subsonic inflow characteristics of the baseline rotor. Note that the summary will cover most of the practical speed range of the rotor and applies only to rotor choking conditions.

Before proceeding, however, this may be a good place to digress slightly and briefly discuss the nature of the "covered-passage starting" as the rotational speed is increased from 60 to 75 percent of design speed. In considering this, it should first of all be recognized that the rotor flow field is actually very three-dimensional during this process, and is not "two-dimensional" as modeled in the above CFD work. In the realistic three-dimensional flow the covered passages at a particular spanwise location do not "start" in a conventional, discontinuous manner as, for example, a supersonic inlet, wind tunnel, or even cascade starts. Rather, the flow field adjusts itself in the spanwise (radial) direction between a started condition at the outer spanwise elements, and an unstarted condition at the inner spanwise elements. The approximate situation corresponding to 65 percent rotational speed is depicted in Figure 5.23, where the mid-gap sonic line in the absolute frame-of-reference is sketched. Notice that the "transonic region" is located somewhere near midspan, as indicated by the s-shaped part of the sonic line. Increasing the rotational speed moves the transonic region towards the hub, thereby increasing the overall mass flow until, at 75 percent speed, the rotor is choked in the leading-edge plane over most of the span. At this point the rotor induces the maximum mass flow. Since the 75 percent speed condition was simulated using the fully three-dimensional CFD code, RVC3D, a computed result can be shown for this case. In Figure 5.24, absolute Mach number contours for the pitchline blade-to-blade plane and the mid-gap plane of the flow field are presented. As can be seen, the computed flow is indeed choked in the leading edge plane, from hub to tip.

Rotor inflow Mach numbers obtained from circumferential-averaging of the three-dimensional viscous CFD flow field for 75 percent of design rotational speed are shown in Figure 5.25, which contains a graph of axial inflow Mach number versus percent annulus

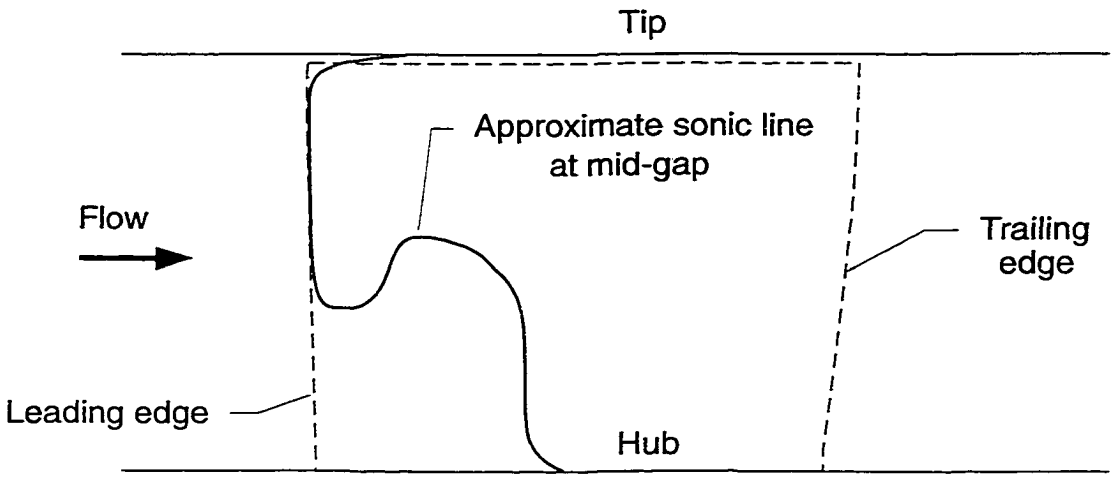

Figure 5.23 Sketch showing approximate mid-gap sonic line (absolute frame-of-reference) corresponding to 65 percent of design rotational speed

height. These Mach numbers were calculated from the computed three-dimensional flow field by circumferential *entropy-averaging* at the *pseudo grid inlet*, located along a straight line between the hub and tip axial coordinates of -0.487 and -0.687 inches, respectively (see Figure 4.12). This location is about 14 percent of axial chord upstream of the rotor. For comparison, the three two-dimensional viscous CFD solutions are also shown.

The overall mass flow for the three-dimensional CFD solution is 52.29 lbm/sec, which agrees closely with the experimental value of 52.17 lbm/sec. The corresponding computational and experimental hub and casing *isentropic wall Mach number* distributions in the inlet duct are compared in Figure 5.26, also demonstrating good agreement and reinforcing the overall mass flow comparison. Using the static pressure tap location 2.0 inches upstream of the rotor, a nominal inflow Mach number (see Chapter 3) of 0.822 is obtained for the computation, compared to the experimental value of 0.819.

In light of the apparent accuracy of the three-dimensional computation, it would appear in Figure 5.25 that the two-dimensional CFD results are consistently too low, although the agreement is still fair ($\Delta M \approx 0.02$). It will now be demonstrated, however, that this difference derives directly from three-dimensional effects not modeled in the two-

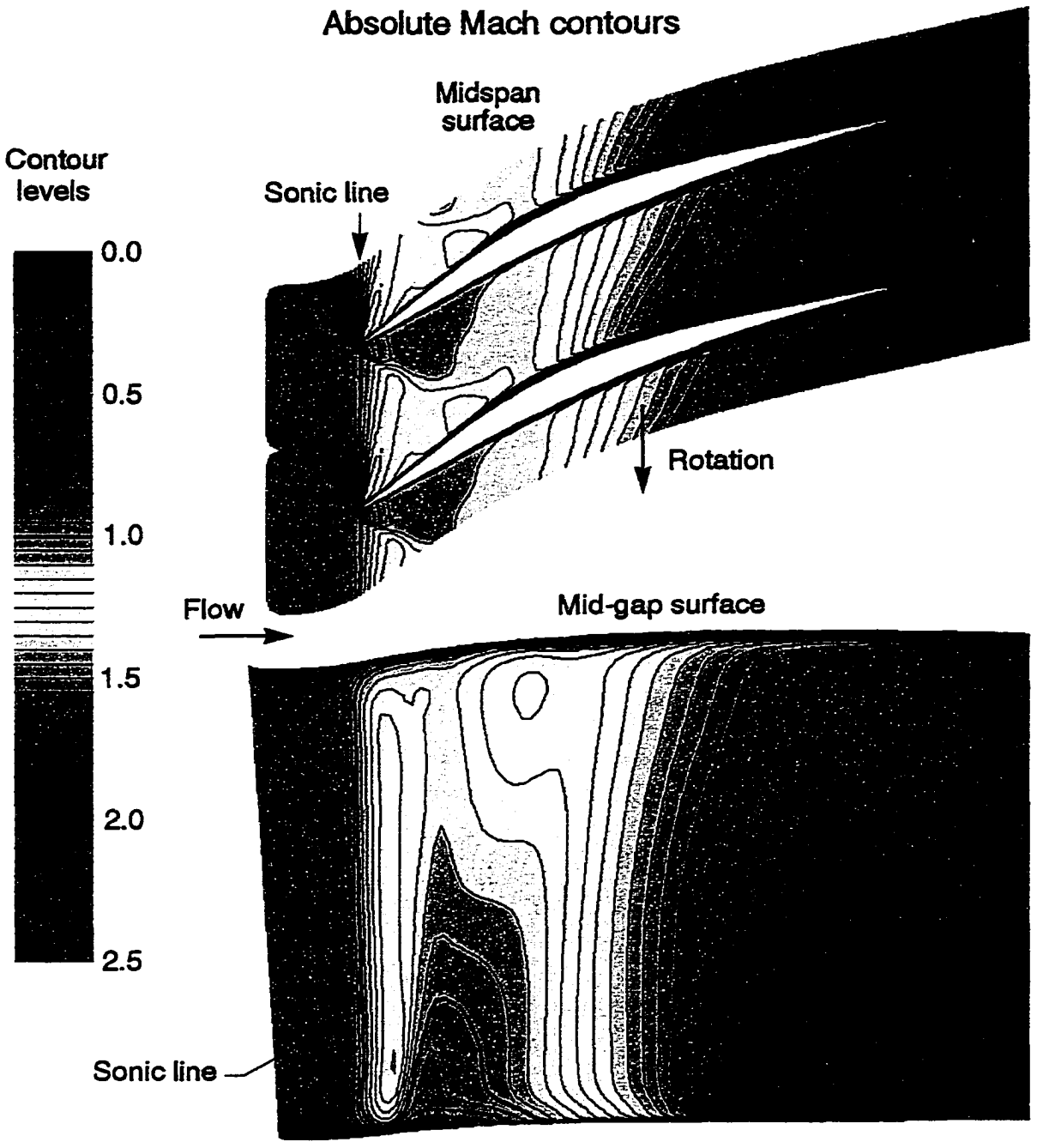

Figure 5.24 Viscous three-dimensional CFD Mach number contours for the rotor at 75 percent of design rotational speed with choked axial-subsonic inflow conditions

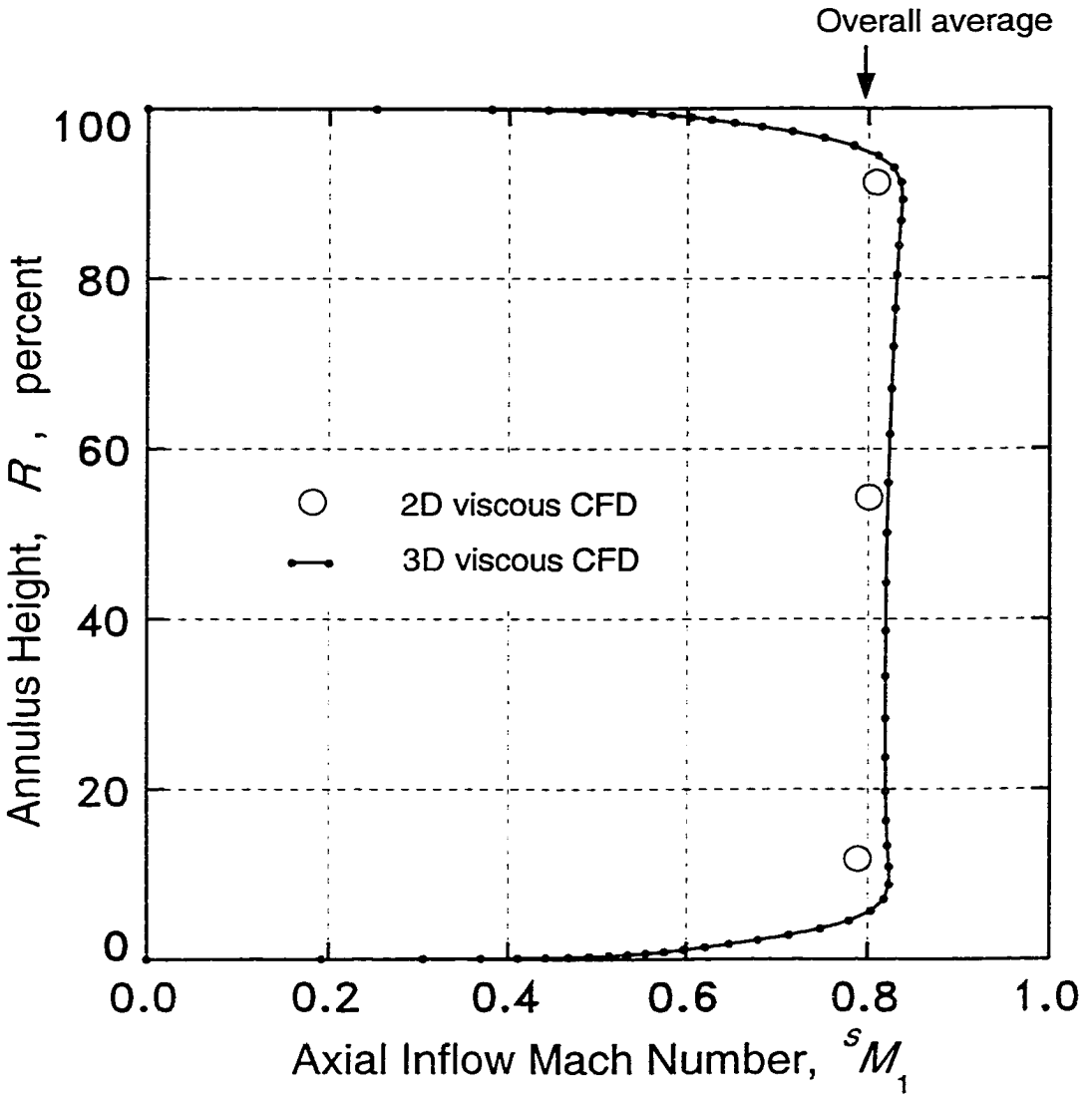

Figure 5.25 Spanwise distribution of axial inflow Mach number for the rotor at 75 percent of design rotational speed; circumferential-average CFD results at a location about 14 percent of axial chord upstream of rotor (entropy average)

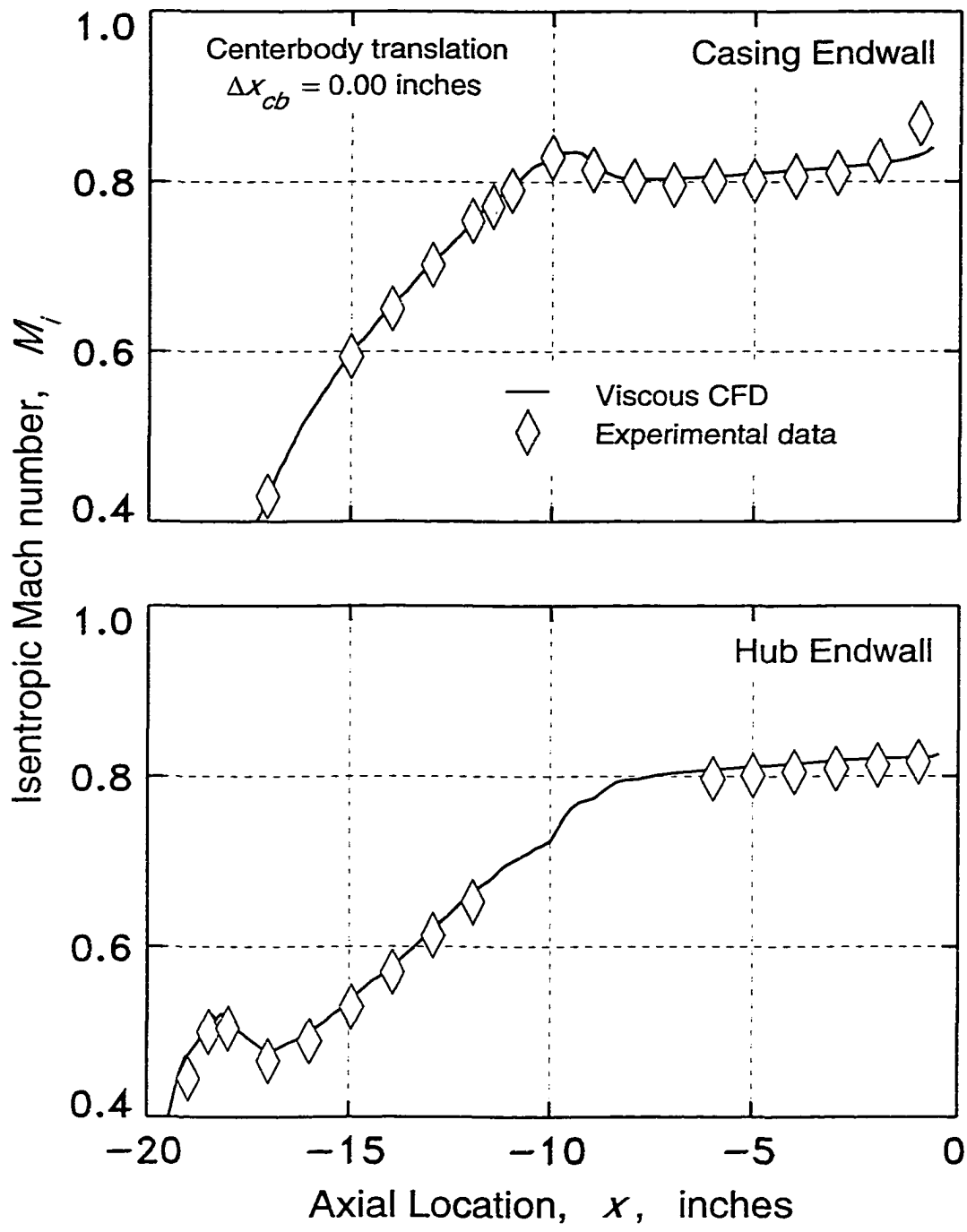

Figure 5.26 Comparison of experimental and computational isentropic endwall Mach number distributions for the inlet duct; rotor operating at 75 percent of design rotational speed

dimensional analysis. Moreover, it will be shown that the two- and three-dimensional CFD solutions are really in much better agreement than they appear to be in Figure 5.25.

The percent variation in streamtube heights, and hence streamtube areas, for three axisymmetric streamtubes at the rotor inlet are shown in Figure 5.27. These streamlines correspond to annulus heights of 16.7, 50.0, and 83.3 percent, and were each determined from the circumferentially-averaged three-dimensional CFD solution. Note that the zero percent axial-chord location is at the rotor leading edge for each streamline. The main result presented in this figure is that all of the core streamtubes from hub to tip undergo a rapid net-area-expansion on the order of about one percent just prior to entering the rotor, which has the effect of diffusing the flow slightly, yet abruptly. Upon entering the rotor, however, the flow then accelerates very rapidly to axial-supersonic velocities. The reason for the sudden area-expansion of the inflow streamtubes can be seen from a graph, shown in Figure 5.28, of the area-blockages factors for the (circumferential-average flow) endwall boundary layers entering the rotor. Observe the rapid decrease in flow area blockage from the hub and casing boundary layers as they approach and enter the blade row, thus increasing the effective flow area in the annulus by a corresponding amount. This effect is a consequence of the sudden drop in static pressure induced by the rotor at its entrance, and which exerts a substantial influence on the viscous flow in the endwall regions.

The quantitative effect of a net increase of 0.75 percent in inflow streamtube area (from grid inlet to rotor leading edge) on axial inflow Mach number is shown in Figure 5.29. The top of this figure shows a streamtube height variation similar to that in Figure 5.27 for the midspan streamtube. The bottom compares circumferentially-averaged [14] viscous CFD results: the fully three-dimensional result from which the streamtube was derived, indicated by the solid line; a quasi-three-dimensional result computed using the same stream tube, indicated by the dash-dotted line; and a two-dimensional result computed assuming no streamtube-height variation, indicated by the dashed line. Note that the pitchline Mach numbers in Figure 5.25 correspond to the Mach numbers in Figure 5.29 at the grid inlet location (-14 percent axial chord). As the comparison in Figure 5.29 demonstrates, the quasi-three-dimensional and fully three-dimensional computations are

---

[14] *Entropy-averaging* procedure (see Appendix C).

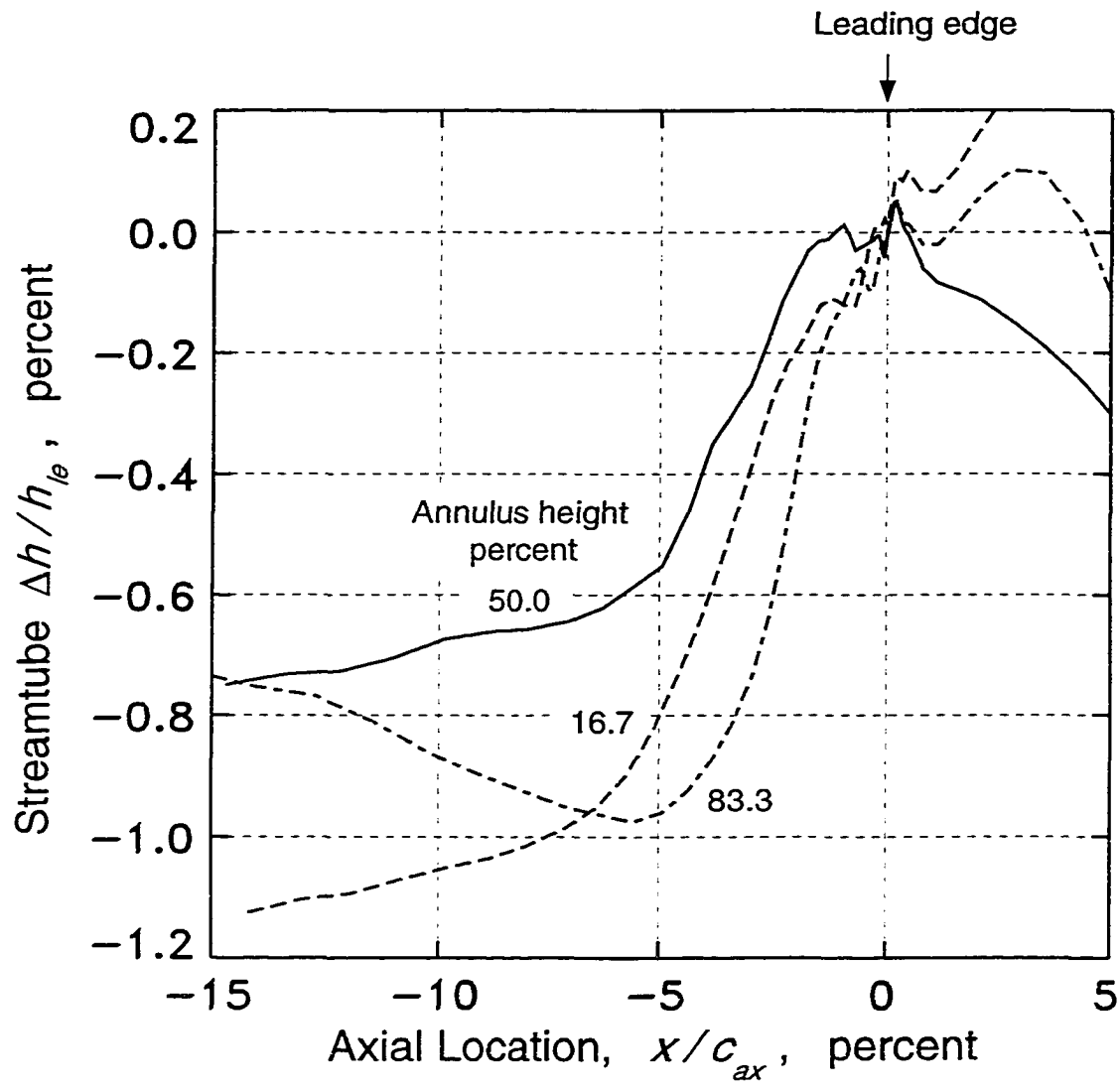

Figure 5.27 Streamtube height variations for three axisymmetric streamtubes at the rotor inlet; streamtubes calculated from circumferentially-averaged three-dimensional viscous CFD solution for the rotor at 75 percent of design rotational speed

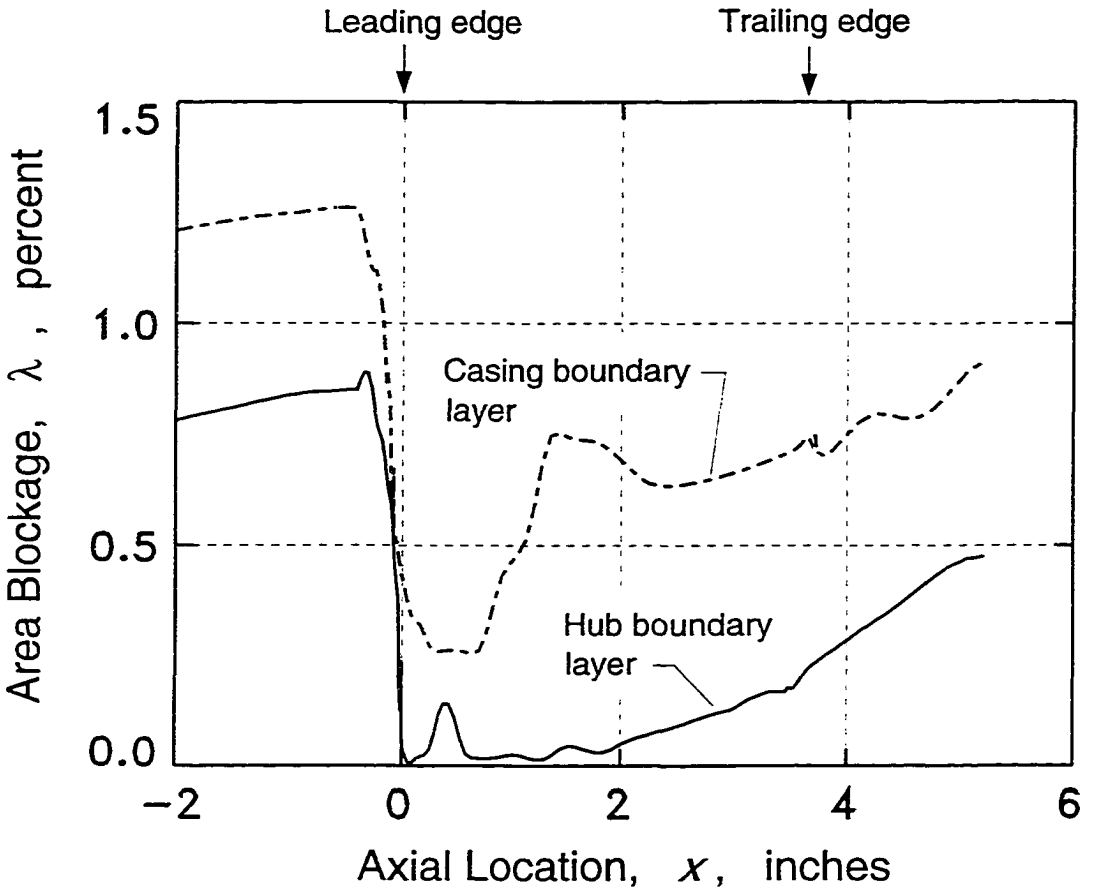

Figure 5.28 Area blockage distributions for the endwall boundary layers entering the rotor; boundary layer displacement thicknesses calculated from circumferentially-averaged three-dimensional viscous CFD solution for the rotor at 75 percent of design rotational speed

in fairly good agreement when the three-dimensional inflow streamtube variation is used for the quasi-three-dimensional computation.

Equally significant in Figure 5.29 are the similar magnitudes of all three sets of Mach numbers at and very near the leading-edge plane (-2 to 0 percent axial chord), suggesting that the Mach number there is almost independent of the streamtube variation upstream. This result is taken as demonstrating that the two- and three-dimensional CFD solutions

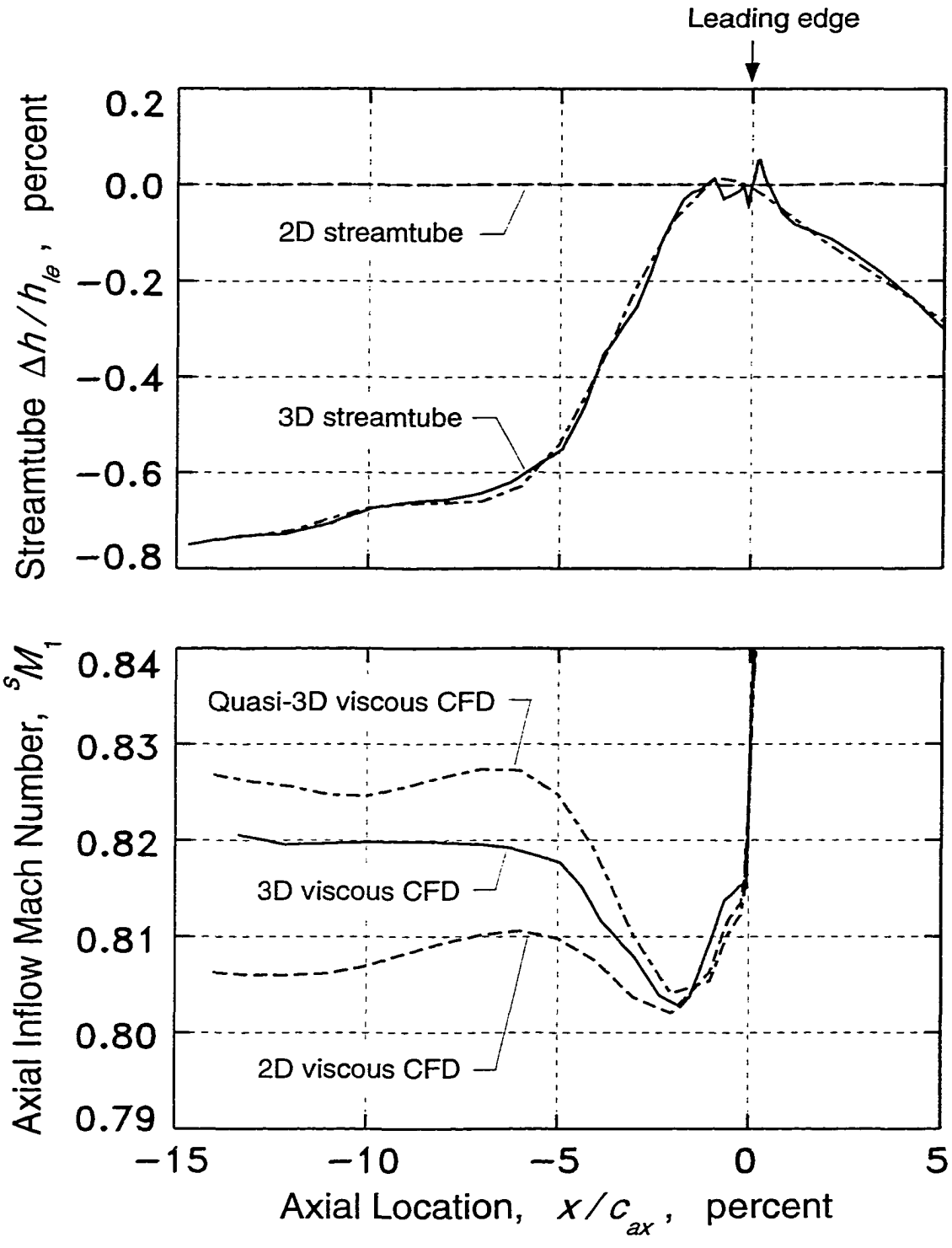

Figure 5.29 Influence of streamtube height variations on axial inflow Mach number

are really in better agreement than that indicated in Figure 5.25; that is, the solutions agree closely when three-dimensional effects are properly accounted for. Furthermore, the result is interpreted as showing that the mass-flow induction capacity of the rotor is determined primarily by two-dimensional blade-to-blade aerodynamic effects in the leading-edge plane, which is why the two-dimensional computation succeeds in predicting the mass-flow per unit area at the rotor face. The three-dimensional effects alter the upstream Mach number levels, but they do not greatly influence the overall mass-flow induced by the rotor. When the two- and three-dimensional CFD solutions of Figure 5.25 are compared just at the inlet plane of the rotor, as shown in Figure 5.30, then the agreement is close. In fact, the Mach number levels at the inlet plane are even indicative of the *overall average* inflow Mach number, which is also included in Figure 5.30 for comparison. Several details regarding the method of calculating an overall average inflow condition are discussed later, in the next subsection.

From simple one-dimensional considerations, the effect of streamtube variations on the upstream inflow Mach number can be shown. For example, consider a one-dimensional, isentropic streamtube. A simple sensitivity study using mass-flow continuity can be used to show that Mach number is fairly sensitive to changes in area. The following equation relating changes in area to changes in Mach number can be derived:

$$\frac{dA}{A} = \frac{-d\phi}{\phi} = 2\left[\frac{M^2-1}{2+(\gamma-1)M^2}\right]\frac{dM}{M} \tag{5.15}$$

Taking a nominal value of 0.800 for the Mach number, a decrease of 0.75 percent in area corresponds to an increase of 0.019 in the Mach number, which is the same increase computed using the more sophisticated CFD (see Figure 5.29 at around -14 percent axial chord). Of course, the amount and direction of streamtube variations are not known *a priori*, but are determined as part of the three-dimensional CFD solution.

The computational and experimental results for 100 percent of design rotational speed are very similar to those for 75 percent speed. Also, in comparing the analytical and experimental results, similar levels of agreement are observed. The spanwise distribution of the axial inflow Mach numbers computed with the three-dimensional code is shown in Figure 5.31, again with two-dimensional CFD results also shown for comparison. The

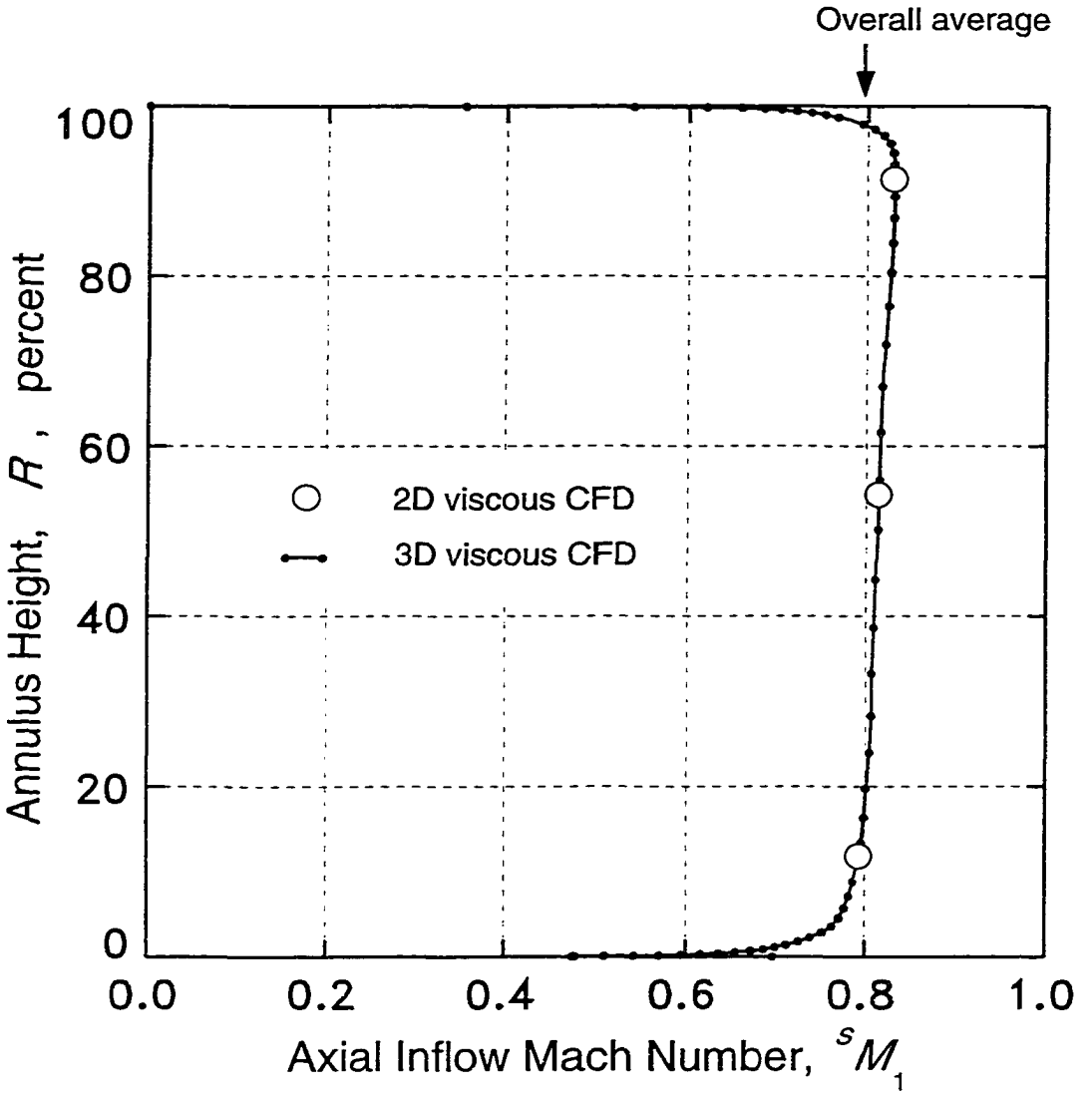

Figure 5.30 Spanwise distribution of axial inflow Mach number for the rotor at 75 percent of design rotational speed; circumferential-average CFD results at the rotor inlet plane (entropy average)

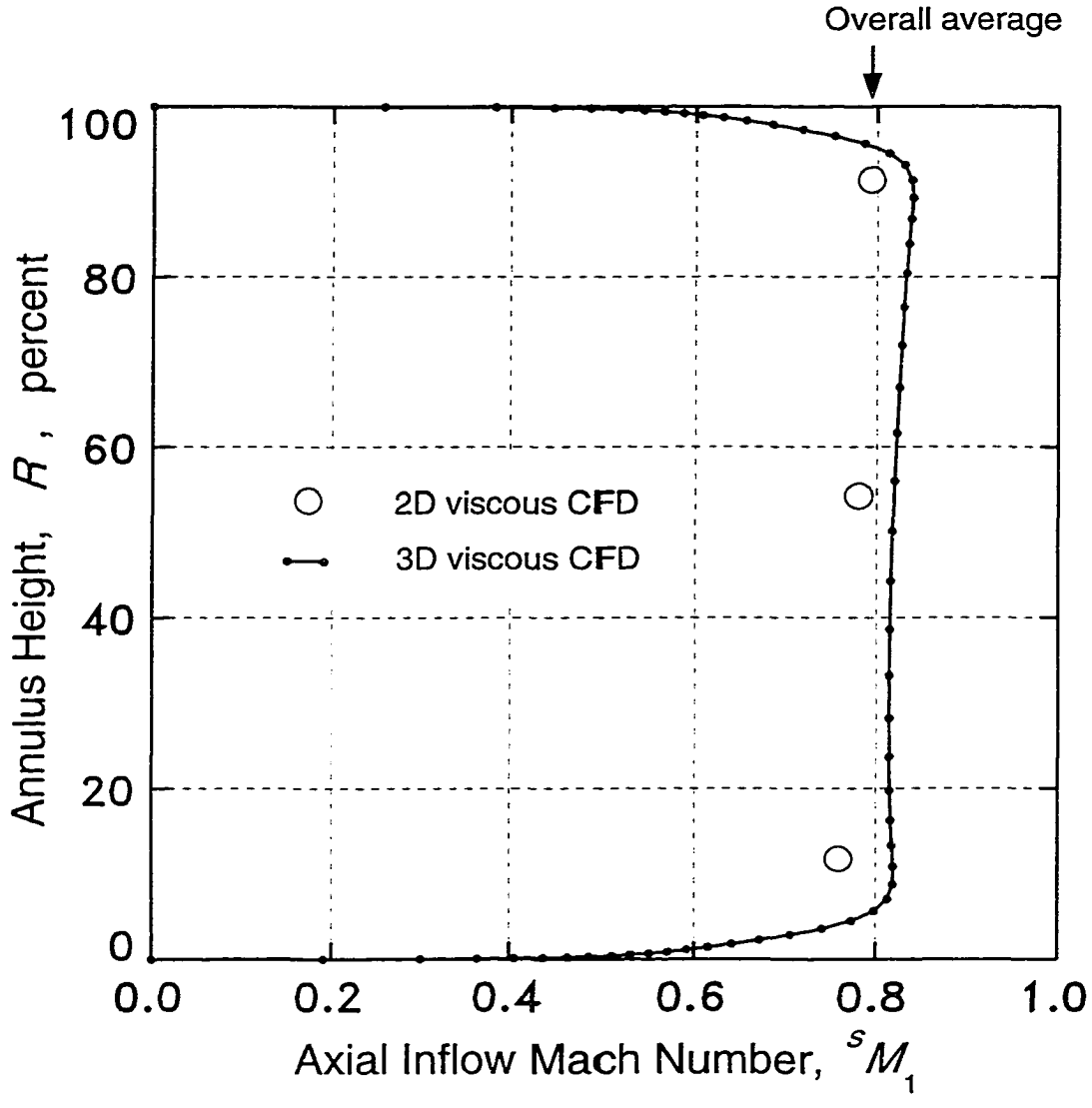

Figure 5.31 Spanwise distribution of axial inflow Mach number for the rotor at 100 percent of design rotational speed; circumferential-average CFD results at a location about 14 percent of axial chord upstream of rotor (entropy average)

same type of result for the upstream location just at the rotor inlet (face) is shown in Figure 5.32. The computed overall mass flow is 52.26 lbm/sec, which compares well with the experimental value of 52.09 lbm/sec. Corresponding computational and experimental hub and casing *isentropic wall Mach number* distributions in the inlet duct are compared in Figure 5.33. The *nominal* inflow Mach number at the 2.0 inch location upstream is 0.820 for the computation, compared to 0.794 for the experiment. Note in Figure 5.33 that the measured and computed distributions for the endwall Mach numbers are not in close agreement, even though the measured and computed overall mass flows are. It would appear that the experimental values are somewhat low, although no specific cause or explanation can be given at this time.

Overall-average inflow conditions

Overall-average inflow conditions for the computed three-dimensional flow fields are obtained by spanwise integration and averaging of the circumferential-average quantities. When determining average quantities upstream of the rotor, the method of circumferential averaging is not very critical since the flow varies little in the circumferential direction, at least as long as the averaging is performed at a location sufficiently far upstream, e.g., at the pseudo grid inlet. In the spanwise direction, however, the method of averaging can be important due to the existence of the endwall boundary layers. Since it is desirable that the average conditions correctly represent the total-pressure deficit (loss) in the endwall boundary layers, the *entropy-averaging* procedure (see Appendix C) would seem to be the preferable method for spanwise averaging.

Applying this averaging procedure to the computed three-dimensional flow field for 75 percent of design speed yields an average axial inflow Mach number $\bar{\bar{M}}_1$ of 0.796. The corresponding inlet total-pressure ratio $\bar{\bar{p}}_{t1}/p_{t0}$ is 0.989. An *effective blockage* λ_{eff} which is related to the average inlet Mach number can also be calculated using mass-flow continuity:

$$\lambda_{eff} = 1 - \frac{\dot{m}}{\rho_{t0} a_{t0} A_1 \phi_1} \tag{5.16}$$

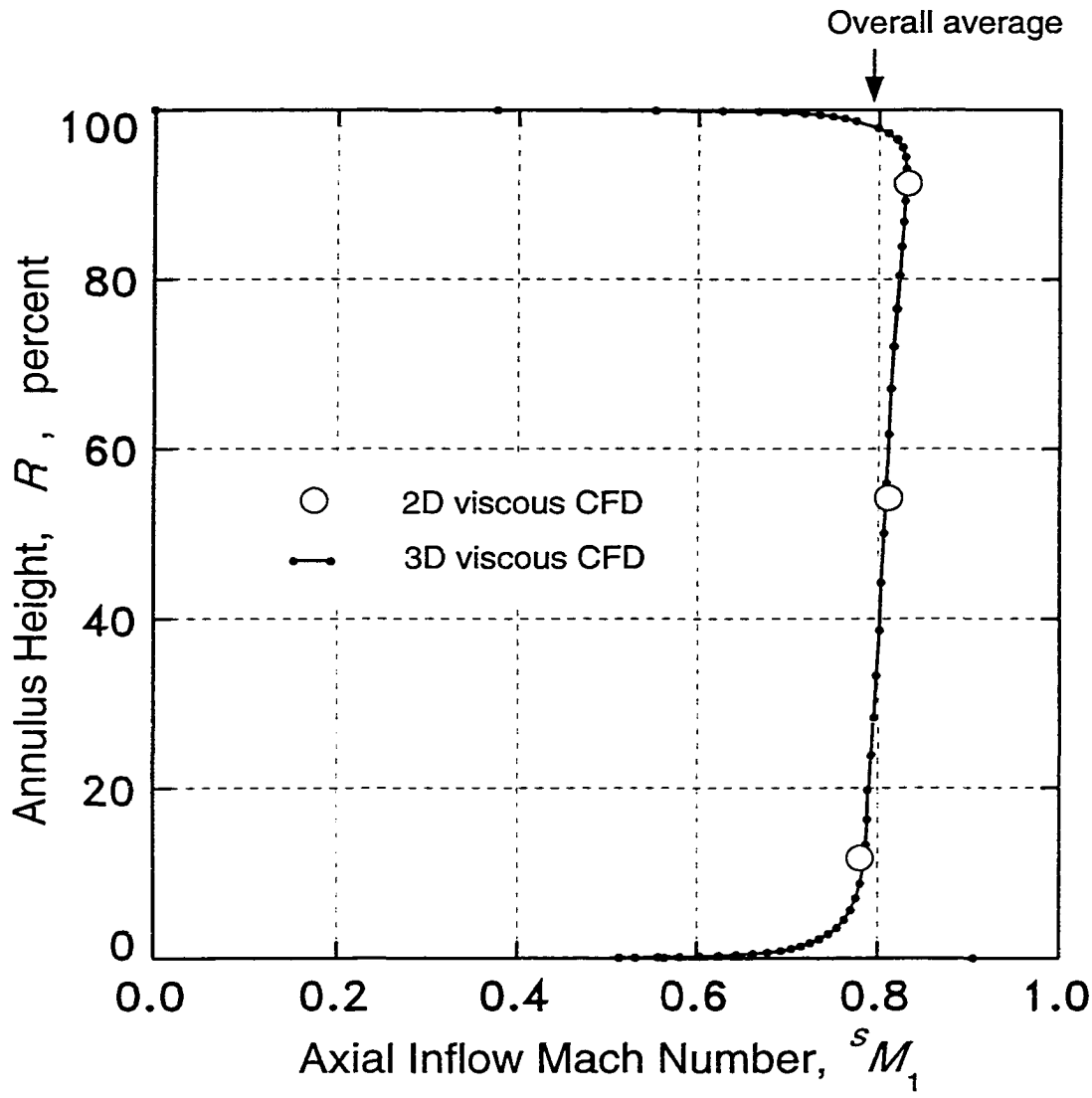

Figure 5.32 Spanwise distribution of axial inflow Mach number for the rotor at 100 percent of design rotational speed; circumferential-average CFD results at the rotor inlet plane (entropy average)

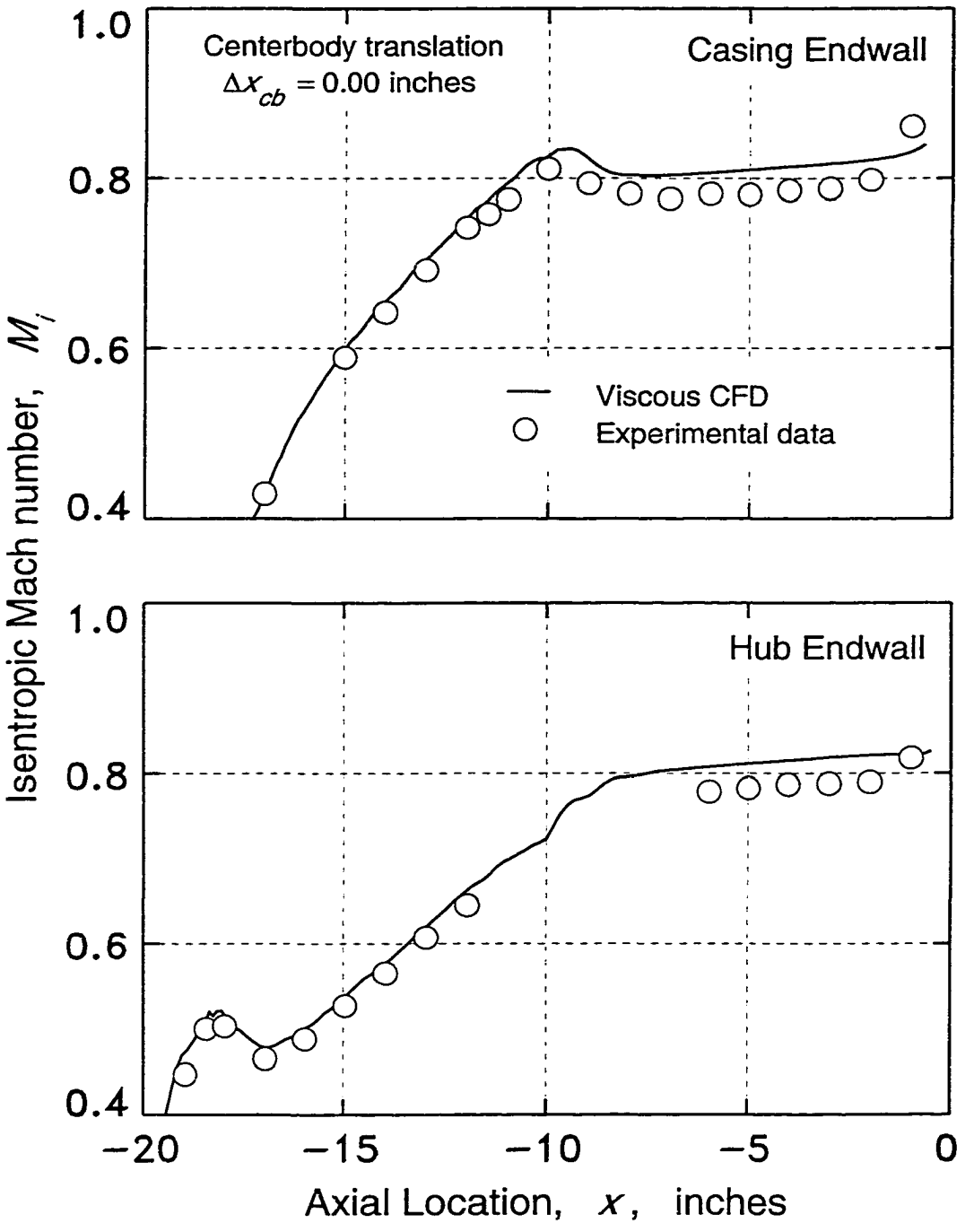

Figure 5.33 Comparison of experimental and computational isentropic endwall Mach number distributions for the inlet duct; rotor operating at 100 percent of design rotational speed

where $\phi_1 = \phi({}^{\bar{ss}}\overline{M}_1)$ and A_1 is the annulus area. The total-pressure ratio (or total-density) ratio is simply related to the effective blockage since the inlet duct flow is isoenergetic:

$$\frac{{}^{\bar{ss}}\bar{p}_{t1}}{p_{t0}} = 1 - \lambda_{eff} \tag{5.17}$$

Therefore, the effective blockage for the 75 percent speed operating point is about one percent.

The computed three-dimensional flow field for 100 percent of design speed can be averaged in the same manner as above, giving an inflow Mach number ${}^{\bar{ss}}\overline{M}_1$ of 0.794 and an inlet total-pressure ratio ${}^{\bar{ss}}\bar{p}_{t1}/p_{t0}$ of 0.989. The effective blockage is therefore about one percent, which is the same as for 75 percent speed.

It should be noted that the effective blockage is different from the boundary layer blockage. As already pointed out, the effective blockage is related to the *overall average* Mach number and total pressure of the inflow. The boundary layer blockage, on the other hand, is the annulus area blockage consistent with the displacement thicknesses of the endwall boundary layers. As such, the boundary layer blockage is related to an average free-stream Mach number, rather than to an overall average Mach number. For the higher flow rates of the baseline fan, the boundary layer blockage at the 2.0 inch location upstream of the rotor is about 2.1 percent [15], which is almost twice the value of the effective blockage.

To conclude this section, overall axial inflow Mach numbers for the choked baseline rotor are presented for several operating points covering most of the practical rotational speed range. The effective blockage just discussed will be useful at this point since it allows the experimental mass flow data to be rendered in the form of an axial inflow Mach number which characterizes well the one-dimensional rotor inflow aerodynamics, and which is also suitable for comparison with the two-dimensional analytical results. It may

---

[15] Hub and casing boundary layer displacement thicknesses of 0.030 and 0.032 inches, respectively.

be recalled that the importance of the inflow Mach number lies in its relationship to rotor inflow starting and unstarting, to be discussed in the next section.

In attempting to quantitatively capture the rotor inflow aerodynamics in a one-dimensional sense, either for the experimental data or the three-dimensional CFD simulations, it would seem appropriate that overall average inflow quantities, rather than free-stream based quantities, be used. The more compelling reasons for this are inherent in the earlier discussion pertaining to three-dimensional inflow effects. Recall from that discussion that the inlet streamtube heights, and thus the free-stream inflow Mach numbers, can vary considerably as the flow approaches the rotor (see Figure 5.29). The streamtube height variations reflect changes in the boundary layer blockage, which decreases rather abruptly as the flow enters the rotor (see Figure 5.28). Conversely, the overall average inflow Mach numbers and total pressures, and the corresponding effective blockages are practically constant near the rotor inlet, exhibiting only a gradual variation due to total-pressure losses as the flow proceeds through the inlet duct. Perhaps most important, however, is the result that the overall average inflow Mach number $^{\bar{ss}}\overline{M}_1$ appears to be a fairly good one-dimensional representation of the inflow Mach number level as it relates to the mass flow induced by the rotor (see Figures 5.30 and 5.32).

The experimental results of References 48 and 49 are summarized in Table 5.2, where $\overline{M}_1$ is the nominal inflow Mach number based on the endwall static taps 2.0 inches upstream of the rotor, and $^{\bar{ss}}\overline{M}_1$ is the overall average inflow Mach number based (using Equation (5.16)) on the orifice measured mass flow rate $\dot{m}$ and an effective blockage λ_{eff} of 1.0 percent. The experimental overall average Mach numbers $^{\bar{ss}}\overline{M}_1$ in Table 5.2 are compared in Figure 5.34 with corresponding computational and analytical results for the same range of rotational speeds. As can be seen in the figure, the experimental, computational, and analytical results are all in good agreement with each other.

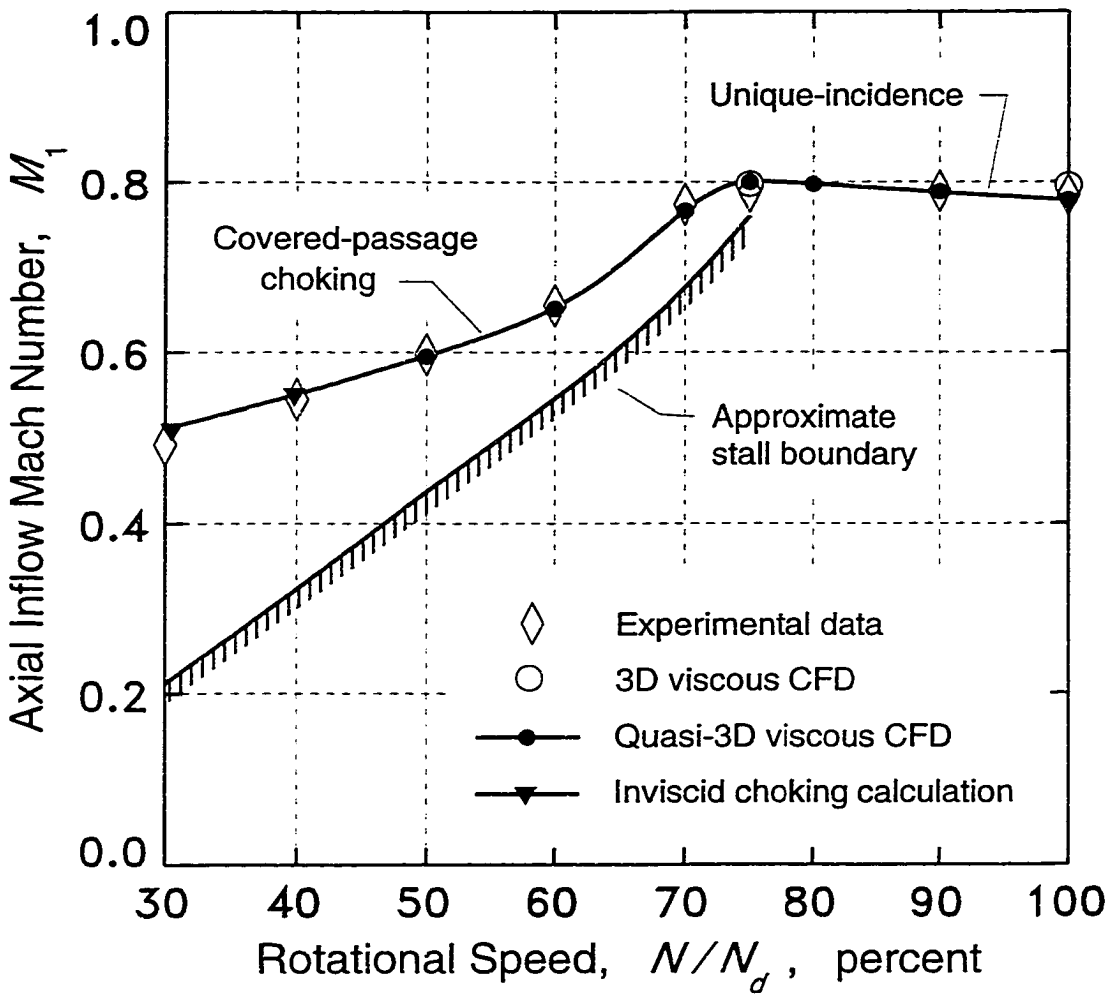

Figure 5.34 Comparison of experimental, computational, and analytical values of overall average inflow Mach numbers for the choked rotor, operating over the 30 to 100 percent rotational speed range

Table 5.2 Experimental values of mass flow rates and axial inflow Mach number

Test Reading	N/N_d percent	$\dot{m}$ lbm/sec	$\bar{ss}\,\overline{M}_1$	$\overline{M}_1$
574	30	40.24	0.493	0.500
587	40	43.14	0.545	0.543
707	50	45.70	0.597	0.602
615	60	48.12	0.655	0.672
681	70	51.84	0.773	0.790
689	75	52.04	0.782	0.810
259 [a]	75	52.17	0.788	0.819
768	90	52.20	0.789	0.816
1307	100	52.09	0.784	0.794

[a] The data for test readings 259, 768, and 1307 were obtained during stage testing. The other data were obtained during isolated rotor testing.

Rotor Inflow Starting and Unstarting

Several of the basic gas dynamic phenomena involved in the supersonic starting of an isoenergetic duct were outlined earlier in this chapter in the section entitled **One-Dimensional Steady-Flow Analysis.** A much more detailed and quantitative analysis of the aerodynamics associated with the starting and unstarting of the rotor inflow, and consequently also the upstream nozzle exit flow, is provided in this section. Although the starting behavior is discussed within the context of an inlet-nozzle such as exists in the baseline SSTF experimental facility, the same general concepts are also involved in the supersonic starting of the inlet and rotor components in an aircraft engine installation.

The primary-inlet and rotor components as they would likely appear in an engine configuration are illustrated in Figure 5.35. The flow features depicted in the figure correspond to supersonic flight with the primary inlet and the rotor inflow in an unstarted mode. The situation in the test facility which relates to that in Figure 5.35 is the condition

where the upstream nozzle is choked and a stable nozzle-shock exists in the diverging section of the c-d nozzle. The inlet shock in Figure 5.35 is analogous to the nozzle shock. Contraction of the nozzle throat increases the Mach number incident on the nozzle shock, as well as its strength, until eventually the nozzle and the rotor inflow start. In the flight propulsion system a similar sequence of events occurs as the supersonic flight Mach number M_0 increases [16]. Since in the propulsion system inlet it is unlikely that an intermediate, stable shock location exists somewhere within the inlet passage upstream of the rotor, then inlet and rotor inflow starting are expected to be simultaneous.

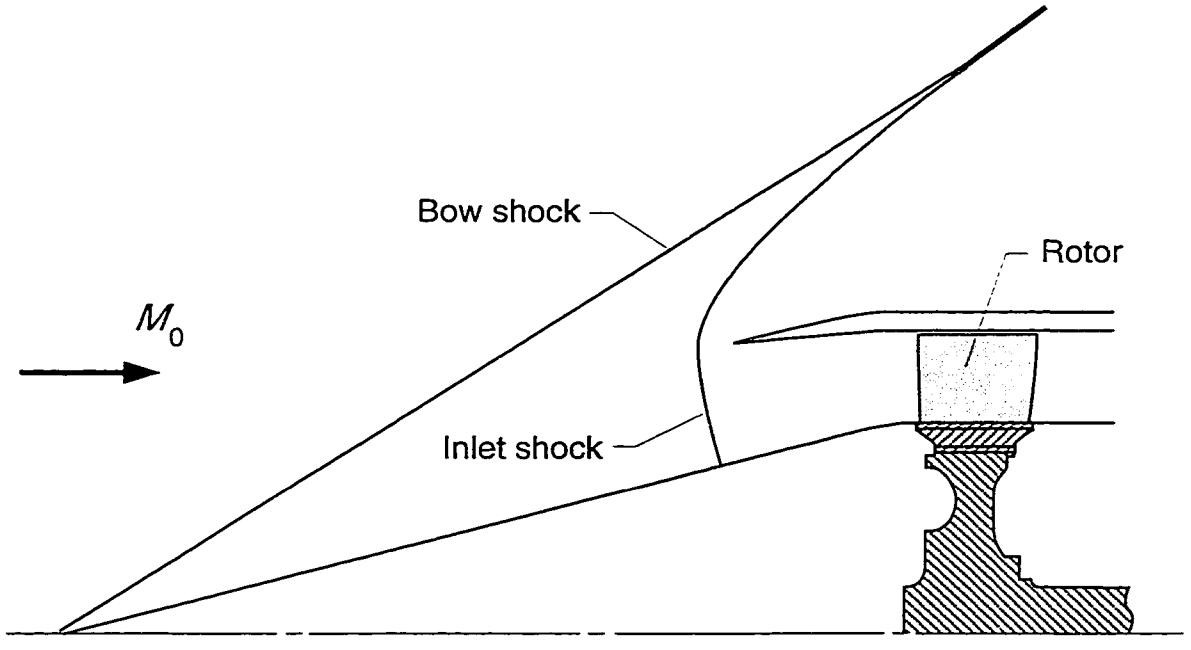

Figure 5.35 Illustration of primary-inlet and rotor components for a supersonic propulsion system; shock structure corresponds to supersonic flight with unstarted inlet and rotor

[16] Variability in the inlet geometry may be used to facilitate inlet starting.

As mentioned earlier, the severity involved in starting the rotor inflow is minimized for a particular rotational speed when the rotor is choked. The reasons for this will be elaborated in this section. The results of the last section demonstrated that, due to unique-incidence, the rotor is practically always choked at rotational speeds at and above 75 percent of design speed unless, of course, it is stalled. At rotational speeds in the 50 to 75 percent range, however, the rotor need not be choked, but for rotor inflow starting it is preferable since even the minimum severity in the start/unstart transition increases dramatically as the rotational speed is reduced below 70 percent of design speed. Details related to this behavior will be discussed in this section, although the experimental rotor was not started, unstarted, or operated with supersonic throughflow conditions at rotational speeds below 70 percent of design. Regarding this, it might be noted that based on theoretical considerations, rotational speeds less than 50 percent of design speed would be associated with a very strong starting shock and would require supersonic Mach numbers exceeding the upper limit of about Mach 2.1 for the test facility nozzle [17].

One-dimensional steady-flow analysis

A one-dimensional steady-flow analysis is very useful for *quantifying*, as well as describing, the first-order behavior of the nozzle flow during the starting process. In considering the rotor inflow for a particular fixed rotational speed, and under rotor choking conditions, an important assumption will be introduced; namely, the overall axial inflow Mach number to the rotor does not change significantly during the entire starting process until the inflow start-transient occurs. The experimental results and computational analyses indicate that this assumption is not strictly true, as expected, but they do confirm that it is a good first-order approximation [18]. An implication of this, as will be shown below, is that the *corrected* mass flow at the rotor inlet does not change appreciably during most of the starting process, although the actual mass flow is continuously reduced as the choked

---

[17] These conditions may be of interest to SSTF systems intended for aircraft with flight Mach numbers extending up into the high-supersonic or low-hypersonic range.

[18] Rotor inflow starting at rotational speeds below 70 percent of design speed involves a stronger nozzle shock, with the consequent shock/boundary-layer interaction effects. Under these conditions the assumption may be less accurate.

nozzle throat is contracted. When the transient "jump" to an axial-supersonic rotor inflow Mach number does occur, terminating the starting process, then the corrected mass flow discontinuously drops to the value of the actual mass flow rate.

The steady-flow situation which is obtained by contracting the nozzle throat beyond the choking threshold (supercritical operation) is illustrated in Figure 5.36. From the figure note that M_0 is the shock-incident Mach number and M_δ is the Mach number at the downstream side of the normal shock. Downstream of the shock the flow is assumed to be isentropic (in the one-dimensional model), and Equation (5.9) can be applied there:

$$A_{*1} = \frac{A_1 \phi_1}{\phi_*} \tag{5.18}$$

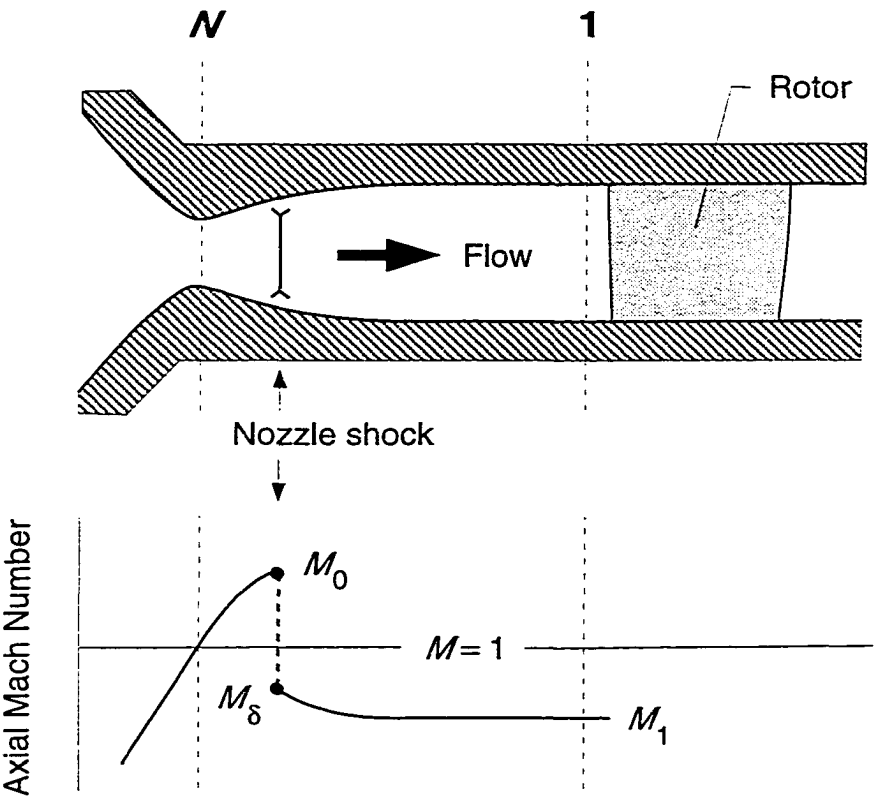

Figure 5.36 Supercritical operation of the upstream converging-diverging (c-d) nozzle; one-dimensional model with normal shock

The critical flow area upstream of the shock is equal to the nozzle throat area since the upstream flow is also assumed to be isentropic. The upstream and downstream critical areas are simply related to the nozzle total-pressure ratio:

$$\frac{A_{*N}}{A_{*1}} = \frac{A_{*0}}{A_{*1}} = \frac{p_{t1}}{p_{t0}} \tag{5.19}$$

Since the nozzle total-pressure ratio in this case is the total-pressure ratio across the normal shock, it can be expressed as a function of the shock-incident Mach number through the following equation, derived from the Rankine-Hugeniot relations [53]:

$$\frac{p_{t1}}{p_{t0}} = \frac{p_{t\delta}}{p_{t0}} = \left[\frac{(\gamma+1)M_0^2}{(\gamma-1)M_0^2+2}\right]^{\gamma/(\gamma-1)} \left[\frac{\gamma+1}{2\gamma M_0^2-(\gamma-1)}\right]^{1/(\gamma-1)} \tag{5.20}$$

The Mach number at the downstream side of the normal shock can also be expressed as a function of the shock-incident Mach number:

$$M_\delta^2 = \frac{(\gamma-1)M_0^2+2}{2\gamma M_0^2-(\gamma-1)} \tag{5.21}$$

The inverse of Equation (5.22) is more useful for the present analysis:

$$M_0^2 = \frac{(\gamma-1)M_\delta^2+2}{2\gamma M_\delta^2-(\gamma-1)} \tag{5.22}$$

Equations (5.18) and (5.19) can be combined to yield a relationship for the *nozzle area ratio* A_1/A_{*N}, which can be expressed as a function of the shock-incident and nozzle-exit Mach numbers:

$$\frac{A_1}{A_{*N}} = \frac{\phi_*}{\phi_1}\frac{p_{t0}}{p_{t1}} = f(M_0, M_1) \tag{5.23}$$

Rotor inflow starting is imminent when the nozzle-exit/rotor-inflow Mach number M_1 equals the Mach number on the downstream side of the shock:

$$M_1 = M_\delta \tag{5.24}$$

where $M_\delta = f(M_0)$ as given in Equation (5.21). This limiting situation occurs when the normal shock is located at the downstream end of the diverging section of the c-d nozzle. Therefore, the *post-start* axial-supersonic rotor-inflow Mach number M_0 is related to the pre-start axial-subsonic rotor-inflow Mach number by the discontinuous jump in flow properties across a normal shock wave (Equations (5.22) and (5.24)).

The *corrected* mass flow rates for the nozzle and rotor are closely related to the nozzle total-pressure ratio. Since the actual mass flow rate equals the nozzle flow rate $\dot{m}_N$, and the total temperature T_{t0} of the steady-flow through the nozzle is constant, then the ratio of the nozzle-to-rotor corrected mass flow rates is equal to the nozzle total-pressure ratio:

$$\frac{\dot{m}_N}{\dot{m}_1} = \frac{\dot{m}_N \sqrt{T_{t0}/T_{t\,ref}} \,/\, (p_{t0}/p_{t\,ref})}{\dot{m}_N \sqrt{T_{t0}/T_{t\,ref}} \,/\, (p_{t1}/p_{t\,ref})} = \frac{p_{t1}}{p_{t0}} \tag{5.25}$$

where $\dot{m}_1$ is the corrected mass flow at the rotor inlet.

An example summarizing the basic ideas discussed above is shown in Figure 5.37. The two graphs in the figure correspond to a subsonic rotor-inflow Mach number of 0.800. The top graph shows corrected mass flow for the nozzle and rotor, both normalized to the corrected mass flow for the initial, subsonic rotor-inflow condition. The bottom graph shows the Mach number variations upstream and downstream of, and across the normal shock over the range of nozzle area ratios A_1/A_{*N} encountered during nozzle starting. As can be seen in the graphs, the nozzle begins to choke at an area ratio of 1.038, and the rotor-inflow starts at an area ratio of 1.055 — representing a 5.5 percent stream-tube area contraction upstream. The discontinuous change in rotor-inflow Mach number is from 0.800 to 1.273 as the nozzle starts, corresponding to a 1.6 percent drop in the corrected mass flow to the rotor.

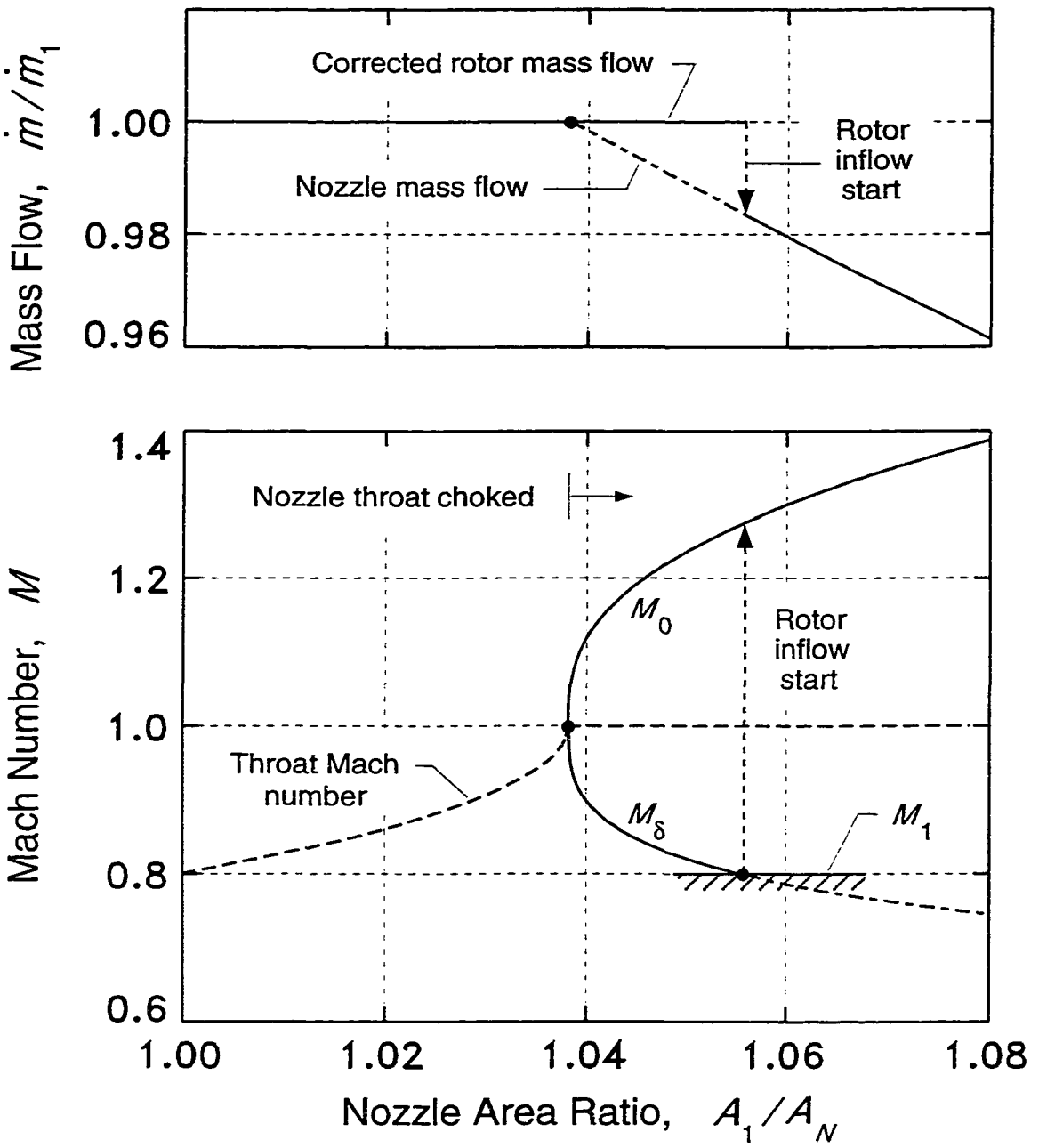

Figure 5.37 Example showing changes in mass flow and inflow Mach number during the nozzle (and rotor inflow) start transition; one-dimensional model with a rotor inflow Mach number of 0.8 prior to starting

Overall-average axial-subsonic rotor-inflow Mach numbers were listed in Table 5.2 in the previous section, for choked-rotor conditions over a wide range of rotational speeds. Using the above set of equations (Equations (5.20) through (5.25)), estimates of the conjugate axial-supersonic inflow Mach numbers and mass flow rates can be determined. Results of this type are listed in Table 5.3 for the same rotational speeds, and they represent the approximate rotor-inflow conditions which are expected at the post-start operating point, just subsequent to the swallowing of the nozzle shock by the choked rotor. More will be said about these results shortly, after first introducing the subject of rotor-inflow unstarting.

Table 5.3 Rotor-inflow post-start conditions based on a one-dimensional analysis using axial-subsonic rotor-inflow Mach numbers

N/N_d percent	$^{ss}\overline{M}_1$	M_0	$\dot{m}_N/\dot{m}_1$	A_1/A_{*N}
30	0.493	2.734	0.4117	3.288
40	0.545	2.215	0.6211	2.033
50	0.597	1.893	0.7706	1.547
60	0.655	1.646	0.8775	1.289
70	0.773	1.326	0.9746	1.078
75	0.782	1.308	0.9780	1.070
75	0.788	1.296	0.9801	1.065
90	0.789	1.294	0.9804	1.064
100	0.784	1.304	0.9787	1.068

Rotor-inflow start/unstart aerodynamics

The axial-supersonic rotor inflow can be unstarted by gradually opening the throat of the upstream nozzle, which is the reverse of the starting process just described above. With reference to the above discussion, and especially to Table 5.3, it seems reasonable to expect that a hysteresis would exists between the *post-start* and the *pre-unstart* conditions, although it is uncertain as to how significant it might be. As will be shown in some detail

below, the experimental and computational results indicate that it is only small, being within the estimated uncertainties of the measurement data, or within the approximations used in the computational analyses. The computational analysis of rotor-inflow unstarting will now be discussed.

By applying the quasi-three-dimensional CFD code RVCQ3D, rotor-inflow unstart simulations were performed over the range of rotational speeds from 50 to 100 percent of design speed. In all cases the rotor inlet region was modeled as two-dimensional. The simulations were aimed at determining the minimum axial-supersonic inflow Mach numbers at which the particular blade-elements examined would remain started. The procedure consisted of performing several numerical simulations for each blade-element, at a given rotational speed, each time incrementally reducing the axial inflow Mach number until an unstart occurred [19], thus establishing the minimum Mach number limit for that blade-element and rotational speed. In all cases three spanwise locations were checked: a near-hub blade-element at 11.8 percent annulus height, a pitchline element at 54.3 percent annulus height, and a near-tip element at 91.4 percent annulus height. The blade-element with the highest unstart Mach number was assumed to be most representative since all elements must unstart together [20]. The results obtained from this computational study are summarized in Table 5.4, and an example from the CFD simulations showing the onset of an unstart at 75 percent of design rotational speed is provided in Figure 5.38. As can be seen in the figure, the unstart is easily recognized.

---

[19] The simulated unstart only established the minimum axial-supersonic Mach number limit. The transient flow simulation itself was not correct since, in order to accelerate convergence, the CFD code was run with a spatially-varying time step.

[20] This was expected *a priori*, but was also demonstrated experimentally. It was considered highly improbable that a nozzle-exit/rotor-inlet shock structure could normally exist which would support a part-span axial-subsonic, and part-span axial-supersonic inlet flow field.

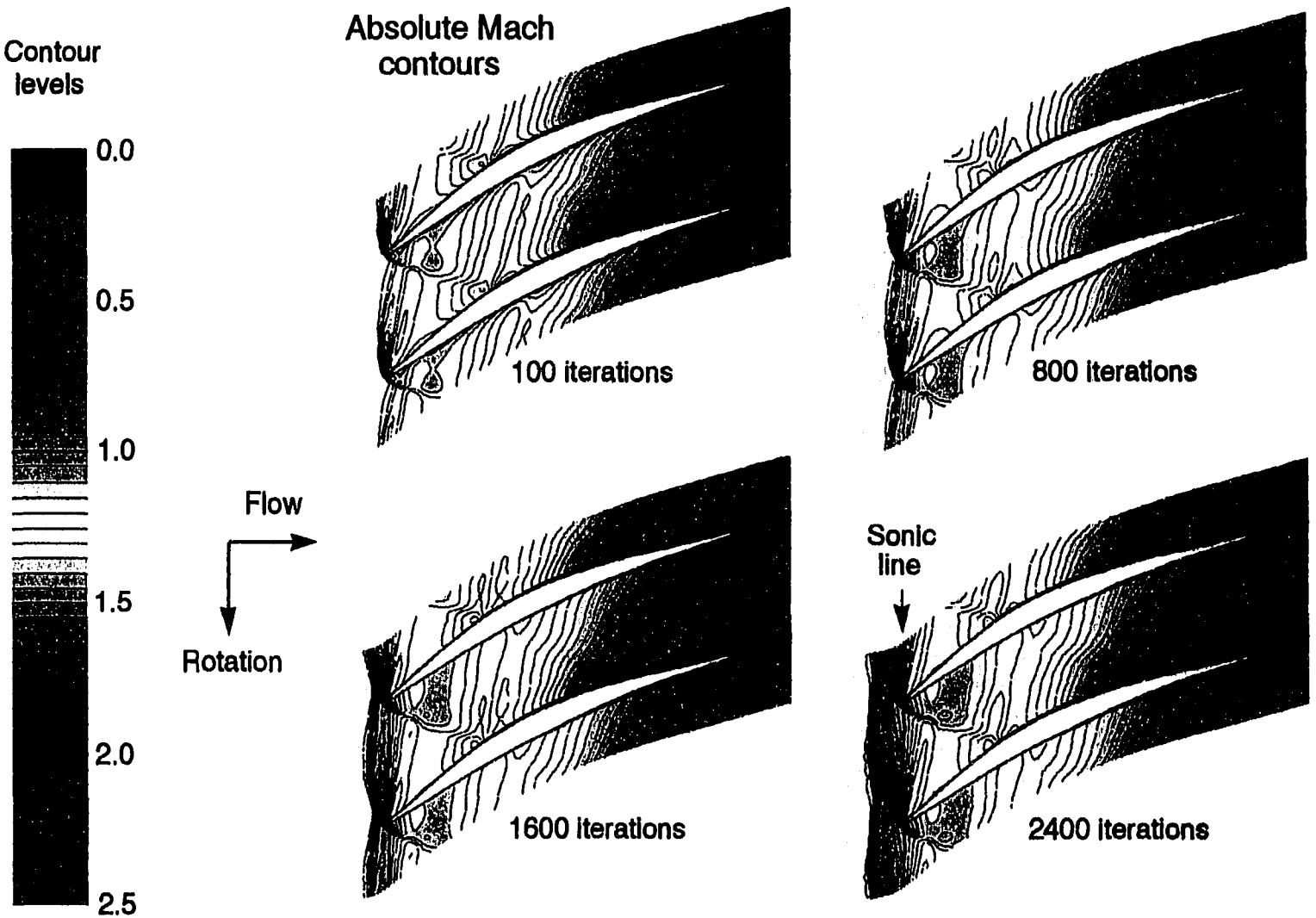

Figure 5.38 Viscous two-dimensional CFD Mach number contours for the rotor pitch-line at 75 percent of design rotational speed; simulated unstart due to an excessively low inflow Mach number (M_1 = 1.26)

Table 5.4 Rotor-inflow unstart Mach numbers determined using two-dimensional CFD simulations

N/N_d percent	$M_{1\ unstart}$	critical blade-element
50	1.93	near-midspan
60	1.53	near-hub
70	1.35	near-hub
75	1.31	near-hub
80	1.31	near-hub
90	1.33	near-hub
100	1.36	near-hub

The results listed in Table 5.4 are graphed in Figure 5.39, which shows axial inflow Mach number versus percent rotational speed. The results from Table 5.3 are also graphed in the figure, as are experimental results and a few other curves.

Referring to Figure 5.39, it is surprising that for rotational speeds exceeding 70 percent of design speed the computed unstart Mach numbers (indicated by filled diamonds) lie *above* the approximate post-start Mach numbers (indicated by filled circles). In actuality that cannot occur since the rotor must be capable of remaining started in order to start in the first place. These discrepancies are relatively minor, however, and could be interpreted as revealing that only a small start/unstart hysteresis should be expected at these rotational speeds. In any case, the computed unstart results will be used to define the theoretical *rotor unstart boundary*, which will also be taken as a reasonably close approximation to the locus of post-start conditions, except perhaps for rotational speeds around 60 percent. At 60 percent of design rotational speed the results indicate that a significant hysteresis may, in fact, be expected. Unfortunately this was not investigated experimentally.

The coordinate space to the upper-right of the unstart boundary in Figure 5.39 is the zone for axial-supersonic inflow operation; that is, either *shock-in-rotor* or *supersonic throughflow* operation. A dashed line indicating zero suction-surface incidence divides

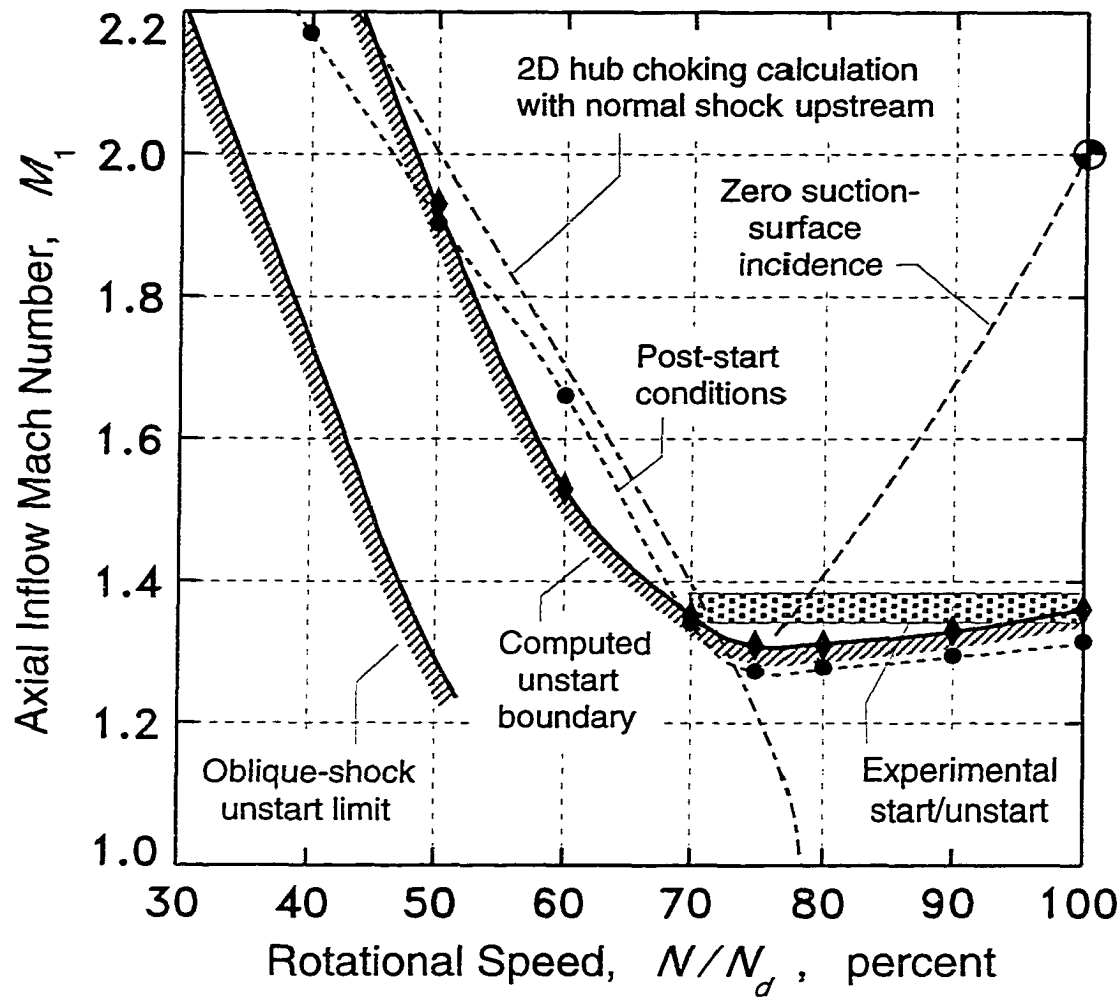

Figure 5.39 Rotor-inflow start/unstart Mach numbers as a function of rotational speed (rotor-inflow unstart boundary); comparison between experimental results, and computational and analytical methods.

this region into two parts: a negative-incidence operation zone to the left of the curve, and a positive-incidence operation zone below the curve.

The experimental results are shown in Figure 5.39 as a band which encompasses the observed post-start and pre-unstart *nominal* supersonic inflow Mach numbers, which lie between 1.34 and 1.37 for the range of rotational speeds tested. As can be seen, there is generally good agreement between the experimental and analytical start/unstart results, especially considering that endwall boundary layer effects were not modeled in the unstart analysis. The good agreement verifies that the first-order effects are two-dimensional in nature, at least for the range of conditions tested. Note, however, that all of the experimental start/unstart transitions involved only positive and near-zero (axial-supersonic) incidence conditions. The most common rotational speed used for transitioning was 75 percent of design speed, which corresponds to a near-zero incidence at the post-start or pre-unstart condition [21].

At the rotational speeds below 70 percent of design speed, the start/unstart boundary in Figure 5.39 has a steep negative slope and is associated with negative incidence conditions. The incidence angles become more negative as the rotational speed is reduced, and the large difference in the slope of the boundary for positive and negative incidences can be attributed to a difference in the aerodynamic mechanism which drives the unstart. This will now be discussed in some detail, first by addressing positive-incidence unstarting, then followed by negative-incidence unstarting.

The basic aerodynamic mechanism involved in positive- (and zero-) incidence unstarting has been analytically considered by Starken and Lichtfuß [71,72] for the case of "sharp" leading edges. The situation is qualitatively the same for the case of blunt leading edges, which case will be considered here and is illustrated in Figure 5.40. Referring to the figure, the blade-to-blade condition which determines the onset of an unstart is when the *left-running* family of weak (expansion) waves generated at and behind the bow of each blade begin to intersect the leading-edge/bow-shock region of the adjacent blade (on the left of each). The unstart-simulation example presented earlier in Figure 5.38 corre-

---

[21] This was optimum since it was the lowest speed with a weak starting shock.

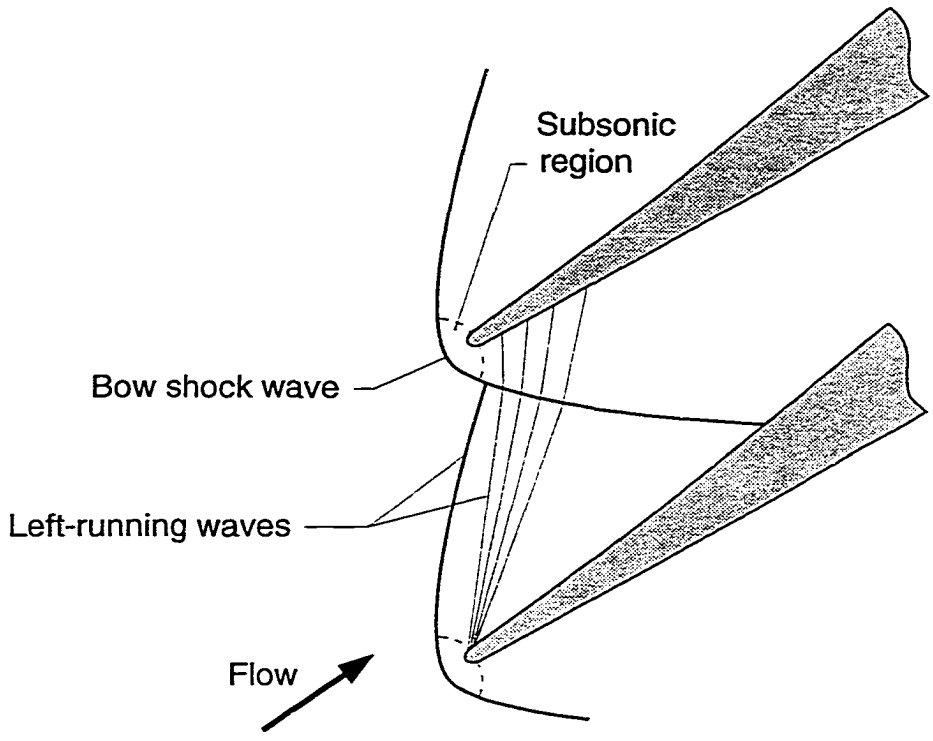

Figure 5.40 Illustration of positive-incidence-unstart flow field for blades with blunt leading edges

sponds to this type of unstart since the incidence angle is nearly zero at 75 percent of design rotational speed.

The negative-incidence unstart involves an entirely different aerodynamic effect, and one which, to the author's knowledge, has not been suggested in the literature. Specifically, as the suction-surface incidence becomes significantly negative an unstart is induced by blade-passage choking, occurring first in the rotor hub region. To demonstrate the first-order nature of this effect, a two-dimensional hub-choking curve is also included in Figure 5.39. This curve was determined using the simple, two-dimensional covered-passage choking calculation method discussed in Appendix D, coupled with the jump relations across a normal shock which is assumed to be just at the rotor inlet. Note that the shock is normal only to the *axial* inflow, but is oblique to the relative inflow. As will be seen in

some of the CFD blade-to-blade flow fields to be presented later, the shock is not exactly normal, but it can be approximated as such for purposes of estimating the choking condition.

There is another theoretical possibility for negative-incidence unstarting which is presented in the open literature [71,72], but which for the baseline SSTF rotor is totally precluded by the choking limit. This other limiting condition involves an oblique shock, i.e., oblique in the relative frame-of-reference, which is situated near, or just in, the leading-edge plane of the blade row, and is therefore approximately normal to the axial direction. A curve representing this limit[22] has been calculated using the oblique shock procedure discussed in Appendix D, and it is included in Figure 5.39 for comparison with the choking limit. As can be seen, the resulting curve lies quite far to the "left" of the choking-unstart limit; thus, the negative-incidence range for supersonic inflow operation is substantially less than might be inferred based on past analytical work, and neglecting the choking aspects of the flow. Note, by the way, that this type of result should generally apply to most practical supersonic throughflow rotor designs where low blade stagger angles can normally be expected.

A generalized summary combining both the axial-subsonic and axial-supersonic rotor inflow characteristics is shown graphically in Figure 5.41. The lower curves are the same as those presented earlier in Figure 5.34, and the upper curves are those just presented in Figure 5.39. Several lines corresponding to various values of suction-surface incidence are also included in the supersonic inflow zone (upper-right). Suction-surface incidence angles corresponding to all of the curves and zones in Figure 5.41 are shown in Figure 5.42, which contains a graph of suction-surface incidence versus axial inflow Mach number. All of the incidence angles graphed in Figure 5.42 were calculated for a near-midspan location, although the exact spanwise location is not important since incidence angle is nearly constant over most of the span at all operating points shown.

---

[22] The near-tip blade sections produced the most restrictive limit. Due to the low suction-surface angles of the baseline rotor, a weak oblique shock solution for a shock lying in the leading-edge plane was not possible at the lower rotational speeds, in which case the limit for shock detachment (from the suction surface) was used instead (see Appendix D).

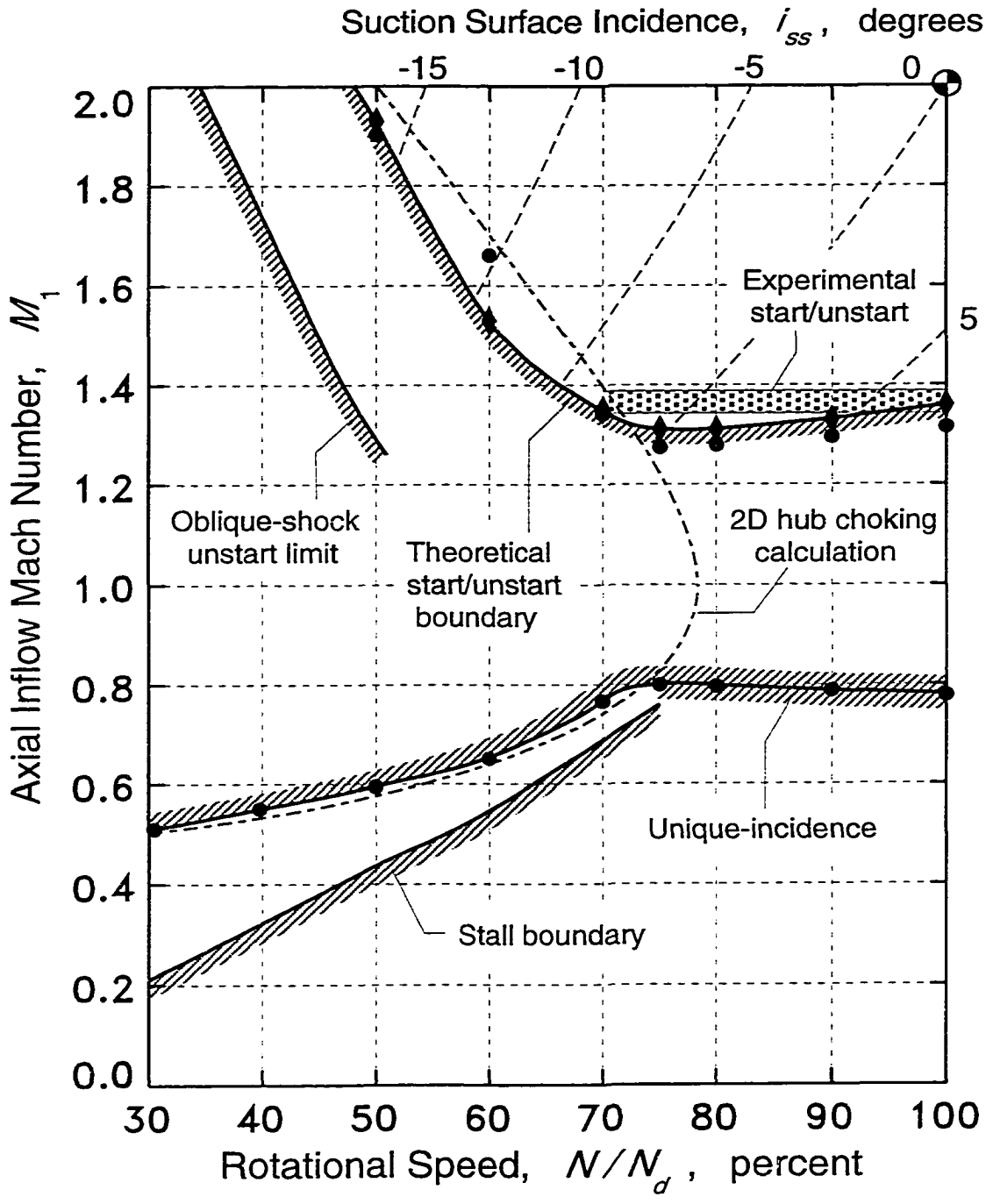

Figure 5.41 Summary of inflow boundaries for baseline rotor operation; axial inflow Mach number versus rotational speed

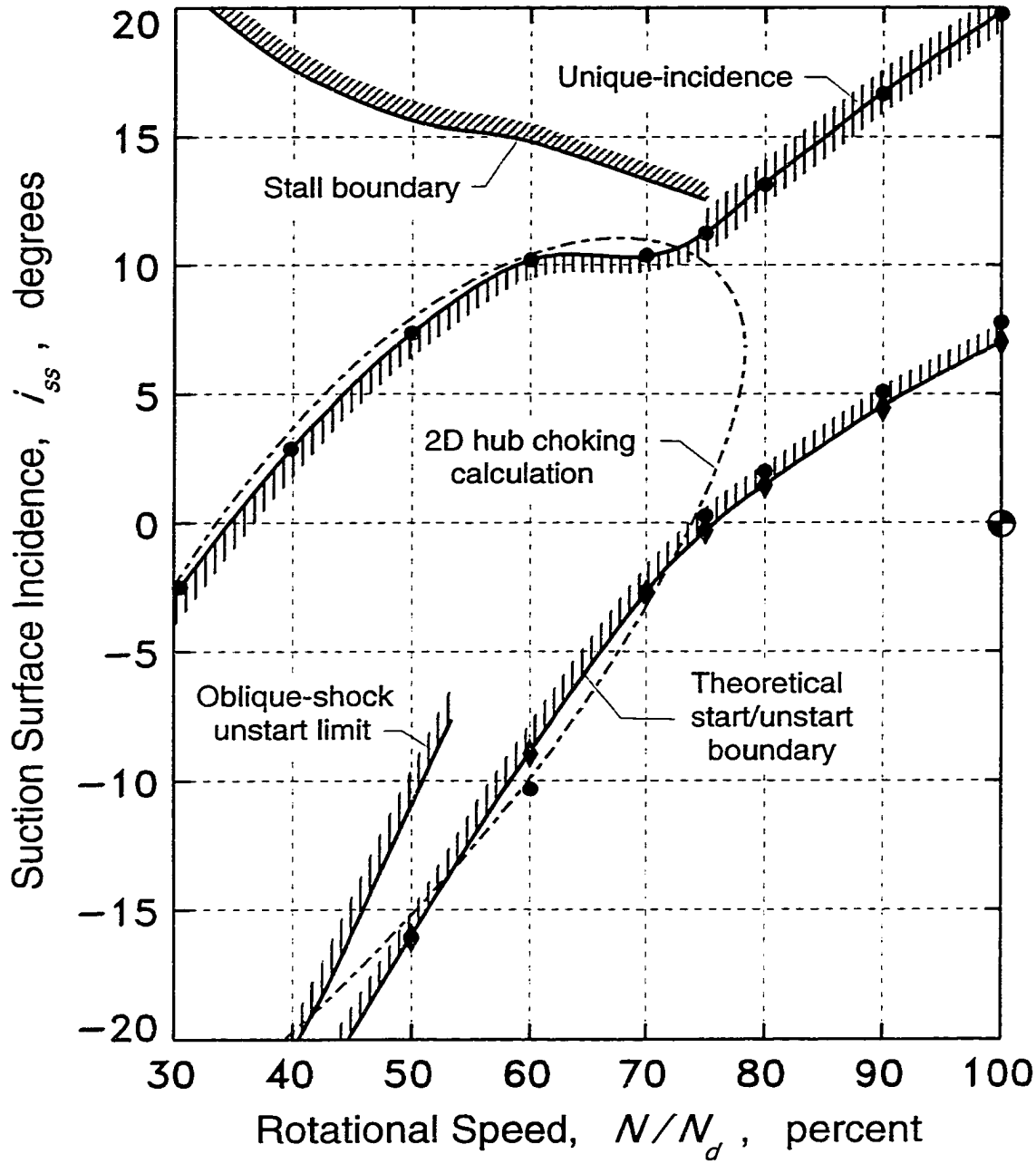

Figure 5.42 Summary of inflow boundaries for baseline rotor operation; suction surface incidence versus rotational speed

Several blade-to-blade flow field solutions obtained using the two-dimensional viscous CFD code RVCQ3D will now be presented for some of the conjugate operating points in Figures 5.41 and 5.42. In particular, the axial-subsonic and axial-supersonic limiting cases for 100, 75, 60, and 50 percent of design rotational speed will be shown and compared. For each rotational speed, *absolute* Mach number contour plots, axial distributions of circumferential-average *absolute* Mach number, and axial distributions of blade surface isentropic Mach number are presented. Most results are for the pitchline location (54.3 percent annulus height), except those for 60 percent speed where the near-hub location (11.8 percent annulus height) is represented. For all solutions the rotor exit flow was axial-supersonic (impulse-type operation).

The CFD results for 100 and 75 percent of design rotational speed are shown in Figure 5.43 and 5.44, respectively. These two rotational speeds are discussed together since in terms of inflow starting/unstarting they are in many ways very similar. Most of this similarity stems from the fact that both represent the maximum-flow unique-incidence condition for axial-subsonic inflow, and the corresponding, conjugate axial-supersonic inflow conditions are both in the zero-to-positive suction-surface incidence range. However, notice in Figure 5.42 the rather large differences in incidence angles for the two speeds, which differences are reflected qualitatively in the blade surface isentropic Mach number distributions.

The most remarkable and interesting feature to be seen in either Figure 5.43 or 5.44 is the change in absolute Mach number which occurs between the started and unstarted states, in the leading-edge region. Observe that the magnitude of the subsonic-to-supersonic expansion into and through the leading-edge plane for axial-subsonic inflow is nearly the same at the magnitude of the starting shock compression — which is the difference between the axial-subsonic and axial-supersonic inflow Mach numbers. Stated differently, the axial flow expansion generated subsonically by the rotor at its inlet has nearly the same magnitude as the shock compression which enters the rotor from the nozzle. The starting shock is therefore strongly attenuated as it enters the blade row, leaving only a weak disturbance to propagate downstream through the rotor[23]. This basic phenomena

---

[23] The weak shock wave propagates downstream with supersonic velocities relative to a flow which, itself, is axial-supersonic.

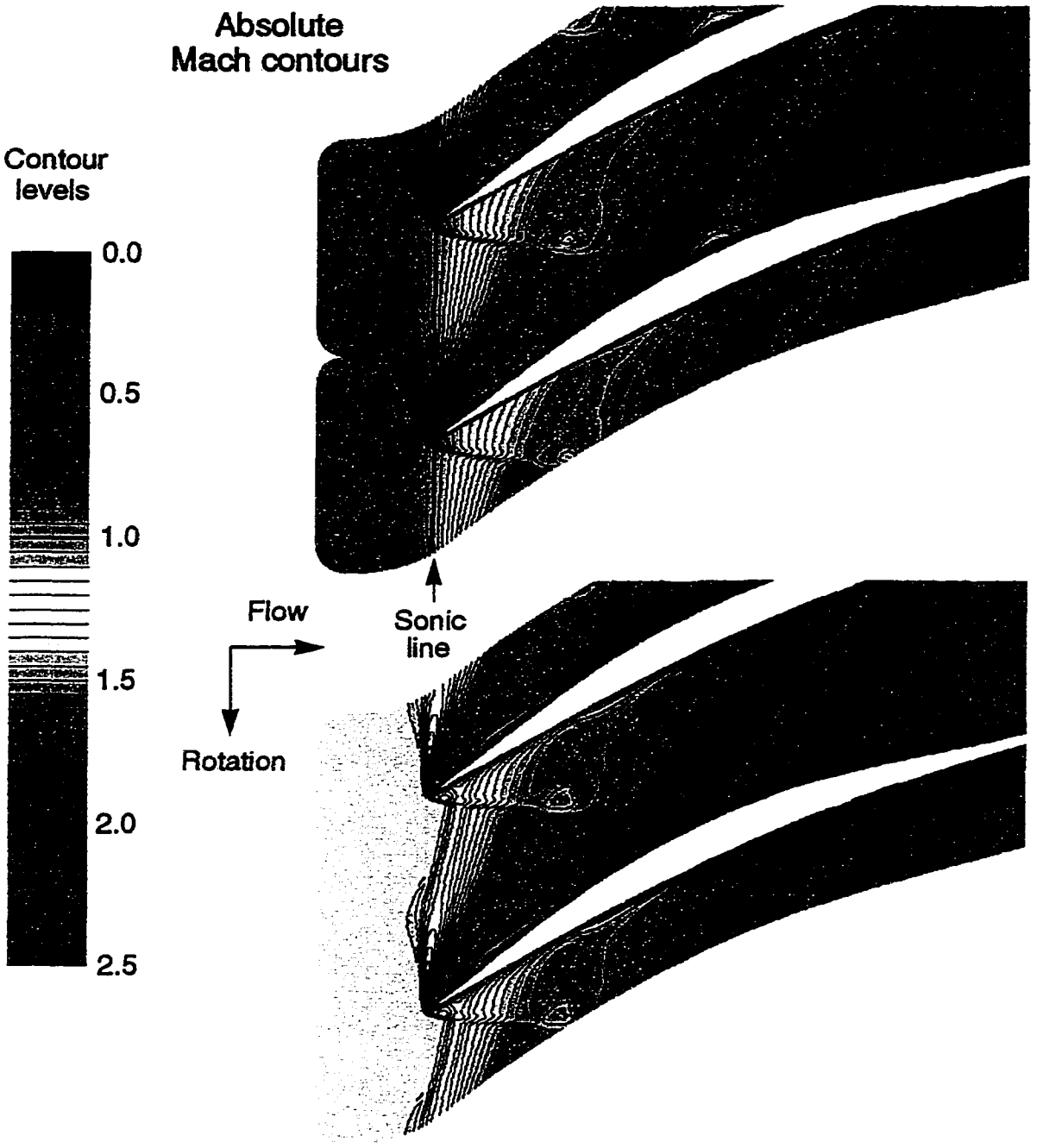

Figure 5.43 Viscous two-dimensional CFD Mach number contours for the rotor pitch-line at 100 percent of design rotational speed; comparison of conjugate axial-subsonic and axial-supersonic limiting inflow conditions

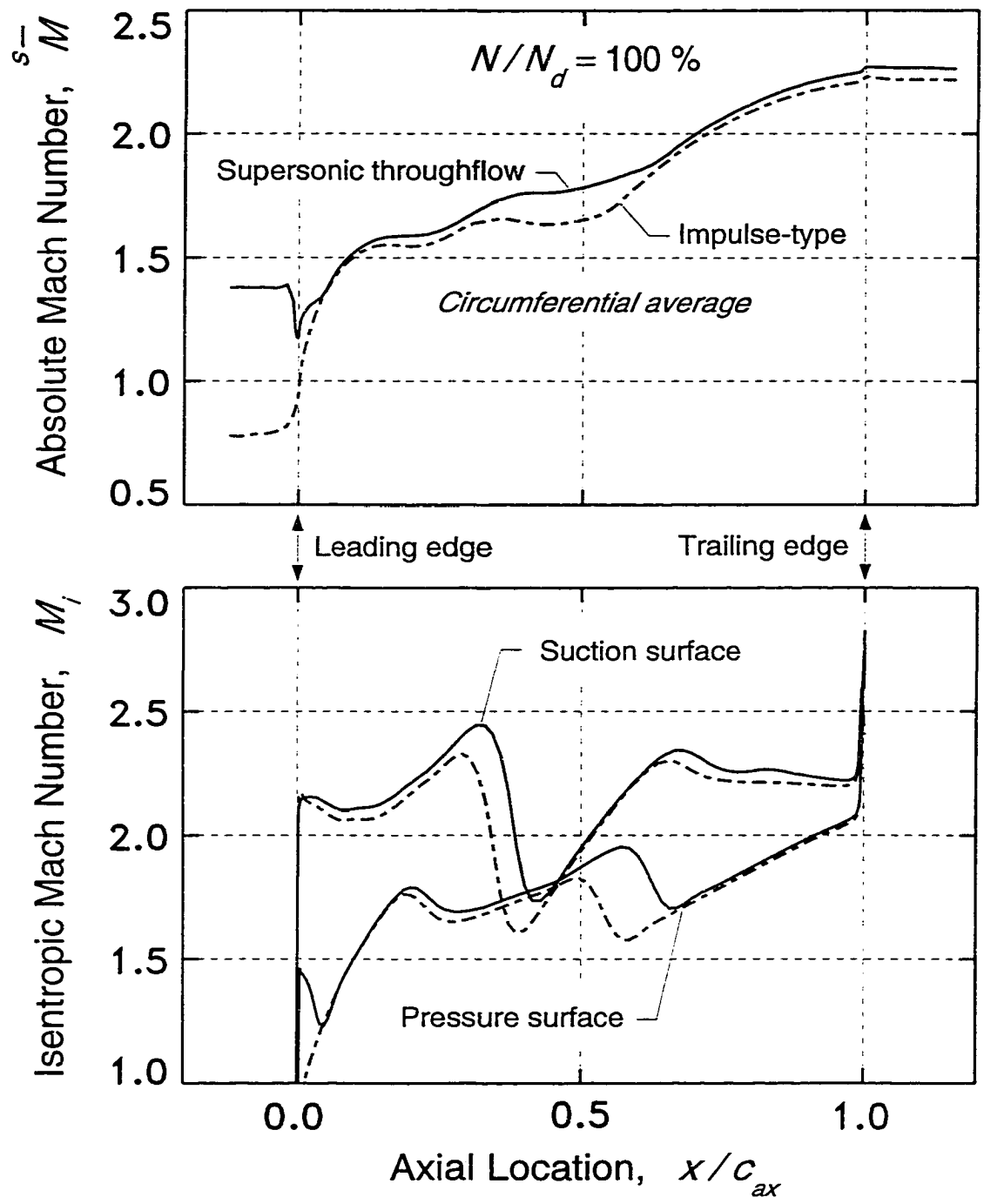

Figure 5.43 (continued)

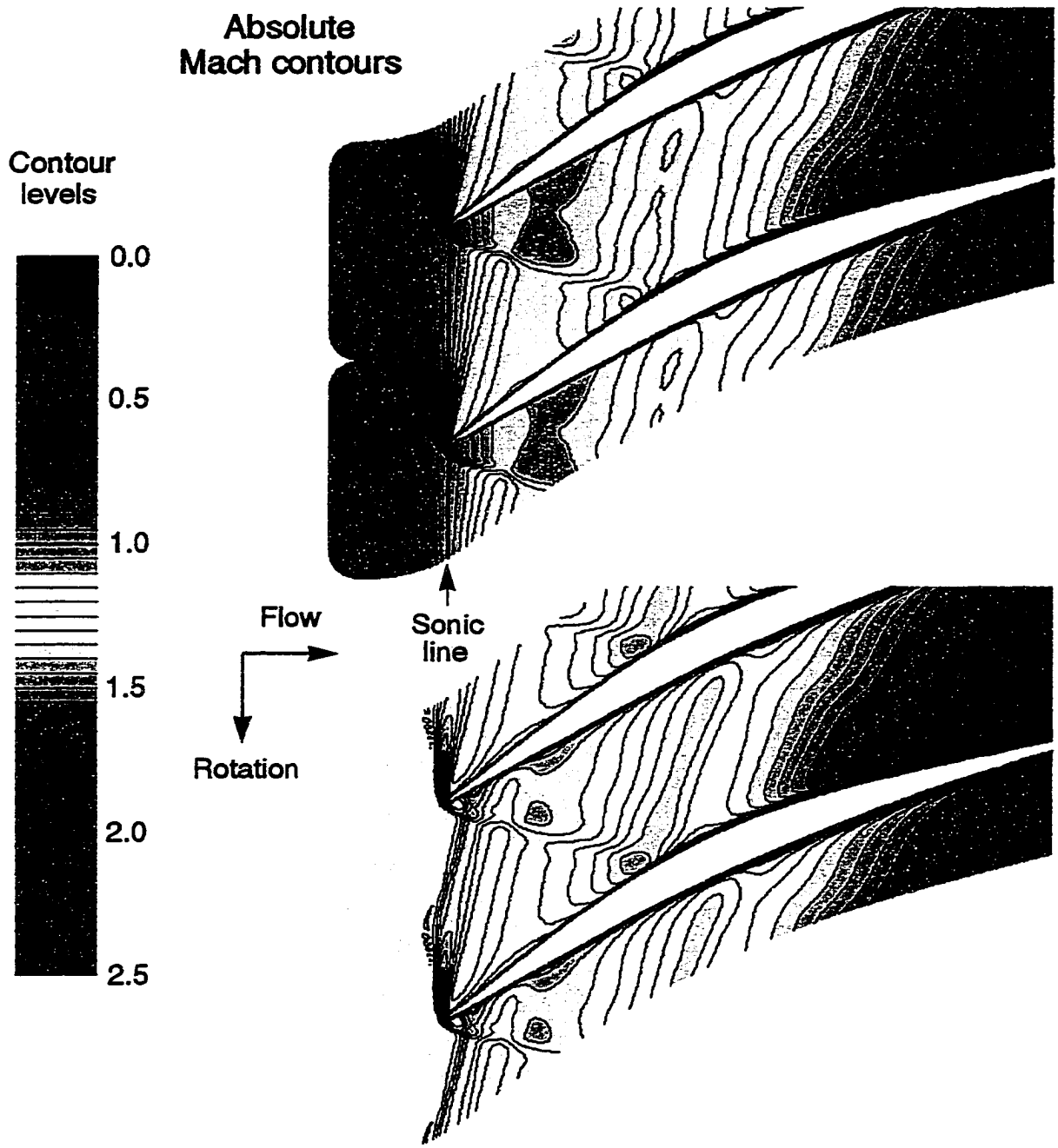

Figure 5.44 Viscous two-dimensional CFD Mach number contours for the rotor pitchline at 75 percent of design rotational speed; comparison of conjugate axial-subsonic and axial-supersonic limiting inflow conditions

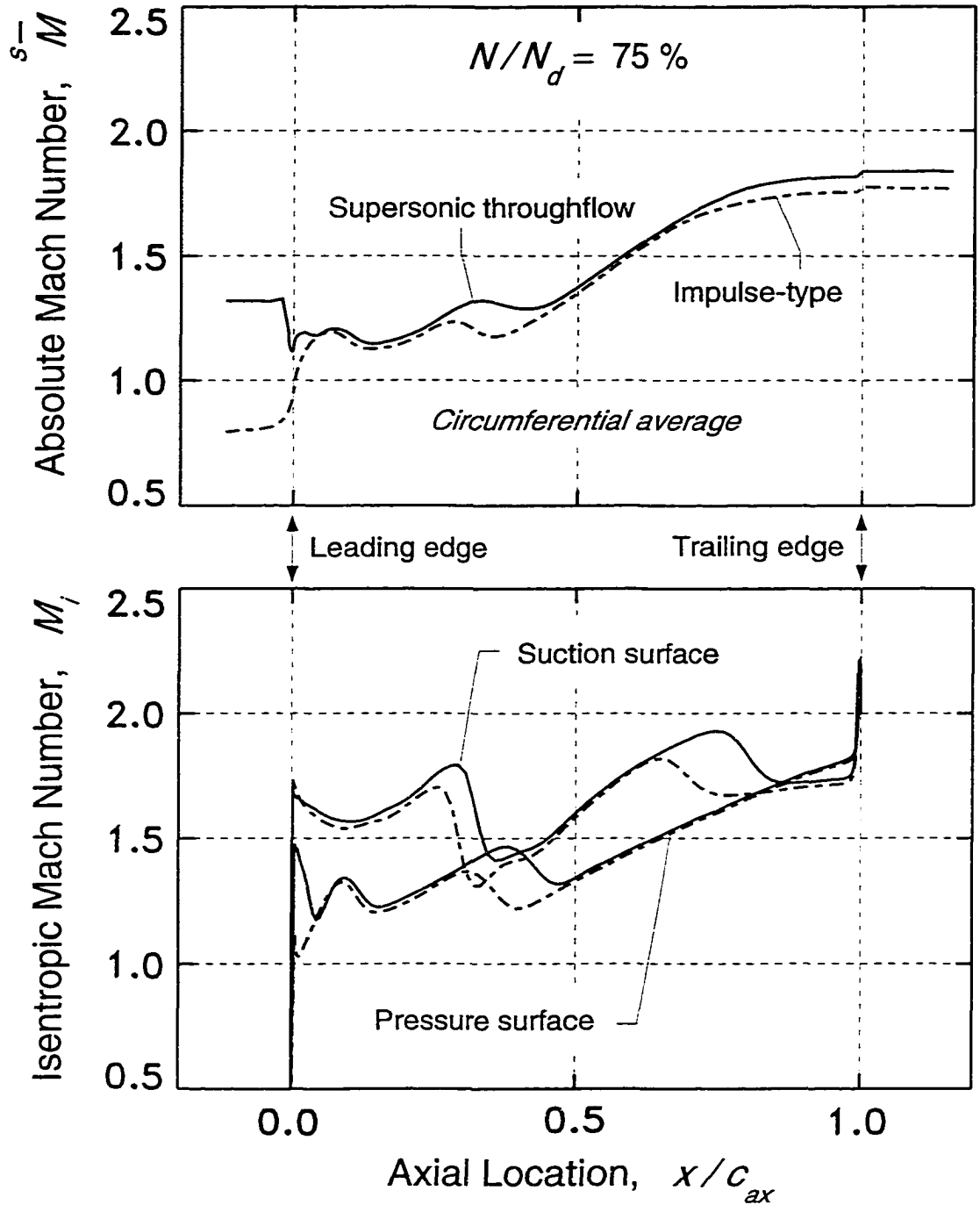

Figure 5.44 (continued)

can be viewed in a different way by examining the blade surface isentropic Mach number distributions. Notice there, in either Figure 5.43 or 5.44, that most of the change in blade loading [24] occurs very close to the leading edge, but that relatively minor changes occur elsewhere downstream. The axial shift in the distribution does not change the *net* blade loading much, and is mostly a reflection of the small shift in the Mach number levels in the blade passage. Compare, also, the contour plots to see this.

The implication of the above result on the practical operability of this type of rotor is very significant: It reveals that no large discontinuity in rotor blade-loading, rotor torque and power, and overall performance should be, or need be, encountered during rotor inflow starting and unstarting. This was verified experimentally, where almost no perceptible change in rotor performance was observed during the rotor-inflow starting and unstarting processes [49].

The CFD results for 60 percent of design rotational speed are shown in Figure 5.45. Observe in the Mach contour plots that the (hub) blade passage is choked around mid-chord for the axial-subsonic inflow case — the thick black line is the sonic line — and that the passage is very close to choking for the axial-supersonic inflow case. Only a slight reduction in the supersonic axial inflow Mach number is needed to choke the passage and induce an unstart. The change in blade loading between the started and unstarted states is more discontinuous than for the higher rotational speeds, but is still reasonably small considering the extent of the flow field adjustment upstream of the passage throat.

The fluid dynamics associated with rotor inflow unstarting at this rotational speed are much more viscous in nature than that encountered at the higher rotational speeds. In the pre-unstart contour plot in Figure 5.45, notice the left-running oblique shock extending from the leading edge on the "lower" blade to the pressure surface on the "upper" blade, where it reflects as *Mach reflection* with a substantial shock/boundary-layer interaction. In the relative frame-of-reference this shock is a weak-oblique wave resulting from the negative suction-surface incidence. It lies, however, almost perpendicular to the absolute, axial rotor-inflow; hence, the "normal shock" approximation mentioned earlier in connec-

---

[24] Local blade loading is related to the vertical distance between the suction and pressure surface curves. The loading is positive (work input from blade to fluid) when the suction surface curve is above the pressure surface curve (for isentropic Mach number).

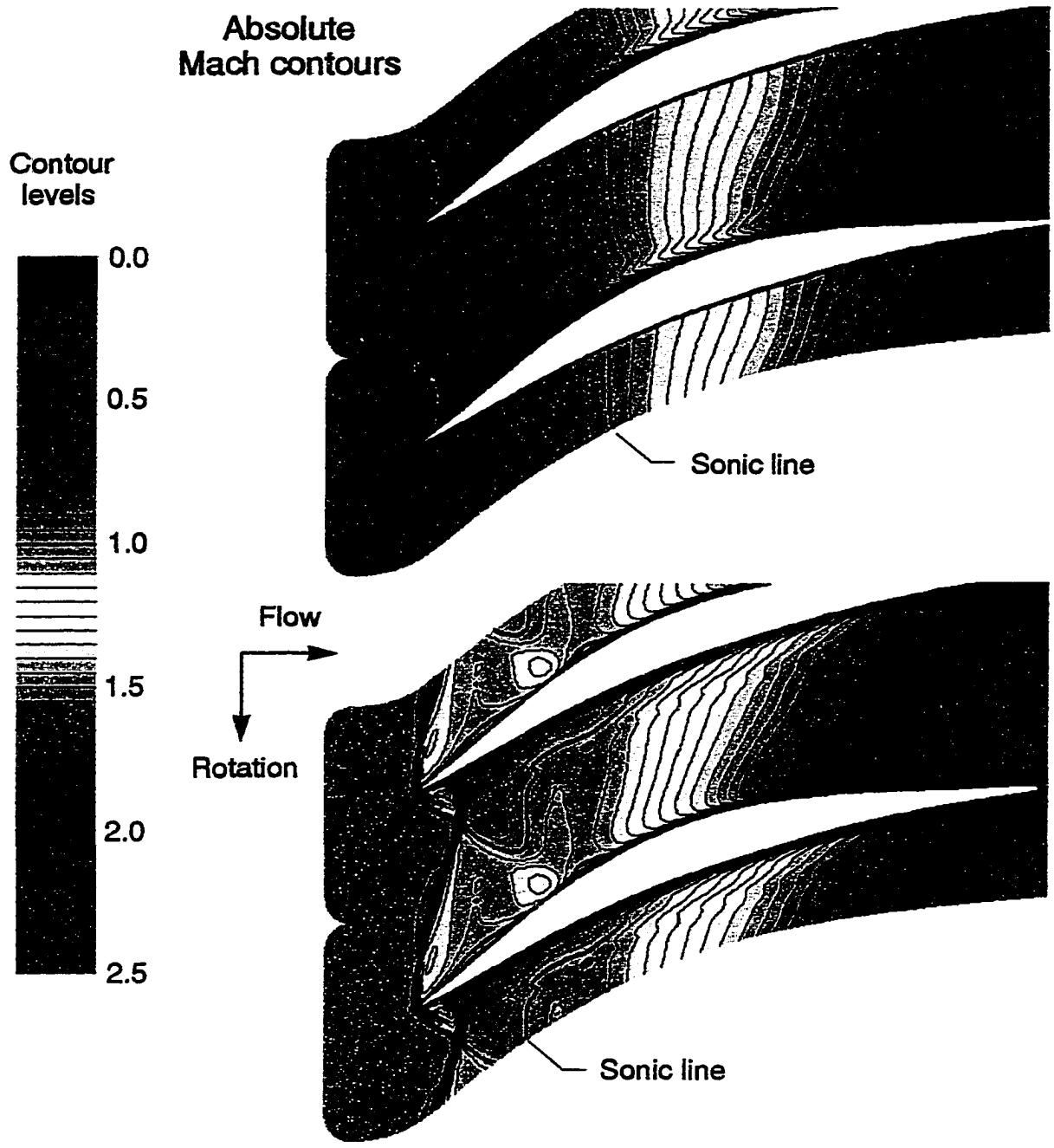

Figure 5.45 Viscous two-dimensional CFD Mach number contours for the rotor near-hub at 60 percent of design rotational speed; comparison of conjugate axial-subsonic and axial-supersonic limiting inflow conditions

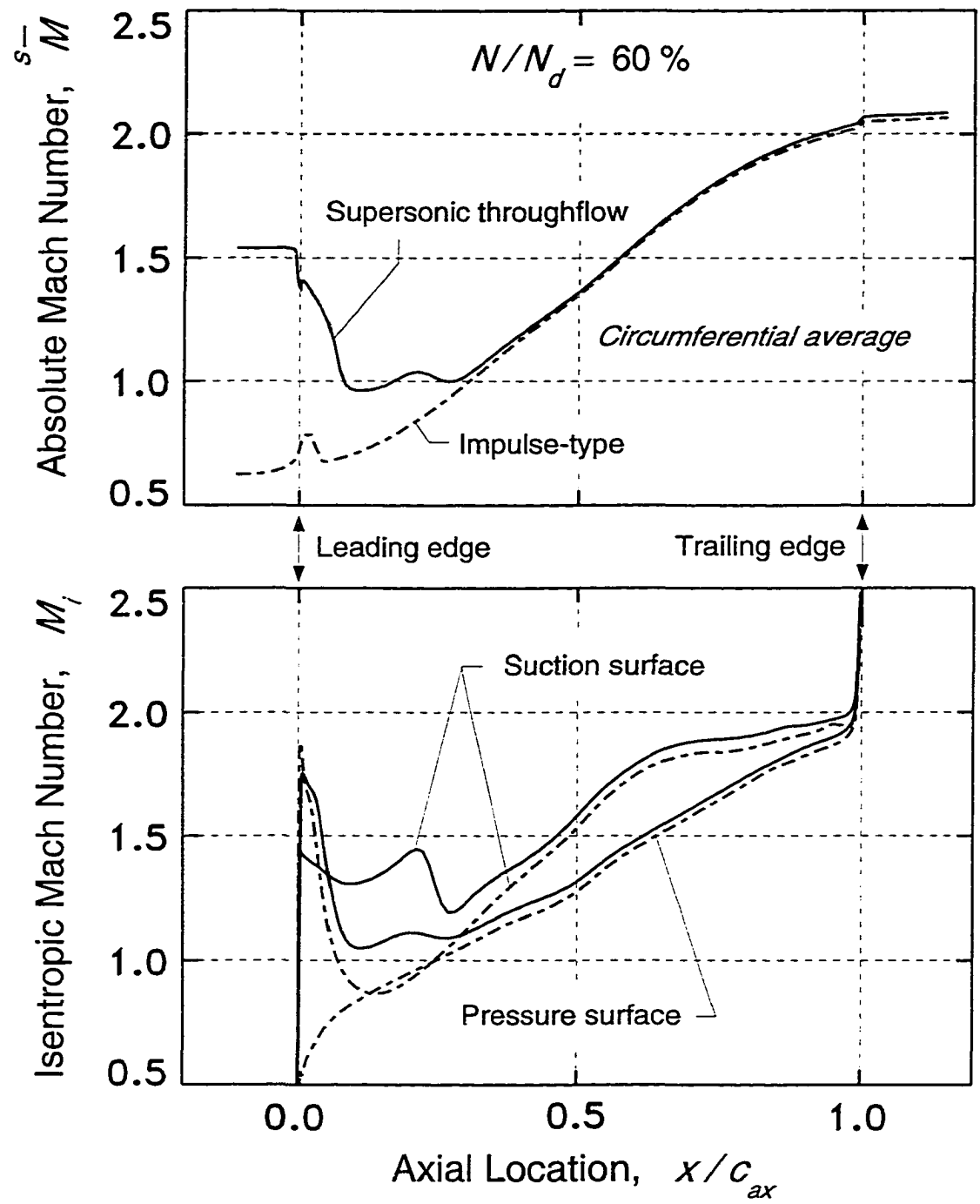

Figure 5.45 (continued)

tion with unstarting and the simple hub-choking calculation procedure (see the dot-dashed curves in Figures 5.41 and 5.42). The absolute Mach numbers between this shock wave and the passage throat are very close to the sonic condition, revealing the marginal nature of this flow condition.

Finally, the CFD results for 50 percent of design rotational speed are shown in Figure 5.46. In a qualitative sense these results are similar to those in Figure 5.45 for 60 percent speed. The extent of the viscous effects is greatly increased, however, and the left-running shock wave (for the axial-supersonic inflow case) is no longer of the weak-oblique type over most of the passage. In fact, about half of this shock wave (the "upper" half in Figure 5.46) is virtually normal to the axial incoming flow, and so has axial-subsonic velocities behind it. Consequently, the *average* absolute Mach numbers are also axial-subsonic behind the shock and upstream of the blade-passage throat. It is only due to the highly two-dimensional nature of the flow field that the passage remains unchoked (in the computed solution).

In its entirety the inlet shock structure is a lambda-type formation, complete with slipline at about mid-gap and extending downstream through the entire blade passage. The shock/boundary-layer interaction in the leading-edge pressure-surface region is very strong, and might lead one to question the veracity of the computed solution in this area of the flow field. Important in this regard is the potential existence of strong three-dimensional effects, including secondary flows in the separated boundary-layer regions. These effects are not modeled in the two-dimensional computation, and if substantial could *qualitatively* alter the flow field, e.g., cause the passage to choke and the inflow to unstart. In order to check this, a fully three-dimensional viscous CFD simulation was performed at an operating condition close to that represented in Figure 5.46; namely, a three-dimensional viscous computation was done for 50 percent of design speed and an axial inflow Mach number of 2.0. A pitchline (54.3 percent annulus height) blade-to-blade contour plot for that solution is shown in Figure 5.47, at the top, and a meridional view of the corresponding mid-gap flow field is shown below it. In general, there is not much difference between the computed quasi- and fully- three-dimensional pitchline flow fields, and the three-dimensional effects are apparently small outside the endwall regions. It might be noted that this result is consistent with related experimental work on a linear supersonic through-flow cascade [73-75], where for *negative* suction-surface incidence angles of up to -10

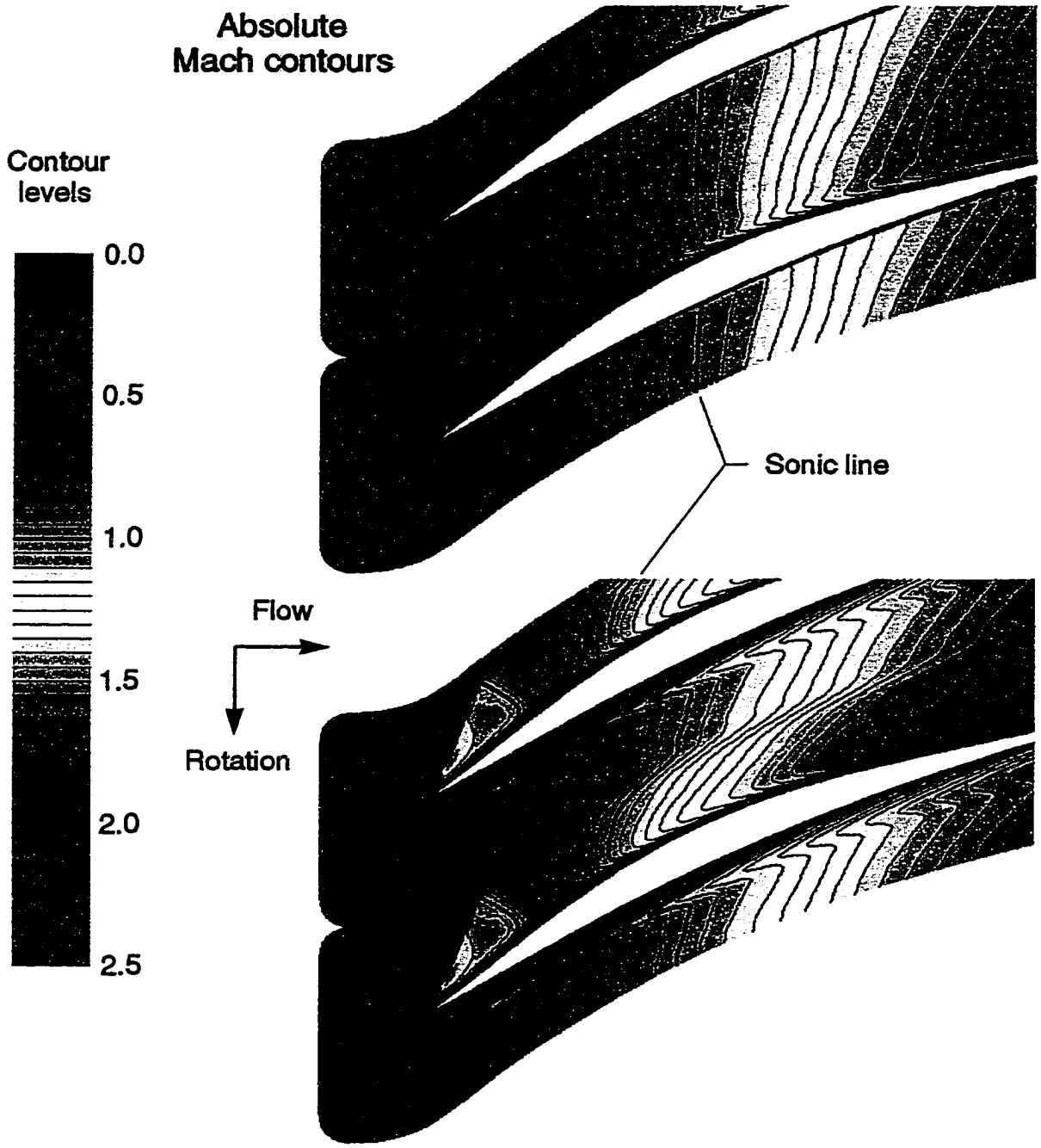

Figure 5.46 Viscous two-dimensional CFD Mach number contours for the rotor pitch-line at 50 percent of design rotational speed; comparison of conjugate axial-subsonic and axial-supersonic limiting inflow conditions

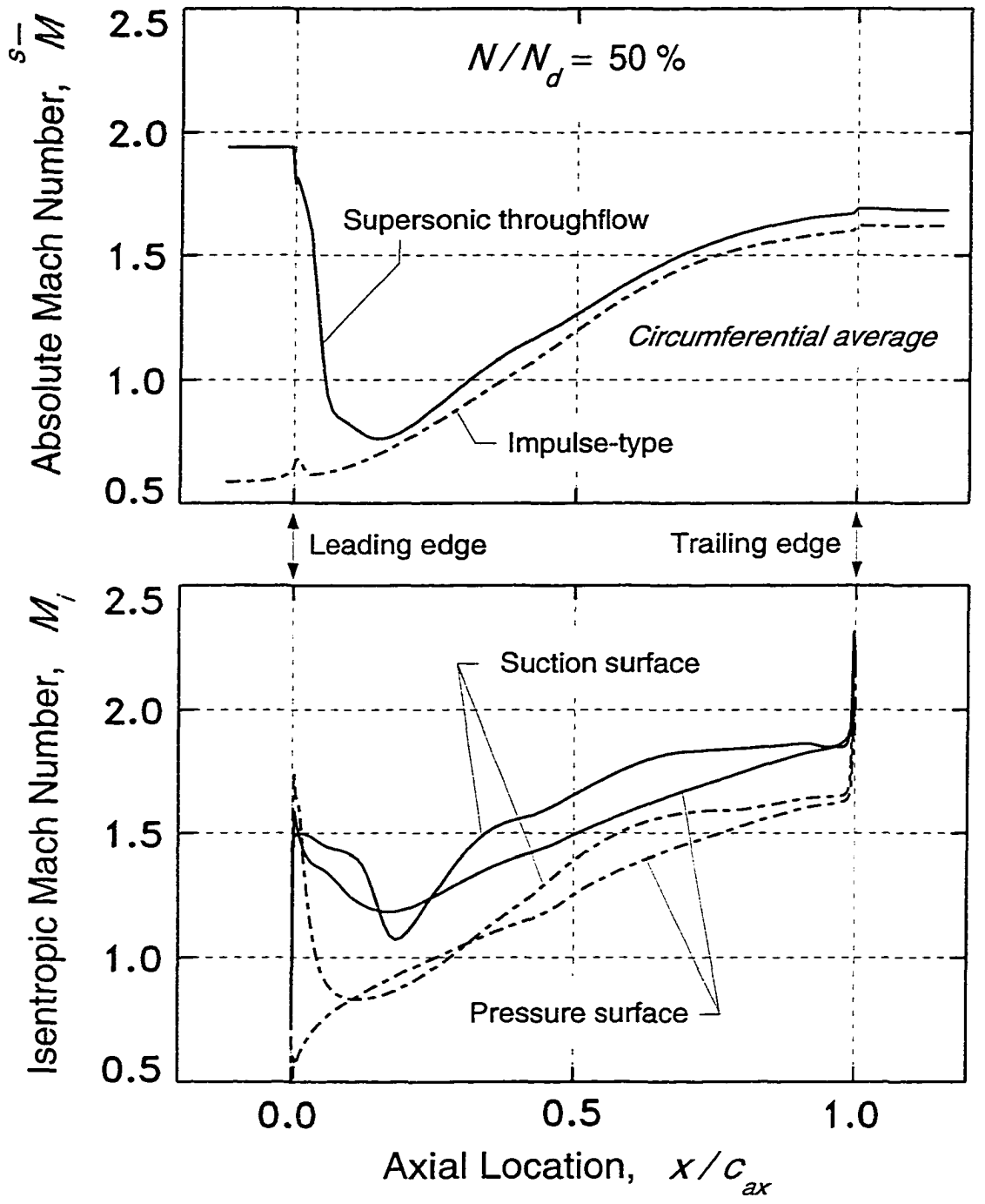

Figure 5.46 (continued)

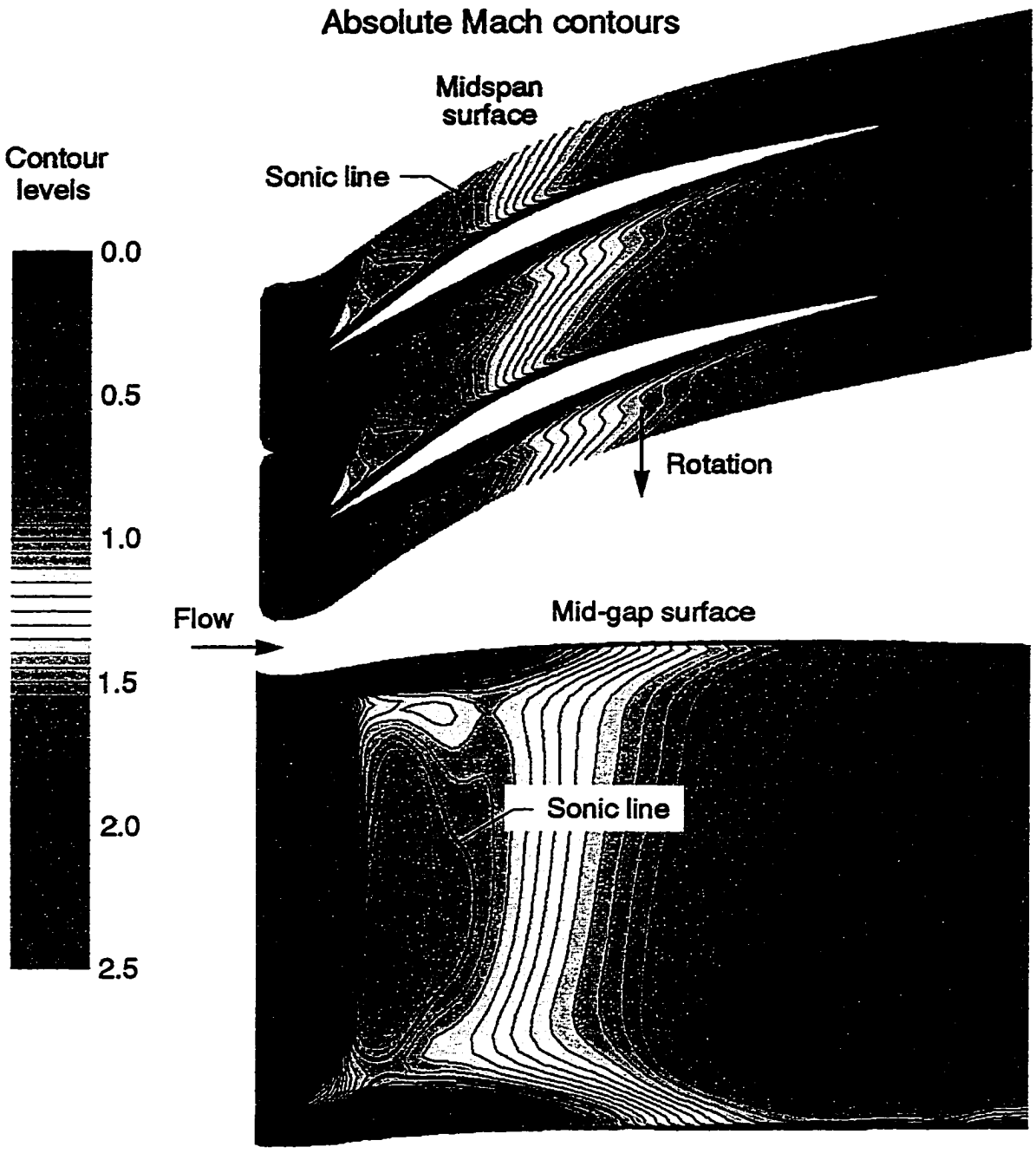

Figure 5.47 Viscous three-dimensional CFD Mach number contours for the rotor at 50 percent of design rotational speed with near-unstart axial-supersonic inflow conditions (M_1 = 2.0)

degrees there were no large-scale three-dimensional effects observed, especially in the separated shock/boundary-layer interaction region on the blade pressure surface [75].

To conclude this particular discussion on the rotor start/unstart aerodynamics at the lower rotational speeds, a couple of final comments might be useful. The comments regard the significance of rotor operation at rotational speeds below 75 percent of design speed, since such operation is clearly less desirable in terms of the start/unstart shock strengths and the associated discontinuities in blade loading. Aside from the more obvious merit attached to acquiring a general knowledge of the SSTF operating envelope, there are also practical aspects of negative-incidence rotor-inflow starting and unstarting which are potentially critical in actual flight applications. For example, consider an SSTF-equipped aircraft cruising supersonically, and experiencing a brief or permanent loss in power to the fan. As the fan rotational speed drops suddenly (along with the flight speed), then at what rotational speed will the rotor, and consequently the entire inlet, unstart? How severe will the unstart be? Furthermore, after unstarting are there any special problems associated with restarting the system?

The next comment relates to the experimental testing of a rotor with supersonic inflow velocities. Specifically, consider the process of rotor inflow starting/unstarting in a facility equipped with, or operated with, a *fixed*-geometry upstream c-d nozzle. This has been done historically, for example, at the NACA Langley Aeronautical Laboratory as discussed in Chapter 1. In such an arrangement the inflow starting/unstarting is practically always associated with negative suction-surface incidence angles. The higher the nozzle exit Mach number, the larger the negative incidence at the start/unstart condition, but also the lower the rotational speed (see Figures 5.41 and 5.42). Note, however, that there is a minimum nozzle Mach number below which the rotor inflow will not start at all, which for the baseline rotor is about Mach 1.35. Finally, as an aside, it is of some interest to add that a fairly accurate description of both positive- and negative- incidence rotor-inflow starting using variable- and fixed- geometry nozzles, respectively, was already published by the early 1960's in Reference 21.

This section will now be concluded by a somewhat detailed description of the nozzle aerodynamics just prior to and after rotor-inflow starting at 75 percent of design rotational speed. In this description, computational and experimental data are used to examine the nozzle shock and its influence on the three-dimensional, axial-subsonic rotor-inflow

characteristics. Also, the *spanwise distribution* of axial-supersonic inflow Mach numbers for the pre-unstart condition is also examined in light of the theoretical unstart boundary (see Figures 5.41 and 5.42).

Contour plots showing a meridional view of absolute Mach numbers for the computed nozzle and rotor flow fields are shown in Figure 5.48. The flow fields in the figure correspond to an operating condition somewhat prior to rotor-inflow starting, and the Mach numbers for the rotor represent the circumferential-average flow field as determined using an approximation to the entropy-averaging procedure. Note that the nozzle and rotor CFD solutions were coupled at the nozzle-exit/rotor-inlet boundary as described in Chapter 4, and the nozzle centerbody was positioned at a pre-start location ($x = 2.44$ inches downstream of the reference position) where experimental data were obtained. The experimental and computational isentropic endwall Mach numbers are compared in Figure 5.49, where it can be seen that the agreement is good, even for the shock location which is fairly sensitive to many parameters. It should be emphasized in this regard that the nozzle-centerbody, not the shock location, was specified for the computational analysis and, furthermore, the rotor computation corresponds to an impulse-type mode so that there is no throttling from downstream — that is, in order to position the nozzle shock. The computed overall mass flow rate of 50.36 lbm/sec also compares fairly well with the experimental value of 50.01 lbm/sec.

Spanwise integration of the computed axial-subsonic inflow just upstream of the rotor yields an overall average axial inflow Mach number of 0.776 and a nozzle total-pressure ratio of 0.961. Comparing this average Mach number with that presented earlier for the nozzle/rotor computation for a fully-open (unchoked) nozzle reveals a small decrease, from 0.796 to 0.776, corresponding to a mass flow decrease from 52.29 to 50.36 lbm/sec, and a nozzle total-pressure ratio decrease from 0.989 to 0.961. Thus there is a quantitative effect of the nozzle shock on the rotor mass-flow induction; the *corrected* flow into the rotor decreases from 52.29 to about 51.83, or about 0.9 percent. At this point the effect is relatively small, substantiating in part the earlier conclusions regarding the constancy of

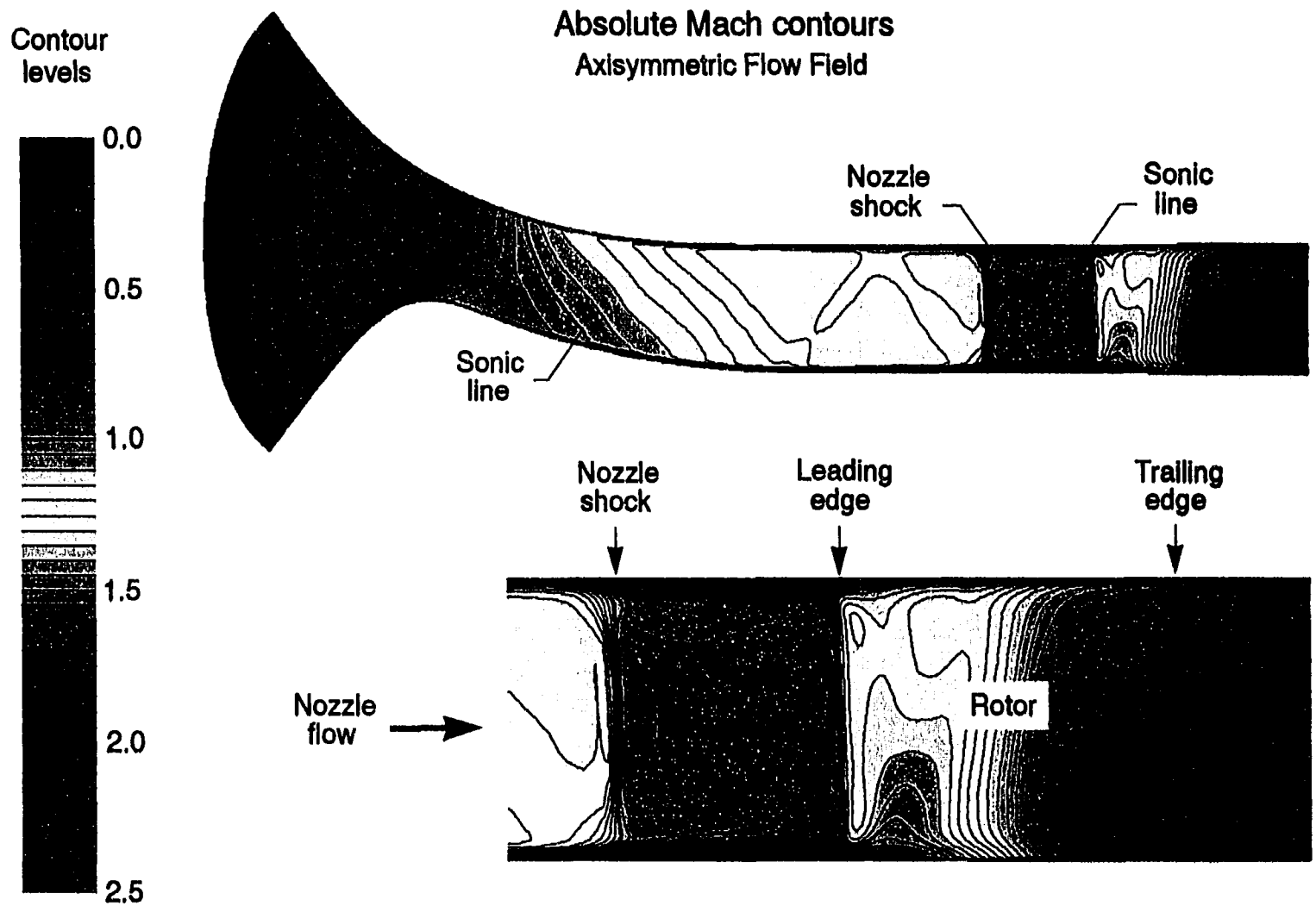

Figure 5.48 Viscous CFD Mach number contours for the nozzle and isolated rotor at 75 percent of design rotational speed; choked nozzle and rotor with steady-state shock in nozzle; condition near rotor-inflow starting

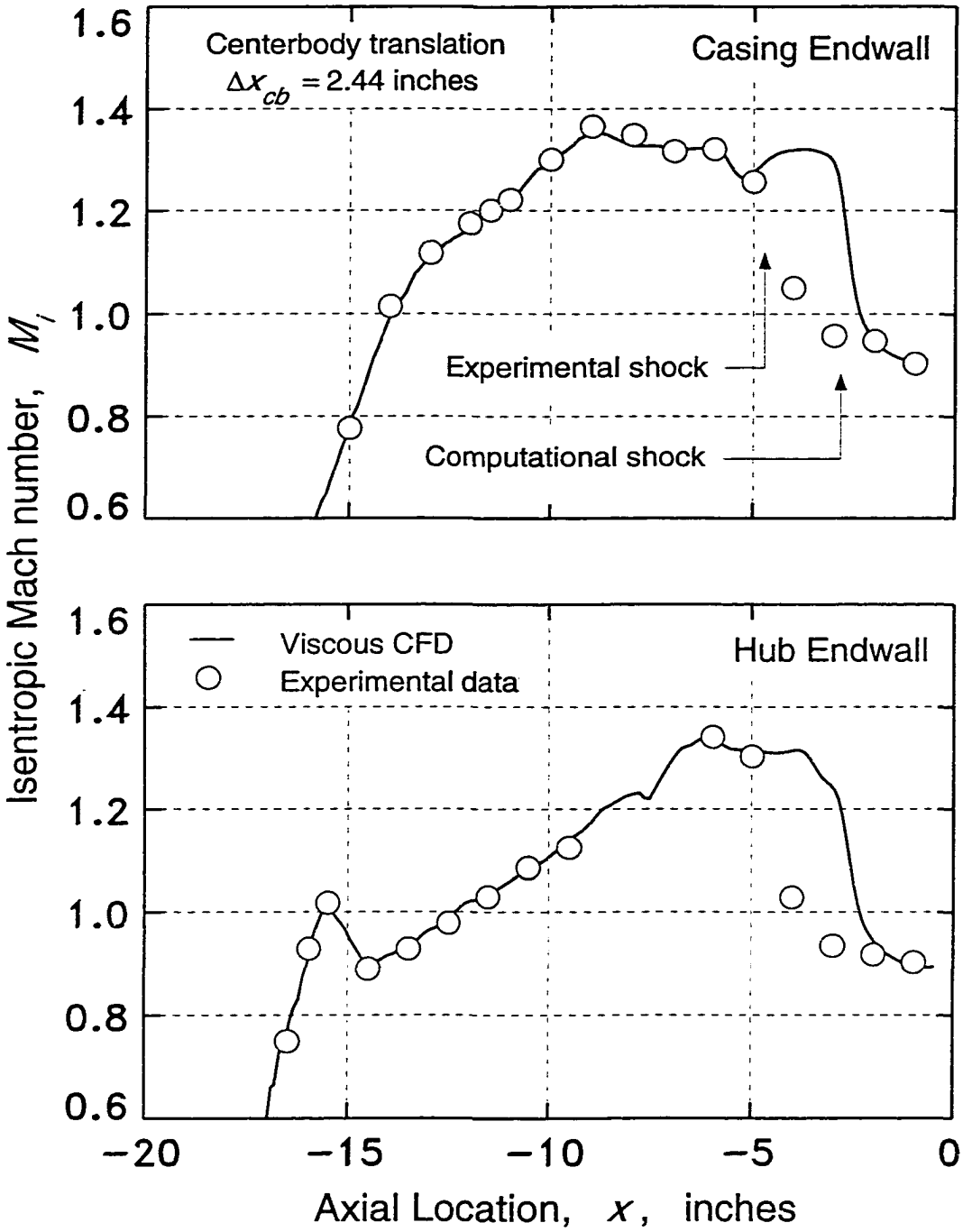

Figure 5.49 Comparison of experimental and computational isentropic endwall Mach number distributions for the inlet nozzle operating with supercritical flow; rotor operating at 75 percent of design rotational speed

the corrected rotor inflow during the starting process [25] (see Figure 5.37, for example). More can be said regarding this, however, as is developed in the following discussion.

Although at the rotor inlet the corrected *overall* inflow conditions are not largely altered by the existence of the upstream nozzle shock, the free-stream conditions are since the shock/boundary-layer interaction causes more boundary layer blockage downstream of the shock. That is, the average rotor inflow Mach number remains fairly constant, but the local free-stream Mach numbers at the rotor inlet increase significantly. This is shown in Figure 5.50 which compares the spanwise Mach number distributions for the two cases. Axial distributions of normalized streamtube height at the inlet pitchline (54.3 percent annulus height) are compared in Figure 5.51, revealing the three-dimensional nature of the effect, similar to that also discussed in the last section. Notice in Figure 5.51 that for the supercritical nozzle flow the pitchline streamtube expands in area by about 1.7 percent as the rotor leading edge is approached, compared to an expansion of about 0.7 percent for all-subsonic nozzle flow.

Computed and measured results for an operating condition just subsequent to rotor-inflow starting are compared in Figure 5.52, where hub and casing isentropic wall Mach number distributions are shown. As can be seen, the agreement is generally very good. In this case the nozzle centerbody has been translated 0.34 inches downstream ($x = 2.78$ inches downstream of the reference position) from that of the previous unstarted condition. As a result of translating the centerbody, the experimental mass flow decreased from 50.01 lbm/sec to 47.93 lbm/sec, which compares to a computed decrease from 50.36 lbm/sec to 48.39 lbm/sec. Based on the CFD results, the *corrected* mass flow decreased from 51.83 lbm/sec to 48.39 lbm/sec, or about 6.6 percent, corresponding to an increase in the *average* axial inflow Mach number from 0.776 to 1.372. At the axial location 1.0 inches upstream of the rotor the computed *nominal* inflow Mach number is 1.380, which compares closely to the experimental value of 1.372.

The above change of 6.6 percent in corrected mass flow encountered in starting the rotor inflow from the condition of Figure 5.48 represents a relatively large departure from

---

[25] Stronger starting shocks at the lower rotational speeds could be expected to produce a larger effect than that exhibited here.

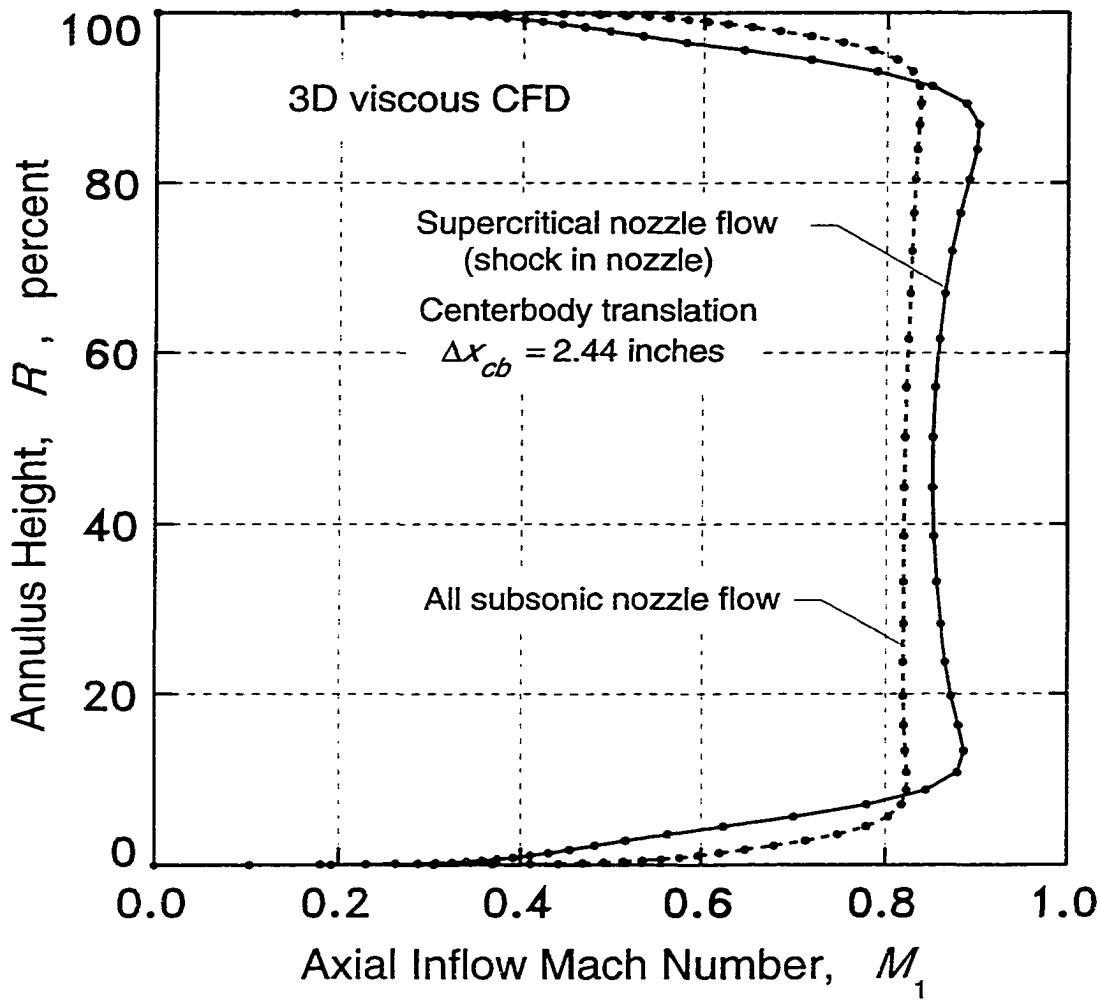

Figure 5.50 Comparison of spanwise distributions of axial inflow Mach number for the rotor at 75 percent of design rotational speed; comparison between all-subsonic and supercritical nozzle flows; circumferential-average CFD results at a location about 14 percent of axial chord upstream of rotor

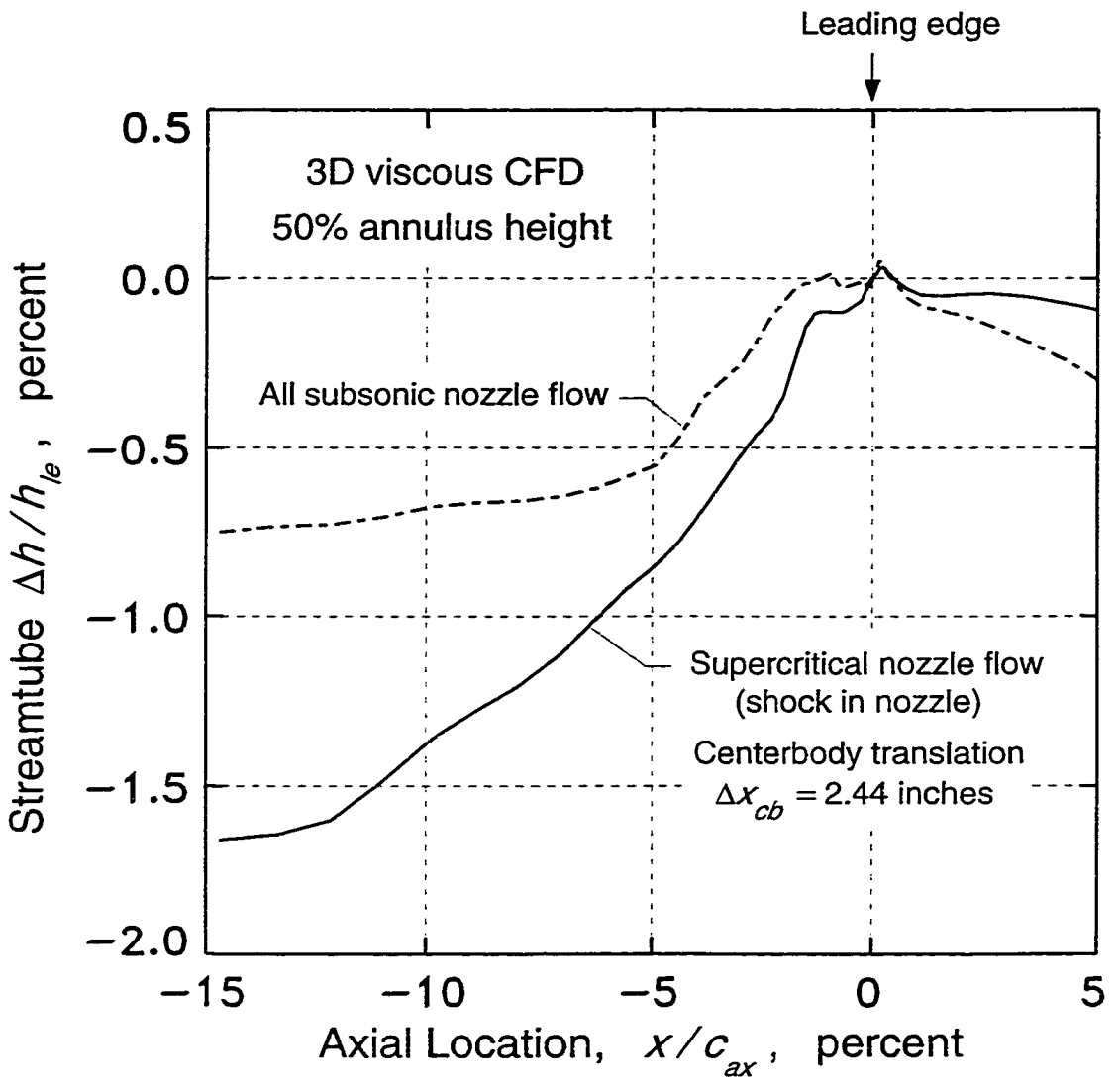

Figure 5.51 Comparison of streamtube height variations at the rotor inlet; comparison between all-subsonic and supercritical nozzle flows; streamtubes calculated from circumferentially-averaged three-dimensional viscous CFD solutions for the rotor at 75 percent of design rotational speed

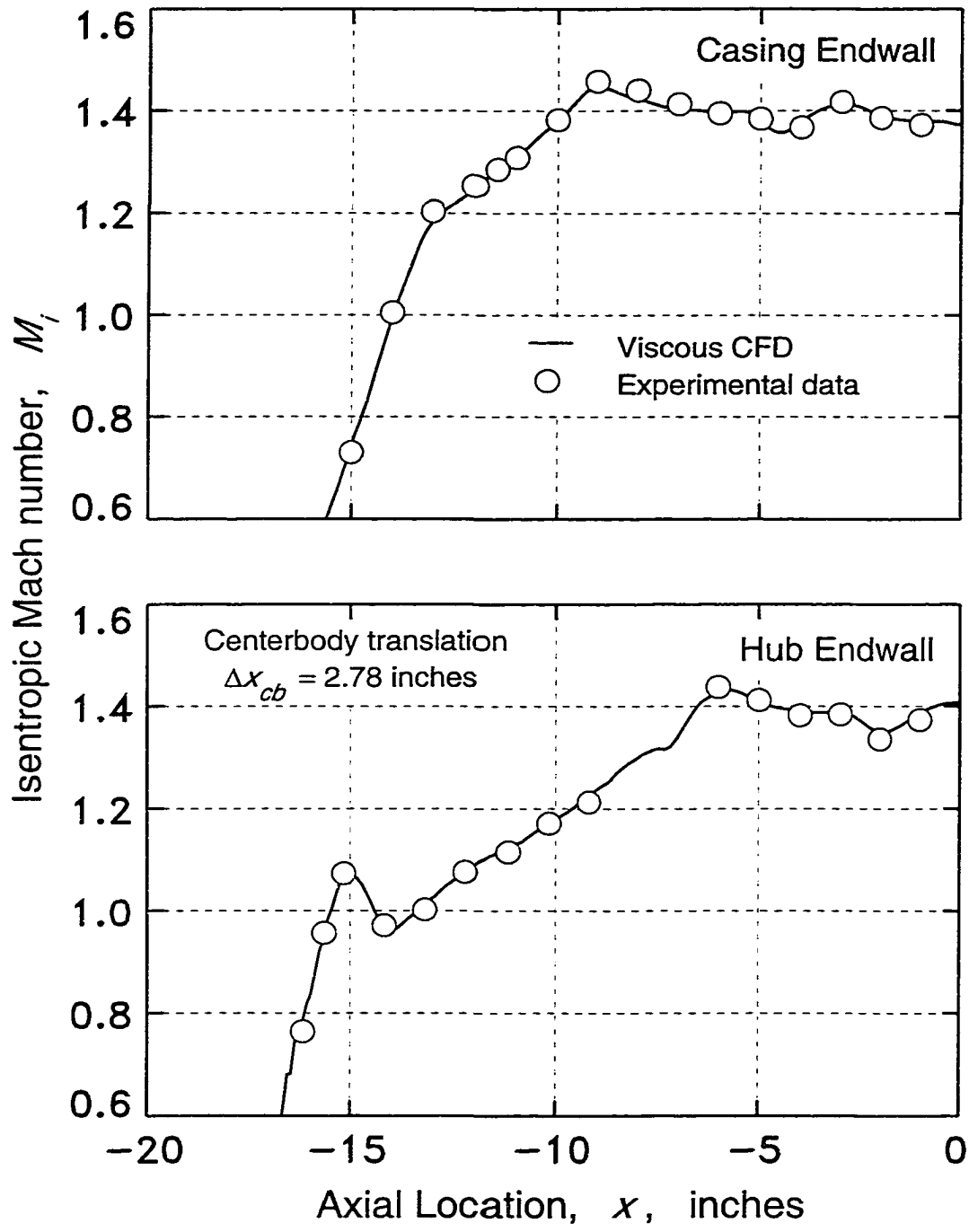

Figure 5.52 Comparison of experimental and computational isentropic endwall Mach number distributions for the inlet nozzle operating with supersonic exit flow; condition just subsequent to rotor-inflow starting

a theoretical one-dimensional value, equal to about 2.4 percent based on the subsonic pre-start Mach number of 0.776; that is, an additional 4.2 percent reduction in corrected mass flow was needed to start the rotor inflow. Apparently, as the nozzle throat area was closed (the centerbody translating the additional 0.34 inches), fairly strong three-dimensional effects developed between the nozzle shock and the rotor. No attempts have been made to simulate this effect numerically, but evidence of it could be seen in the experimental end-wall static pressure data. It is suspected that strong shock/boundary-layer interaction effects at the endwalls are the primary cause.

The spanwise distribution of computed axial inflow Mach numbers at the rotor leading edge plane for the above post-start case is presented in Figure 5.53. For similar CFD results at a slightly higher Mach number level see Appendix A, where experimental radial-traverse data are also included and compared. Since the operating condition corresponding to the results in Figure 5.53 is marginal in terms of rotor inflow unstarting [26], it is of interest to examine the spanwise variations in Mach number. In particular, the minimum level of the free-stream Mach number is critical since, presumably, it should be where the rotor inflow is first induced to unstart. Using this assumption for the computed solution, the minimum local (spanwise) Mach number at which the unstart occurs is slightly below 1.362, which agrees well with the theoretical (two-dimensional) number of 1.32 for 75 percent of design rotational speed (see Figure 5.39 or 5.41). Note that the corresponding *nominal* axial inlet Mach number is slightly higher at 1.380.

Impulse-Type Operation

In general, the impulse-type operating mode is associated with axial-supersonic outflow velocities, whether the inflow is axial-subsonic or axial-supersonic. As defined at the beginning of the chapter, however, the usage of the term *impulse-type* is normally being reserved for the special case of axial-subsonic inflow conditions, with the term *supersonic throughflow* being applied in the other case. Despite this distinction, the two operating

---

[26] The start/unstart hysteresis is small.

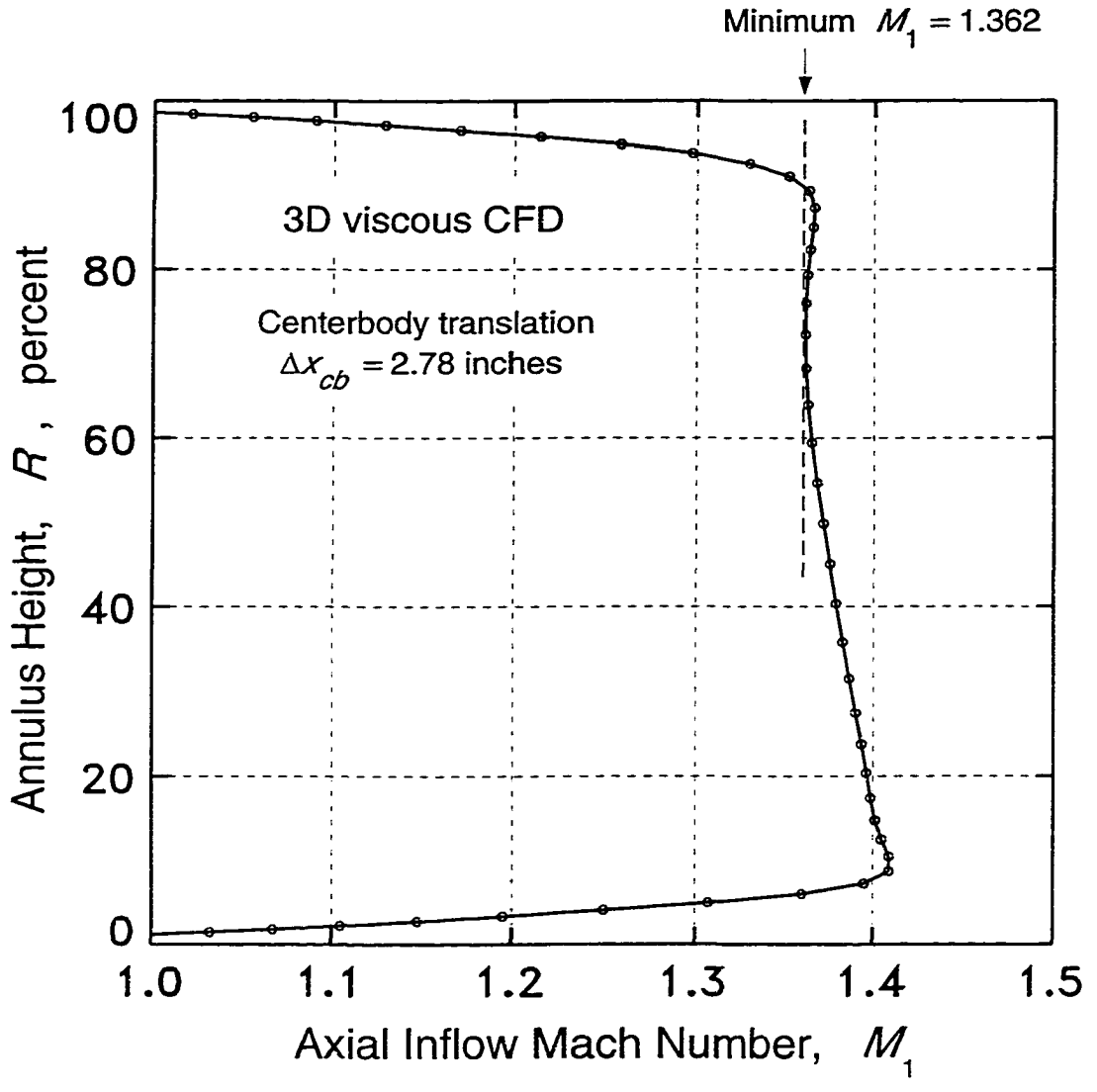

Figure 5.53 Spanwise distribution of axial inflow Mach number for the rotor at a near-unstart condition at 75 percent of design rotational speed; axisymmetric two-dimensional CFD solution at the rotor leading edge plane

modes are very similar in many ways as will become apparent in the following subsection entitled **General theoretical considerations** . In that subsection the more general usage of the term *impulse-type* will often be temporarily employed, where appropriate, since the supersonic throughflow operating mode is actually a subset of the impulse-type mode.

Impulse-type operating modes with both axial-subsonic and axial-supersonic rotor inflow conditions have been simulated computationally and were commonly encountered experimentally. In the experimental facility during the fan starting sequence, axial-supersonic outflow conditions were usually established while the rotor inflow remained axial-subsonic; that is, the downstream diffuser was started while the upstream nozzle was in the open configuration A fan starting sequence involving nozzle starting prior to diffuser starting [27] was rarely done experimentally, although no difficulties were observed in connection with it.

General theoretical considerations

The general form of the rotor outflow vector diagram for impulse-type operation is illustrated in Figure 5.54, in terms of Mach number vectors. Note that the relative outflow angle β_2, as it is shown in the figure, is in the positive circumferential direction and the absolute flow angle α_2 and the wheel speed U_2 are in the negative direction. The necessary conditions for axial-supersonic outflow can be expressed in terms of the relative flow quantities as a simple function:

$$M_2' = M_{ax\,2} / \cos\beta_2 \tag{5.26}$$

where $M_{ax\,2}$ must exceed unity. A graph of this function for several different axial-supersonic Mach numbers is provided in Figure 5.55. As can be seen, the graph is symmetrical about the zero relative outflow angle, and the cross-hatch regions indicate axial-subsonic outflow conditions. Also indicated in the figure is the approximate zone where the baseline rotor operates while in the impulse-type mode.

---

[27] Shock-in-rotor operation results as an intermediate mode during this sequence.

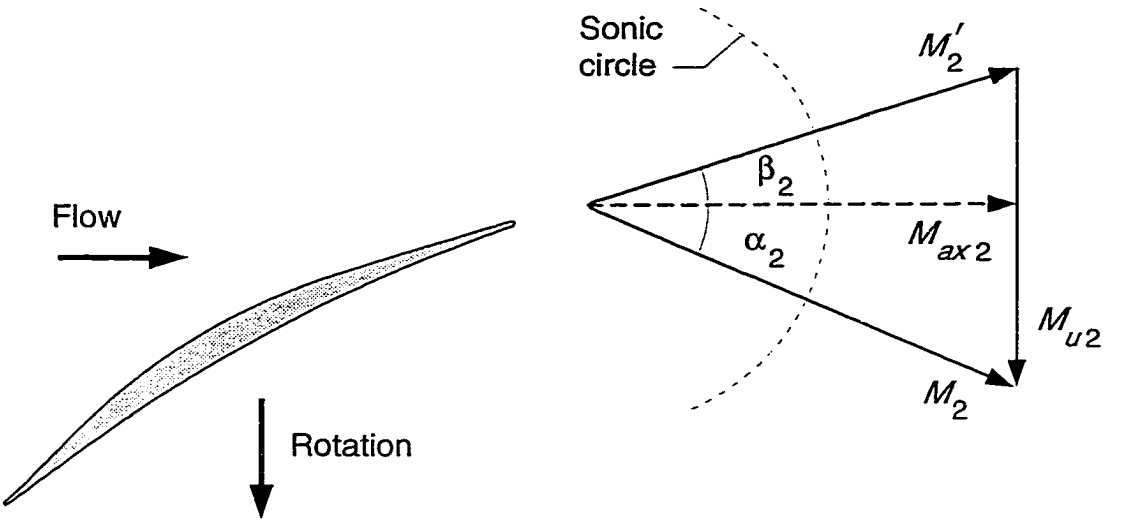

Figure 5.54 Rotor outflow Mach number vector diagram for impulse-type operation

Typically, during impulse-type operation the relative outflow angle for a particular blade element is more-or-less aligned with the blade exit angle, and may even exceed that angle (positive deviation) by several degrees. Referring to Figure 5.55, therefore, it can be seen that with highly staggered blades the impulse-type mode is unattainable, except at unusually high exit Mach numbers. A conventional transonic fan rotor, for example, with its fairly large blade stagger angles at the outer half of the span could not be expected to operated in an impulse-type mode, even under very low back-pressure conditions, as long as the inflow velocities were axial-subsonic. In contrast, the baseline SSTF rotor has small blade-element stagger angles, and even smaller blade exit angles, making impulse-type operation naturally attainable as the blade row is unthrottled to the point of relative supersonic exit velocities; that is, the relative exit Mach number is nearly equal to the axial component of the absolute exit Mach number.

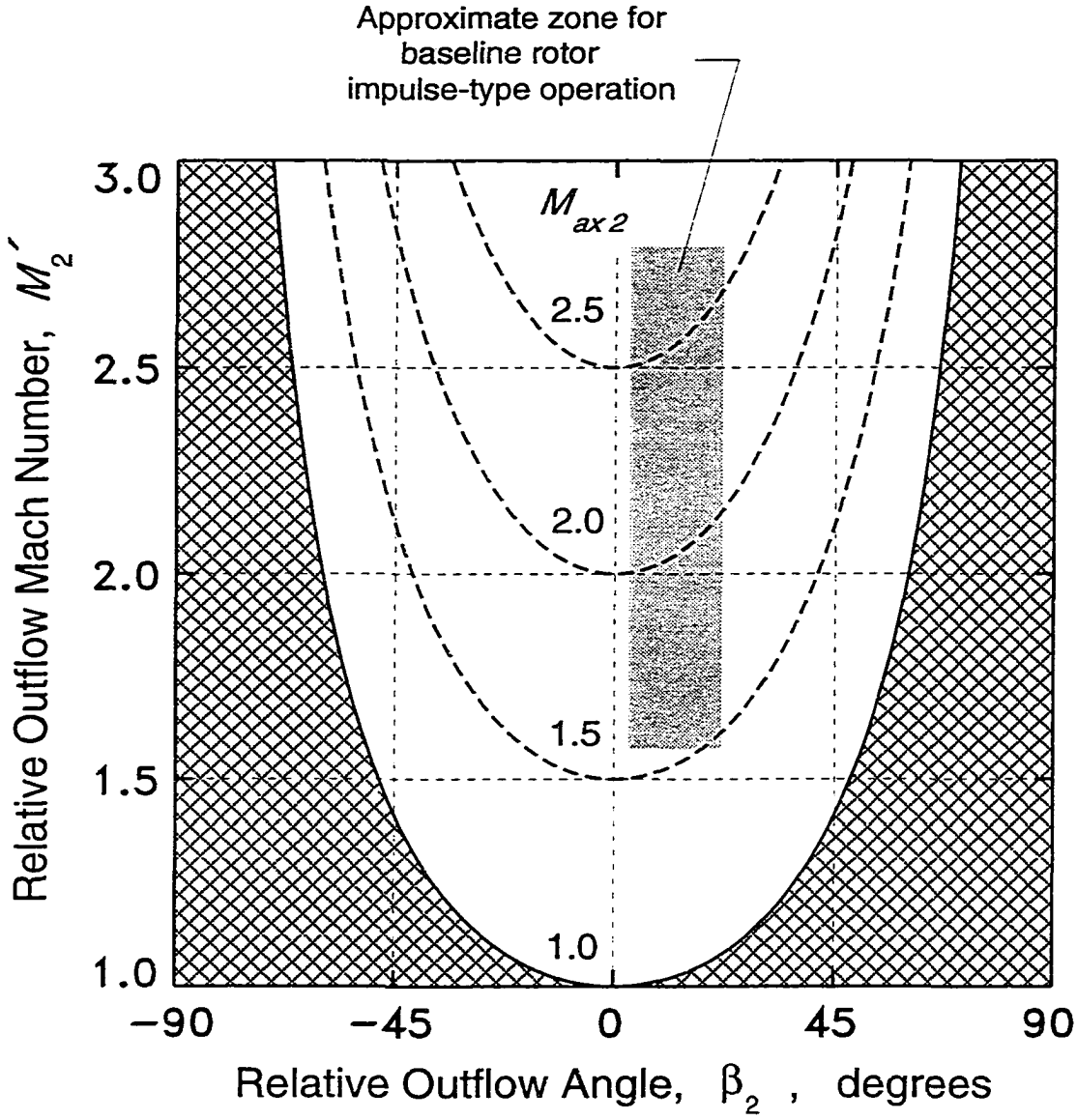

Figure 5.55 Rotor outflow conditions necessary for impulse-type operation (cross-hatch regions indicate axial-subsonic outflow conditions)

The work done on the fluid by the rotor when it operates in an impulse-type mode is of much practical interest, given that such operation is readily attainable. A relatively simple pitchline calculation of the work, or equivalently, the rotor total-temperature ratio, can be performed by considering only the rotor outflow velocity diagram since, for the cases considered here, the inflow to the rotor has no swirl. The Euler momentum equation for a rotor with no inlet swirl has already been given in a useful form in Equation (5.6), which is repeated here for convenience:

$$\frac{V_{\theta 2}}{a_{t2}} = \frac{(T_{t2}/T_{t1}) - 1}{(\gamma - 1)\,(U_2/a_{t1})\sqrt{T_{t2}/T_{t1}}} \tag{5.27}$$

Note that in this equation the total-temperature ratio is the dependent parameter to be determined. Two more equations derived from the outflow velocity diagram are also useful:

$$\frac{U_2/a_{t1}}{\sqrt{T_{t2}/T_{t1}}} - \frac{V_{\theta 2}}{a_{t2}} = \frac{M_2' \sin\beta_2}{\sqrt{1 + \frac{\gamma - 1}{2} M_2^2}} \tag{5.28}$$

$$M_2^2 = \frac{(V_{\theta 2}/a_{t2})^2 + (M_2' \cos\beta_2)^2}{1 - \frac{\gamma - 1}{2}(V_{\theta 2}/a_{t2})^2} \tag{5.29}$$

The relative flow quantities M_2' and β_2 are treated as known independent parameters, leaving three non-linear equations and three unknowns to be solved for. The solution procedure is iterative, but can be quickly performed on a computer. Several results are graphed in Figure 5.56, which also contains experimental data for the baseline rotor at the 75 and 100 percent of design rotational speeds. In this figure the rotor total-temperature ratio is graphed as a function of the axial outflow Mach number, for a particular relative outflow angle β_2. The analysis applies to the rotor midspan ($r/r_{tip} = 0.85$), and for the experimental data the Mach numbers at the midspan (rake) location were used.

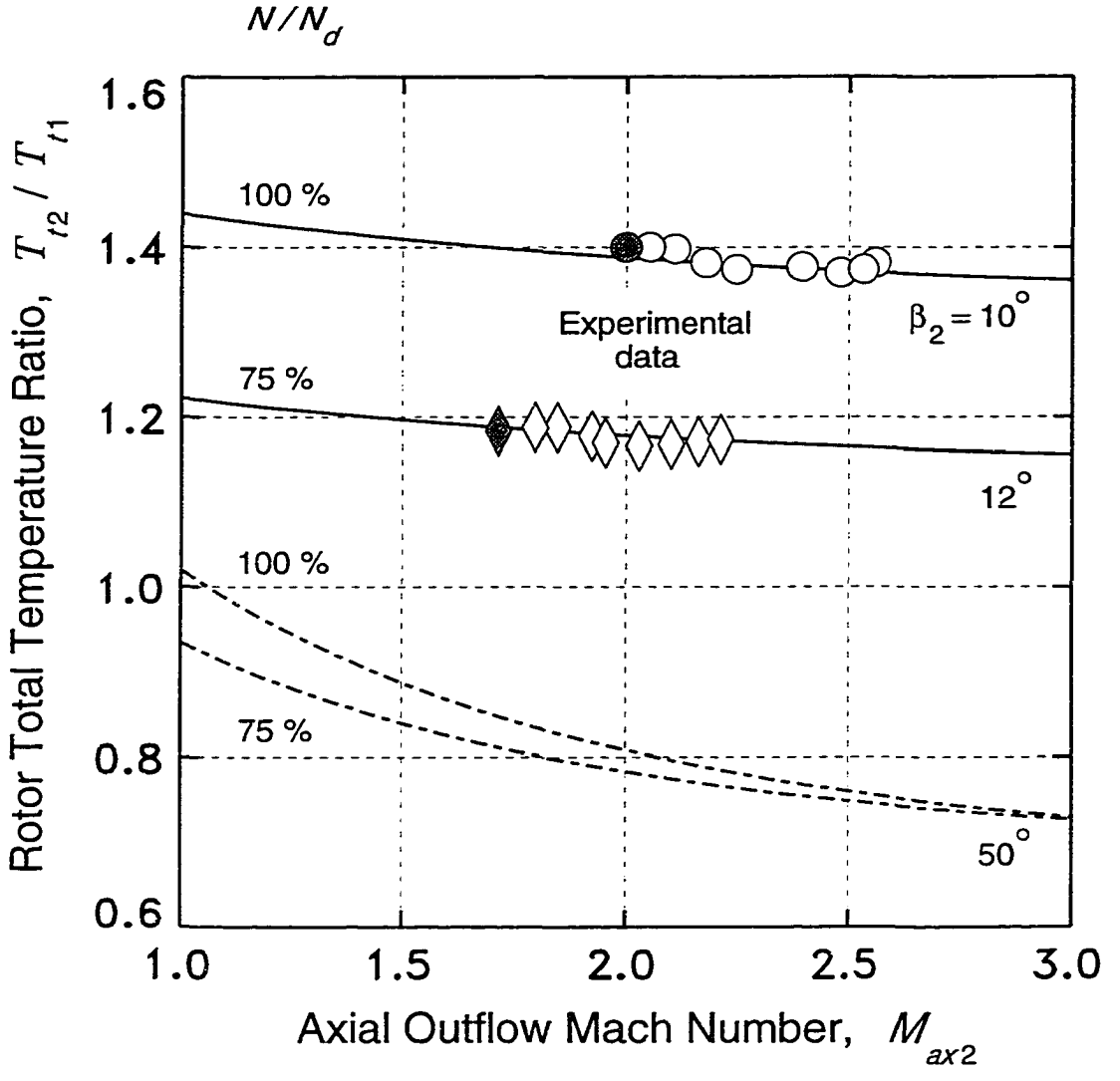

Figure 5.56 Rotor total-temperature ratio as a function of axial outflow Mach number for impulse-type operation of the baseline rotor; experimental data and analytical results at midspan for 75 and 100 percent of design rotational speed (unfilled symbols denote supersonic throughflow operation)

The two solid curves in Figure 5.56 correspond to the baseline SSTF rotor at the conditions indicated. The outflow angles were selected to give the good agreement shown, although they are close to the value of the pitchline blade exit angle of 15 degrees. The comparisons reveal that the relative outflow angle has a fairly constant value over a wide range of impulse-type operating conditions — the high blade-element solidities contribute much to this effect — and that the rotor total-temperature ratio is only weakly dependent on the axial outflow Mach number. This latter effect results from the low relative outflow angle. In fact, for a zero outflow angle ($\beta_2 = 0$) there would be no Mach number dependency at all, so that the curves would be flat and at a level determined solely by the tangential blade speed at the rotor exit:

$$\frac{T_{t2}}{T_{t1}} - 1 = (\gamma - 1)\left(\frac{U_2}{a_{t1}}\right)^2 \tag{5.30}$$

Relative outflow angles opposite the direction of rotation decrease the rotor work below that calculated using Equation (5.30), whereas relative outflow angles in the direction of rotation increase the work.

Finally, notice in Figure 5.56 the two dashed curves corresponding to a relative outflow angle of 50 degrees opposite the direction of rotation [28]. As can be seen, such a condition must be accompanied by a work extraction; that is, the rotor must operate as a turbine. The general implication of this is that any "normal" axial-flow rotor with no inlet swirl, and which has blade exit angles greater than around 40 degrees opposite the direction of rotation must operate in a shock-in-rotor mode in order to function as a practical fan or compressor, regardless of whether the inflow Mach number is axial-subsonic or axial-supersonic. The exception to this would be the case of a rotor with an unusually high rotational speed.

---

[28] Note that 100 percent rotational speed is referenced in this case to the baseline SSTF rotor which has a corrected tip speed of 1500 ft/sec ($U_{tip}/a_{t1} = 1.344$).

Baseline rotor operation and performance

The operation of the baseline SSTF rotor in an impulse-type mode[29] was normally established through a reduction in the rotor back-pressure, as obtained by opening the downstream diffuser throat and thereby unthrottling the rotor. The changes which occur in the rotor performance and the internal blade-passage flow field as the rotor is unthrottled will now be discussed. The rotational speed of 75 percent of design is used to show the basic features since it is at that speed that subsonic-throughflow to impulse-type operation was commonly induced. This is, however, of only minor importance since the basic phenomena associated with the transition to the impulse-type mode are nearly the same for all practical rotational speeds.

A pitchline CFD analysis of the baseline rotor produces trends and performance levels which are very similar to those observed in the experimental test facility. Therefore, several CFD results will be used to explain and demonstrate the basic aerodynamic changes involved in transitioning the rotor to the impulse-type mode.

Computed performance results for four different operating points at 75 percent of design rotational speed are shown in Figure 5.57. The three operating points indicated by *A*, *B*, and *C* are states encountered while progressively unthrottling the rotor (see Figure 5.17 for the subsonic performance of the experimental rotor at several rotational speeds). In the CFD analyses this unthrottling was simulated by decreasing the downstream static pressure at the grid exit boundary. The corresponding blade-to-blade flow fields for each of these cases are presented in Figure 5.58 where absolute Mach number contour plots are shown. The fourth operating point indicated by *D* was obtained from the same CFD solution as point *C*, except that the downstream axial location for determining the rotor performance was not taken as the grid exit, as in the other three cases, but instead was taken at an axial location between the blade row exit and the grid exit. This axial location is indicated in the contour plot associated with the operating points *C* and *D*.

The overall aerodynamic performance results graphed in Figure 5.57 were calculated from the blade-to-blade numerical solutions by circumferential integration and averaging using the methods described in Appendix C. These results represent so-called *entropy*

---

[29] Axial-subsonic inflow, as per the more restricted definition.

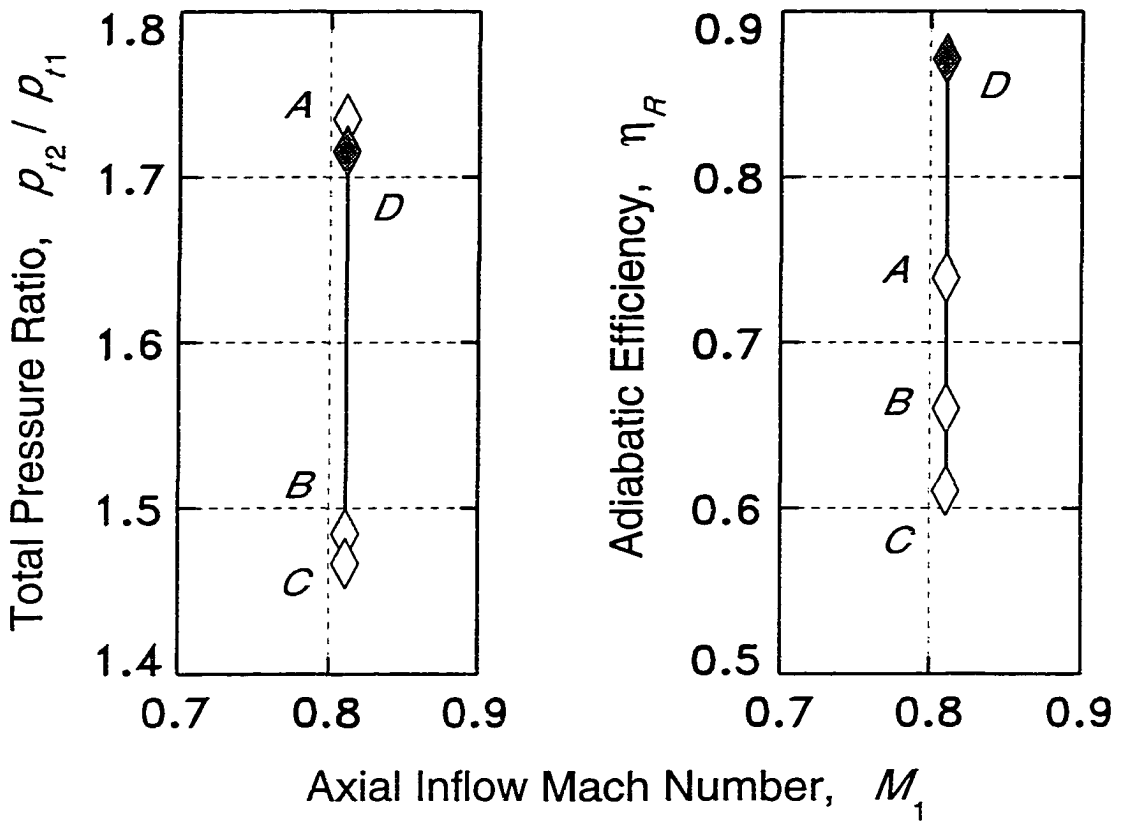

Figure 5.57 Typical operating points in the process of unthrottling the baseline rotor at 75 percent of design rotational speed, in order to obtain impulse-type operation; pitchline quasi-three-dimensional viscous CFD analysis

averages, and as such should reflect the "correct" overall performance for the computed flow field between the upstream and downstream stations. The circumferential averaging can also be performed at various locations throughout the blade row, thus revealing how the average flow and performance develop through the rotor. Results of this type are shown in Figure 5.59 for the three cases, *A*, *B*, and *C*, where graphs for absolute Mach number and total-pressure ratio are presented. Note that the performance levels at the right extremity of each curve are the same as those contained in Figure 5.57, with the exception of point *D*.

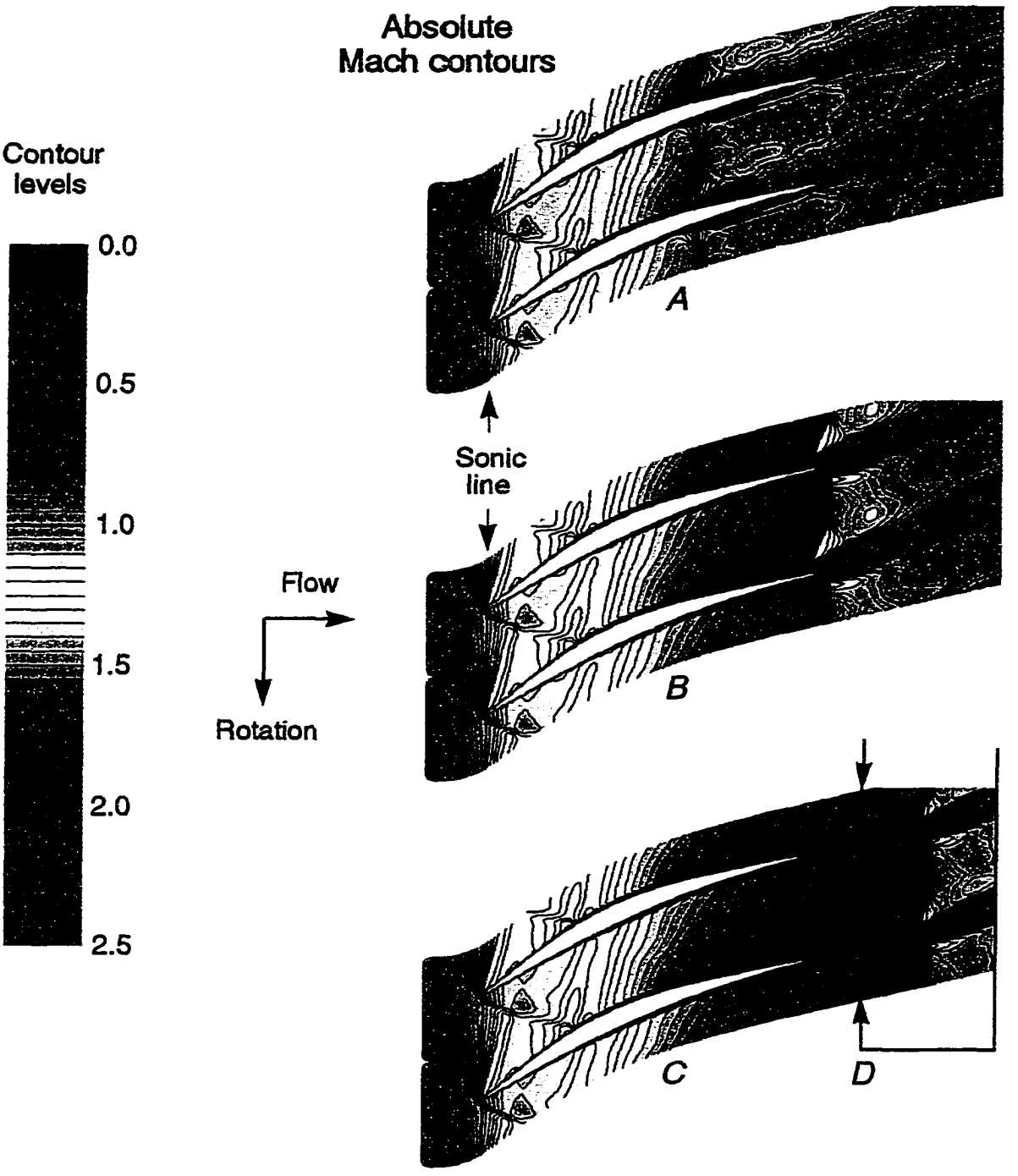

Figure 5.58 Viscous quasi-three-dimensional CFD Mach number contours for the rotor pitchline at 75 percent of design rotational speed; rotor choked with axial-subsonic inflow and three different back-pressure conditions

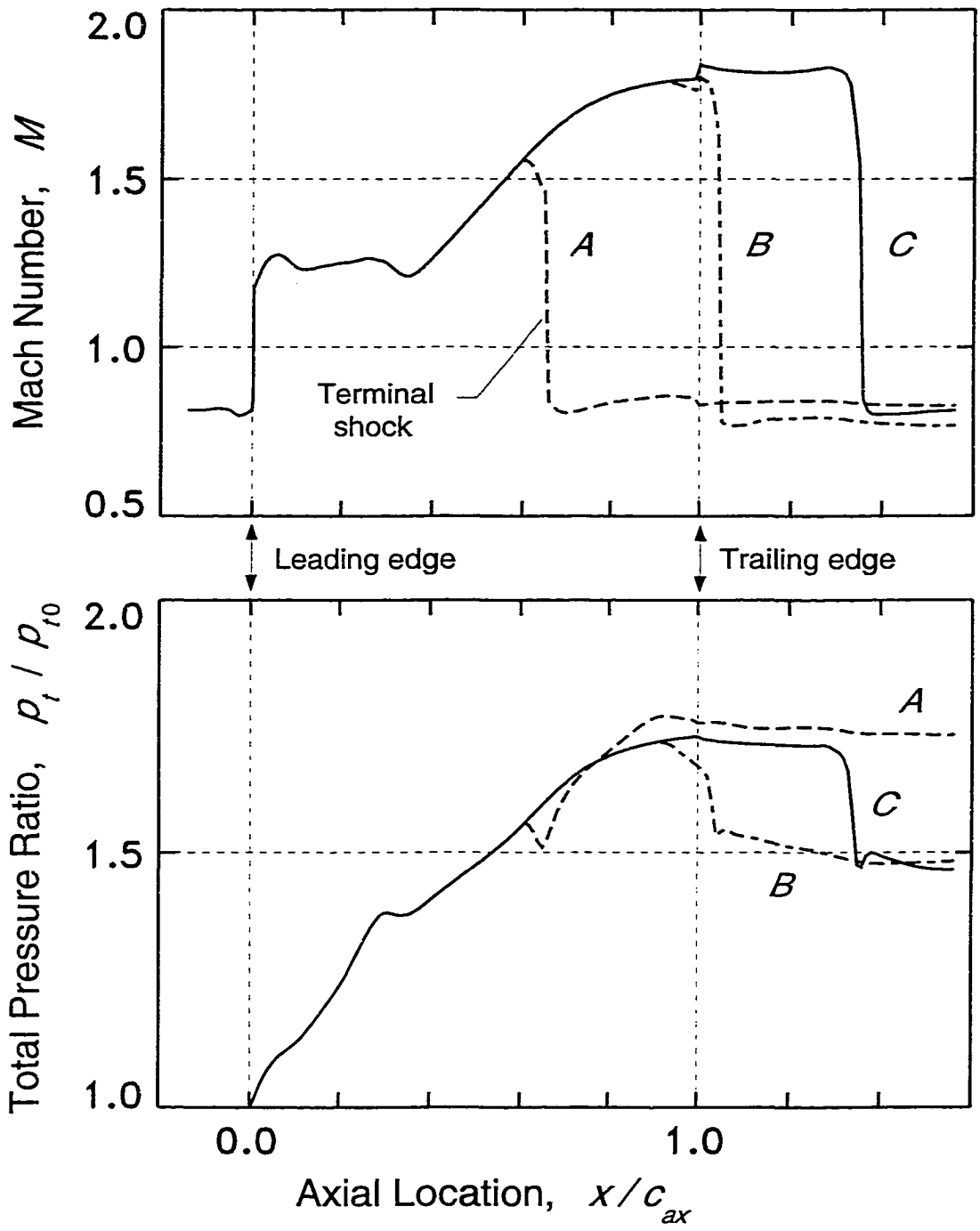

Figure 5.59 Axial distributions of circumferential-average pitchline CFD results (entropy average) for the baseline rotor at 75 percent of design rotational speed

Several features are worth noting from Figures 5.58 and 5.59. First, the rotor is choked in the leading-edge plane, as discussed rather extensively in the earlier section entitled **Axial-Subsonic Rotor-Inflow Characteristics.** Behind this choking plane the flow remains at low supersonic Mach numbers (around Mach 1.2) until reaching the blade-passage minimum area located near mid-chord. The supersonic flow then expands steadily and rapidly to higher Mach numbers in the downstream half of the passage, before finally terminating in a strong normal-shock system The flow expansion and stable normal-shock-structure both require an effectively increasing flow area in the relative frame-of-reference. Indeed, such an increase is expected due to the relative flow turning toward the axial direction, and to the substantial decrease in the blade-metal blockage from the maximum-blade-thickness location to the trailing edge. Notice that upstream of the terminal shock the flow fields are identical, as expected for relative supersonic flow.

Decreasing the rotor back-pressure moves the terminal shock system (further) downstream until, eventually, it becomes located somewhere just downstream of the blade row (operating point *B* to *C*). During this unthrottling process the operating point moves down the vertical (choking) part of the speed line (see Figure 5.57) to lower total-pressure ratios and efficiencies until reaching a minimum at point *C*. The performance reduction is due to increasing Mach number levels incident on the terminal shock as it relocates further and further downstream; that is, the shock system increases in strength with a corresponding increase in total pressure loss. Since the blade loading also decreases at the same time, as can be seen by inspection of the (dimensionless) blade static pressure distributions shown in Figure 5.60, the performance drops rapidly.

From the standpoint of blade-row aerodynamics, impulse-type operation already exists at point *C* because the flow exiting the blade row is axial supersonic, and the blade loading and energy input are uninfluenced by back pressure. Since, however, the downstream integration and averaging are being carried out at the grid exit, which is downstream of the normal-shock system, the performance values include the relatively large total-pressure loss generated by the shock system. The performance of the rotor without this loss, point *D* in Figure 5.57, was obtained by circumferential averaging at a location 0.5 inches downstream of the blade row, which is just upstream of the shock system (see Figure 5.58).

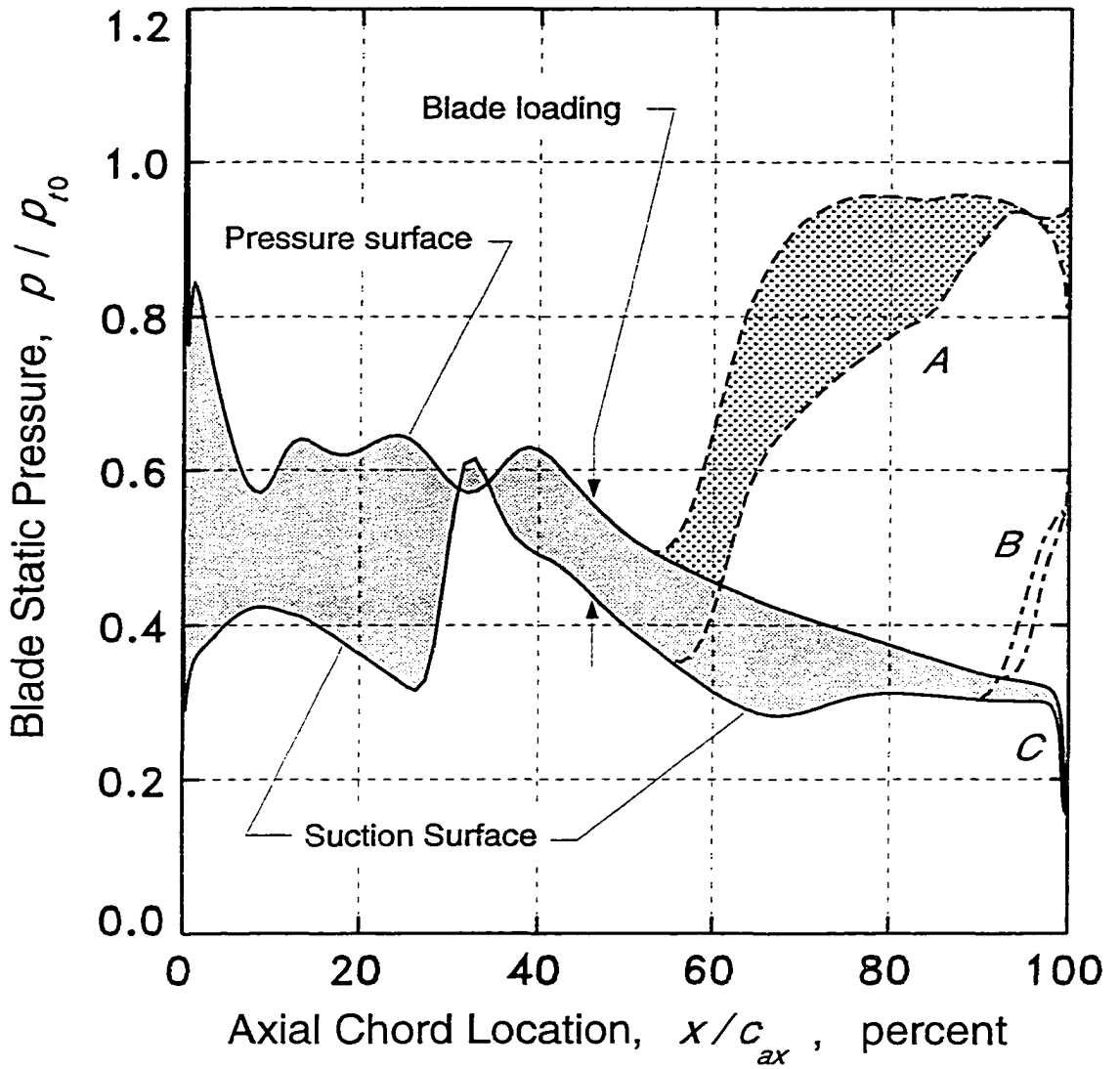

Figure 5.60 Rotor pitchline blade loading distributions before and after the transition to impulse-type operation at 75 percent of design rotational speed; quasi-three-dimensional viscous CFD analysis

A similar improvement in aerodynamic performance was observed for the experimental rotor when impulse-type operation was induced. As the rotor was unthrottled in the test facility, a jump in measured performance occurred when the rotor terminal-shock moved downstream past the measurement rakes (located approximately 3.5 inches downstream of the rotor). Diffuser starting coincided with this jump in performance since the shock system did not relocate in the diffuser duct downstream of the rakes. Interestingly, however, the terminal-shock system did find stable locations in the duct section just downstream of the rotor exit, as the pitchline CFD results implied would be the case (Figure 5.58, point *C*). This fact was evidenced in the experiment by rotor strain-gage instrumentation which indicated a substantial four-cycles-per-revolution signal at the more highly-throttled conditions. The disturbances were due to perturbations in blade loading from the four measurement rakes downstream. As the rotor was unthrottled, a point was reached at which the strain-gage signal abruptly disappeared and the blade stress fluctuations became quiescent, thus indicating that the shock system had moved downstream of the rotor blade row. Further unthrottling was still needed, however, to induced the diffuser to swallow the shock, with the accompanying discontinuous improvement in measured rotor performance.

A more three-dimensional picture of the transition to impulse-type operation can be seen using the experimental hub and casing static-pressure data. Measured endwall static pressures in the diffuser just before and after diffuser-starting are shown in Figure 5.61, which also includes hub and casing static pressure distributions within the rotor as computed using the three-dimensional viscous CFD methods (see Chapter 4). Note that dimensionless static pressures are presented here, rather than isentropic wall Mach numbers, because the total pressure increases through the rotor.

Measured and computed overall performance results for the baseline rotor in the impulse-type operating mode are compared in Figure 5.62 for several rotational speeds. Rotor total-pressure ratio as a function of axial inflow Mach number is shown on the left in Figure 5.62, and the corresponding adiabatic efficiencies are shown on the right. Quasi-three-dimensional and fully three-dimensional viscous CFD results are both compared with the experimental data, as indicated, and the agreement is generally quite good. Apparently the quasi-three-dimensional approximation is fairly accurate for this particular rotor and operating mode, as implied by the good agreement.

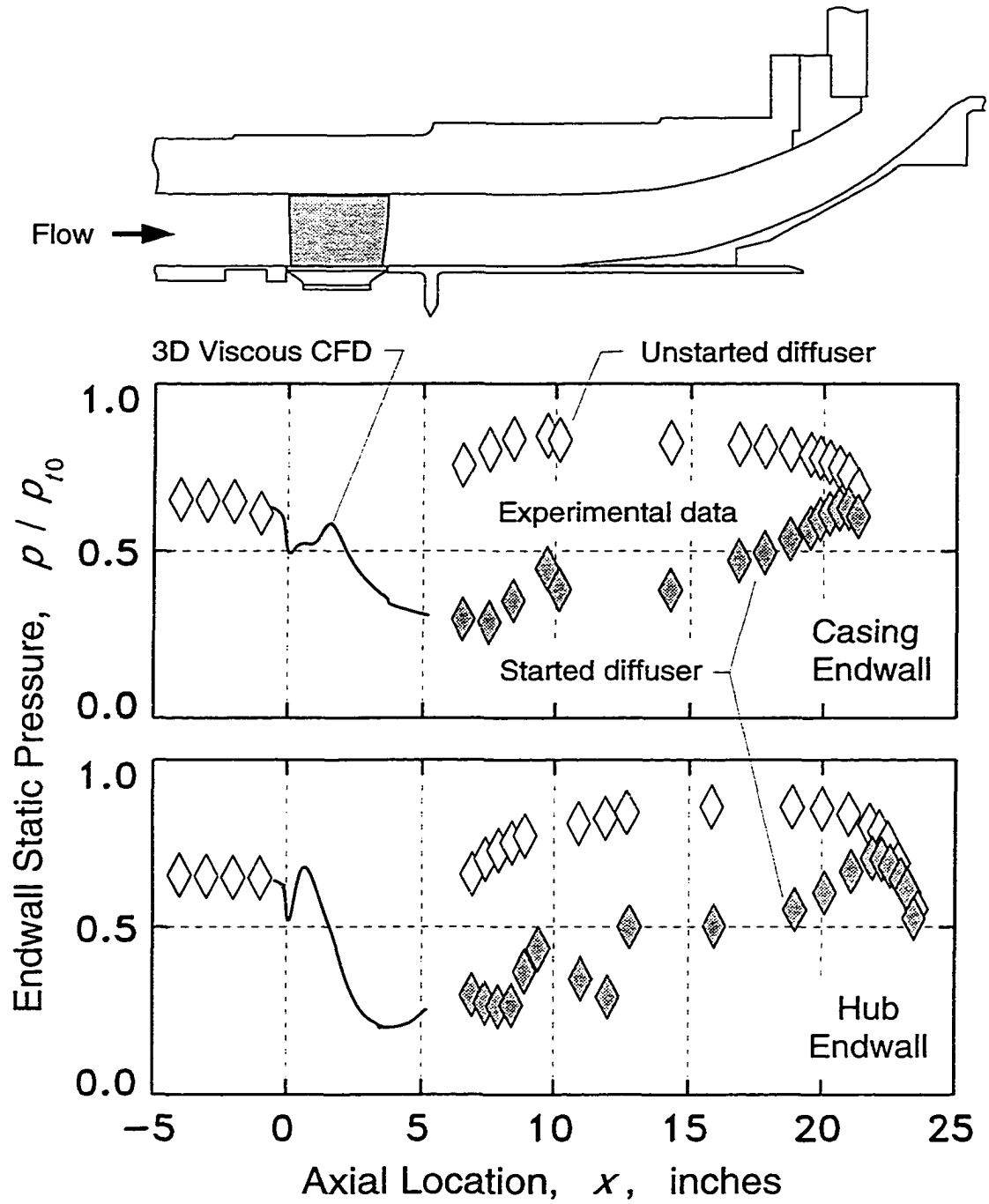

Figure 5.61 Experimental endwall static pressure distributions before and after diffuser starting at 75 percent of design rotational speed; computed endwall static pressure distributions within the rotor (operating in impulse-type mode)

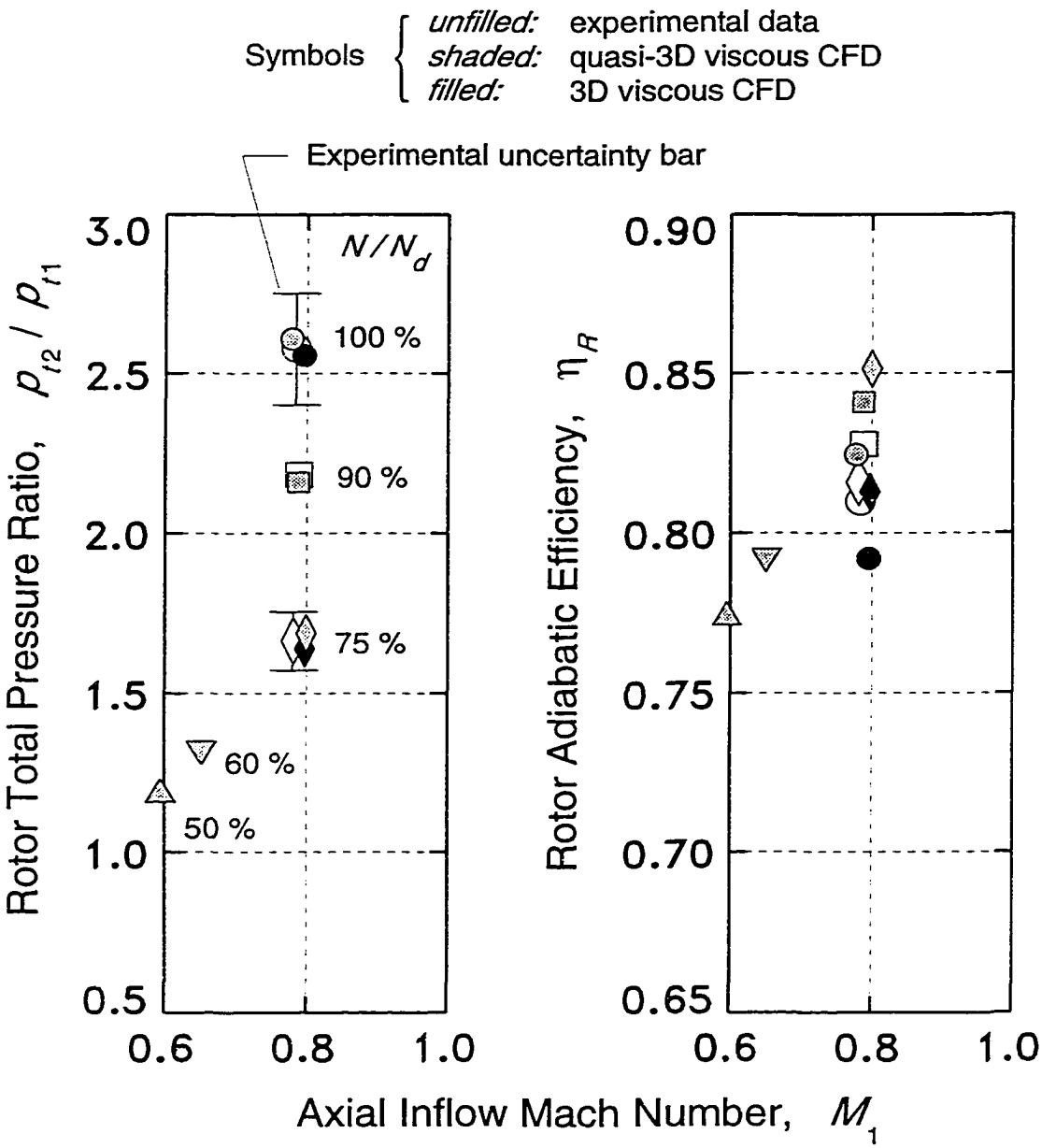

Figure 5.62 Computed and measured overall performance of the baseline rotor in the impulse-type operating mode; total-pressure ratio and adiabatic efficiency versus axial inflow Mach number

Many of the aerodynamic performance aspects inherent in Figure 5.62 have already been discussed in one form or another. For example, the axial inflow Mach number levels for choked-rotor operation over much of the rotational speed range have been described, as have the general rotor-work (total-temperature ratio) characteristics. More specific results for the rotor total-temperature ratios corresponding to the operating points in Figure 5.62 are shown in Figure 5.63. For simplicity, only the pitchline quasi-three-dimensional CFD results are presented[30] in Figure 5.63, where at each operating point an outflow angle β_2 and a deviation angle δ_2 are indicated. Observe that for the entire range from 50 to 100 percent of design rotational speed, the outflow angle is almost constant at between 11 and 15 degrees, which is close to the blade exit angle of 15 degrees.

To conclude this section there is one remaining aspect of the rotor aerodynamic performance which is of major importance and which should be addressed; namely, the rotor total-pressure loss, or similarly, the rotor adiabatic efficiency. The adiabatic efficiency relates the rotor total-temperature ratio (see Figure 5.63) to the total-pressure ratio (see Figure 5.62), and is remarkably constant ($\eta_R = 0.77$ to 0.85) for the impulse-type operating mode over a wide range of rotational speeds. Since adiabatic efficiency is fundamentally determined by the total-pressure loss in the relative frame-of-reference, the loss characteristics of the baseline rotor will be briefly discussed.

Rotor pitchline total-pressure loss coefficients are graphed against relative inflow Mach numbers in Figure 5.64, for the same operating points shown in Figure 5.63. Only the pitchline quasi-three-dimensional CFD results are presented for the sake of simplicity, and because they are considered adequate to represent the rotor aerodynamic performance. Also shown in Figure 5.64 is a rough break-down of the total-pressure losses, particularly for relative-supersonic inflow conditions where three basic loss sources are indicated: skin-friction, bow-shock, and oblique-shock. These loss-source magnitudes were estimated by analyzing the CFD flow field solutions, and by using a

---

[30] The close agreement between the experimental and computational results justifies this simplification, in the author's opinion.

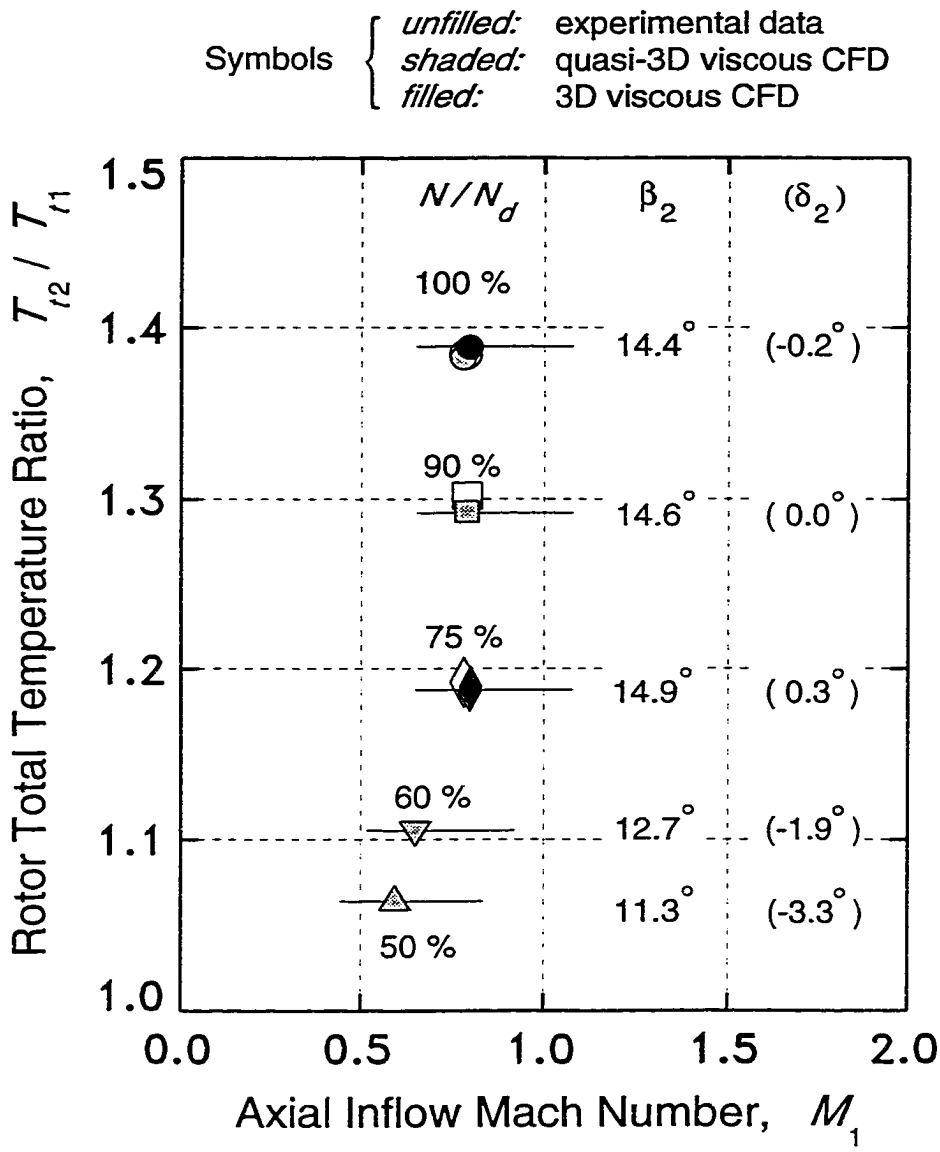

Figure 5.63 Computed and measured overall performance of the baseline rotor in the impulse-type operating mode; total-temperature ratio versus axial inflow Mach number

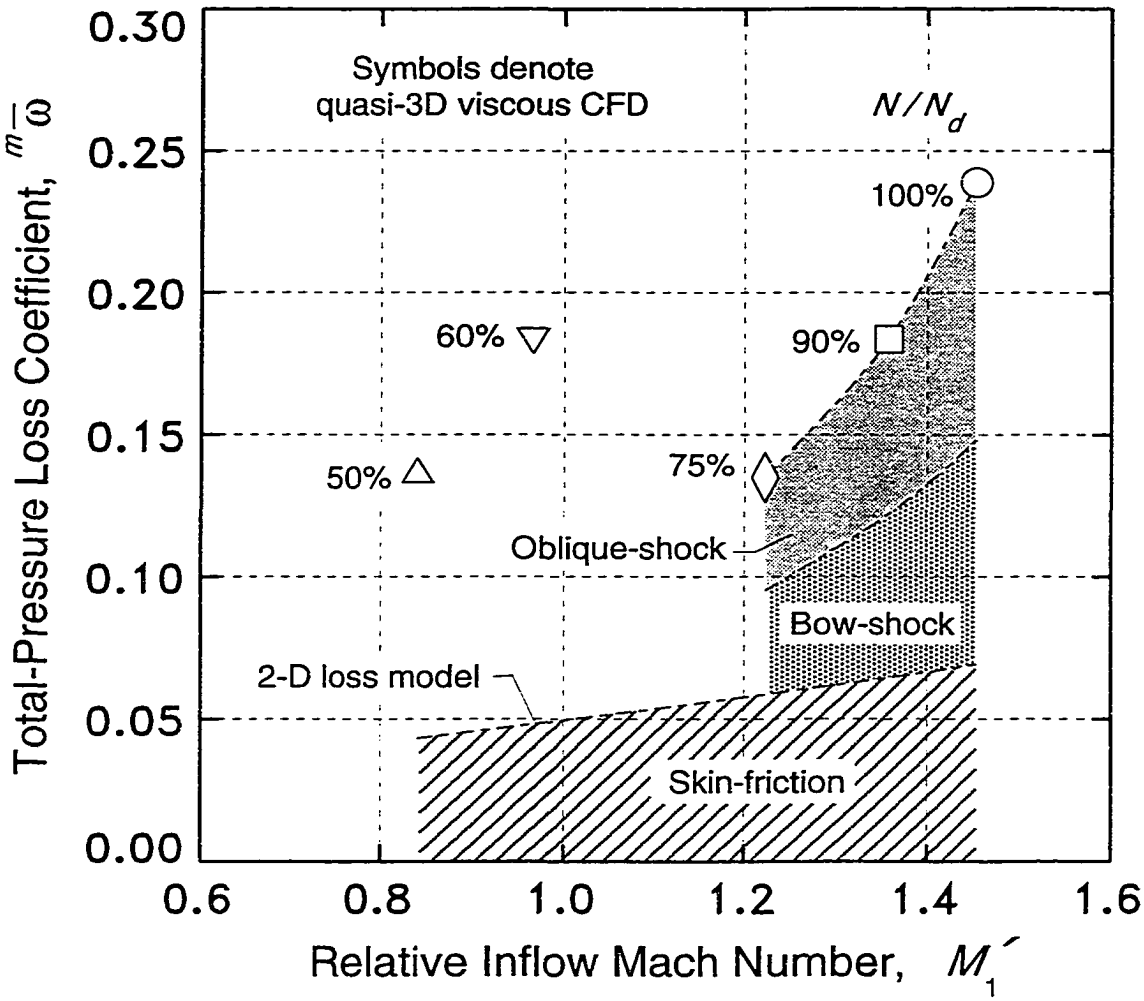

Figure 5.64 Rotor pitchline total-pressure loss coefficient as a function of relative inflow Mach number, for impulse-type operation; quasi-three-dimensional viscous CFD analysis, and two-dimensional loss-model analysis for the skin-friction loss (see Appendix E)

fairly simple loss model [31], described in Appendix E, for the skin-friction losses. In general it can be seen that the bow- and oblique- shock losses have similar magnitudes at a particular rotational speed, with both increasing rapidly as rotational speed increases. The skin-friction loss (modeled using a compressible flat-plate boundary layer), however, increases only slowly as rotational speed increases. At 75 percent of design rotational speed the approximate quantitative breakdown of the total loss into the three components is as follows: skin-friction loss 43 percent, bow-shock loss 27 percent, and oblique-shock loss 30 percent. Similarly, at 100 percent of design speed the approximate breakdown is as follows: skin-friction loss 29 percent, bow-shock loss 33 percent, and oblique-shock loss 38 percent. Notice that for the lower rotational speeds (50 and 60 percent of design speed, and relative-subsonic inflow conditions), no attempt was made to estimate the shock losses. At these lower speeds the shock losses are generated in a transonic flow field with supercritical flow on the forward suction-surfaces of the blades (see Figures 5.19 and 5.20).

Supersonic Throughflow Operation

Rotor operation in the supersonic throughflow mode involves a fairly wide range of mass flow and rotational speed conditions. The design condition represents a specific point within this range, and due to its importance will be given special consideration in a subsection entitled **Design-point performance and aerodynamics**, which describes the design-point aerodynamics in more detail than otherwise is done for off-design conditions. The general design/off-design point performance and aerodynamics are discussed first, however, providing a framework within which to discuss the design-point aerodynamics.

---

[31] The model was not used to estimate the shock losses for these cases since the rotor inflow is axial-subsonic. As described in Appendix E, the complete model includes shock losses and applies only to supersonic throughflow conditions.

General performance and aerodynamics

The supersonic throughflow regime is bounded by the *rotor unstart boundary*, which is composed of a locus of minimum axial-supersonic inflow Mach numbers depending on the rotational speed, as discussed earlier in the section entitled **Rotor-Inflow Starting and Unstarting**. The supersonic through flow operating points which are at or near this boundary were referred to as either *post-start* or *pre-unstart*, whichever was applicable, although for all practical purposes they are nearly the same since there is normally little start/unstart hysteresis. To begin this section it is of some interest to discuss the aerodynamic performance associated with these near-rotor-unstart (NRU) operating points, particularly as it relates to the impulse-type performance just discussed in the previous section. The impulse-type and NRU supersonic throughflow operating points are closely related to each other, forming a type of conjugate pair for a given rotational speed. This can be seen, for example, in Figures 5.43 through 5.46 where the aerodynamic similarities are apparent. Of key interest are the performance and blade-loading discontinuities encountered in transitioning between conjugate points, which was also briefly discussed in connection with rotor inflow starting and unstarting. At that time, however, no performance results were presented.

Rotor performance maps showing the conjugate operating points in terms of total-pressure ratio and total-temperature ratio as a function of axial inflow Mach number are shown in Figure 5.65. Experimental and circumferentially-averaged computational results are both graphed, as indicated, and are in good agreement. As can be seen there is only a relatively small discontinuity in the rotor performance between the impulse-type and NRU operating points (at a particular rotational speed). Notice the general appearance of symmetry from left-to-right about the sonic axial inflow condition. This symmetry is due to the lack of any large change in performance between the started and unstarted states (see also Figure 5.41). The reason that there is little change in the total-temperature ratio has already been addressed in the general discussion on impulse-type operation, where supersonic throughflow was considered to be a special category of impulse-type operation. Since the total-temperature ratios are nearly the same for conjugate operating points, then any differences in the total-pressure ratios (and adiabatic efficiencies) are due to differences in the rotor total-pressure losses. These differences, therefore, must be small, at least for rotational speeds above 50 percent of design speed.

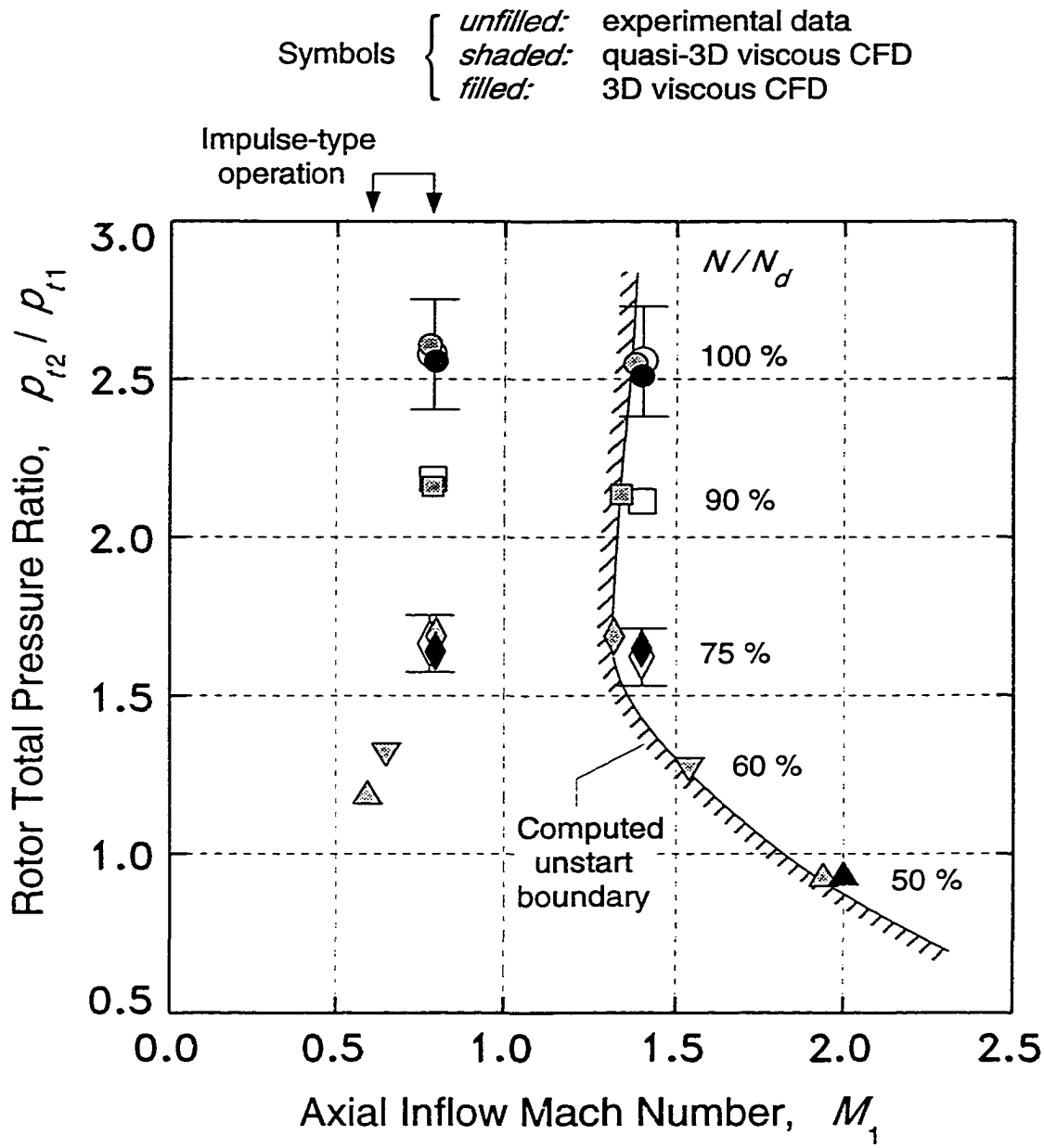

Figure 5.65 Rotor performance for impulse-type operation and supersonic throughflow operation at near-rotor-unstart conditions

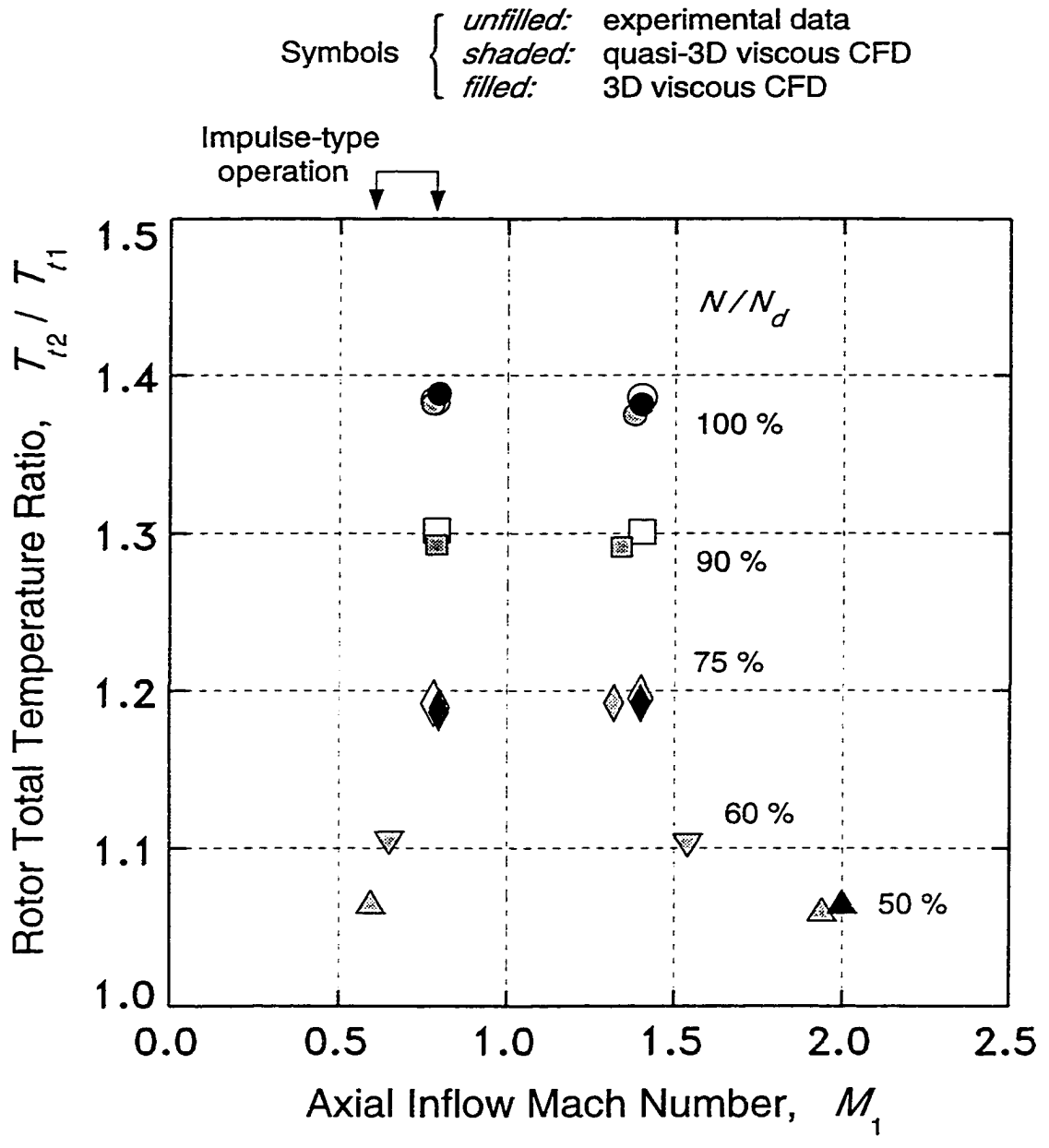

Figure 5.65 (continued)

Total-pressure loss coefficients for the rotor pitchline at NRU operating points for 75, 90, and 100 percent of design rotational speed are shown in Figure 5.66, where they are graphed against relative inflow Mach number. These results were obtained using the quasi-three-dimensional CFD code and are direct counter-parts to the impulse-type results presented above in Figure 5.64. Also in Figure 5.66 is an approximate break-down of the losses as determined using the two-dimensional loss model (see Appendix E). The magnitudes of the pitchline losses and of the three contributing loss-sources can be directly compared with the conjugate impulse-type points in Figure 5.64, which are also shown in Figure 5.66 for easier comparison. As expected, the differences in the total-pressure losses between conjugate points are relatively small, although there are substantial differences in the split between the bow-shock and oblique-shock losses.

In view of the substantial differences in the relative inflow Mach number levels between impulse-type and NRU points in Figure 5.66, it is perhaps surprising that the loss levels are so similar. This can be explained in part by recognizing that for impulse-type operation the inflow Mach number levels are lower, but at the same time the flow incidence angles are much higher (see Figure 5.42 for incidence angles). The high incidence causes a bow-shock wave which is locally "detached" off the pressure side of the blade, thereby producing a larger bow-shock loss than would occur for the same relative inflow Mach number at a lower incidence. This effect occurs only in the leading-edge region of the blade row where the impulse-type and NRU cases are qualitatively different. Downstream of the leading-edge plane the two related cases become remarkably similar, however, as can be seen for example in the pitchline blade-to-blade contour plots of Figures 5.43 and 5.44. A more comprehensive view of this general similarity in flow fields is shown in Figures 5.67 and 5.68, for the 75 and 100 percent of design rotational speeds, respectively. These figures compare meridional contour plots of circumferential-average absolute Mach number for the impulse-type and the NRU supersonic throughflow operating points, as computed using the three-dimensional viscous CFD code. Corresponding hub and casing static-pressure distributions are compared in Figures 5.69 and 5.70 for the 75 and 100 percent rotational speeds, respectively, with measured static pressures also shown to verify and compliment the CFD results.

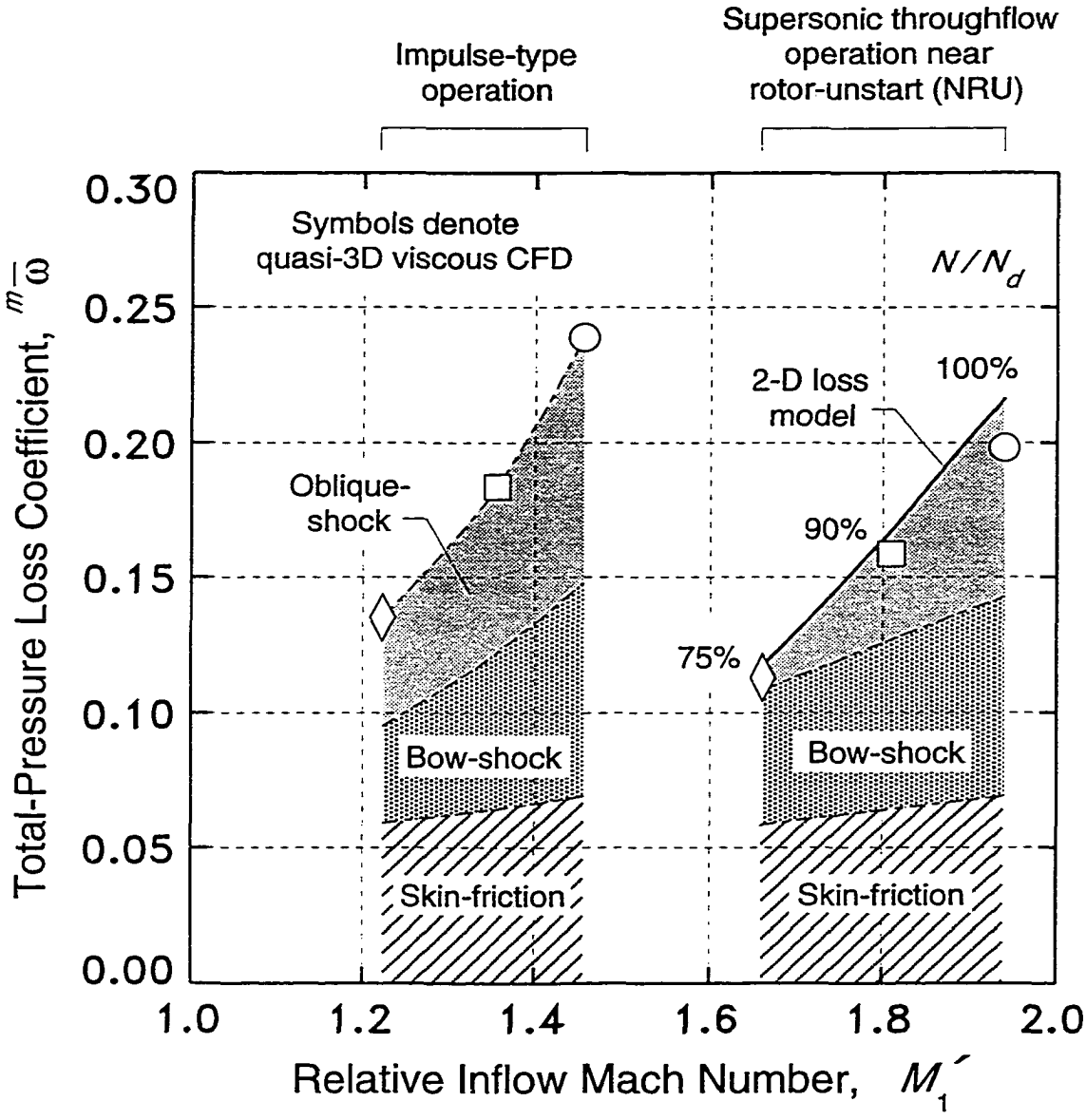

Figure 5.66 Rotor pitchline total-pressure losses for impulse-type operation and supersonic throughflow operation at near-rotor-unstart conditions; quasi-three-dimensional viscous CFD analysis, and a two-dimensional loss-model analysis (see Appendix E)

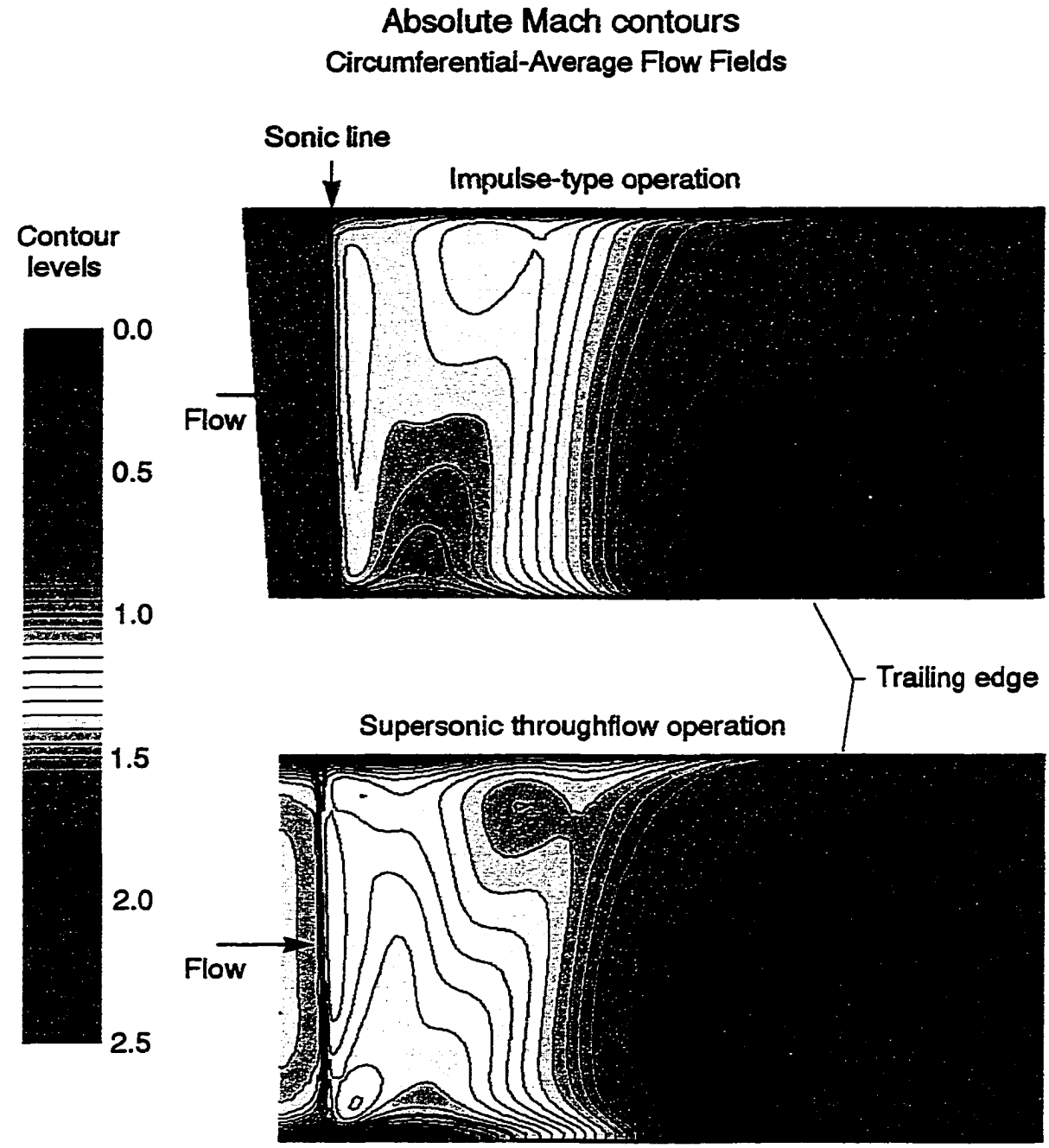

Figure 5.67 Viscous three-dimensional CFD Mach number contours for the circumferential-average rotor flow field at 75 percent of design rotational speed; comparison of impulse-type and NRU supersonic throughflow operation

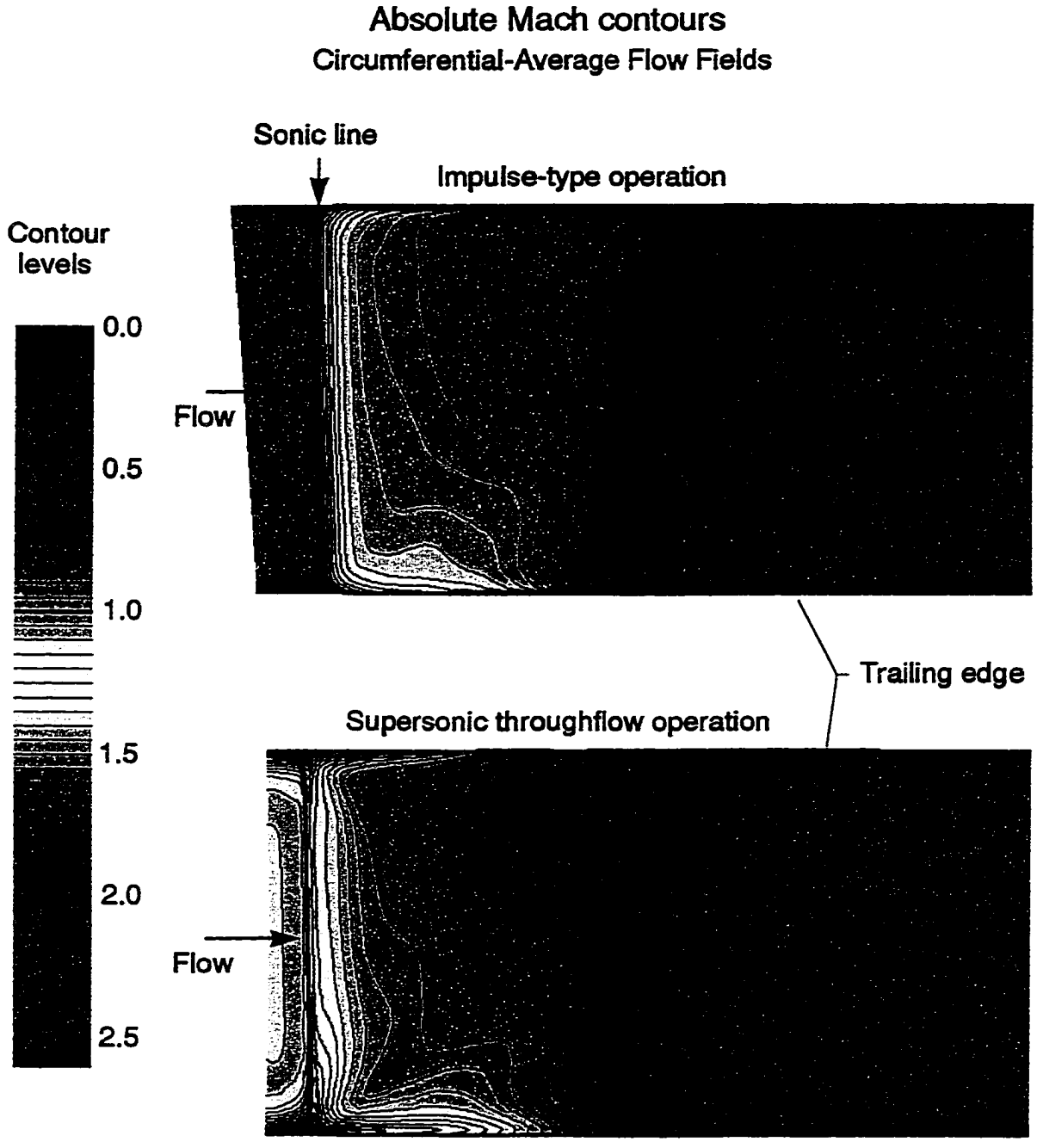

Figure 5.68 Viscous three-dimensional CFD Mach number contours for the circumferential-average rotor flow field at 100 percent of design rotational speed; comparison of impulse-type and NRU supersonic throughflow operation

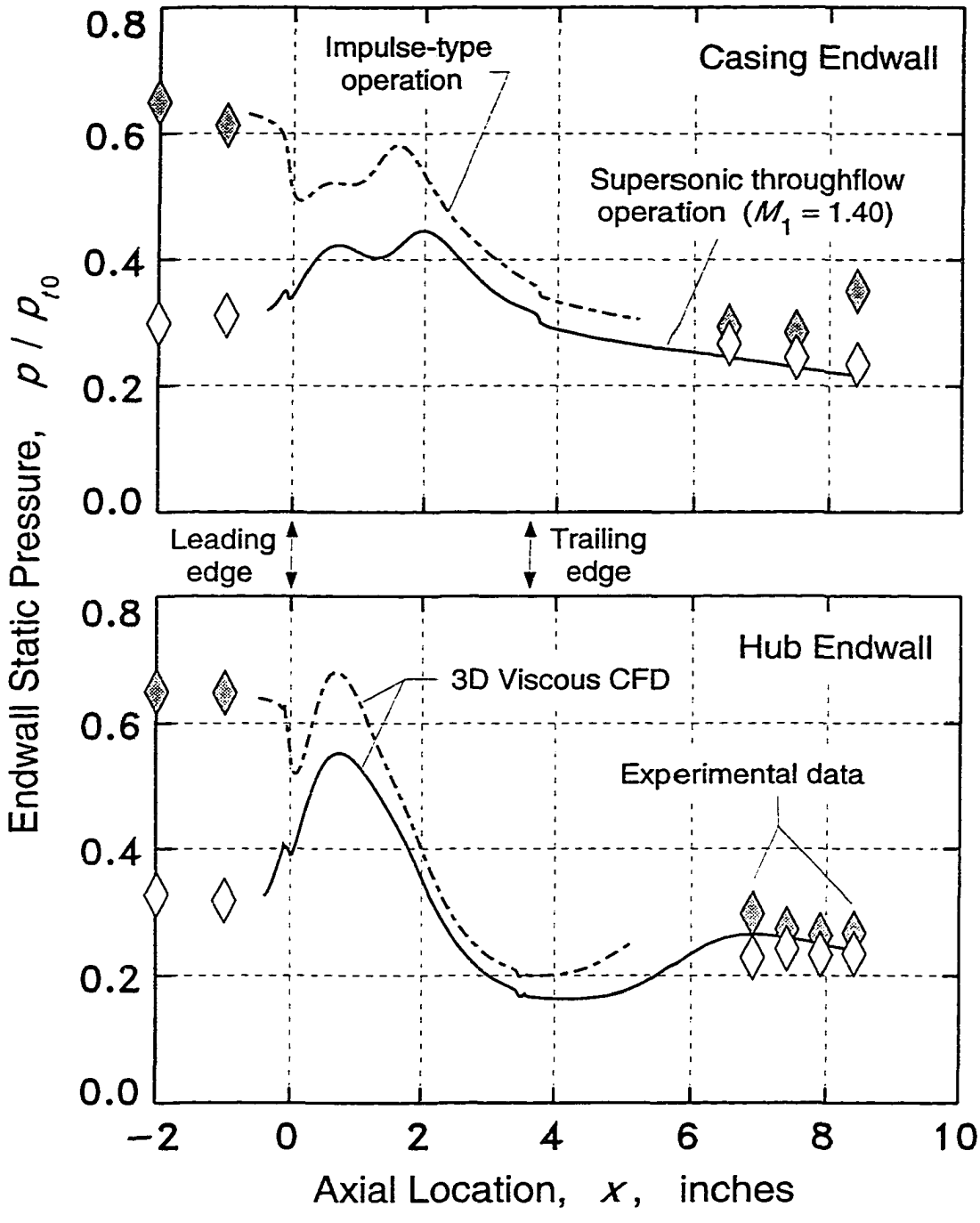

Figure 5.69 Endwall static pressure distributions for impulse-type operation and supersonic throughflow operation at near-rotor-unstart conditions, at 75 percent of design rotational speed; experimental and three-dimensional viscous CFD results

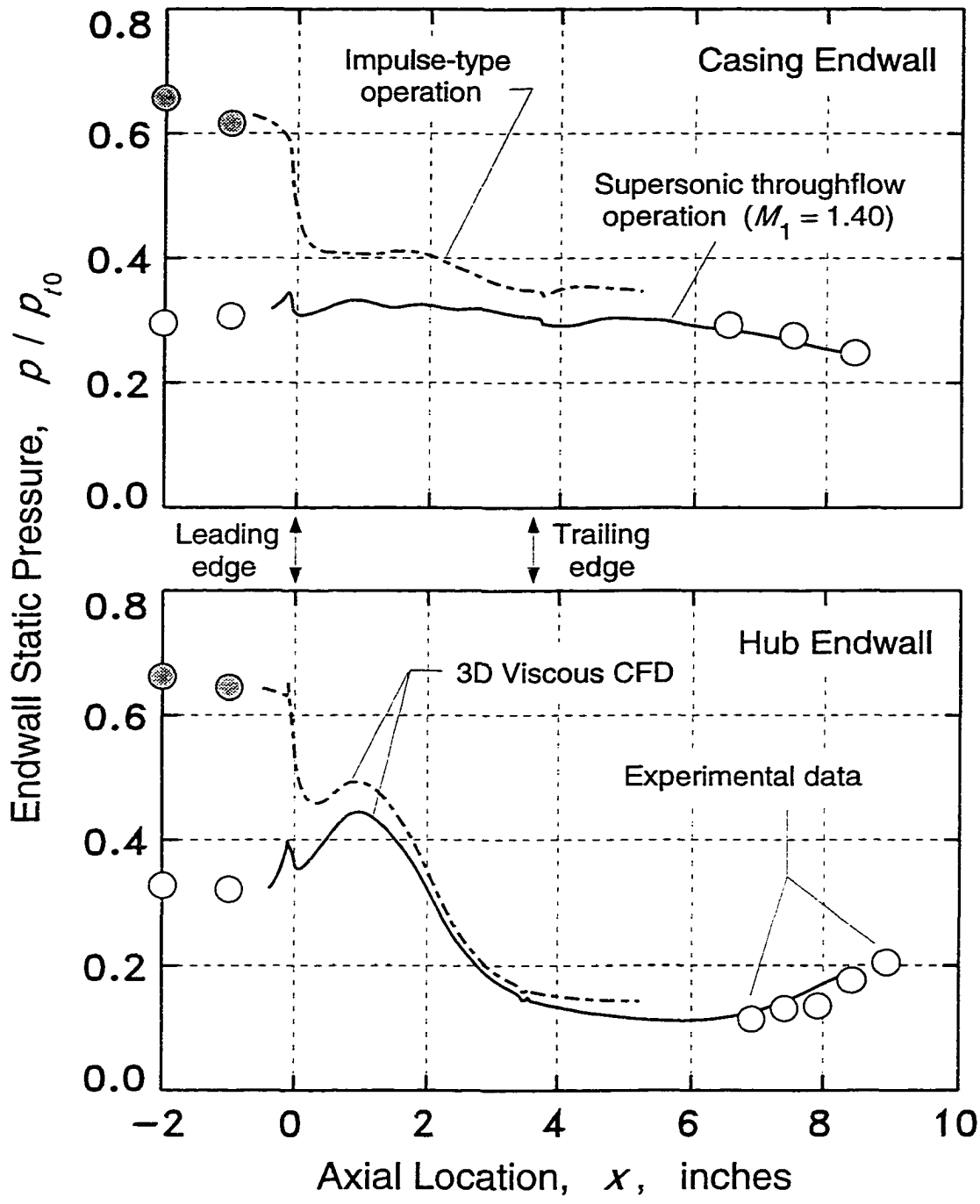

Figure 5.70 Endwall static pressure distributions for impulse-type operation and supersonic throughflow operation at near-rotor-unstart conditions, at 100 percent of design rotational speed; experimental and three-dimensional viscous CFD results

The aerodynamic performance of the baseline rotor over the entire range of measured and computed supersonic throughflow conditions is presented in Figure 5.71, which shows maps for total pressure ratio, total temperature ratio, and adiabatic efficiency, as a function of axial inflow Mach number. In this figure the experimental and computational results are compared, demonstrating good agreement. Note that the experimental data represent slow-response rake-instrumentation measurements fairly far downstream of the isolated rotor[32] (see Chapter 3), and the CFD flow field results have been circumferentially and radially *energy-averaged* at the rake location (see Appendix C). The curves show performance calculations obtained using an axisymmetric off-design performance analysis code[33]. These curves, involving an empirical correlation for deviation angle, will be discussed below after first covering some preliminary considerations.

The experimental uncertainty bars in Figure 5.71 are only rough approximations and represent a 1.0 percent of full-scale measurement uncertainty in the basic measurement quantities, which is the same as the experimental uncertainties reported in Reference 48 and listed in Chapter 3. The uncertainty bars indicate the *potential* for large errors due to error propagation into the total-pressure results (see Appendix B). In general, the higher the Mach number at the measurement location, the larger the propagated uncertainty.

The constant-speed lines for supersonic throughflow operation are relatively flat, i.e., horizontal, which is a direct consequence of the work-input characteristics of an impulse-type rotor. This behavior was described in the last section entitled **Impulse-Type Operation**, where it was ascribed to the low exit flow angles resulting from low blade exit angles. The rotor exit blade angles range almost linearly from about 0 degrees at the hub to 23 degrees at the tip, and deviation angles are virtually always negative over the entire range of experimental supersonic throughflow conditions, as will be shown below.

---

[32] Total-temperature data based on the slow-response probe measurements downstream of the fan *stage* are shown, rather than the rake total-temperature data for the isolated rotor. The stage data are used because the near-hub rake-element appears to have given erroneous total-temperatures in at least some cases. Combining the rotor and stage data introduces a slight error in the inflow Mach numbers (the rotor and stage inflow Mach numbers were not identical), but the effects are negligible.

[33] The off-design code is based on the streamline-curvature method and typically uses eleven axisymmetric streamlines from hub to tip. The code is undocumented.

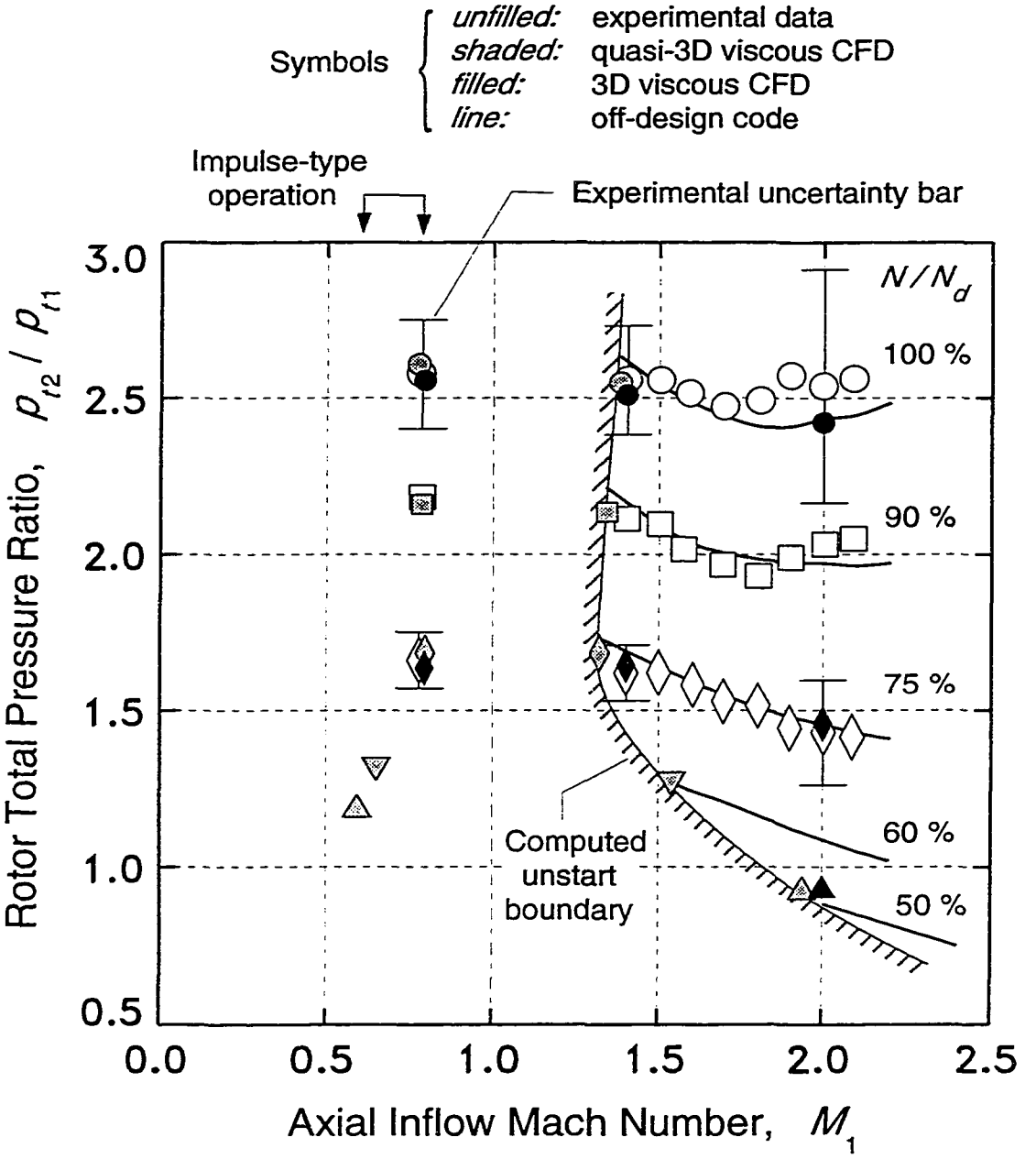

(a) total pressure ratio

Figure 5.71 Rotor performance for supersonic throughflow operation

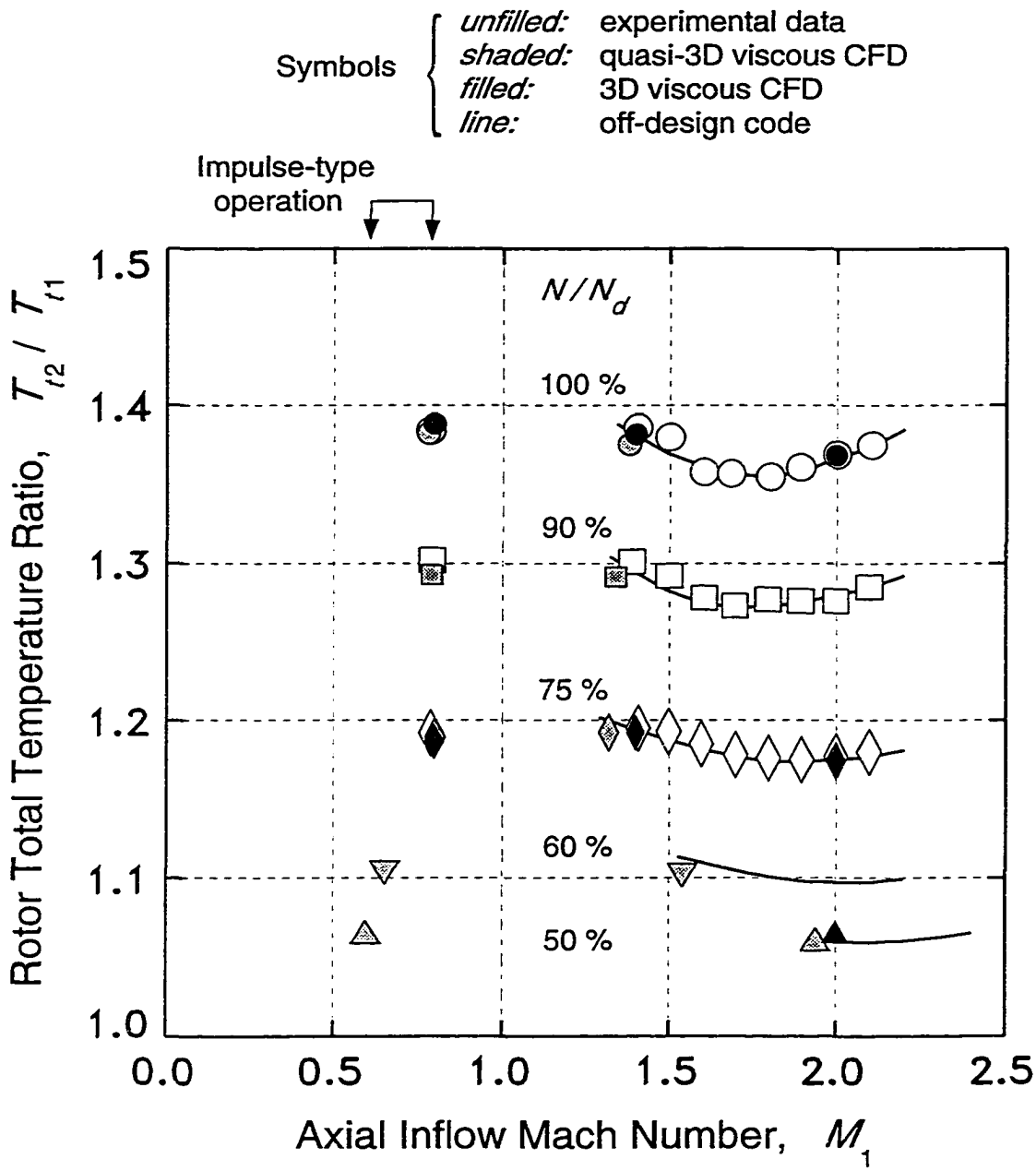

(b) total temperature ratio

Figure 5.71 (continued)

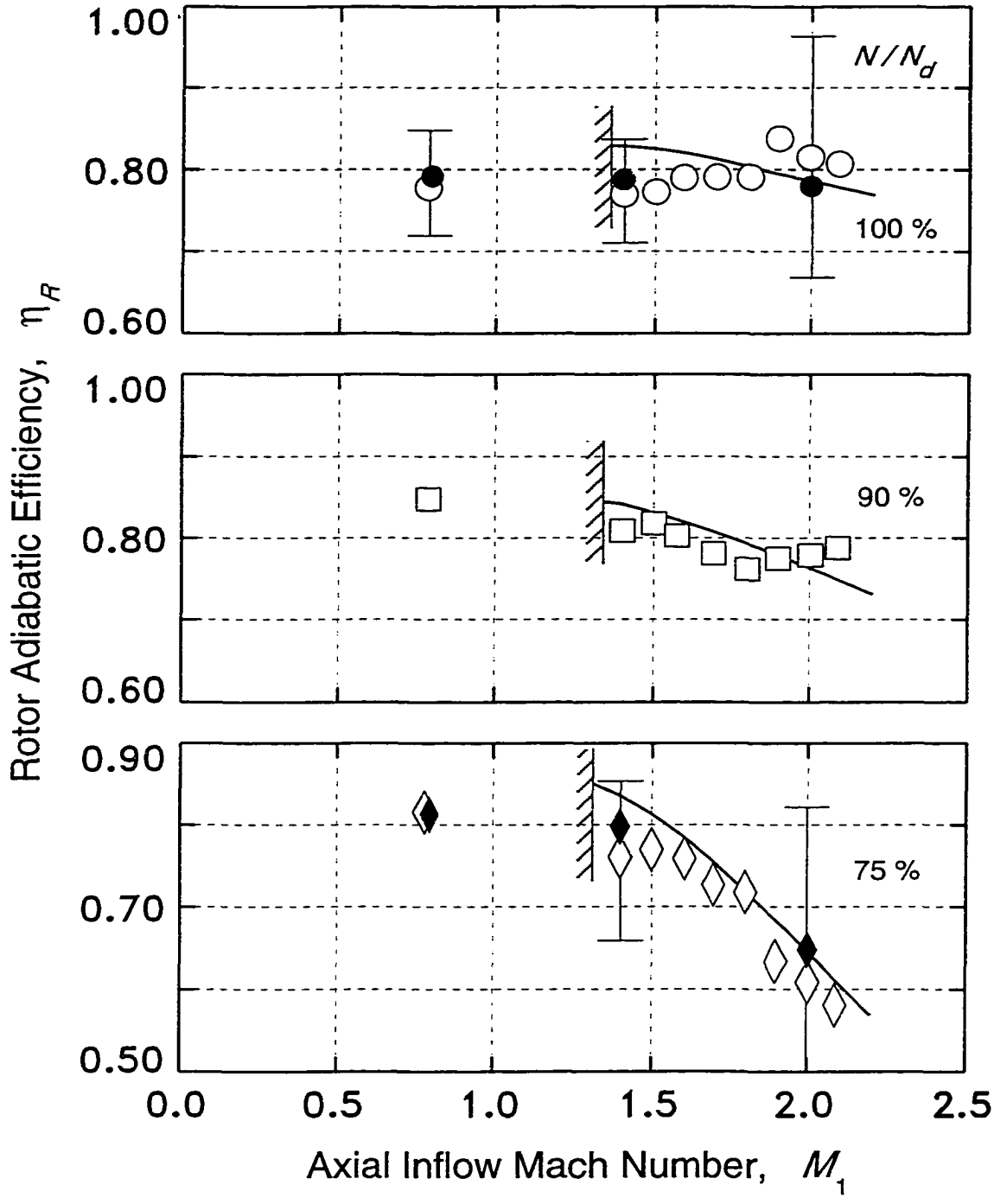

(c) adiabatic efficiency

Figure 5.71 (continued)

Using the experimental data at the three rake-element locations, approximate rotor exit deviation angles were calculated using Equations (5.27) to (5.29). Note that it was necessary to re-formulate Equations (5.28) and (5.29) to solve for the exit flow angle β_2 as a function of the rotor total-temperature ratio and the absolute Mach number at the rotor exit. The difference between the exit flow angle (at the rake location) and the blade exit angle κ_2 is the deviation angle δ_2:

$$\delta_2 = \beta_2 - \kappa_2 \tag{5.31}$$

The resulting experimental-based deviation angles for the near-hub (16.7 percent height), mid (50.0 percent height), and near-tip (83.3 percent height) spanwise locations are graphed in Figure 5.72 for supersonic throughflow operation at the three rotational speeds of 75, 90, and 100 percent design speed. As can be seen, the deviation angles are always negative (or zero). The abscissa in the graph is relative inflow Mach number, which was chosen in an effort to correlate the deviation angles.

The angles graphed in Figure 5.72 correlate reasonably well with relative inflow Mach number for a particular spanwise location, so that a fairly successful empirical-fit has been achieved for purposes of calculating the baseline rotor work input (total-temperature ratio) over the wide range of supersonic throughflow conditions. Unfortunately, no fundamental and physically meaningful relationship was found to generally model the deviation, as for example was done with the total-pressure loss coefficient (see Appendix E). The empirical model correlates the deviation angle as a function of the relative inflow Mach number M_1' and the spanwise location R:

$$\delta_2 = -0.5 + (1.6R - 8.6)\ [M_1' + 0.2R - 2.2]^{(1.4R + 1.3)} \tag{5.32}$$

where $R = (r - r_{tip}) / (r_{hub} - r_{tip})$ at the rake location. An adjustment term based on suction-surface incidence i_{ss} (for a particular blade element) is subtracted when the incidence is positive:

$$\delta_2 = \delta_2 - 0.33 \max(0, i_{ss}) \tag{5.33}$$

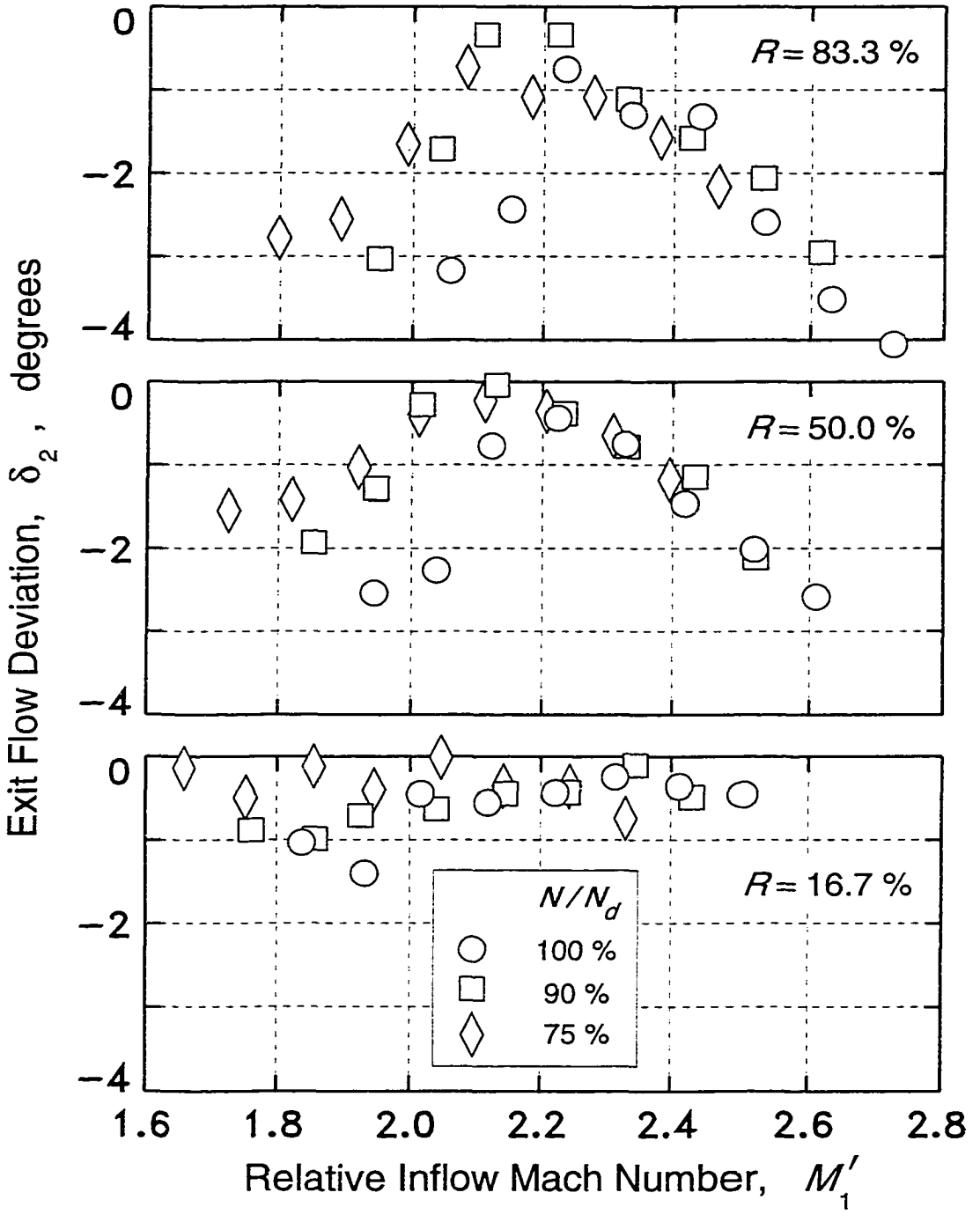

Figure 5.72 Rotor exit flow deviation angles based on absolute Mach numbers and total temperatures at the rake location

The success of the correlation is apparent in the total temperature performance map in part (b) of Figure 5.71. The curves in that figure are practically a direct consequence of the deviation angle correlation as it was incorporated into the off-design performance code. Notice how well the total-temperature ratios from the off-design calculations reproduce the experimental values [34]. The primary usefulness of the deviation-angle correlation, however, is that it eliminates total-temperature ratio (rotor work input) as a consideration when comparing the measured and calculated total-pressure ratios and adiabatic efficiencies; that is, the differences in the experimental and calculated total-pressure ratios and adiabatic efficiencies in Figure 5.71 are due solely to differences in the experimental and analytically modeled total-pressure losses. Good agreement in terms of the overall total-pressure ratios can thus be interpreted as at least a partial verification of the loss model (see Appendix E).

The performance of the rotor at 100 and 75 percent of design rotational speed is now examined in some detail, with an emphasis on the total-pressure losses. Total pressure ratio and adiabatic efficiency results for the rotor at these two speeds are shown in Figure 5.73, which repeats many of the data in Figure 5.71, but with some additional information. In regard to Figure 5.73, a few comments about the analytical loss model are relevant. First, as described in Appendix E, the loss model is formulated in a manner which is consistent with momentum conservation, and as such yields loss and performance predictions which correspond closely to complete mixing-out of the rotor exit flow, especially the wakes (see Appendix C). The experimental and computational flow fields, on the other hand, still contain well-defined wakes at the rake location, such that the flow is characterized to a significant degree by non-axisymmetry. It is therefore expected that the loss model predictions be somewhat high in total-pressure loss, corresponding to somewhat low rotor total-pressure ratios, when compared to the CFD and experimental results. The magnitude of this difference has been estimated by using the three-dimen-

---

[34] An attempt was made initially to apply the off-design code to the SSTF by assuming constant deviation angles and using the design-point values. The constant-deviation rules, however, did not provide total-temperature ratios which adequately matched the experimental data.

sional viscous CFD flow field solution at the design-point condition. Taking into consideration the average loss coefficients at several spanwise locations, an approximate factor for reducing the mixed-out (momentum based) total-pressure loss coefficient to a corresponding entropy-based loss coefficient at the rake location was determined:

$$ {}^{s}\overline{\omega}_{R} \approx 0.90 \; ({}^{m}\overline{\omega}_{R}) \tag{5.34} $$

The dash-dotted lines in Figure 5.73 reflect the adjustment of Equation (5.34), whereas the solid lines do not. As can be seen, the adjustment is significant even though the rake location is relatively far downstream of the rotor (more than one rotor-blade chord), but no clear improvement in the comparison with the experimental and CFD results is gained by it. In any case the agreement between the experimental, computational, and analytical results is considered to be good in view of the experimental uncertainty levels.

Direct comparisons can be made in Figure 5.73 between the CFD and off-design-code results, as long as similar types of data are compared. For example the solid curves should be compared with the momentum-average CFD results (solid filled symbols), and the dot-dashed curves should be compared with the energy-average CFD results (shaded symbols). In all four cases where this can be done, the total-pressure ratios are somewhat over-predicted by the off-design code, implying that the loss-model tends to under-predict the total-pressure losses as compared to the three-dimensional viscous CFD. This tendency *might* be attributed partly to the two-dimensionality of the loss model, which neglects any secondary flow effects as well as the frictional losses at the hub and casing endwalls. Another significant observation can also be made regarding the four cases. Notice that the *difference* between the momentum- and entropy-average CFD results at each operating point is the same as the corresponding difference between the solid and dot-dashed curves. Apparently Equation (5.34) is valid over the entire operating range shown in Figure 5.73.

The general capability of the total-pressure loss model to allow reasonable predictions of the rotor performance leads to perhaps the most useful application of the model to the baseline rotor; namely, good first-order estimates can be made for the relative (and absolute) magnitudes of the various total-pressure loss sources within the rotor. It is these losses which cumulatively determine the rotor aerodynamic (adiabatic) efficiency. Since

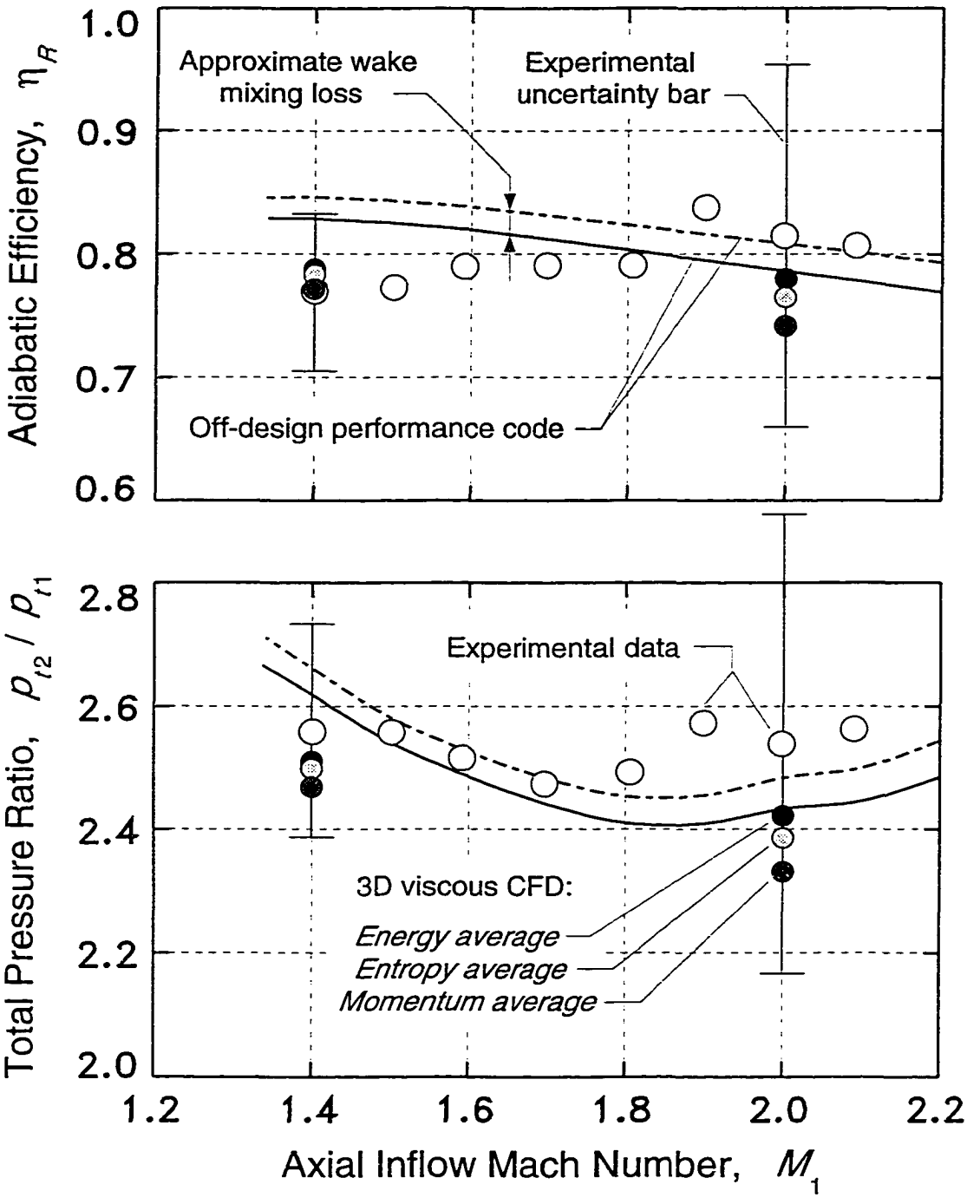

(a) 100 percent of design rotational speed

Figure 5.73 Rotor performance for supersonic throughflow operation at 100 and 75 percent of design rotational speed

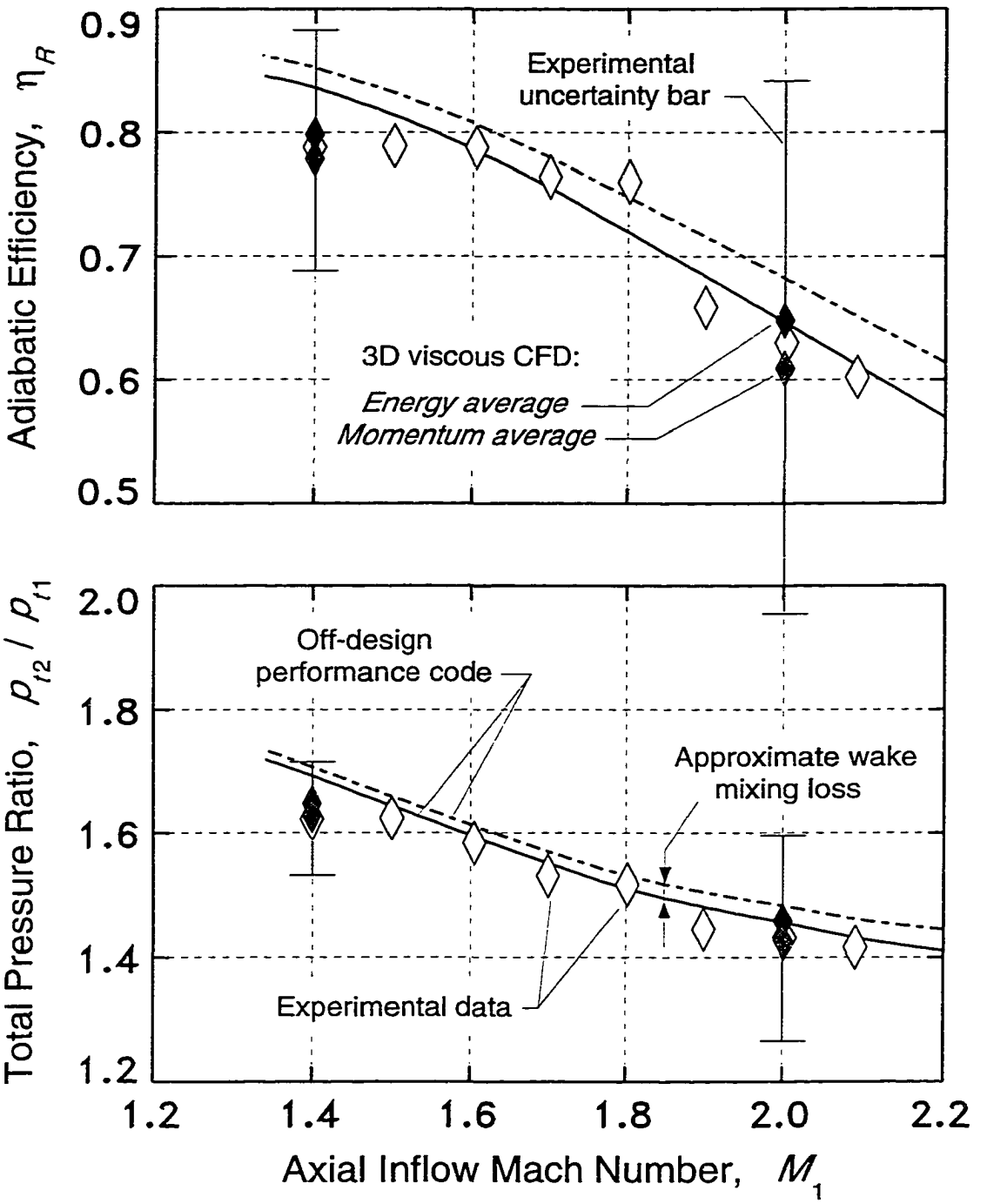

(a) 75 percent of design rotational speed

Figure 5.73 (continued)

the rotor pitchline losses represent fairly well the rotor losses in general, the modeled pitchline losses are shown in Figure 5.74 for the 75, 90, and 100 percent rotational speed off-design curves of Figure 5.71. The break-down of the total loss at each point into the three major loss source components (skin-friction, bow-shock, and oblique-shock) is also shown. Based on these results it is clear that any large gains in the overall rotor performance must be made by reducing either the skin-friction losses, the bow-shock losses, or both. Some ideas and concepts are being considered in order to accomplish this, but it is beyond the scope of this dissertation to discuss them. More will be said about the bow shock losses (at the design point) in the next subsection, however.

Design-point performance and aerodynamics

The aerodynamics and performance of the rotor at its design operating point are of special interest since it is there that an assessment of the aerodynamic design system and the associated design methodologies can be made. This is especially important in the case of the baseline supersonic throughflow fan and rotor since no empirical data base was accessed or available at the time of the design. In terms of the overall aerodynamic performance, much of the above discussion applies to the design point, and in fact many design-point results were presented. In this subsection, however, the experimental, CFD, and analytical results will be examined in more detail.

Spanwise distributions of several different flow quantities at the downstream rake location are compared in Figures 5.75 through 5.78. Note that Pitot-pressure distributions (see Figure 5.75) are also shown because Pitot pressure is a direct measurement in the supersonic flow, whereas total pressure is not. In general, the agreement between the three-dimensional viscous CFD [35] and the experimental results [36] is very good, lending much credibility to the CFD as a tool for predicting absolute levels of performance for this type of blade row. The design distributions for each quantity are also indicated on several of the graphs, although it should be noted that they strictly apply to the trailing-edge location of the rotor. As is apparent, the experimental rotor performs reasonably close to the

---

[35] *Energy-average* in the circumferential direction (see Appendix C).

[36] The uncertainty bars, like those for the overall results, represent a one-percent of full-scale uncertainty in the primary measurement quantities (see Appendix B).

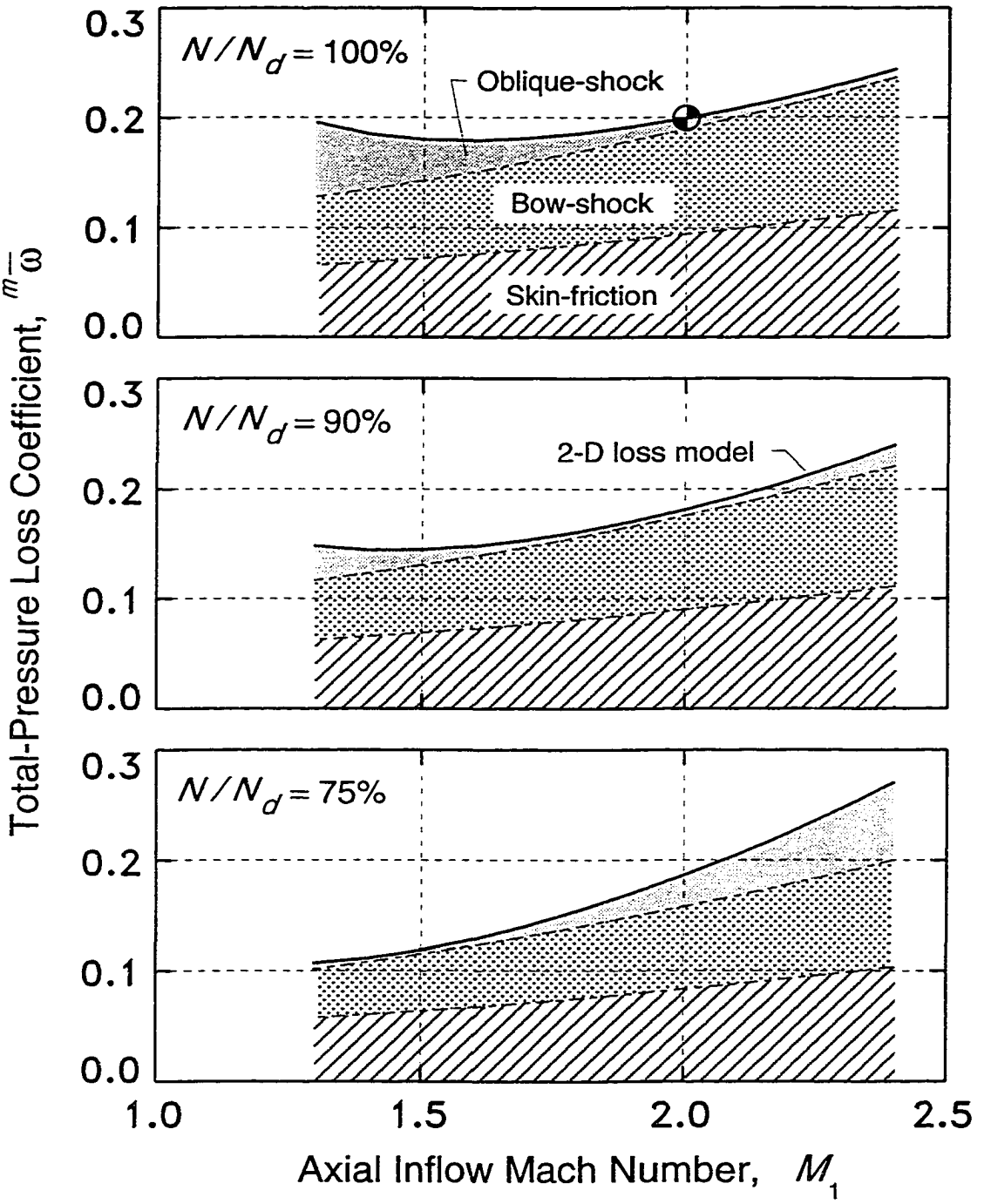

Figure 5.74 Rotor pitchline total-pressure losses for supersonic throughflow operation; losses based on analytical loss model

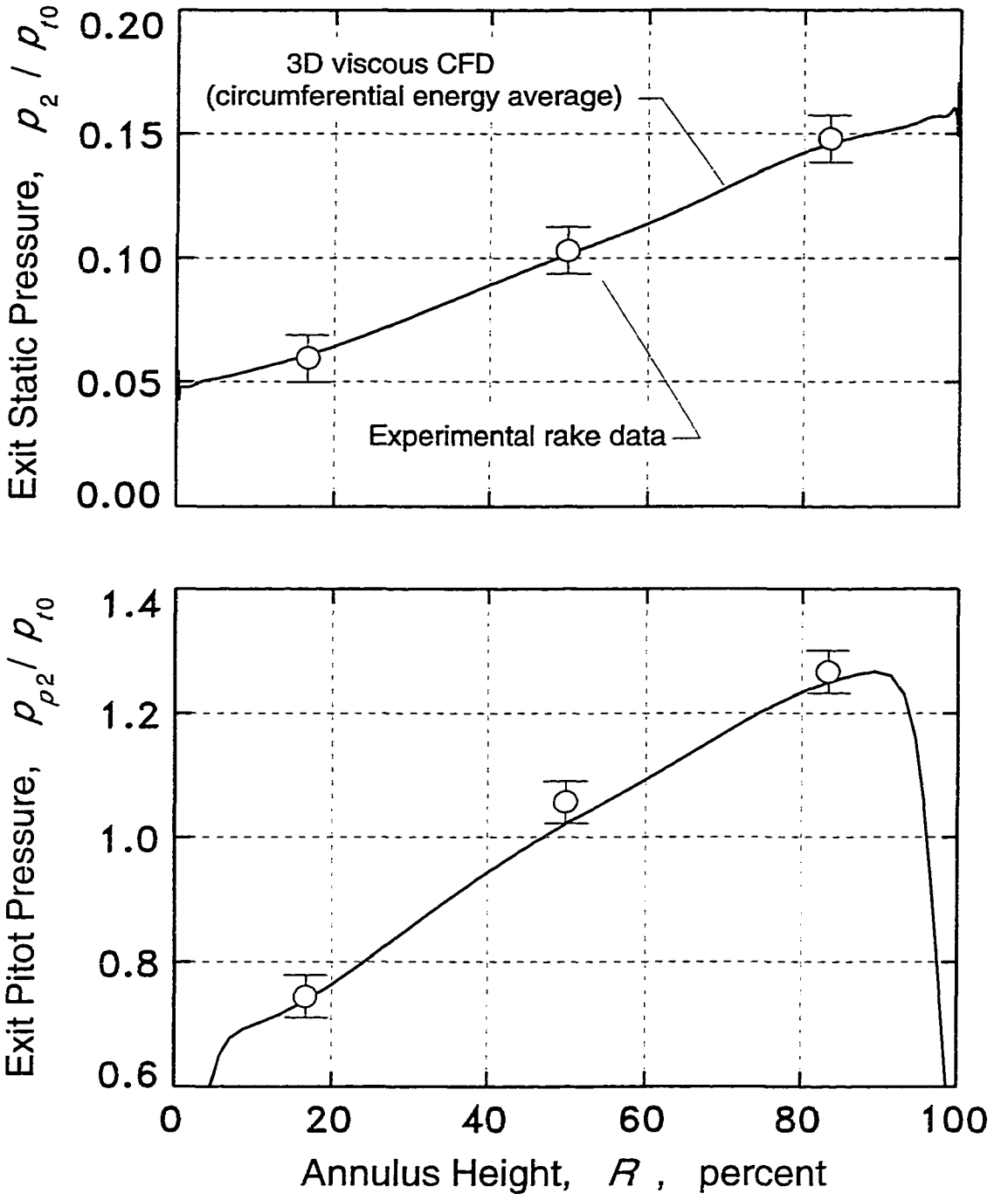

Figure 5.75 Computed and measured spanwise distributions of static and Pitot pressures at the downstream rake location; design-point rotor operation

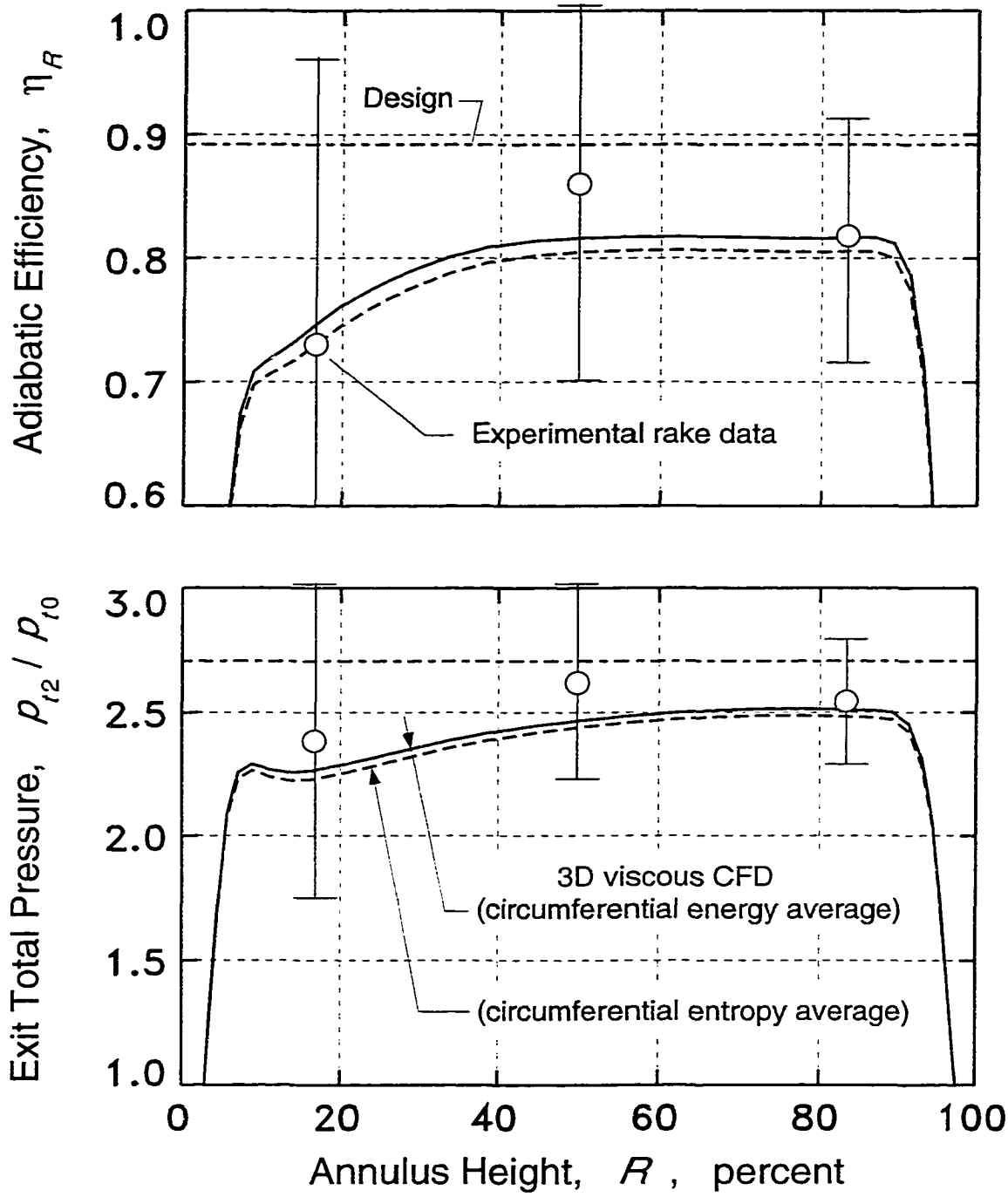

Figure 5.76 Computed and measured spanwise distributions of adiabatic efficiency and total pressure at the downstream rake location; design-point rotor operation

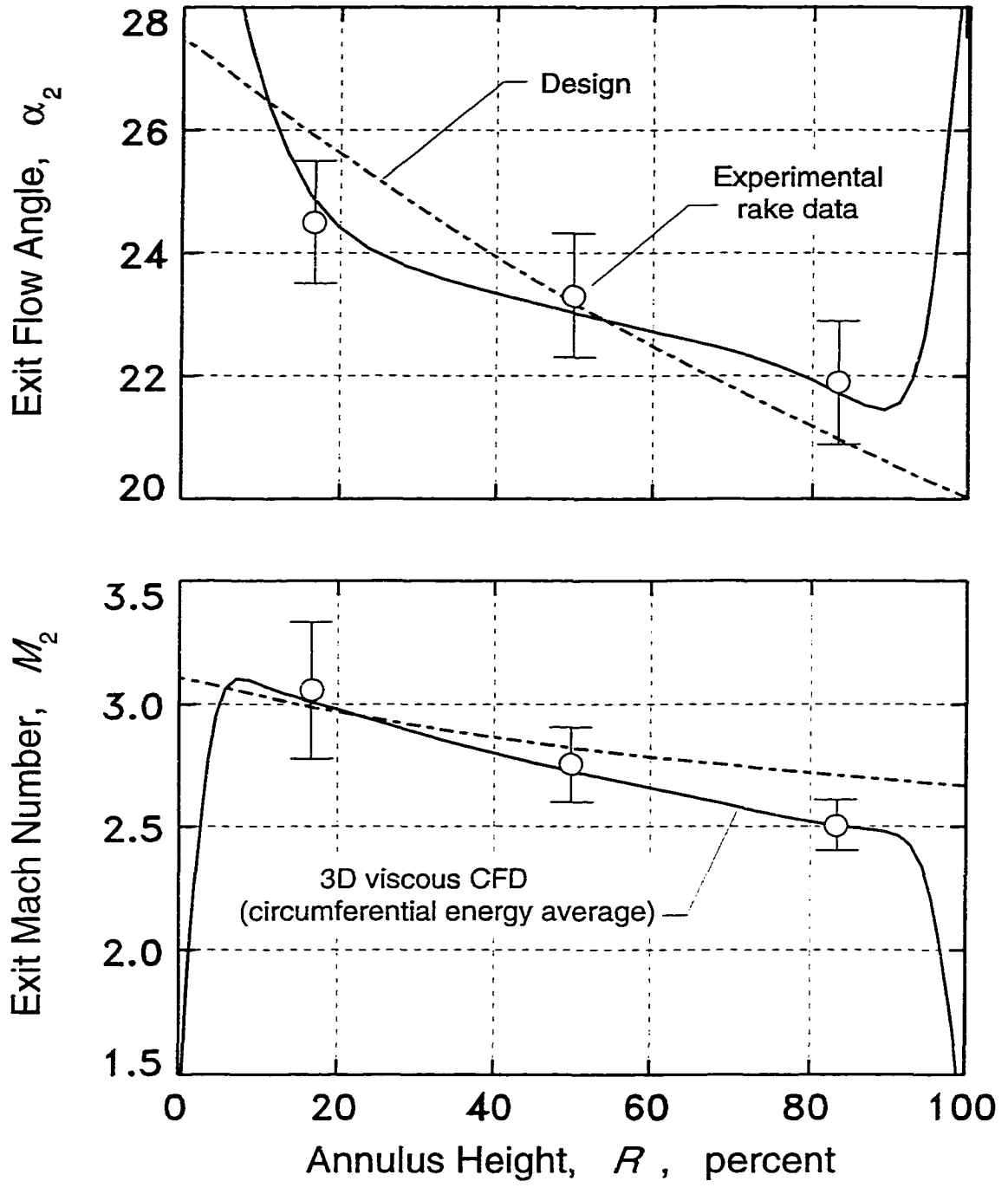

Figure 5.77 Computed and measured spanwise distributions of flow angle and Mach number at the downstream rake location; design-point rotor operation

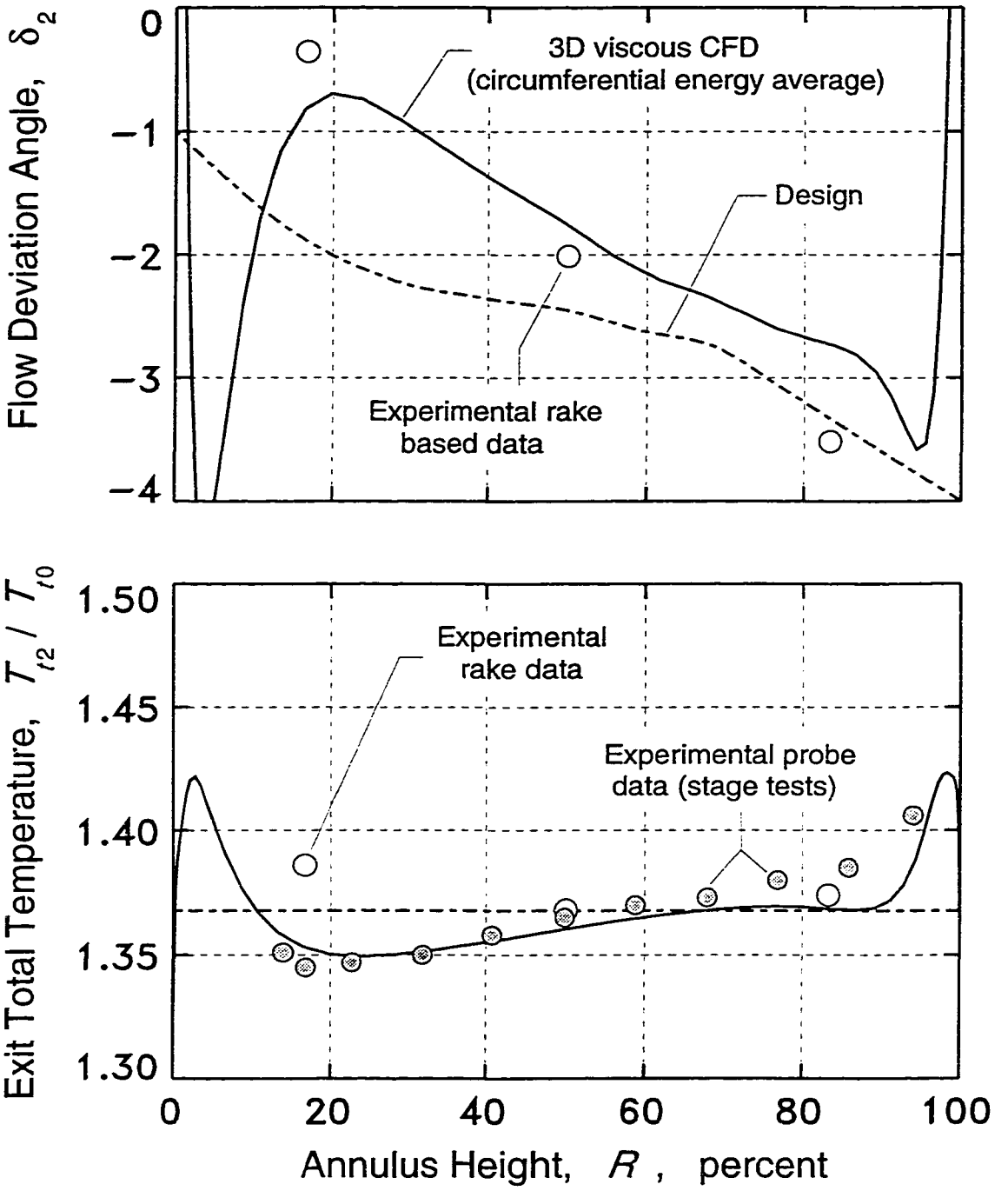

Figure 5.78 Computed and measured spanwise distributions of flow deviation angle and total temperature at the downstream rake location; design-point rotor operation

intended design conditions. In this regard, note especially the total-temperature and deviation-angle distributions [37] (see Figure 5.78).

A Mach number contour plot for the circumferential-average of the three-dimensional viscous CFD flow field is shown in Figure 5.79. This flow field can be considered as an "axisymmetric" representation of the flow, and was determined using the entropy-averaging procedure (see Appendix C). From this flow field, axisymmetric streamlines for mass flow fractions of 20, 50, and 80 percent were calculated, and are compared with the design streamlines in the bottom half of the figure. Note that the design code determined the streamline locations only at the blade leading- and trailing-edge locations, using simple radial-equilibrium, so that the agreement between the design and CFD streamline locations is quite good considering the aerodynamic approximations used in the design method.

Rotor pitchline blade-to-blade and mid-gap hub-to-tip relative Mach number contours computed from the three-dimensional viscous CFD flow field are shown in Figure 5.80. In general, the computed flow field indicates that all oblique passage shock waves are weak, and strong wave reflections from the blade surfaces were avoided in the design, as was intended (see Chapter 2). Corresponding isentropic Mach number distributions along the blade surfaces at the 20, 50, and 80 percent mass flow fraction locations (see Figure 5.79) are also shown in Figure 5.80, in part (b) of the figure. As can be seen, the isentropic Mach number distributions (or similarly, static pressure distributions) "close" fairly well as the trailing edge is approached. Again, this was a design goal, although it might be emphasized that the aerodynamic design was performed using a *two-dimensional* viscous CFD code in the design process. The three-dimensional CFD solution confirms the original assumption that three-dimensional effects would not determine the first-order aerodynamics of the baseline rotor.

Spanwise distributions of the total-pressure loss coefficient for the CFD solution are shown in Figure 5.81. Two graphs are shown. The top graph compares three different loss distributions, corresponding to different types of circumferential-averaging methods,

---

[37] The experimental deviation angles were determined from the exit total temperatures, as discussed in the last subsection. Note that the total temperature from the near-hub rake-element is thought to be erroneous.

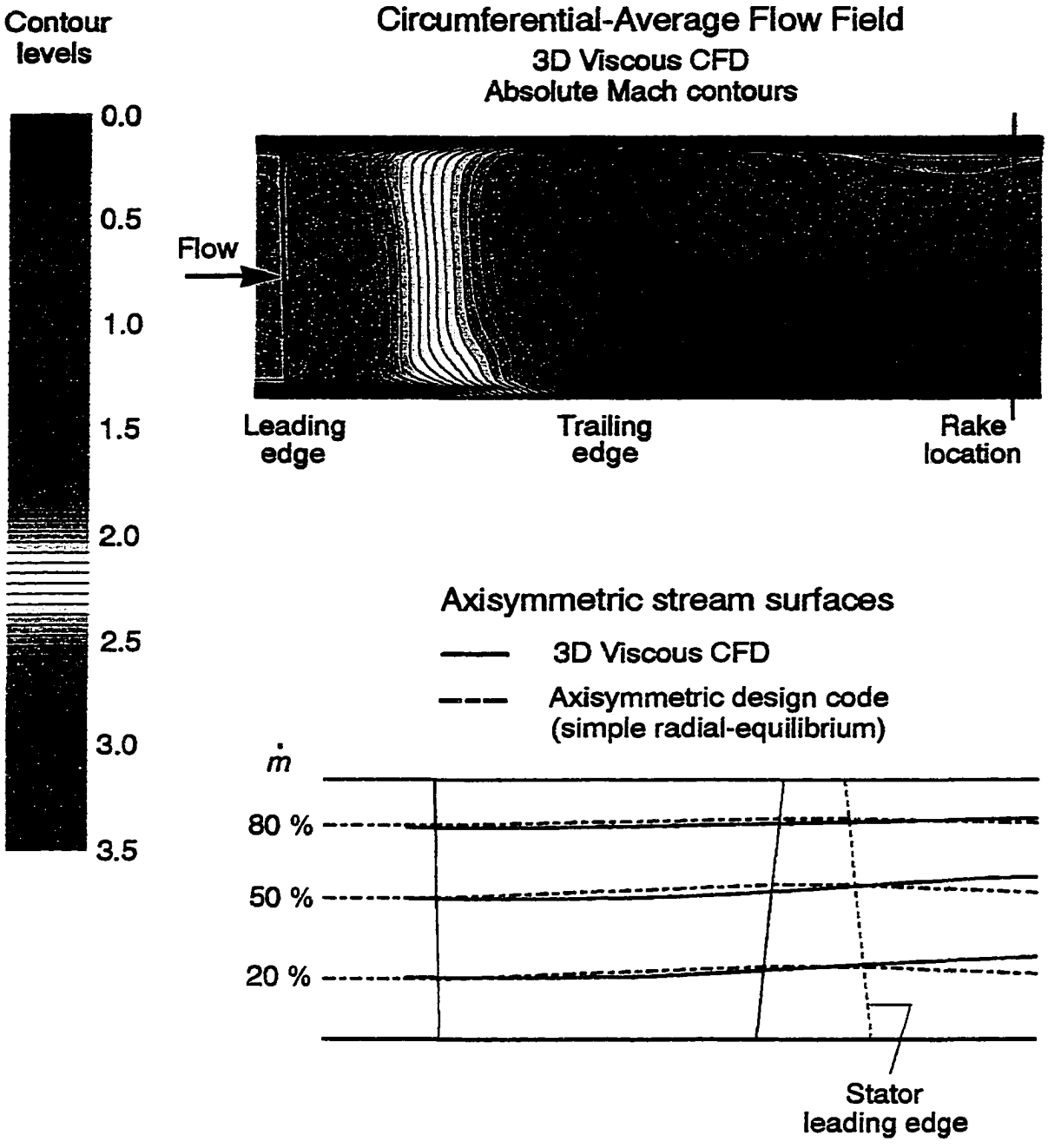

Figure 5.79 Viscous three-dimensional CFD Mach number contours and axisymmetric stream surfaces for the circumferential-average rotor flow field at design conditions

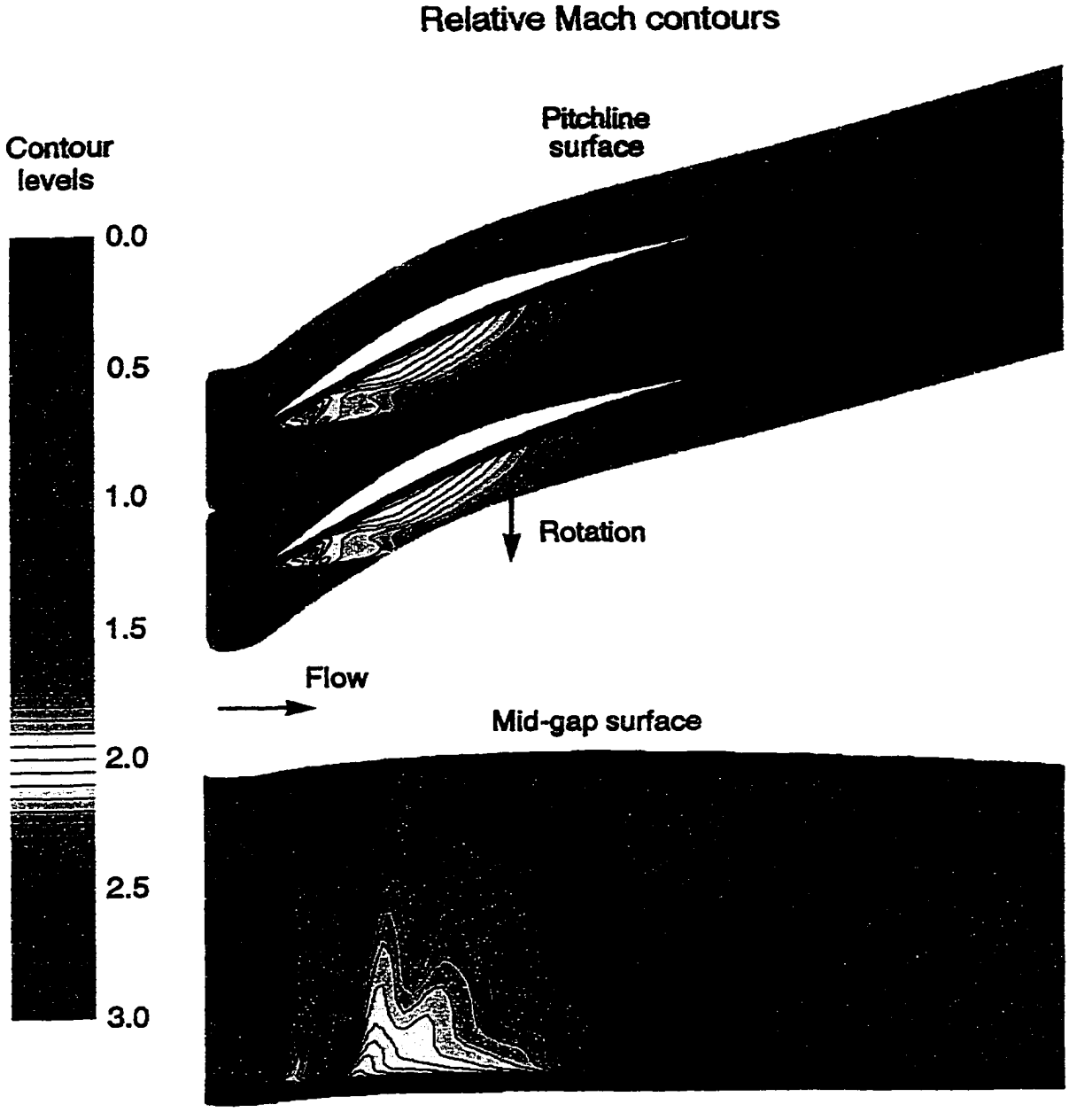

(a) Mach number contours

Figure 5.80 Viscous three-dimensional CFD Mach number contours and blade-surface isentropic Mach number distributions for the rotor at design conditions; contours on pitchline blade-to-blade and mid-gap hub-to-tip surfaces

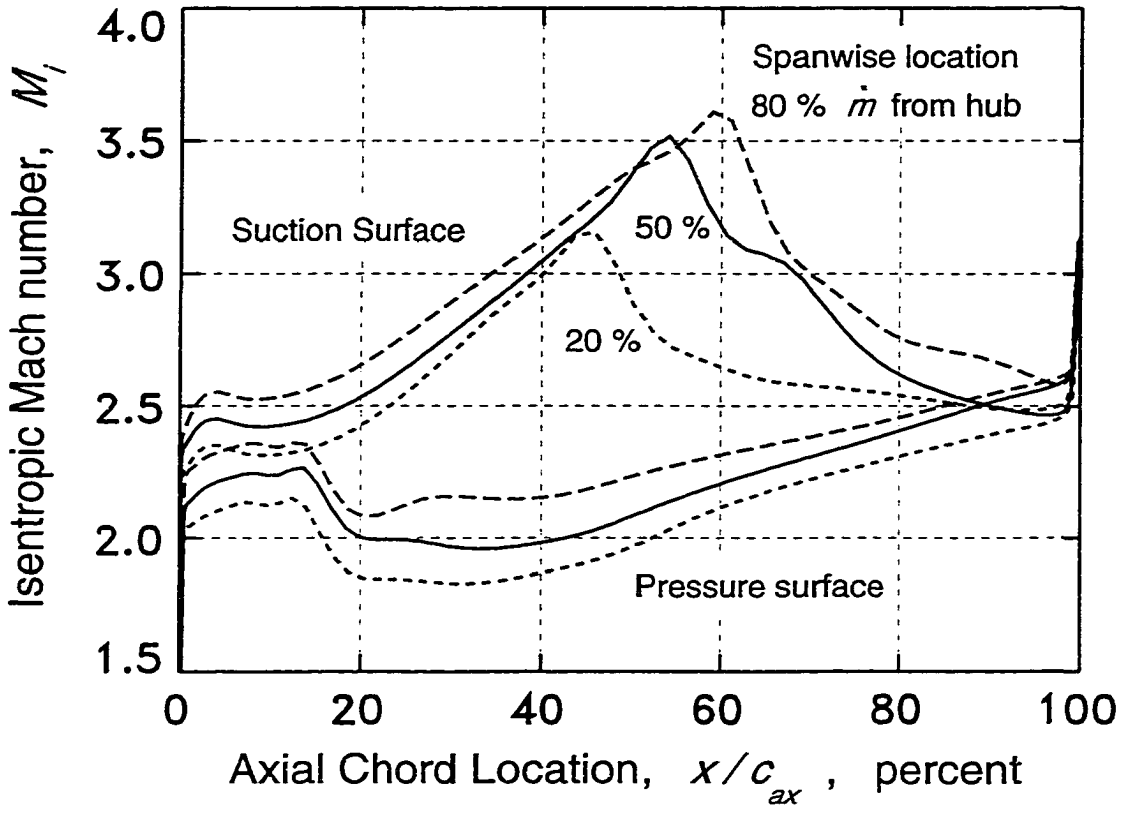

(b) blade-surface isentropic Mach number distributions

Figure 5.80 (continued)

with the design distribution. The bottom graph shows a comparison between total mixed-out (momentum-average) losses from the CFD analysis and losses calculated using the two-dimensional, analytical loss-model (see Appendix E). The loss model also provides a break-down of the total loss into the three major loss-source components, as discussed earlier. Note that the off-design performance analysis code, incorporating the loss model, was used for calculating the analytical losses. In general, the conclusions stated earlier regarding the pitchline loss sources (see Figure 5.74, top graph) can be seen here to apply across much of the span, with the exception of the endwall regions and a substantial portion of the hub region where significant three-dimensional effects are involved. Also, it is

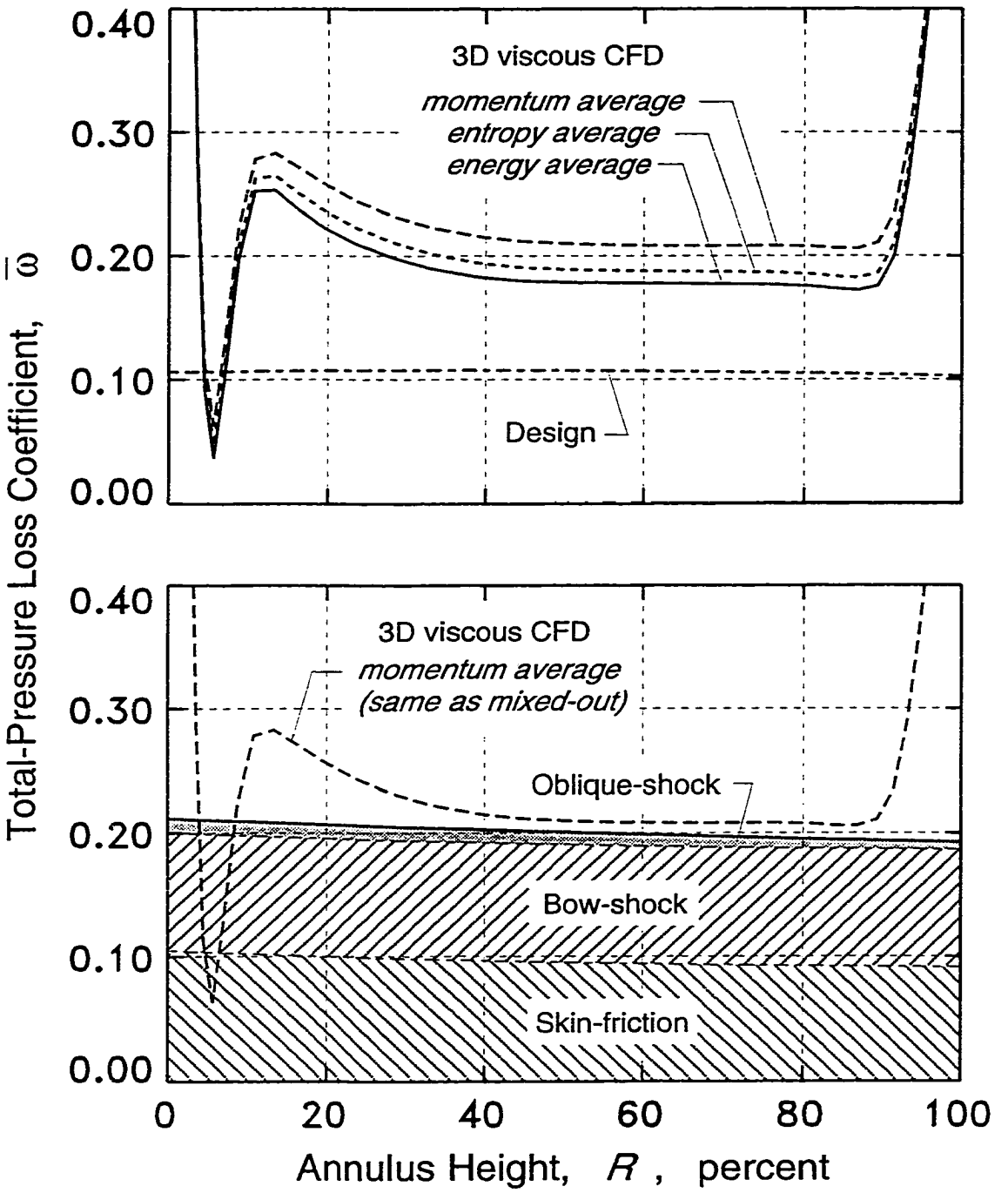

Figure 5.81 Spanwise distributions of total-pressure loss for design-point rotor operation; three-dimensional viscous CFD and analytical loss-model results

apparent that the loss levels assumed in the design of the rotor were too low, leading to a rotor total-pressure ratio less than the design value (see Figure 5.76).

As Figure 5.81 reveals, the bow shock losses are very substantial for the baseline rotor, accounting for up to about 44 percent of the total mixed-out losses at the design point. Some of this bow shock loss is a mixing loss, with the mixing occurring in the blade wakes; that is, the shear flow from the *curved* bow wake is fully intermingled with the shear flow from the blade surface. A more complete quantitative of this can be gained by examining the chordwise development of the total-pressure losses through the blade row. The loss development for the rotor pitchline element is shown in Figure 5.82, where the conditions at the various axial locations were determined from a circumferential-average of the three-dimensional viscous CFD flow field. From this figure, the following approximate loss analysis results [38]: 36 percent bow shock loss, 31 percent skin friction loss, 5 percent oblique shock loss, and 28 percent mixing loss. Around 8 counts of the 28 percent mixing loss can be attributed to the bow shock wave. If the remaining mixing loss is combined with the skin friction loss, then the total skin-friction loss amounts to about 51 percent of the total, which is consistent with the previous figures showing a break-down of the losses into the various components.

The reason the bow shock losses are so large is that the blade leading edges are fairly "blunt", considering the relative inflow Mach number levels at which the rotor blades operate. The pitchline bow shock wave for the three-dimensional CFD flow field is shown in Figure 5.83 in terms of relative Mach number and total-pressure contours. Observe that the total-pressure losses generated by the curved bow wave form a shear layer which convects downstream along the blade surfaces and within which the blade-surface boundary layers develop.

The bow shock loss model of Appendix E provides a simple, explicit formula for estimating the bow shock loss:

$$ {}^{m}\bar{\omega}_{bwv} \approx [1.81 + 3.72\,(M_1' - 1) + 1.08\,(M_1' - 1)^2]\ \frac{r_{le}}{s_0 \cos\beta_1} \qquad (5.35) $$

---

[38] Percentages are based on the total mixed-out loss.

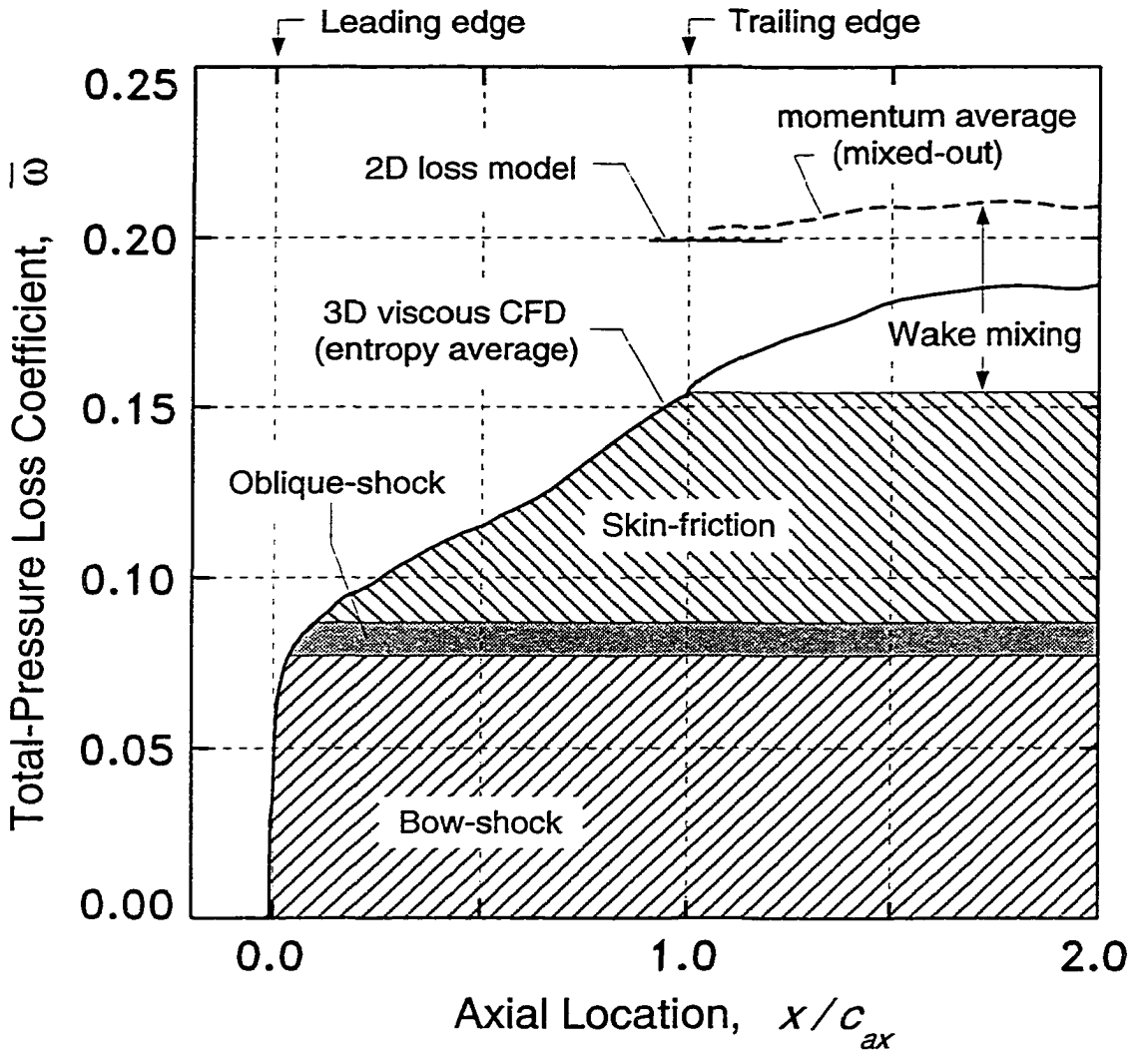

Figure 5.82 Chordwise development of the rotor pitchline total-pressure losses; loss coefficients calculated from three-dimensional viscous CFD flow field

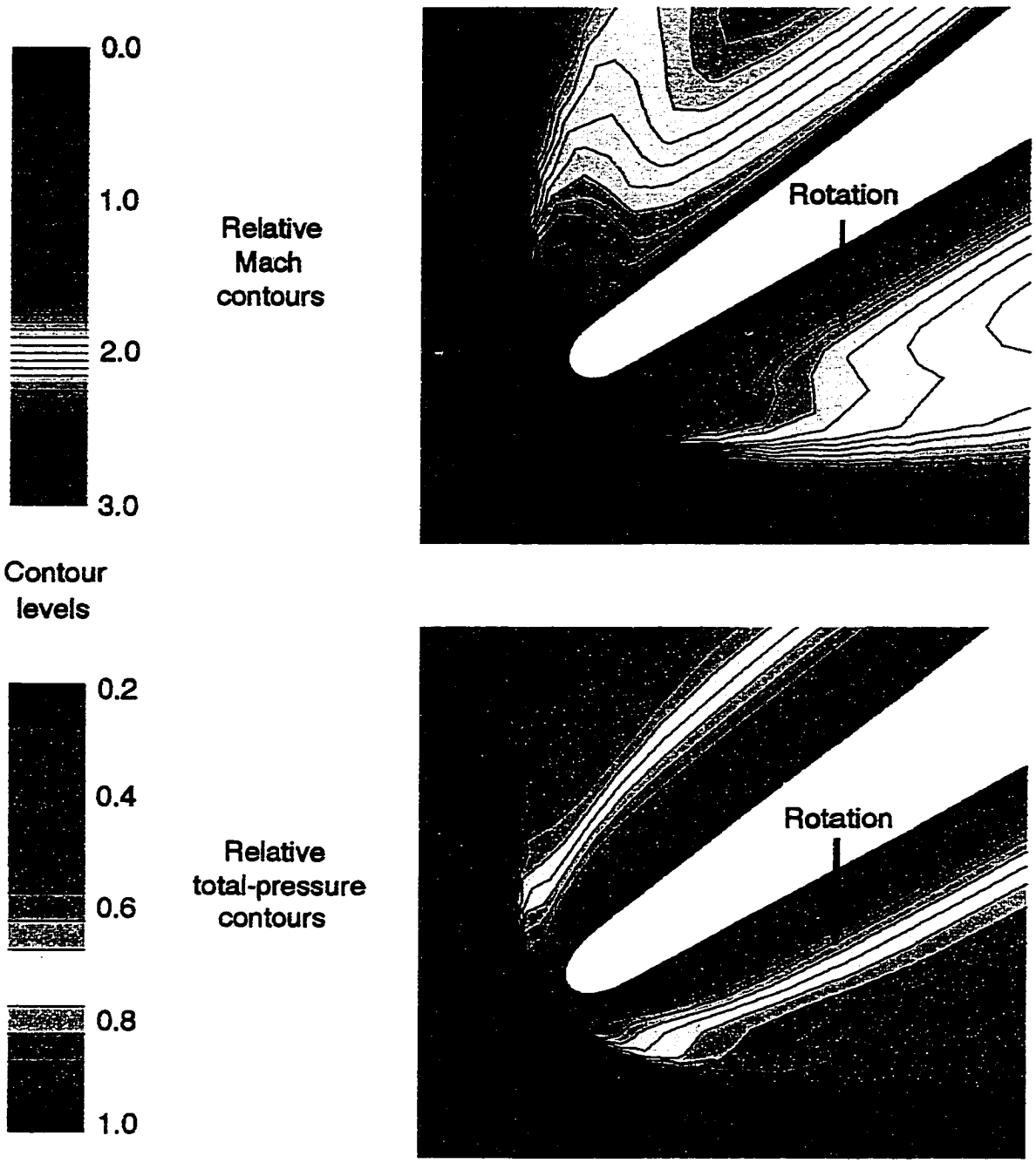

Figure 5.83 Viscous three-dimensional CFD Mach number and total-pressure contours for the rotor pitchline at design conditions; leading-edge bow shock wave region in the relative frame-of-reference

The parameter s_0 is the circumferential blade spacing (gap) between the leading edges, and the parameter r_{le} is an effective leading-edge radius which includes an adjustment for edge-ellipse eccentricity:

$$r_{le} \approx a_{le} \exp\left(-0.18\varepsilon^{0.84}\right) \tag{5.36}$$

where a_{le} is the half-thickness of the leading edge, and the parameter ε is related to the aspect ratio of the edge-ellipse:

$$\varepsilon = \left(\frac{b}{a}\right)_{le} - 1 \tag{5.37}$$

From Equation (5.35), the significant *geometric* parameter determining the bow shock loss is the ratio of effective leading-edge radius to blade-spacing. For a particular relative inflow Mach number, inflow angle, and blade spacing, the relationship between the leading-edge radius and the total-pressure loss is approximately linear, so that first-order estimates of leading-edge radius on loss coefficient are easily obtained once the approximate fractional extent of the bow-shock losses are known. For example, the expected improvement in performance due to using "sharp" leading edges would be to decrease the mixed-out pitchline loss coefficient from about 0.215 to 0.120 (see Figure 5.81), which translates into an improvement in (pitchline) rotor adiabatic efficiency from about 79 percent to near 88 percent. Sharp leading edges are impractical in any real application, but the potential gains in performance associated with sharper edges provides much incentive to reduce the edge thickness, i.e., the effective "edge-bluntness", to the minimum practical limit.

Particle traces of fluid streamlines deep within the viscous regions of the three-dimensional CFD flow field are presented in Figure 5.84, which shows the blade pressure- and suction-surfaces. No significant secondary flows appear in the blade pressure surface boundary layer (blue-violet traces), while conversely, near the blade suction surface the (red and yellow) traces reveal radial flow migrations toward midspan. Note that the yellow traces lie deeper within the boundary layer than do the red traces, but both are well within the boundary layer. Much of the boundary-layer fluid very near the suction surface is migrated from the hub endwall boundary layer, as revealed by the green particle traces in Figure 5.84. A more comprehensive view of the hub endwall and suction-surface sec-

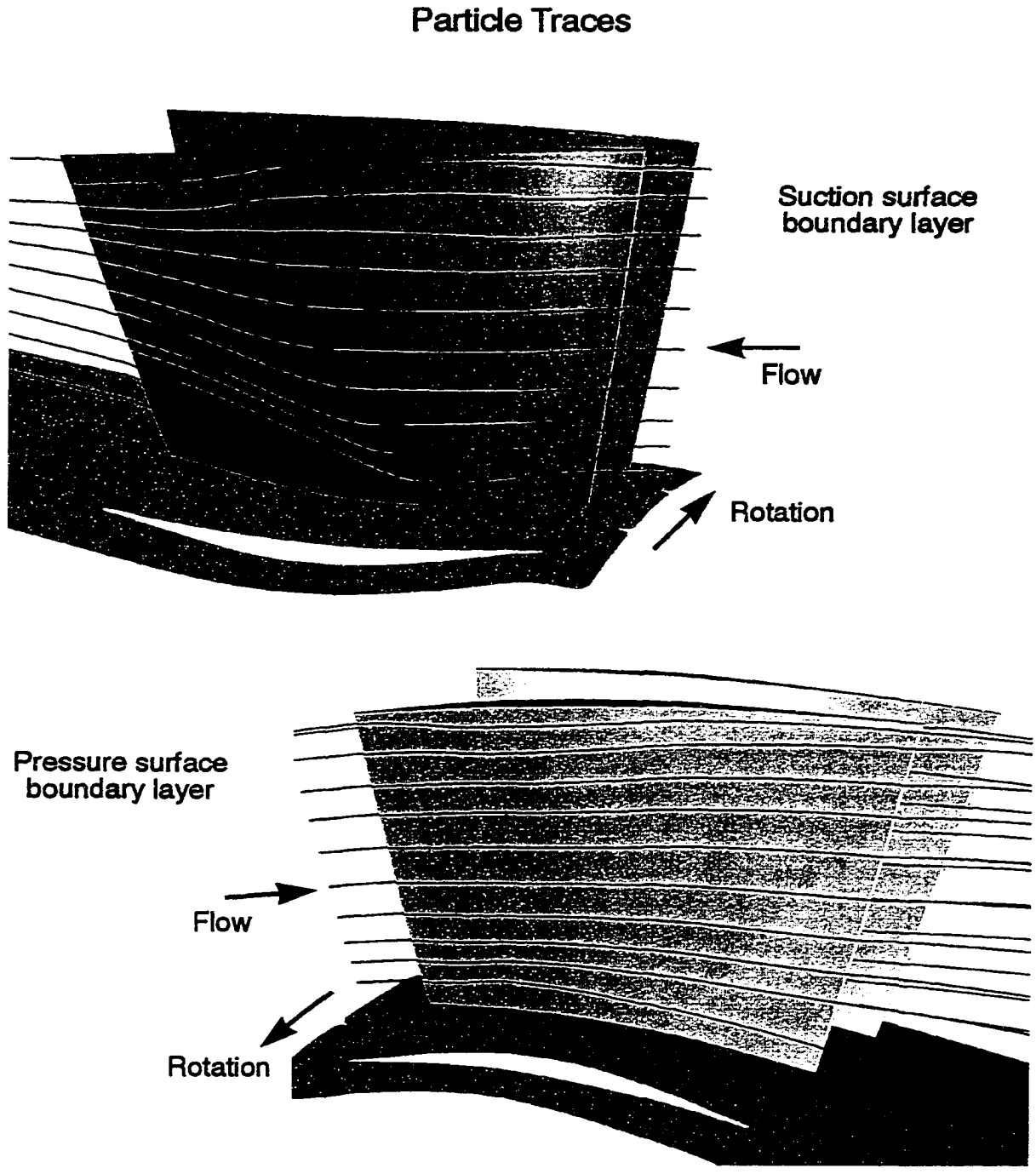

Figure 5.84 Viscous three-dimensional CFD particle traces for the rotor at design conditions; traces showing blade and hub surface boundary-layer streamlines

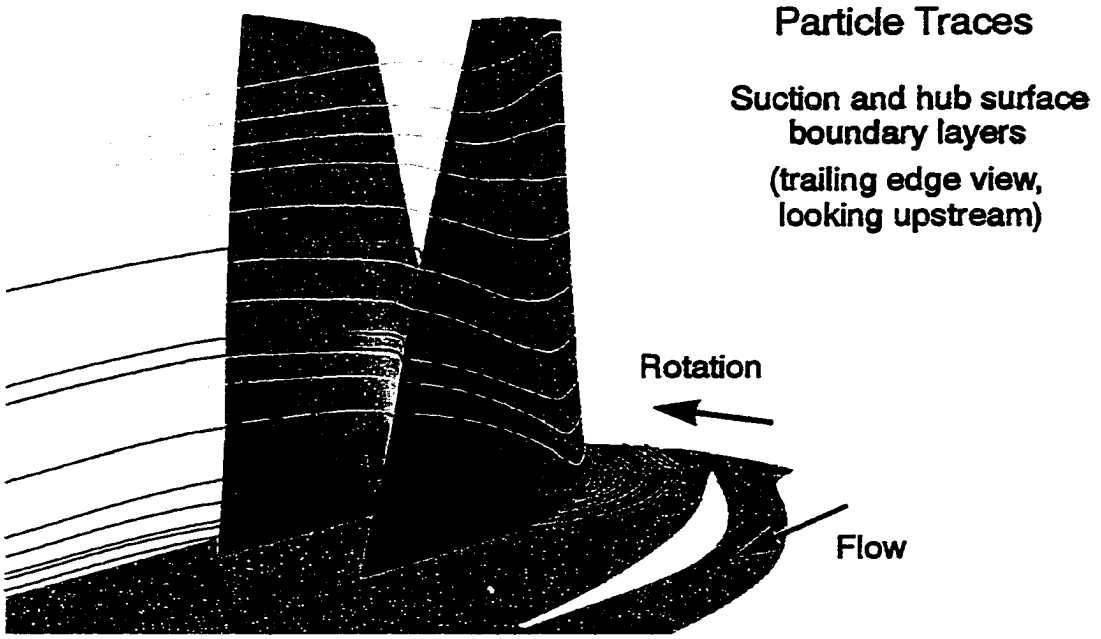

Figure 5.84 (continued)

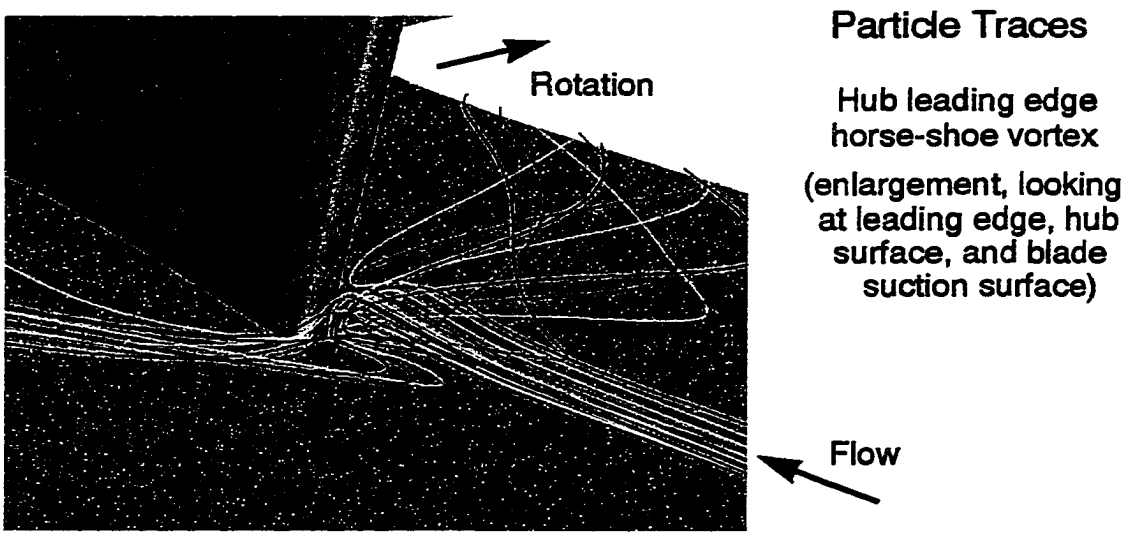

Figure 5.85 Viscous three-dimensional CFD particle traces for the rotor at design conditions; traces showing the hub leading edge horse-shoe vortex and the downstream migration of the vortex particles

Particle Traces

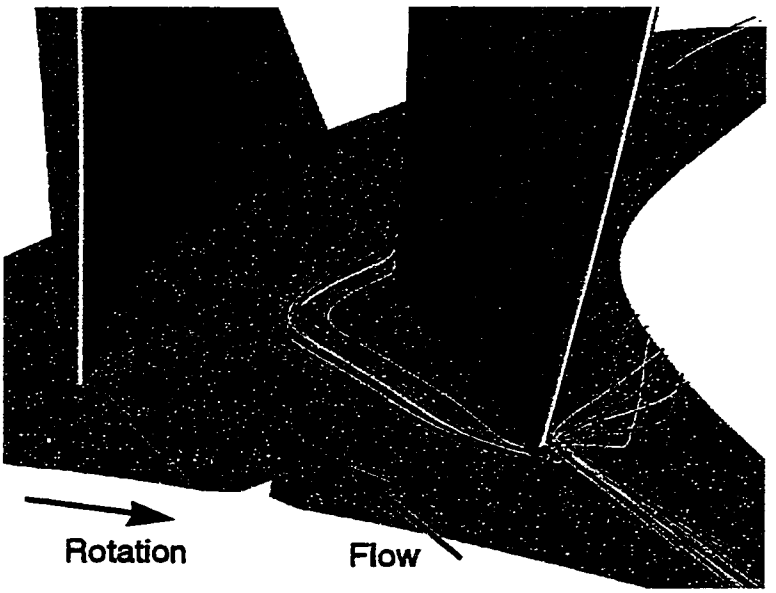

Hub leading edge horse-shoe vorticies and the downstream migration of the vortex particles

(leading edge view, looking downstream)

Downstream migration of the hub leading edge vortex particles

(trailing edge view, looking upstream)

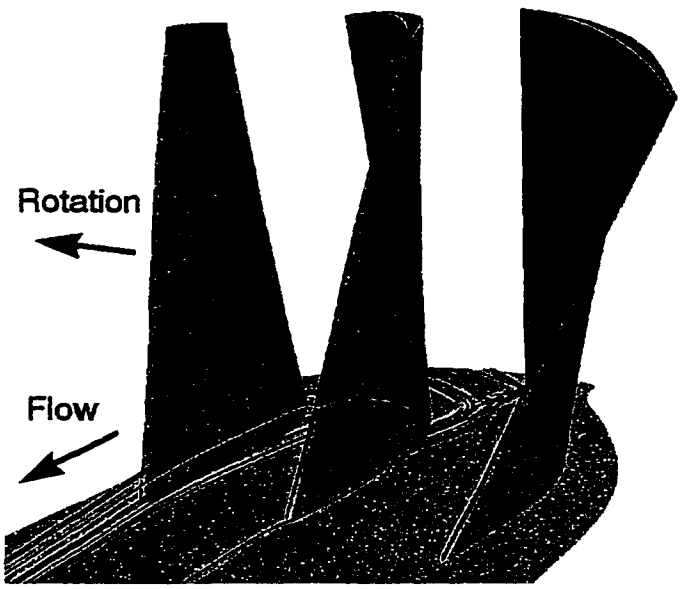

Figure 5.85 (continued)

ondary flow can be seen in Figure 5.85, which shows particle traces through the hub leading edge horse-shoe vortex, and the subsequent migration of those particles downstream. As can be seen, the fluid from the horse-shoe vortex composes part of the boundary-layer fluid transported from pressure to suction surface along the hub endwall, and then up the aft part of the blade suction surface. Notice, however, that the vortex itself does not appear to persist for any significant distance away from the leading edge. Finally, in Figure 5.86, particle traces through the rotor tip clearance gap are shown. These traces reveal that only minor aerodynamic effects are associated with the tip clearance flow, at least according to the CFD simulation.

It should be emphasized that the above secondary-flow migrations are fairly close to the bounding surfaces. Nevertheless, the secondary flow on the hubward, aft part of the suction surface involves the transport of a significant amount of low-momentum fluid. This fluid migration is large enough to influence the spanwise distribution of total-pressure loss, as will be presented below. First, however, a general explanation for the existence of the secondary flow is given since it can be understood within the context of classical fluid dynamics.

Blade surface pressures on the suction and pressure sides of the blade are shown as static pressure contours in Figure 5.87. On both surfaces the more densely clustered contours lines indicate shock impingement locations, as can be seen by comparison with pitchline and near-hub blade-to-blade contour plots of static pressure, shown in Figure 5.88. Since secondary flows are of interest, the key features to notice are static pressure gradients near the wall, and particularly those gradients which are skewed relative to the primary flow direction. It is these gradients which tend to drive the lower-momentum viscous flows from regions of higher to regions of lower static pressures, in directions along the surface but transverse to the main flow direction (typically in the radial direction). Such gradients exist on the blade suction surface at the shock impingement locations where the spanwise-running shock is axially swept [39]. On the hubward side of the suction surface the shock is swept axially-back from hub to midspan, driving a secondary flow

---

[39] Notice the lack of any shock sweep (skew) on the pressure surface. The shock intersects the pressure surface at about 15 percent chord and is oriented virtually normal to the axial direction.

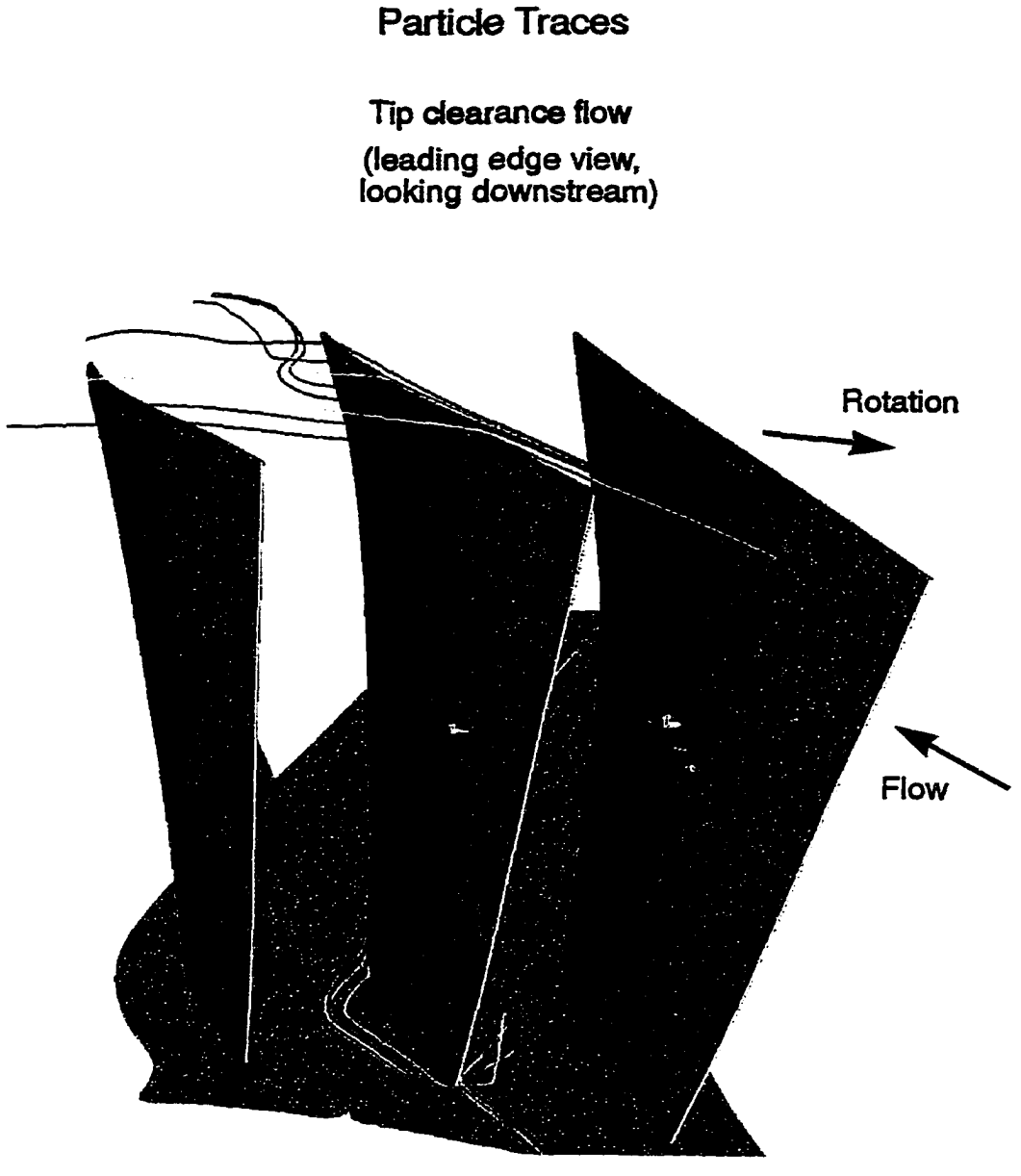

Figure 5.86 Viscous three-dimensional CFD particle traces for the rotor at design conditions; traces showning the rotor tip clearance flow

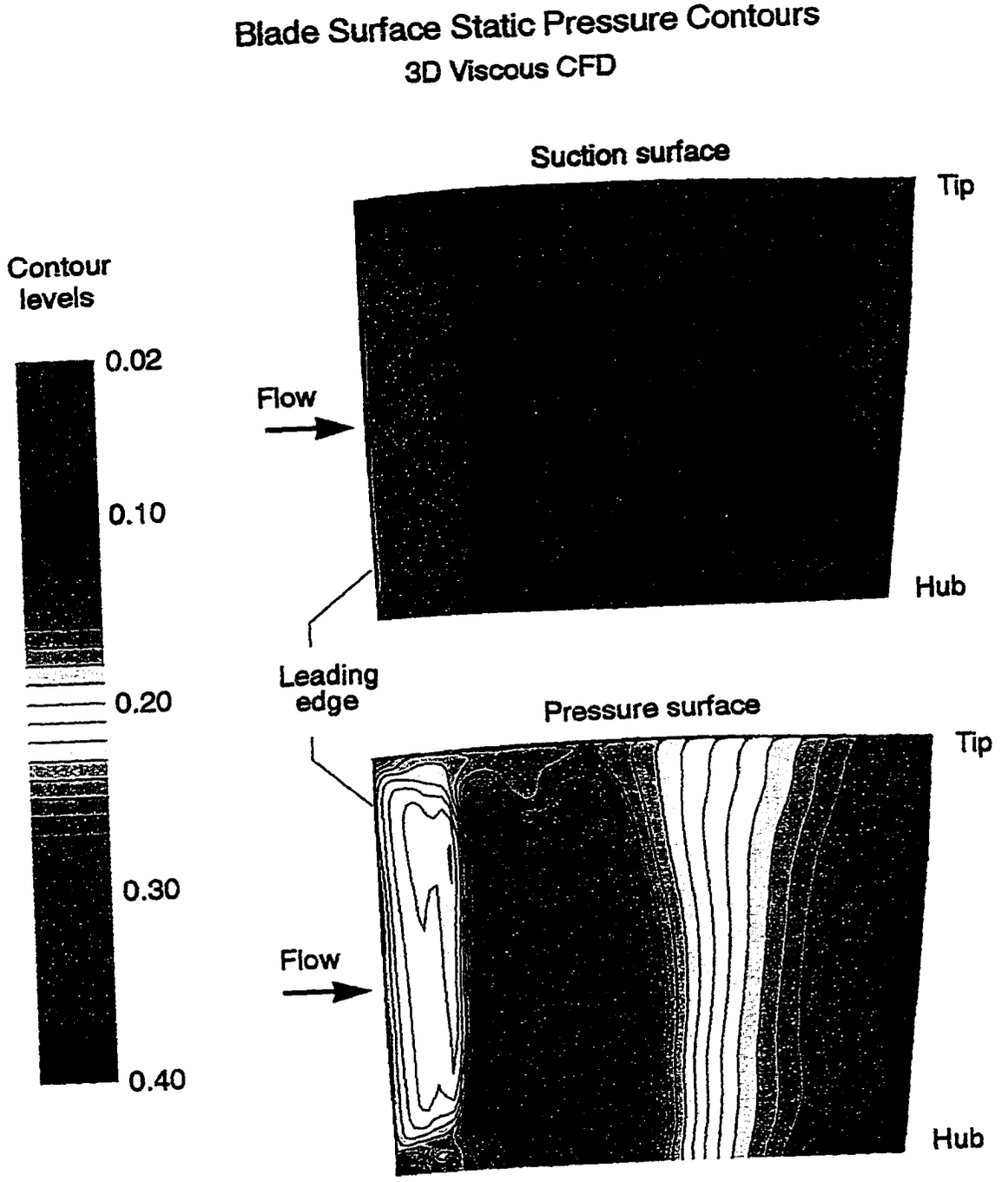

Figure 5.87 Viscous three-dimensional CFD static-pressure contours (dimensionless) for the rotor blade surfaces at design conditions

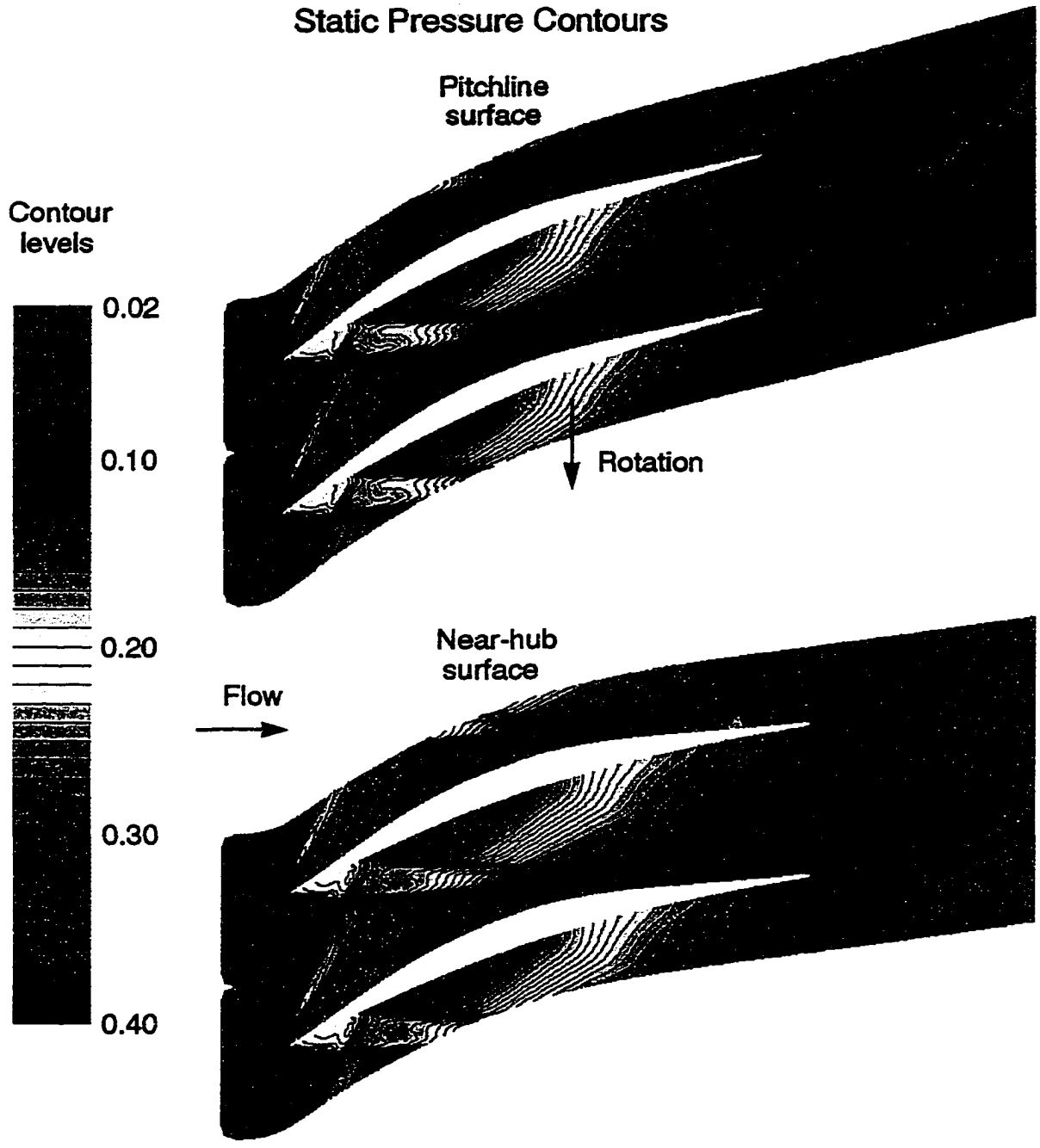

Figure 5.88 Viscous three-dimensional CFD static-pressure contours (dimensionless) for the rotor at design conditions; blade-to-blade distributions at pitchline and near-hub locations (50 and 20 percent mass flow fractions)

toward midspan. Notice in Figure 5.84 that the (red and yellow) particle traces are more-or-less aligned with the primary flow direction until reaching the shock-impingement location, at which point they are bent radially outward, i.e., fluid particles are deflected toward larger radii. Near the tip the opposite trend is observed because the shock is swept axially-back from tip to midspan, causing a mild secondary flow migration toward midspan. Again, the upstream boundary-layer flow is aligned more-or-less with the primary flow until encountering the swept shock.

Another, perhaps simpler, way to consider the secondary flow is to realize that the blade suction surface induces a low-pressure region, especially around mid-chord. The endwall flows are drawn into this low pressure region in the classical pressure-to-suction surface endwall flow migration associated with secondary flows in turbomachine blade rows. Thus some of the low-momentum fluid which ends up in the blade wakes originates from the endwalls, as clearly seen for example in Figures 5.84 and 5.85. A cross-channel contour plot showing radial flow velocity magnitudes near the trailing-edge plane, at the 95 percent axial-chord location, is shown in Figure 5.89. Corresponding velocity vectors near the hub are also included in the figure. In general, the primary flow has a small positive (outward) radial velocity component due to the effects of flow swirl (see also the streamlines in Figure 5.79). Close to the blade suction surface (*SS*), however, the boundary-layer flow can be seen to have a considerably larger radial velocity component over much of the span, and especially near the hub where the peak magnitudes are encountered. The velocity vectors in the figure provide further details about this secondary flow, showing directly the secondary-flow directions. In the tip region near the suction surface, a negative (inward) radial flow can be observed, but the radial velocity magnitudes indicate a much weaker secondary flow than at the hub. This result was also indicated in Figure 5.84 by the (red and yellow) particle traces since near the blade tip only small radial migrations are observed.

A simple cross-channel sketch depicting generalized secondary-flow directions is shown in Figure 5.90. From this sketch it can be explained, qualitatively, why the secondary flows in the tip region are weaker than those in the hub region. The explanation is brief. The relative motion of the casing, and even the tip clearance flow, counter-act the basic pressure-surface (*PS*) to suction-surface (*SS*) endwall flow migration; that is, there are opposing secondary-flow influences in the tip region.

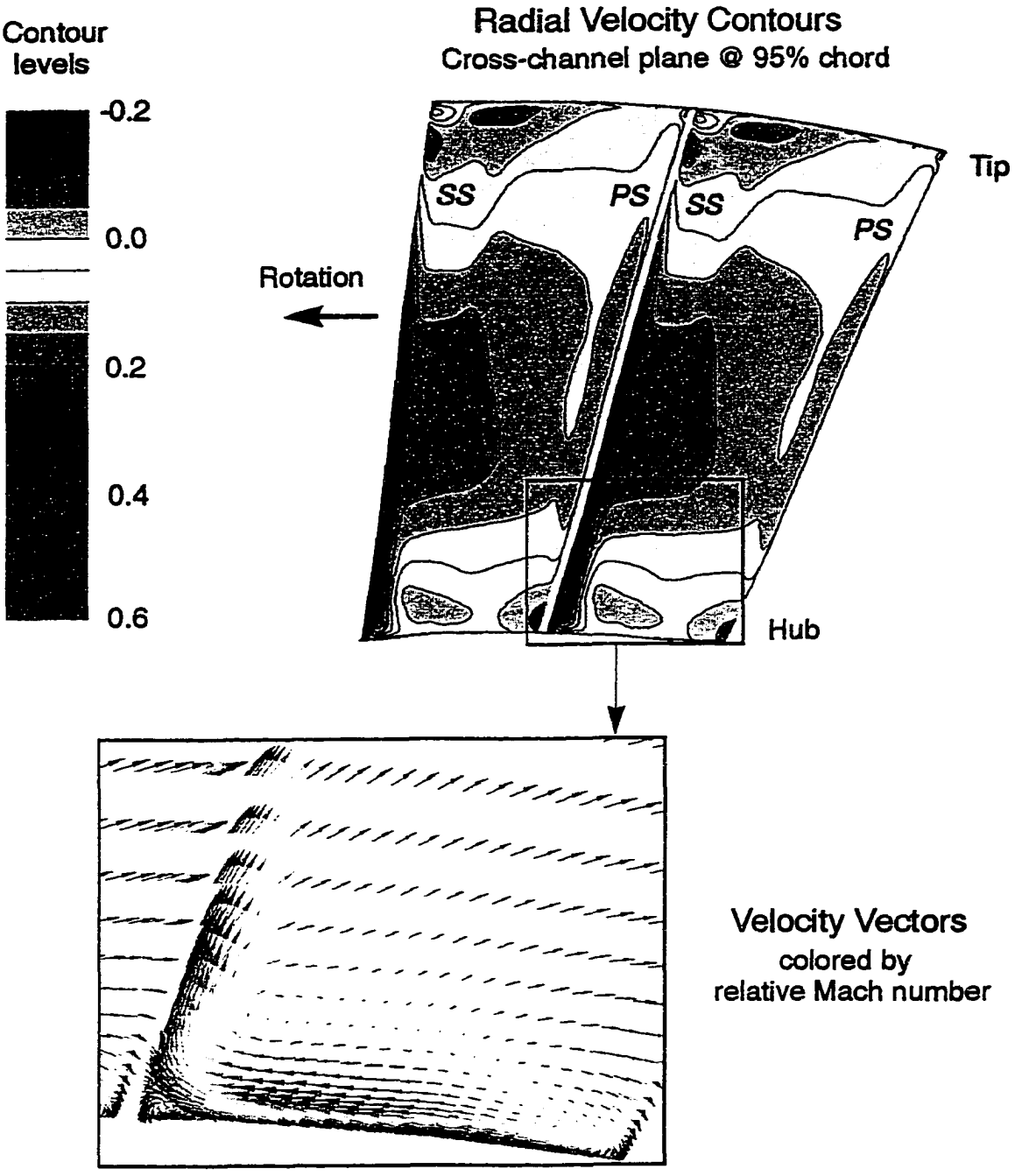

Figure 5.89 Viscous three-dimensional CFD radial velocity contours (dimensionless) and velocity vectors (colored according to relative Mach number; see Figure 5.80) at the rotor exit cross-channel for design conditions

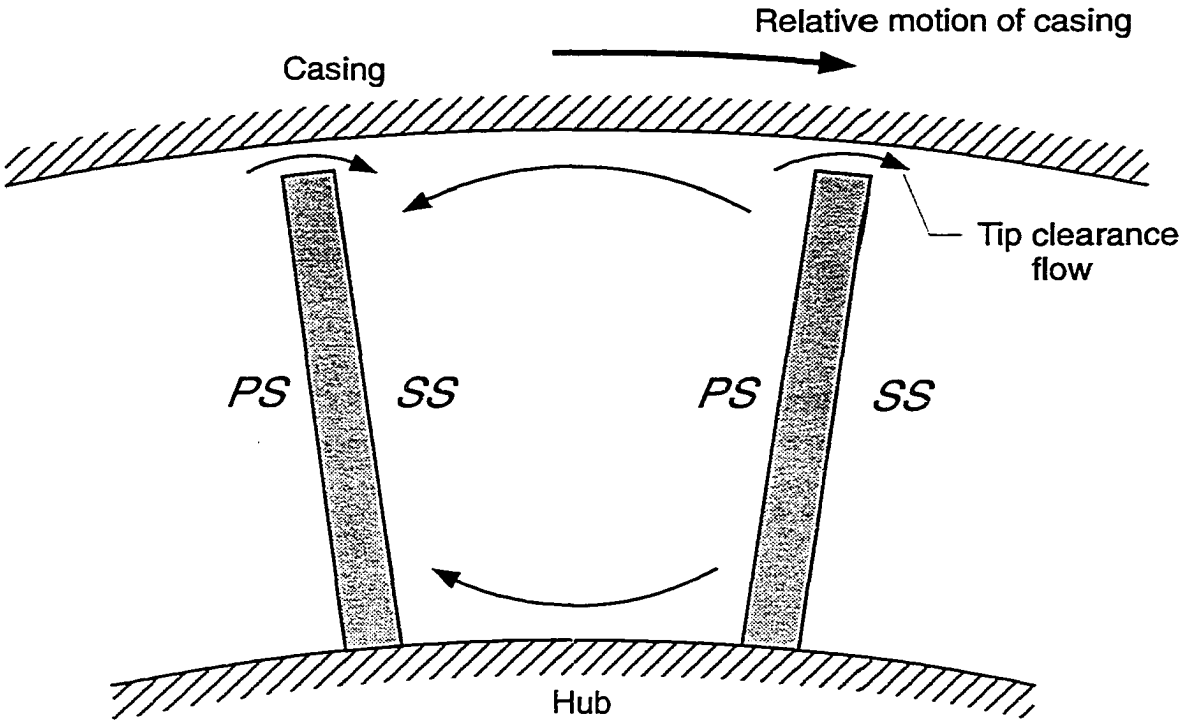

Figure 5.90 Sketch of cross-channel showing generalized secondary-flows

It was mentioned earlier that the secondary flow on the hubward, aft portion of the blade is substantial enough to transport a sufficient amount of low-momentum fluid to influence the spanwise distribution of total-pressure loss. A graph showing several spanwise distributions of loss coefficient at various chordwise locations is shown in Figure 5.91. The influence of the secondary flow can be seen in the near-hub loss distribution as the flow develops through the blade row. At the 55 percent chordwise location, which is upstream of most of the secondary flow on the blade surface, the spanwise loss distribution is fairly flat between about 10 and 90 percent annulus height. At the 95 percent axial-chord location (the trailing edge), however, the flat region extends only from about 30 to

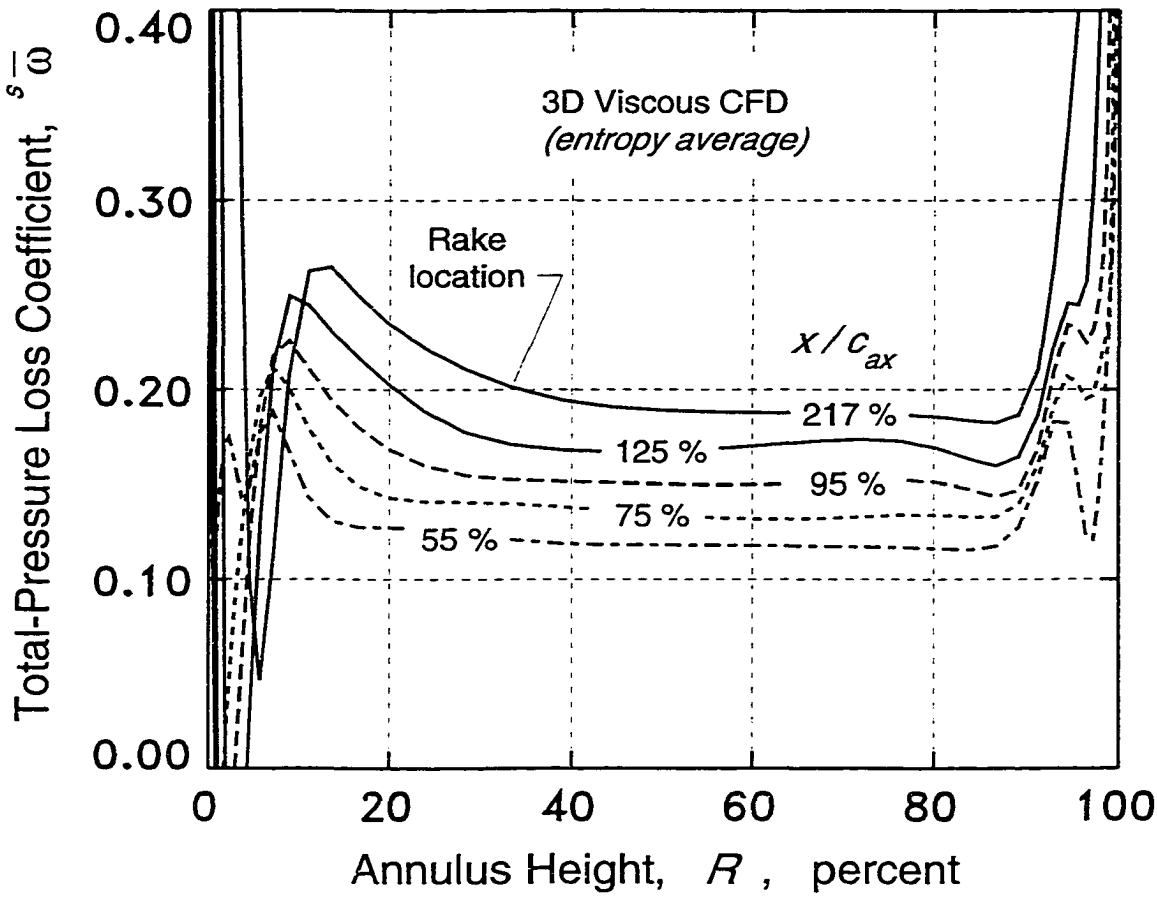

Figure 5.91 Spanwise distributions of total-pressure loss at several chordwise locations; three-dimensional viscous CFD for design-point rotor operation

90 percent annulus height; that is, a region of higher loss near the hub extends to almost 30 percent annulus height. By the time the flow reaches the rake location (at 217 percent of axial chord), the secondary flow, transporting low-momentum fluid from the hub toward midspan, has acted to extend the higher-loss region to about 45 percent annulus height. In contrast, notice that no such effects occur in the tip region.

Shock-in-Rotor Operation

The shock-in-rotor operating mode is of only limited interest for the baseline rotor, although it is potentially important as it relates to rotor inflow unstarting induced by downstream throttling. This mode is easily obtained and apparently quite stable at the higher rotational speeds, but little experimental testing was done to determine the shock-in-rotor performance and operational characteristics. The experimental *stage* was operated in this mode in a few rare cases, but no detailed performance measurements were performed. As an isolated blade row, the baseline rotor was not operated in this mode.

In discussing the turbomachinery literature in Chapter 1, it was pointed out that axial-supersonic inflow velocities have been obtained in at least two isolated rotor cases in the past; namely, the experimental rotor tested at the Langley Aeronautical Laboratory [21] in the 1950's and the experimental rotor tested at the von Karman Institute [38] in the 1970's. In both cases shock-in-rotor operation was the intended and demonstrated operating mode, which is in contrast to the baseline SSTF rotor designed for operation without a strong (normal or quasi-normal) rotor shock. Historically, therefore, the shock-in-rotor mode is of some interest and consequence.

A fairly brief description of the operational characteristics of this mode as it relates to the baseline rotor is presented in this section. Much of the description is mostly qualitative in nature, although pitchline quasi-three-dimensional CFD simulations have been conducted in order to obtain rough approximations of the performance levels. The major focus is on the 75 percent of design rotational speed since it is adequate to provide a picture of the general features.

From the standpoint of rotor operation and the associated performance map, the primary difference between shock-in-rotor and supersonic throughflow operation is that in the former case there is an additional independent parameter; namely, the downstream static pressure. Thus with shock-in-rotor operation there are *three* first-order, independent aerodynamic parameters [40], the other two being rotational speed and axial inflow Mach

---

[40] This is also in contrast to subsonic throughflow operation where there are only two first-order independent parameters: rotational speed and downstream static pressure.

number (or mass flow). The implication of this is that on the performance map it is no longer possible to depict the aerodynamic performance using "constant speed lines", but rather "constant speed regions" are needed since axial inflow Mach number and downstream static pressure can both be varied for a particular rotational speed. Such a region can be seen in Figure 5.92 which shows a performance map for the baseline rotor operating at 75 percent of design speed. These performance results were estimated using quasi-three-dimensional viscous CFD analyses at the rotor pitchline. Relative Mach number contours showing the blade-to-blade flow field for one of the computed shock-in-rotor cases (axial inflow Mach number 1.60) are presented in Figure 5.93.

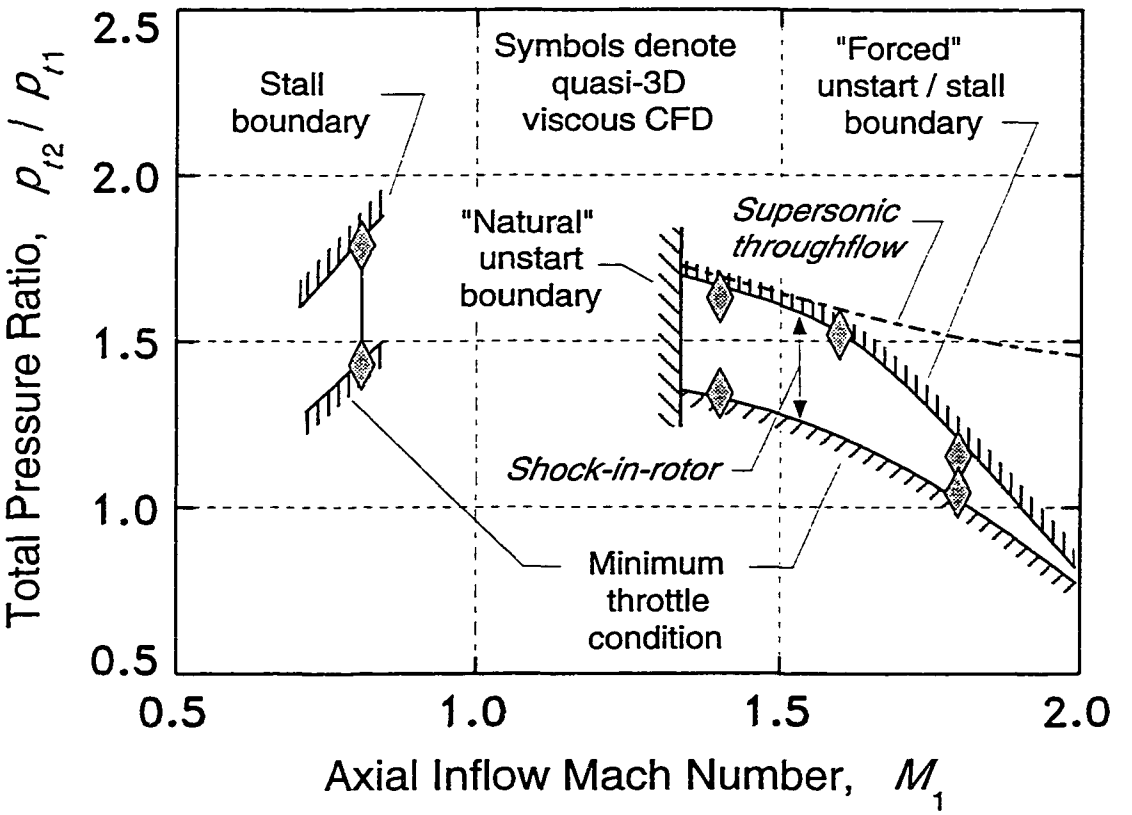

Figure 5.92 Shock-in-rotor operating region for the baseline rotor at 75 percent of design rotational speed; results based on quasi-three-dimensional viscous CFD at the rotor pitchline

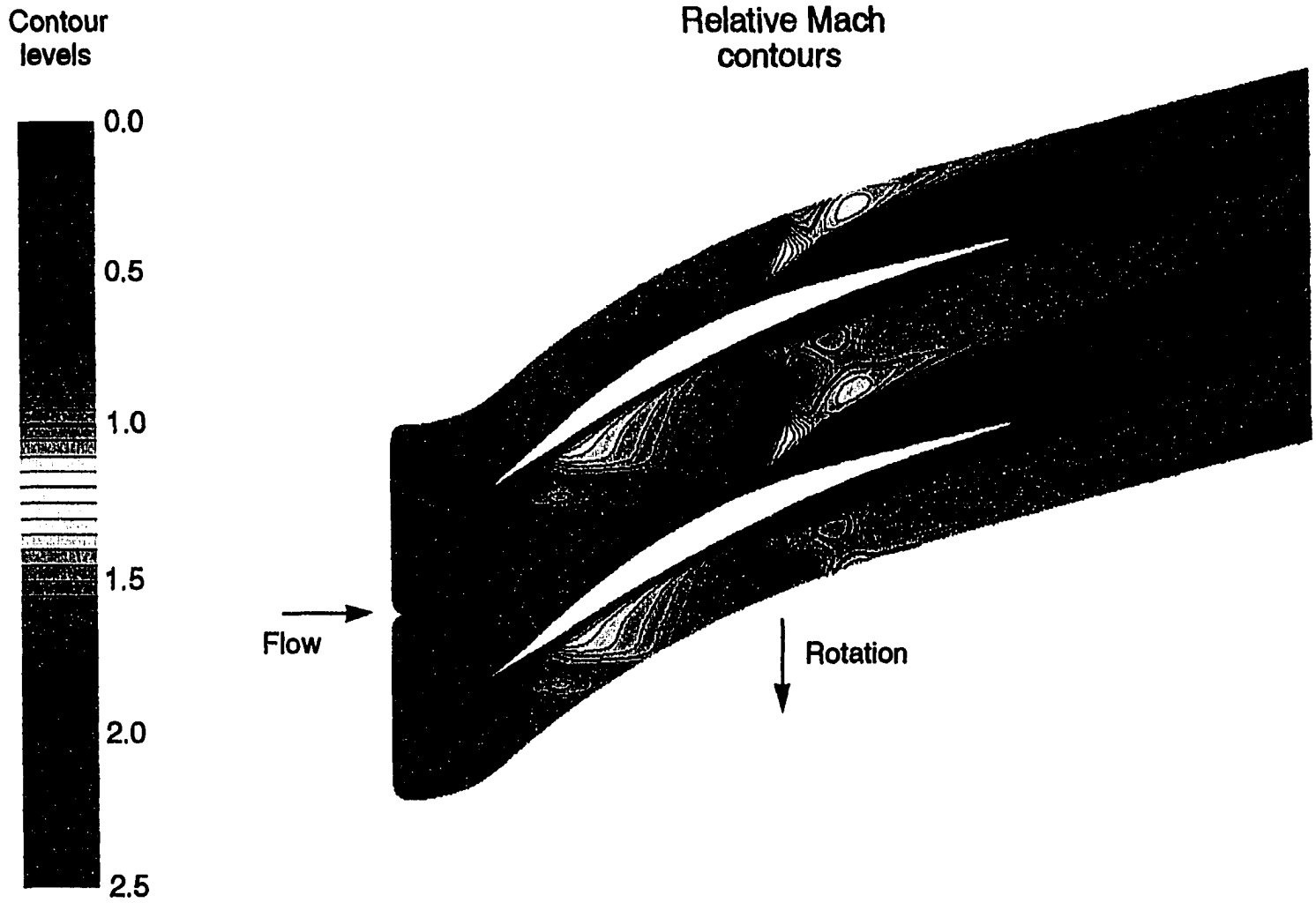

Figure 5.93 Viscous quasi-three-dimensional CFD Mach number contours for the rotor pitchline at 75 percent of design rotational speed, with shock-in-rotor conditions (M_1 = 1.60)

The constant speed zone in Figure 5.92 can be seen to be bounded above, below, and on the "left", where the left boundary is the *rotor unstart boundary* discussed throughout much of the chapter. The upper boundary is also a type of rotor unstart boundary, but aerodynamically the unstart mechanism is different. At the left boundary the unstart is induced from *upstream* by minimum supersonic axial inflow Mach numbers for which the rotor cannot sustain the axial-supersonic inflow condition. The rotor unstart in that case is closely related to the blade row geometry and the rotational speed, as discussed earlier. At the upper boundary the unstart is induced from *downstream* by a maximum back-pressure which forces the rotor shock upstream. This unstart boundary does not involve a single, minimum inflow Mach number (at a particular rotational speed), but rather involves the whole range of axial inflow Mach numbers also associated with supersonic throughflow operation. In light of the difference between these two types of rotor inflow unstarting, it may be desirable to denote the latter type of unstart as *forced rotor-inflow unstarting*, so as to distinguish it from the former type which may, perhaps, be termed *natural rotor-inflow unstarting* due to its more "natural" occurrence and relationship to the rotor geometry. Note that the natural unstart always supersedes the forced unstart, and that it represents the unstart of least severity for a particular rotational speed. Furthermore, depending on the rotational speed, the forced unstart may cause the rotor to stall (or surge). The higher the axial inflow Mach number, the more likely that the forced unstart will terminate in stall.

The lower boundary for the constant speed zone in Figure 5.92 corresponds to the minimum back-pressure (throttle) condition for axial-subsonic outflow. Opening the downstream throttle beyond that point causes the rotor to begin operating in the supersonic throughflow mode; that is, the performance jumps (vertically on the map) from the lower boundary to the constant speed line for supersonic throughflow operation. A performance jump very similar to this also occurs on the "subsonic" side of the performance map when the rotor transitions from subsonic throughflow to impulse-type operation.

CHAPTER 6.
CONCLUDING REMARKS

The baseline supersonic throughflow rotor was operated and tested over a wide range of operating conditions. At the design point the rotor performed much as designed, and off-design operation involved stable operational characteristics with no unusual instabilities, even during transitional phases of operation where transient discontinuities traversed the rotor flow field. Rotor inflow starting, involving the propagation of a normal shock into the rotor from upstream, was accompanied by only minor discontinuities in rotor performance and blade loading.

Two- and three-dimensional viscous CFD simulations were performed for several of the rotor operating points, and the resulting solutions exhibited good agreement with the experimental data. The lack of harsh dynamic effects on rotor blade loading and performance during rotor inflow starting was also predicted using the analytical methods.

The application of a simple two-dimensional total-pressure loss model in conjunction with the experimental and CFD results allowed a fairly accurate determination of the first-order loss sources for a wide range of operating conditions. For design-point operation it was shown that viscous (skin-friction) losses account for about 51 percent of the total mixed-out losses, and that bow shock wave losses account for about 44 percent. Oblique shock wave losses contribute only about 5 percent to the total loss, which is expected considering that the aerodynamic design objectives included the goal that oblique waves be maintained at weak levels. Mixing losses, which are included as part of the viscous and the bow shock losses in the simple model, account for about 28 percent of the total mixed-out loss.

Attempts to improve the aerodynamic performance of supersonic throughflow rotors must inevitably address the different loss sources, particularly the two dominant mechanisms: skin-friction and bow shock waves. As a general design guideline, the relative Mach number levels should be reduced to the minimum levels possible subject to the constraints of the overall propulsion system. All three major loss sources are favorably

influenced by lower relative Mach numbers. Practically considered, this implies designing for lower rotational speeds and axial inflow Mach numbers. Convergence of the annulus area through the blade row should also prove beneficial in this regard.

From the standpoint of a practical propulsion system, lower design rotational speeds will almost certainly be required due to the effects of supersonic flight on the total-temperature conditions upstream of the fan. A graph of mechanical tip speed versus flight Mach number is shown in Figure 6.1 for several constant corrected tip speeds, as indicated. For example, in order to cruise at Mach 2.4 between the altitudes of 40,000 and 80,000 ft, the corrected tip speed of 1500 ft/sec (the baseline fan design speed) would require a mechanical tip speed of 1908 ft/sec, which most would agree is excessive. Furthermore, the fairly high hub-tip radius ratios and the large number of blades associated with supersonic throughflow rotors result in large and heavy rotor disks. The higher the rotational speed requirements, the greater becomes the problem of disk weight. From Figure 6.1, it seems reasonable to conclude that a practical rotor design would involve a cruise (design) corrected tip speed of around 1350 ft/sec or less.

The skin-friction losses for the baseline rotor are determined largely by the blade-element solidity parameter σ, in conjunction with the relative Mach number levels. Reynolds number effects due to scaling, although potentially significant, are not expected to be large since no large variations in Reynolds numbers occur between the sub-scale test facility with sea-level-standard (SLS) inlet conditions and a full-scale fan in supersonic flight. The experimental (sub-scale) rotor blade-chord Reynolds numbers are on the order of about 1.7×10^6, and the full-scale (cruise) flight Reynolds numbers are larger by an amount depending on the flight altitude and Mach number. Curves showing the approximate factor by which the Reynolds number increases as a function of flight Mach number and altitude are shown in Figure 6.2, which also includes a length scale factor of 3.6 between the sub-scale experimental fan and a full-scale fan. From the figure it can be seen, for example, that Mach 2.4 flight at 60,000 ft involves an increase in the Reynolds number (from the sub-scale experiment) by a factor of about two.

Since the blade-element solidities are relatively large, it is tempting to consider reducing the skin friction losses by reducing the solidity. This is, however, not possible since reducing the solidity results in a progressive increase in the shock/boundary-layer interaction on the aft part of the blade suction surface, as described in Reference 28. In fact,

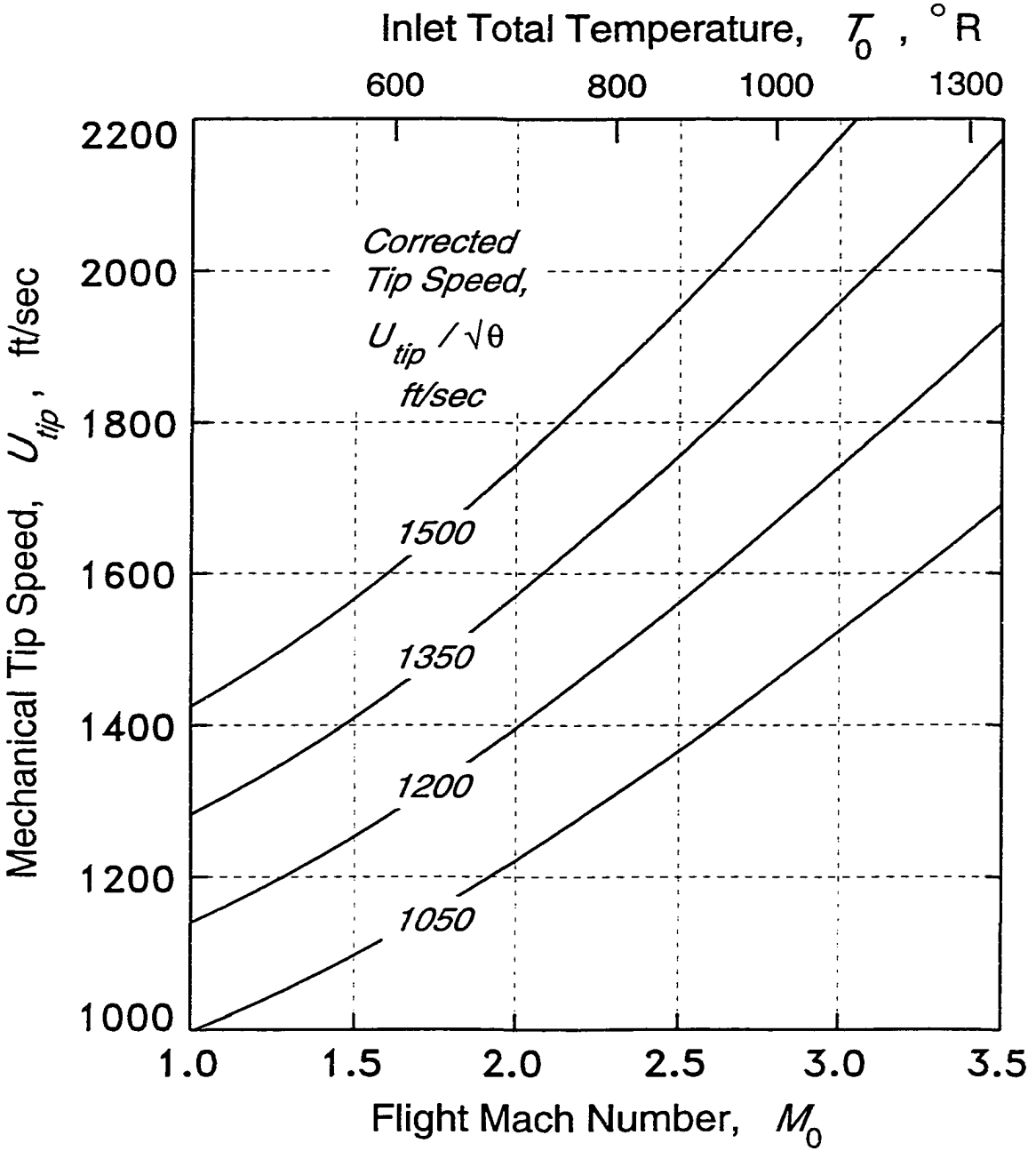

Figure 6.1 Mechanical tip speed as a function of flight Mach number and corrected tip speed; flight altitudes 40,000 to 80,000 ft

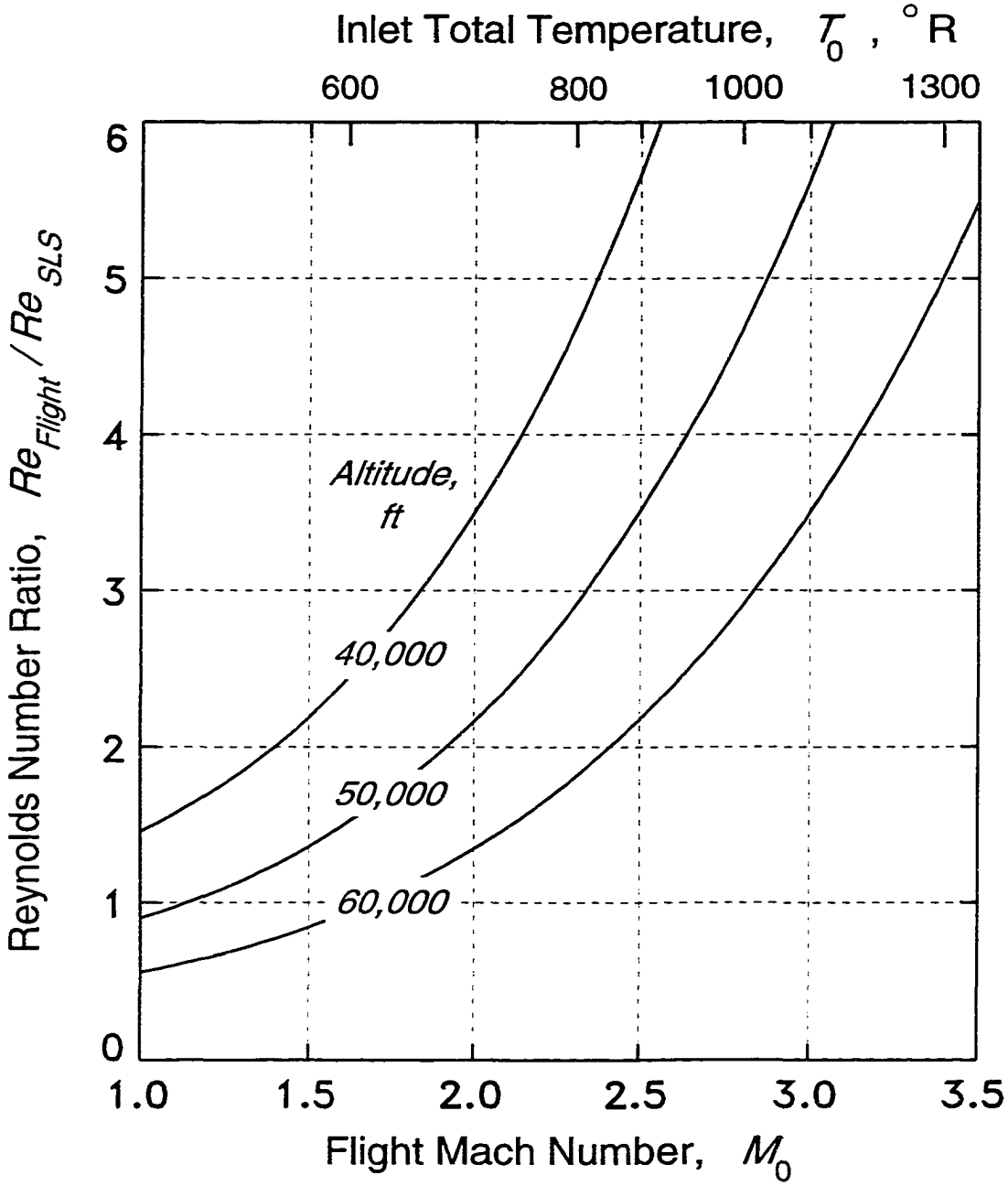

Figure 6.2 Approximate factor by which Reynolds number increases as a function of flight Mach number and altitude; curves include a length scale factor of 3.6 between the sub-scale experimental fan (SLS) and a full-scale (flight) fan

more recent studies (currently undocumented) reveal that the solidity chosen for the baseline rotor is near the optimum (at that tip speed and inflow Mach number) for minimum total-pressure losses. It would appear, therefore, that little can be done to reduce the skin-friction losses, other than designing for lower relative Mach number levels through the blade row. However, an experimental investigation into surface riblets on the blades of a supersonic throughflow cascade [76], similar to the midspan blade element of the baseline rotor, revealed a significant reduction in the skin-friction losses: about an 8 percent decrease in the loss coefficient at the design condition (relative Mach number 2.36 and zero suction-surface incidence). This loss decrease is equivalent to an improvement of about one point in rotor adiabatic efficiency.

The bow shock loss levels associated with the baseline rotor are large, at around a total-pressure loss coefficient of 0.095, producing a 9 point reduction in the adiabatic efficiency of the rotor. The blunt leading edges of the rotor blades are the cause of this, and as discussed in Chapter 5, the bow shock losses should scale linearly with the effective leading edge bluntness — all other geometric features remaining fixed. The practical implications of this are immense when scaling effects from the experimental sub-scale hardware to full-scale hardware are considered. Specifically, a scale factor of about 3.6 is involved, except for the leading-edges which should be capable of meeting foreign object damage (FOD) requirements with only a partial scaling-up in size, and incorporating more edge-ellipse eccentricity. Optimistic estimates [1] indicate an improvement of up to 6 points in adiabatic rotor efficiency by scaling up to a full-size fan [2].

---

[1] Optimistic in terms of leading edge "bluntness". As discussed in Chapter 5, and mentioned again here, a zero-thickness (sharp) leading edge corresponds to about a 9 point improvement in adiabatic efficiency over that of the blunt edge.

[2] The performance and operation of the fan stage was not addressed in this dissertation, but a comment about the stator performance in regard to this discussion is worth adding. In general the baseline stator performed with loss levels similar to, and actually greater than, the baseline rotor. This basic behavior is not typical of transonic turbomachinery where stator losses tend to be considerably less than the rotor losses for a given stage. It is, however, a consequence of the high Mach number levels in the stator, and can be accounted for in the same manner as for the rotor. In scaling up the stage, therefore, an improvement in stage adiabatic efficiency on the order of 12 points is expected (6 points for the rotor and 6 points for the stator).

Finally, as a closing remark it should be emphasized that the main objectives in designing and testing the baseline rotor (and stage) were to demonstrate the proof-of-concept, provide an experimental data base, and obtain a basic understanding of the aerodynamics associated with supersonic throughflow fans. These objectives have been achieved with a good measure of success. Much future work remains, however, if the adiabatic efficiency levels are to be improved to the levels required for practical applications, at least in a commercial supersonic transport. Furthermore, many practical issues related to system integration and operability have yet to be investigated, although considerable progress toward these goals has been made.

REFERENCES

1. Driver, C., "How Different a Modern SST Would Be," *Aerospace America*, Vol. 24, Nov. 1986, pp. 26-29.

2. Boeing Company, "High-Speed Civil Transport Study," NASA CR-4233, 1989.

3. McDonnell-Douglas Company, "Study of High-Speed Civil Transports," NASA CR-4235, 1989.

4. McLean, F. Edward, "Supersonic Cruise Technology," NASA SP-472, 1985.

5. Howlett, R. A., and Smith, M. G., Jr., "Advanced Supersonic Transport Propulsion Systems," SAE Paper 771010, 1977.

6. Calder, P. H., and Gutpa, P. C., "Engine Options for Supersonic Cruise Aircraft," AIAA Paper 78-1054, 1978.

7. Franciscus, Leo C., "The Turbine Bypass Engine — New Supersonic Cruise Propulsion Concept," NASA TM-82608, July 1981.

8. Smith, M. G., Jr., "21st Century High Speed Transport Propulsion," AIAA Paper 88-2987, July 1988.

9. Lowrie, B. W., "Future Supersonic Transport Propulsion Optimisation," in *European Symposium on the Future of High Speed Air Transport, Strasbourg, France, November 6-8, 1989, Proceedings*, pp. 203-209, Cepadues-Editions, Toulouse, France, 1990.

10. Habrard, Alain, "The Variable-Cycle Engine — A Solution to the Economical and Environmental Challenges of the Future Supersonic Transport," in *European Symposium on the Future of High Speed Air Transport, Strasbourg, France, November 6-8, 1989, Proceedings*, pp. 211-218, Cepadues-Editions, Toulouse, France, 1990.

11. Office of Science and Technology Policy, "National Aeronautical R&D Goals: Agenda for Achievement," Executive Office of the President, Washington, D. C., Feb. 1987.

12. Trucco, Horacio, "Studies of Variable Cycle Engines Equipped with Supersonic Fans," NASA CR-134777 (also Advanced Technology Laboratories, ATL TR 201), Sept. 1975.

13. Franciscus, Leo C., "Supersonic Through-Flow Fan Engines for Supersonic Cruise Aircraft," NASA TM-78889, April 1978.

14. Franciscus, Leo C., "The Supersonic Fan Engine — An Advanced Concept in Supersonic Cruise Propulsion," NASA TM-82657 (also AIAA Paper 81-1599), July 1981.

15. Franciscus, Leo C., "Supersonic Fan Engines for Military Aircraft," NASA TM-83499, Oct. 1983.

16. Franciscus, Leo C., "The Supersonic Through-Flow Turbofan for High Mach Propulsion," NASA TM-100114 (also AIAA Paper 87-2050), June 1987.

17. Tavares, Theodore S., "A Supersonic Fan Equipped Variable Cycle Engine for a Mach 2.7 Supersonic Transport," NASA CR-177141, 1985.

18. Champagne, G. A., "Payoffs for Supersonic Through-Flow Fan Engines in High Mach Transports and Fighters," AIAA Paper 88-2945, 1988.

19. Seiner, John M., and Krejsa, Eugene A., "Supersonic Jet Noise and the High Speed Civil Transport," AIAA Paper 89-2358, July 1989.

20. Wilcox, Ward W., Tysl, Edward R., and Hartmann, Melvin J., "Résumé of the Supersonic-Compressor Research at NACA Lewis Laboratory," *Journal of Basic Engineering*, Vol. 81, Dec. 1959, pp. 559-568.

21. Savage, M., Boxer, E., and Erwin, J. R., "Résumé of Compressor Research at the NACA Langley Laboratory," *Journal of Engineering for Power*, Vol. 83, July 1961, pp. 269-285.

22. Klapproth, J. F., "A Review of Supersonic Compressor Development," *Journal of Engineering for Power*, Vol. 83, July 1961, pp. 258-268.

23. Broichhausen, K.-D., Gallus, H. E., and Mönig, R., "Off-Design Performance of Supersonic Compressors With Fixed and Variable Geometry," *Journal of Turbomachinery*, Vol. 110, July 1988, pp. 312-322.

24. Kantrowitz, Arthur, "The Supersonic Axial-Flow Compressor," NACA Report 974, 1950 (supersedes NACA ACR L6D02, 1946).

25. Ferri, Antonio, "Three Dimensional Effects in Supersonic Compressors, Part 1 — Introductory Remarks on the Design Problem of Supersonic Compressors," PIBAL Report No. 233, Oct. 1953.

26. Ferri, Antonio, "Problems Related to Matching Turbojet Engine Requirements to Inlet Performance as a Function of Flight Mach Number and Angle of Attack," in *Air Intake Problems in Supersonic Propulsion*, (Fabri, J.,ed.), pp. 48-62, AGARD, Agardograph No. 27, 1956.

27. Wood, Jerry R., Schmidt, James F., Steinke, Ronald J., Chima, Rodrick V., and Kunik, William G., "Application of Advanced Computational Codes in the the Design of an Experiment for a Supersonic Throughflow Fan Rotor," NASA TM-88915 (also ASME Paper 87-GT-160), May 1987.

28. Schmidt, James F., Moore, Royce D., Wood, Jerry R., and Steinke, Ronald J., "Supersonic Through-Flow Fan Design," NASA TM-88908 (also AIAA Paper 87-1746), June 1987.

29. Ball, Calvin L., and Moore, Royce D., "Supersonic Throughflow Fans for High-Speed Aircraft," Aeropropulsion '87, NASA CP-3049, 1990.

30. Ball, Calvin L., and Moore, Royce D., "Supersonic Throughflow Fans," Lecture Series 1988-03, von Karman Institute for Fluid Dynamics, Feb. 1988.

31. Saunders, Neal T., and Glassman, Arthur J., "Turbomachinery Technology for High-Speed Civil Flight," NASA TM-102092, June 1989.

32. Lipfert, F. W., "Supersonic Axial Velocity Compressor Study, Volume I — Summary and Aerodynamic Design Studies," AFAPL-TR-67-68, Volume I, Aug. 1967.

33. Short, Frederick R., and Poste, Edward A., et al., "Supersonic Axial Velocity Compressor Study, Volume II — Mechanical Design, Control, and Weight Analyses," AFAPL-TR-67-68, Volume II, Aug. 1967.

34. Lipfert, F. W., "Supersonic Axial Velocity Compressor Study, Volume IV — Two-Dimensional Cascade Test Results," AFAPL-TR-67-68, Volume IV, Aug. 1967.

35. LaRocca, Aldo, "Three-Dimensional Effects in Supersonic Compressors, Part 3 — The Design of Two Stator Passages and Comparison between Theory and Experiment," PIBAL Report No. 271, Dec. 1954.

36. Beder, Earl, "Theoretical and Experimental Investigation of a Two-Dimensional All-Supersonic Diffusing Cascade at Mach Number 2.5," AFOSR TN-56-15 (also Propulsion Research Corporation, PRC-R-155), June 1955.

37. Iura, T., and Beder, Earl, "Experimental Investigation of a Three-Dimensional All-Supersonic Diffusing Cascade," AFOSR TR-58-132, May 1958.

38. Breugelmans, F. A. E., "The Supersonic Axial Inlet Component in a Compressor," ASME Paper 75-GT-26, March 1975.

39. Shaw, R. J., "Overview of Supersonic Cruise Propulsion Research," Aeropropulsion '91, NASA CP-10063, 1991.

40. Moore, Royce D., Schmidt, James F., and Tweedt, Daniel L., "Aerodynamic Performance of a Supersonic Throughflow Fan Stage," NASA TP-3308, 1993.

41. Moore, Royce D., and Tweedt, Daniel L., "Effect of Operational Variations on the Supersonic Throughflow Fan Stage Aerodynamic Performance," NASA TP-3382, 1993.

42. Chima, Rodrick V., "Explicit Multigrid Algorithm for Quasi-Three-Dimensional Viscous Flows in Turbomachinery," *AIAA Journal of Propulsion and Power*, Vol. 3, Sept.-Oct. 1987, pp. 397-405.

43. Crouse, James E., and Gorrell, William T., "Computer Program for Aerodynamic and Blading Design of Multistage Axial-Flow Compressors," NASA TP-1946, 1981.

44. Ramsey, J. K., and Kielb, R. E., "A Computer Program for Calculating Unsteady Aerodynamic Coefficients for Cascades in Supersonic Axial Flow," NASA TM-100204, 1987.

45. Kielb, R. E., and Ramsey, J. K., "Flutter of a Fan Blade in Supersonic Axial Flow," ASME Paper 88-GT-78, June 1988.

46. Urasek, Donald C., Cunnan, Walter S., Lantz, Richard L., Fronek, Dennis L., Dawson, Ronald A., and Brown, Jeffrey C., "Supersonic Throughflow Fan Test Facility at NASA Lewis Research Center," NASA TP-3038, 1990.

47. Moore, Royce D., "Flow Tests for a Supersonic Throughflow Fan Test Facility," NASA TP-3097, 1991.

48. Fronek, D. L., Setter, R. N., Blumenthal, P. Z., and Smalley, R. R., "A Distributed Data Acquisition System for Aeronautics Test Facilities," NASA TM-88961, 1987.

49. Moore, Royce D., and Tweedt, Daniel L., "Aerodynamic Performance of a Supersonic Throughflow Fan Rotor," NASA TP-3115, 1991.

50. Vahl, W. A., and Weirich, R. L., "Calibration of 30° Included-Angle Cone for Determining Local Flow Conditions in Mach Number Range of 1.51 to 3.51," NASA TN D-4679, 1968.

51. Burcham, F. W., Jr., "Wind-Tunnel Calibration of a 40° Conical Pressure Probe at Mach Numbers from 3.5 to 7.4," NASA TN D-4678, 1968.

52. Stickney, T. M., "Recovery and Time-Response Characteristics of Six Thermocouple Probes in Subsonic and Supersonic Flow," NACA TN-3455, 1955.

53. Ames Research Staff, "Equations, Tables, and Charts for Compressible Flow," NACA Report 1135, 1953.

54. Chima, Rodrick V., "Viscous Three-Dimensional Calculations of Transonic Fan Performance," NASA TM-103800, May 1991.

55. Chima, Rodrick V., and Yokota, Jeffrey W., "Numerical Analysis of Three-Dimensional Viscous Internal Flows," *AIAA Journal*, Vol. 28, May 1990, pp. 798-806 (also NASA TM-100878).

56. Moore, Royce D., Tweedt, Daniel L., and Chima, Rodrick V., "NASA Lewis Supersonic Throughflow Fan Program," NASA TM-103248 (Paper presented at 1990 JANNAF Propulsion Meeting in Anaheim, California, Oct. 3-5, 1990), 1990.

57. Jorgenson, Philip C. E., and Chima, Rodrick V., "An Unconditionally Stable Runge-Kutta Method for Unsteady Flows," NASA TM-101347 (also AIAA Paper 89-0205), 1989.

58. Denton, J. D., "An Improved Time-Marching Method for Turbomachinery Flow Calculations," *Journal of Engineering for Gas Turbines and Power*, Vol. 105, July 1983, pp. 514-524.

59. Whitfield, D. L., Swafford, T. W., Janus, J. M., Mulac, R. A., and Belk, D. M., "Three-Dimensional Unsteady Euler Solutions for Propfans and Counter-rotating Propfans in Transonic Flow," AIAA Paper 87-1197, 1987.

60. Baldwin, B. S., and Lomax, H., "Thin-Layer Approximation and Algebraic Model for Separated Turbulent Flows," AIAA Paper 78-257, Jan. 1978.

61. Chima, R. V., Giel, P. W., and Boyle, R. J., "An Algebraic Turbulence Model for Three-Dimensional Viscous Flows," NASA TM-105931, Jan. 1993.

62. Sorenson, R. L., "A Computer Program to Generate Two-Dimensional Grids About Airfoils and Other Shapes by the Use of Poisson's Equation," NASA TM-81198, 1980.

63. Nietubicz, C. J., Pulliam, T. H., and Steger, J. L., "Numerical Solution of the Azimuthal-Invariant Thin-Layer Navier-Stokes Equations," *AIAA Journal*, Vol. 18, Dec. 1980, pp. 1411-1412.

64. Miller, D. P., and Reddy, D. R., "The Design/Analysis of Flows Through Turbomachinery — A Viscous/Inviscid Approach," NASA TM-104447 (also AIAA Paper 91-2010), June 1991.

65. Schlichting, Hermann, *Boundary-Layer Theory.* New York: McGraw-Hill, Inc., 1968, p. 674.

66. Shapiro, Ascher H., *The Dynamics and Thermodynamics of Compressible Fluid Flow.* Vol. 1, New York: The Ronald Press Company, 1953.

67. Owczarek, Jerzy A., *Fundamentals of Gas Dynamics.* International Textbook Company, Scranton, Pennsylvania, 1964.

68. Zucrow, Maurice J., and Hoffman, Joe D., *Gas Dynamics.* Vol. 1, New York: John Wiley & Sons, Inc., 1976.

69. Starken, H., Zhong, Y., and Schreiber, H. A., "Mass Flow Limitation of Supersonic Blade Rows due to Leading Edge Blockage," ASME Paper 84-GT-233, 1984.

70. Zhong, Y., and Starken, H., "Die Überschallanströmung stumpfer Plattengitter," IB 325-2-1982, Deutsche Forschungs- und Versuchsanstalt für Luft- und Raumfahrt (DFVLR), Cologne, Germany, June 1982.

71. Starken, H., and Lichtfuß, H. J., "Supersonic Cascade Performance," AGARD Lecture Series 39 on Advanced Compressors, Brussels, Belgium, and Kongsberg, Norway, June 1970.

72. Lichtfuß, H. J., and Starken, H., "Supersonic Cascade Flow," in *Progress in Aerospace Science*, Vol. 15, (Kuchemann, D.,ed.), pp. 37-149, Pergamon Press Ltd., New York, 1974.

73. Bowersox, Rodney D., "Meanflow and Turbulence Measurements in the Wake of a Supersonic Through-Flow Cascade," Master of Science Thesis, Virginia Polytechnic Institute and State University, Jan. 1990.

74. Chesnakas, Christopher J., "Experimental Studies in a Supersonic Through-Flow Fan Blade Cascade," Doctoral Dissertation, Virginia Polytechnic Institute and State University, May 1991.

75. Andrew, Philip L., "Experimental and Numerical Investigations of the Off-Design Flow Physics in a Supersonic Through-Flow Fan Cascade," Doctoral Dissertation, Virginia Polytechnic Institute and State University, Aug. 1992.

76. Ninnemann, Todd, and Ng, Wing, "Supersonic Throughflow Fan Blade Cascade Studies Part II: Riblet Effects," To be published as a high-number NASA CR, 1993.

77. Zierke, W. C., and Deutsch, S., "An Analysis to Facilitate the Interpretation of Boundary Layer Measurements," NASA TM 85-85 (Applied Research Laboratory, Pennsylvania State University, NASA Grant NSG-3264), May 1985.

78. Saravanamutto, H. I. H., editor, "Recommended Practices for Measurement of Gas Path Pressures and Temperatures for Performance Assessment of Aircraft Turbine Engines and Components," Report of the Propulsion and Energetics Panel Working Group 19, AGARD Advisory Report No. 245, June 1990.

79. Grant, H., "Measuring Time-Average Stagnation Pressure in Pulsatile Air Flow," paper presented at the Instrument Society of America 23rd International Instrumentation Symposium, Las Vegas, Nevada, May, 1977.

80. Kline, S. J., and McClintock, F. A., "Describing Uncertainty in Single Sample Experiments," *Mechanical Engineering*, Vol. 75, 1953, pp. 3-8.

81. Zucrow, Maurice J., and Hoffman, Joe D., *Gas Dynamics*. Vol. 2: Multidimensional Flow, New York: John Wiley & Sons, Inc., 1977.

82. Schimming, P., and Starken, H., "Data Reduction of Two-Dimensional Cascade Measurements," in *Modern Methods of Testing Rotating Components of Turbomachines (Instrumentation)*, (Pianko, M., ed.), pp. 1-46, AGARD, Agardograph No. 207, 1900.

83. Gerald, Curtis F., *Applied Numerical Analysis*. second edition, Addison-Wesley Publishing Company, 1978, pp. 15-20.

84. Gelder, T. F., and Lewis, G. W., "Aerodynamic Performance of a 0.5-Meter Diameter, 337-Meter-per-Second Tip Speed, 1.5-Pressure-Ratio, Single-Stage Fan Designed for Low Noise Aircraft Engines," NASA TN D-7836, Dec. 1974, p. 7.

85. Levine, P., "Two-Dimensional Inflow Conditions for a Supersonic Compressor with Curved Blades," *Journal of Applied Mechanics*, Vol. 24, June 1957, pp. 165-169.

86. Novák, O., "Flow in the Entrance Region of a Supersonic Cascade," *Strojnicky Casopis*, Vol. 19, C. 2-3, Slovenskej Académic vied Bratislava, 1967, pp. 138-150.

87. Starken, H., "Untersuchung der Strömung in ebenen Überschallverzögerungsgittern," DLR-FB 71-99, Deutsche Forschungs- und Versuchsanstalt für Luft- und Raumfahrt (DFVLR), Cologne, Germany, 1971.

88. York, R. E., and Woodard, H. S., "Supersonic Compressor Cascades — An Analysis of the Entrance Region Flow Field Containing Detached Shock Waves," *Journal of Engineering for Power*, Vol. 98, April 1976, pp. 247-257.

89. Moeckel, W. E., "Approximate Method for Predicting Form and Location of Detached Shock Waves Ahead of Plane or Axially Symmetric Bodies," NACA TN 1921, July 1949.

90. Love, Eugene S., "A Reexamination of the Use of Simple Concepts for Predicting the Shape and Location of Detached Shock Waves," NACA TN 4170, Dec. 1957.

91. White, Frank M., *Viscous Fluid Flow.* New York: McGraw-Hill, Inc., 1974.

92. Kim, Chul-Soo, "Experimental Studies of Supersonic Flow Past a Circular Cylinder," *Journal of the Physical Society of Japan*, Vol. 11, April 1956, pp. 439-445.

93. Wellmann, J., "Vereinfachung von Rechnungen am schiefen Verdichtungsstoß," *Deutsche Luft- und Raumfahrt*, Forschungsbericht 72-11, Deutsche Forschungs- und Versuchsanstalt für Luft- und Raumfahrt, Institut für Aerodynamik, Braunschweig, Germany, Jan. 1972.

94. Wolf, T., "Comment on 'Approximate Formula of Weak Oblique Shock Wave Angle'," *AIAA Journal*, Vol. 31, 1993, p. 1363.

ACKNOWLEDGEMENTS

A large number of people have participated in the supersonic throughflow fan program at the NASA Lewis Research Center. It would be impractical to acknowledge them all, or even most of them, by name, but I am nevertheless greatly indebted to them for their contributions to this project. The work done by them was outstanding, and I hold all participants in high regard.

The baseline fan program, funded under NASA RTOP 505-62-20, has been ongoing since about 1986. Since the program's inception, Mr. Calvin L. Ball has served actively as a key technical advocate, and therefore deserves much credit for the program's existence and continuance. The experimental project manager and principle research engineer has been Mr. Royce D. Moore, whose experience, planning, and engineering work were essential to the success and efficiency of the experimental research. Mr. James F. Schmidt performed the aerodynamic design of the baseline fan, and so his work has been foundational to the overall success of the program.

Computational fluid dynamics (CFD) codes have been used extensively throughout the project, from the design of the baseline fan to the subsequent analyses of the off-design aerodynamics. The viscous CFD codes applied to the fan were written and developed by Dr. Rodrick V. Chima, who has also provided continual support in the application of the codes. Dr. Chima contributed much in the way of helpful discussions regarding the CFD methods and results, and regarding flow field averaging techniques.

Special thanks are reserved for Dr. Lonnie Reid, who was my supervisor at the time the decision was made to select the supersonic throughflow fan as the research topic for this dissertation. Dr. Reid encouraged the selection, and facilitated its approval despite limitations on the public distribution of information about the fan research. My current supervisor, Dr. Lawrence J. Bober, Chief of the Turbomachinery Technology Branch, also deserves many thanks for his continued patience and encouragement during the last two years. Dr. Bober ensured that priority was maintained and abundant opportunity provided for the timely completion of this work.

I am very grateful to Professor Theodore H. Okiishi, my major professor in charge of this work, for all his efforts, patience, and encouragement in helping to bring the dissertation to completion. His flexibility regarding the selection of a research topic is greatly appreciated, as are his contributions to the final manuscript.

I would like to acknowledge my parents, Mr. and Mrs. M. L. Tweedt, and my wife, Julie, for their indirect but valuable contributions. Much of my higher education and many of my abilities were provided and encouraged by my parents, who also provided love and security, and continually demonstrated the value and rewards of diligent, hard work. Julie has been a faithful wife and friend for the past seven years, and her fellowship, support, and encouragement have been wonderful. Her example of humility and perseverance in daily ministering to our three children, Katherine, Joseph, and Jonathan, have meant much to me, and have been a constant reminder that the things of real value are not worldly success and recognition, or even personal pleasure and satisfaction. Rather, it is our faithful service and devotion to God, our Father, and His Son Jesus Christ, our Savior, which are of infinitely greater value, resulting someday in eternal rewards.

Finally, and most importantly, I acknowledge almighty God as having ultimately provided all that was necessary for this accomplishment. Indeed, all of life's expressions, from each unnoticed breath to the most sophisticated of intellectual endeavors, are a testimony to His amazing grace, His unmerited favor, which He constantly demonstrates toward us. Apart from His continued grace, sustenance, and provision, nothing truly worthwhile could be accomplished by any of us. God is merciful and good, however, and has proved once and for all His love for every member of the human race by sending His only Son, Jesus Christ, to suffer on our behalf the just penalty of death, carried out on a Roman cross for all our offenses against God. Through the death of His Son, God offers to all the free gift of eternal life, to be received simply by believing in Jesus Christ to be their righteousness and to secure their complete acceptance before an exceedingly righteous God. Therefore, to my God, who gives me hope and purpose by having already delivered me from condemnation and death, I offer thanks for abundantly providing everything I needed to complete this dissertation to the best of my ability.

APPENDIX A.
SUPERSONIC NOZZLE PERFORMANCE AND EXIT FLOW QUALITY

The variable-geometry inlet nozzle in the SSTF test facility functions as a subsonic inlet duct when in the fully-open (nozzle centerbody forward) configuration, and as a converging-diverging (c-d) supersonic nozzle when in the partially- to fully-closed range of positions (see Chapter 3), provided that the static pressures at the nozzle exit are low enough to sustain supersonic flow there. While operating as a supersonic nozzle, the nozzle is choked at its throat and the nozzle flow field is independent of the conditions at the nozzle exit.

In this appendix the performance of the nozzle and the quality of the nozzle exit flow field are documented for the range of *supersonic* nozzle-exit conditions corresponding to the supersonic range of the SSTF fan. Experimental data are presented and compared with CFD results obtained using the axisymmetric duct code DVC2D, described in Chapter 4. Note that it is important to document the supersonic nozzle-exit flow field because the downstream flow field in the SSTF rotor are determined by it.

The nozzle was designed for an exit Mach number of 2.0 with near-uniform flow from hub to tip, as described in Reference 27. As will be shown here, the experimental and computational results confirm that the nozzle performs much as designed, and that it performs well over the range of exit Mach numbers from 1.4 to 2.0. Furthermore, there is generally very good agreement between the computational and experimental data, thus enabling inferences to be made from the CFD results regarding specific flow field details; for example, the CFD solutions supply information about the nozzle total-pressure ratio and the endwall boundary layers at the nozzle exit [1].

---

[1] These boundary layers are ingested by the fan.

The experimental data discussed in this appendix were taken from Reference 47. In that reference the data indicated a significant total-pressure loss in the free-stream region of the nozzle flow field, for conditions where the exit flow was supersonic [2]. Since there are no reasonable explanations [3] for such a loss to exist, an alternate data reduction method has been used to calculate some of the experimental results presented herein. Specifically, spanwise (radial) traversing probe [4] measurements at the nozzle exit have been reduced using the alternate method, while the endwall results (isentropic Mach numbers) are the same as originally reported.

The alternate method assumed negligible total-pressure losses in the free-stream region. Thus, differences between the plenum total pressure and the probe "Pitot" pressures were all attributed to the probe bow shock, which is always virtually "normal" to the small portion of flow impacting the Pitot tube. The free-stream Mach numbers were iteratively calculated using the well-known equation for the total-pressure ratio across a normal shock [53], the total-pressure ratio in this case being that of the pitot pressure to the plenum total pressure. In the endwall boundary-layer regions the assumption of negligible total-pressure loss was not valid, however, so that a different approach was taken; namely, the Rayleigh Pitot equation [53] was applied using the 'known" static pressure nearest the Pitot-tube location. Note that in all cases the known static pressures were reduced values from the edge of the free-stream region, rather than directly measured values from the endwall static taps.

---

[2] The measured total-pressure losses within the free-stream were typically between 2 and 5 percent.

[3] Other than humidity effects (condensation shocks), there are no plausible aerodynamic features which could produce the levels of total-pressure loss indicated by the experimental data. The dry air supplied to the facility leaves the possibility of significant humidity effects very small, however. The experimental (and computational) endwall static pressures (isentropic Mach numbers) confirm that all shock waves in the nozzle were oblique and very weak (nearly isentropic).

[4] Five-hole cone probes (see Chapter 3 and Appendix B) measured cone-surface static pressures and the total pressure *behind the bow shock wave of the probe.* The "undisturbed" flow conditions were determined using aerodynamic calibration curves.

Experimental nozzle exit Mach numbers determined using the alternative method are listed in Table A.1, where the values calculated using the Rayleigh Pitot equation are in parenthesis. Average Mach numbers are also included at the bottom of the table, these values being determined by arithmetic averaging as noted.

Table A.1 Radial distributions of experimental Mach numbers at the nozzle exit (modified from Reference 47)

Radial Position	Radius (inches)	Reading Number			
		462	461	460	459
1	9.803	(1.331) [a]	(1.608)	(1.747)	(2.032)
2	9.704	(1.377)	(1.625)	1.764	2.051
3	9.403	1.385	1.636	1.775	2.046
4	9.104	1.410	1.614	1.778	2.033
5	8.805	1.430	1.658	1.776	1.992
6	8.507	1.417	1.570	1.776	1.997
7	8.209	1.415	1.581	1.759	1.988
8	7.910	1.433	1.594	1.781	1.998
9	7.608	1.412	1.600	1.813	1.986
10	7.305	1.435	1.602	1.813	1.979
11	7.154	(1.311)	(1.506)	(1.725)	(1.901)
Average [b]		1.413	1.599	1.782	2.008

[a] Numbers in parenthesis indicate that the Rayleigh Pitot equation was used with the nearest free-stream static pressure.

[b] Arithmetic average of Mach numbers for radial positions 2 through 10.

The four cases listed in Table A.1, involving nozzle exit Mach numbers ranging from 1.4 to 2.0, are examined in this appendix. The experimental conditions for these cases are listed in Table A.2 where Δx_{cb} is the nozzle centerbody position, which is the distance relative to the fully-open position that the centerbody has been translated in the downstream

direction. Note that these tests were conducted with the nozzle bleed inserts [5] installed (see Chapter 3), but with no operational bleed flow.

Table A.2 Experimental results for the supersonic nozzle

Reading Number	Δx_{cb} (inches)	$\dot{m}$ (lbm/sec)	M_N [a]	$\overline{M}$ [b]	λ [c] percent
462	2.92	47.47	1.403	1.413	3.1
461	3.70	42.76	1.602	1.599	2.9
460	4.70	37.44	1.801	1.782	3.3
459	6.22	31.48	2.002	2.008	2.8

[a] Nominal Mach number based on an arithmetic average of the hub and casing endwall static pressures for the taps located 1.0 inch upstream of the nozzle exit (see Chapter 3).

[b] Arithmetic average of Mach numbers at the nozzle exit for "free-stream" radial positions 2 through 10 (see Table A.1).

[c] Area-blockage factor based on $\dot{m}$ and $\overline{M}$, as calculated using Equation (A.1).

Results obtained by post-processing of CFD flow-field data are listed in Table A.3, where the parameters are the same as those shown in Table A.2. Mach number contour plots for two of the CFD flow fields — exit Mach numbers 2.0 and 1.4 — are shown in Figure A.1. Comparing Tables A.2 and A.3, the corresponding experimental and computational mass flow rates $\dot{m}$ are in good agreement, with discrepancies of less than 0.25 lbm/sec (0.8 percent), which is well within the experimental uncertainty of 0.5 lbm/sec reported in Reference 47. Similarly, the *nominal* Mach numbers M_N, the "average" Mach numbers $\overline{M}$, and the area blockage factors λ at the nozzle exit also exhibit good agreement between experiment and computation. The area blockage was essentially constant at about 3 percent over the entire range of supersonic exit Mach numbers.

[5] Tests were also performed using solid inserts in place of the bleed-ring inserts, but these results are not included since the fan was tested with the bleed inserts installed.

Table A.3 Computational results for the supersonic nozzle

Δx_{cb} (inches)	$\dot{m}$ (lbm/sec)	M_N [a]	$\overline{M}$ [b]	λ [c] percent
2.92	47.49	1.405	1.421	2.7
3.70	42.82	1.596	1.595	3.0
4.70	37.66	1.775	1.778	3.1
6.22	31.71	1.980	1.995	3.1

[a] Nominal Mach number based on an arithmetic average of the hub and casing endwall static pressures at a location 1.0 inch upstream of the nozzle exit.

[b] Average nozzle exit Mach number based on $\dot{m}$ and λ, as calculated using Equation (A.2).

[c] Area-blockage factor based on boundary-layer displacement thicknesses.

The experimental area-blockage factors λ in Table A.2 were calculated from the average Mach numbers and the orifice-measured mass flow rates using the following form of the one-dimensional continuity equation for a perfect gas:

$$\lambda = 1 - \frac{\dot{m}}{\rho_{t0}\, a_{t0}\, A_1 \bar{\phi}} \tag{A.1}$$

where $\bar{\phi} = \phi(\overline{M})$, and the mass-flux parameter ϕ is defined in the **Symbols and Notation**. This same equation, albeit rearranged, was also used in connection with the CFD results to calculate the average Mach numbers $\overline{M}$ in Table A.3, from the computed mass flow rates and the area blockage factors:

$$\bar{\phi} = \frac{\dot{m}}{\rho_{t0}\, a_{t0}\, A_1 (1-\lambda)} \tag{A.2}$$

where $\overline{M} = M(\bar{\phi})$. The area blockages for Equation (A.2) were determined from the computed (CFD) boundary-layer displacement-thicknesses at the nozzle exit. These displacement thicknesses as well as other boundary-layer features of the nozzle flow will be discussed after first comparing more experimental and computational results.

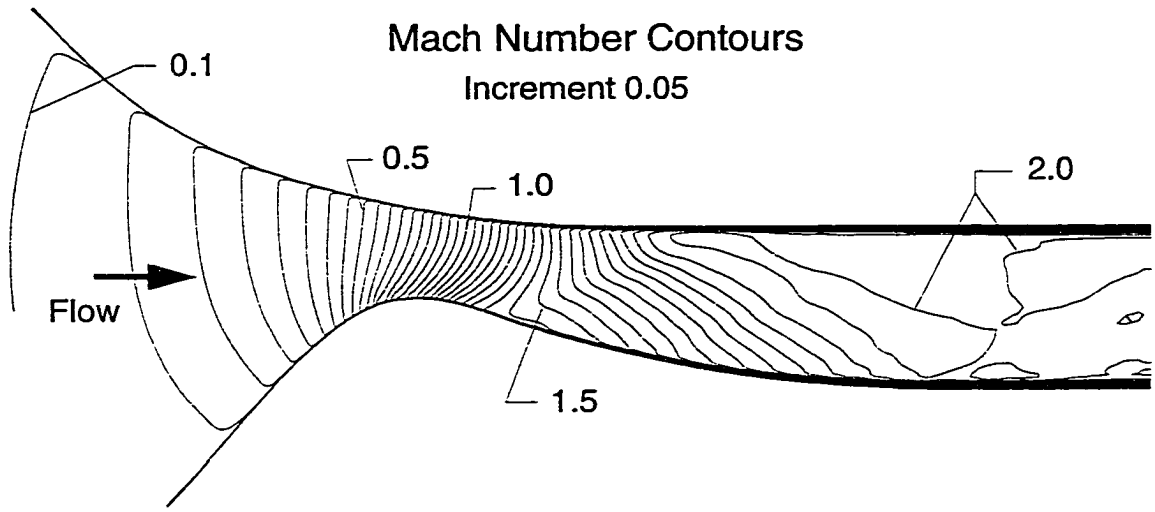

(a) design condition with centerbody position Δx_{cb} at 6.22 inches

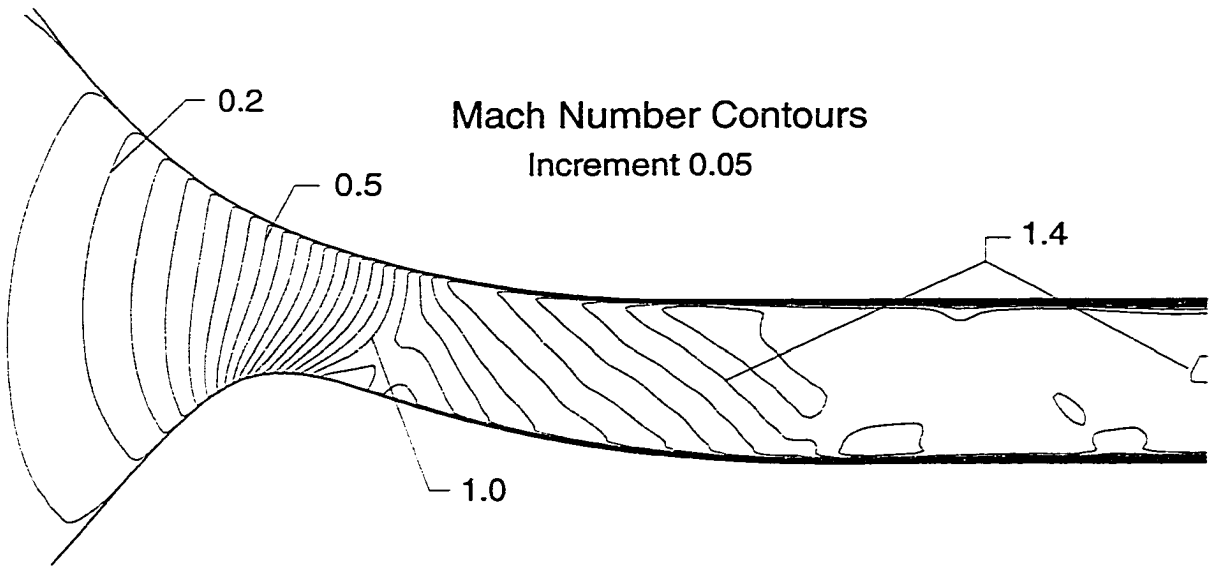

(b) off-design condition with centerbody position Δx_{cb} at 2.92 inches

Figure A.1 Computed nozzle Mach number contours for two centerbody positions

The tabular results compared so far represent global, or integrated, parameters. Two basic types of *local* distributed results are now compared: isentropic endwall Mach numbers along the length of the nozzle, and the spanwise Mach number distributions at the nozzle exit. The computational and experimental distributions of isentropic wall Mach numbers are shown in Figures A.2 and A.3 for the hub and casing, respectively. As can be seen the agreement is good in all four of the cases. The spanwise Mach number distributions in the annulus at the nozzle exit (rotor hub leading edge; axial coordinate $x = 0.000$ inches) are compared in Figure A.4. Again the agreement is good, being similar in magnitude to that for the endwall data where Mach number differences less than 0.05 (2 to 4 percent) are observed. The corresponding spanwise distributions of (dimensionless) total-pressure are shown in Figure A.5, where it should be noted that the alternate data-reduction method has resulted in the experimental free-stream total pressures being identically equal to one; that is, the experimental total pressures in the figure were not measured, but are assumed (to be equal to the plenum total pressure).

The endwall boundary-layer development along the length of the nozzle can be seen by graphing the displacement and overall boundary-layer thicknesses against axial location. Results of this type are presented in Figures A.6 and A.7 for two of the computed flow fields. To estimate the boundary layer thicknesses an approximate method was used, which is currently undocumented, but is very similar to an experimental data reduction procedure described by Zierke and Deutsch [77]. The first case, shown in Figure A.6, is for the design operating configuration with Δx_{cb} at 6.22 inches, corresponding to an exit Mach number of 2.0. The upper curves in the figure show the hub and casing endwall boundary-layer thicknesses, and the bottom curves show the corresponding displacement thicknesses. The second case, shown in Figure A.7, is for the configuration with Δx_{cb} at 2.92 inches, corresponding to an exit Mach number of 1.4. Notice that both cases are very similar and the boundary layers at the nozzle exit were computed to be between 0.20 to 0.25 inches thick, which agrees reasonably well with the experimental hub and casing boundary-layer thicknesses of 0.25 inches reported in Reference 47.

A list of the nozzle-exit hub and casing endwall displacement and overall boundary-layer thicknesses is provided in Table A.4 for all four CFD cases. The table also contains the corresponding overall average total-pressure ratios computed for the nozzle. Notice that the average total-pressure ratio decreases almost linearly with increasing exit Mach

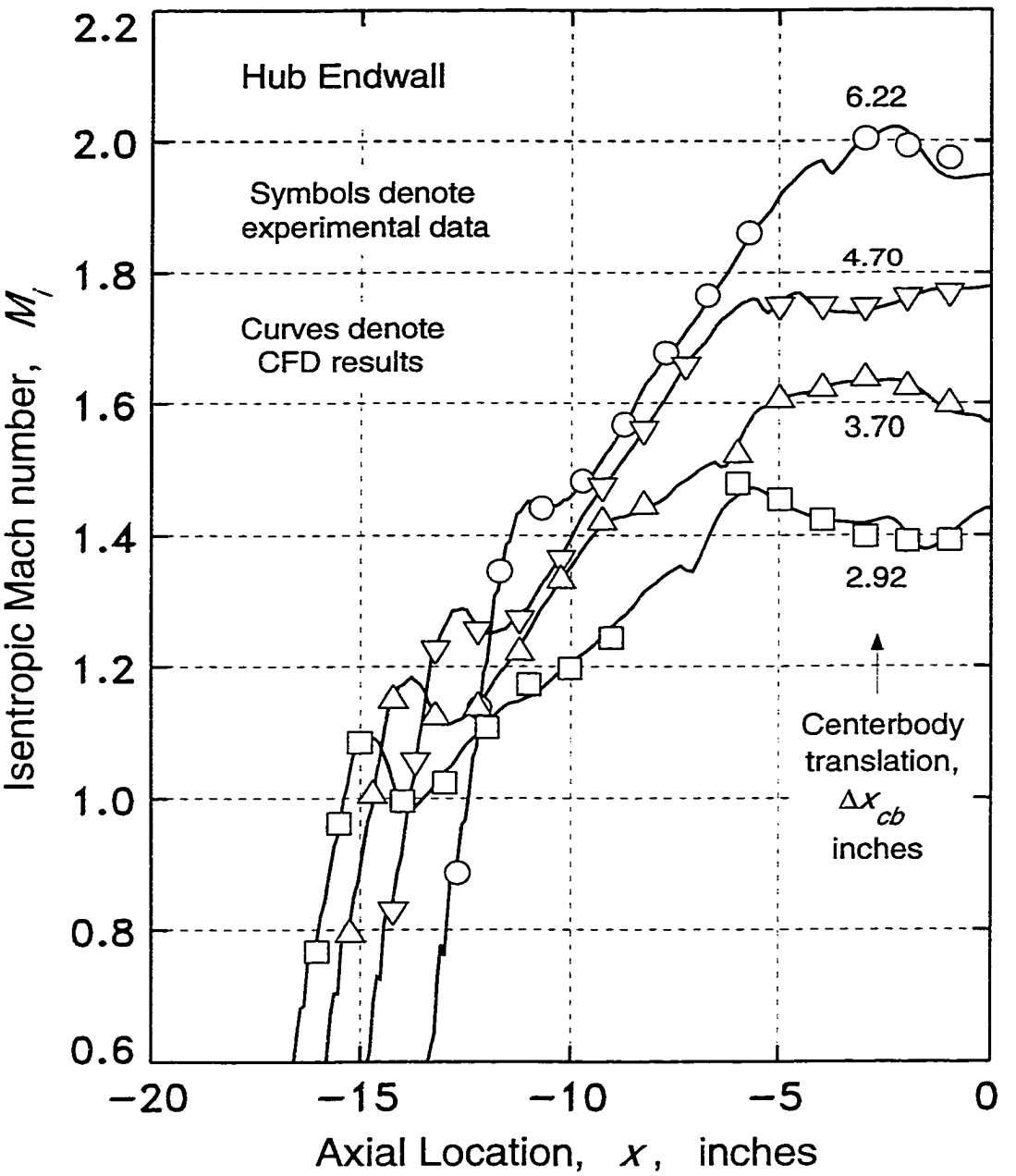

Figure A.2 Comparisons of experimental and CFD isentropic Mach number distributions along the hub endwall of the supersonic nozzle

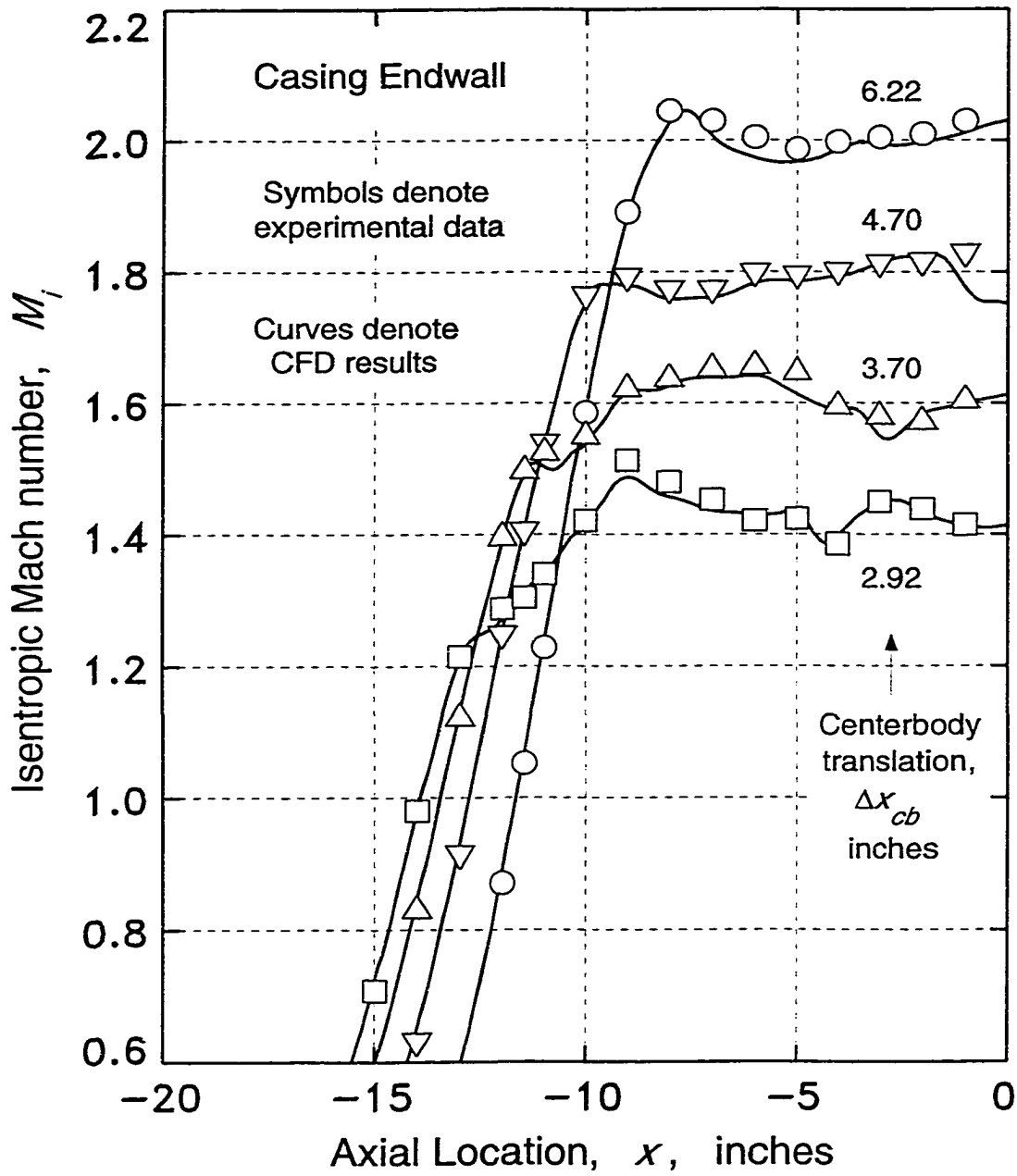

Figure A.3 Comparisons of experimental and CFD isentropic Mach number distributions along the casing endwall of the supersonic nozzle

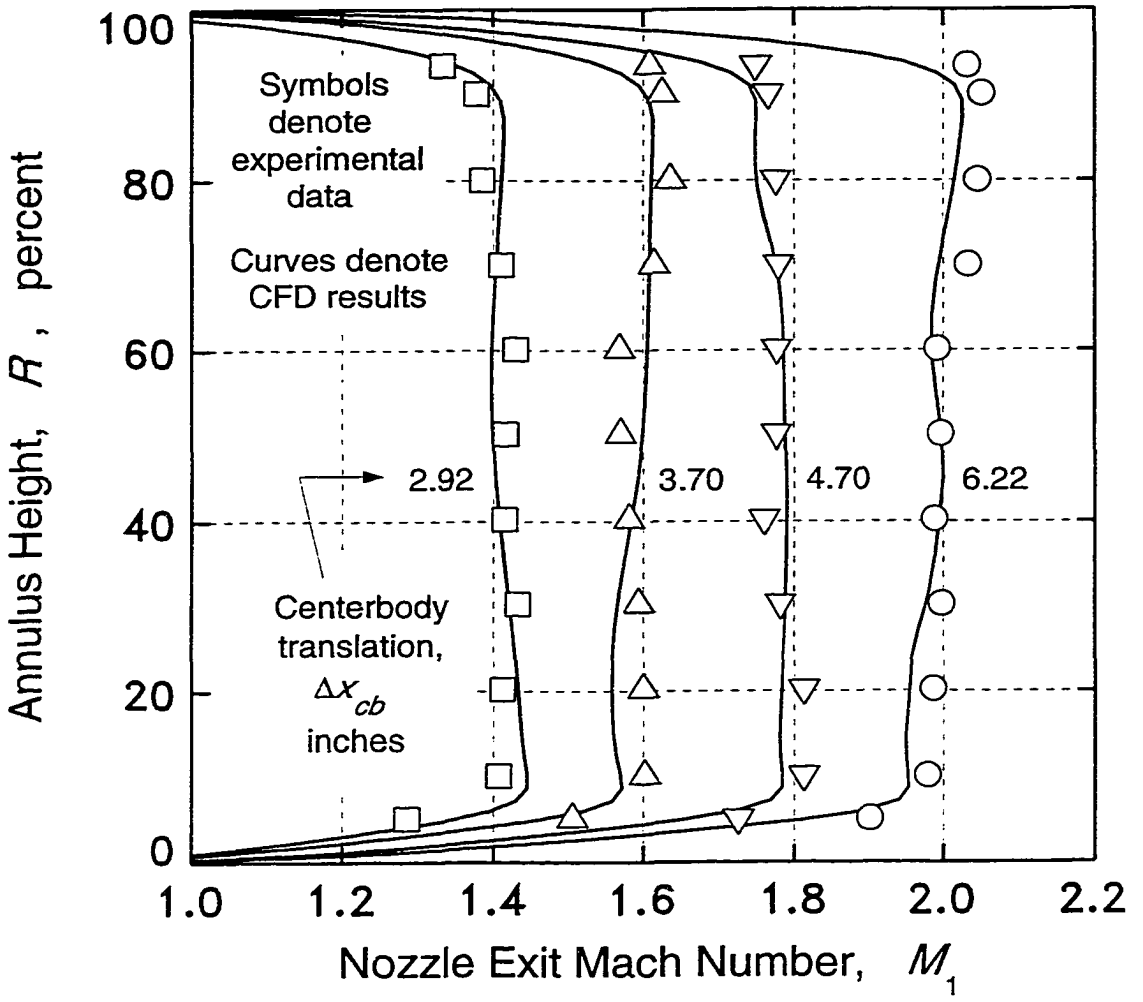

Figure A.4 Comparisons of experimental and CFD Mach number radial distributions at the supersonic nozzle exit

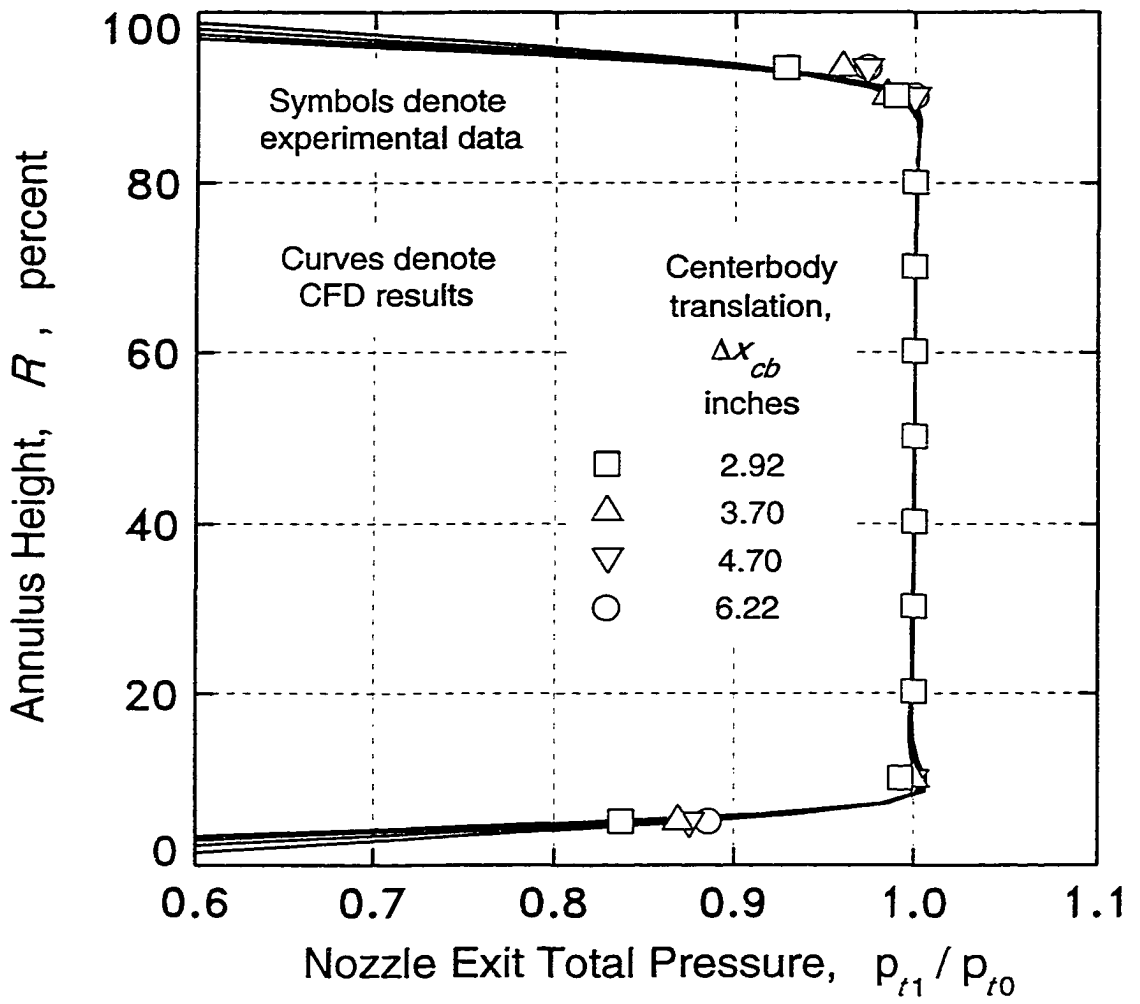

Figure A.5 Comparisons of experimental and CFD total-pressure radial distributions at the supersonic nozzle exit

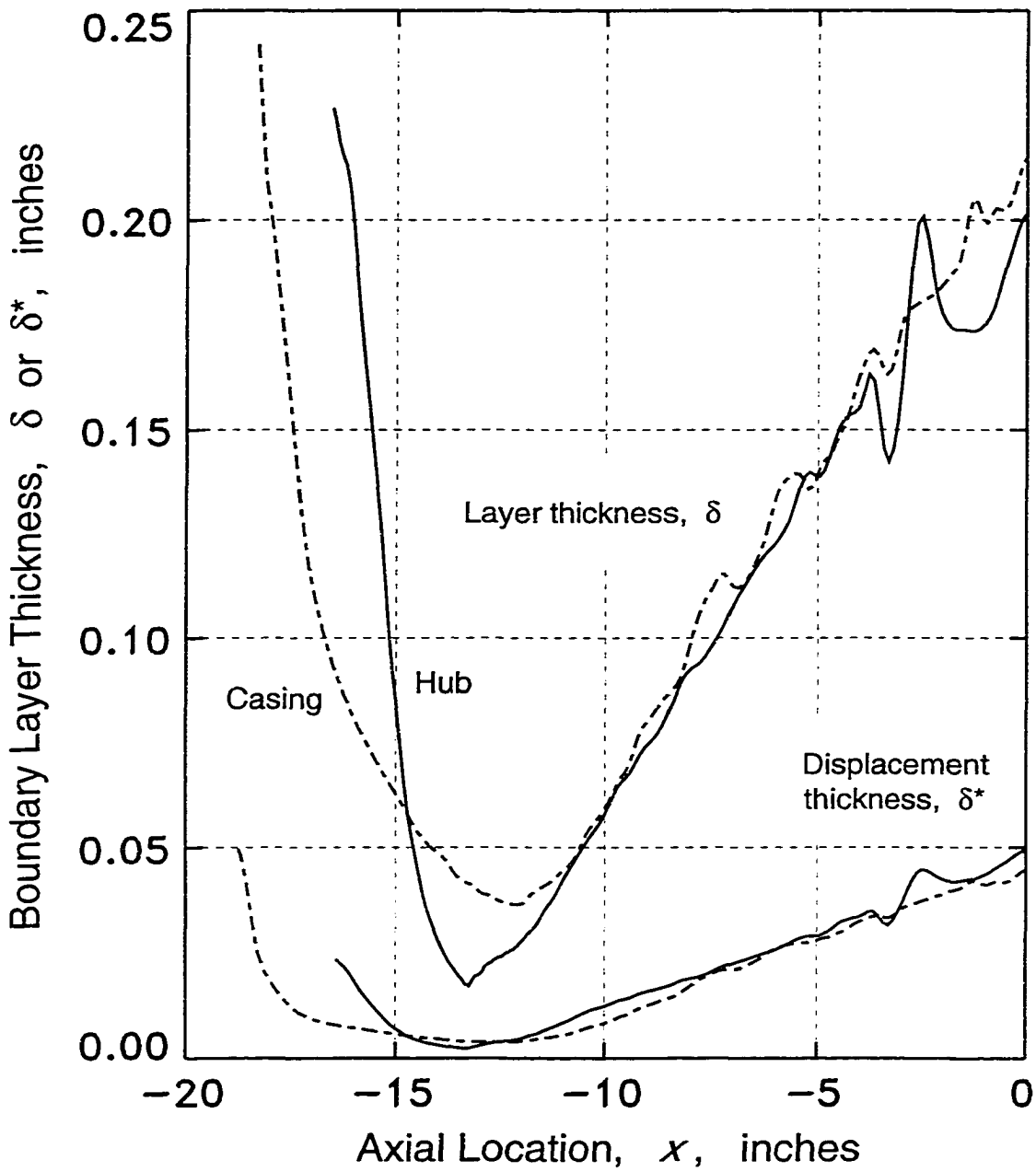

Figure A.6 Computed boundary-layer development along the supersonic nozzle end-walls for the design operating condition (Δx_{cb} = 6.22 inches; exit Mach number 2.0)

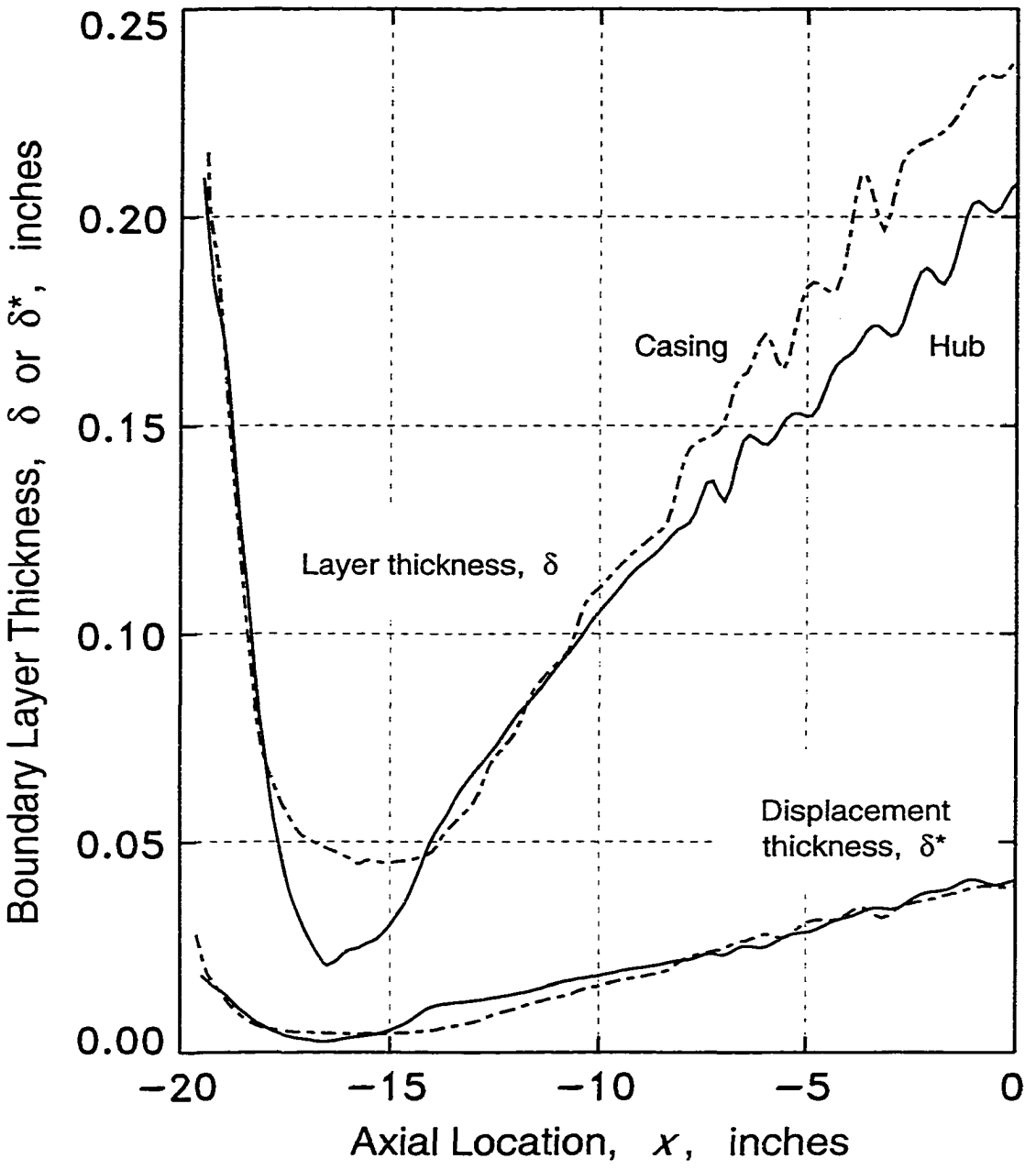

Figure A.7 Computed boundary-layer development along the supersonic nozzle end-walls for an off-design operating condition (Δx_{cb} = 2.92 inches; exit Mach number 1.4)

number (see Table A.3 for the corresponding Mach numbers). Although this trend is certainly in the right direction, no experimental assessment of the computed total-pressure results can be made due to the many difficulties inherent in attempting to measure this type of data.

Table A.4 Nozzle exit parameters derived from CFD flow fields

Δx_{cb} (inches)	δ^*_{hub} (inches)	δ^*_{tip} (inches)	δ_{hub} [a] (inches)	δ_{tip} (inches)	$\bar{s}\,\bar{p}_t / p_{t\,0}$ [b]
2.92	0.041	0.040	0.208	0.237	0.967
3.70	0.047	0.043	0.212	0.248	0.961
4.70	0.046	0.046	0.202	0.223	0.956
6.22	0.049	0.045	0.202	0.215	0.950

[a] The hub and tip boundary-layer thicknesses are based on the distance from the endwall where the velocity is 99 percent of the free-stream velocity.

[b] The overall total pressures are based on an *entropy-averaging* procedure (see Appendix C), which is denoted by the upper-left superscript, $\bar{s}$.

To conclude this appendix, a graph of the free-stream-average Mach number $\overline{M}$ verses the nozzle centerbody position Δx_{cb} is presented in Figure A.8. Two sets of data are shown in the figure, one set for the experimental results (listed in Table A.2) and the other for the CFD results (listed in Table A.3). Both sets are nearly the same. The quadratic curve through the data was obtained by a least-squares regression of the CFD results and represents the approximate schedule for setting the average nozzle-exit Mach number. The inverse form of the quadratic equation in Figure A.8 can be used to determine the nozzle centerbody translation (in inches) as a function of the nozzle exit Mach number:

$$\Delta x_{cb} = 9.128 - \sqrt{83.319 - 52.219\,(\overline{M} - 0.5607)} \qquad \text{(A.3)}$$

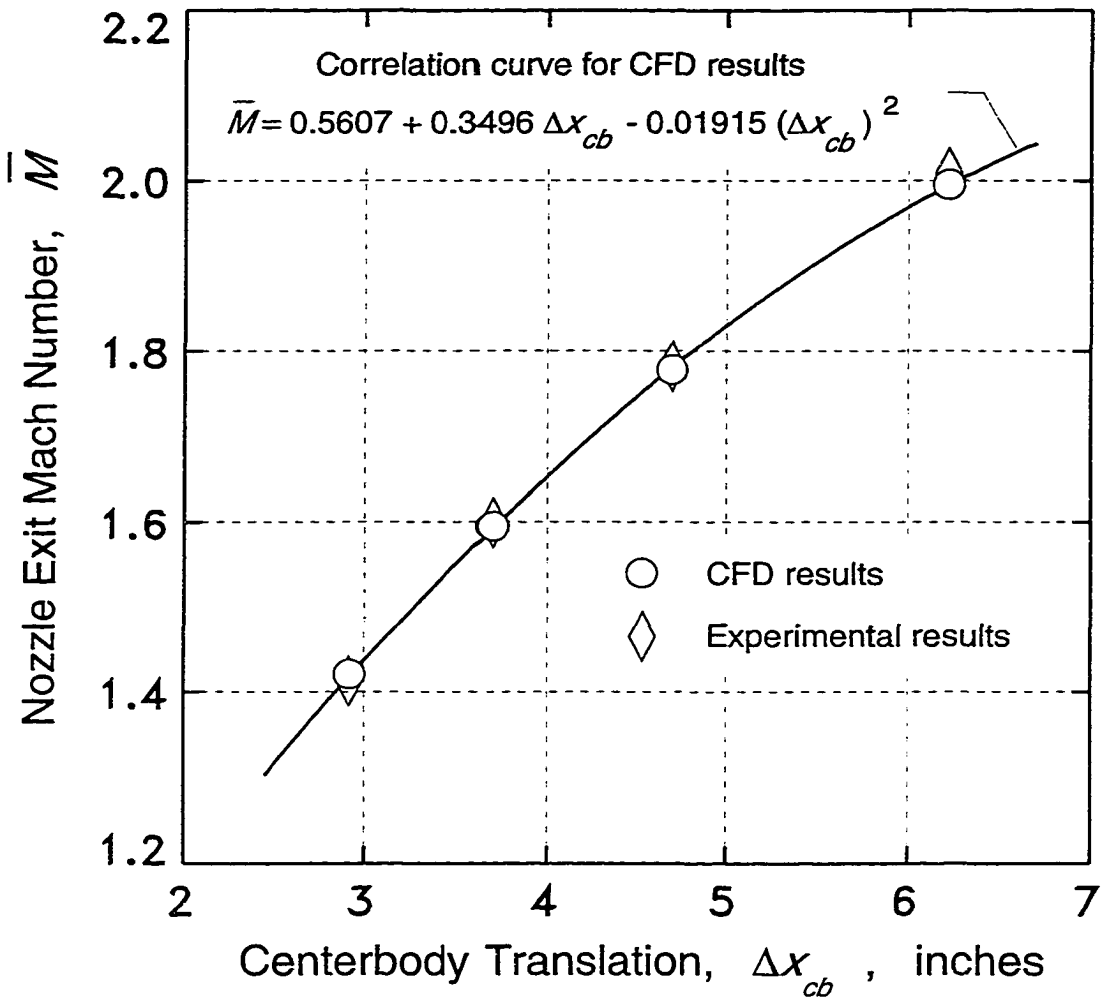

Figure A.8 Approximate centerbody schedule for setting average nozzle-exit Mach number

APPENDIX B.
PROBLEMS IN COMPARING COMPUTATIONAL AND EXPERIMENTAL RESULTS

An important aspect of the SSTF research program is the application and assessment of computational fluid dynamics (CFD) codes. Any attempts to assess the accuracy of the computational results by comparisons with the experimental data, however, presuppose some knowledge about the accuracy of the experimental data. The purpose of this appendix is to address some of the baseline SSTF experimental uncertainties and the associated problems in making valid quantitative comparisons of computational and experimental results. Note that the scope of this investigation precludes a complete and detailed analysis of experimental uncertainties, so only an approximate first-order analysis is presented.

At the outset it should be emphasized that many of the problems encountered in making valid comparisons of computational and experimental results ensue from experimental measurement difficulties and practical limitations, the majority of which are common to aerodynamic measurements in high-speed turbomachinery. The presence of supersonic probe-relative velocities, however, results in significantly larger measurement errors. These larger errors occur in part because of the nature of the flow field being measured (large flow gradients in shock and expansion waves, and in deep, narrow blade-wakes), and in part because of the propagation of primary measurement errors into the reduced (calculated) quantities.

Before proceeding further, a general comment regarding the contents of this appendix is appropriate. Specifically, the focus of this appendix is on experimental problems and weaknesses, rather than on computational limitations. The main reason for this focus is that according to conventional wisdom in turbomachinery fluid dynamics, the experimental data are normally assumed to be the proper standard for comparison. Although this may be a good general approach, it could lead to incorrect conclusions when axial-supersonic (supersonic probe-relative) velocities are involved.

The accuracy of the CFD results cannot be assessed in an absolute sense apart from comparisons with accurate experimental data. It is possible, however, to identify several major sources of uncertainty related to the computational analyses, as is done next in order to provide some "balance" to this critical discussion of experimental problems and uncertainties. The experimental issues are then discussed in a subsequent section. Note that the treatment of CFD-related issues is only brief and qualitative, whereas the treatment of experimental problems is more extensive and includes some equations for determining quantitative information about error propagation.

Factors Influencing Computational Uncertainties

The computational methods involve several simplifying assumptions which may be important, depending on the sensitivity of the aerodynamics and performance of the rotor to these assumptions. Some of the factors which may lead to significant errors in the computational results, or to significant differences between the computational and experimental results, are listed below in their approximate order of importance:

- Boundary-layer turbulence modeling, including boundary-layer transition effects and wake (free shear-layer) turbulence modeling. This category may also partially relate to an inability of CFD to correctly simulate shock/boundary-layer interaction regions in many cases.

- Grid density. The grids around turbomachinery blade surfaces are typically "coarse" in the streamwise direction at locations where shock wave impingement occurs. This has an impact on the spatial resolution of the associated shock/ boundary-layer interaction regions. Note that the thin-layer approximation used in the CFD code formulation assumes *a priori* that the streamwise grid resolution is too low to resolve the streamwise viscous effects, which are therefore neglected.

- Geometric deviations from design coordinates. The design coordinates, assuming perfect blade-to-blade periodicity, were used for CFD simulations. The experimental rotor lacked perfect blade-to-blade periodicity, did not deform under operational loading to the exact design ("hot") coordinates, and had blade-root fillets. The fillets were not included in the geometry analyzed using the CFD codes.

- Rotor tip clearance model. Only a simple, first-order model was used in the CFD simulation for design-point operation. No tip clearance model was used in the off-design simulations.
- Artificial dissipation effects in the CFD solutions.
- Surface roughness and free-stream turbulence effects in the experimental results. These effects were not modeled in the CFD methods.
- Rotor inlet boundary condition for CFD simulations. It was only approximate and not identical to the nozzle exit flow profile (see Appendix A).
- Experimental rotor blade geometric variations from design-point blade deflections to off-design deflections. This category applies only to CFD simulations at off-design operating points.

The above list is based on the subjective judgement of the author and is not considered exhaustive. Furthermore, it applies only to the baseline SSTF rotor. It should be noted that the top three categories are believed to be *potentially* more influential than the others. The fifth factor is also potentially large, but is believed to have been kept small by using relatively fine grids and giving careful attention to the artificial dissipation scheme implemented in the codes. Although unproven and uncertain, most of the factors are thought to be of only second- or third- order significance *for this particular type of fan* operating with a tight tip-clearance. Finally, as a closing comment a disclaimer might be issued; that is, since the above list is subjective there is considerable room for misjudgment. Nevertheless, the conclusions are presented in an attempt to provide the reader with the benefit of at least some of the author's recent experience in this area.

Factors Influencing Experimental Uncertainties

The experimental uncertainties stem from an entirely different set of factors than do the CFD-related uncertainties. As just discussed, in the latter case the difficulties are in the realm of numerically simulating the "physically correct" flow field, including also the proper modeling of all geometric and aerodynamic boundary conditions. In the experimental situation, on the other hand, the "correct" flow field always exists, but there is the problem of accurately controlling all the important boundary conditions (i.e., the problem

of performing a controlled experiment) and the problem of accurately measuring the flow field at the desired locations. Regarding these issues, namely the design and instrumentation of an experimental facility, practical considerations and the state-of-the-art measurement technology play major roles.

The accurate aerodynamic measurement of high-speed turbomachinery flow fields and the associated aerodynamic performance has long been considered a difficult task involving several complex issues [78]. The purpose here is not to discuss these issues *per se*, except as they directly relate to the measurement problems peculiar to the baseline SSTF experiments. Briefly stated, the basic measurement problem can be summarized as follows: "Using stationary aerodynamic instrumentation, accurately measure the kinematic and thermodynamic properties of an unsteady, highly non-uniform, supersonic flow field." As is well known, the influences of flow unsteadiness and three-dimensionality are generic to turbomachinery flow field measurement, and in themselves create difficulties. Unfortunately, the supersonic velocities of the SSTF flow result also in relatively large primary measurement errors, which are then amplified through the data reduction equations. Note, however, that this effect is confined mostly to measurements involving intrusive probes (traversing probes and rakes), and not so much to the non-intrusive measurements of endwall and blade surface static pressures.

Aerodynamic measurement problems

Descriptions of the SSTF experimental facility, its instrumentation, and the methods for reducing the experimental data are given in Chapter 3. For the present discussion it should be noted that most of the aerodynamic measurements in the SSTF facility, and all of the measurements under consideration, involved *slow-response* instrumentation. Furthermore, all measurements downstream of the rotor involved a highly-unsteady flow field with relatively large fluctuations in flow properties. The coexistence of shock waves, rapid supersonic-expansions, and deep, narrow blade-wakes [1] (in the relative frame-of-

[1] CFD results indicate that supersonic wakes dissipate much less with downstream distance than do subsonic wakes. Even though the turbulence model might be underpredicting the turbulent wake diffusion, this effect would still be very pronounced.

reference of the rotor), all contributed to a flow field with large temporal variations in quantities measured in the absolute frame-of-reference.

The unsteadiness of the flow does not appear in any of the experimental data since the slow-response instrumentation integrates out the unsteadiness, thereby providing a form of steady-state measurement. The exact type of average provided by the instrumentation is unknown, but is often *assumed* to be a time-average for each particular quantity measured [79]. Since, however, the resulting steady-state measurement values *may* in fact depend on the form of the unsteady signal [2] being processed by the instrumentation, an uncertainty exists which is difficult to quantify. Furthermore, it might be expected that the level of this uncertainty in these steady-state measurements would be larger for larger unsteady fluctuations.

In measuring the supersonic flow with the rake downstream of the SSTF rotor, the above "commonly occurring" unsteady flow measurement problem existed and was aggravated by the additional complexity of the measurement-probe (rake-element) aerodynamics. The steady-state total pressure of the flow, for example, was not measured directly since each rake-element generates a bow shock wave upstream of itself, as illustrated in Figure B.1. The bow shock produces a total-pressure loss so that the Pitot-tube pressure is substantially less, depending on the supersonic Mach number, than the total pressure of the upstream flow. An aerodynamic calibration of the rakes was used to circumvent this fundamental problem, but it should be recognized that the calibration was performed in a steady flow, and the influences of various forms and magnitudes of unsteadiness on the accuracy of the calibration are unknown. When it is realized that the strengths of normal and oblique shock waves are highly non-linear with variations in incident Mach number — consider here the probe-generated bow shock wave and the fact that it moves (relative to the probe) due to the unsteadiness — then it is reasonable to infer that the unsteadiness *could have* a significant impact on the measurement accuracy.

To demonstrate the unsteadiness levels (magnitudes) involved in the SSTF experiments, graphs showing computed [3] (temporal) variations in Pitot pressure, static pressure,

---

[2] This implies that the steady-state values are not correct time-averages.

[3] The computations were performed using the three-dimensional viscous CFD code.

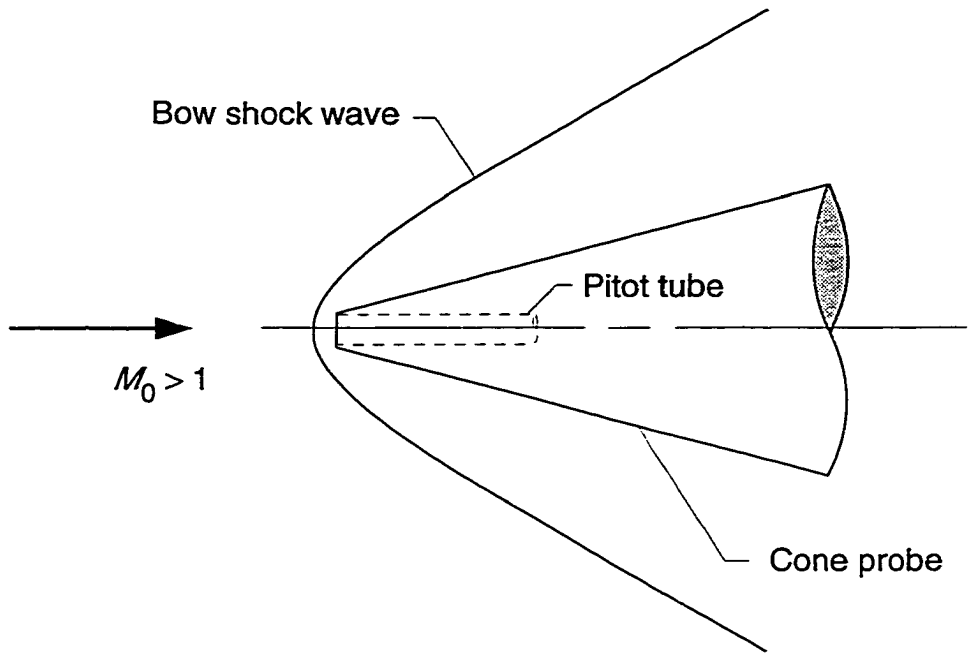

Figure B.1 Rake-element (cone probe) with bow shock wave

and flow Mach number are shown in Figure B.2. These results are for the design operating point, they apply to the midspan rake location downstream of the rotor, and are in the stationary (rake) frame-of-reference.

Propagation of errors (uncertainties)

The errors encountered in primary measurement quantities, especially those described above, are propagated into several reduced quantities of immense practical interest. One of the most important of these reduced quantities is total pressure, from which rotor aerodynamic performance is determined. In the interest of clarity and generality, a few distinctions need to be outlined first before addressing the approximate methods for estimating error propagation.

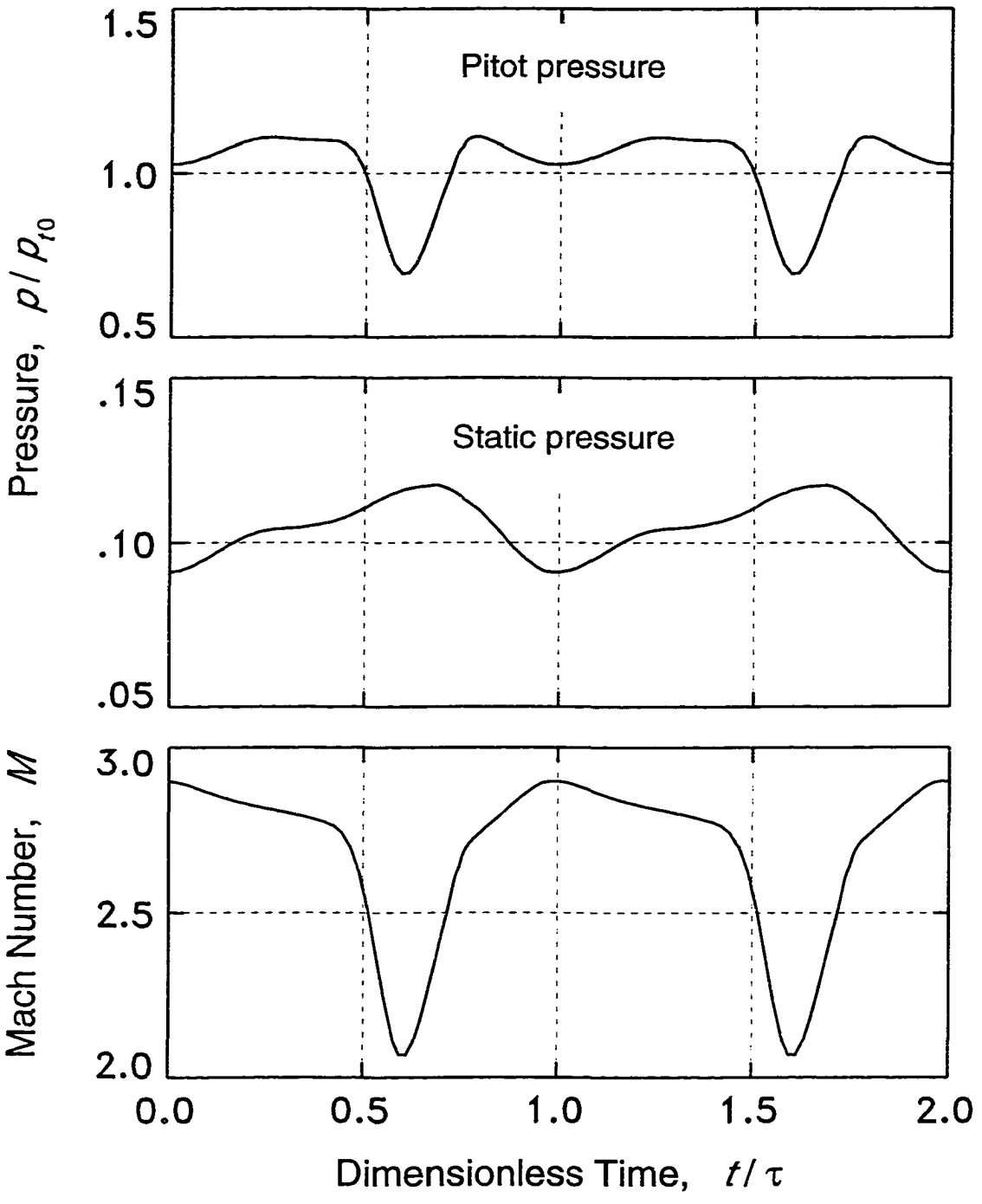

Figure B.2 Flow unsteadiness at the midspan rake location behind the isolated SSTF rotor; three-dimensional CFD solution for design-point conditions

The first distinction relates to the different types of experimental results included as output from the data reduction process. These results may in general be divided into three major groups; namely, *plenum* quantities, *local* quantities, and *spatial-average* quantities. The local quantities, in turn, can be broken down into three basic subgroups:

- Static pressures and corresponding isentropic wall Mach numbers based on static-pressure tap measurement data.
- Mach numbers, static pressures, and total pressures based on five-hole cone probe (pressure rake-element) measurement data.
- Total temperatures based on total-temperature probe measurement data.

Note that other local quantities could be mentioned, but they all follow from the quantities listed above. Also, it might be noted that most of the previous subsection on aerodynamic measurement problems pertained to the second subgroup, i.e., the five-hole cone probe.

The plenum quantities consist of average values for the plenum total-pressure and total-temperature. For convenience, the orifice-measured mass flow rate is also considered as a plenum quantity, even though it is not measured there.

In the case of spatial-average quantities, errors (or uncertainties) in local quantities are propagated through the integration process into the average quantity. Although it is possible to numerically compute this error propagation, this was not done for any of the SSTF results because the difficulties and approximations involved did not warrant such an effort. The uncertainties determined for several of the key local quantities are only rough approximations in the first place, used primarily to show the quantitative effects of the local error (uncertainty) propagation. Therefore, as an approximate procedure the uncertainties in average quantities were obtained by averaging the local uncertainty values in the same manner as the local quantities were averaged.

The errors in local quantities are propagated from the corresponding local primary measurement data, including also a plenum quantity in some cases. Estimated primary-measurement uncertainties due solely to the data acquisition system were given in Chapter 3, in Table 3.1, as obtained from Reference 40 (or 41, 47, 49). The values in Table 3.1 represent a one percent of full-scale measurement uncertainty, and should actually be construed as minimum uncertainty levels because they do not include any of the aerodynamic measurement problems (related to flow unsteadiness) previously discussed.

However, since the reported values are conservative estimates, and since no quantitative assessment of the magnitudes of the aerodynamic-related errors has been performed, the values in Table 3.1 are used as rough overall estimates for purposes of quantifying the effects of error (uncertainty) propagation.

Based on the relative magnitudes of different uncertainties, several simplifications can be made in performing a propagation-of-uncertainty analysis. One such simplification is to neglect the uncertainty in the plenum quantities since, virtually always, the uncertainties in other quantities are relatively much larger. Another simplification is to neglect the uncertainty in total-temperature measurements, which in general is relatively small [4]. For example, in calculating adiabatic efficiencies the total-pressure uncertainty produces virtually all of the uncertainty in efficiency, the plenum and total-temperature measurement uncertainties being negligibly small.

The methods for determining the propagation of uncertainty into isentropic wall Mach numbers, and into the (rake-element) cone-probe measured quantities of Mach number, total pressure, and static pressure will now be discussed. Notice that these two cases are the first two subgroups of local quantities listed earlier. Since the uncertainty calculation for the isentropic Mach number is the simplest and can be done analytically (in closed form), it will be described first.

Isentropic wall Mach number — Letting W_p and W_{pt} denote the uncertainties in the wall static-pressure and reference total-pressure measurements, respectively, the uncertainty W_{Mi} in the isentropic Mach number can be estimated as follows using the uncertainty propagation methods of Kline and McClintok [80] for single-sample measurements:

$$W_{Mi}^2 = \left(\frac{\partial M_i}{\partial p}\right)^2 W_p^{\,2} + \left(\frac{\partial M_i}{\partial p_t}\right)^2 W_{pt}^{\,2} \tag{B.1}$$

---

[4] Total temperature is basically a direct measurement, even for supersonic flow. Some error can be introduced into the measurements, however, through the correction for the probe recovery factor. Based on the probe calibration curve, this correction cannot be expected to normally exceed ± 2°R, suggesting that an overall uncertainty in total temperature might be ± 3°R for supersonic conditions. Even if the total-temperature uncertainty were ± 5°R, it would still be relatively small and insignificant compared to other uncertainties.

where the partial derivatives can be evaluated analytically from the gas dynamic relation used to calculate the isentropic Mach number:

$$M_i = \sqrt{\frac{2}{\gamma - 1}\left[\left(\frac{p_t}{p}\right)^{(\gamma-1)/\gamma} - 1\right]} \tag{B.2}$$

The partial derivatives are the following:

$$-\frac{\partial M_i}{\partial p} = \frac{2 + (\gamma - 1) M_i^2}{2\gamma M_i p} \tag{B.3}$$

$$\frac{\partial M_i}{\partial p_t} = \frac{2 + (\gamma - 1) M_i^2}{2\gamma M_i p_t} \tag{B.4}$$

Cone-probe quantities — The cone-probe quantities of Mach number, total pressure, and static pressure were calculated using empirical calibration curves rather than analytical functions, but the propagation-of-uncertainty can be fairly well estimated by modeling the rake-element flow field as depicted in Figure B.3. The model involves two basic assumptions:

- The vertex-port measures the total pressure downstream of a normal shock wave.
- The flow over the cone approximates that of a Taylor-Maccoll[5] flow [81]. This implies that the vertex-port is small relative to the size of the cone.

Under these two assumptions, and assuming perfect gas behavior, the upstream Mach number, total pressure, and static pressure can be determined from the vertex Pitot pressure p_p and the cone-surface static pressure p_c:

$$M = f_1(p_p, p_c) \tag{B.5}$$

$$p_t = f_2(p_p, p_c) \tag{B.6}$$

$$p = f_3(p_p, p_c) \tag{B.7}$$

---

[5] Taylor-Maccoll flow is an axisymmetric conical flow with a uniform supersonic upstream flow and an attached shock wave at the vertex of the cone.

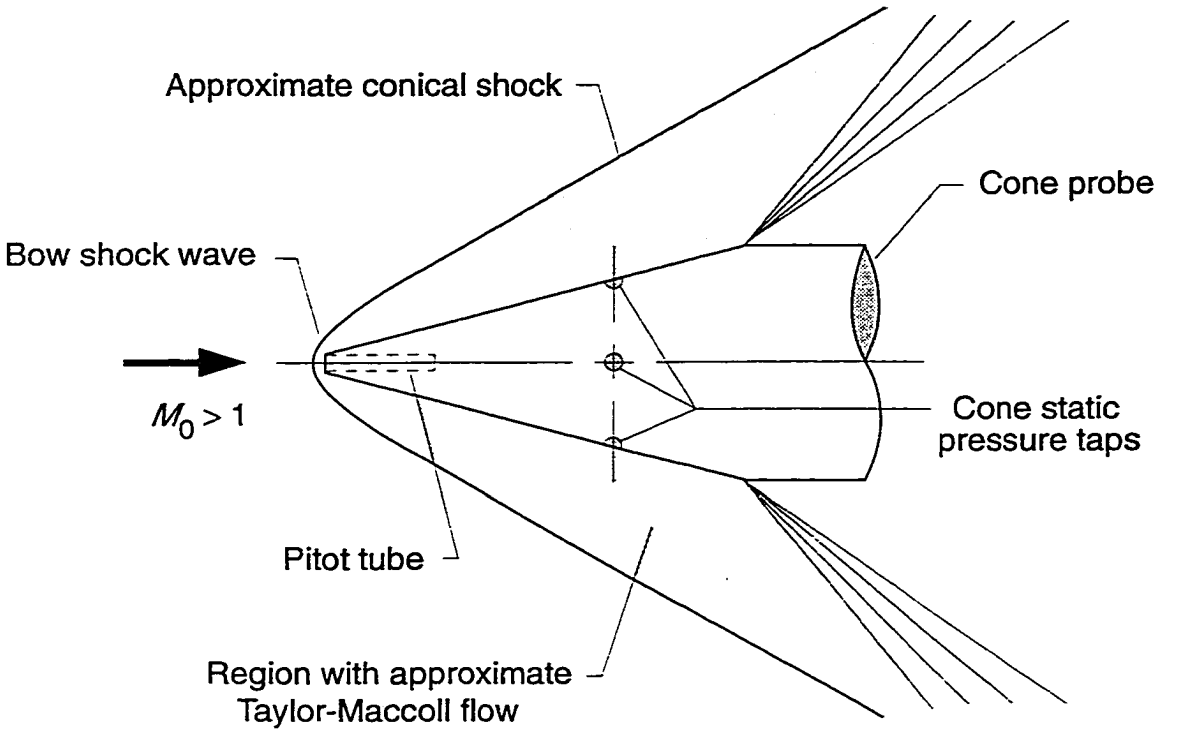

Figure B.3 Rake-element (cone-probe) flow field with conical shock wave

The evaluation of these upstream properties, however, cannot be accomplished in closed form since an iterative procedure, including a numerical integration of an ordinary differential equation at each iteration, is involved [81]. Nevertheless, accurate numerical solutions can be found quickly (1 to 2 seconds) on a small computer. Letting W_{pp} and W_{pc} denote the uncertainties in the primary measurement quantities p_p and p_c, respectively, then the uncertainty for each of the reduced flow properties can be estimated as follows, again using the uncertainty propagation methods of Kline and McClintok:

$$W_M^2 = \left(\frac{\partial M}{\partial p_p}\right)^2 W_{pp}^2 + \left(\frac{\partial M}{\partial p_c}\right)^2 W_{pc}^2 \tag{B.8}$$

$$W_{pt}^2 = \left(\frac{\partial p_t}{\partial p_p}\right)^2 W_{pp}^2 + \left(\frac{\partial p_t}{\partial p_c}\right)^2 W_{pc}^2 \tag{B.9}$$

$$W_p^2 = \left(\frac{\partial p}{\partial p_p}\right)^2 W_{pp}^2 + \left(\frac{\partial p}{\partial p_c}\right)^2 W_{pc}^2 \tag{B.10}$$

where the partial derivatives must be evaluated numerically using Equations (B.5) to (B.7); that is, finite difference approximations are used to approximate the partial derivatives.

At supersonic Mach numbers less than about 1.3, the above approach will not work because the cone shock becomes detached. In this case the uncertainty in the flow static pressure can be assumed equal to the uncertainty in the cone-surface static pressure. With this assumption, which is actually quite good at all supersonic Mach numbers, the uncertainties can be evaluated in closed form as follows:

$$W_p \approx W_{pc} \tag{B.11}$$

$$W_M^2 \approx \left(\frac{\partial M}{\partial p_p}\right)^2 W_{pp}^2 + \left(\frac{\partial M}{\partial p}\right)^2 W_p^2 \tag{B.12}$$

$$W_{pt}^2 \approx \left(\frac{\partial p_t}{\partial M}\frac{\partial M}{\partial p_p}\right)^2 W_{pp}^2 + \left(\frac{\partial p_t}{\partial M}\frac{\partial M}{\partial p}\right)^2 W_p^2 \tag{B.13}$$

where the partial derivatives *at constant static pressure* (used in the W_{pp} terms) are the following:

$$\frac{\partial M}{\partial p_p} = \frac{(\gamma-1)}{2\gamma}\frac{M}{p_p}\left[1 - \frac{2M^2}{2\gamma M^2 - (\gamma-1)}\right]^{-1} \tag{B.14}$$

$$\frac{\partial p_t}{\partial M} = \frac{2\gamma M p_t}{2 + (\gamma-1)M^2} \tag{B.15}$$

and the partial derivatives *at constant Pitot pressure* (used in the W_p terms) are the following:

$$\frac{\partial M}{\partial p} = -\frac{(\gamma-1)}{2\gamma}\frac{M}{p}\left[1-\frac{2M^2}{2\gamma M^2-(\gamma-1)}\right]^{-1} \tag{B.16}$$

$$\frac{\partial p_t}{\partial M} = -\frac{2\gamma}{(\gamma-1)}\frac{p_t}{M}\left[1-\frac{2M^2}{2\gamma M^2-(\gamma-1)}-\frac{(\gamma-1)M^2}{2+(\gamma-1)M^2}\right] \tag{B.17}$$

Note that these derivatives were obtained by differentiation of the well-known gas dynamic equations for either an isentropic flow or the flow through a normal shock wave, whichever was appropriate.

Finally, one last propagation-of-uncertainty formulation will be presented for the special case of Pitot pressure measurements at the exit of the inlet-nozzle. In Appendix A, an alternate data reduction method for calculating the supersonic Mach numbers within the annulus at the nozzle exit was discussed. The method involved the assumption of no total-pressure loss in the free-stream flow, so that the measured plenum total pressure was used with the measured cone-probe Pitot pressure to calculate a free-stream Mach number. In this case the uncertainty in the Mach number can be estimated as follows:

$$W_M^2 = \left(\frac{\partial M}{\partial p_t}\right)^2 W_{pt}^2 + \left(\frac{\partial M}{\partial p_p}\right)^2 W_{pp}^2 \tag{B.18}$$

where the partial derivatives determined from the normal-shock relations for a perfect gas are as follows:

$$\frac{\partial M}{\partial p_t} = -\frac{(\gamma-1)}{2\gamma}\frac{M}{p_t}\left[1-\frac{2M^2}{2\gamma M^2-(\gamma-1)}-\frac{(\gamma-1)M^2}{2+(\gamma-1)M^2}\right]^{-1} \tag{B.19}$$

$$\frac{\partial M}{\partial p_p} = \frac{(\gamma-1)}{2\gamma}\frac{M}{p_p}\left[1-\frac{2M^2}{2\gamma M^2-(\gamma-1)}-\frac{(\gamma-1)M^2}{2+(\gamma-1)M^2}\right]^{-1} \tag{B.20}$$

APPENDIX C.
AVERAGING METHODS FOR COMPUTED FLOW FIELDS

The methods used for obtaining spatially averaged results from the computed flow fields are defined and described in this appendix. To give a broader perspective on the subject of flow field integration and averaging, a brief introductory discussion is provided first, followed by descriptions of the methods for interpolating and averaging the computed flow fields. This appendix concludes with a description of the notation for indicating the various types of averages.

Introduction

As is well known, turbomachinery fluid dynamics routinely involves the consideration or representation of the internal flow fields in *axisymmetric* form. The flow fields are not axisymmetric, of course, but much progress has been made over the past half-century in the design of virtually all types of turbomachinery by employing an axisymmetric flow model in one form or another. Closely related to this axisymmetric representation of turbomachinery fluid dynamics is the *circumferential*, or *blade-to-blade*, averaging of the non-axisymmetric flow fields actually involved. Graphs showing spanwise distributions of various flow quantities are commonly encountered and, although not often explicitly stated, these distributions usually incorporate some type of circumferential averaging, the exact type of which is frequently unspecified. In any case, it should be stressed that circumferential averaging is a very common feature deeply ingrained in the design, analysis, and even measurement methodologies associated with turbomachinery fluid dynamics. Similarly, *spanwise* averaging is also routinely performed on both computed and measured flow fields so as to determine *overall* flow quantities and performance levels for a particular blade row, stage, or series of stages.

There are some general difficulties involved in the averaging of any non-uniform flow field. One of the more elusive of these arises when the attempt is made, either conceptually or otherwise, to equate the "average" flow with the actual flow itself, as is often done, for example, when considering the "axisymmetric" flow through turbomachinery blade rows. Although the properties of the average (bulk) flow usually correspond approximately to many of the local flow properties, the average and distributed flow cases as such are in many respects different. In fact, due to nonlinear relationships between several flow properties it is generally not possible to reduce a particular non-uniform flow field to an equivalent one with fewer degrees of freedom. A consequence of this limitation is that in the integration process certain physical features of the flow field are lost (integrated out) as it were, and it therefore becomes impossible to simultaneously satisfy all of the physical characteristics of the actual flow in a *global*, or *lumped*, set of properties. This basic problem has long been recognized in fundamental fluid dynamics. One common method of partially circumventing the problem has been to introduce coefficients into lumped-parameter equations or systems of equations [1].

For a fluid flow in three spatial dimensions, any three independent kinematic properties (velocity components) and two independent thermodynamic properties completely characterize the state of the fluid. Five such properties may therefore be averaged to determine an average fluid state, where the selection of the properties to be integrated determines (or preserves) five basic characteristics of the fluid dynamic system. As already mentioned above, however, the other characteristics of the original system are not generally maintained by the average properties since some flow properties are nonlinearly related. It is possible to average additional properties and thereby preserve more of the system characteristics, but this over-specification of independent properties introduces inconsistencies into the property relationships and is therefore highly undesirable. For brevity, the fully-consistent set of properties resulting from using the minimum number of

---

[1] Consider as an example the standard "one-dimensional" approach to pipe flow analysis. In the energy equation for the total pressure of the flow there is a coefficient on the kinetic-energy term. This coefficient must be adjusted to account for the difference between the *average* kinetic energies of laminar and turbulent pipe flows, for the "same" *average* velocity based on mass flow rate.

independent property integrations (averages) will be referred to as a *coherent* set in later discussion.

Noting, therefore, that it is generally not possible to average in such a way as to correctly characterize all of the integral properties of the flow field [82], attention can be focused on the more relevant issue; namely, the determination of the most suitable type(s) of average(s). In many cases this issue is relatively unimportant because only small differences exist between the various types of average results. This is often the situation, for example, in the inter-blade-row and downstream flow fields of conventional turbomachinery, as long as the circumferential averaging is performed "far enough" downstream of blade trailing edges. There are cases, however, such as the supersonic throughflow fan or in the inter-blade-row regions of closely-coupled blade rows, where the flow fields are highly non-uniform in the circumferential direction. Under such conditions the selection of an "appropriate" averaging scheme (or schemes) is usually important and should be performed considering the intended use for the averaged results. This selection can be difficult, involving unwanted compromises, and it is associated with an increased complexity in the interpretation and presentation of the final average results.

Interpolation of Computed Flow Fields

Given a computed blade-row flow field, it is typically desired that average flow and performance-related quantities be calculated for two or more "axial" locations. Usually this involves one location upstream of a blade row and one or more locations downstream of a blade row. If the desired locations do not coincide with the grid inlet or exit, then it is necessary to interpolate the flow field solution [2]. To accomplish this, a linear interpolation of the *conservation variables* is adequate since it maintains the second-order spatial accuracy of the numerical scheme. The conservation variables $\hat{q}$ are standard to CFD, and for three dimensions in a cylindrical coordinate system are the following:

---

[2] The C-type grid makes this necessary since, in general, none of the interior grid lines have a constant axial coordinate.

$$\hat{q} \equiv \begin{bmatrix} \rho \\ \rho V_x \\ \rho V_\theta \\ \rho V_r \\ \rho h_t - p \end{bmatrix}$$

Averaging Schemes

Three basic averaging schemes are described below. Each scheme and its designation refers to a *coherent system* of averaging several quantities, rather than to a method for averaging a single quantity as is normally the case. The schemes are designated by the following terms: *momentum average*, *entropy average*, and *energy average*. In defining the averages, a perfect gas is assumed and the three-dimensional formulations are presented since they are the most general.

Momentum average

The term *momentum average* denotes here, by definition, a scheme for averaging several quantities so as to provide a coherent set of average properties which are consistent with (preserve) the integrated flows of mass, energy, and (three components of) momentum through the area being considered [3]. Thus, the average properties applied uniformly over the area of integration represent total flows of mass, energy, and momentum [4] which are equivalent to those occurring through the non-uniformly distributed local properties over the same area. Application of this scheme to a control volume results in average quantities which can be used in conjunction with balances of mass, energy, and (the three components of) momentum for that control volume. In fact, the momentum averaging scheme is derived by using balances for each of the conserved quantities, the conservation laws being applied to an infinitesimally thin control volume bounded on both sides by the

---

[3] This correspondence also applies to an unsteady flow field at an instant in time.

[4] The momentum terms also include a static-pressure force.

area of integration. In a cylindrical coordinate system, the following five equations can be derived:

mass:

$$\dot{m} = \bar{\rho}\,(\overline{V_x}A_x + \overline{V_r}A_r) = \int \delta\dot{m} = \int \rho\,(V_x dA_x + V_r dA_r) \tag{C.1}$$

energy:

$$\dot{m}\,\overline{h_t} = \int h_t \delta\dot{m} \tag{C.2}$$

tangential momentum:

$$\dot{m}\,\overline{rV_\theta} = \int rV_\theta \delta\dot{m} \tag{C.3}$$

axial momentum:

$$\dot{m}\,\overline{V_x} + A_x\bar{p} = \int V_x \delta\dot{m} + \int p dA_x \equiv I_x \tag{C.4}$$

radial momentum:

$$\dot{m}\,\overline{V_r} + A_r\bar{p} = \int V_r \delta\dot{m} + \int p dA_r \equiv I_r \tag{C.5}$$

To complete the system of equations, the equation of state is applied to the average thermodynamic properties:

$$\bar{h} = \frac{\bar{a}^2}{\gamma - 1} = \frac{\gamma}{\gamma - 1}\frac{\bar{p}}{\bar{\rho}} \tag{C.6}$$

and the standard definition of total enthalpy further relates the average thermodynamic and kinematic properties to each other:

$$\overline{h_t} = \bar{h} + \frac{1}{2}\left(\overline{V_x}^2 + \overline{V_r}^2 + \overline{V_\theta}^2\right) \tag{C.7}$$

Notice that Equations (C.1) to (C.5) are the minimum number necessary to solve for a complete set of properties, and the integral term(s) on the right-hand-side of each equation represents a known quantity obtained through integration. The area parameters A_x and A_r represent area projections in the axial and radial directions, respectively.

By inspection it can be seen that the mass flow rate $\dot{m}$, and the average total-enthalpy $\overline{h_t}$, are directly determined. The average tangential velocity $\overline{V_\theta}$ is also calculated directly using a mass-averaged radius:

$$\dot{m}\,\bar{r}^2 = \int r^2 \delta\dot{m} \tag{C.8}$$

where it is assumed [5] that $\bar{r}\,\overline{V_\theta} = \overline{rV_\theta}$. [6] The other average properties must be determined by solving the remaining set of simultaneous equations. A solution to the equation set is obtained in closed form by solving for the average static pressure $\bar{p}$, resulting in the following solution to a quadratic equation:

$$\bar{p} = b \pm \sqrt{b^2 + c} \tag{C.9}$$

where the constants b and c are defined as follows:

$$b \equiv \frac{1}{\gamma+1}\left[\frac{I_x A_x + I_r A_r}{A_x^2 + A_r^2}\right] \tag{C.10}$$

$$c \equiv \frac{\gamma-1}{\gamma+1}\left[\frac{I_x^2 + I_r^2 - \dot{m}\,(2\overline{h_t} - \overline{V_\theta}^2)}{A_x^2 + A_r^2}\right] \tag{C.11}$$

The two roots of the equation correspond to the axial-subsonic and axial-supersonic solutions for mass flow continuity. The positive sign should be used to obtain an axial-subsonic root when the bulk of the flow is axial-subsonic, and conversely, the negative sign

---

[5] Except for averages over the entire annulus area, this assumption is not really necessary since all circumferential integrations are performed at a constant radius.

[6] For adiabatic flow, changes in tangential momentum and total enthalpy across a turbomachinery blade row are related to each other through the rotational speed Ω of the blade row:

$$\Delta\overline{h_t} = \Omega\Delta\,(\overline{rV_\theta})$$

Therefore the mass-averaging of tangential momentum in Equation (C.3) is fundamentally consistent with the mass-averaging of total enthalpy in Equation (C.2).

should be used to obtain an axial-supersonic solution. With the average pressure known, the remaining velocities can be calculated from the corresponding momentum equations:

$$\overline{V_x} = \frac{I_x - A_x \bar{p}}{\dot{m}} \tag{C.12}$$

$$\overline{V_r} = \frac{I_r - A_r \bar{p}}{\dot{m}} \tag{C.13}$$

Finally, the density is determined using the equation of state:

$$\bar{\rho} = \frac{\gamma}{\gamma - 1} \frac{\bar{p}}{\bar{h}} \tag{C.14}$$

where the static enthalpy is calculated from the average total-enthalpy and the average velocities using a slight variation of Equation (C.7).

Entropy average

The *entropy average* is similar to the momentum average in that it results in a coherent set of flow properties, and is compatible with mass and energy conservation. The integrations for mass, energy, and tangential momentum (Equations (C.1), (C.2), and (C.3)) are the same, but the axial and radial momentum integrations (Equations (C.4) and (C.5)) are replaced with an integration for the average entropy:

$$\dot{m}\,\bar{s} = \int s \delta \dot{m} \tag{C.15}$$

The specific entropy for a perfect gas can be expressed as a simple logarithmic function of *dimensionless* [7] total pressure and total enthalpy:

$$\frac{s}{c_p} = \ln\left[\frac{h_t}{p_t^{(\gamma-1)/\gamma}}\right] = \ln\left[\frac{h_t}{h_{t\,i}}\right] \tag{C.16}$$

---

[7] These quantities are non-dimensionalized by some arbitrary reference state which is defined to have zero entropy at that state.

where the *ideal total enthalpy* $h_{t\,i}$ is defined as follows:

$$h_{t\,i} \equiv p_t^{(\gamma-1)/\gamma} \tag{C.17}$$

Using Equation (C.16), the local values of entropy are determined from local total pressures and total enthalpies. The average total pressure is determined from the average entropy and the average total enthalpy:

$$\overline{h_{t\,i}} = \overline{h_t} e^{-\bar{s}/c_p} \tag{C.18}$$

$$\overline{p_t} = \overline{h_{t\,i}}^{\,\gamma/(\gamma-1)} \tag{C.19}$$

Note that the entropy averaging scheme correctly lumps the flow of entropy through the area of integration, and is thus compatible with the second law of thermodynamics. Since two equations are being replaced, one more relationship is required. It is obtained by using the meridional flow angle $\overline{\psi}$ from the momentum averaging scheme:

$$\overline{\psi} \equiv \tan^{-1} \frac{\overline{V_r}}{\overline{V_x}} \tag{C.20}$$

where the velocities are from Equations (C.12) and (C.13). That is, the meridional flow angle for the entropy average is assumed to be the same as that for the momentum average. Note that Equation (C.20) does not imply that the axial and radial velocity components for the entropy and momentum averages are equal, but rather only that they are proportionately related.

Unlike for the momentum-averaging scheme, the system of equations for the entropy average cannot be solved in closed form. A concise formulation for solving the equations iteratively using a Newton-iteration method [83] can be derived, however. The final formulation can be expressed as follows:

$$g(\Phi) + \Phi - 1 = 0 \tag{C.21}$$

where

$$\Phi \equiv \frac{\overline{V}^2}{2\overline{h_t}} = 1 - \frac{\bar{h}}{\overline{h_t}} \tag{C.22}$$

The function g is defined in terms of the parameter Φ and two known constants, b and c:

$$g \equiv \left[\frac{b\,(1-\Phi)}{\sqrt{\Phi - c}} \right]^{(\gamma-1)/\gamma} \tag{C.23}$$

$$b \equiv \frac{\gamma - 1}{\gamma} \frac{\bar{\rho}\,\overline{V_m}}{\overline{p_t}} \sqrt{\frac{\overline{h_t}}{2}} \tag{C.24}$$

$$c \equiv \frac{\overline{V_\theta}^{\,2}}{2\overline{h_t}} \tag{C.25}$$

Note that the root value of Φ must be between zero and one, where a value of one corresponds to a Mach number of infinity. The product $\bar{\rho}\,\overline{V_m}$ in the constant b is identical to that for the momentum average, and therefore can be determined from the momentum-averaged axial and radial components (Equations (C.12) and (C.13)):

$$\bar{\rho}\,\overline{V_m} = \bar{\rho}\sqrt{\overline{V_x}^{\,2} + \overline{V_r}^{\,2}} \tag{C.26}$$

Once the root value for Φ is determined, all other average properties follow explicitly:

$$\overline{V}^{\,2} = 2\overline{h_t}\Phi \tag{C.27}$$

$$\overline{V_m} = \sqrt{\overline{V}^{\,2} - \overline{V_\theta}^{\,2}} \tag{C.28}$$

$$\bar{p} = \overline{p_t}\, g^{\gamma/(\gamma-1)} \tag{C.29}$$

$$\bar{\rho} = \frac{\bar{\rho}\,\overline{V_m}}{\overline{V_m}} \tag{C.30}$$

The equation of state (Equation C.6) can be used to calculate the average static enthalpy and the average speed of sound. Finally, the axial and radial velocity components are calculated from the meridional velocity and flow angle:

$$\overline{V_x} = \overline{V_m}\cos\overline{\psi} \tag{C.31}$$

$$\overline{V_r} = \overline{V_m}\sin\overline{\psi} \tag{C.32}$$

Energy average

The general formulation of the *energy average* is almost the same as that of the entropy average, except that the ideal total enthalpy is mass-averaged instead of the entropy:

$$\dot{m}\,\overline{h_{t\,i}} = \int h_{t\,i}\delta\dot{m} \tag{C.33}$$

Equation (C.19) is then used to calculate an average total pressure. All other quantities are calculated in a manner identical to that in the entropy averaging scheme. It might be noted that both schemes can be thought of as different ways of obtaining an average total pressure, although the energy averaging scheme does not correctly lump the total flow of entropy through the area of integration, as does the entropy average. The energy average, however, is preferable to the common method of directly mass-averaging total pressure, which method has a fundamental weakness: it involves the mass-averaging of an intensive property, namely total pressure, which is not a *specific* property [8].

There is, apparently, no formal basis for performing an energy average, but an informal rationale for it [84] can be seen from the definition of adiabatic efficiency. For exam-

---

[8] The adjective *specific* typically indicates an *intensive*, or point-valued, property derived from an *extensive* property, normally by expressing it on a per-unit-mass basis. The process of integrating (summing) mass-flow-weighted specific properties, such as specific enthalpy, for example, is physically sound and is equivalent to summing the distributed elements of an extensive property.

ple, the overall average adiabatic efficiency for a compressor can be written in the following dimensionless form:

$$\overline{\eta}_c = \frac{\overline{h_{t\,i}} - 1}{\overline{h}_t - 1} \tag{C.34}$$

where the averages are performed at an exit station of the compressor and the efficiency is relative to some upstream reference state by which the quantities are non-dimensionalized. Noting that the mass-average total enthalpy (see Equation (C.2)) in the denominator of Equation (C.34) is rigorously consistent with the first law of thermodynamics (energy conservation), it seems somewhat reasonable to also mass average the ideal total enthalpy in the numerator. This approach, however, cannot be defended on fundamental grounds.

Notation for Averaging Schemes

A simple notation for clearly indicating the different types of averages described above has been devised. The averaging schemes are listed in Table C.1 along with italicized lower-case letters for denoting each scheme. The notation assumes a *coherent set* of average properties, and the basic form is as follows:

$$^{s}\bar{q}$$

The overbar indicates that the quantity q is an average, and the upper-left superscript indicates the type of averaging scheme. In this example the entropy averaging scheme is indicated by the "*s*" (see Table C.1).

Table C.1 Upper-left superscript abbreviations used for denoting the various averaging schemes

m	*momentum* averaging scheme
s	*entropy* averaging scheme
e	*energy* averaging scheme

The superscript can involve a single letter as in the above example, or two letters if two spatial directions are involved. The two different directions, spanwise and circumferential, are distinguished as follows:

$^{s}\bar{q}$ *circumferential* average (no diacritical mark on superscript)

$^{\tilde{s}}\bar{q}$ *spanwise* average (small bar over the superscript)

Examples

A few examples are now provided in order to demonstrate the usage of the notation. In all cases the generic flow quantity q will be used to show the notation.

Example 1: steady, axisymmetric duct flow

$^{\tilde{s}}\bar{q}$ spanwise entropy-average — gives overall-average quantities

$^{\bar{m}}\bar{q}$ spanwise momentum-average — gives overall-average quantities

Example 2: steady, quasi-three-dimensional blade-to-blade flow; downstream of isolated blade row

$^{e}\bar{q}$ circumferential energy-average — gives circumferential-average quantities

Example 3: steady, three-dimensional flow; downstream of isolated blade row

$^{e}\bar{q}$ circumferential energy-average — gives spanwise distribution of circumferential-average quantities

$^{\tilde{s}m}\bar{q}$ circumferential momentum-average and spanwise entropy-average — gives overall-average quantities

APPENDIX D.
APPROXIMATE TWO-DIMENSIONAL CALCULATION METHODS

Approximate methods for rapidly calculating three different types of two-dimensional blade-to-blade inflow conditions are briefly described in this appendix. The three conditions of interest are cascade unique-incidence, cascade choking at the minimum blade-passage area, and cascade (axial-supersonic) unstart with an oblique-shock wave just in or near the inlet plane of the cascade. Each of these conditions is a potentially important limit or constraint to the relationship between the relative inflow Mach number and inflow direction to the cascade. A major reason for considering these simpler methods, as a supplement to the more sophisticated CFD methods, is that they can provide additional insight into the inflow aerodynamics, as well as aid in the interpretation of the computational results.

Unique-Incidence Calculation Procedure

Unique-incidence conditions are established for a cascade inflow when the blade-relative inflow velocities are supersonic and the covered passage is started. The axial Mach number component must be subsonic, however, in which case a functional relationship exists between the relative inflow Mach number and the relative inflow direction; that is, the incidence angle is dependent on the relative inflow Mach number [71-72, 85-88].

An approximate procedure for calculating this relationship for a particular cascade geometry has been developed by Starken, et al. [69,70], incorporating significant refinements over the earlier work of Levine [85] to account for the influence of leading-edge bluntness. The basic approach assumes the steady flow of a perfect gas and combines two-dimensional, simple-wave gas dynamic theory with the detached bow-shock model of Moeckel [89]. The Moeckel bow-shock model can be slightly improved by incorporating

some of the refinements discussed by Love [90], and this has been done for the present work. The basic flow field model from which the scheme is formulated is illustrated in Figure D.1. The flow region in the vicinity of the blade leading edge is depicted in more detail in Figure D.2. Only a superficial description of the method will be given here since more detailed descriptions can be found in the literature [69,70].

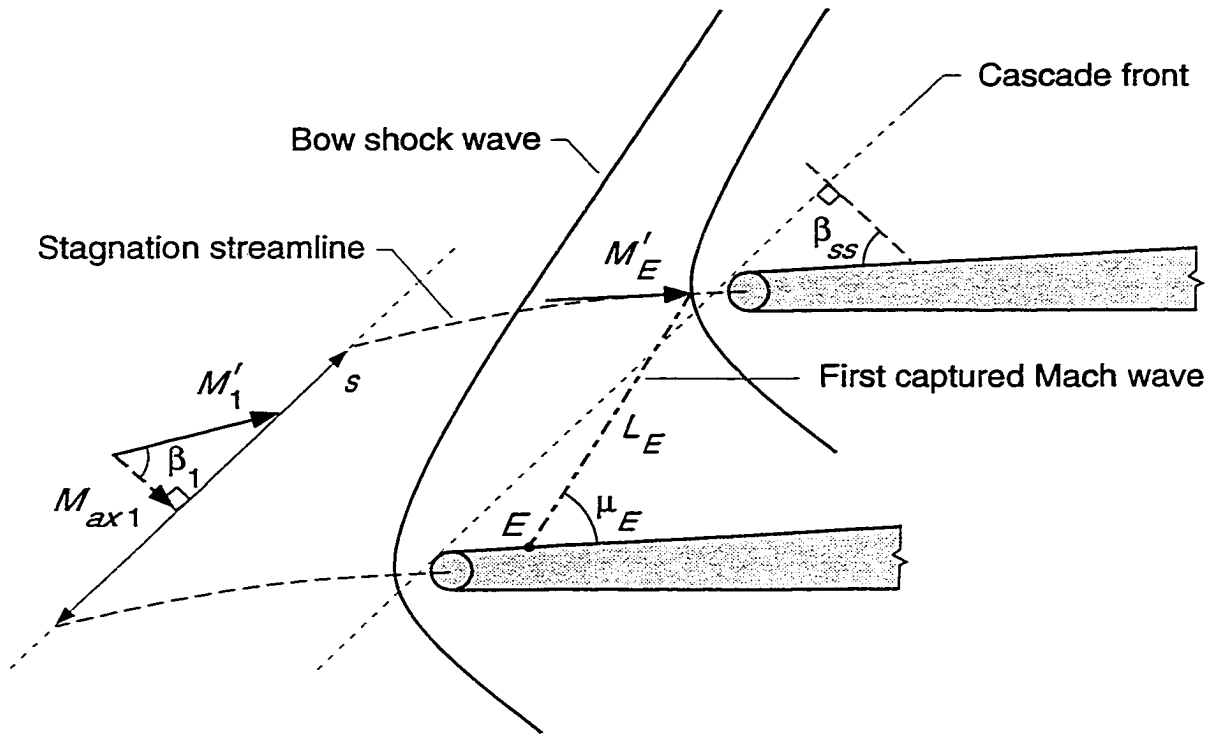

Figure D.1 Flow field model used for formulation of the unique-incidence calculation procedure

Referring to Figures D.1 and D.2, note that except for the subsonic regions located just behind the strong portions of the bow shock waves, the entire inlet flow is relative supersonic, but axial-subsonic as evidenced by the left-running waves propagating out in front of the cascade. A left-running Mach wave is shown emanating from the blade suction surface at point *E*, and running across the entrance region to intersect the bow shock wave of

the adjacent blade. This Mach wave is assumed to be straight with constant flow properties along it, which is equivalent to assuming a simple-wave inlet flow field and neglecting the entropy gradients generated by curved bow shocks. By definition, this *first captured Mach wave* intersects the bow shock wave at the stagnation streamline so that the amount of flow entering the blade passage is determined by the length L_E of the Mach wave. The shock detachment distance D_E, shown in Figure D.2, is a function of the shock-incident Mach number $M_E^{\prime}$, according to the bow shock model, so for a particular point E on the blade suction surface there is a unique first captured Mach wave. The procedure for determining a solution for a particular point E is iterative, and for a solution to exist the point must lie within a limited range of positions on the blade surface. Given such a solution,

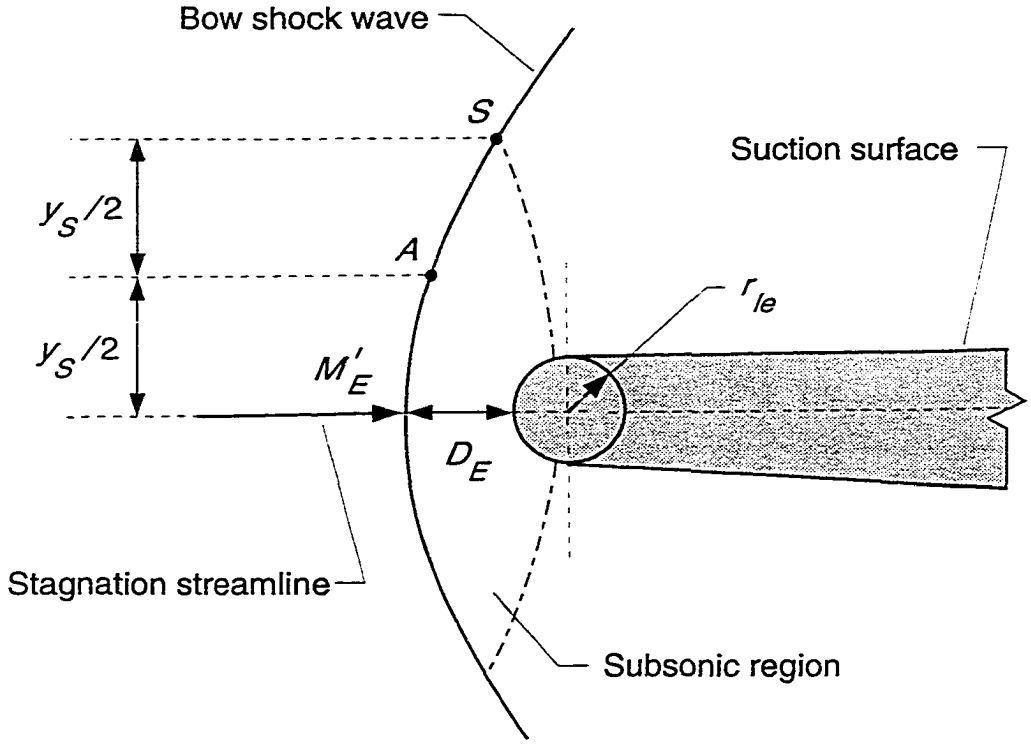

Figure D.2 Bow shock wave flow field for unique-incidence model

the mass flow (per unit width) entering the passage can be described using the following form of the continuity equation:

$$\dot{m} = \rho'_{tE} a'_{tE} \phi_E L_E \sin\mu_E \tag{D.1}$$

where $\phi_E = \phi(M'_E)$ and $\sin\mu_E = 1/M'_E$. The function defining the mass-flux parameter ϕ is given in the **Symbols and Notation.**

The upstream flow conditions for the cascade are determined by applying mass flow continuity to a control volume bounded by the first captured Mach wave and by an axial station "far" upstream where uniform conditions exist blade-to-blade (see Figure D.1). Upstream of the cascade the control volume is circumferentially periodic, and a constant streamtube height in the circumferential and axial directions is assumed. Note that this latter constraint is not absolutely necessary if an additional degree-of-freedom be admitted; that is, the formulation could include streamtube height variations in the axial direction. The continuity equation for the upstream station can be written as follows:

$$\dot{m} = \rho'_{t1} a'_{t1} \phi_1 (s) \cos\beta_1 \tag{D.2}$$

where $\phi_1 = \phi(M'_1)$. Conservation of mass for the control volume requires that the right hand sides of Equations (D.1) and (D.2) be equal to each other. Since no change in relative total temperature occurs for the flow through the control volume, the total sonic speed a'_t is constant. Thus, Equations (D.1) and (D.2) can be combined to give the following conservation-of-mass equation:

$$\phi_1 \cos\beta_1 = \frac{\rho'_{tE}}{\rho'_{t1}} \frac{L_E}{s} \frac{\phi_E}{M'_E} \tag{D.3}$$

The total-density ratio is estimated by using the total-density loss from the strong portion of the bow shock wave, which corresponds in Figure D.2 to the segment of the bow shock between the stagnation streamline and point *S*. An approximate nominal total-density ratio ρ'_{tA} / ρ'_{t1} for the shock segment is calculated using the shock wave angle at midpoint *A* (see Figure D.2) along with the incident Mach number. The shock angle at point *A* is known from the bow shock model. Mass-averaging this bow shock total-density ratio,

for the flow through area y_S, with the remaining "no loss" passage flow yields a simple relationship for the "average" inlet total-density ratio [1]:

$$\frac{\rho'_{tE}}{\rho'_{t1}} = 1 + \frac{M'_E y_S}{L_E}\left[\frac{\rho'_{tA}}{\rho'_{t1}} - 1\right] \tag{D.4}$$

Thus, the right hand side of Equation (D.3) can be determined for a particular point E on a given geometry. The left hand side contains the desired two unknowns, M'_1 and β_1, where M'_1 is implicit in the parameter ϕ_1. The second equation necessary for determining these two unknowns follows directly from the simple-wave model for the inlet flow field:

$$\beta_1 + \nu_1 = \beta_E + \nu_E \tag{D.5}$$

where ν_1 and ν_E are the Prandtl-Meyer angles (see **Symbols and Notation**) for M'_1 and M'_E, respectively, and β_E is the blade suction-surface angle β_{ss} at point E (see Figure D.1). Although the solution to Equations (D.3) and (D.4) is iterative, it can be obtained almost instantaneously on a computer. The axial component of the inlet Mach number, or the inlet Mach number itself if axial, follows from the relative Mach number and flow angle:

$$M_{ax\,1} = M'_1 \cos\beta_1 \tag{D.6}$$

---

[1] This simplified approach is justified on the grounds that the left-running bow shock wave attenuates rapidly with distance from the leading edge generating it. This rapid attenuation occurs because of the left-running expansion waves intersecting the shock on the upstream, as well as the downstream side. This is a characteristic of cascade aerodynamics and is not encountered with isolated airfoils.

Unique-Incidence for a Flat Plate Cascade

In most practical applications the unique-incidence behavior of a two-dimensional blade element is determined by the blade suction-surface geometry in the *entrance region* of the blade passage, and by the leading edge radius-to-gap ratio r_{le}/s (see Figure D.1). If the curvature of the suction surface on the forward part of the blade is small, then a flat plate approximation gives a fair estimate of the unique-incidence behavior. By using such an approximation, a simple parametric study [69,70] can be performed with only two independent parameters: the blade suction surface angle β_{ss} and the leading edge radius-to-gap ratio r_{le}/s. Results from this type of parametric study will be shown below, where the range of parameters bracket values representative for the baseline SSTF. These results provide both qualitative and quantitative information, and help to explain several basic characteristics of the baseline fan with respect to its subsonic mass flow induction capability.

A simplified blade geometry is adequate for the analysis, and so a circular leading edge is used. Tangent to the circle is a straight suction-surface segment for the entrance region (uncovered portion) of the blade passage (see Figure D.1). Graphs of suction-surface incidence and axial inflow Mach number (component) versus relative inlet Mach number are presented in Figures D.3 and D.4, where Figure D.3 shows the influence of suction-surface angle for a constant leading edge radius-to-gap ratio of 0.007, and Figure D.4 shows the influence of leading-edge radius-to-gap ratio for a constant suction surface angle of 38 degrees. Note that the suction-surface angles for the baseline SSTF vary from about 32 degrees at the hub to 42 degrees at the tip, and the leading-edge radius-to-gap ratios vary from about 0.010 at the hub to 0.007 at the tip.

Several key observations and conclusions can be made about these results. First, all of the unique-incidence curves exhibit a maximum axial inflow Mach number at some relative inflow Mach number. For the cases with thicker leading edges or low suction-surface angles, the maximums are at the sonic end of the curves. Relative Mach numbers higher than this "maximum flow" condition are associated with a trend of gradually decreasing axial inflow Mach number with increasing relative Mach number (see part (b) of Figures D.3 and D.4). Simultaneously, there is a rapid increase in incidence (see part (a) of Figure D.3 and D.4). Considered from the standpoint of a rotor, such behavior implies that the

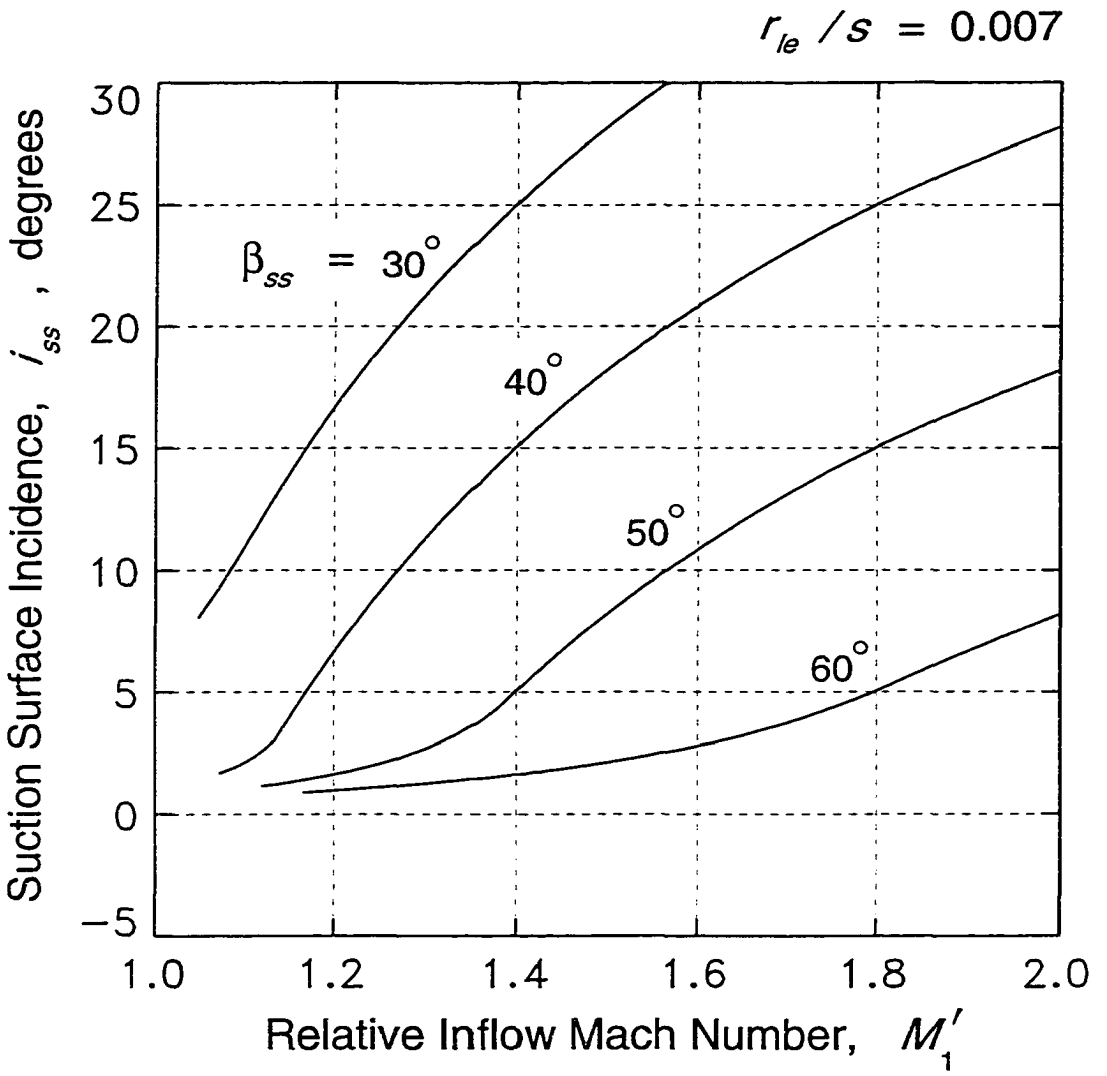

(a) suction-surface incidence

Figure D.3 Influence of suction-surface angle on unique-incidence for a flat plate cascade with a leading edge radius-to-gap ratio of 0.007

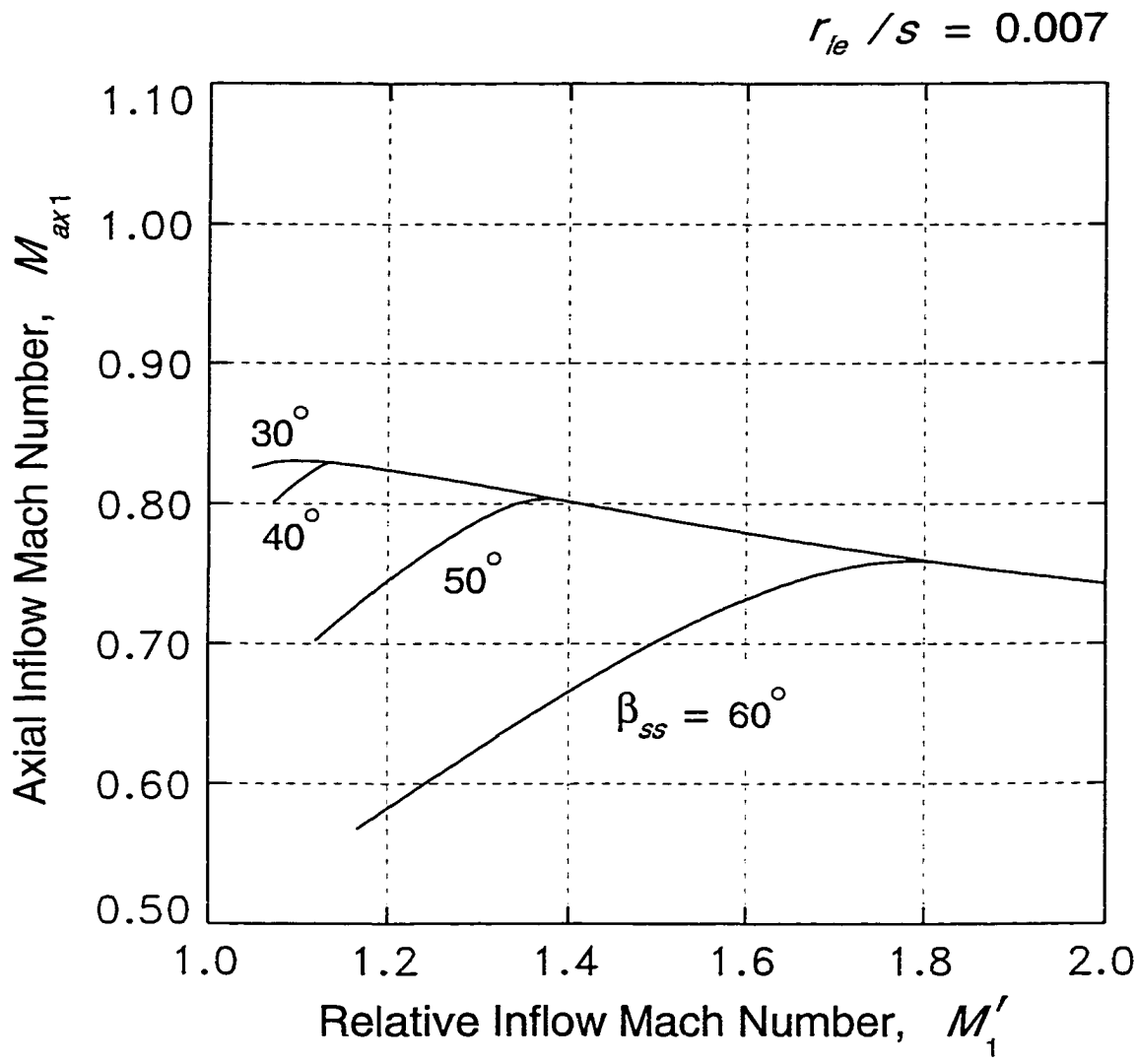

(b) axial inflow Mach number

Figure D.3 (continued)

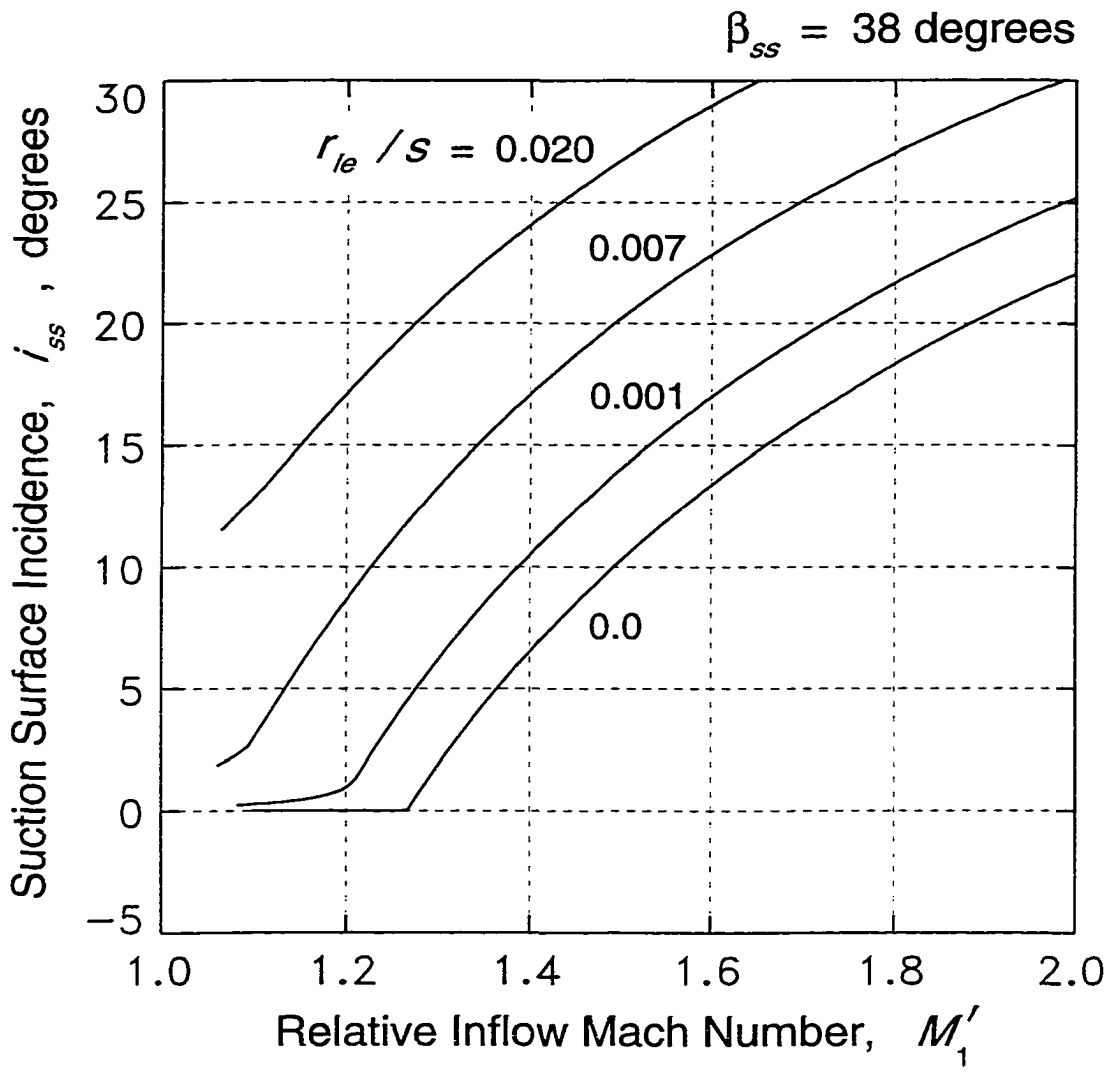

(a) suction surface incidence

Figure D.4 Influence of leading edge radius-to-gap ratio on unique-incidence for a flat plate cascade with a 38 degree suction-surface angle

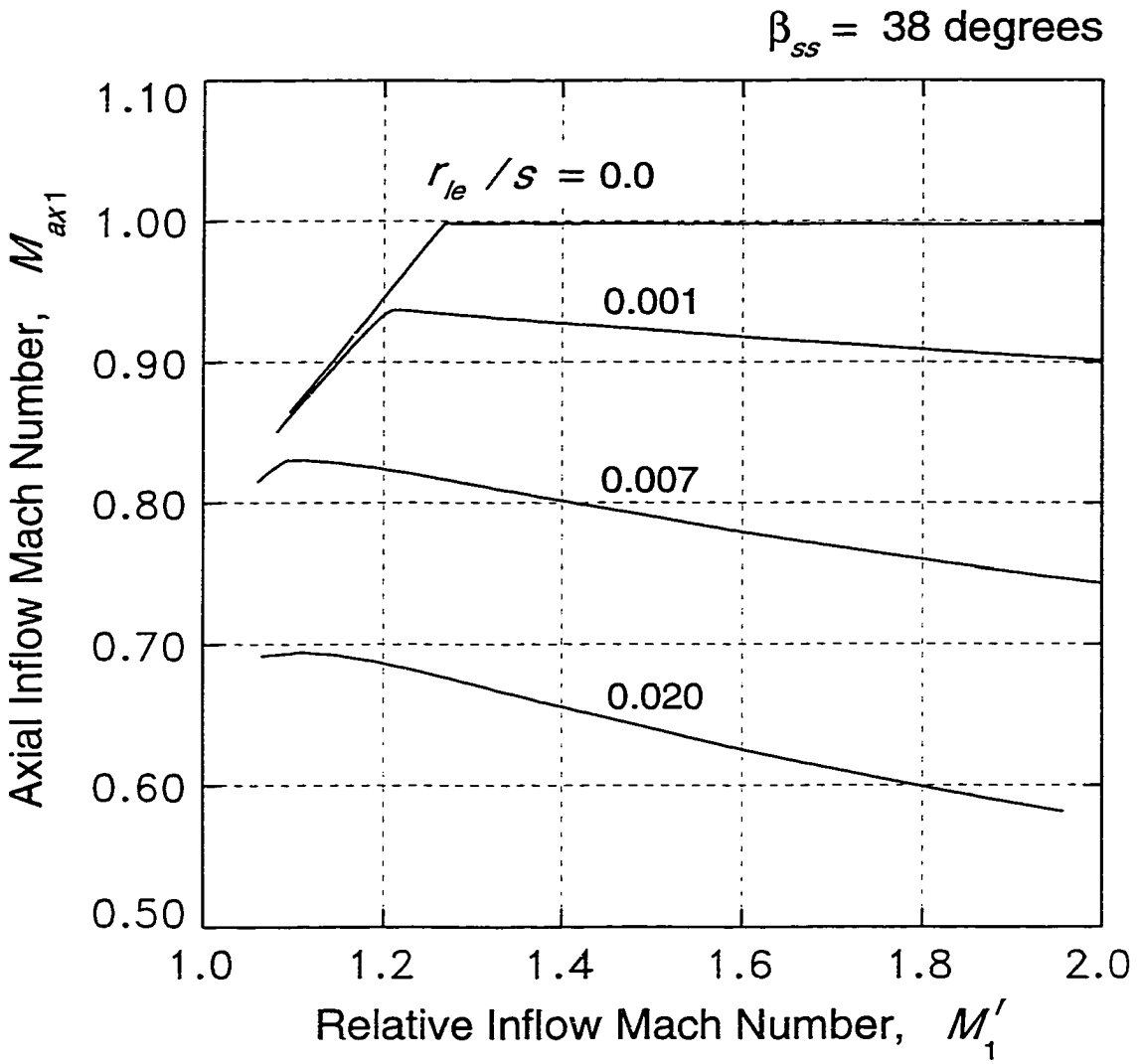

(b) axial inflow Mach number

Figure D.4 (continued)

mass flow induced by the rotor will increase with rotational speed (relative inlet Mach number) to some maximum flow condition, beyond which increases in rotational speed will actually reduce the mass flow slightly. For blades with low suction surface angles this condition is reached at low relative inlet Mach numbers (see part (b) of Figure D.3), i.e., relative Mach numbers just above one, and the maximum flow condition occurs concurrently with the establishment of unique-incidence.

The above behavior can be explained fairly well in terms of the first captured Mach wave discussed in the previous section (see Figure D.1). In general, assuming that unique-incidence is established, increasing the (supersonic) relative inlet Mach number, for example through increases in rotational speed, causes the first captured Mach wave to originate from a point E located further and further upstream on the blade suction-surface. As this occurs, the length L_E of the wave becomes longer and, since the Mach number component normal to a Mach wave is always unity, the mass flow into the passage increases. The increasing trend continues until the point E reaches the leading edge, at which position the Mach wave is nearly normal to the axial direction and its length becomes more-or-less fixed. Furthermore, the axial component of the flow is then sonic in the leading-edge plane of the cascade, between the blade leading edges where blockage is minimal. It is the onset of this axially-choked condition that corresponds to the maximum attainable mass flow. Relative Mach numbers exceeding this choking threshold tend to increase the effective leading-edge blockage slightly by increasing the bow-shock total-pressure loss, and thus decreasing the mass flow slightly.

A second observation is that larger leading edge radius-to-gap ratios reduce the maximum attainable axial inlet Mach number (component), and thus the maximum attainable mass flow (see part (b) of Figure D.4). Somewhat less significant is a modest shift in the maximum condition to lower relative inlet Mach numbers. The decrease in maximum axial inlet Mach number with "thicker" blade leading edges can be understood in light of the above discussion. More specifically, since at that condition the cascade is choked in the leading-edge plane, then effectively thicker edges reduces the critical area where the cascade is choked.

Finally, one last comment. It was noted earlier that low suction-surface angles are associated with a maximum mass flow occurring at near-sonic relative inlet Mach numbers. In such cases unique-incidence is always equivalent to "leading-edge choking",

and the onset of unique-incidence from a previously choked condition involves the relocation of a sonic line from the blade-passage minimum-area to the leading-edge plane.

Blade Passage Choking Calculation Procedure

A simple, two-dimensional choking model is useful for analyzing the mass-flow choking characteristics of the baseline fan at rotational speeds too low for unique incidence. The relationship between the relative inflow direction, or incidence, and the relative inflow Mach number, for the limiting condition where the blade passage is choked, can be approximately determined using the "one-dimensional" minimum-area of the blade passage. The steady, two-dimensional flow field assumed for this scheme is depicted in Figure D.5, where it can be seen that the passage throat area t_* is approximated as a straight line with uniform sonic flow normal to it. As in the unique-incidence formulation, a control volume is defined which extends upstream to uniform inflow conditions, and

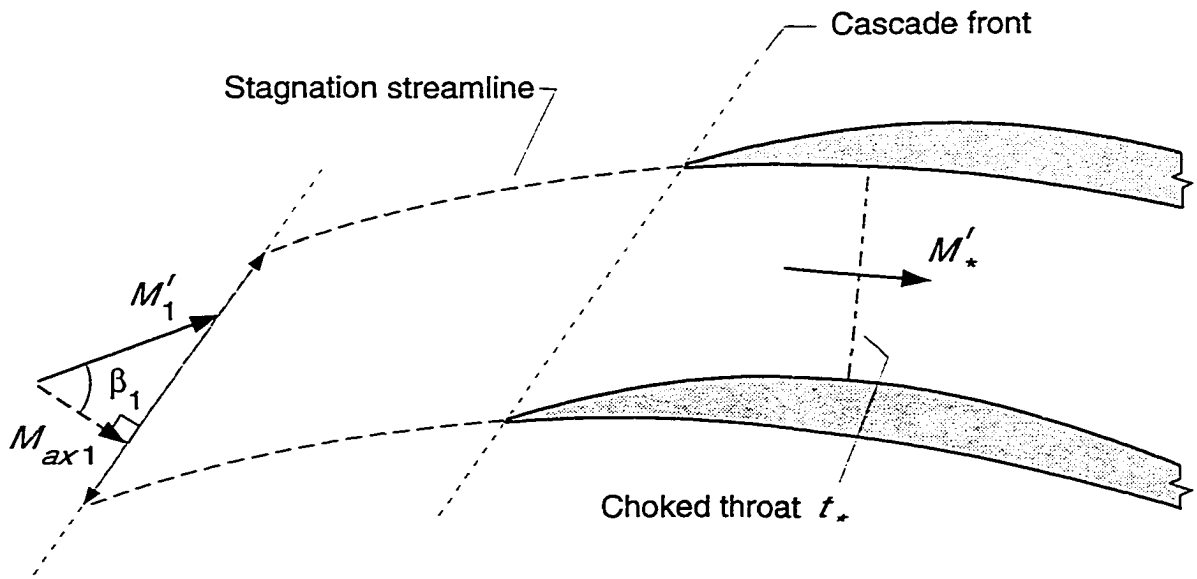

Figure D.5 Flow field model used for formulation of the blade passage choking calculation procedure

which in this case is bounded downstream by the sonic line. Since the control volume is periodic upstream of the cascade, the mass flow rates at the upstream and downstream boundaries must be equal. Assuming a perfect gas, the mass flow rate at the upstream boundary is described by Equation (D.2), and the continuity equation applied to the sonic line yields the following relationship:

$$\dot{m} = \rho'_{t*} a'_{t*} \phi_* t_* \tag{D.7}$$

where $\phi_* = \phi(M'_*)$ and $M'_* = 1.0$. Noting that the relative sonic speed is a constant for this flow field, Equations (D.2) and (D.7) can be combined to give the following expression for the relative inlet flow angle:

$$\beta_1 = \cos^{-1}\left[\frac{\rho'_{t*}}{\rho'_{t1}} \frac{t_*}{s} \frac{\phi_*}{\phi_1}\right] \tag{D.8}$$

If the relative total-density (or total-pressure) loss upstream of the choked area is neglected, as was done in this work, then the total-density ratio in Equation (D.8) is unity and the relative inlet flow angle becomes a simple function of the relative inlet Mach number.

Oblique Shock Wave in Inlet Plane of Cascade

A potentially important limit for axial-supersonic flow into a cascade is the condition where an oblique shock wave lies in or near the inlet plane of the blade row [71,72]. Axial-supersonic inlet Mach numbers below this limit cause the *axial* inflow to the blade row to unstart. By considering the inviscid, steady flow of a perfect gas into a cascade of blades with infinitesimally-thin leading edges, i.e., neglect leading-edge bluntness, an estimate of this limit can be obtained. The inlet flow field model is illustrated in Figure D.6, where it is assumed that the forward portion of the blade suction surface is straight and that the blade passage is not choked downstream.

The relative Mach number incident on the oblique shock can be expressed [52] as a function of the shock wave angle θ, and the angular flow deflection δ through the shock (see Figure D.6):

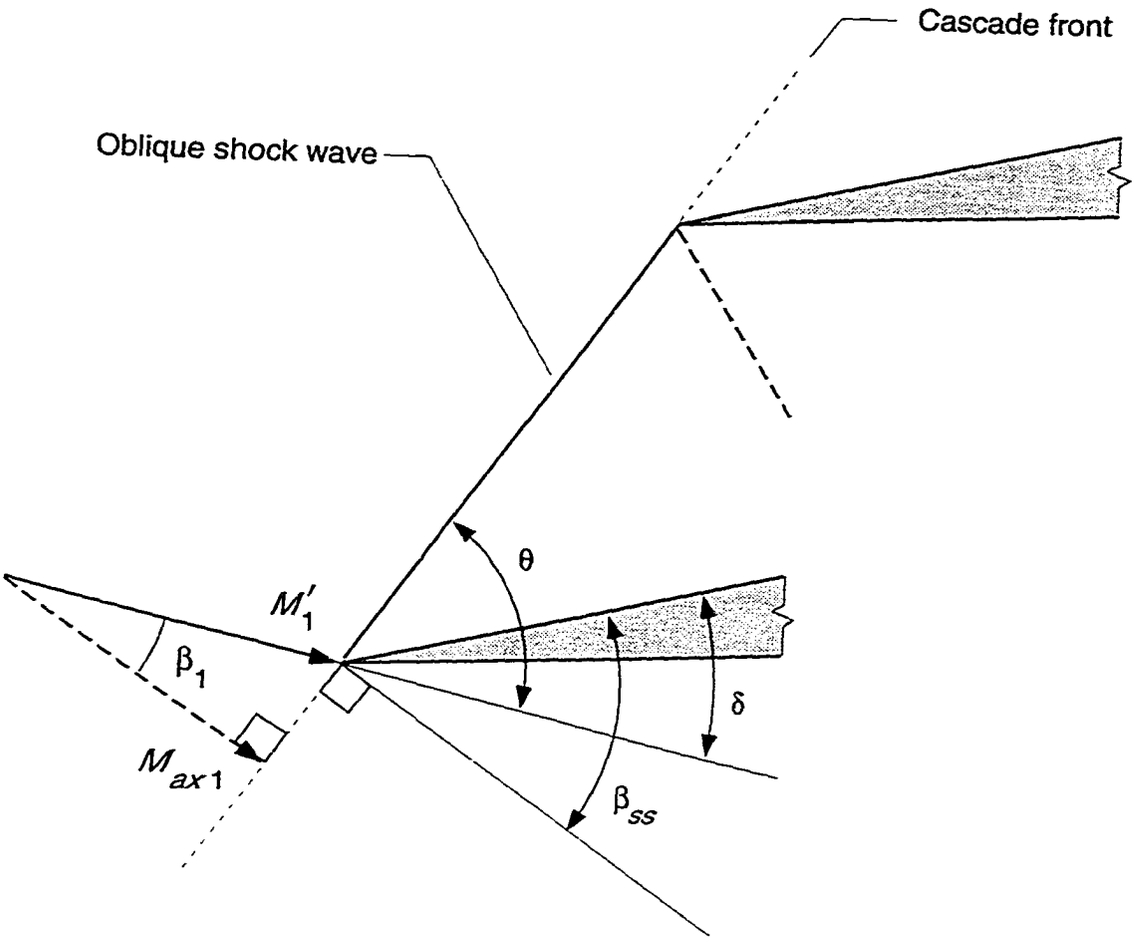

Figure D.6 Oblique shock wave in inlet plane of cascade

$$\frac{1}{M_1'} = \sqrt{\sin^2\theta - \frac{\gamma+1}{2}\frac{\tan\theta}{\tan\theta + \cot\delta}} \tag{D.9}$$

Given the relative flow angle β_1, the following relationships exist:

$$\theta = \frac{\pi}{2} - \beta_1 \tag{D.10}$$

$$\delta = \beta_{ss} - \beta_1 \tag{D.11}$$

Note that for a particular incident Mach number there is a maximum flow deflection angle δ_{max}, and corresponding shock wave angle $\theta_{\delta\, max}$, above which an attached (weak) shock does not exist; that is, only strong oblique-shock solutions exist. From Reference 52, the shock wave angle for maximum flow deflection is given by the following equation:

$$\sin^2\theta_{\delta\, max} = \frac{1}{4\gamma M_1'^2}\left\{ (\gamma+1)M_1'^2 - 4 + \sqrt{(\gamma+1)\left[(\gamma+1)M_1'^4 + 8(\gamma-1)M_1'^2 + 16\right]} \right\} \tag{D.12}$$

and the maximum flow deflection angle can be approximated as follows:

$$\delta_{max} \approx \frac{4}{3\sqrt{3}(\gamma+1)}\frac{(M_1'^2-1)^{3/2}}{M_1'^2} \tag{D.13}$$

If the shock wave angle (or flow deflection angle) corresponding to a shock lying in the leading-edge plane exceeds the weak wave limit, then a solution corresponding to a maximum flow deflection angle is sought. In this case the constraint of a shock lying in the leading-edge plane is ignored (Equation D.10) and the flow deflection angle (Equation D.11) is defined as being at the maximum limit. The solution for the incident Mach number M_1' is iterative (using Equations D.9 and D.12) and corresponds to an oblique shock wave with near-sonic exit conditions, and which does not lie in the inlet plane but is instead swept back into the blade passage.

APPENDIX E.
A TOTAL-PRESSURE LOSS MODEL FOR SUPERSONIC THROUGHFLOW FAN BLADE ROWS

The supersonic throughflow fan belongs in a general sense to the subclass of compressors often referred to as impulse-type compressors. Characteristic of the impulse-type compressor is a high-solidity, low-diffusion rotor with moderate to high degrees of relative-flow turning. In the special case of the supersonic throughflow fan, the stator blade row is aerodynamically similar to the rotor.

Efforts aimed at analyzing and understanding the aerodynamic performance of the supersonic throughflow fan have resulted in the development of a fairly simple and approximate total-pressure-loss model. The model is generally applicable to blade-elements with axial-supersonic throughflow velocities, high solidity, low diffusion, and moderate-to-low levels of relative-flow turning. The flow is assumed to be compressible air, and in the practical application of the model to all elements in a blade row, secondary flow effects are neglected.

Experimental and computational results for a two-dimensional supersonic throughflow cascade [73-75] are used to assess the model. Overall the results agree well with the experimental data, which is somewhat remarkable considering the model's simplicity. An important benefit derived from the model is that it allows the determination of first-order loss sources and their relative magnitudes. This information is useful in estimating the practical upper limits in performance for the supersonic throughflow type of fan, and it provides a basis for effectively directing efforts to improve the fan aerodynamic performance.

Loss-Model Description

The basic assumption underlying the model is that only four sources of loss exist, and that they add linearly to produce the total loss. The summation of loss contributions is performed in terms of the loss coefficient parameter as follows:

$$\bar{\omega} = \bar{\omega}_{skf} + \bar{\omega}_{bwv} + \bar{\omega}_{obq} + \bar{\omega}_{sbl} \tag{E.1}$$

where

$\bar{\omega}_{skf}$ = viscous skin-friction loss for a zero-incidence thin-flat-plate cascade.

$\bar{\omega}_{bwv}$ = bow shock-wave loss for a zero-incidence blunt-flat-plate cascade with inviscid flow.

$\bar{\omega}_{obq}$ = free-stream shock loss due to oblique shock waves generated by incidence and leading-edge "wedge" effects.

$\bar{\omega}_{sbl}$ = additional viscous loss caused by shock/boundary-layer interactions from the oblique shock waves.

The theory and equations used to determine each of the above loss source terms are now described in turn. In each case air is assumed to be a perfect gas ($\gamma = 1.4$), and all quantities are in the frame-of-reference relative to the blade, modeled as a plate or wedge unless otherwise noted.

Skin-friction loss model

Skin-friction losses are estimated by assuming a steady, compressible turbulent boundary layer [1] on a smooth flat plate. A formula developed by van Driest [2] is applied to determine the drag coefficient C_D for adiabatic airflow over the plate:

---

[1] A laminar boundary layer model can also be used for low blade chord Reynolds numbers (less that about 10^5). This is, however, seldom relevant for the high-speed turbomachinery applications being considered here.

[2] The formula has been taken from White [91], who references the work of van Driest.

$$\frac{\sin^{-1}A}{\sqrt{C_D\,(T_{aw}/\,T_e-1)}} \approx 4.13\log\left(Re_{Le}C_D\,\frac{\mu_e}{\mu_{aw}}\right) \tag{E.2}$$

where

$$A \equiv \left(\frac{\gamma-1}{2}\,M_e^2\,\frac{T_e}{T_{aw}}\right)^{1/2} \tag{E.3}$$

$$\frac{T_{aw}}{T_e} \approx 1+f_{rt}\,\frac{\gamma-1}{2}\,M_e^2 \tag{E.4}$$

The turbulent recovery factor f_{rt} is estimated using the Prandtl number Pr [91]:

$$f_{rt} \approx Pr^{1/3} \tag{E.5}$$

The viscosity ratio is estimated using the well-known power law [53,91]:

$$\frac{\mu_e}{\mu_{aw}} \approx \left(\frac{T_e}{T_{aw}}\right)^n \tag{E.6}$$

where for air, $n \approx 2/3$. In the above equations the subscript "*aw*" denotes an adiabatic wall condition, and the subscript "*e*" denotes the free-stream condition at the edge of the boundary layer. An iterative procedure is necessary for calculating C_D from Equation (E.2), but convergence is rapid and easily obtained.

The independent parameters needed to solve for the drag coefficient are the freestream Mach number M_e, the freestream Reynolds number Re_{Le} based on the length of the plate, and the Prandtl number *Pr*, which is assumed to have the nominal value of 0.71 for air. In applying Equation (E.2) to the turbomachinery environment, however, the "freestream" flow is not uniform along the blade surface and, furthermore, is generally quite different for the two surfaces of the blade, i.e., the suction and pressure surfaces. The simplifying approximation is to arithmetically average the relative flow conditions upstream and downstream of the blade element, and to use that average condition on both sides of the blade; that is, the flat-plate drag is doubled to account for both sides. The length L of the plate is taken as the aerodynamic chord c, but with a minor adjustment for blade camber $\Delta\kappa$:

$$L = \frac{c\,(\Delta\kappa)/2}{\sin\dfrac{\Delta\kappa}{2}} \tag{E.7}$$

where $\Delta\kappa = |\kappa_2 - \kappa_1|$, the absolute difference between the blade inlet and exit metal angles.

In order to calculate a total-pressure loss coefficient from the drag coefficient it is necessary to consider the array (cascade) of plates with spacing *s*, and to convert the drag coefficient to an appropriate drag force parameter. The circumferential periodicity of the flow field then allows a formulation of the conservation equations for mass, energy, and momentum, from which the total-pressure loss can be determined.

An appropriate control volume for formulating the conservation equations is shown in Figure E.1. In order to avoid additional axial-force terms the streamtube must be modelled as two-dimensional, in which case the drag force *D* (for both sides of the plate) is balanced by the upstream and downstream static pressure forces and the net flow of

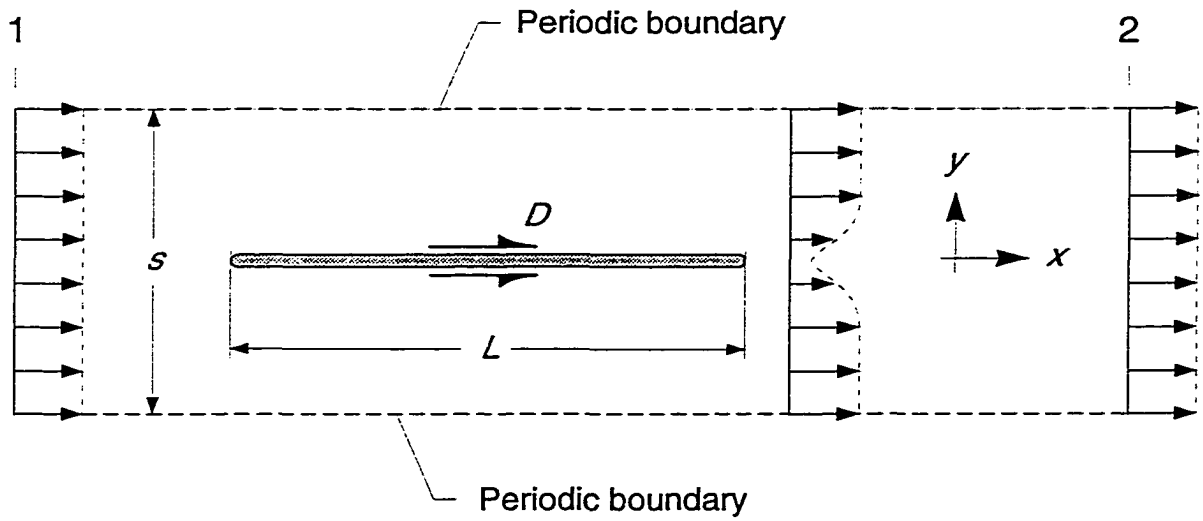

Figure E.1 Two-dimensional control volume for formulating conservation equations, used to determine skin-friction total-pressure loss from flat-plate drag

momentum through the upstream and downstream boundaries [3]. Tangential-momentum is trivial in this case due to the flow field symmetry and periodicity. The conservation equations for mass, axial-momentum, and energy are as follows:

$$\rho_1 u_1 = \rho_2 u_2 \tag{E.8}$$

$$-D/s = \rho_2 u_2^2 - \rho_1 u_1^2 + p_2 - p_1 \tag{E.9}$$

$$h_{t1} = h_{t2} \tag{E.10}$$

Adiabatic flow has been assumed and the total enthalpy h_t can be expressed in terms of the other flow variables:

$$h_t = \frac{\gamma}{\gamma - 1}\frac{p}{\rho} + \frac{u^2}{2} \tag{E.11}$$

Using the definition for drag coefficient, as well as the definition for blade solidity σ, the drag force parameter D/s is related to the drag coefficient:

$$D/s = \sigma C_D \rho_e u_e^2 \approx \sigma C_D \rho_1 u_1^2 \tag{E.12}$$

Note from Equation (E.12) that state "1" is assumed to be approximately the same as state "e", which is consistent with the flat-plate model. After some algebraic manipulations, the following set of equations can be derived:

$$u_1 \equiv M_1 \left(1 + \frac{\gamma - 1}{2} M_1^2\right)^{-1/2} \tag{E.13}$$

$$I_x \equiv u_1 \left(1 + \frac{1}{\gamma M_1^2} - \sigma C_D\right) \tag{E.14}$$

$$u_2 = \frac{\gamma I_x \pm \sqrt{(\gamma I_x)^2 - 2(\gamma + 1)}}{\gamma + 1} \tag{E.15}$$

---

[3] The Mach number effects which are induced by streamtube area variations and radius changes are included in a first-order sense by the averaging of the upstream and downstream flow conditions.

$$M_2 = \left(\frac{u_2^2}{1 - \frac{\gamma - 1}{2} u_2^2} \right)^{\frac{1}{1/2}} \tag{E.16}$$

Finally, the skin-friction loss coefficient can be calculated from the total-pressure ratio:

$$\left(\frac{p_{t2}}{p_{t1}} \right)_{skf} = \frac{u_2}{u_1} \frac{M_1^2}{M_2^2} \left(\frac{2 + (\gamma - 1) M_2^2}{2 + (\gamma - 1) M_1^2} \right)^{\frac{\gamma}{\gamma/(\gamma-1)}} \tag{E.17}$$

$$\bar{\omega}_{skf} = \frac{1 - (p_{t2}/p_{t1})_{skf}}{1 - p_1/p_{t1}} \tag{E.18}$$

where

$$\frac{p_1}{p_{t1}} = \left(1 + \frac{\gamma - 1}{2} M_1^2 \right)^{-\gamma/(\gamma-1)} \tag{E.19}$$

Note that the above set of equations can be solved explicitly, in sequence, and that the positive sign in Equation (E.15) is used for axial-supersonic outflow conditions. The resulting loss coefficient is consistent with momentum conservation, by definition, and as such represents the "mixed-out" wake losses.

Bow shock wave loss model

An approximate method for estimating the bow shock wave losses for an array of blunt flat plates is formulated by assuming that each bow shock is independent of the other plates (or blades) and that each wave extends to infinity in a uniform upstream flow field. The model is an inviscid, linear, two-dimensional approximation and implicitly assumes that the upstream flow is axial-supersonic and the blade leading edges are "thin" relative to the plate spacing. A schematic depicting the basic flow field is shown in Figure E.2.

As illustrated in Figure E.2, the basic arrangement involves no stagger in the cascade of plates, and the plate leading-edge profiles are circular. This basic model is discussed

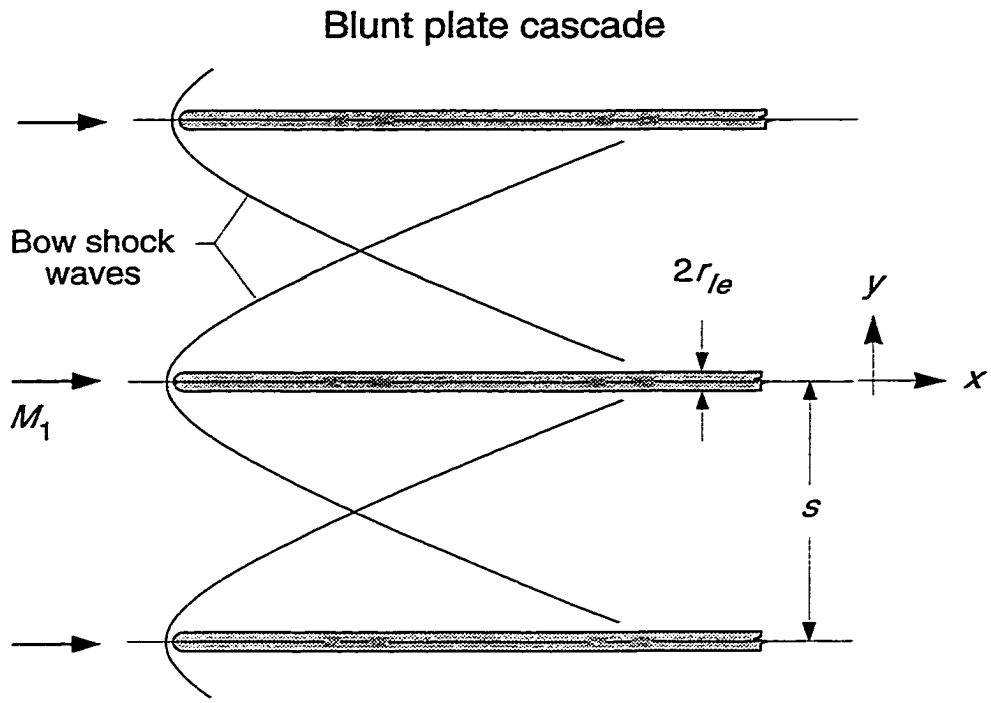

Figure E.2 Two-dimensional blunt-plate cascade for formulating the bow-shock total-pressure loss

first, followed by a description of adjustments to the model in order to account for the influence of non-zero relative inflow angles [4] and for elliptically-shaped leading edges.

The bow shock loss coefficient is a parameter representing the average total-pressure loss generated by the circumferentially-periodic system of bow shocks:

$$\bar{\omega}_{bwv} = \frac{1 - (p_{t2}/p_{t1})_{bwv}}{1 - p_1/p_{t1}} \tag{E.20}$$

[4] This is not an incidence effect, but rather a flow-area reduction effect due to non-zero relative inflow angles. The incidence angle is assumed to be always zero for this model.

The linear approximation involves considering each shock as independent, and furthermore as being symmetrical and in a uniform upstream flow field. Under this set of assumptions the total-pressure loss coefficient becomes a function of the upstream Mach number M_1, the dimensionless shock wave shape, and the dimensionless leading-edge bluntness parameter r_{le}/s:

$$\bar{\omega}_{bwv} \approx \frac{r_{le}}{s} f(M_1) \tag{E.21}$$

In Equation (E.21) the dimensionless shape of the shock wave is imbedded in the function, which involves some form of flow integration and averaging in the direction normal to the incident flow; namely, in the y-direction in Figure E.2. It is assumed that the integration can be extended to virtual infinity, which in the practical sense requires that the thickness parameter r_{le}/s be much less than unity; thus, "thin" leading edges are defined in terms of the thickness parameter:

$$r_{le}/s \ll 1 \tag{E.22}$$

Inherent in Equation (E.21) is the basic assumption that the shape of the bow shock wave is independent of the leading-edge bluntness parameter, and thus depends only on the upstream Mach number M_1. This is based on the thin leading-edge assumption, and is ultimately where the model derives most of its utility. Specifically, the functional dependency of loss coefficient on upstream Mach number needs to be determined for only one particular "reference" value of the bluntness parameter:

$$\left(\frac{\bar{\omega}_{bwv}}{r_{le}/s}\right)_{ref} \approx f(M_1) \tag{E.23}$$

The general approach taken here involved correlating the loss coefficient with the upstream Mach number, for a bluntness parameter $(r_{le}/s)_{ref}$ value of 0.010. Initially this was done by using an approximate, semi-empirical model for the shape of the bow shock wave, namely, the model developed by Moeckel [89] and later improved somewhat by Love [90]. However, since this model is fairly accurate only for the "near-field" portion of the bow wave, it was reasoned that a better approximation might be obtained through CFD methods. Therefore, several two-dimensional, inviscid CFD simulations were performed for different upstream Mach numbers on a blunt flat-plate cascade. The

computations were performed using the quasi-three-dimensional, finite-difference CFD code developed by Chima [42] for the viscous or inviscid analysis of turbomachinery blade-to-blade flows. The code solves the Euler equations or the thin-layer formulation of the Navier-Stokes equations on a C-type grid, which in this case had dimensions 225×75. Half of the (symmetrical) grid is shown in Figure E.3. Note that viscous effects were deliberately excluded for the present analysis.

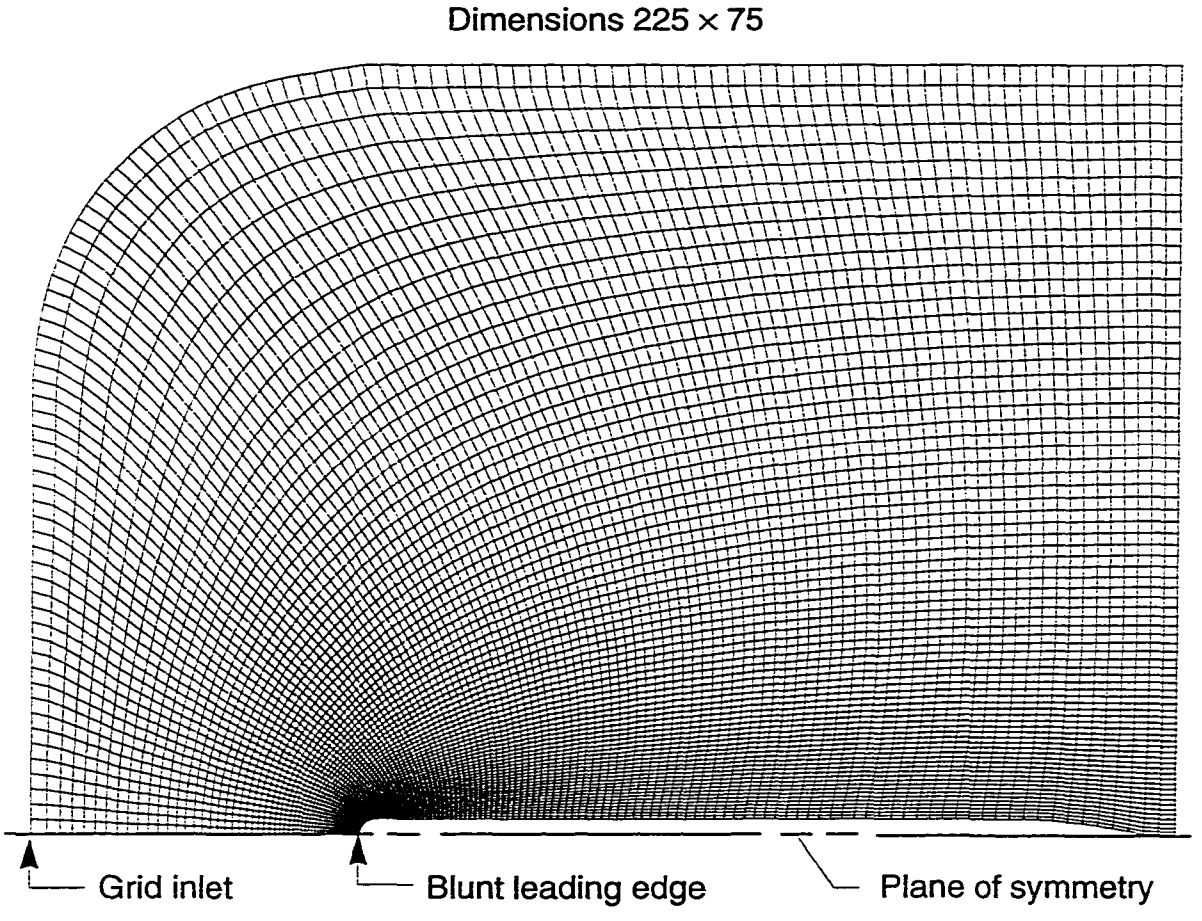

Figure E.3 Computational grid for two-dimensional inviscid CFD analysis of blunt-plate bow shock wave (only upper half of grid is shown)

Dimensionless total-pressure contour plots for two cases are shown in Figures E.4 and E.5, representing upstream Mach numbers of 1.80 and 2.70, respectively. In Figure E.6 the near-field shock wave shapes for these two cases, and an additional case for upstream Mach number 1.35, are compared with experimentally determined shapes [90,92] and with the shapes modeled semi-empirically [5]. As expected, the computed shocks are smeared over several grid lines due to the central-difference scheme employed in the numerical algorithm, but the agreement between all three shapes at all three Mach numbers is very good in the leading-edge region.

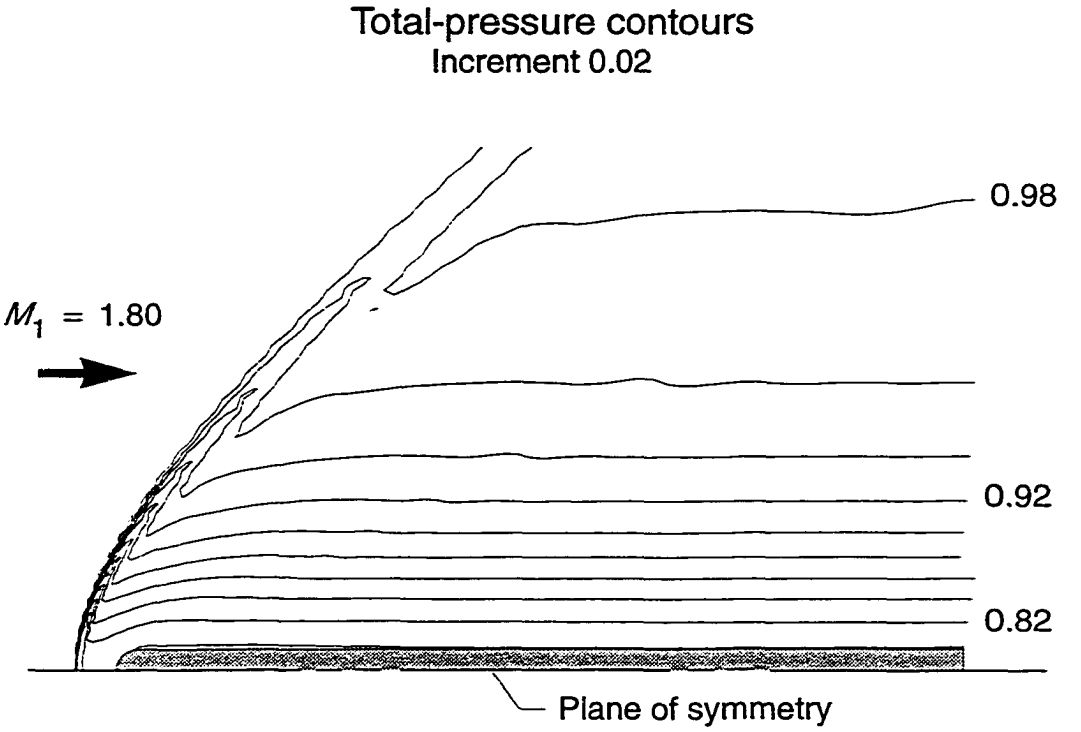

Figure E.4 Dimensionless total-pressure contours for computed bow shock with upstream Mach number 1.80

[5] The improvements suggested in Reference 90 have been incorporated into this model.

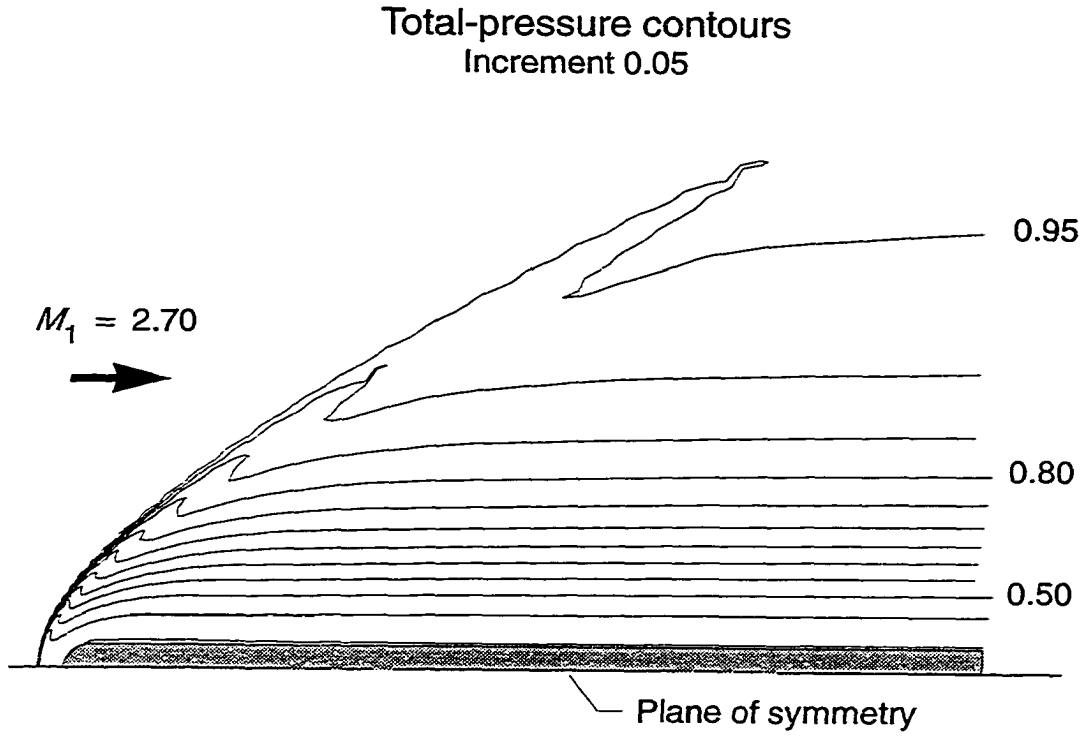

Figure E.5 Dimensionless total-pressure contours for computed bow shock with upstream Mach number 2.70

Flow-field integrations in the circumferential direction have been performed on all of the CFD solutions — for upstream Mach numbers 1.35, 1.60, 1.80, 2.40, 2.70, and 3.20 — and, for comparison, on corresponding shock wave shapes as approximated using the semi-empirical fit. The resulting average loss coefficients are graphed in Figure E.7 against upstream Mach number. The solid lines in Figure E.7 represent correlations for the CFD results, for two different types of averaging procedures, and the dashed line represents the results derived from the semi-empirical shock wave shapes. The so-called *entropy-average* results for both the semi-empirical model and the lower CFD correlation curve can be directly compared, and thus reveal that the computed shock waves are significantly stronger than those of the semi-empirical model. This result is not surprising since it is generally accepted that the hyperbolic curve used in the semi-empirical model does

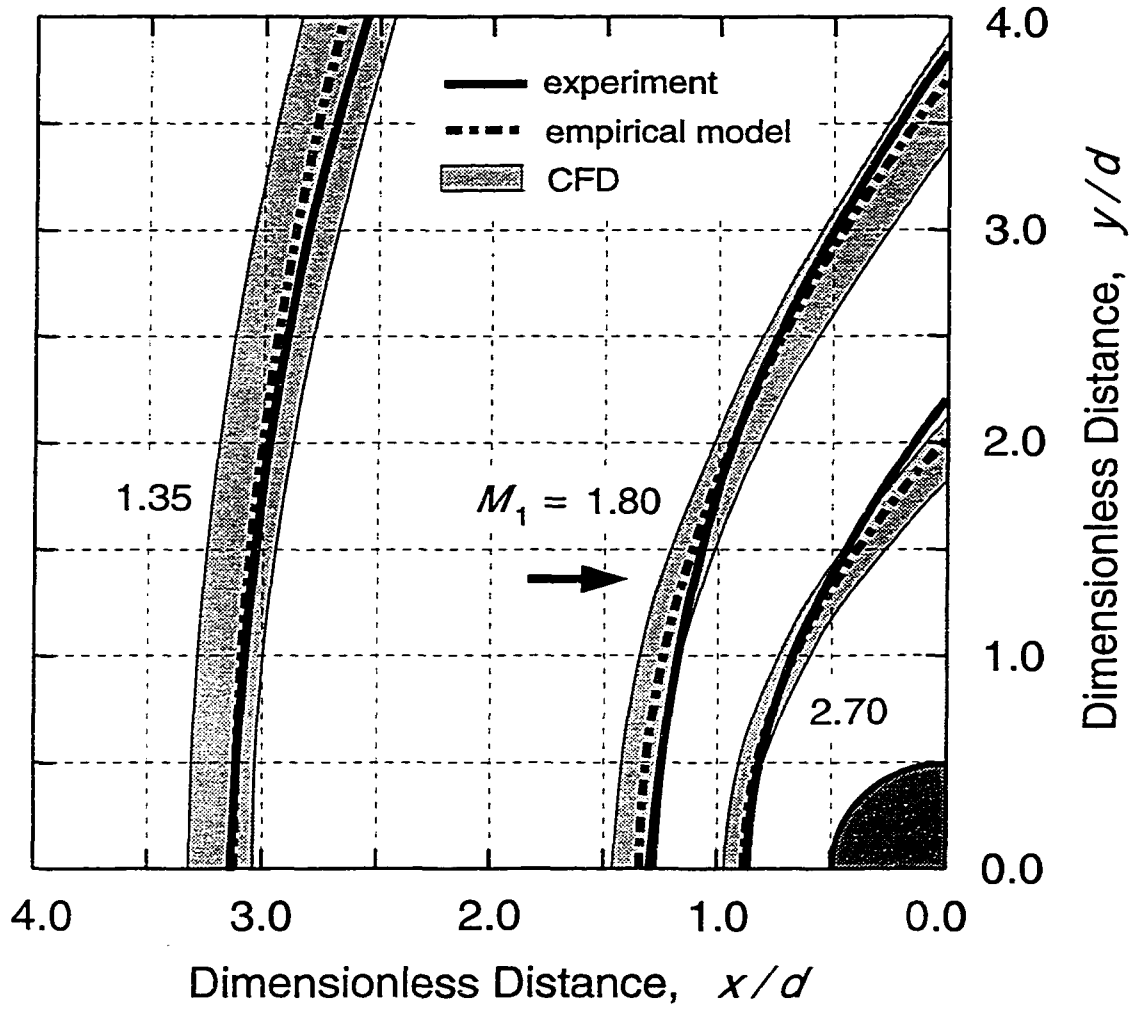

Figure E.6 Comparison of experimental [92], modeled [90], and computed (CFD) detached shock wave shapes and locations at different Mach numbers for a two-dimensional circular cylinder

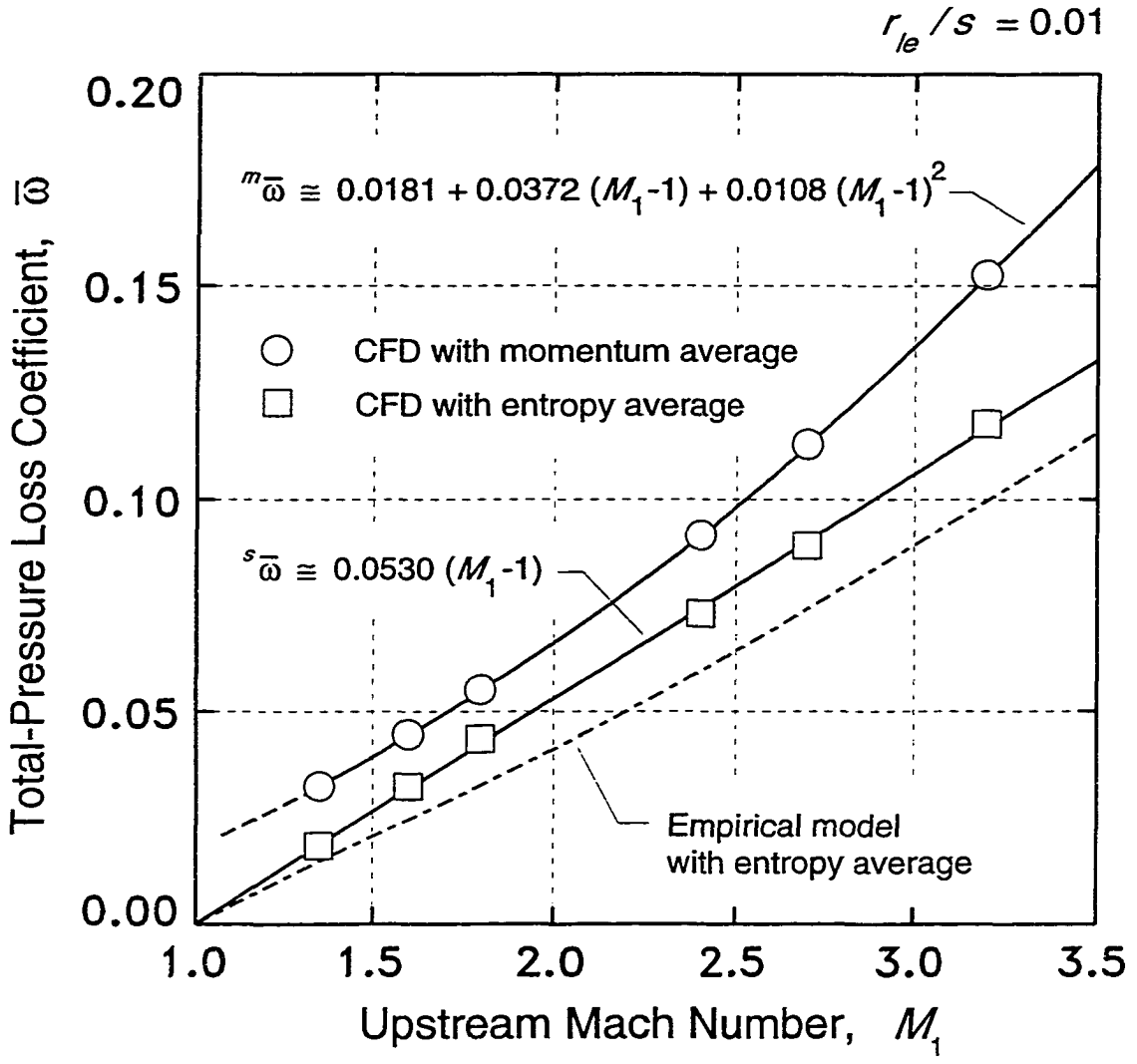

Figure E.7 Total-pressure loss correlation for an inviscid flat-plate cascade with blunt circular leading edges (leading-edge radius equal to one percent of plate spacing), with zero plate stagger, and at zero incidence

not accurately fit the shock wave shape in the "far-field" region. Apparently, the hyperbolic-fit shock wave attenuates too rapidly with distance from the plate leading edge.

The entropy-averaging procedure provides a total-pressure loss which reflects the mass-average entropy rise for the entire blade-to-blade flow; therefore, it is believed to correctly represent the actual total-pressure loss generated by the (computed) shock, apart from any viscous mixing in the rotational flow field downstream of the curved bow-shock. As indicated in Figure E.7, the correlation of entropy-average CFD results is linear:

$$({}^{s}\bar{\omega}_{bwv})_{ref} \approx 0.0530\,(M_1 - 1) \tag{E.24}$$

Thus, from Equations (E.21) and (E.23), the general equation for the entropy-average loss coefficient follows:

$${}^{s}\bar{\omega}_{bwv} \approx 5.30\,(M_1 - 1)\,(r_{le}/s) \tag{E.25}$$

A description of the entropy-averaging procedure used here can be found in Appendix C. Also contained in Appendix C is a description of a so-called momentum-averaging procedure, which is so named because it averages the results in a way consistent with momentum conservation. The momentum-average CFD loss coefficients in Figure E.7 correctly reflect the momentum deficit produced by the bow waves. This type of loss coefficient is similar to that discussed earlier in regard to the skin-friction loss which, it will be recalled, was related to the viscous drag force on the thin-flat-plate cascade. To obtain these results the CFD flow field was averaged at an axial location upstream of the plate trailing edges so as to avoid the additional total-pressure losses produced by the trailing edges. In effect, it is as if the plates extended to downstream infinity, and the rotational flow behind the curved bow shock allowed to mix-out completely. The additional total-pressure losses incurred in this constant-area, adiabatic mixing process are embodied by the differences between the momentum- and entropy-average results. The momentum-average losses have been correlated as indicated in Figure E.7, resulting in the following general formulation:

$${}^{m}\bar{\omega}_{bwv} \approx [1.81 + 3.72\,(M_1 - 1) + 1.08\,(M_1 - 1)^2]\,(r_{le}/s) \tag{E.26}$$

It should be pointed out that Equation (E.26), rather than Equation (E.25), will be used as the accepted model for the bow shock loss. This selection provides fundamental consistency between the "momentum-based" bow-shock loss coefficient and the "drag-based" skin-friction loss coefficient of the previous subsection.

An adjustment to the leading-edge spacing can be made in order to account for the first-order effects of a non-zero inflow angle. The adjustment is simple and consists of correcting the actual spacing s_0 to an effective spacing s, corresponding to the relative inflow angle β_1 as illustrated in Figure E.8. From the figure, the following relationship is apparent:

$$s = s_0 \cos\beta_1 \tag{E.27}$$

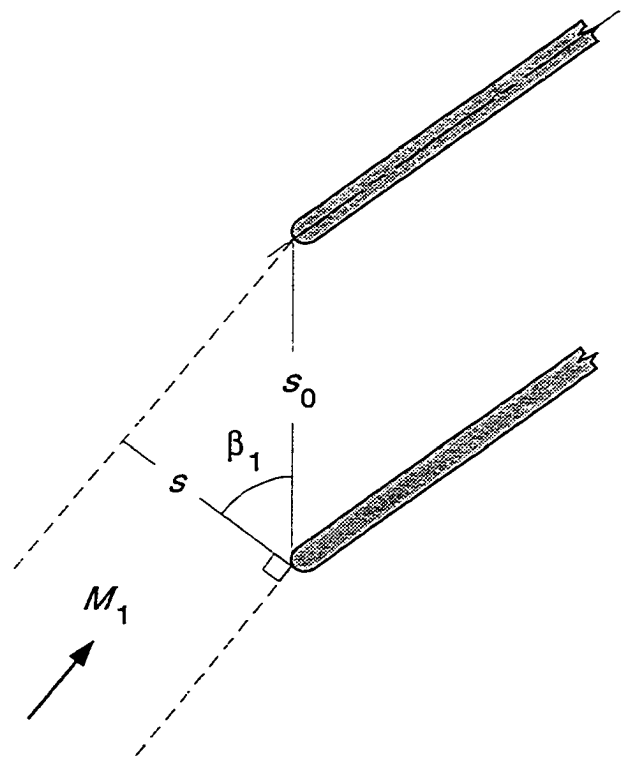

Figure E.8 Geometric relationship between the actual and effective blade spacing for use in the bow-shock loss model

An adjustment to account for the influence of leading-edge ellipse eccentricity is also modeled. This is done using a correlation of CFD results for two upstream Mach numbers, 1.6 and 2.4, and several different leading-edge ellipse eccentricities. The ellipse parameter ε is used:

$$\varepsilon \equiv (b/a)_{le} - 1 \tag{E.28}$$

where b and a are the ellipse major and minor axis lengths, respectively, as depicted in Figure E.9. The computational analysis was virtually the same as that conducted for the circular leading edges, except for the changes in the leading-edge geometry. Three different values for the ellipse parameter were examined; namely, values of 1, 3, and 5.

The correlation assumes that Mach number effects are second-order, and thus can be neglected. The effects of increasing ellipse eccentricity are modeled as an "effective" circular leading-edge radius r_{le}, so that the bow-shock loss correlation of Equation (E.26) can be applied. The following relationship can be deduced from Equation (E.21), under the assumption of negligible Mach number influence:

$$\frac{r_{le}}{a_{le}} \approx \left(\frac{\bar{\omega}}{\bar{\omega}_0}\right)_{bwv} = f(\varepsilon) \tag{E.29}$$

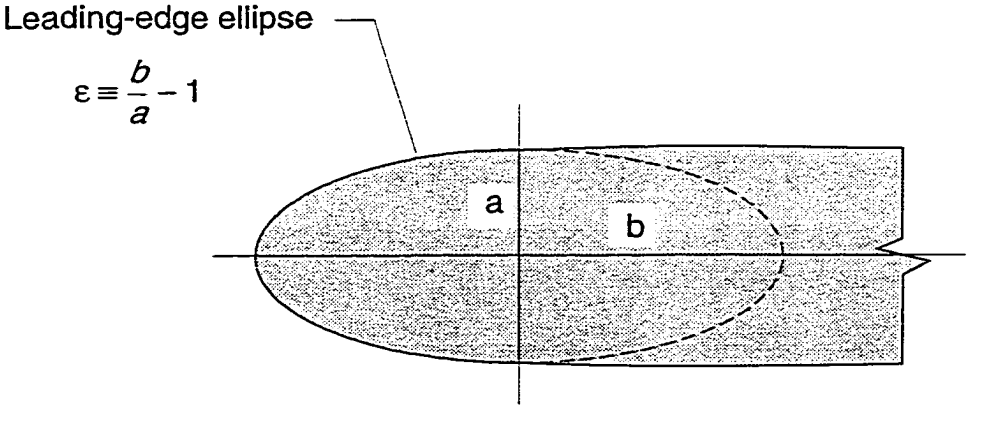

Figure E.9 Definition of leading-edge ellipse parameter ε

where $\bar{\omega}_0$ is the loss coefficient for a circular leading edge. The dimensionless loss-coefficient results obtained from the CFD solutions are graphed in Figure E.10 as a function of the ellipse parameter. As can be seen, there is a significant Mach number effect, but it is within the general accuracy of the overall loss model being attempted here; hence, it is not unreasonable to neglect it. An exponential curve fit has been made to the data for Mach 2.4 — considered to be a representative mean Mach number for the model in general — with the following result:

$$\left(\frac{\bar{\omega}}{\bar{\omega}_0}\right)_{bwv} \approx \exp\left(-0.18\varepsilon^{0.84}\right) \tag{E.30}$$

An exponential function was chosen because it has the desirable characteristic of approaching zero as the ellipse parameter goes to infinity (a sharp leading edge), as well as having a value of one for a circular leading edge. From Equations (E.29) and (E.30), the effective leading-edge radius becomes a simple function of the leading-edge half-thickness a_{le} and the ellipse parameter:

$$r_{le} \approx a_{le} \exp\left(-0.18\varepsilon^{0.84}\right) \tag{E.31}$$

As a concluding remark to this subsection, note that at upstream Mach numbers below about 1.5 the bow-shock loss model begins to loose much of its validity. As transonic conditions are approached even "thin" leading-edges produce large flow-field disturbances. In fact, for the particular blunt plate cascade considered above, inflow Mach numbers in the range of about 0.85 to 1.20 are not even possible due to the 2 percent plate blockage. Thus, it should be emphasized that the model is intended only for cases with relative inflow Mach numbers exceeding transonic conditions by a sufficient margin.

Oblique-shock loss model

The total-pressure losses due to oblique shock waves which extend across most of the blade passage are modeled by applying several simplifying assumptions. The first is that the upstream flow is axial-supersonic, which is consistent with the bow shock model. The second, and probably most important assumption, involves the concept that all oblique shocks of significant strength originate at the leading edges of the blades. Although at first glance this may seem unreasonable, it proves to be a consequence of high-solidity blade

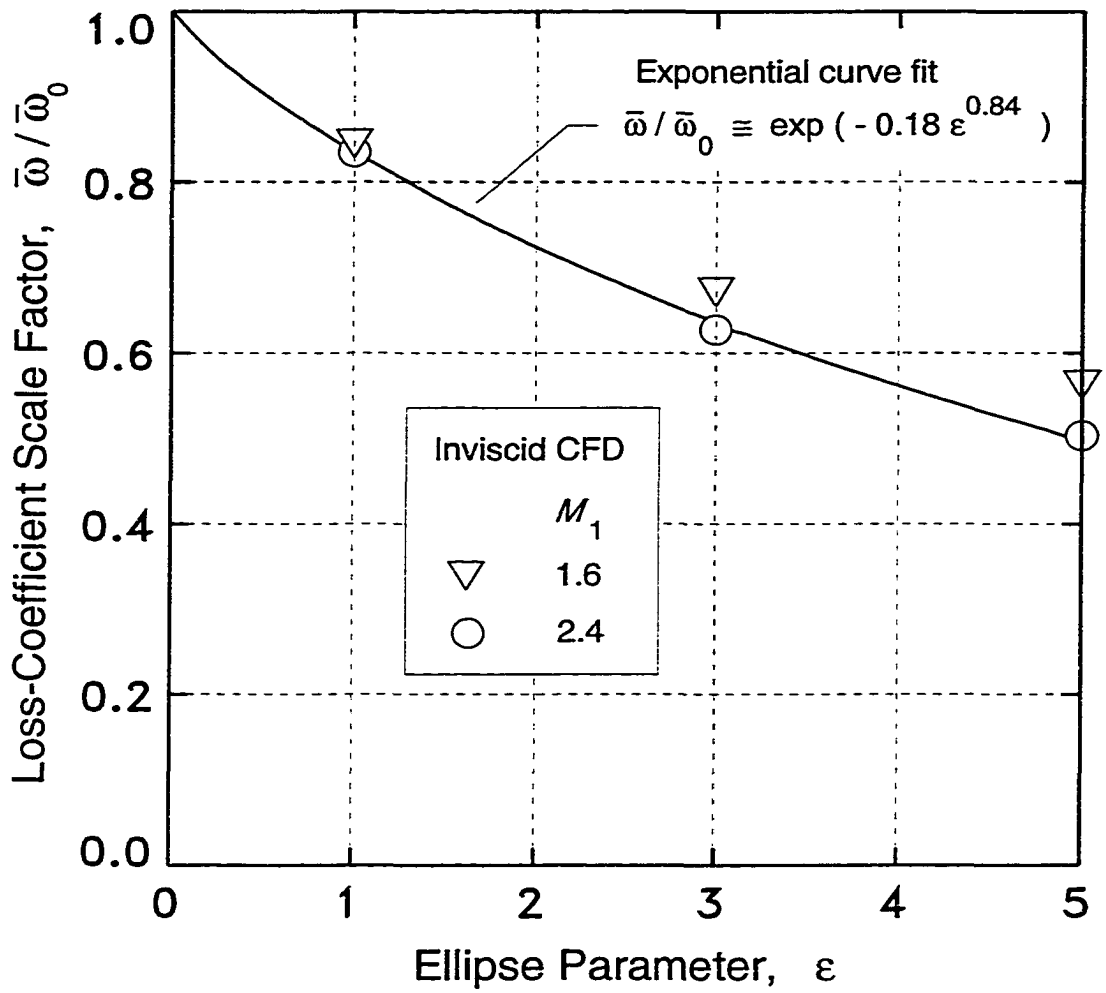

Figure E.10 Bow shock wave total-pressure loss correlation for the influence of leading-edge ellipse eccentricity, based on two-dimensional inviscid CFD results for an upstream Mach number of 2.4

elements with low-to-moderate blade camber. In essence, the model presupposes that any fairly strong oblique shocks generated by incidence and blade leading-edge "wedge-angle" effects are completely cancelled by the blade suction-surface, whether the waves are left- or right-running, because of the high length-to-width ratio of the blade channel. This effect is largely a consequence of the fact that such blade channels are normally *designed* to cancel any waves generated off the bow of the blades, at least for design point operation.

The simplified flow-field model considers all oblique shock waves to extend across the entire blade passage and to be straight with uniform flow conditions immediately upstream and downstream. Blade leading edges are treated as sharp since bluntness effects are modeled separately in the bow-shock loss term. The suction and pressure surfaces downstream of the leading edges are assumed to be approximately straight, thus forming a two-dimensional wedge as illustrated in Figure E.11. Referring to this figure,

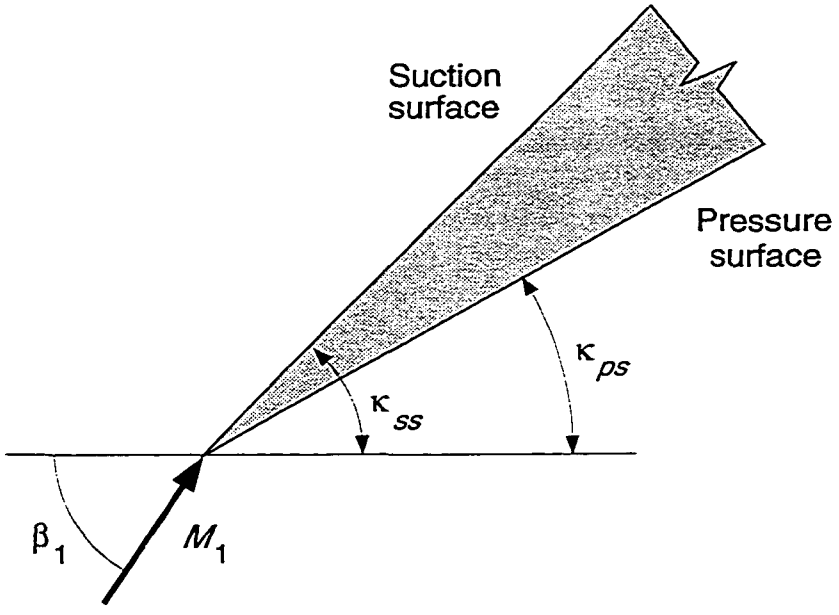

Figure E.11 Illustration of the sharp leading-edge wedge model and definitions of blade metal angles

flow deflection angles δ_{ss} and δ_{ps} for each surface are simple functions of the relative inflow angle β_1 since the blade surface angles are known for a particular blade geometry:

$$\delta_{ss} = \kappa_{ss} - \beta_1 \tag{E.32}$$

$$\delta_{ps} = -\kappa_{ps} + \beta_1 \tag{E.33}$$

Positive deflection angles produce an oblique shock which emanates from the leading edge on that side, whereas negative deflection angles produce a Prandtl-Meyer expansion fan centered at the edge. The pertinent equations for oblique shock waves and Prandtl-Meyer expansions are now reviewed, although they can be found in most standard textbooks or references on compressible fluid flow or gas dynamics. For example, see Reference 53 or 68. The equations are included here for completeness and convenience. These descriptions are followed by a discussion of the basic "frontal" wave combinations and the approximate total-pressure losses generated by each.

Prandtl-Meyer expansion — A "negative" flow deflection produces a Prandtl-Meyer expansion fan, which is depicted in Figure E.12. Since the value of the deflection angle δ is negative, the following equation applies:

$$\nu_2 = \nu_1 - \delta \tag{E.34}$$

where ν is the Prandtl-Meyer angle and is a function of Mach number:

$$\nu = \sqrt{\frac{\gamma+1}{\gamma-1}}\ \tan^{-1}\sqrt{\frac{\gamma+1}{\gamma-1}(M^2-1)} - \tan^{-1}\sqrt{M^2-1} \tag{E.35}$$

The downstream value of the Prandtl-Meyer angle ν_2 is determined from Equation (E.34), from which the downstream Mach number M_2 is calculated iteratively using Equation (E.35). There is no total-pressure loss through the expansion:

$$\frac{p_{t2}}{p_{t1}} = 1 \tag{E.36}$$

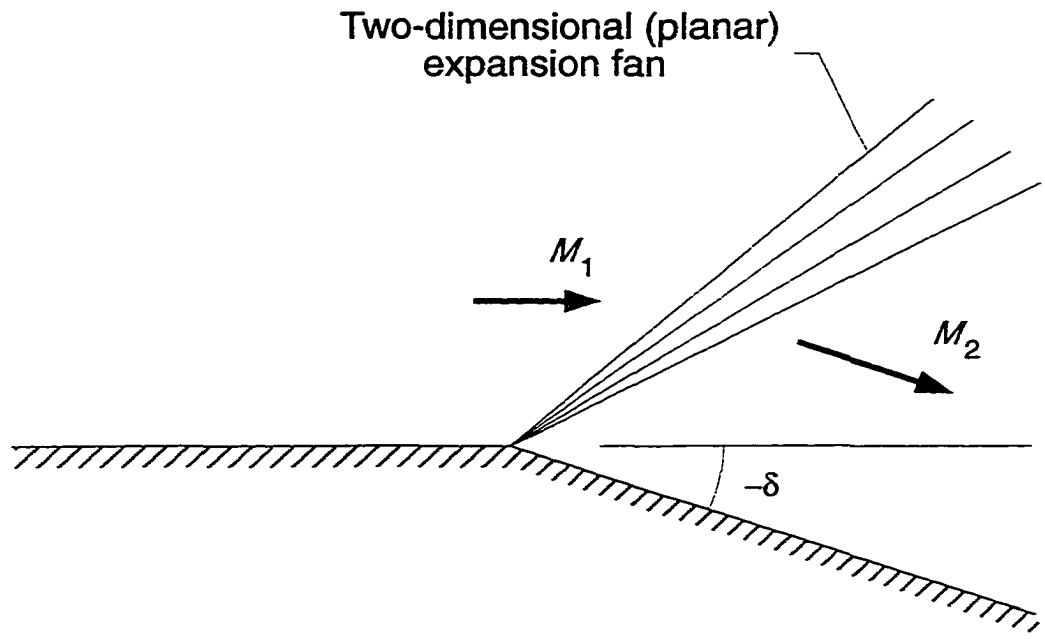

Figure E.12 Prandtl-Meyer expansion fan

Oblique shock wave — A positive flow deflection causes an oblique shock wave to be generated, as long as the deflection is not too large or the Mach number is not too low, i.e., too close to transonic conditions. The shock wave angle θ, depicted in Figure E.13, can be determined [6] from the upstream Mach number M_1 and the flow deflection angle δ:

$$\tan\theta\left(\frac{(\gamma+1)M_1^2}{2\,(M_1^2\sin^2\theta-1)}-1\right)=\frac{1}{\tan\delta} \tag{E.37}$$

---

[6] Most standard references present some form of this implicit formula, which requires an iterative solution procedure to solve for θ. As of 1972, however, an explicit and analytically exact expression has existed as derived by Wellmann [93], and published more recently in a brief technical paper by Wolf [94].

The downstream Mach number M_2 can be explicitly calculated using the upstream Mach number component normal to the shock wave:

$$M_{n1} = M_1 \sin\theta \tag{E.38}$$

$$M_2 = \left(\frac{(\gamma-1)M_{n1}^2 + 2}{2\gamma M_{n1}^2 - (\gamma-1)} \right)^{\frac{1}{1/2}} \frac{1}{\sin(\theta-\delta)} \tag{E.39}$$

The total-pressure ratio across the shock is also calculated explicitly using the relationship for a normal shock wave:

$$\frac{p_{t2}}{p_{t1}} = \left(\frac{(\gamma+1)M_{n1}^2}{(\gamma-1)M_{n1}^2 + 2} \right)^{\gamma/(\gamma-1)} \left(\frac{\gamma+1}{2\gamma M_{n1}^2 - (\gamma-1)} \right)^{1/(\gamma-1)} \tag{E.40}$$

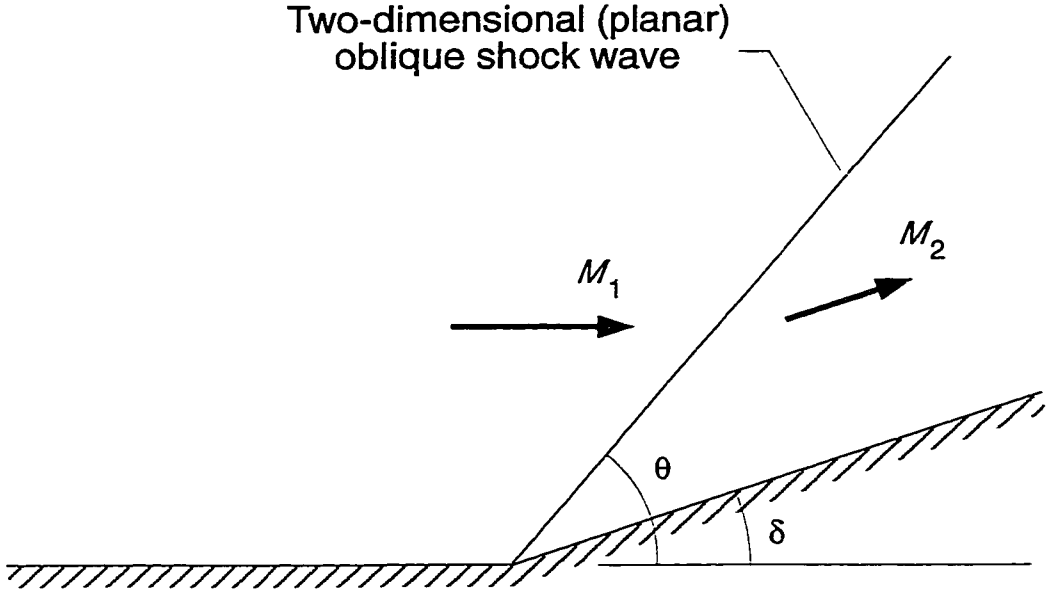

Figure E.13 Two-dimensional (planar) weak oblique shock wave

Frontal wave systems — Basically there are three different frontal wave systems, that is, shock and expansion wave combinations, that form in the front half of the blade passage. The formation which occurs depends on the flow deflection angles for each surface just behind the leading edge:

Case 1: $\delta_{ss} \leq 0$ and $\delta_{ps} > 0$

Case 2: $\delta_{ss} > 0$ and $\delta_{ps} \leq 0$

Case 3: $\delta_{ss} > 0$ and $\delta_{ps} > 0$

These three cases are illustrated in Figures E.14 to E.16, respectively, and they are now discussed in that order. Note that in all cases the influence of blade camber on Mach numbers and flow angles are neglected.

The first case, depicted in Figure E.14, occurs at zero and positive suction-surface incidence angles i_{ss} . The Prandtl-Meyer expansion relations are used to determine the Mach

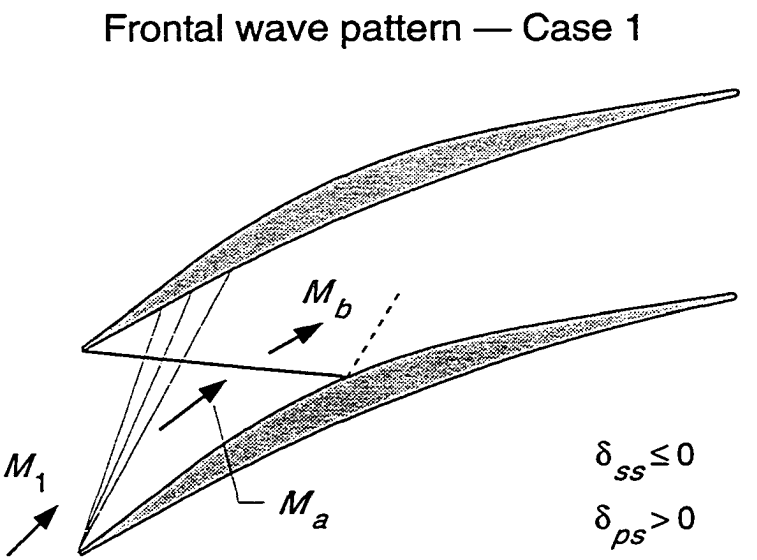

Figure E.14 Frontal wave pattern for zero and positive suction-surface incidence angles

number M_a , which is then used in the oblique shock relations with the pressure-surface deflection angle δ_{ps} to estimate the free-stream total-pressure ratio:

$$\left(\frac{p_{t2}}{p_{t1}}\right)_{obq} \approx \frac{p_{tb}}{p_{t1}} = \frac{p_{tb}}{p_{ta}} \frac{p_{ta}}{p_{t1}} \approx f_{obq}(M_a, \delta_{ps}) \tag{E.41}$$

The second case, depicted in Figure E.15, occurs at moderate-to-large negative suction-surface incidence angles. The oblique shock and Prandtl-Meyer expansion relations are used as needed, according to Figure E.15, in order to estimate the cumulative total-pressure loss in the free stream:

$$\left(\frac{p_{t2}}{p_{t1}}\right)_{obq} \approx \frac{p_{tc}}{p_{t1}} = \frac{p_{tc}}{p_{tb}} \frac{p_{tb}}{p_{ta}} \frac{p_{ta}}{p_{t1}} \tag{E.42}$$

where

$$\frac{p_{ta}}{p_{t1}} \approx f_{obq}(M_1, \delta_{ss}) \tag{E.43}$$

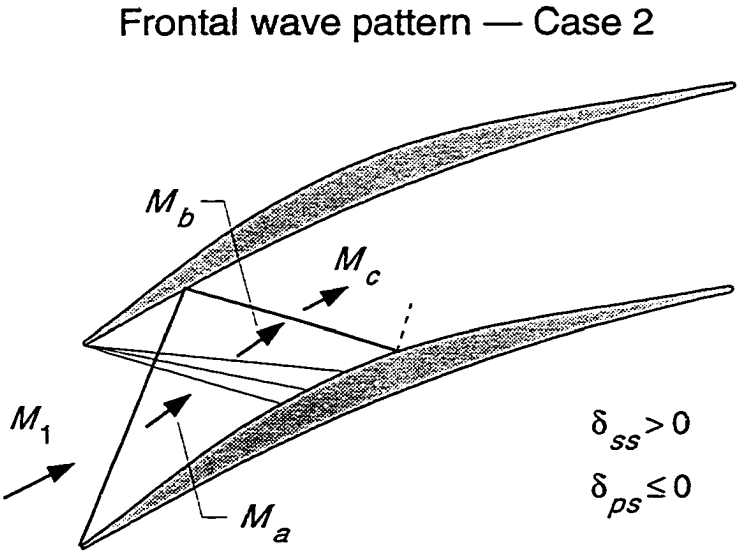

Figure E.15 Frontal wave pattern for moderate-to-large negative suction-surface incidence angles

$$\frac{p_{tb}}{p_{ta}} = 1 \tag{E.44}$$

$$\frac{p_{tc}}{p_{tb}} \approx f_{obq}(M_b, \delta_{ss}) \tag{E.45}$$

The third and last case, depicted in Figure E.16, occurs at small, negative suction-surface incidence angles. This case is similar to the second one, except that no expansion fan is encountered. Therefore Equations (E.42) through (E.45) still apply, except that the total-pressure ratio from state *(a)* to *(b)* is no longer unity; that is, Equation (E.44) must be replaced by the equation for the total-pressure ratio across an oblique shock:

$$\frac{p_{tb}}{p_{ta}} \approx f_{obq}(M_a, \delta_{ps}) \tag{E.46}$$

It was mentioned earlier that an iterative procedure is required to solve the equations for the Prandtl-Meyer expansion (or the oblique shock wave if the implicit formula is

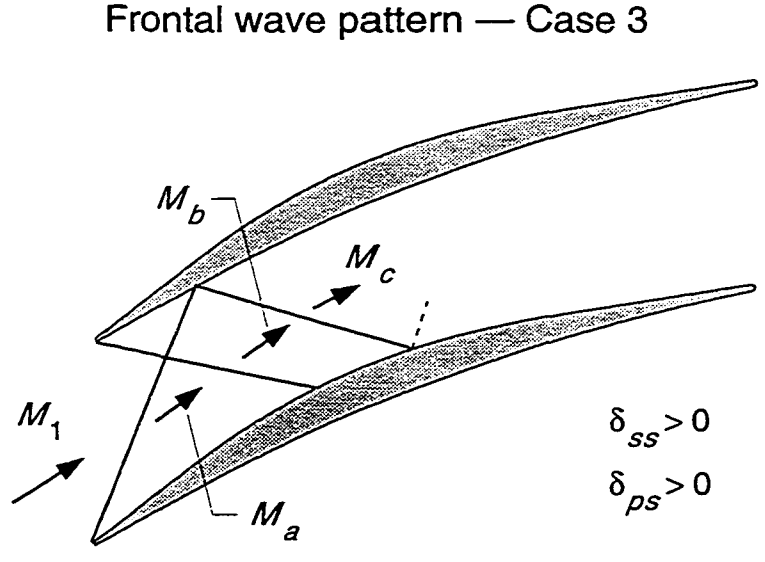

Figure E.16 Frontal wave pattern for small negative suction-surface incidence angles

used). Thus, each of the above cases actually involves a sequence of two or three iterative steps. These solutions, however, present no difficult problems and are easily and quickly obtained on even a small computer. Finally, the oblique-shock loss coefficient is calculated from the cumulative total-pressure ratio:

$$\bar{\omega}_{obq} = \frac{1 - (p_{t2}/p_{t1})_{obq}}{1 - p_1/p_{t1}} \tag{E.47}$$

Shock/boundary-layer interaction loss model

No serious effort has been made to physically model the shock/boundary-layer interaction term in Equation (E.1), although it is realized that this term could in many cases become very significant as the strengths of the oblique shocks in the blade passages increase, especially at large positive or negative incidence angles. A first-order approach to estimate its magnitude, however, is attempted here in a simple linear[7] relationship to the oblique shock loss:

$$\bar{\omega}_{sbl} \approx k\,\bar{\omega}_{obq} \tag{E.48}$$

where k is a constant. This approximation implies that the added viscous loss resulting from shock/boundary-layer interaction effects increases in direct proportion to the strength (total-pressure loss) of the oblique shock waves. Such a linear model seems reasonable as long as the interactions are not too strong, which is generally consistent with the requirement that only low diffusion levels exist.

Viscous CFD studies of a two-dimensional supersonic throughflow cascade, to be discussed in the next subsection, have indicated that in some cases the shock/boundary-layer term may not be very significant. Based on the computational results, the value of the constant k appears to be small, at about 0.1 for positive suction-surface incidence angles and zero for negative incidence angles. Indeed, for that particular cascade the shock/boundary-layer loss term could be neglected. The primary reason for including the loss term, however, is to provide a means, whether empirical or theoretical, for potential adjustments to the loss model as it is more generally applied.

---

[7] A non-linear equation could be used instead.

Two-Dimensional Supersonic Throughflow Cascade

Experimental and computational (CFD) results for a two-dimensional, linear, supersonic throughflow cascade are now compared with results obtained using the loss model. The experimental cascade has an inflow Mach number of 2.36 and an inflow angle of 37 degrees at the zero suction-surface incidence condition. The cascade Reynolds number is about 4.2×10^6 based on the upstream flow conditions and the blade chord.

A variety of experimental data have been acquired and analyzed, as reported in References 73 through 75; however, only a very limited amount of the data are discussed here in order to stay within the scope of this work. Specifically, only experimental loss coefficient results are presented, mainly to confirm the validity of the CFD total-pressure loss results. The viscous CFD simulations were performed using the quasi-three-dimensional code of Chima [42], on a C-type grid with dimensions 385×49 and assuming two-dimensional streamtubes.

The experimental and CFD total-pressure loss coefficient results are compared in Figure E.17. These results correspond to incidence angles i_{ss} of -10, -5, 0, and 5 degrees, as referenced to the blade suction surface near the leading edge. The axial location is 38.7 percent of axial chord downstream of the cascade. A computational result for 10 degrees incidence is also shown. This incidence condition was also attempted experimentally, but only about 7 degrees positive incidence was possible while still maintaining axial-supersonic inflow, as indicated by flow-field observations using Schlieren photography. Based on theoretical and computational considerations, coupled with experimental oil-flow traces on the blade surfaces [75], it is believed that three-dimensional, secondary-flow effects cause a very premature transition of the cascade inflow from axial-supersonic to axial-subsonic conditions. This conclusion is also significant for the experimental results shown in Figure E.17, particularly the result for the 5 degrees incidence setting. As can be seen, there is good agreement between the experimental and computational results at the zero and negative incidence conditions, but at the 5-degrees incidence setting the experimental losses are considerably larger than the computed losses. The surface oil-flow traces for the 5 degrees incidence case indicate a strong secondary flow, with substantial boundary-layer separations and large amounts of low-momentum boundary-layer fluid being convected to the midspan region where the total-pressure losses are measured

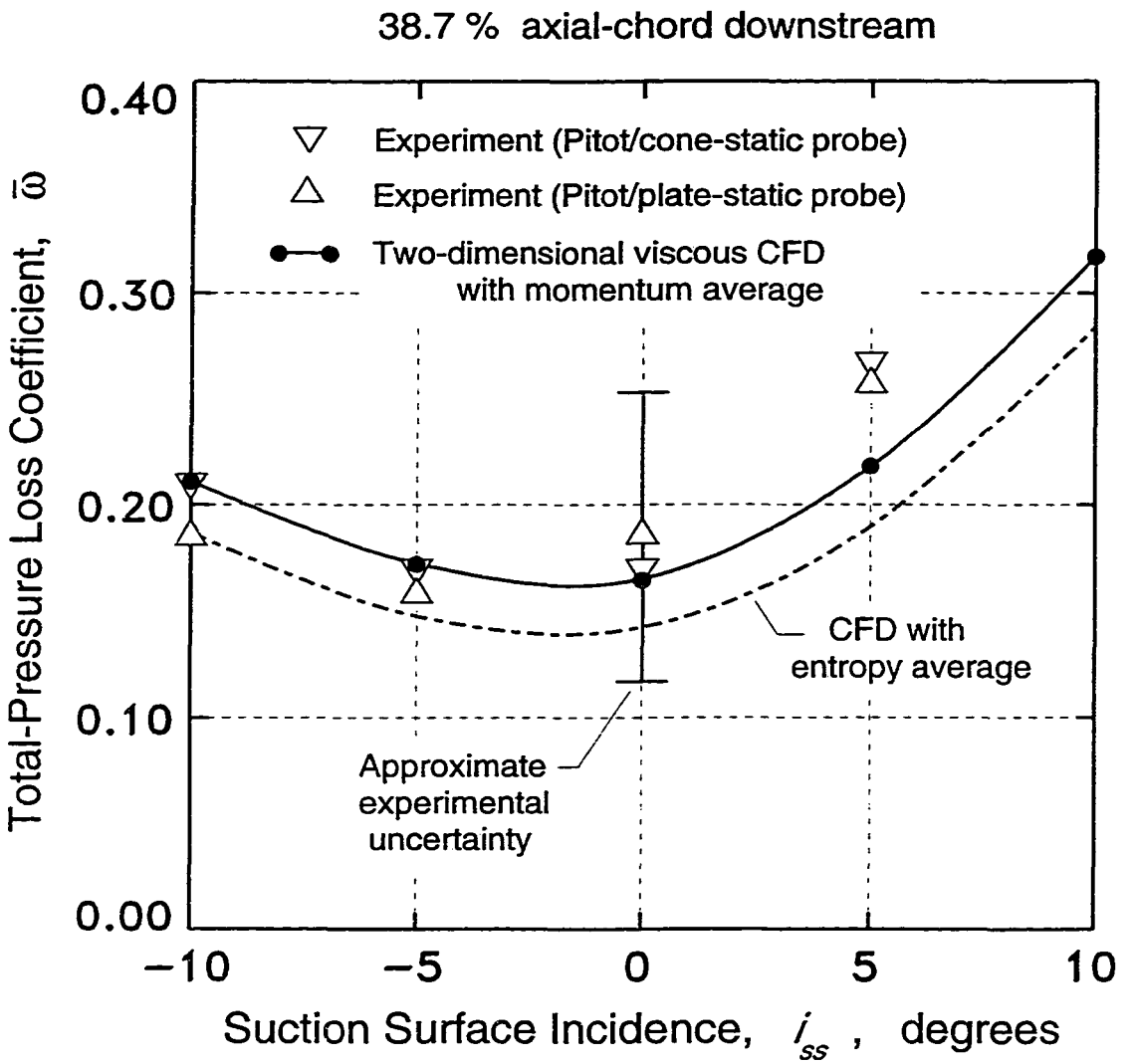

Figure E.17 Comparison of experimental [73,74] and CFD total-pressure losses for a linear, two-dimensional supersonic throughflow cascade with relative Mach number 2.36

(downstream). Therefore, even though unsupported by experimental data, the CFD results for the 5 and 10 degrees incidence angles are assumed to provide fairly good approximations of the cascade total-pressure losses *under two-dimensional flow conditions*, and thus are used to assess the loss model.

The loss coefficients graphed in Figure E.17 were obtained through circumferential integrations of the measured and computed flow fields. As indicated in the figure, the results were averaged using the momentum-averaging procedure (see Appendix C), and as such represent the mixed-out losses. It is these momentum-based losses which are most appropriate for comparisons with the loss model.

Loss coefficient results which were determined through entropy-averaging of the computed flow fields are also shown in Figure E.17, as indicated by the dash-dotted line. Experimental results averaged in the same manner could be compared to this curve, with virtually the same agreement as that exhibited for the momentum-average results. The entropy-based loss coefficients, when compared to the momentum-based loss coefficients, reveal the extent of the wake mixing losses downstream of the measurement plane (38.7 percent of axial chord downstream). Over most of the incidence range shown, the difference between the momentum- and entropy-based loss coefficients — which is the two-dimensional, constant-area, adiabatic mixing loss — is between 0.022 and 0.028, or between 11 and 14 percent of the total mixed-out loss at the zero (design) incidence angle. Entropy-based results corresponding to the cascade trailing edge plane reveal differences between 0.036 and 0.042 (17 to 23 percent of the total mixed-out loss) in the loss coefficient, which differences represent the total mixing-losses occurring under two-dimensional, adiabatic conditions. Based on the CFD, therefore, at the measurement plane location between 60 and 70 percent of the mixing-loss has actually occurred, with another 30 to 40 percent remaining. It should be apparent from these results that supersonic wake flows can involve a substantial mixing loss which requires significantly greater (axial) distances downstream to accomplish the mixing, than do subsonic wake flows. This aspect should not be overlooked when considering either computational or experimental results for turbomachinery blade rows with axial-supersonic velocities at the blade-row exit.

Total-pressure losses calculated using the loss model are compared in Figure E.18 with the experimental and CFD loss results. The curved, solid-line is the total, mixed-out loss predicted using the model, but while neglecting any contribution from the shock/bound-

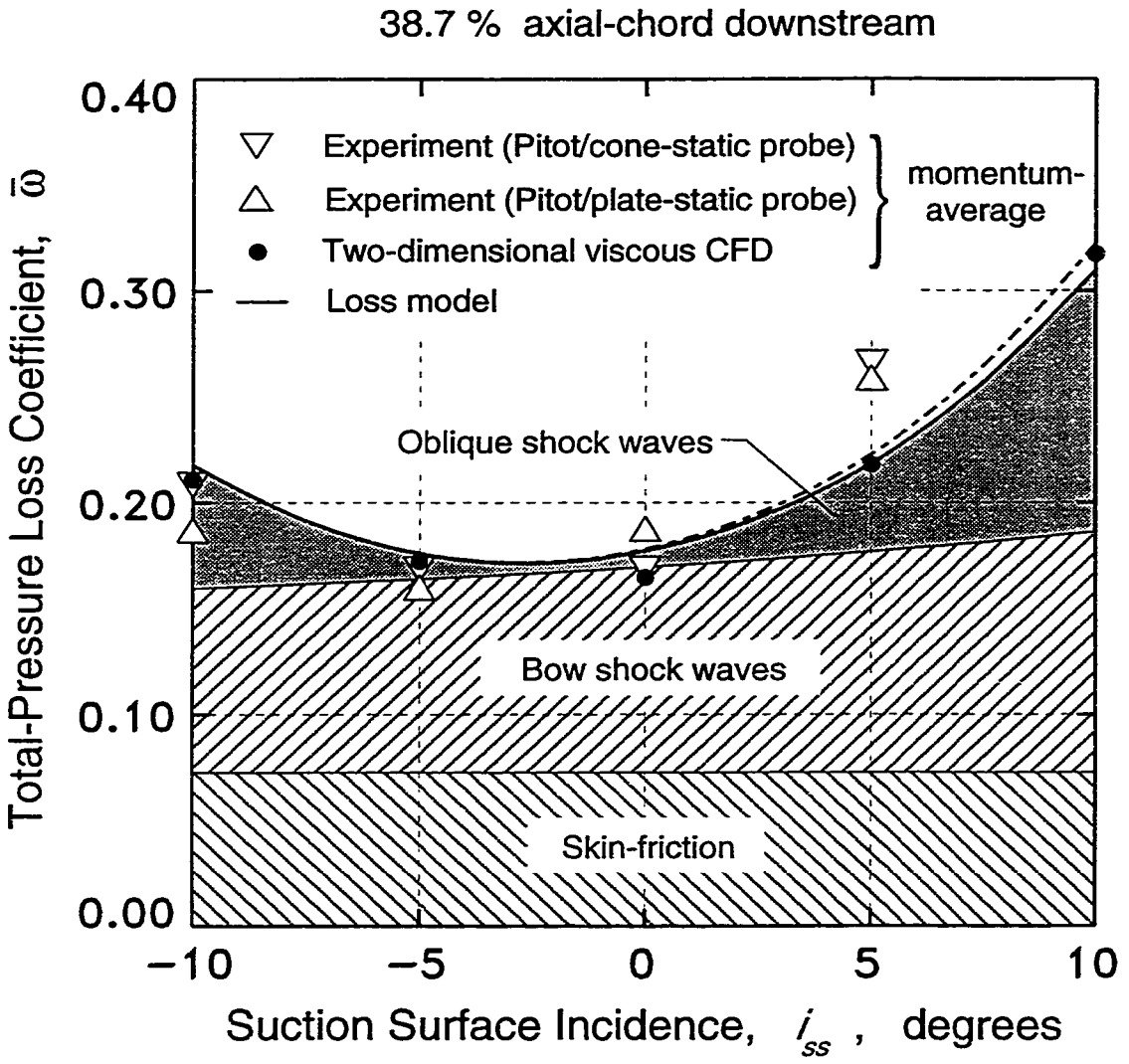

Figure E.18 Comparison of experimental, CFD, and modeled total pressure losses for a linear, two-dimensional supersonic throughflow cascade with relative Mach number 2.36

ary-layer term $\overline{\omega}_{sbl}$. The dashed-line just above it includes a small contribution from this term under positive incidence conditions; specifically, the constant k in Equation (E.48) is given a value of 0.1 for positive suction-surface incidence angles. The contributions from the other loss components are also indicated, where it can be seen that at zero incidence the skin-friction and bow-shock losses are about 40 and 55 percent, respectively, of the total loss. The oblique shock losses at near zero incidences are fairly small, as would be expected near the design point. The skew in the oblique shock loss distribution is due mostly to the incidence being referenced to the suction surface, rather than to the mean camber line. Since the leading-edge "wedge" angle is about 8 degrees, there is about an 8-degree-flow-deflection shock from the leading-edge pressure surface at the zero suction-surface incidence angle. This effect can be easily seen in Figure E.19 which shows Mach

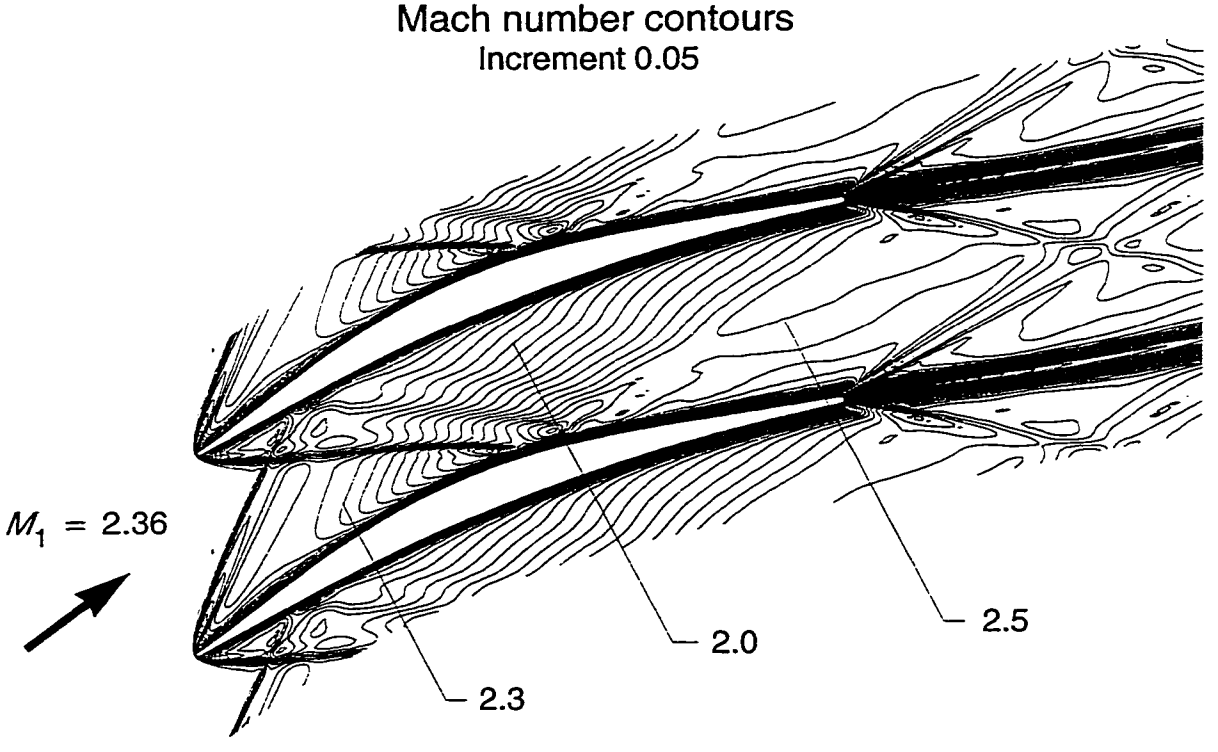

Figure E.19 Two-dimensional viscous CFD Mach number contours for the supersonic throughflow cascade with inflow Mach number 2.36 at zero-incidence

number contours for the zero-incidence CFD flow-field solution. At the negative 10 degrees incidence condition the maximum shock strength corresponds to a 10-degree flow-deflection, whereas at the positive 10 degrees incidence condition the maximum shock strength corresponds to an 18-degree flow-deflection; hence, the larger oblique shock losses at positive incidence angles. The oblique shock strengths, and consequently the oblique shock losses, are at a minimum at about the -4 degree incidence angle, which is about where the inflow is symmetrically divided by the leading-edge wedge.

In order to more closely examine the accuracy of the oblique shock loss model, circumferential distributions of the computed (CFD) losses are shown in Figure E.20. In the free-stream region of the downstream blade-to-blade flow field, approximate zones which bracket the free-stream loss range are indicated for each incidence condition. Using the upper and lower limits of each of these zones, the computed oblique shock losses are graphed versus suction-surface incidence in Figure E.21 for comparison with the oblique shock loss model. As can be seen from the figure, the loss model provides a remarkably good loss prediction considering its relative simplicity and the extent of the assumptions made in its derivation. This seems to verify, at least partially, that the assumptions were reasonable.

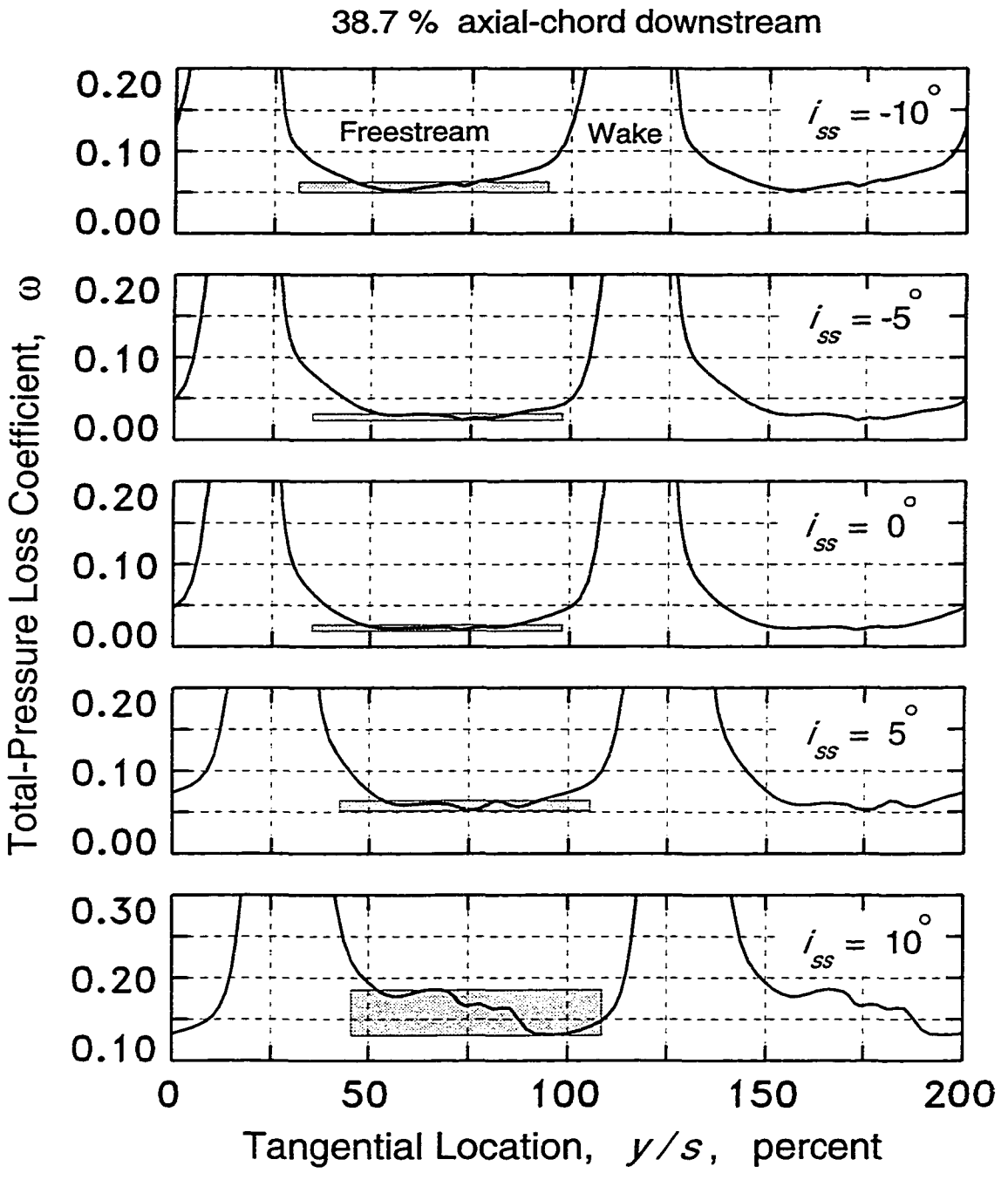

Figure E.20 CFD blade-to-blade total-pressure loss distributions at several incidence angles for the supersonic throughflow cascade with inflow Mach number 2.36 (wake regions clipped at top of each graph)

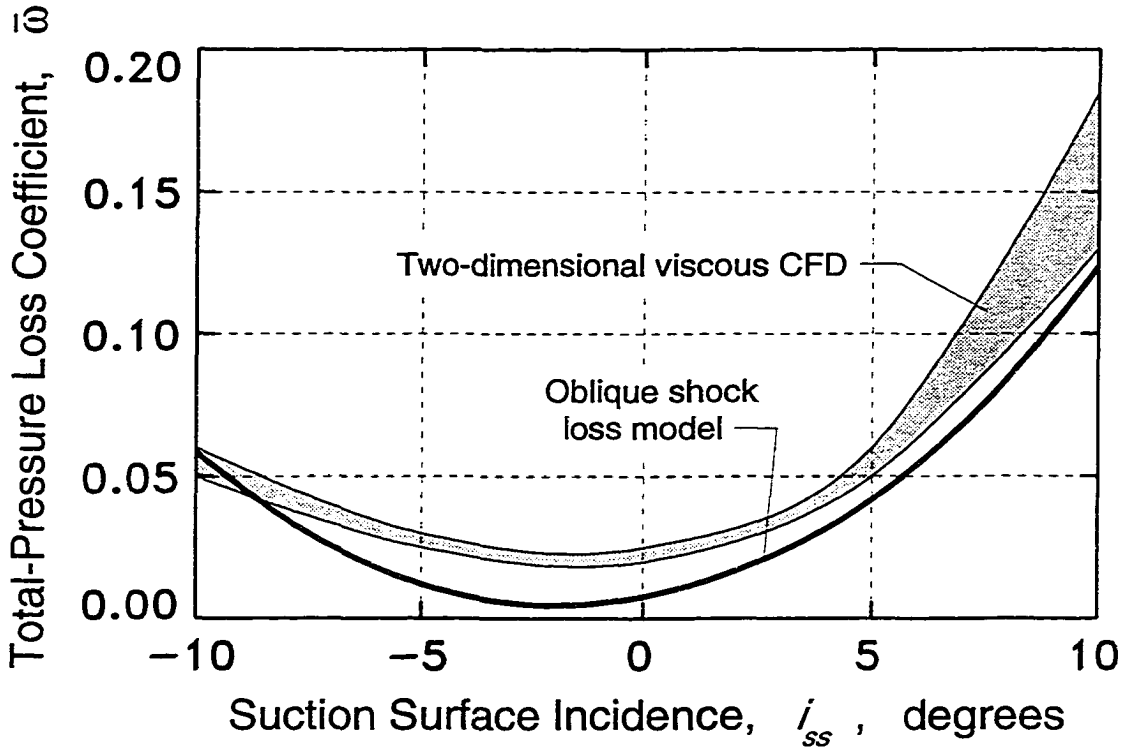

Figure E.21 Comparison of CFD and modeled oblique shock total-pressure losses for the supersonic throughflow cascade with inflow Mach number 2.36